Origin, emplacement and tectonic relevance of the Mt. Kinabalu granitic pluton of Sabah, Borneo

BURTON-JOHNSON, ALEXANDER

Origin, emplacement and tectonic relevance of the Mt. Kinabalu granitic pluton of Sabah, Borneo

A thesis submitted for the degree of Doctor of Philosophy

by

Alex Burton-Johnson

Department of Earth Sciences

Durham University

2013

“Kinabalu’s granite is beautiful rock”

Sir David Attenborough, 1975

Declaration

No part of this thesis has previously been submitted for a degree at this or any other University. The work described in this thesis is entirely that of the author, except where reference is made to previously published or unpublished work.

Alex Burton-Johnson, 2013

Abstract

The generation of granitic melts, their evolution and emplacement in the crust are investigated here through a detailed multi-disciplinary study on the geology of the Mt Kinabalu pluton in the Malaysian state of Sabah, North Borneo. Implications of our findings for the tectonic history of SE Asia and the generation of continental crust are also discussed.

New field data, geochemical analyses and gravity interpretations conclude that the ophiolitic basement of Sabah is not underlain by felsic crust. The ophiolite's geochemistry and existing geochronological data support initial ophiolite emplacement at approximately 200 Ma during early Pacific subduction.

A new geological map and field observations on Mt Kinabalu show construction in a laccolith style but with complex three-dimensional forms of its composite units.

AMS and structural data indicate emplacement during regional NW-SE extension.

Geochemical data disputes an anatectic origin. The magma of Mt Kinabalu was produced by crystallisation of hornblende and plagioclase rich cumulates from an enriched basaltic primary melt with simultaneous assimilation of biotite-rich meta-sediments. The primary melt was derived by low degree melting of a fertile mantle source, probably through extensional melting. Similar melts have occurred across South China and the South China Sea region since at least the Jurassic.

Implications of the results for the generation of continental crust show both the upper and lower crust to be derived through variable degrees of fractional crystallisation from mantle melts, not through intra-crustal differentiation.

Acknowledgements

Within these pages are the work and conclusions from what has to have been both the most enjoyable and challenging piece of work that I have ever done. Mt Kinabalu is a truly inspirational big lump of rock, and this project has been an amazing opportunity to try and tell its story.

There are many people I wish to thank for the last four years. First and foremost I thank my supervisor, Colin Macpherson for giving me this opportunity, all his support during the project and for teaching me a lot about the scientific method. I would like to thank Robert Hall for his helpful discussions and all his support for the project and Carl Stevenson for kindly supporting my AMS work, as well as Mike Cottam for his assistance with the project. I would also like to thank Andrew Cullen for his discussions and the opportunity to work on the Usun Apau samples.

My fieldwork in Borneo was the most incredible experience, and I would like to thank everyone in Sabah who assisted me. I would particularly like to thank Alim Biun, Felix Tongkul, Alijen "Jen", Halli, Jasirin, Sokaibin, Maklarin Lakim, Sapinus, Samuel, Nicholas and the D'Villa Lodge as well as Antony van der Ent. Oh, and Osprey rucksacks for making incredibly tough bags…

There are many people in Durham I wish to thank, particularly Chris Otley and Geoff Nowell for all their support and advice in the labs, and the many people with whom I've discussed my work and from whom I've learnt a lot about the complex avenues of geology. I would particularly like to thank Scott Dempsey, Pierre Bouilhol, Ken McCaffrey, Clayton Grove, Tim Watton, Ian McNeill, Pete Tollan, Kevin Burton, Neill Goulty, Jing Zhang, Hui Huang, Vali Memeti and everyone involved in "Volcanology Coffee". I would also like to thank Nic Odling and Adrian Boyce for their assistance with my major element and oxygen analyses.

I would like to thank all my mates up here in Durham for providing me with such an enjoyable four years and keeping me stocked up on free food! In addition to those already mentioned I would like to thank Baker, Damby, Harriet, Natters, Kris, Sam, Ben, Ben, Viv, Amy, Suzy, Iona, Helen, Helen, Mark, Peace, Jordan, Jack, Jess, Claire, Kathy, Iza, Lawley, Bob, Paul, Pete, Cat, Leo, Ian , Bansri, Sian, Stefan, Andy, Alice, Amelie, all the guys from the Cheese Society and Caving Club and Tom and Cassie for being the best landlords ever while I was working in Brum. Just don't expect me to buy you all a beer!

But above all I would like to thank my family for all of their love and support, even though I choose to spend my time playing with rocks!

Chapter Contents

Chapter 1:.....1

Chapter 1: Introduction and Thesis Outline.....2

Chapter 2:.....7

Chapter 2. Nature of the Basement of Borneo and the Initiation of Western Pacific Subduction: Evidence from the Sabah Ophiolite and Segama Valley Felsic Intrusions.....8

Abstract.....8

Introduction.....9

Regional Geological History and Previous Studies.....12

Field data and petrography.....13

Ophiolite in the Segama Valley.....13

The Segama Valley Felsic Intrusives.....13

The S. Purut Intrusion.....15

S. Danum Intrusion.....15

The Litog Klikog Kiri (S. LKK) Intrusion.....16

Ophiolite surrounding Mt Kinabalu.....17

Analytical methodology.....17

Results.....19

Major Elements and Classification.....19

Trace elements.....20

Radiogenic Isotopes.....22

Discussion.....23

The Felsic Intrusions.....23

Mafic Samples.....24

Implications for the age of the Sabah ophiolite.....27

Is there a continental basement under Sabah?.....31

Conclusions.....35

Chapter 3:.....41

Chapter 3: The complex structure and emplacement of composite granitic plutons:

Field evidence from Mt Kinabalu, Borneo 42

Abstract.....42

Introduction 43

Regional Geological History and Tectonic Setting 45

Previous Studies on Mt Kinabalu 48

Geology 51

Country rocks 52

Ophiolitic Basement.....52

Crocker Formation 54

The Granitic Units 54

Dykes.....63

Satellite Intrusions 64

Enclaves and xenoliths.....64

Contacts 65

External Contacts 65

Internal Contacts.....66

Structures.....70

Country rocks 70

Granite 71

Discussion.....73

Emplacement depth.....73

Contact metamorphic conditions 74

Internal structure of the pluton and Emplacement Mechanism 75

Stress field during emplacement 79

Conclusions 81

Chapter 4:.....86

Chapter 4: Anisotropy of Magnetic Susceptibility of the Mt Kinabalu Pluton, Borneo:

Constraining the stress field during granitic emplacement.....87

Abstract.....87

Introduction 88

Structure of the Mt Kinabalu pluton 89
Methodology 92
Results 93
AMS ellipsoid 93
Mineralogical source of the AMS fabric 96
AMS fabrics of the composite units 100
Discussion 102
Implications 105
Conclusions 107

Chapter 5: 110

Chapter 5: Sourcing granitic melts from basalt fractionation, development of isotopic disequilibrium and the problems with crustal anatexis: Evidence from Mt Kinabalu, Borneo
..... 111
Abstract 111
Introduction 113
Regional Geological History and Tectonic Setting 115
Field relations, emplacement and previous work 118
Methodology 120
Results 122
Major and trace elements 122
Radiogenic Isotopes 127
Oxygen Isotopes 130
Country rocks 131
Alteration 132
Discussion 134
Crustal anatexis 134
Modelling anatexis of felsic crust and isotopic disequilibrium 135
Other sources of anatectic melting 140
Basaltic fractionation 143
Modelling basalt fractionation and assimilation 144
Major element modelling 144
Results 152

Primary magma 152
Assimilant 153
Fractionating assemblages 155
Further constraints on the assimilant 157
Discussion and Implications of the Model 159
The formation of Mt Kinabalu 159
Global implications for granitic magmatism and formation of the continental crust 164
Conclusions 174
Supplementary A – Modelling the evolution of isotopic heterogeneities and disequilibrium partial melting 185
Supplementary B – Modelling major element fractionation 188

Chapter 6 - Regional Synopsis: 195
Chapter 6: Regional Synopsis: Magmatism in SE Asia: An Extended History 196
Abstract 196
Introduction 198
The Capoas Granite of Palawan 199
Methodology 200
Results 201
Discussion 205
Regional signature 213
Conclusions 216

Chapter 7: 222
Chapter 5: Conclusions 223
1. What processes produced the felsic magma of Mt Kinabalu? 223
2. How was this magma emplaced in the crust? 224
3. What implications do these findings have for the generation and emplacement of granitic melts globally? 224
4. What implications do they have for the generation of continental crust? 225
5. What can we learn from this study about the regional geology and tectonic history of Borneo and SE Asia? 226
Future Work 228

Figure Contents

Chapter 2

Fig. 2.1. Simplified geological map of Sabah 10

Fig. 2.2. Regional map of magmatism in the SE Asia and South China Sea region 11

Fig. 2.3. Regional map of the Segama Highlands, Sabah 14

Fig. 2.4. IUGS QAP classifications of the Segama ophiolite felsic intrusions 14

Fig. 2.5. Danum Gorge contact photo 16

Fig. 2.6. Major element classification diagrams for the Segama ophiolite and S. Mansahaban ophiolite samples 19

Fig. 2.7. Normalised multi-element plots for the Sabah ophiolite samples 21

Fig. 2.8. Radiogenic isotope plots of the Segama Highlands cal-alkaline intrusives and regional magmatism 22

Fig. 2.9. Subduction initiation illustration 26

Fig 2.10. Comparison of determined ages of the Sabah Ophiolite with ages of Mesozoic magmatism in SE Asia and South China 27

Fig. 2.11. Proposed line of the Mesozoic Pacific forearc and subduction zone 30

Fig 2.12. Bouguer anomaly gravity map of Sabah 31

Fig. 2.13. Stratigraphic columns illustrating the crustal structure used in the gravity models 34

Chapter 3

Fig. 3.1. Regional map of Borneo, Palawan and the South China Sea 44

Fig. 3.2 Simplified geological map of Sabah 46

Fig. 3.3. Miocene tectonic illustrations of the proposed models for the opening of the South China Sea 47

Fig. 3.4. Geological map of the region around Mt Kinabalu 49

Fig. 3.5. Geological Map of Mt Kinabalu 50

Fig. 3.6. New geological map overlain on DEM of the mountain 51

Fig. 3.7. Summit map of the Western and Eastern plateaus of Mt Kinabalu 52

Fig. 3.8. Classification diagrams of the Mt Kinabalu granitoids 56

Fig. 3.9. Selected field photos from Mt Kinabalu 61

Fig. 3.10. Rose diagrams of strike measurements for faults from the sedimentary country rocks around Mt Kinabalu from Jacobson 71

Fig. 3.11. Rose diagrams of strike measurements for faults and dykes on Mt Kinabalu 72

Fig. 3.12. Interpreted geological cross-sections of the mountain 75

Fig. 3.13. Exploded view illustration of the pre-erosional structure of the Mt Kinabalu pluton 76
Fig. 3.14. Simplified illustration of emplacement mechanism 78

Chapter 4

Fig. 4.1. Illustration of the relationship between the stress field and the strain ellipse 89
Fig. 4.2. Geological map of Mt Kinabalu showing transects taken during mapping and sample sites for AMS analyses 91
Fig. 4.3. Illustrations of the shape ellipsoids used to describe the magnetic fabrics 95
Fig. 4.4. Plots of the degree of magnetic anisotropy (*P'*) against K_{mean} 95
Fig. 4.5. Mapped Anisotropy of Magnetic Susceptibility (AMS) fabrics 97
Fig. 4.6. Stereographic projections of the mean K_1 and K_3 values measured 100
Fig. 4.7. Rose diagrams of strikes to the measured planes of faults and dykes from Mt Kinabalu with interpreted principal stress directions 103
Fig. 4.8. K_1 and K_3 values for all units excluding excluding contact orientated samples and interpreted principal stress directions (σ_1 and σ_3) 106

Chapter 5

Fig. 5.1. Regional map of Borneo, Palawan and the South China Sea 114
Fig. 5.2 Simplified geological map of Sabah 116
Fig. 5.3. Miocene tectonic illustrations of the proposed models for the opening of the South China Sea 117
Fig. 5.4. Aerial photograph looking and 3D geological map of Mt Kinabalu showing units and emplacement ages 119
Fig. 5.5. (a) TAS and (b) IUGS classifications of the Mt Kinabalu granitic units 123
Fig. 5.6. Selected major element vs SiO_2 for the Mt Kinabalu granitic units 124
Fig. 5.7. Selected trace elements element vs SiO_2 for the Mt Kinabalu granitic units 125
Fig. 5.8. Multi-element, primitive mantle normalised trace element plots and chondrite normalised REE plots for the Mt Kinabalu granitic units 126
Fig. 5.9. Initial isotope values and respective trace element concentrations for the Mt Kinabalu units. 128
Fig. 5.10. Isotopic values at t = 7.5Ma for Mt Kinabalu, and regional lithologies for comparison 129
Fig. 5.11. δ-δ plot for quartz and hornblende 131
Fig. 5.12. Experimentally determined phase disappearance and appearance during dehydration partial melting of a tonalite at 10kbar 137
Fig. 5.13. Isotopic disequilibrium models 138
Fig. 5.14. Comparison of Mt Kinabalu with collated melting experiment data 142

Fig. 5.15. Frequency chart of Al in hornblende pressure estimates 146

Fig. 5.16. Selected variation diagrams comparing the Mt Kinabalu data with the combined major, trace and isotope AFC models 148

Fig. 5.17. Multi-element trace and REE plots comparing the Mt Kinabalu fractionation models 150

Fig. 5.18. Images of the conglomerate xenolith, A098, from Mt Kinabalu 153

Fig. 5.19. FMM normalised plot showing the composition of the average lower continental crust (LCC) and the 99% confidence intervals (CI) of Neogene volcanics 163

Fig. 5.20. Multi-element trace and REE plots, comparing the estimated average composition of the lower continental crust with compositions of the bulk cumulate assemblages and the Linau Balui basalt 166

Fig. 5.21. Schematic diagram illustrating our proposed model for continental arc magmatism and generation of the continental crust 167

Fig. 5.22. Selected variation diagrams showing modelling of the generation of the average upper continental crust (UCC) through fractional crystallisation of the average lower continental crust (LCC) without assimilation 169

Fig. 5.23. Multi-element trace and REE plots, comparing the LCC to UCC fractionation models 170

Fig. 5.24. Global dataset for granites, granodiorites, diorites and tonalites 173

Chapter 6

Fig. 6.1 Location and geological maps of the granitic bodies of the Capoas intrusion, Palawan 200

Fig. 6.2. TAS and QAP classifications of the Capoas Gt 202

Fig. 6.3. Multi-element, primitive mantle normalised trace element plots and chondrite normalised REE plots for the Capoas Granite 203

Fig. 6.4. Isotopic values (t = 7.5Ma, the age of Mt Kinabalu's emplacement) for the Capoas Gt, Usun Apau, Mt Kinabalu and regional lithologies for comparison 204

Fig. 6.5. Comparison of the Capoas Gt and Usun Apau data with the Mt Kinabalu granitoids and collated melting experiment data 206

Fig. 6.6. Selected variation diagrams comparing the measured major element data with the combined major, trace and isotope AFC models for the Capoas Gt and Usun Apau dacites 211

Fig. 6.7. Multi-element trace and REE plots comparing the Capoas Gt and Usun Apau dacite fractionation models 212

Fig. 6.8. Distribution, magmatic ages and trace element chemistry of mafic magmatism in the South China Sea region since the Jurassic 215

Table and Appendix Contents

Chapter 3

Table 3.1. Summary of ages, volumes and mineralogies of the major granitic units 60

Chapter 5

Table 5.1. Summary of fractionating assemblages and parameters used in the fractionation models. 151
Table 5.2. Results of the models discussed with target compositions, both normalised to 100%, and sum of the differences squared for each major element oxide for comparison 152
Table 5.3. Calculations used for major element modelling 194

Chapter 6

Table 6.1. Modal mineral proportions from point counting of stained thin sections of the Capoas Gt 202
Table 6.1. Summary of fractionating assemblages and parameters used in the fractionation models for the Capoas Gt and Usun Apau dacites 209
Table 6.2. Results of the major element models discussed with target compositions 210

Appendices

Appendix A1: Major and trace element QC data

A1.1. Major element standards for QC 230

A1.2. QC data for trace element analysis, including standards, blanks and repeated samples for both standard dissolution sample preparation and by flux fusion prior to acid dissolution 231
A1.2.1a. QC data from standards prepared for ICP-MS analysis by flux fusion prior to HF and HNO3 acid dissolution 231
A1.2.1b. QC data on blanks, fusion blanks and fused repeat samples from the flux fusion procedure of sample preparation 232
A1.2.1c. QC data from standards prepared for ICP-MS analysis by the standard HF and HNO3 acid dissolution procedure without prior flux fusion 233
A1.2.1d. QC data on blanks and repeat samples from the acid dissolution procedure without prior flux fusion of the samples 234
Appendix A2: Whole rock elemental and isotopic data for the Sabah ophiolite samples from the Segama Valley and Mt Kinabalu area
A2.1.a. Major and trace elements for the Segama Valley felsic intrusions 235

A2.1.b. Major and trace elements for the Segama Valley ophiolite 236

A2.1.c. Major and trace elements for ophiolite samples from S. Mansahaban and Mt Kinabalu 237
A2.2. Isotopic data from the ophiolite samples of the Segama Valley, Mt Kinabalu and S. Mansahaban 238
Appendix A3: AMS results and calculated parameters
A3.1. AMS data, 95% confidence ranges and shape parameters 239
Appendix A4: Geochemical data from Mt Kinabalu
A4.1. Whole rock Major and trace element data from Mt Kinabalu 242
A4.2. Mineral separate trace element data collected from crushed and handpicked minerals prepared by the standard acid dissolution procedure prior to ICP-MS analysis 252
A4.3. Radiogenic isotope data from Mt Kinabalu 254
A4.4. Oxygen isotope values for different phases from of Mt Kinabalu 255
A4.5. Mineral separate ion microprobe data on selected phases of the Mt Kinabalu granite. 256
A4.6.a Kd values used to model melt at <63wt% SiO2 259
A4.6.b. Kd values used to model melt at >63wt% SiO2 260
Appendix A5: Whole rock geochemical data from The Capoas Granite
A5.1. Whole rock major and trace element compositions of the Capoas Granite, Palawan 261
A5.2. Whole rock radiogenic isotope data from the Capoas Granite of Palawan 262
Appendix A6: 263
Cullen, A., Macpherson, C., Taib, N.I., Burton-Johnson, A., Geist, D., Spell, T. and Banda, R.M. (2013). Age and Petrology of the Usun Apau and Linau Balui Volcanics: Windows to Central Borneo's Interior. *Journal of Asian Earth Sciences*

Chapter 1:

Introduction and Thesis Outline

Aerial photograph of Mt Kinabalu, looking NE
(courtesy of Dr Tony Barber, SEARG)

Chapter 1: Introduction and Thesis Outline

The 4095m peak of Mt Kinabalu in the Malaysian state of Sabah in northern Borneo is the highest mountain between the Himalayas and Papua New Guinea. Its prominence in the region, standing 1.5km higher than any of its surrounding peaks, has made it an internationally famous landmark and a national symbol. The range of elevations and microclimates present on the mountain from lowland primary rainforest at its base to high altitude montane and sub-alpine vegetation on its upper flanks and summit plateau (Van Steenis, 1964) and its range of soil types, most notably those developed on ultramafic bedrock, has resulted in the most biodiverse place in the world in terms of species per unit area (van der Ent, 2011). However, despite its fame, prominence and ecological importance the origin of the granitic pluton from which it is formed is still unknown.

The aim of this study is to constrain the processes involved in the generation of the magma from which the Mt Kinabalu pluton developed, how this magma evolved and how it was emplaced in the upper crust. We will test the plausibility of different mechanisms for generating granitic melts, discuss implications for these processes in developing continental crust and will investigate how our results affect interpretations of the tectonic history of SE Asia.

The principal questions to be answered are:

1. What processes produced the felsic magma of Mt Kinabalu?
2. How was this magma emplaced in the crust?
3. What implications do these findings have for the generation and emplacement of granitic melts globally?
4. What implications do they have for the generation of continental crust?
5. What can we learn from this study about the regional geology and tectonic history of Borneo and SE Asia?

Each chapter will discuss the following:

- **Chapter 2:**

  Nature of the Basement of Borneo and the Initiation of Western Pacific Subduction: Evidence from the Sabah Ophiolite and Segama Valley Felsic Intrusions

  Before any interpretation can be made on the generation of Mt Kinabalu's granitic melts it is first necessary to constrain the basement lithologies underlying the region as these have implications for both potential sources and contaminants.

  An ophiolitic basement underlies much of Sabah including around Mt Kinabalu. However, based on field evidence, geochemistry and regional gravity anomalies previous studies have suggested that older felsic continental crust underlies the ophiolite (e.g. Leong, 1974, Milsom *et al.*, 2001, Macpherson *et al.*, 2010). To investigate this fresh field observations and geochemical analyses are made of felsic intrusions within the Segama Valley ophiolite of eastern Sabah, previously interpreted as either partial melts or windows of this underlying crust, and gravity data from Borneo is reinterpreted.

  In addition, geochemical and geochronological data on the Sabah ophiolite and associated regions are discussed to determine their tectonic implications for Pacific subduction.

- **Chapter 3:**

  The complex structure and emplacement of composite granitic plutons: Field evidence from Mt Kinabalu, Borneo

  Over the last decades our understanding of the emplacement of granitic plutons has moved from slowly ascending diapirs to rapid dyke fed ascent and laccolith-style emplacement of plutons from multiple composite units (e.g. Petford *et al.*, 2000, Cruden and McCaffrey, 2001). The 2900m vertical range of granitic exposure at Mt Kinabalu and the complete exposure on its glaciated summit provide an opportunity to investigate how composite

granitic plutons are constructed in three dimensions. Consequently, this chapter presents new field observations and the first geological map of the mountain since Jacobson (1970). The pluton and its country rocks are re-mapped, their contacts and field relations assessed and structural evidence for the tectonic stresses present during emplacement are discussed.

- **Chapter 4:**

  Anisotropy of Magnetic Susceptibility of the Mt Kinabalu Pluton, Borneo: Constraining the stress field during granitic emplacement

  The mineral fabric of granitic plutons can provide details on the stress field acting on the magma during crystallisation. The origin of this stress field is a combination of magmatic stress from the ascending magma column and regional tectonic stresses (Paterson *et al.*, 1998). Which of these stresses the mineral fabric records depends on their relative dominance and can change between plutons and within the same intrusion.

  Although mineral fabrics were mapped from some outcrops on the mountain most units do not display a visible common orientation. However, the anisotropy of magnetic susceptibility (AMS) of an outcrop allows us to determine the fabric of its magnetic mineral phases even when they cannot be observed visually. In this chapter AMS analysis is carried out on samples from Mt Kinabalu, the fabric is mapped across the mountain and the origin of the stress field producing it determined.

- **Chapter 5:**

  Sourcing granitic melts from basalt fractionation, development of isotopic disequilibrium and the problems with crustal anatexis: Evidence from Mt Kinabalu, Borneo

  Despite over 200 years of research (e.g. Hutton, 1788, Pitcher, 1997) the processes involved in the generation of granitic melts and their contribution to the generation of continental crust remain a subject of discussion. Geochemical data on Mt Kinabalu collected during this study is presented

and discussed in this chapter including major elements, trace elements and radiogenic and stable isotope data. Different processes proposed for the generation of granitic melts are tested for their viability in producing the chemical signatures of Mt Kinabalu's composite units. The relevance and implications of the processes involved in generating the Mt Kinabalu pluton are then discussed with relation to the generation of the continental crust and granitic intrusions globally.

- **Chapter 6 – Regional Synopsis:**

  Magmatism in SE Asia: An Extended History

  Having discussed the processes involved in generating and emplacing the Mt Kinabalu pluton this chapter puts these findings in their regional tectonic context to investigate how widespread they are in SE Asia and South China and for how long they have persisted. The genesis of other examples of felsic magmatism along the southern margin of the South China Sea (the Capoas Granite of Palawan and the Usun Apau Dacites of Sarawak, NW Borneo) and evidence for regional magmatism since at least the Jurassic is discussed and new data presented.

- Finally, the principal findings of each chapter are collated in **Chapter 7: Conclusions**.

Cruden, A. and McCaffrey, K. (2001). Growth of plutons by floor subsidence: implications for rates of emplacement, intrusion spacing and melt-extraction mechanisms. *Physics and Chemistry of the Earth, Part A: Solid Earth and Geodesy*. **26**, 4, 303-315.

Hutton, J. (1788). Theory of the Earth; or an Investigation of the Laws observable in the Composition, Dissolution, and Restoration of Land upon the Globe. *Transactions of the Royal Society of Edinburgh*.

Jacobson, G. (1970). *Gunung Kinabalu area, Sabah, Malaysia*. Sabah, Geological Survey of Malaysia.

Leong, K. (1974). *The geology and mineral resources of the Upper Segama Valley and Darvel Bay area, Sabah, Malaysia*. US Government Printing Office.

Macpherson, C.G., Chiang, K.K., Hall, R., Nowell, G.M., Castillo, P.R. and Thirlwall, M.F. (2010). Plio-Pleistocene intra-plate magmatism from the southern Sulu Arc, Semporna peninsula, Sabah, Borneo: Implications for high-Nb basalt in subduction zones. *Journal of Volcanology and Geothermal Research*. **190**, 1-2, 25-38.

Milsom, J., Holt, R., Hutchison, C.S., Bergman, S.C., Swauger, D.A. and Graves, J.E. (2001). Discussion of a Miocene collisional belt in north Borneo: uplift mechanism and isostatic adjustment quantified by thermochronology: Journal, Vol. 157, 2000, 783-793. *Journal of the Geological Society*. **158**, 2, 396-400.

Paterson, S.R., Fowler Jr, T.K., Schmidt, K.L., Yoshinobu, A.S., Yuan, E. and Miller, R.B. (1998). Interpreting magmatic fabric patterns in plutons. *Lithos*. **44**, 1, 53-82.

Petford, N., Cruden, A.R., McCaffrey, K.J.W. and Vigneresse, J.L. (2000). Granite magma formation, transport and emplacement in the Earth's crust. *Nature*. **408**, 6813, 669-673.

Pitcher, W.S. (1997). *The nature and origin of granite*. Springer.

van der Ent, A. (2011). Ecology of ultramafic outcrops at Mount Kinabalu, Sabah, Malaysia. *International Conference on Serpentine Ecology (7th, ICSE, 2011)*. 81-81.

Van Steenis, C. (1964). Plant geography of the mountain flora of Mt Kinabalu. *Proceedings of the Royal Society of London. Series B, Biological Sciences*. 7-38.

Chapter 2:

Nature of the Borneo Basement and the Initiation of Western Pacific Subduction: Evidence from the Sabah Ophiolite and Segama Valley Felsic Intrusions

S. Danum, Segama Valley

Chapter 2. Nature of the Basement of Borneo and the Initiation of Western Pacific Subduction: Evidence from the Sabah Ophiolite and Segama Valley Felsic Intrusions

Abstract

The nature of the basement in Sabah, Malaysian Borneo, has been disputed on the grounds of field evidence, geochemistry and regional gravity anomalies. To investigate this, fresh field observations were made of Late Jurassic intrusions in the Segama Valley outcrops, previously interpreted as partial melts or windows of an unexposed old continental crust underlying Sabah's ophiolitic basement. These were found to be tonalite intrusions into the ophiolite suite. Geochemical analysis of their trace, REE and radiogenic isotopes shows them to be arc-like mantle melts of a subduction zone enriched mantle source, disputing the evidence for an underlying continental crust. Likewise, modelling of airborne gravity data for Sabah shows that the regional gravity lows invoked to represent this low density crust can be explained by a combination of the overlying sedimentary basins and asthenospheric upwelling, both associated with continuing regional extension.

The ophiolite was emplaced during the early stages of subduction in a forearc setting, with initial rifting resulting in MORB type magmatism followed by arc magmatism once subduction had developed and enriched the mantle wedge. A wide range of ages exist for the ophiolite, from 210 Ma into the Cenozoic, but the old ages and arc-like elemental signature of the felsic intrusions imply that when the earlier intrusions of this range were emplaced the arc was already developed and that arc magmatism continued within the ophiolite throughout the duration of Pacific subduction in the region. This supports initiation of the western Pacific subduction beneath SE Asia and SE China (during which the ophiolite was emplaced) at approximately 200 Ma, in agreement with ophiolite and arc granitoid ages from Kalimantan. This also implies that although a period of magmatic quiescence exists in SE China between 205 and 180 Ma during the transition from Tethyan to Pacific / Panthalassa subduction related magmatism there was no such quiescence along the subduction zone, with Tethyan subduction leading directly to the initiation of Pacific subduction.

Introduction

Before interpretations can be made on the Cenozoic magmatism of Borneo, including that of Mt Kinabalu, it is first important to constrain the composition of the region's basement lithologies. The nature of the basement of the Malaysian state of Sabah, north Borneo has been discussed numerous times in the literature (Leong, 1974, Leong, 1998, Graves *et al.*, 2000, Milsom *et al.*, 2001, Hutchison, 2005). The exposed geology is predominantly of Cenozoic marine sediments underlain by an ophiolite sequence exposed in the Segama Valley, Darvel Bay, Telupid and Kudat (Fig. 2.1). However it has been suggested on multiple occasions that the region is underlain by unexposed, granitic continental crust, similar to the granitic crust forming the Schwaner Mountains of Kalimantan, SW Borneo.

This interpretation is based on three lines of evidence: (1) Gravity data (Holt, 1998, Milsom *et al.*, 2001) shows an extensive low gravity anomaly over much of Sabah interpreted to result from low density continental crust beneath the region. (2) Plio-Pleistocene volcanics of the Semporna peninsula in E Sabah and the Usun Apau plateau of Sarawak, NW Borneo have anomalously low Nd isotopic values (Macpherson *et al.*, 2010, Cullen *et al.*, 2013) interpreted to be inherited through assimilation of Proterozoic continental crust by mantle melts. And (3), Leong (1974) and Kirk (1968) recorded the presence of calc-alkaline granitic bodies within the ophiolite of the Segama Valley. These intrusive bodies were deemed too potassic to be mantle derived and so it was postulated that they were partial melts of an underlying continental basement intruded into the ophiolite (Hutchison, 2005).

These intrusive bodies have not been revisited since those early publications and so this work presents the first new data on them including reinvestigation of their field relations, major and trace element and isotopic chemistry, plus a reinterpretation of the nature of the basement of Sabah based on this data and gravity data.

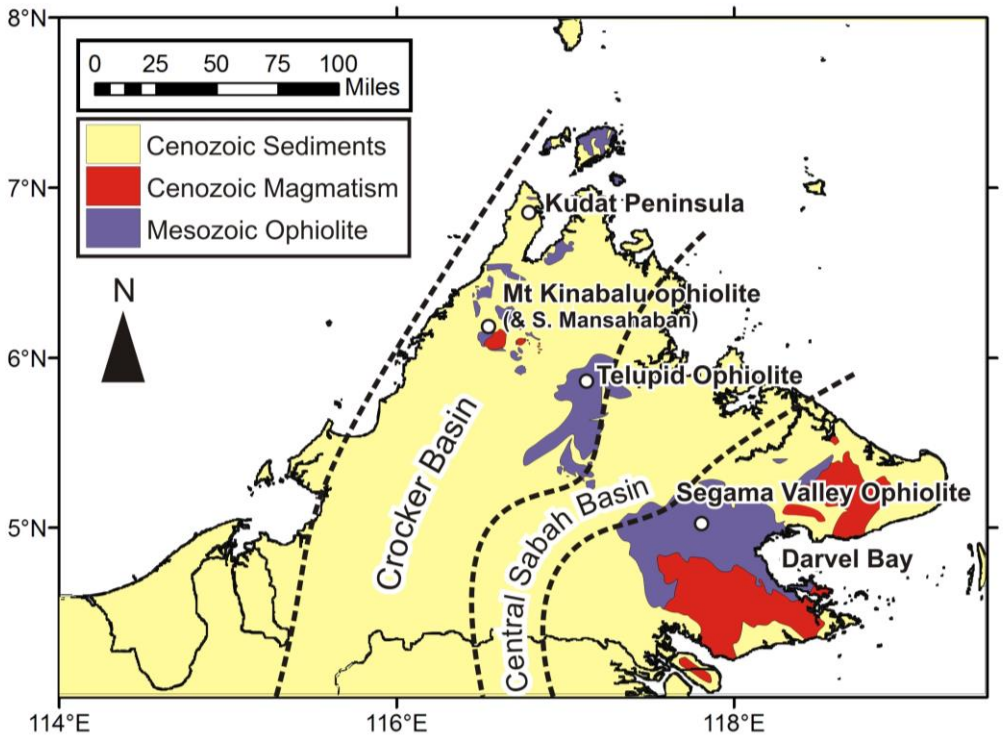

Fig. 2.1. Simplified geological map of Sabah, showing the distribution of Mesozoic ophiolite outcrops, Cenozoic magmatism and sediments (Kirk, 1968, Hutchison, 2005), and the localities discussed in the text.

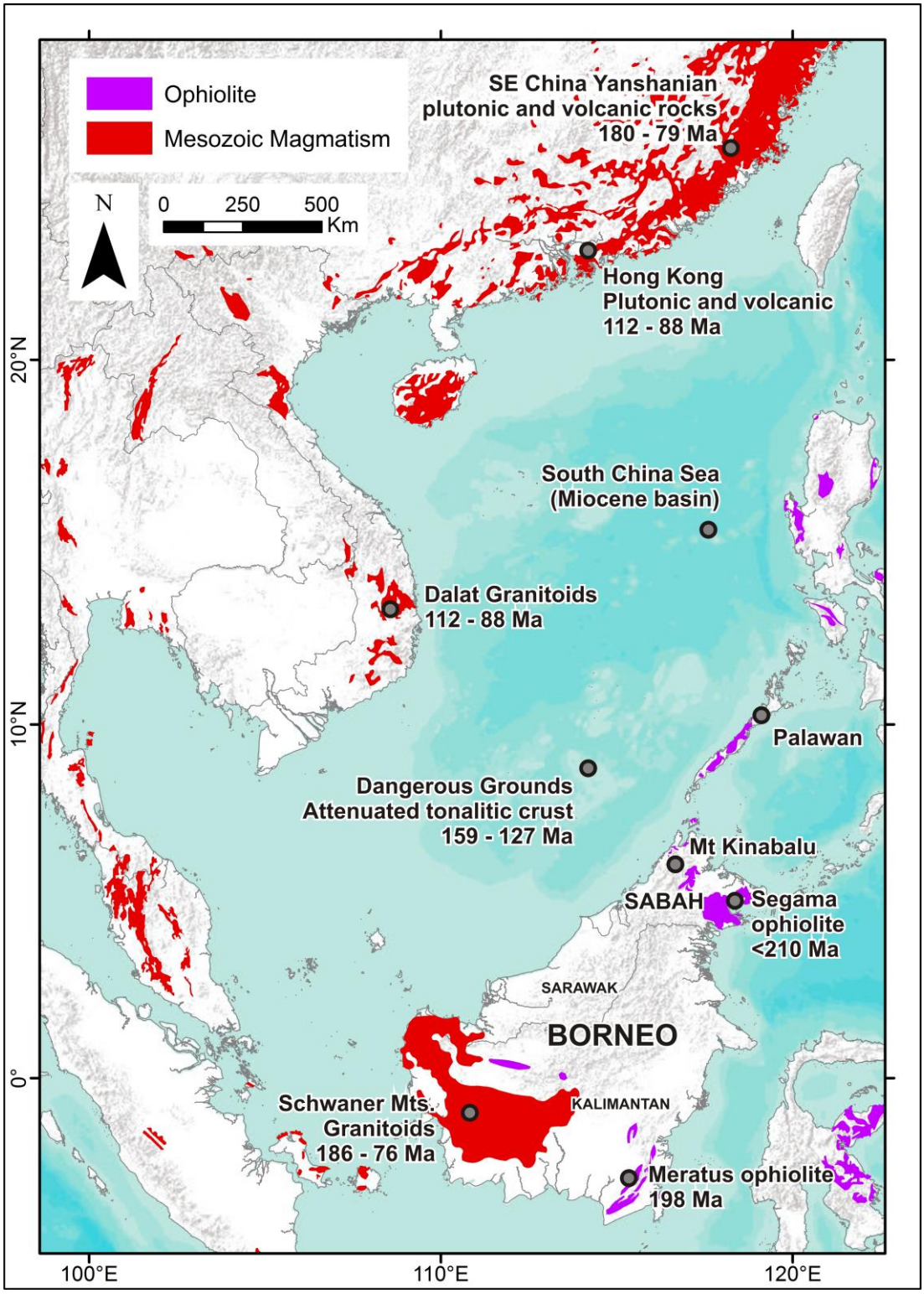

Fig. 2.2. Regional map of SE Asia and the South China Sea region, showing localities discussed in the text. Also shown are the loactions of mesozoic volcanic and plutonic magmatism and ophiolitic crust, along with age data discussed in the text (Kirk, 1968, Leong, 1974, Hutchison, 1975, Davis *et al.*, 1997, Steinshouer *et al.*, 1997, Moss, 1998, Parkinson *et al.*, 1998, Wakita *et al.*, 1998, Encarnación, 2004, Nguyen *et al.*, 2004, Zhou *et al.*, 2006, Yan *et al.*, 2010, Coggon *et al.*, 2011, Davies *et al.*, 2012, Suggate *et al.*, 2013). Basemap data from the ESRI ArcGIS® software (Copyright © Esri).

Regional Geological History and Previous Studies

The geological history of Borneo and its relationship to Sundaland and the regional tectonics of SE Asia is a continuing subject of discussion. During the Mesozoic a large destructive margin existed across the whole region from the Yanshanian province of SE China across the now attenuated, continental crust of the South China Sea continental shelf, along Vietnam and Peninsular Malaysia to the Schwaner Mountains of Kalimantan in SW Borneo (Metcalfe, 2011). This marked the location of magmatism derived from subduction of Pacific oceanic crust and produced a belt, hundreds of kilometres wide, of arc granites and lesser volcanics across SE Asia (Fig. 2.2).

As well as development of this continental-type crust, it was during the Mesozoic that the ophiolitic basement of the northern and eastern ends of Borneo were emplaced, including that of Sabah, forming a belt of ophiolitic basement stretching from central Java, across Borneo and into Palawan and the Philippines (Fig. 2.2). Although some studies have proposed a mid-ocean ridge setting for formation of the ophiolite (Graves *et al.*, 2000), LILE and HFSE data has shown this to have been in a supra-subduction zone setting (Omang and Barber, 1996). The age of the ophiolite is unclear and although outcrops in Sabah give K-Ar radiometric ages of 33 to 217 Ma (Hutchison, 2005) clearly not all of these ages can be correct. Due to the susceptibility of K to fluid alteration some dates may have been reset. Subsequently, Hutchison (2005) neglects ages younger than 127 Ma as they post-date the 127-135 Ma radiolarian age of the overlying cherts (Basir, 1992), although magmatic activity may have persisted. Whether this ophiolite was emplaced on top of older continental crust will be discussed below.

The region ceased to be an active arc in the Late Cretaceous when the Pacific subduction zone migrated east. Subsequently, Borneo became the location of extensive marine sedimentation through the Tertiary, during which most of its extensive cover of marine mudstones and turbidites were deposited (Fig. 2.1). This deposition is dominated by the Late Cretaceous to Late Eocene Rajang group, a sequence of deep marine turbidite sedimentation into the large SW-NE trending Crocker Basin. Following the Eocene inversion event of the Sarawak Orogeny further turbidite sedimentation formed the Kinabatangan Group. A shallower marine setting during the Miocene

deposited the carbonates and shallow marine to fluvial deltaic deposits of the Serudong Group (Balaguru, 2001).

Field data and petrography

Ophiolite in the Segama Valley

The Segama Valley of Eastern Sabah forms part of the Darvel Bay ophiolite suite. Kirk (1968) and Leong (1974) differentiated the Mesozoic basement of Sabah into a sequence of dolerites, gabbros and variably serpentinised peridotites, an underlying crystalline basement of amphibolites, schists and gneisses, plus the felsic intrusives of this study and the Chert-Spilite Formation of marine sediments and basaltic submarine volcanism. However, current understanding of ophiolite stratigraphy, whereby ophiolites represent oceanic crust emplaced in a submarine spreading centre or marginal basin, commonly in a forearc setting (Pearce, 2003), implies that these are all constituent parts of the ophiolite and represent its variably metamorphosed mafic intrusive crust and associated extrusive magmatism and overlying marine sedimentation. As noted by Hutchison (2005), ribbon cherts represent the first sediments to be deposited on newly emplaced seafloor, explaining the abundance of this lithology in the Chert-Spilite Formation

The Segama Valley Felsic Intrusives

Intrusive bodies up to 5km long of tonalite, granodiorite and granite were are recorded by Leong (1974) as river outcrops within the Segama Valley ophiolite. These outcrops were mapped in Dismal Gorge and the Barrier Falls on S. Segama; S. Purut; Danum Gorge; S. Telewas; and the S. Litog Klikog Kiri and S. Babayas tributaries of S. Segama (Fig. 2.3). For this study, the S. Purut, S. Danum, Barrier Falls and the S. Litog Klikog Kiri/S. Babayas intrusions were visited, although it transpired that the meander mapped as the Barrier Falls intrusion was composed of mudstone and chloritised mafics. Mineral abundances given here were calculated from point counted sections

stained for plagioclase and K- feldspar. QAP modal mineral classifications are shown in Fig. 2.4.

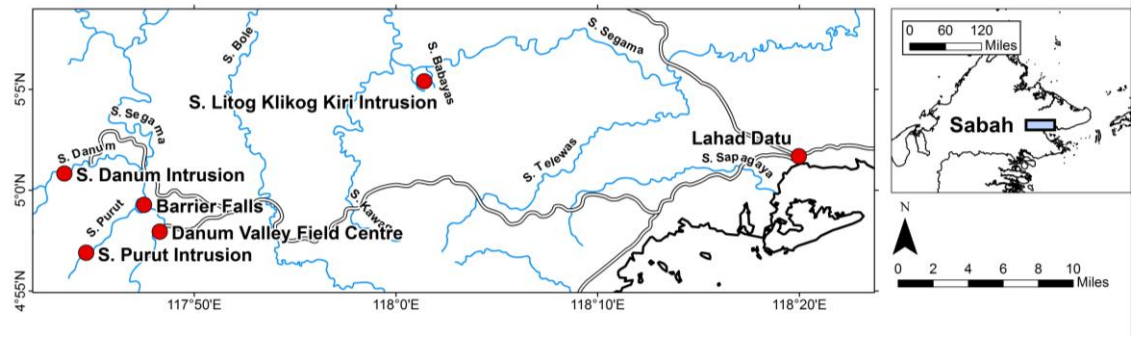

Fig. 2.3. Regional map of the Segama Highlands, Sabah, and the locations of the intrusions discussed in the text.

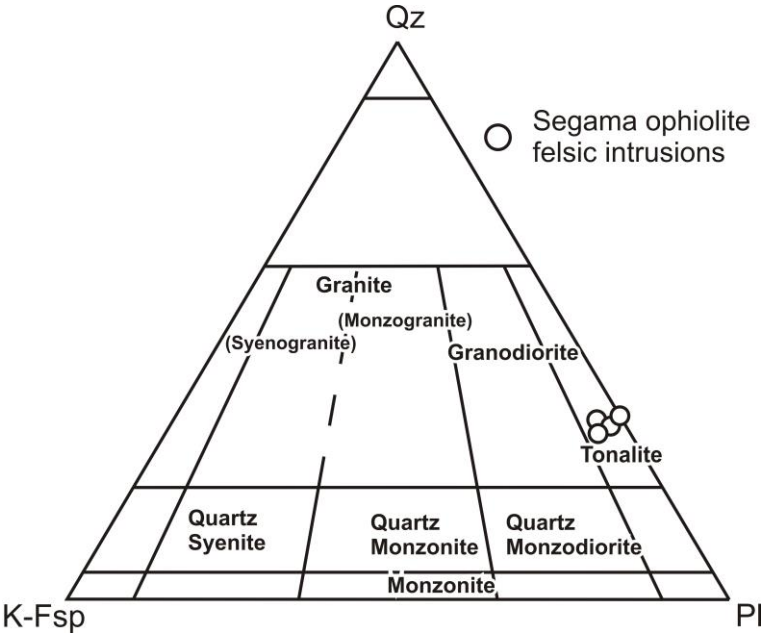

Fig. 2.4. IUGS QAP (Streckeisen, 1976) classifications of the Segama ophiolite felsic intrusions. Point counting based on 300 points per sample.

The S. Purut Intrusion

S. Purut is a tributary of the Upper S. Segama and can be reached from the Danum Valley Field Centre (DVFC). It is a medium grained tonalite composed of 11% quartz, 22% plagioclase and 16% hornblende plus 13% chlorite and 38% sericite, which if derived solely from the plagioclase and hornblende puts their respective percentages at 60% and 29%. The body shows a clear intrusive contact with amygdale-rich basaltic country rocks, which have altered to a highly chloritised hornfels along the contact. This basalt is what is referred to in previous literature as the spilite of the "Chert-Spilite formation" and contains amygdales of chlorite, zeolite and quartz. Therefore the intrusion post-dates the ophiolite. A smaller intrusion similar to the main body but only 100m across is found 700m downstream and has been itself intruded by later mafic dykes.

The S. Danum Intrusion

S. Danum is another tributary of the Upper S. Segama and can be reached from the Borneo Rainforest Lodge. The S. Danum Intrusion forms the walls of the narrow, 800m long Danum Gorge (Fig. 2.5) and is another medium grained tonalite composed of 25% quartz, 56% plagioclase, 5% alkali feldspar and 14% variably chloritised hornblende.

The body has intruded the microcrystalline quartzite forming the country rock and a 5m thick margin of chloritised hornfels exists on its margin with wispy xenoliths of this material within the granite. Further downstream smaller dykes and intrusions 10-40m across intrude the quartzite with magma mingling textures of two dark, fine grained phaneritic lithologies revealing at least two phases of intrusion. The largest of these bodies is located at the contact of the quartzite with the red chert unit that continues to form the outcrops downstream. However, they do not appear in contact with the tonalite and so the relationship of these two magmatic events is unknown.

Fig. 2.5. Downstream end of the Danum Gorge, showing the intrusive contact of the S. Danum tonalite intrusion with the quartzite overlying the mafic sequences of the ophiolite.

The Litog Klikog Kiri (S. LKK) Intrusion.

Of all the felsic bodies in the Segama Valley, the Litog Klikog Kiri intrusive has attracted the most attention, largely due to the biotite rich aureole noted by Hutchison (2005). Its contacts are marked in the topography by S. LKK and S. Babayas, two small tributaries of the Middle S. Segama. An interesting note is that during the Second World War many of the citizens of Lahad Datu escaped to small villages (now long gone) on the banks of the river in this region and some of the refugees of Kampung Kadang were successful in panning gold from the confluence of S. LKK with S. Segama, implying that this body is mineralised (local resident, pers. comms.). The intrusions lie outside the Danum Valley national park and can only be accessed by boat from the Lower S. Segama, 30km downstream.

The intrusion is a medium grained tonalite, composed of 28% quartz, 61% plagioclase, 3% alkali feldspar and 8% chloritised hornblende, although its upstream outcrops show a much higher biotite content, composed of 22% quartz, 44% plagioclase, 3% alkali feldspar, 17% hornblende, 7% biotite and 7% chlorite. These distinct units may represent construction of the intrusion from multiple pulses of magma. The S. Litog

Klikog Kiri stream follows the contact between the intrusion and the hornfelsed country rock, a highly chloritised basalt composed of a plagioclase-rich groundmass and variably chloritised clinopyroxene phenocrysts and calcite amygdales. In one occurrence the protolith appears to have been entirely altered to a mass of biotite. Based on these contact relationships the S. LKK tonalite, like the S. Purut intrusion, intruded the volcanic sequence of the ophiolite.

The S. Babayas stream follows the biotite rich hornfels of the eastern contact but, although granitic dykes are observed, the main body is not exposed here. Intriguingly, the stream follows an exposure of calc-silicates for 25m. These are in faulted contact with the hornfels to either side, implying that carbonates were deposited on top of the ophiolite prior to the emplacement of the intrusion and incorporated into the mafic sequence by later deformation.

Ophiolite surrounding Mt Kinabalu

For comparison to the intrusive and country rock samples collected from the Segama valley, additional ophiolite samples were collected and analysed from around the Mt Kinabalu pluton in west Sabah near Mt Kinabalu (Fig.2.1) where the ultramafic sequence of the ophiolite also outcrops (Jacobson, 1970). This sample set includes variably serpentinised peridotites from the flanks of the mountain as well as float from S. Mansahaban to the east where a near-complete suite of ophiolite rocks occurs as float (Imai and Ozawa, 1991). These include garnet pyroxenites, amphibolite, garnet amphibolite, garnet-zeolite amphibolite and amphibolite-plagioclase gneiss, amygdale-rich basaltic volcanics and chert. The location of the source of this float in the dense rainforest upstream is unclear.

Analytical methodology

Samples of the intrusives and country rock were analysed for major element composition by XRF at Edinburgh University and by ICP-MS and PIMMS (Plasma

Ionisation Multi-collector Mass Spectrometry) at Durham University to obtain trace element and radiogenic isotope data, respectively.

Samples were crushed and milled to a fine powder using a fly press and agate ball mills. For XRF analysis the samples were dried at 1100^{o}C to calculate Loss On Ignition (LOI) before being mixed with $LiBO_2$ flux and fused into glass discs for analysis (Gill, 1997). Trace element analysis followed the procedure presented in Ottley *et al.* (2003). Samples were dissolved using HF and HNO_3, and analysed on a ThermoScientific X-Series 2 ICP-MS using blanks, repeated samples and the standards BHVO-1, W2 and AGV-1 for calibration and quality control. For felsic samples where significant and observable depletions in Zr and Hf in the data resulted from incomplete dissolution of zircon crystals, trace elements were determined by standard HF dissolution for all elements except those highly compatible in zircon (Ta, Cs, Zr, Hf, Th, U, Nb, Y and the REE except La, for which the $LiBO_2$ flux during flux fusion affects analytical accuracy). To analyse these elements the samples were prepared again but fused in the same way as for XRF to break down zircon and resistant accessory phases prior to dissolution. To determine accuracy and reproducibility the standards AGV-1, BHVO-1 and W2 as well as two samples from Mt Kinabalu were analysed multiple times in each analytical batch of samples as well as acid blanks and the flux material used for flux fusion prior to dissolution. This QC data is presented in Appendix A1.2.

Sample preparation for analysis of Sr and Nd radiogenic isotopes followed the column chemistry procedures detailed in Charlier *et al.* (2006). Whole rock powders were dissolved in HF and HNO_3 SpA acid and separated by column chemistry using Sr-spec resin and Hf-Nd cation resin (AG50 X-8). The lead fraction was collected in 100µl 8N HCl from the Sr columns following collection of the Nd and Sr fractions and waste elution using 200µl 2.5N HCl. The Pb fraction was then dried down, dissolved in 500µl 3% HNO_3, and spiked with ^{206}Tl to correct for mass bias (Hirata, 1996). PIMMS analytical procedures are as detailed in Nowell *et al.* (2003). For $^{87}Sr/^{86}Sr$ and $^{143}Nd/^{144}Nd$, measured values for the NBS987 and J&M standards (±2SD error) during the same run as the samples were 0.710267 ±23 (n=35) and 0.511109 ±10 (n=44) respectively. Data are corrected to the respective NBS987 and J&M standard values of 0.71024 (Thirlwall, 1991) and 0.511110 (Royse *et al.*, 1998). For Pb, measured values for the NBS981

standards ±2SD for $^{206}Pb/^{204}Pb$, $^{207}Pb/^{204}Pb$, $^{208}Pb/^{204}Pb$, $^{207}Pb/^{206}Pb$ and $^{208}Pb/^{206}Pb$ (n=12) are 16.9405 ±9, 15.4983 ±9, 36.7181 ±21, 0.9149 ±1 and 2.1675 ±5 respectively. Data are corrected to values of NBS981 of 16.94051, 15.49800, 36.71744, 0.91485 and 2.16743 respectively (Galer, 1997).

Results

Major Elements and Classification

Data for all geochemical analyses are presented in Appendix A2. The felsic intrusion samples of Leong (1974) and Kirk (1968) give K_2O contents of up to 2.25 wt.% and SiO_2 contents of 55.10 to 72.7 wt. %, classifying them according to their K content and TAS as tholeiitic to calc-alkaline diorite, syeno-diorite, granodiorite and granite (Fig. 2.6). The new data demonstrate ranges of 55.59 to 71.39 wt.% SiO_2 and 1.30 to 2.11 wt.% K_2O. This classifies the felsic plutons as calc-alkaline to high-K calc-alkaline syeno-diorite, granodiorite and granite, the S. Purut and S. Mansahaban volcanics as calc-alkaline basalt, and the S. Danum dyke as a calc-alkaline dacite based on their K_2O content and the TAS classification of Stauffer (1968).

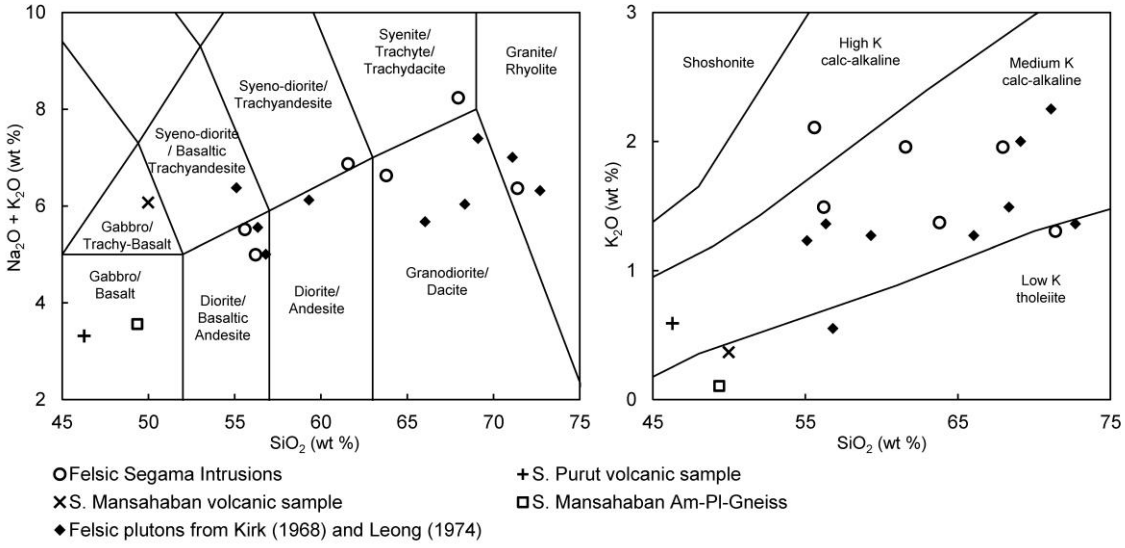

Fig. 2.6. Major element classification diagrams for the Segama ophiolite and S. Mansahaban ophiolite samples. Classification fields from Le Maitre *et al.* (1989) and Rickwood (1989). Am-Pl-Gneiss – Amphibole-plagioclase gneiss. Felsic plutons from the Segama Valley ophiolite from Kirk (1968) and Leong (1974) plotted for comparison.

Trace elements

Primitive mantle (PM) multi-element plots and chondrite normalised REE plots for the intrusive bodies (Fig. 2.7) show the LILE and LREE enrichment and HFSE and HREE depletions characteristic of arc magmatism and continental crust, as does the S. Mansahaban chert. The plot for the S. Purut basalt shows a similar pattern, but a lower degree of LILE enrichment. In contrast, the amphibole-plagioclase gneiss, garnet amphibolite and two of the peridotite samples from Kinabalu and S. Mansahaban show relatively flat REE profiles with depletion in their LREE, typical of N-MORB magmatism, and also show the steady MORB-like depletion in more mantle incompatible trace elements (e.g. high PM normalised La/Nb), except for enrichments in the most mantle-incompatible and fluid mobile elements (e.g. Cs, Rb, U, K and Pb).

Unlike the other mafic samples, the S. Mansahaban trachy-basalt shows a smooth OIB-type signature for trace and REE profiles, increasing in concentration towards more mantle-incompatible elements (e.g. Cs, Rb, Ba), and the eclogite shows a flat, low concentration profile with a prominent peak for Eu

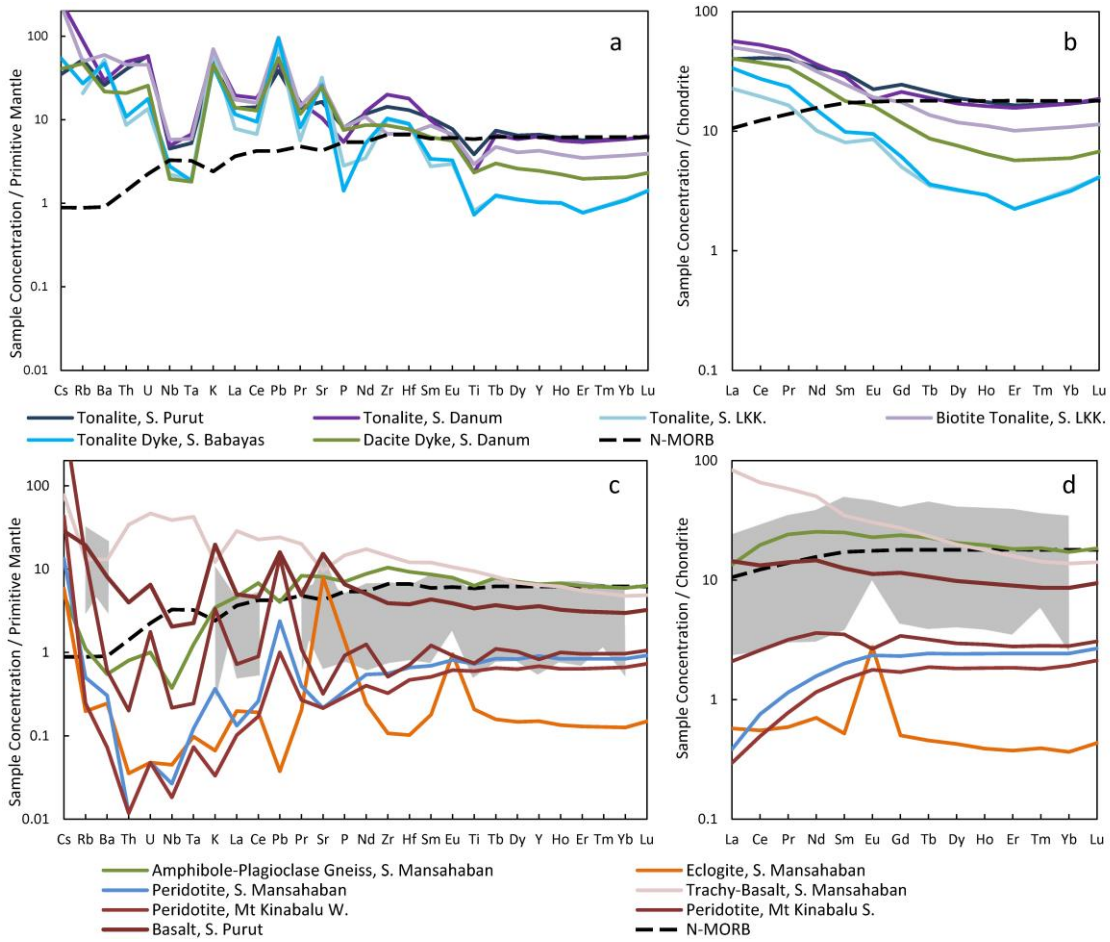

Fig. 2.7. Normalised multi-element plots for the felsic Segama ophiolite intrusion (a & b) and the mafic and ultramafic igneous and metamorphic ophiolite samples from the Segama ophiolite, Mt Kinabalu and S. Mansahaban (c & d). Shaded area indicates the compositions of mafic and ultramafic igneous and metamorphic ophiolite samples from the Sabah ophiolite in Graves *et al.* (2000) for comparison. Normalising values and N-MORB composition from Sun and McDonough (1989)..

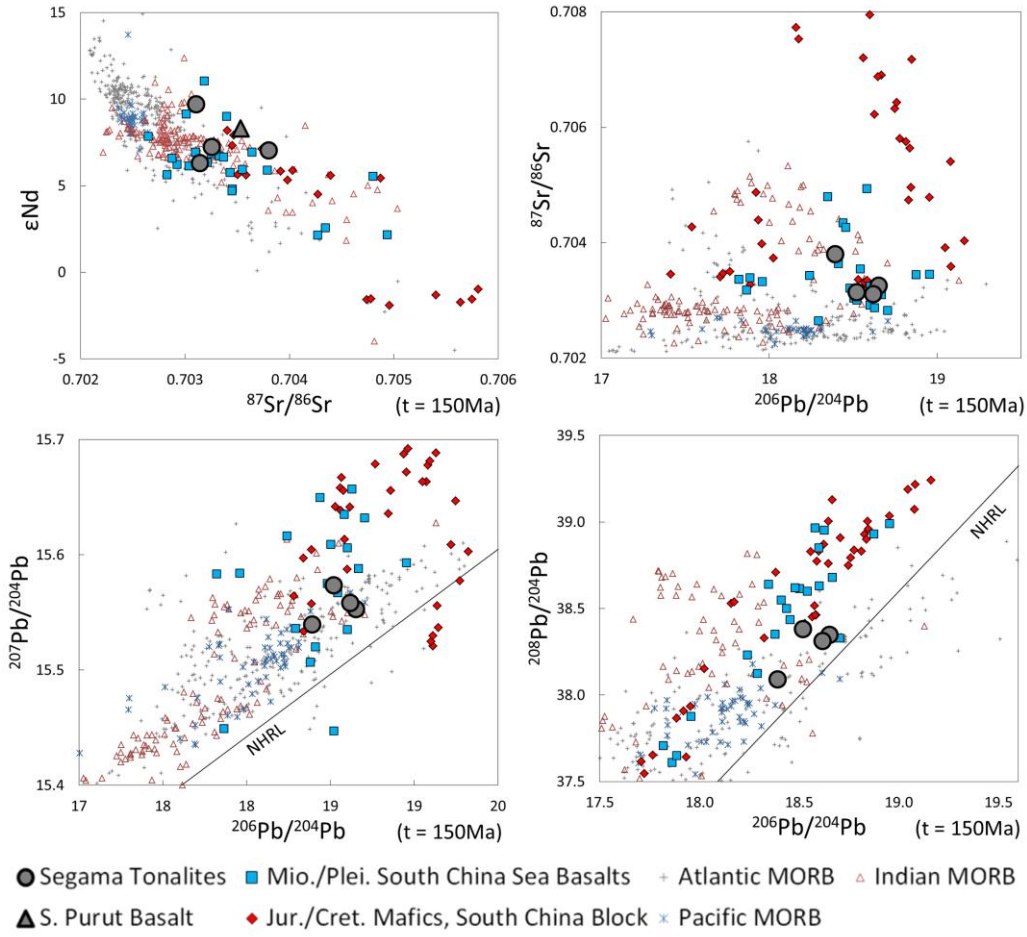

Fig. 2.8. Comparison of isotopic signatures of the Segama Highlands cal-alkaline intrusives with values for South China Sea basalts (Tu *et al.*, 1992, Yan *et al.*, 2008); South China Block mafics (Wang *et al.*, 2008) and spreading ridge basalts of the Indian, Pacific and Atlantic Oceans (data from PetDB).

Radiogenic Isotopes

Fig. 2.8 shows the isotopic data acquired for the intrusive rocks and the S. Purut basalt. Assuming an age of 150 Ma for the samples analysed (see below), the initial $^{87}Sr/^{86}Sr$, $^{143}Nd/^{144}Nd$, $^{206}Pb/^{204}Pb$, $^{207}Pb/^{204}Pb$, and $^{208}Pb/^{204}Pb$ values for the Segama Valley intrusives and the S. Purut spilite all have mantle-like signatures, with lower Sr and Pb isotope ratios and higher Nd isotopes than bulk earth. They lie within the calculated field of Plio-Pleistocene basaltic rocks dredged from the South China Sea (Tu *et al.*, 1992, Yan *et al.*, 2008) backdated to 150 Ma. They also plot within the field of the initial isotopic values of Mesozoic mafic rocks from the South China Block around the

Chenzhou-Linwu Fault of S. China (Wang *et al.*, 2008) but with lower Sr and Pb and higher Nd isotopic values than most of these Chinese samples.

Discussion

The Felsic Intrusions

Previous studies have postulated that the Segama ophiolite felsic intrusions are either partial melts of older, continental crust or outcrops of it within the ophiolite. However, the clear intrusive contacts of the Segama Valley plutonic rocks into the ophiolite sequence supports the interpretation that they are partial melts post-dating the formation of the ophiolite rather than windows into an underlying granitic basement. Although the relative HFSE depletions and LILE enrichments observed could be attributed to either an arc setting or inheritance from continental crust, the isotopic signatures of the intrusions plot consistently within the spread of data for global MORB values and within the spread that present day oceanic crust of the South China Sea would occupy if backdated to an estimated age of ophiolite formation of 150 Ma (Hutchison, 2005). This indicates a mantle source for the intrusions instead of being derived from a partial melt of an underlying continental crust for which much more evolved Sr and Pb and depleted Nd isotopic signatures would be expected.

Early interpretations of ophiolites understood them to represent oceanic crust formed at mid-ocean ridges and later obducted on to continental crust at subduction zones. Consequently, interpretation of the felsic intrusions proposed that they must be derived through partial melting of the crust on to which they were obducted because mid-ocean ridge magmatism predominantly produces melts of the tholeiitic series. However, the development of our understanding of ophiolite emplacement (e.g. Dewey and Bird, 1971, Pearce and Cann, 1971, Miyashiro, 1973, Moores *et al.*, 1984, Pearce *et al.*, 1984, Pearce, 2003) has concluded that almost all ophiolites form in supra-subduction zone spreading centres. Consequently, although early magmatism displays N-MORB like affinity, as the subduction zone develops the melt becomes more enriched and oxidised and begins to produce calc-alkaline magmas of more arc-like

affinity. Once fully developed, the Sabah ophiolite would have been located within a continental arc on the margins of SE Asia, a setting in which calc-alkaline intermediate magmatism, such as these intrusions, is not unusual. These mantle-derived arc melts provide an alternative process for ophiolitic plagiogranite derivation to that proposed by previous studies whereby they are derived through partial melting of gabbros, metamorphosed gabbros or amphibolites of the crustal sequence (Flagler and Spray, 1991, Floyd et al., 1998, Koepke et al., 2004, Koepke et al., 2007).

Mafic Samples

The intrusive and metamorphosed mafic and ultramafic samples show a range of trace element enrichments between MORB and arc-like signatures. The amphibole-plagioclase gneiss and two of the peridotite samples from Kinabalu show MORB signatures in their trace and REE patterns. This REE pattern is very similar to gabbroic, ultramafic and basaltic samples from the ophiolite outcrops of the Segama Highlands, Telupid and NE Sabah, and the metagabbros of the Darvel Bay ophiolite from previous studies (Omang and Barber, 1996, Graves *et al.*, 2000). However, the MORB-like samples of this and earlier studies show variable relative enrichment of Cs, Rb, Ba, Th, U, Pb and K. Enrichment of these fluid mobile incompatible elements is characteristic of subduction zone magmatism, supporting the interpretation of ophiolite emplacement in a supra-subduction zone setting. Enrichment of LILE and incompatible elements superimposed on an otherwise MORB-like signature probably indicates the enrichment of a previously depleted mantle source, although may also result from hydrothermal alteration post-emplacement. As the isotopic signature of the S. Purut basalt shares the mantle affinity of the tonalites, the trace element enrichments observed in both lithologies are not inherited through assimilation of continental crust.

As illustrated in Fig. 2.9, the progression of MORB-type to arc-type magmatism has been interpreted by previous authors to represent the progressive contribution of slab derived fluids to the mantle wedge (e.g. Whattam and Stern, 2011), and so a forearc spreading centre initially of MORB like affinity will start to display more arc-like affinities as subduction progresses. Thus, the apparent superposition of MORB and arc

signatures in these samples may imply emplacement relatively early in the history of this subduction zone.

In contrast to the other samples, the basalt sample from S. Mansahaban shows enrichment of its more mantle-incompatible trace elements, similar to OIB magmatism. None of the other samples from this study or previous work on the ophiolite has found Mesozoic samples of this signature. However, OIB signatures are prevalent in Neogene magmatism from Borneo and the South China Sea region (Hoang *et al.*, 1996, Macpherson *et al.*, 2010, Cullen *et al.*, 2013), and so it is probable that this sample represents later magmatism not associated with emplacement of the ophiolite.

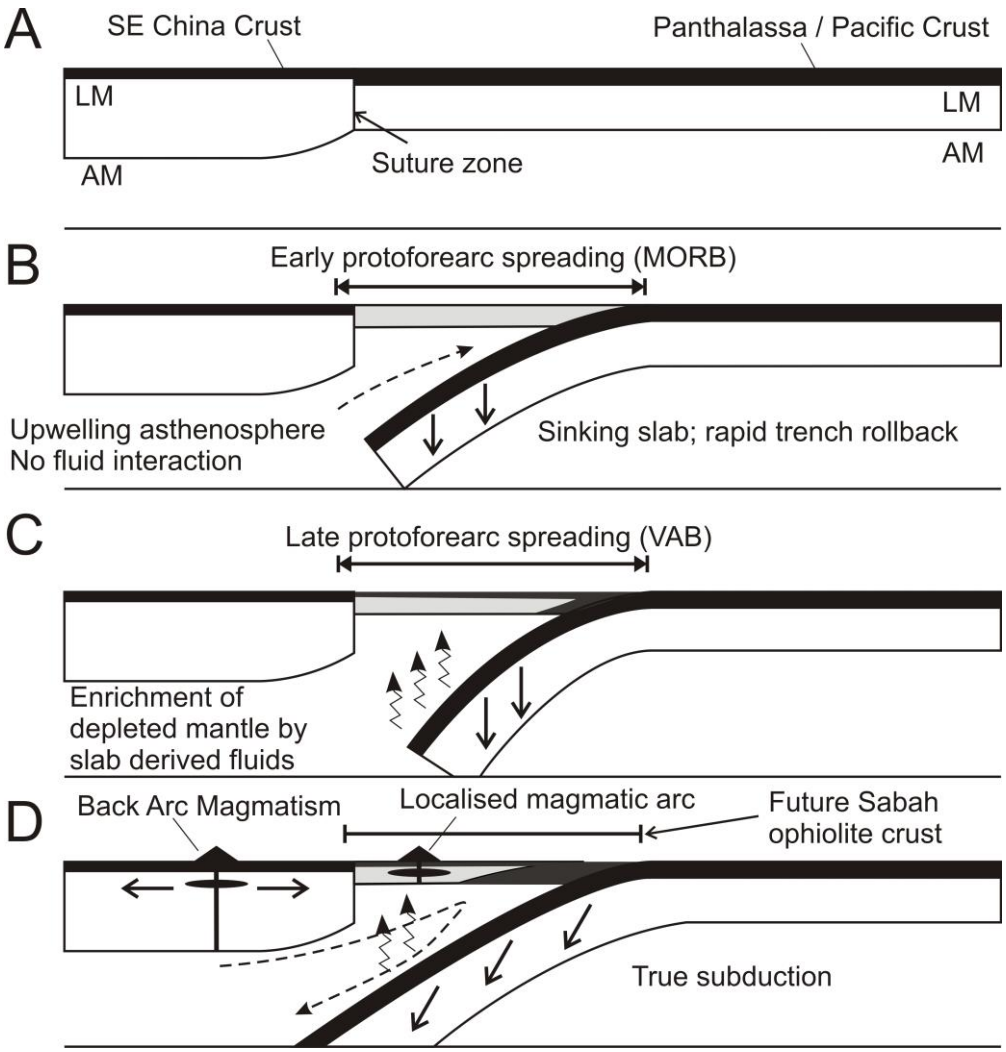

Fig. 2.9. Subduction initiation of the western Pacific crust beneath SE China and emplacement of the Supra-subduction zone forearc crust forming the Sabah ophiolite. (A) Suture of old, cold Panthalassa oceanic lithosphere – referred to after subduction initiation as the Pacific. (B) Subsidence of the old oceanic lithosphere, resulting in asthenosphere upwelling, MORB-type magmatism and proto-forearc spreading. (C) Dehydration of the subducting slab enriches the mantle wedge - now depleted in incompatible elements - with fluid mobile elements. This superimposes elemental enrichments on the depleted chemical signature, as shown in the trace element plots of Fig. 2.7. (D) Downdip motion of the sinking slab and continued slab dehydration results in true subduction and magmatic arc development. Back arc spreading results in extensional magmatism behind the arc, inland in SE China (Zhou *et al.*, 2006). LM – Lithospheric Mantle; AM – Asthenospheric Mantle; MORB – Extrusive and intrusive Mid Ocean Ridge Basalt magmatism; VAB - Extrusive and intrusive Volcanic Arc Basalt magmatism. Adapted from Stern *et al.* (2012).

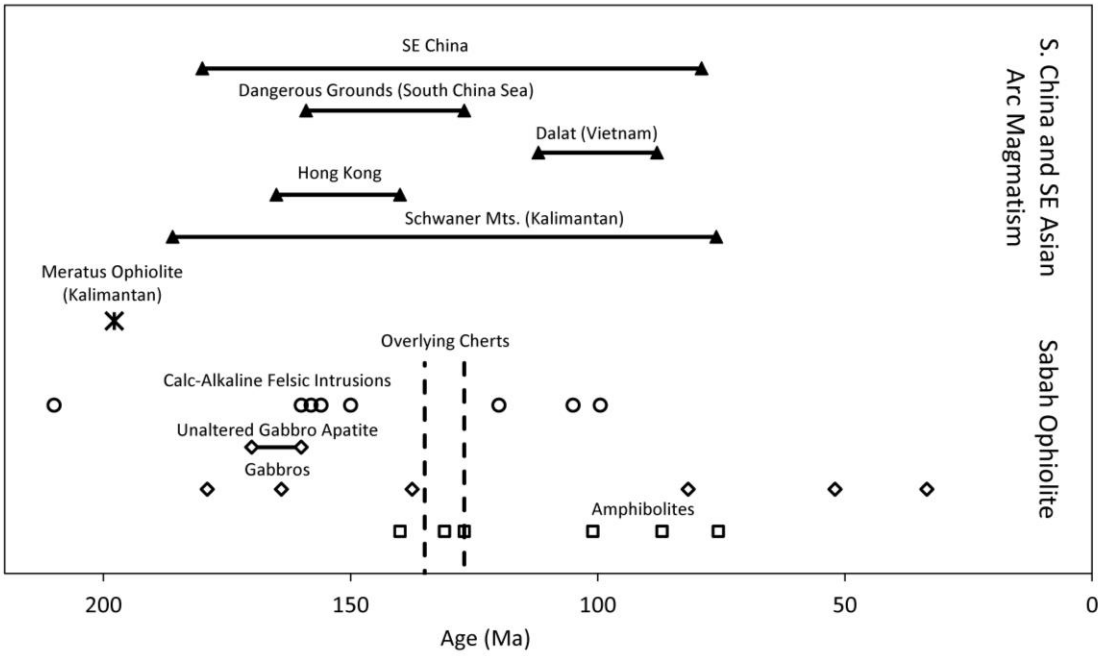

Fig 2.10. Comparison of determined ages of the Sabah Ophiolite with ages of Mesozoic magmatism in SE Asia and South China. Age data is from: SE China granites, Zhou and Li (2000); Dangerous Grounds tonalites and monzogranites, Yan *et al.* (2010); Hong Kong volcanics and intrusives, Davis *et al.* (1997); Schwaner Mountain Granites of Kalimantan, Moss (1998); Meratus ophiolite, Coggon *et al.* (2011); Radiolarian age range of overlying chert from Hutchison (2005); Unaltered gabbro apatite fission track ages, Hutchison (2005); Felsic intrusives of the Segama Highlands K-Ar dates from Kirk (1968), Leong (1974), Leong (1998) and Graves *et al.* (2000); Sabah ophiolitic gabbro K-Ar dates from Rangin *et al.* (1990), Omang (1993) and Graves *et al.* (2000); Sabah ophiolitic amphibolite K-Ar dates from Kirk (1968), Leong (1974), Omang (1993) and Swauger *et al.* (1995).

Implications for the age of the Sabah ophiolite

Oceanic crust can develop in forearc extensional settings during slab rollback and consequent supra-subduction zone extension (Fig. 2.9). If there is a period of inversion and this extensional setting becomes compressive then this forearc oceanic crust will be thickened or obducted on to the crust further from the arc, resulting in an ophiolite (Stern *et al.*, 2012). Thus, it is the periods of extension that produce both forearc and ophiolite crust, and it is this that is recorded by the Sabah ophiolite. However, to understand the emplacement history of the Sabah ophiolite it is first important to understand when it occurred. As discussed previously a range of dates exist for units of the ophiolite sequence and are summarised in Fig. 2.10. The radiolarian age of the

overlying cherts of 127 – 135 Ma (Basir, 1992) gives a minimum age of initial emplacement (Hutchison, 2005). However, the mafic and ultramafic samples have undergone varying degrees of alteration and metamorphism so the K-Ar dates from these low K samples are susceptible to being reset. Hutchison (2005) published apatite fission track ages for gabbros of the ophiolite, of which almost all had been reset to <110 Ma, although four samples interpreted to still represent the original age were dated at 160 – 170 Ma. The gabbros dated at <100Ma and 217 Ma are neglected by Omang (1993) on the basis of alteration are also likely to have been reset. Although Leong (1998) reported another 210Ma K-Ar age from a later study, the anomalously old 210Ma tonalite sample of Leong (1974) was also neglected by previous authors as it was much older than the majority of ages from the ophiolite (Hutchison, 1988, Hutchison, 1989, Omang and Barber, 1996).

However, when considering these dates it is important to look at the Sabah ophiolite in a wider context. Being a region of prolonged subduction and extension, outcrops of ophiolite in SE Asia are widespread, including, but not limited to, Sumatra, Java, Kalimantan and Palawan (Hutchison, 1975). Application of the ^{190}Pt-^{186}Os geochronometer has allowed accurate dating of the Meratus ophiolite in SE Kalimantan to 197.8 ± 8.1 Ma (2 σ) (Coggon *et al.*, 2011). This is in agreement with the associated arc magmatism in the Schwaner mountains of SW Kalimantan, which have bimodal U-Pb in zircon dates of 186 and 76 Ma (Davies *et al.*, 2012). As these outcrops in Kalimantan reflect the continuation of the subduction zone forearc that formed the Sabah ophiolite to the SW there is no reason to disregard similar ages in Sabah.

With this in mind, there still remains a very wide range of measured ages. Omang (1993) concluded that the ophiolite was emplaced between 179 and 164 Ma, although he determined that the gabbros from which these dates were obtained had an arc-like affinity and so were late stage intrusions. As shown by this study, the felsic intrusions also represent arc magmatism and so although these higher K samples are less susceptible to alteration of the K-Ar dates they cannot confirm the initial date of ophiolite formation, although they do provide a minimum age. Thus, given the two dates from the felsic intrusions at 210 Ma (Leong, 1974, Leong, 1998) and the similar ages for the Meratus Ophiolite and Schwaner Mountains in Kalimantan we conclude

that the ophiolite was emplaced in the Early Jurassic at the latest, and propose an approximate age of emplacement of 200 Ma. This age is much older than that advocated by previous authors, but we propose that the later ages measured for igneous samples from the Sabah Ophiolite result from continuing arc magmatism beneath Sabah throughout the Mesozoic.

An Early Jurassic age of emplacement for both the Sabah and Kalimantan ophiolites is of particular importance when the regional geological history of this Mesozoic arc is considered. The volume of largely granitic igneous crust formed during this period of subduction is vast, extending across SE China and SE Asia (Fig. 2.2). The region of Jurassic and Cretaceous magmatism in SE China alone covers an area of 220,000km^2 (Zhou *et al.*, 2006). Various ages for magmatic activity related to the early Pacific arc exist, including: 180 to 79 Ma for the S. China Yanshanian magmatism (Zhou and Li, 2000); 165 to 140 Ma for magmatism in Hong Kong (Davis *et al.*, 1997); 159 to 127 Ma for attenuated granitic crust of the South China Sea (Yan *et al.*, 2010); 112 to 88 Ma for the Dalat granitoids of Vietnam (Nguyen *et al.*, 2004) and 186 to 76 Ma for the Schwaner Mountains granites of Kalimantan (Moss, 1998, Davies *et al.*, 2012). This puts the emplacement age of the ophiolite at the start of the non-Tethyan Mesozoic arc magmatism and at the start of subduction of the old Panthalassa oceanic crust, subsequently referred to as the Pacific. This is in agreement with models of ophiolite emplacement as protoforearc crust during subduction zone initiation, as illustrated in Fig. 2.9 (Stern and Wyllie, 1981, Pearce *et al.*, 1984, Stern *et al.*, 2012), and disagrees with tectonic models indicating initiation of Pacific subduction in the Permian (e.g. Li and Li, 2007, Metcalfe, 2011). It also disagrees with models proposing a Cretaceous age for subduction initiation and that Jurassic magmatism was related to crustal extension following the Indosinian Orogeny (Chen *et al.*, 2008). It does however support the model of Zhou *et al.* (2006), who proposed that between 205 and 180 Ma magmatism in SE China switched from being derived though the Tethyan subduction processes, which formed the Permian and Triassic Indosinian magmatism, to processes associated with subduction of the Pacific Plate. However, it does indicate that there was not the proposed period of magmatic quiescence between 205 and 180 Ma observed in SE China, and so Tethyan subduction may have led directly to the initiation of Pacific

subduction. From the observations discussed we propose that the Mesozoic Pacific subduction zone and forearc are recorded by the supra-subduction zone ophiolites of Sabah and Kalimantan, and probably also by those of Palawan and Java further along this trend (Fig. 2.11). However, initial emplacement ages of the latter two are unclear as their oldest measured ages are Cretaceous, but like the Cretaceous ages of the Sabah ophiolite these may represent post-emplacement arc magmatism.

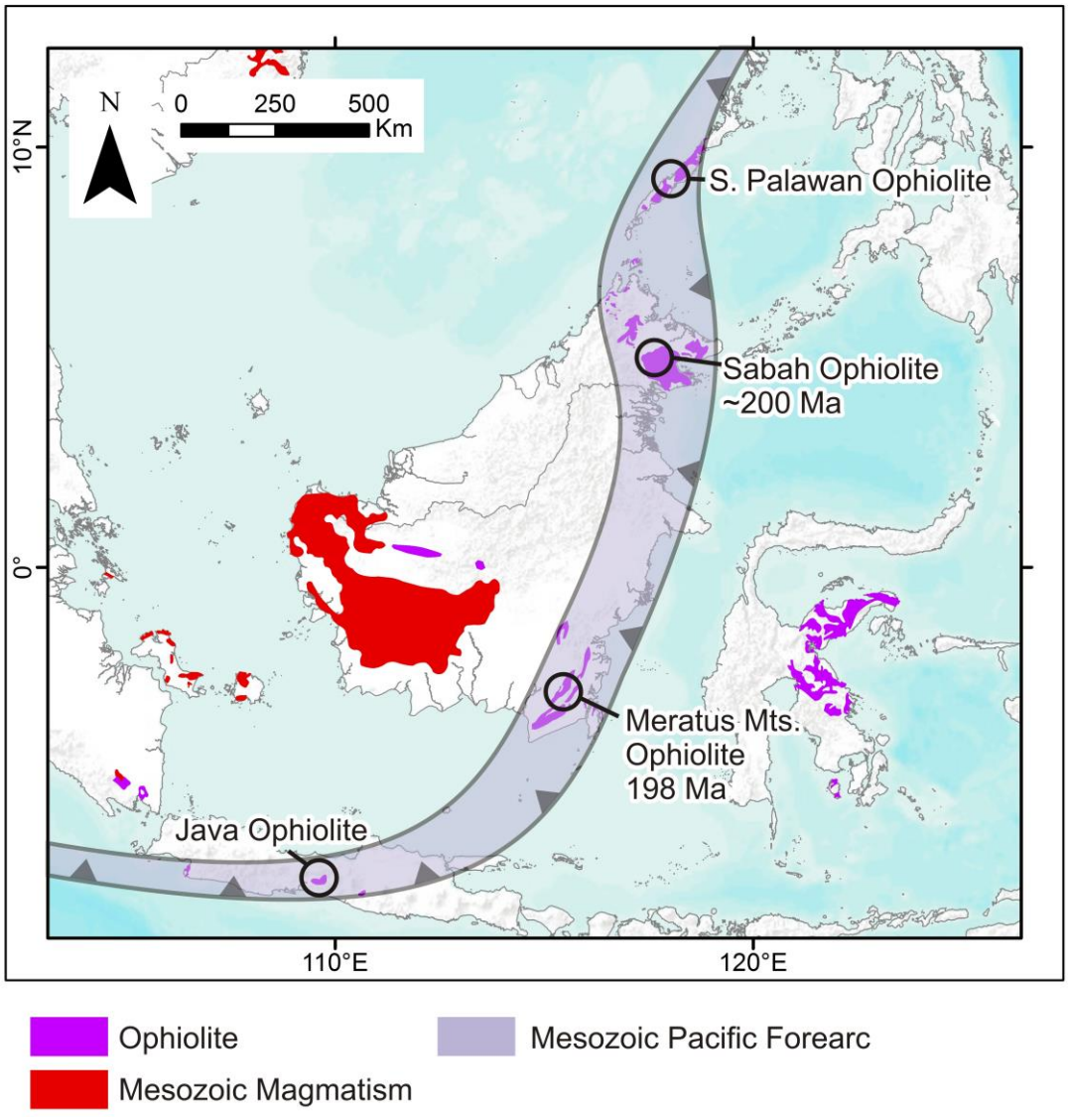

Fig. 2.11. Proposed line of the Mesozoic Pacific forearc and subduction zone, as marked by the ophiolites of Sabah, the Meratus Mountains, Java and Palawan, along with emplacement ages. Map and age data from Kirk (1968), Steinshouer *et al.* (1997), Moss (1998), Parkinson *et al.* (1998), Wakita *et al.* (1998), Coggon *et al.* (2011) and Suggate *et al.* (2013). Basemap data from the ESRI ArcGIS® software (Copyright © Esri).

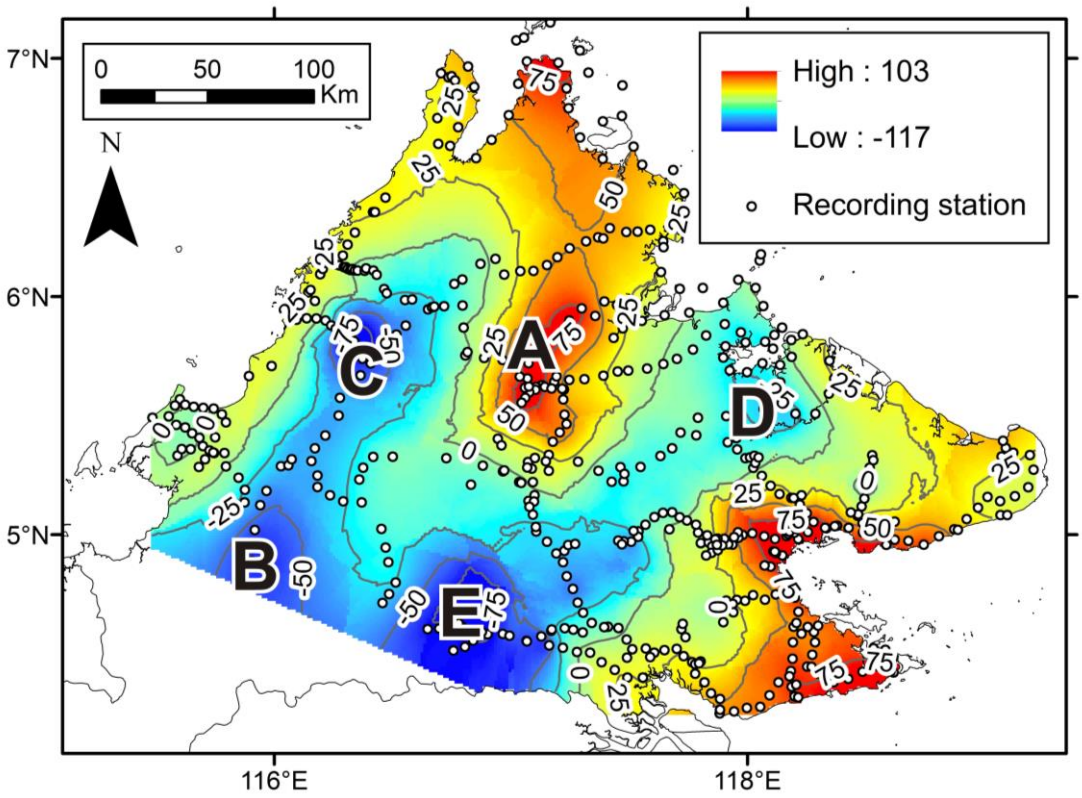

Fig 2.12. Terrain corrected Bouguer anomaly gravity map of Sabah. Data from Holt (1998).

Is there a continental basement under Sabah?

It is clear from the geochemical data presented here that even the more evolved rocks of the ophiolite sequence are mantle derived, with no geochemical evidence for involvement of an older continental crust underlying Sabah. Holt (1998) and Milsom *et al.* (2001) interpreted the presence of underlying continental crust from their land-based gravity data, in which it was shown that a large negative gravity anomaly was present in Sabah (Fig. 2.12). It is interesting to note the close relationship between the high gravity values with the regions of ophiolite outcrop and the low values with the main sedimentary basins (Compare Fig 2.12 with Fig. 2.1). Aerial gravity data collected by the Malaysian Department of Surveying and Mapping (JUPEM) shows similar anomalies and shows the large low gravity anomaly continuing through Sarawak to the SW (pers. comms.). It is well known that sedimentation rates onshore and offshore in this region are exceptionally high, with the stratigraphic thickness of sediments in South Sabah reported as 6000-7000m (Balaguru and Nichols, 2004). As such we

propose an alternative hypothesis that the low Bouguer anomalies simply represent thick sedimentary sequences deposited during the Late Cretaceous and Cenozoic in basins formed by prolonged regional NW-SE extension in Sabah (Balaguru, 2001, Hall, 2013). Thus, during this extension the ophiolite was deformed into a horst-graben structure with the surface outcrops of ophiolite representing the horsts and the sedimentary basins infilling the grabens.

As the detailed structure of the basement beneath the Tertiary sediments is unclear, it would not be suitable to attempt complex geophysical modelling of the subsurface. However, the validity of the hypothesis can be tested by a simple slab model using the following equation (Kearey *et al.*, 2009):

$$t = \Delta g / 2\Pi G \Delta \rho$$

[Eq. 1]

where t is the thickness of the sediments, Δg change in observed gravity (m s^{-2}), G is the gravitational constant (6.67 x 10^{-11} $m^3kg^{-1}s^{-2}$) and $\Delta \rho$ is the density contrast between the sediments and ultramafic sequence (kg m^{-3}). Taking density values of 3000 kg m^{-3} for the ophiolite and 2300 kg m^{-3} for the sediments, and a gravity contrast from Holt (1998) of 155mgal (0.00155 m s^{-2}) between the Telupid Ophiolite and the SW Crocker Basin we derive a maximum thickness of 5.3km of sediments overlying the ophiolite in the SW Crocker Basin (Fig. 2.13). This is a plausible figure given the known stratigraphic thicknesses (Balaguru and Nichols, 2004).

A potentially important additional factor producing the strong negative gravity anomalies beneath the Sabah basin is the nature of the underlying mantle. These basins are an upper crustal expression of prolonged crustal extension in Borneo (Hall, 2013). The presence of Neogene OIB magmatism in Sabah (Macpherson *et al.*, 2010, Cullen *et al.*, 2013) has led previous authors to advocate the upwelling of asthenosphere into lithospheric thin spots beneath the crust. The arrival of this warm mantle into zones of extension would have a similar effect to that observed beneath mid-ocean ridges (Wang *et al.*, 1996) and produce a lower than expected gravity anomaly. Heat flow is elevated beneath much of SE Asia (Hall and Morley, 2004),

supporting this hypothesis. However, for Borneo most of the data is from offshore and so this data cannot specifically determine regions of likely mantle upwelling in Sabah (Sperber, 2009). Seismic velocities provide low resolution data for SE Asia but do indicate a low velocity region in SW Borneo, in agreement with high crustal heat flow along the coast of this region (Kenyon and Beddoes, 1977, Rutherford and Qureshi, 1981, Pollack *et al.*, 1990, Lebedev and Nolet, 2003, Sperber, 2009)

By assuming there is a density contrast between upwelling asthenosphere and the sub-continental mantle lithosphere and assuming a thickness of upwelling mantle it is possible to show the effect of this process with the slab model used previously and modifying the density of the lower lithospheric mantle to that of the asthenosphere. Seismic tomography (Lebedev and Nolet, 2003) indicates a depth of approximately 150km for the lithosphere-asthenosphere boundary (the seismic Moho) beneath Sabah and a 30km for the Mohorovičič discontinuity (the petrological Moho). Sabah shows surface heat flow values of 40 to 70mWm^{-2}. The lower values of this range are comparable to the 45 to 50mWm^{-2} heat flow values of tectonically active Phanerozoic terrains from which lithospheric mantle densities were modelled by Poudjom Djomani *et al.* (2001), and so are suitable proxies for regional heat flows unaffected by mantle upwelling. For modelling the basement of Sabah, we have replaced the lower 50km of lithospheric mantle with isothermally upwelling asthenosphere (Fig. 2.13). From the model of Poudjom Djomani *et al.* (2001), the difference in density between the 1300^{o}C asthenospheric adiabat and the lithospheric mantle varies between 10 to 40kg m^{-3} for depths of 150 and 100km. Therefore we use a conservative overall density contrast between the lithospheric mantle and the upwelling asthenosphere of 20kg m^{-3}.

By rearranging Eq. 1 we can determine that replacing the lower 50km of the mantle lithosphere with asthenosphere beneath extended sedimentary basins reduces the thicknesses of sediment required to explain the negative Bouguer anomalies. For instance, calculated sedimentary thickness required to explain the SW Crocker Basin would be reduced from 5.3 to 3.9km (Fig. 2.13).

Using this model for the other basins of Sabah shows that all may be explained by a combination of upwelling asthenosphere and reasonable sedimentary thicknesses (Fig.

2.13) without the requirement for an underlying continental crust. Consequently, neither the gravity data nor the field evidence supports the presence of an underlying continental basement beneath Sabah. This leaves the isotopic evidence for an old assimilant in the volcanic samples of the Semporna Peninsula (Macpherson *et al.*, 2010) as the only remaining indication for such material. This may imply that such material is either more localised or incorporated within the ophiolite and overlying sediments as attenuated crust or sedimentary material rather than being a more widespread underlying crust. The nature of this assimilant will be discussed further with regard to its implications for Mt Kinabalu in Chapter 5.

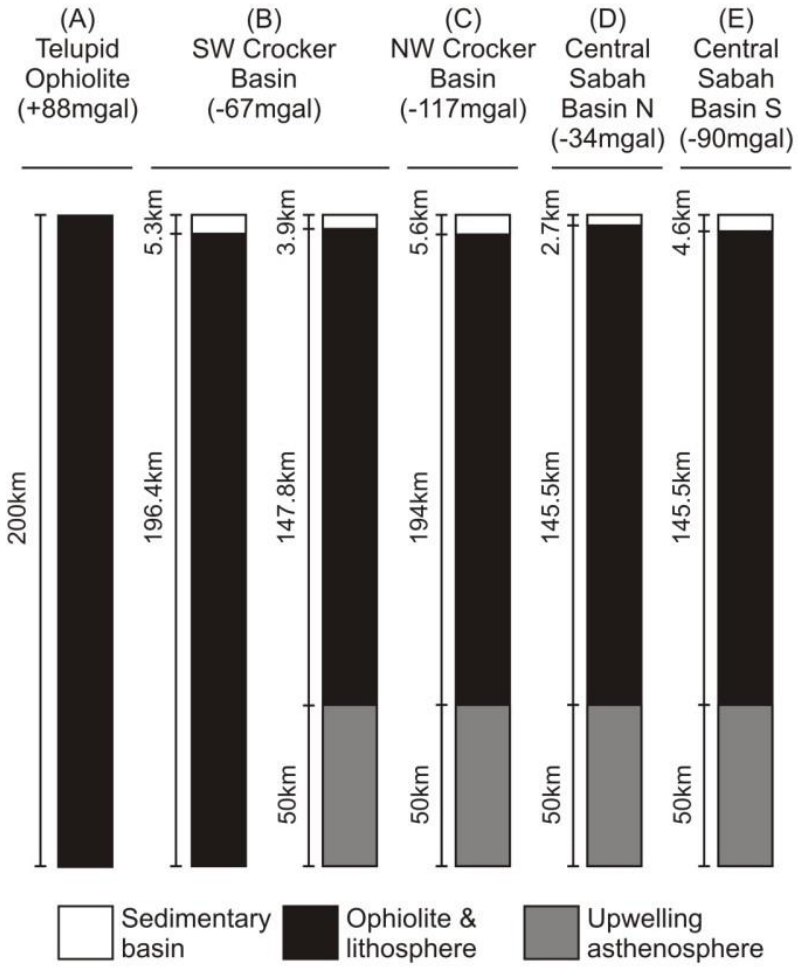

Fig. 2.13. Stratigraphic columns illustrating the crustal structure used in the gravity modelling of the observed negative Bouguer anomalies and contrasting observed gravitational strengths in Sabah, with and without asthenospheric upwelling. The density contrast used between the sediments and ophiolite at the same depth is 700kg m^{-3}, and between the deep lithosphere and upwelling asthenosphere is 20kg m^{-3}.

Conclusions

Granitic rocks, previously interpreted as windows into or partial melts of an underlying continental basement beneath the ophiolite of Sabah, are actually arc tonalites intruded into the ophiolite during Mesozoic subduction of the Pacific beneath SE Asia and SE China. Ophiolitic plagiogranites have previously been interpreted as partial melts of the gabbro sequence, but this indicates that they are more likely to be arc mantle melts in a SSZ setting, similar to arc dacites.

Low Bouguer anomalies in Sabah have also previously been advocated as evidence for underlying continental crust beneath Sabah but gravity modelling has shown that reasonable basin thicknesses and upwelling asthenosphere, both consequences of regional extension, can explain the observed negative gravity anomalies.

Our interpretation of the tonalites as felsic arc magmatism within a MORB ophiolite requires that the emplacement age of the Sabah ophiolite be re-examined. We propose that this supports an early Jurassic emplacement age of approximately 200 Ma, older than generally accepted, but that mafic magmatism continued within the ophiolite throughout the history of Pacific subduction beneath the region, producing the published range of gabbro ages. This agrees with dates of other ophiolites marking the trace of the paleo-subduction zone. Comparison of the ophiolite with age and distribution of regional magmatism in SE Asia and SE China indicates that the Sabah ophiolite is part of a continuous belt of ophiolites in Kalimantan and Palawan, and represents forearc magmatism emplaced during the early stages of Pacific subduction. These observations also imply that although a period of magmatic quiescence exists in SE China during the transition from Tethyan to Pacific subduction related magmatism no such inactivity exists along the arc.

Balaguru, A. (2001). Tectonic Evolution and Sedimentation of the Southern Sabah Basin, Malaysia. *Department of Geology, Royal Holloway, University of London.* PhD.

Balaguru, A. and Nichols, G. (2004). Tertiary stratigraphy and basin evolution, southern Sabah (Malaysian Borneo). *Journal of Asian Earth Sciences*. **23**, 4, 537-554.

Basir, J. (1992). Significance of radiolarian chert from the Chert-Spilite Formation, Telupid, Sabah. *Bulletin of the geological Society of Malaysia*. **31**, 67-84.

Charlier, B., Ginibre, C., Morgan, D., Nowell, G., Pearson, D., Davidson, J. and Ottley, C. (2006). Methods for the microsampling and high-precision analysis of strontium and rubidium isotopes at single crystal scale for petrological and geochronological applications. *Chemical Geology*. **232**, 3, 114-133.

Chen, C.-H., Lee, C.-Y. and Shinjo, R. (2008). Was there Jurassic paleo-Pacific subduction in South China?: Constraints from 40Ar/39Ar dating, elemental and Sr–Nd–Pb isotopic geochemistry of the Mesozoic basalts. *Lithos*. **106**, 1, 83-92.

Coggon, J., Nowell, G., Pearson, D. and Parman, S. (2011). Application of the 190Pt-186Os isotope system to dating platinum mineralization and ophiolite formation: an example from the Meratus Mountains, Borneo. *Economic Geology*. **106**, 1, 93-117.

Cullen, A., Macpherson, C., Taib, N.I., Burton-Johnson, A., Geist, D., Spell, T. and Banda, R.M. (2013). Age and Petrology of the Usun Apau and Linau Balui Volcanics: Windows to Central Borneo's Interior. *Journal of Asian Earth Sciences*.

Davies, L., Hall, R. and Armstrong, R. (2012). *Cretaceous crust beneath SW Borneo: U-Pb dating of zircons from metamorphic and granitic rocks*. AGU Autumn Meeting, San Francisco, United States.

Davis, D.W., Sewell, R.J. and Campbell, S.D.G. (1997). U-Pb dating of Mesozoic igneous rocks from Hong Kong. *Journal of the Geological Society*. **154**, 6, 1067-1076.

Dewey, J.F. and Bird, J.M. (1971). Origin and emplacement of the ophiolite suite: Appalachian ophiolites in Newfoundland. *Journal of Geophysical Research*. **76**, 14, 3179-3206.

Encarnación, J. (2004). Multiple ophiolite generation preserved in the northern Philippines and the growth of an island arc complex. *Tectonophysics*. **392**, 1, 103-130.

Flagler, P.A. and Spray, J.G. (1991). Generation of plagiogranite by amphibolite anatexis in oceanic shear zones. *Geology*. **19**, 1, 70-73.

Floyd, P., Yaliniz, M. and Goncuoglu, M. (1998). Geochemistry and petrogenesis of intrusive and extrusive ophiolitic plagiogranites, Central Anatolian Crystalline Complex, Turkey. *Lithos*. **42**, 3, 225-241.

Galer, S. (1997). Optimal triple spiking for high precision lead isotope ratio determination. *Terra Nova*. **9**, 441.

Gill, R. (1997). *Modern Analytical Geochemistry: an introduction to quantitative chemical analysis techniques for Earth, environmental and materials scientists*. Addison Wesley Longman.

Govindaraju, K. (1994). 1994 compilation of working values and sample description for 383 geostandards. *Geostandards newsletter*. **18**, S1, 1-158.

Graves, J.E., Hutchison, C.S., Bergman, S.C. and Swauger, D.A. (2000). Age and MORB geochemistry of the Sabah ophiolite basement. *Bulletin of the Geological Society of Malaysia*. **44**, 151-158.

Hall, R. and Morley, C.K. (2004). Sundaland basins. *Continent-Ocean Interactions Within East Asian Marginal Seas*. **149**, 55-85.

Hall, R. (2013). Contraction and extension in northern Borneo driven by subduction rollback. *Journal of Asian Earth Sciences*.

Hirata, T. (1996). Lead isotopic analyses of NIST standard reference materials using multiple collector inductively coupled plasma mass spectrometry coupled with a modified external correction method for mass discrimination effect. *Analyst*. **121**, 10, 1407-1411.

Hoang, N., Flower, M.F. and Carlson, R.W. (1996). Major, trace element, and isotopic compositions of Vietnamese basalts: Interaction of hydrous EM1-rich asthenosphere with thinned Eurasian lithosphere. *Geochimica et Cosmochimica Acta*. **60**, 22, 4329-4351.

Holt, R.A. (1998). The Gravity Field of Sundaland - Acquisition, Assessment and Interpretation. *Research School of Geological and Geophysical Sciences, Birkbeck College and University College London.* PhD.

Hutchison, C. (1988). Stratigraphic-tectonic model for eastern Borneo. *Geological Society of Malaysia Bulletin*. **22**, 135-151.

Hutchison, C.S. (1975). Ophiolite in Southeast Asia. *Geological Society of America Bulletin*. **86**, 6, 797-806.

Hutchison, C.S. (1989). *Geological evolution of South-east Asia*. Clarendon Press Oxford.

Hutchison, C.S. (2005). *Geology of North-West Borneo: Sarawak, Brunei and Sabah*. Elsevier Science.

Imai, A. and Ozawa, K. (1991). Tectonic implications of the hydrated garnet peridotites near Mt Kinabalu, Sabah, East Malaysia. *Journal of Southeast Asian Earth Sciences*. **6**, 3, 431-445.

Jacobson, G. (1970). *Gunung Kinabalu area, Sabah, Malaysia*. Sabah, Geological Survey of Malaysia.

Kearey, P., Brooks, M. and Hill, I. (2009). *An introduction to geophysical exploration*. Wiley. com.

Kenyon, C.S. and Beddoes, L.R. (1977). *Geothermal Gradient Map of Southeast Asia*. Southeast Asia Petroleum Exploration Society.

Kirk, H.J.C. (1968). The igneous rocks of Sarawak and Sabah. *Geological Survey Malaysia Bulletin*. **Memoir 14**,

Koepke, J., Feig, S., Snow, J. and Freise, M. (2004). Petrogenesis of oceanic plagiogranites by partial melting of gabbros: an experimental study. *Contributions to Mineralogy and Petrology*. **146**, 4, 414-432.

Koepke, J., Berndt, J., Feig, S.T. and Holtz, F. (2007). The formation of SiO 2-rich melts within the deep oceanic crust by hydrous partial melting of gabbros. *Contributions to Mineralogy and Petrology*. **153**, 1, 67-84.

Le Maitre, R.W., Bateman, P., Dudek, A., Keller, J., Lameyre, J., Le Bas, M., Sabine, P., Schmid, R., Sorensen, H. and Streckeisen, A. (1989). *A classification of igneous rocks and glossary of terms: Recommendations of the International Union of Geological Sciences Subcommission on the Systematics of Igneous Rocks*. Blackwell Oxford.

Lebedev, S. and Nolet, G. (2003). Upper mantle beneath Southeast Asia from S velocity tomography. *Journal of Geophysical Research*. **108**, B1, 2048.

Leong, K. (1974). *The geology and mineral resources of the Upper Segama Valley and Darvel Bay area, Sabah, Malaysia*. US Government Printing Office.

Leong, K. (1998). Sabah crystalline basement: “Spurious” radiometric ages? Continental? *Warta Geologi (Geological Society of Malaysia Newsletter)*. **24**, 5-8.

Li, Z.-X. and Li, X.-H. (2007). Formation of the 1300-km-wide intracontinental orogen and postorogenic magmatic province in Mesozoic South China: a flat-slab subduction model. *Geology*. **35**, 2, 179-182.

Macpherson, C.G., Chiang, K.K., Hall, R., Nowell, G.M., Castillo, P.R. and Thirlwall, M.F. (2010). Plio-Pleistocene intra-plate magmatism from the southern Sulu Arc, Semporna peninsula, Sabah, Borneo: Implications for high-Nb basalt in subduction zones. *Journal of Volcanology and Geothermal Research*. **190**, 1-2, 25-38.

Metcalfe, I. (2011). Tectonic framework and Phanerozoic evolution of Sundaland. *Gondwana Research*. **19**, 1, 3-21.

Milsom, J., Holt, R., Hutchison, C.S., Bergman, S.C., Swauger, D.A. and Graves, J.E. (2001). Discussion of a Miocene collisional belt in north Borneo: uplift mechanism and isostatic

adjustment quantified by thermochronology: Journal, Vol. 157, 2000, 783-793. *Journal of the Geological Society*. **158**, 2, 396-400.

Miyashiro, A. (1973). The Troodos ophiolitic complex was probably formed in an island arc. *Earth and Planetary Science Letters*. **19**, 2, 218-224.

Moores, E., Robinson, P.T., Malpas, J. and Xenophonotos, C. (1984). Model for the origin of the Troodos massif, Cyprus, and other mideast ophiolites. *Geology*. **12**, 8, 500-503.

Moss, S.J. (1998). Embaluh group turbidites in Kalimantan: evolution of a remnant oceanic basin in Borneo during the Late Cretaceous to Palaeogene. *Journal of the Geological Society*. **155**, 509-524.

Nguyen, T.T.B., Satir, M., Siebel, W. and Chen, F. (2004). Granitoids in the Dalat zone, southern Vietnam: age constraints on magmatism and regional geological implications. *International Journal of Earth Sciences*. **93**, 3, 329-340.

Nowell, G., Pearson, D., Ottley, C., Schweiters, J. and Dowall, D. (2003). Long-term performance characteristics of a plasma ionisation multi-collector mass spectrometer (PIMMS): the ThermoFinnigan Neptune. *Plasma Source Mass Spectrometry: Applications and Emerging Technologies. Cambridge: Royal Society of Chemistry*. 307-320.

Omang, S.A.K. (1993). Petrology, Geochemistry and Structural Geology of the Darvel Bay Ophiolite, Sabah, Malaysia. *Department of Geology, Royal Holloway, University of London.* PhD.

Omang, S.A.K. and Barber, A. (1996). Origin and tectonic significance of the metamorphic rocks associated with the Darvel Bay Ophiolite, Sabah, Malaysia. *Geological Society, London, Special Publications*. **106**, 1, 263-279.

Ottley, C., Pearson, D. and Irvine, G. (2003). A routine method for the dissolution of geological samples for the analysis of REE and trace elements via ICP-MS. *Plasma source mass spectrometry: Applications and emerging technologies*. 221-230.

Parkinson, C., Miyazaki, K., Wakita, K., Barber, A. and Carswell, D. (1998). An overview and tectonic synthesis of the pre-Tertiary very-high-pressure metamorphic and associated rocks of Java, Sulawesi and Kalimantan, Indonesia. *Island Arc*. **7**, 1-2, 184-200.

Pearce, J. and Cann, J. (1971). Ophiolite origin investigated by discriminant analysis using Ti, Zr and Y. *Earth and Planetary Science Letters*. **12**, 3, 339-349.

Pearce, J.A., Lippard, S. and Roberts, S. (1984). Characteristics and tectonic significance of supra-subduction zone ophiolites. *Geological Society, London, Special Publications*. **16**, 1, 77-94.

Pearce, J.A. (2003). Supra-subduction zone ophiolites: The search for modern analogues. *Special Papers-Geological Society of America*. 269-294.

Pollack, H., Hurter, S. and Johnson, J. (1990). The new global heat flow data compilation. *Eos Trans. AGU*. **71**, 1604.

Potts, P.J., Tindle, A.G. and Webb, P. (1992). *Geochemical Reference Material Compositions: Rocks, minerals, sediments, soils, carbonates, refractories, and ores used in research and industry*. Taylor & Francis US.

Poudjom Djomani, Y.H., O'Reilly, S.Y., Griffin, W. and Morgan, P. (2001). The density structure of subcontinental lithosphere through time. *Earth and Planetary Science Letters*. **184**, 3, 605-621.

Rangin, C., Bellon, H., Benard, F., Letouzey, J., Muller, C. and Sanudin, T. (1990). Neogene arc-continent collision in Sabah, Northern Borneo (Malaysia). *Tectonophysics*. **183**, 1-4, 305-319.

Rickwood, P.C. (1989). Boundary lines within petrologic diagrams which use oxides of major and minor elements. *Lithos*. **22**, 4, 247-263.

Royse, K., Kempton, P. and Darbyshire, D. (1998). Procedure for the analysis of rubidium–strontium and samarium–neodymium isotopes at the NERC Isotope Geosciences Laboratory. *NIGL Report Series*. **121**, 28.

Rutherford, K.J. and Qureshi, M.K. (1981). *Geothermal gradient map of southeast Asia*. Southeast Asia Petroleum Exploration Society.

Sperber, C.M. (2009). The thermotectonic development of Mount Kinabalu, Sabah, Malaysia: Constraints from low-temperature thermochronology. *Department of Earth Science, Royal Holloway, University of London.* PhD.

Stauffer, P.H. (1968). Studies in the Crocker Formation, Sabah, Borneo Region. *Malaysia. Geol. Surv. Bull.* **8**, pp. 1-13.

Steinshouer, D.W., Qiang, J., McCabe, P. and Ryder, R.T. (1997). Maps showing geology, oil and gas fields, and geological provinces of the Asia Pacific Region. *US Geological Survey Open-File Report*. **97**, 470F.

Stern, C.R. and Wyllie, P.J. (1981). Phase relationships of I-type granite with H2O to 35 kilobars: The Dinkey Lakes biotite-granite from the Sierra Nevada Batholith. *Journal of Geophysical Research*. **86**, B11, 10412-10,422.

Stern, R.J., Reagan, M., Ishizuka, O., Ohara, Y. and Whattam, S. (2012). To understand subduction initiation, study forearc crust: To understand forearc crust, study ophiolites. *Lithosphere*.

Streckeisen, A. (1976). To each plutonic rock its proper name. *Earth-Science Reviews*. **12**, 1, 1-33.

Suggate, S., Cottam, M., Hall, R., Sevastjanova, I., Forster, M., White, L., Armstrong, R., Carter, A. and Mojares, E. (2013). South China continental margin signature for sandstones and granites from Palawan, Philippines. *Gondwana Research*.

Sun, S.-S. and McDonough, W. (1989). Chemical and isotopic systematics of oceanic basalts: implications for mantle composition and processes. *Geological Society, London, Special Publications*. **42**, 1, 313-345.

Swauger, D., Bergman, S.C., Graves, J., Hutchison, C.S., Surat, T., Morillo, A.P., Benavidez, J.J. and Pagado, E.S. (1995). Tertiary stratigraphic, tectonic, and thermal history of Sabah, Malaysia: results of a 10 day reconnaissance field study and laboratory analyses. *ARCO International Oil and Gas Co. and ARCO Exploration and Production Technology, unpublished report TRS 95-0036*.

Thirlwall, M. (1991). Long-term reproducibility of multicollector Sr and Nd isotope ratio analysis. *Chemical Geology: Isotope Geoscience section*. **94**, 2, 85-104.

Tu, K., Flower, M.F.J., Carlson, R.W., Xie, G., Chen, C.-Y. and Zhang, M. (1992). Magmatism in the South China Basin: 1. Isotopic and trace-element evidence for an endogenous Dupal mantle component. *Chemical Geology*. **97**, 1–2, 47-63.

Wakita, K., Miyazaki, K., Zulkarnain, I., Sopaheluwakan, J. and Sanyoto, P. (1998). Tectonic implications of new age data for the Meratus Complex of south Kalimantan, Indonesia. *Island Arc*. **7**, 1-2, 202-222.

Wang, X., Cochran, J.R. and Barth, G.A. (1996). Gravity anomalies, crustal thickness, and the pattern of mantle flow at the fast spreading East Pacific Rise, 9°–10° N: Evidence for three-dimensional upwelling. *Journal of Geophysical Research: Solid Earth (1978–2012)*. **101**, B8, 17927-17940.

Wang, Y., Fan, W., Cawood, P.A. and Li, S. (2008). Sr–Nd–Pb isotopic constraints on multiple mantle domains for Mesozoic mafic rocks beneath the South China Block hinterland. *Lithos*. **106**, 3, 297-308.

Whattam, S.A. and Stern, R.J. (2011). The 'subduction initiation rule': a key for linking ophiolites, intra-oceanic forearcs, and subduction initiation. *Contributions to Mineralogy and Petrology*. **162**, 5, 1031-1045.

Yan, Q., Shi, X., Wang, K., Bu, W. and Xiao, L. (2008). Major element, trace element, and Sr, Nd and Pb isotope studies of Cenozoic basalts from the South China Sea. *Science in China Series D: Earth Sciences*. **51**, 4, 550-566.

Yan, Q.S., Shi, X.F., Liu, J.H., Wang, K.S. and Bu, W.R. (2010). Petrology and geochemistry of Mesozoic granitic rocks from the Nansha micro-block, the South China Sea: Constraints on the basement nature. *Journal of Asian Earth Sciences*. **37**, 2, 130-139.

Zhou, b.X., Sun, T., Shen, W., Shu, L. and Niu, Y. (2006). Petrogenesis of Mesozoic granitoids and volcanic rocks in South China: a response to tectonic evolution. *Episodes*. **29**, 1, 26.

Zhou, X.M. and Li, W.X. (2000). Origin of Late Mesozoic igneous rocks in Southeastern China: implications for lithosphere subduction and underplating of mafic magmas. *Tectonophysics*. **326**, 3-4, 269-287.

Chapter 3:

The complex structure and emplacement of composite granitic plutons: Field evidence from Mt Kinabalu, Borneo

"While we were gathering more firewood outside, to keep the stove going through the night, the rain stopped and the clouds blew first into tatters and then into rents big enough to give us a glimpse of the upper mountain for the first time since we had been on its slopes. High above reared a vast naked flank of silver grey rock, like the glistening side of a beached whale breaching the surface of the sea, white-striped with water-falls roaring and glissading down the sheer face"

Sir David Attenborough, 1975

Nature Walk Up Mt Kinabalu, Time-Life Books

Chapter 3: The complex structure and emplacement of composite granitic plutons: Field evidence from Mt Kinabalu, Borneo

Abstract

The three dimensional structure and emplacement history of large silicic plutons is often obscured by erosion, alteration and indistinct composite units. Here we investigate their construction using fresh field observations from the Mt Kinabalu pluton of Sabah, N Borneo, and compare with existing geobarometric estimates and U-Pb zircon ages. The pluton was emplaced at shallow depths (<12km) at the contact between the ultramafic basement and overlying sediments between 7.85 and 7.22 Ma as five major units in a top-down, laccolith style. Field evidence shows that each unit was emplaced laterally and accommodated by upward deformation of the overlying sediments, with each subsequent pulse emplacing beneath those that precede it and intruding around their external contacts. Remapping the mountain revealed a later porphyritic unit, (not previously mapped), forming the SE of the mountain and a vertical planar biotite granite body in its central region. These new units and interpreted structure contrast with previous work on the mountain. Almost all internal intrusive contacts are sharp, implying crystallisation of each unit in the ~0.2 My intervals between each composite pulse of magma. Structural data indicates emplacement in an extensional setting related to regional Neogene extension in SE Asia.

Introduction

The 4095m high granite mountain of Mt Kinabalu in the Malaysian state of Sabah, NW Borneo (Fig. 3.1), is a striking landmark and a national symbol. Standing 1500m higher than the surrounding peaks of the Crocker Mountains, it is the highest peak between the Himalayas and Papua New Guinea. However, no detailed mapping of the pluton has been published for four decades, largely due its relief and the inaccessibility of its rainforest covered flanks. Here we present the first new map of the pluton since Jacobson (1970), describing the petrology of the multiple granitic units composing it, their relationship to each other and the surrounding country rock, and the structures within them.

Our understanding of the ascent and emplacement of granitic intrusions has changed drastically in the past decades from models of large diapirs ascending slowly through the crust to models of rapid dyke-fed ascent and layered, laccolith-style emplacement of composite plutons (e.g. Clemens and Mawer, 1992, McCaffrey and Petford, 1997, Cruden, 1998, Petford and Clemens, 2000, Petford *et al.*, 2000, Cruden and McCaffrey, 2001). However, as most of this understanding is based on highly eroded bodies missing much of their upper and peripheral material the large scale construction of intrusive bodies in three dimensions is still being investigated (e.g. Leuthold *et al.*, 2012). Mt Kinabalu provides an opportunity to study this further as its glaciated summit provides almost total exposure and a vertical range of 2900m of granitic outcrops allows the potential to map its structure in three dimensions. Existing U-Pb zircon dates for its composite units also allow us to place temporal constraints on the pluton's emplacement.

The regional tectonics of SE Asia in the Cenozoic are ambiguous, but given the geological complexity of the region and its substantial petroleum reserves they are of continuing interest. By combining structural data and field observations of this pluton's emplacement with published U-Pb zircon ages for the different units more precise interpretations of the regional tectonics can be made for the region.

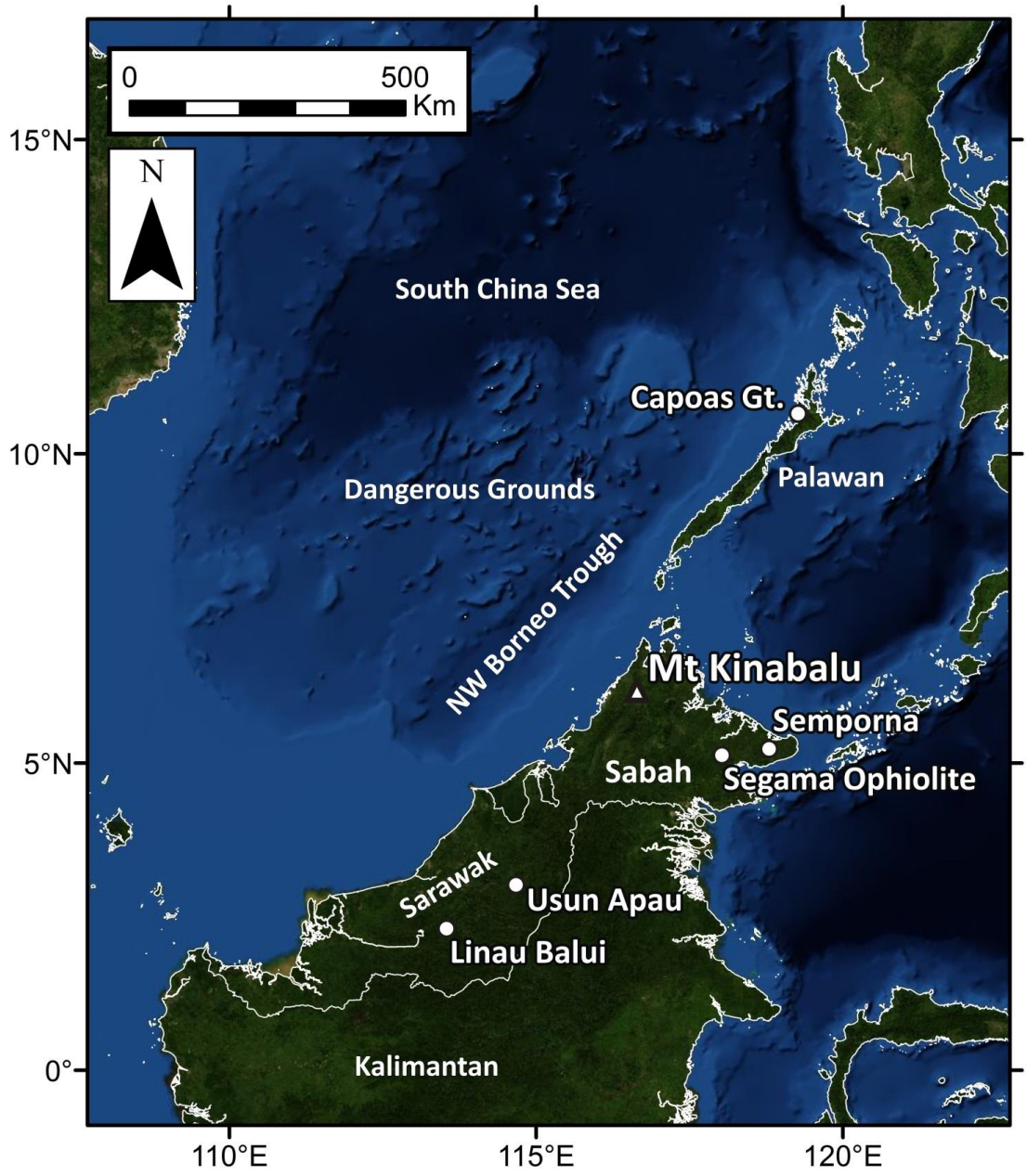

Fig. 3.1. Regional map of Borneo, Palawan and the South China Sea, with localities referred to in the text.

Regional Geological History and Tectonic Setting

The formation of Mt Kinabalu is intrinsically related to the geological and tectonic history of Sabah in N Borneo and the South China Sea region (Fig. 3.1). Most of Sabah is underlain by an ophiolitic basement (Fig. 3.2), dominantly composed of peridotites with associated amphibolitised gabbroic and basaltic units and overlying submarine volcanic rocks and cherts. This supra-subduction zone ophiolite was emplaced at approximately 200 Ma (Leong, 1974, Leong, 1998, Coggon *et al.*, 2011, see Chapter 1) during the initiation and early period of subduction of the western Pacific plate beneath South China and SE Asia. The development of the early Pacific arc in this region resulted in later intrusive and extrusive arc magmatism in the ophiolite and the development of prolonged and extensive magmatism in East Asia (see Chapter 2), stretching from the Schwaner granite mountains of Kalimantan in SW Borneo (Moss, 1998), the Dalat granites of Vietnam (Nguyen *et al.*, 2004), the granitic crust of the South China Sea continental shelf (Yan *et al.*, 2010), the volcanic and intrusive magmatism of Hong Kong (Davis *et al.*, 1997) and the widespread, largely granitic Yanshanian belt in S. China (Zhou and Li, 2000). This magmatic belt persisted across S. China and SE Asia until 79 Ma (Zhou and Li, 2000) when the arc migrated eastwards.

Following this period the region underwent extension, resulting in deposition of the Late Cretaceous to Late Eocene Rajang group (Balaguru, 2001). This is a sequence of deep marine turbidite sedimentation into the large SW-NE trending Crocker Basin of NW Borneo (Fig. 3.2). The Late Eocene unconformity marking its uppermost stratigraphic limit resulted from the Sarawak orogeny (Hutchison, 1996). This regional extension also resulted in the Paleogene volcanism of South China between 64 and 43 Ma (Chung *et al.*, 1997) followed by spreading of the South China Sea (SCS), dated using marine magnetic anomalies to between 31 and 20.5 Ma (Taylor and Hayes, 1983, Briais *et al.*, 1993, Barckhausen and Roeser, 2004). Three models are proposed for this extension (Fig. 3.3): (1) The extrusion model (Tapponnier *et al.*, 1986) in which the India-Asia collision resulted in the South China Sea being pulled open by displacement along laterally extensive strike slip faults; (2) The subduction model (Hall, 2009), in which southward directed subduction of the Proto-SCS along NW Borneo resulted in rifting through slab pull; (3) The continental rift basin model (Cullen *et al.*, 2010) in

which a combination of far-field stresses from slab roll back along Java and Sumatra and extrusion in SE Asia resulted in southward crustal extension. Whichever model is true, extension of the SCS thinned and rifted continental crust that had originally formed along the Mesozoic arc of S. China, ultimately forming the SCS oceanic basin along its SW-propagating spreading centre and causing NW-SE extension.

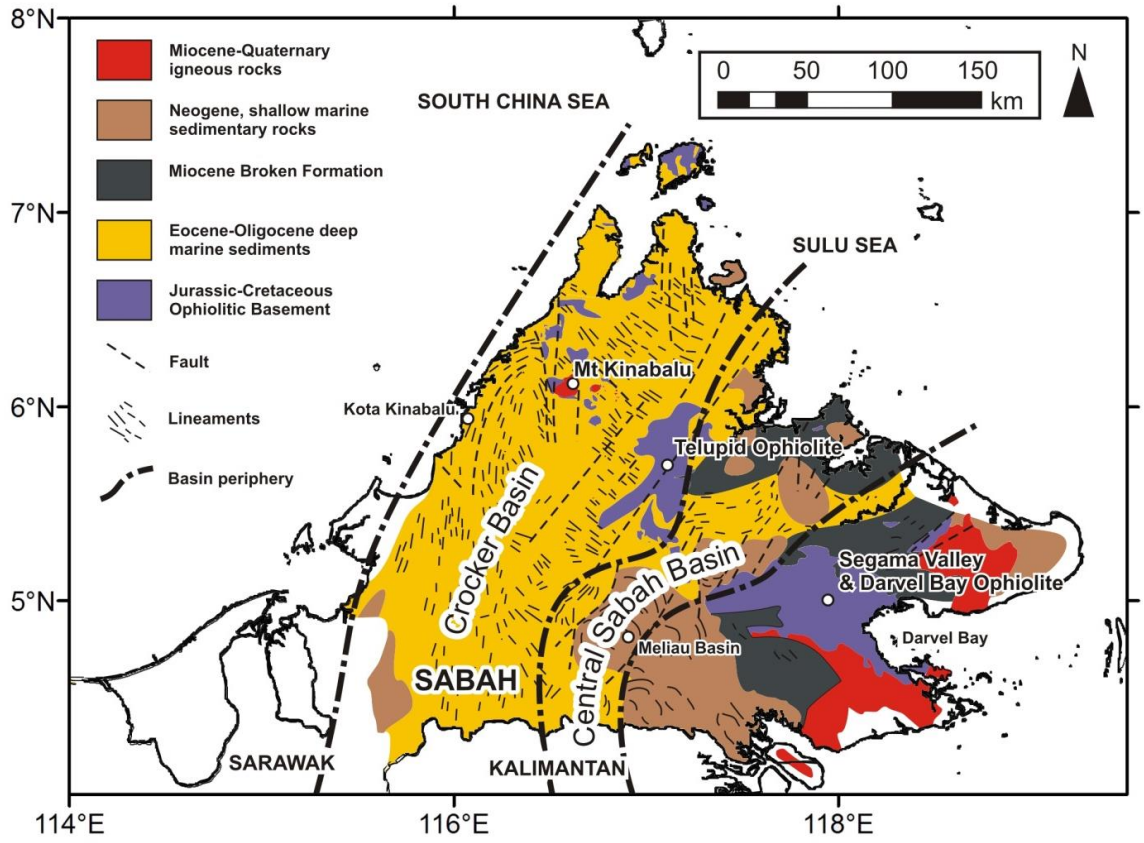

Fig. 3.2 Simplified geological map of Sabah, adapted from Kirk (1968), Balaguru and Nichols (2004) and Hutchison (2005).

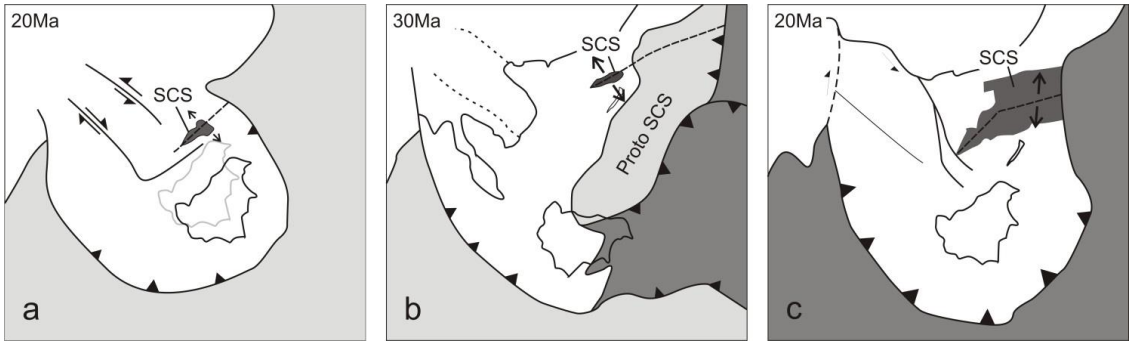

Fig. 3.3. Miocene tectonic illustrations of the proposed models for the opening of the South China Sea: (a) The extrusion model (Tapponnier *et al.*, 1986), (b) The subduction model (Hall, 2002), and (c) the continental rift model (Cullen, 2010). Adapted from Cullen (2010).

During this period of SCS extension, turbidite deposition of the Crocker Formation continued in Sabah (van Hattum *et al.*, 2013). The cessation of extension and SCS spreading is recorded in the sediments of onshore and offshore Sabah by the multiple unconformities of the protracted inversion event of the Sabah Orogeny between ~20 and 9 Ma (Hutchison, 1996, van Hattum *et al.*, 2013). In the subduction model this is attributed to the collision of the Dangerous Grounds continental crust attenuated from the S. China margin, which now forms the continental shelf of the southern South China Sea (Fig. 3.1), with NW Borneo. Alternatively the unconformities may represent far-field compression associated with the NW-directed subduction of the Celebes Sea beneath SE Sabah (Cullen, 2010).

Renewed extension following the Sabah Orogeny in the Late Miocene (Hall, 2013) resulted in regional uplift in Sabah and progradation through the Miocene into the Pliocene and led to increasingly shallower deposition of carbonates and shallow marine to fluvial deltaic deposits of the Serudong Group (Balaguru, 2001). This renewed extension also coincided with the production of scattered Late Cenozoic magmatism in the South China Sea region (Fig. 3.1), including the Mt Kinabalu intrusion (7.85 - 7.22Ma, Cottam *et al.*, 2010), the Capoas intrusion of Palawan (13.5Ma, Suggate *et al.*, 2013), the Scarborough Sea Mounts in the SCS (13.9 - 1.6Ma, Tu *et al.*, 1992, Yan *et al.*, 2008), extrusive and intrusive magmatism in Sarawak (Kirk, 1968) including the Usun Apau volcanics of Sarawak (4Ma, Cullen *et al.*, 2013), the Semporna volcanics of Eastern Sabah (3Ma, Chiang, 2002, Macpherson *et al.*, 2010) and magmatism in Kalimantan,

including the Metulang Plateau and Nuit volcanics (4.9Ma, Moss *et al.*, 1997) and the Keramu river minette dykes (8Ma, Bergman *et al.*, 1988).

Previous Studies on Mt Kinabalu

A limited number of field studies on the geology of Mt Kinabalu have been published since 1951 (Reinhard and Wenk, 1951, Collenette, 1958, Kasama *et al.*, 1970), the most detailed being the study by Jacobson (1970), which includes the most recent and detailed geological map of the mountain and the lithologies to the south on the Pinosuk plateau. The mountain was even less accessible in 1970, with the park boundary being 20km further to the south, covering the present Mesilau village (Fig. 3.4) and extensive Menteki cabbage fields with dense, extremely diverse lowland rainforest. In addition, Sayap village and its access road were also non-existent, so the study was unable to reach the north flank of the mountain and the lack of the Mesilau trail on the southern flanks limited observations away from the streams in this area. With more extensive rainforest and a much poorer transport system, access was very limited and mainly followed the lowland streams south of the mountain.

In addition, geochemical studies have been published by Vogt & Flower (1989) (using the samples of Jacobson, 1970), Chiang (2002) and Sperber (2009) using new samples, and (Cottam *et al.*, 2010, 2013) (using the samples of Sperber, 2009) who also published a new interpretation of the structure of the pluton and its uplift rates based on U-Pb and fission track ages.

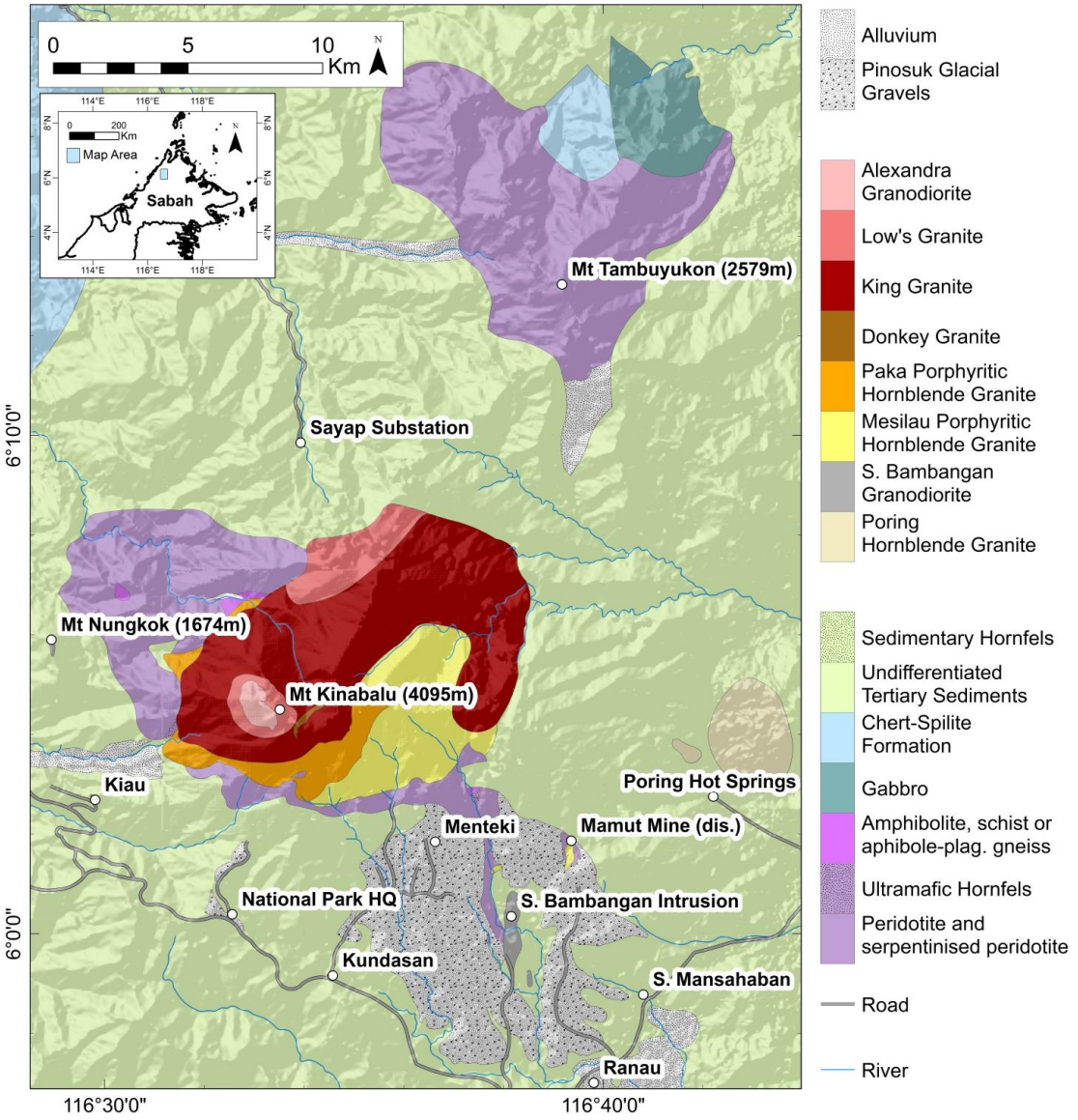

Fig. 3.4. Geological map of the region around Mt Kinabalu, combining observations of this study with the maps of Kirk (1968) and Jacobson (1970).

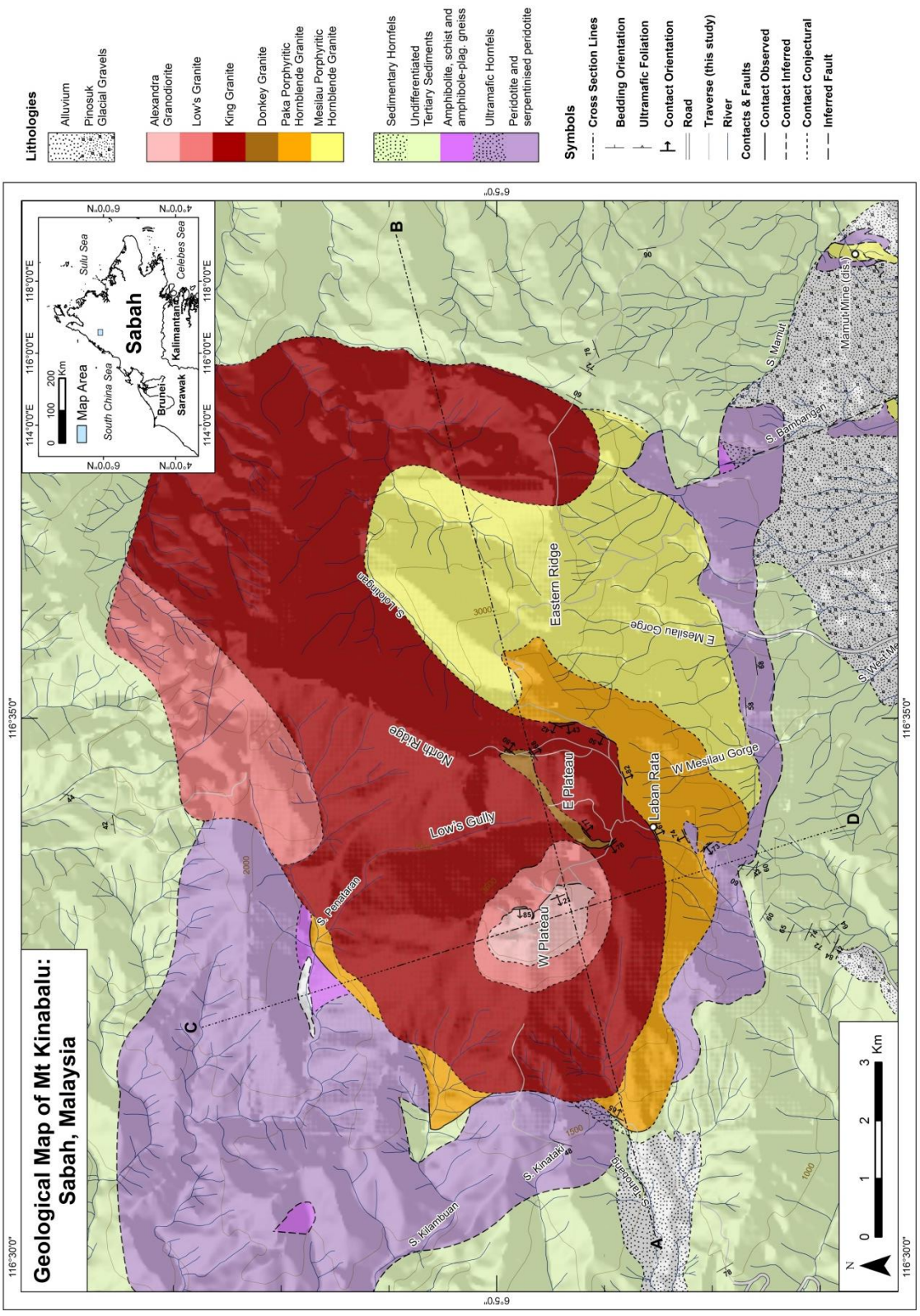

Fig. 3.5. Geological Map of Mt Kinabalu, combining observations of this study with the map of Jacobson (1970). Inset shows regional geography and study area.

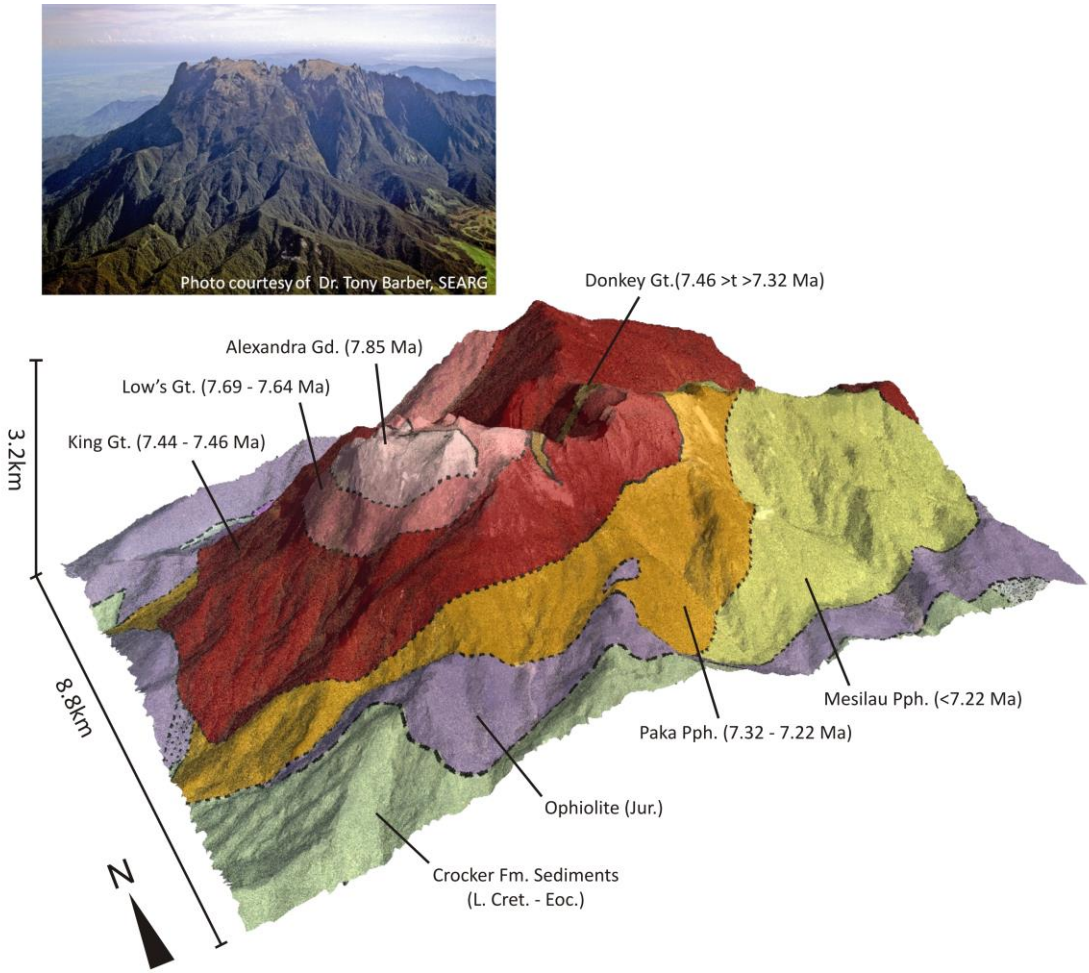

Fig. 3.6. New geological map overlain on DEM of the mountain and aerial photo of the same view for comparison (photo courtesy of Dr Tony Barber, SEARG). Symbols as in Fig. 3.2. Ages of granitic units from Cottam *et al.* (2010).

Geology

The pluton is composed of multiple granitic units with scattered satellite intrusions, and is intruded into a predominantly ultramafic ophiolitic basement overlain by turbidite sediments. A new geological map of the mountain is shown in Fig. 3.5, and Fig. 3.4 shows the geology of the local area and localities around Mt Kinabalu. In Fig.3.6 the map of the pluton is overlain on a digital elevation model of the mountain, illustrating the relationship between the geology and the topography. The summit plateaux are shown in more detail in Fig. 3.7 including the peak names referred to in the text. Due to the inaccessibility of most of the mountain, observations were restricted to the plateaux regions and the routes of traverses made on the mountain's ridges, valleys

and flanks, as indicated on Fig. 3.5. The primary focus was to observe the nature of each unit's contacts and their distribution, as well as observe structures within the pluton and collect samples for geochemical and Anisotropy of Magnetic Susceptibility (AMS) analysis (Chapter 4). The map is constructed by integrating new field observations with the maps of previous studies (Kirk, 1968, Jacobson, 1970, Imai, 2000). Contacts marked as "observed" include those of this study and Jacobson (1970).

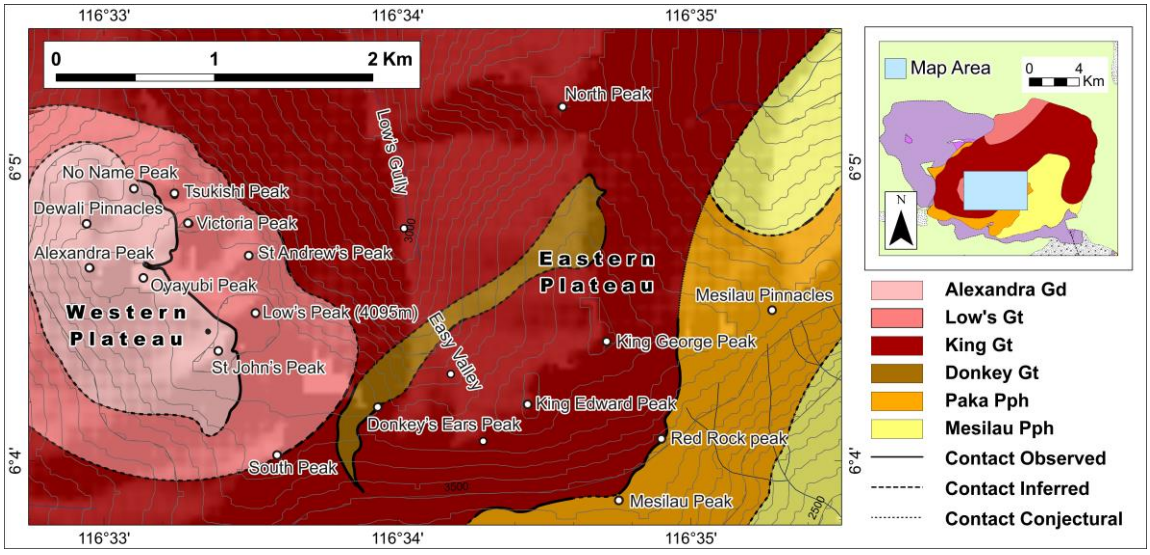

Fig. 3.7. Summit map of the Western and Eastern plateaux of Mt Kinabalu, separated by Low's Gully, showing the geological interpretation and peak names referred to in the text.

Country rocks

Ophiolitic Basement

The ophiolitic basement is the oldest lithological suite in Sabah, and underlies much of the region (Fig. 3.2). Its age, chemistry and emplacement are discussed further in Chapter 2. It is dominantly composed of peridotites with associated amphibolitised gabbroic and basaltic units and overlying submarine volcanic basalts and cherts. This supra-subduction zone ophiolite was initially emplaced at approximately 200 Ma (Leong, 1974, Leong, 1998, Coggon *et al.*, 2011, see Chapter 2) during the initiation and early period of subduction of the western Pacific Plate beneath South China and SE Asia

and continued to be intruded by mafic arc magmatism throughout the Jurassic and Cretaceous.

The ophiolite outcrops in the Mt Kinabalu area are ultramafic rocks with varying degrees of serpentinisation, forming a 0.5km to 2km thick band on the south of the mountain and a large area to the north-west. The most predominant ultramafic lithology is lherzolite, but wehrlites, harzburgites and dunite also occur (Jacobson, 1970). The ophiolite also forms the country rock of the mineralised Mamut satellite body to the SE (Imai, 2000) and Mt Tambuyukon to the NE (Fig. 3.4). Mt Tambuyukon is a large NW-SE trending fault block of ophiolite composed mainly of ultramafics with gabbro and dolerite on its eastern flank (Kirk, 1968), and is the second highest peak in Borneo (2579m). The extent of the ultramafic outcrops around Mt Kinabalu can be easily determined in the field and from satellite photographs due to the appearance of the different vegetation. Ultramafic soils are nutrient poor and enriched in Mg and Ni, rendering them toxic for most plants that have not evolved an adaptation (Baillie *et al.*, 2000). This change in vegetation results in a noticeably darker appearance in aerial photographs which was confirmed in the field by vegetation changes over just a few metres at the contact. In the field the extent of the unit is also easily determined by the bright orange soils it produces.

Imai and Ozawa (1991) recorded hydrated garnet peridotite float in the S. Mansahaban riverbed, south-east of Mt Kinabalu. These were located and sampled in the field during this study, and are discussed in Chapter 2. Although none of the rocks were seen in outcrop the river contained a varied mix of lithologies representing a near-complete suite of ophiolite rocks, including granite, garnet pyroxenites, amphibolite, garnet amphibolite, garnet-zeolite amphibolite and amphibolite-plagioclase gneiss, amygdale-rich basaltic volcanics and chert. Similar rocks are described from the ophiolite in the Darvel Bay region by Leong (1974), Hutchison (1978) and Omang and Barber (1996).

Jacobson (1970) maps a unit described as “crystalline basement” at a small number of locations within the ophiolite. The unit is described as comprising actinolite schist, plagioclase-hornblende gneiss and biotite-hornblende schist and is interpreted by Jacobson (1970) as small wedges of an older crystalline basement beneath the

ultramafic sequence. The outcrops described were not observed on the traverse to S. Bambangan where it is mapped by this previous study and the S. Penataran outcrop is inaccessible except during particularly dry periods. However, the descriptions are very similar to the Mansahaban river float and so may also represent metamorphosed units of the ophiolite sequence.

Crocker Formation

Overlying the ophiolitic basement is an extensive formation of turbidite sediments. Collenette (1958) and Jacobson (1970) differentiate this Eocene to Lower Miocene sedimentary sequence into the Crocker Formation and the Trusmadi Formation. The Trusmadi Formation is a sequence of slates and dark mudstone beds with occasional volcanics and sandstone beds, and the Crocker Formation is a sequence of interbedded shales, mudstones and sandstones with occasional massive sandstone units. The traverses of this study only crossed the Crocker Formation, which was observed as a sequence of interbedded mudstones and sandstones. The mudstones are grey or orange in appearance, whilst the sandstones weather to a pale orange, but usually appear pale grey on fresh surfaces. Point counting of 29 sandstone samples by Jacobson (1970) classified them as quartzarenite to subarkose in composition, composed of poorly sorted, very fine to coarse (0.1 – 0.5mm) subrounded to subangular grains, with the coarser beds being more poorly sorted and angular than the finer beds. Their point counted modal mineral composition is 48% quartz, 4% feldspar, 3% chert grains, 2% other lithics and 40% matrix and cement, composed of an aggregate of sericite, chlorite, silica and carbonate, plus varying detrital grains of biotite, muscovite, hornblende, zircon, monazite, rutile and tourmaline.

The Granitic Units

The main body of the Mt Kinabalu can be divided into five distinct granitic units. These are: the “Alexandra Peak” Biotite Tonalitic Granodiorite (Alexandra Gd); the hornblende granite units of the “Low’s Peak” High Ti Hornblende Granite (Low’s Gt)

and the “King George Peak” Low Ti Hornblende Granite (King Gt); the “Donkey’s Ears Peak” Biotite Granite (Donkey Gt); the “Paka” Porphyritic Hornblende Granite (Paka Pph), and the “Mesilau” Porphyritic Hornblende Granite (Mesilau Pph). In all previous work, the Paka Pph and the Mesilau Pph were both classified as variants of a single porphyritic unit with minor areas of larger phenocrysts. However, we observed both units to be distinct in their mineralogy and extent. Additionally, the two hornblende granites (Low’s Gt and King Gt) are principally distinguished based on their major element composition and magnetic mineral fabrics (see Chapters 4 and 5) as they are indistinguishable in hand specimen. Of the geochemical distinctions between the two units Ti is the clearest (Chapter 5) showing a distinctly higher concentration in the Low’s Gt (0.63-0.83wt% Ti) than the King Gt (0.41-0.55wt% Ti).

The granitic units have been classified and named in the literature under different terms with different modal assemblages (compared in Cottam *et al.*, 2010). The most comprehensive modal abundance data is that of Sperber (2009) which was based on point counting of 36 sections of which 22 were stained for K-feldspar. The modal proportions for these units are presented in Fig. 3.8a. Mineralogy discussed here is largely based on the Sperber (2009). However, the Donkey Gt and the Mesilau Pph were not identified as separate units prior to this study, so thin sections were stained according to the methodology of Hutchison (1974) for K-feldspar and plagioclase and point counted for classification. It is important to note that there is a discrepancy between the modal mineralogical classification and classification by major elements (Fig. 3.8b) as the modes give granite to tonalitic granodiorite classifications according to the IUGS-Streckeisen system (Streckeisen, 1976), whereas the TAS major element classification gives more mafic diorite to granodiorite classifications.

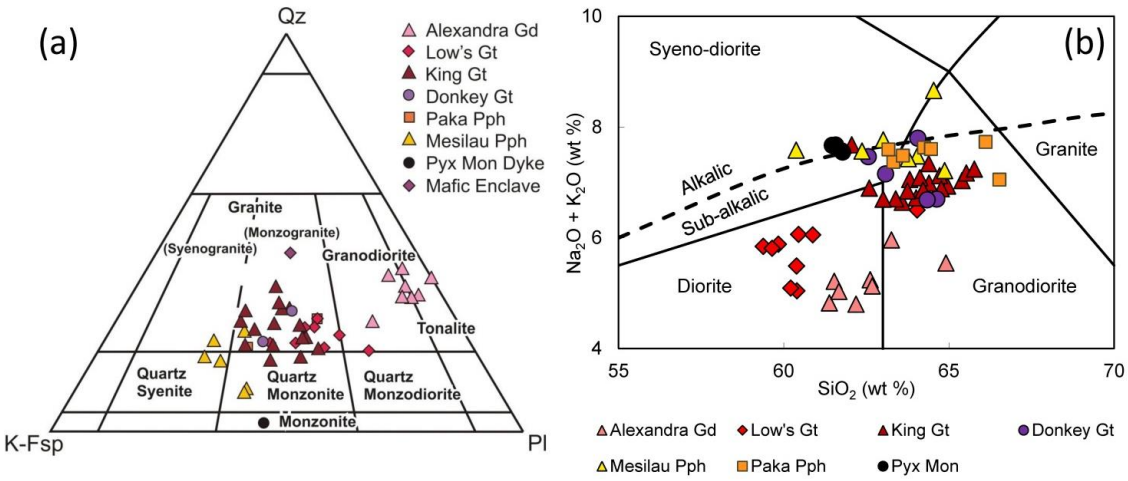

Fig. 3.8. Classification of the Mt Kinabalu granitoids, according to: a, the modal IUGS-Streckiesen classification (Streckeisen, 1976) and b, the TAS classification (Hutchison, 1988, Hutchison, 1989).

Ages presented here for each unit are from SHRIMP U-Pb dating of zircon (Cottam *et al.*, 2010) from nine different locations on the mountain. They are summarised, along with the approximate volume of each major unit and their mineralogy in Table 3.1. In order of emplacement, the main granitic units are described as follows:

(1) The **Alexandra Gd** was the emplaced at 7.85 ± 0.08 Ma and crops out over an area of 2km by 1km and a vertical range of 300 to 600m. The unit forms some of the highest elevations on the Western Plateau, encapsulating the western summit peaks (Fig. 3.7). It is composed of crystals 1 to 3mm in length, with modal proportions of 4-7% K-feldspar, 40-45% plagioclase, 23-28% quartz, 4-13% hornblende, 9-19% biotite and apatite and epidote observed as accessory phases. In the field foliation of the biotite crystals is observed to dip at ~40-65^{o} to the south-west in agreement with Jacobson (1970). All of the granite units show some alteration of hornblende to secondary biotite, but this is particularly prevalent in the Alexandra Gd.

(2) The **Low's Gt** was emplaced at 6.69 ± 0.07 Ma – 7.64 ± 0.11 Ma below and around the Alexandra Gd on the Western Plateau, encapsulating its eastern and southern peaks (including Low's peak, the highest point on the mountain). It covers an area of approximately 2km by 3km, with a maximum vertical range of

~200m, although due to its identical appearance to the King Gt and location of its contacts on the steep flanks of the Western Plateau much of its contact is inferred from chemical and magnetic data. The Low's Gt also crops out in a separate, unconnected region on the northern flank of the mountain (Fig. 3.5) but the contact here is even less accessible and is inferred from topography. The Low's Gt is composed of 4 to 7mm long hornblende phenocrysts in a groundmass of 1 to 4mm long K-feldspar, plagioclase, hornblende and biotite crystals. Modal proportions on the Western Plateau are 18-22% K-feldspar, 30-32% plagioclase, 16-21% quartz, 21-27% hornblende, 5-7% biotite and accessory apatite, epidote and zircon. The proportions in the northern outcrop samples are more K-feldspar and quartz rich than samples from the Western Plateau indicating a more evolved melt for the northern body with 21-29% K-feldspar, 25-33% plagioclase, 21-28% quartz, 21-28% hornblende and 4-7% biotite.

(3) The **King Gt** was emplaced at 7.46 ± 0.08 Ma – 7.44 ± 0.09 Ma beneath the Low's Gt and is the most extensive unit on the mountain, covering an area of approximately 15km by 8km with a maximum interpreted vertical extent of approximately 2500m (observed maximum extent is 2100m). This encapsulates the majority of the western and northern flanks, the North Ridge and the Eastern Plateau. It has the same crystal sizes as the Low's Gt, with modal proportions of 26-36% K-feldspar, 21-38% plagioclase, 14-27% quartz, 9-21% hornblende, 0-5% biotite and observed accessory apatite, epidote and zircon.

Although Jacobson (1970) and Sperber (2009) noted common hornblende lineations in the King Gt, none were observed in this study. This lack of a common observable crystal orientation was confirmed by thin section image analysis, implying that visible orientation of the mafic minerals in this unit is sparse and localised.

(4) The **Donkey Gt** has not been dated, but its intrusive contact with the Low's Gt implies that the Donkey Gt followed this intrusion. It was previously described by Jacobson (1970) as the minor "biotite adamellite porphyry". It has been found to be much more extensive than previously mapped, cropping out on the Western Plateau, Easy Valley 600m below it (the glaciated hanging valley forming the top end of the infamous Low's Gully), and on the Eastern Plateau,

although it is impossible to map a contact between these points given the enormous cliffs of the gully separating the two plateaux. The relative locations of these outcrops imply the unit to be a large NE trending sub-vertical planar unit, 2.5km long and 200m thick.

Mineralogically the Donkey Gt is very similar to the Alexandra Gd but has an appearance and crystal size more similar to the King Gt it intrudes. The unit is slightly darker than the King Gt and flow banding is common, especially near the contacts. It is composed of hornblende, biotite and plagioclase phenocrysts up to 4mm long in a finer groundmass of hornblende, biotite, plagioclase, quartz and K-feldspar. The modal proportions are 25% K-feldspar, 26% plagioclase, 23% quartz, 11% hornblende, 13% biotite (plus an additional 2% of secondary biotite derived from magmatic hornblende) and apatite was observed as an accessory phase.

(5) The **Paka Pph** was emplaced at 7.32 ± 0.09 Ma – 7.22 ± 0.07 Ma along the southern flank of the mountain, along the southern and eastern flanks of the Eastern Plateau and as occasional dykes in the country rock. It was also found by Jacobson (1970) to crop out at lower elevations in river valleys on the north western flanks of the mountain, although was not found during this study when ascending the ridges between these valleys. The unit ranges in width up to 2km and covers an area of about 10km^2. It forms the lowest elevation of the granite at ~1150m at its westernmost outcrop in S. Tahobang (06^{o}03’54”N 116^{o}31’17”E, Fig. 3.5) and has a maximum vertical outcrop range of approximately 2500m.

The Paka Pph appears darker grey in outcrop than the King Gt. It contains conspicuous megacrysts of K-feldspar 10 to 15mm in length in a groundmass of 2 to 5mm crystals of K-feldspar (23-35%), plagioclase (23-33%), quartz (15-21%), hornblende (22-24%), biotite (1-2%) and accessory apatite. A preferential lineation of the megacrysts is often observed, as noted by Jacobson (1970) and Sperber (2009). This alignment of this lineation often deviates in orientation across a single outcrop, but its plunge was invariably shallow (<26^o) and when near a contact the azimuth would be orientated sub-parallel to the contact surface.

(6) **The Mesilau Pph** has not been dated, but was emplaced after the Paka Pph within the southeast of the pluton where it forms the Eastern Ridge and is in contact with a lobe of King Gt to the east and the Paka Pph to the west. Previous studies have mapped the **Mesilau Pph** as a variation of the Paka Pph, but there are clear distinctions in their mineralogy, chemistry and field relations. The Mesilau Pph crops out over an 18km^2 area with a maximum vertical outcrop range of ~1500m. The unit also forms the mineralised satellite stock of the disused Mamut porphyry copper mine, south-east of the mountain (Fig. 3.5). The northern extent of this unit is unknown but two sizeable ridges running north from the eastern ridge between the eastern and western contacts of the Mesilau Pph are interpreted the margins of this unit. The contact with the King Gt in the north-west is inferred from the prominent linear NE-SW trending valley of the Upper Lolotingan River. However, reaching the Upper Lolotingan to test this hypothesis would be very difficult.

The Mesilau Pph differs most notably from the Paka Pph in possessing large 20-30mm long K-feldspar megacrysts, which make up about 30% of the rock. The groundmass consists of 3 to 5mm long crystals with modal proportions of 38-48% K-feldspar, 24-28% plagioclase, 7-21% quartz, 8-23% hornblende, 0-5% biotite, 0-2% climopyroxene and observed accessory apatite and sphene. A preferential megacryst lineation is also commonly observed, although like the Paka Pph this often deviates in orientation across an outcrop.

Unit	Alexandra Gd	Low's Gt	King Gt	Donkey Gt	Paka Pph	Mesilau Pph
U-Pb Age (Ma)	7.85	7.69 – 7.64	7.44 – 7.46	7.46 > t > – 7.32	7.32 – 7.22	-
Approx. Vol. (Km^3)	1	10	75	0.5	40	40
Mineralogy (Modal %)	23 – 28% Qz 40 – 45% Plag 4 – 7% K-Fs 4 – 13% Hb 9 – 19% Bt Accessory ap & ep	16 – 28% Qz 25 – 33% Plag 18 – 29% K-Fs 21 – 28% Hb 4 – 7% Bt Accessory ap, ep & zr	14 – 27% Qz 21 – 38% Plag 26 – 36% K-Fs 9 – 21% Hb 0 – 5% Bt Accessory ap, ep & zr	23% Qz 26% Plag 25% K-Fs 11% Hb 13% Bt Accessory ap	15 – 21% Qz 23 – 33% Plag 23 – 35% K-Fs 22 – 24% Hb 1 – 2% Bt Accessory ap	7 – 21 % Qz 24 – 28% Plag 38 – 48% K-Fs 8 – 23% Hb 0 – 5% Bt 0 – 2% Cpx Accessory ap & sph

Table 3.1. Summary of ages, volumes and mineralogies of the major granitic units. Mineral abbreviations used: Qz – quartz; Plag – plagioclase; K-Fs – Potassium Feldspar; Hb – Hornblende; Bt – Biotite; Cpx – Clinopyroxene; ap – Apatite; ep – Epidote; zr – Zircon; sph – Sphene.

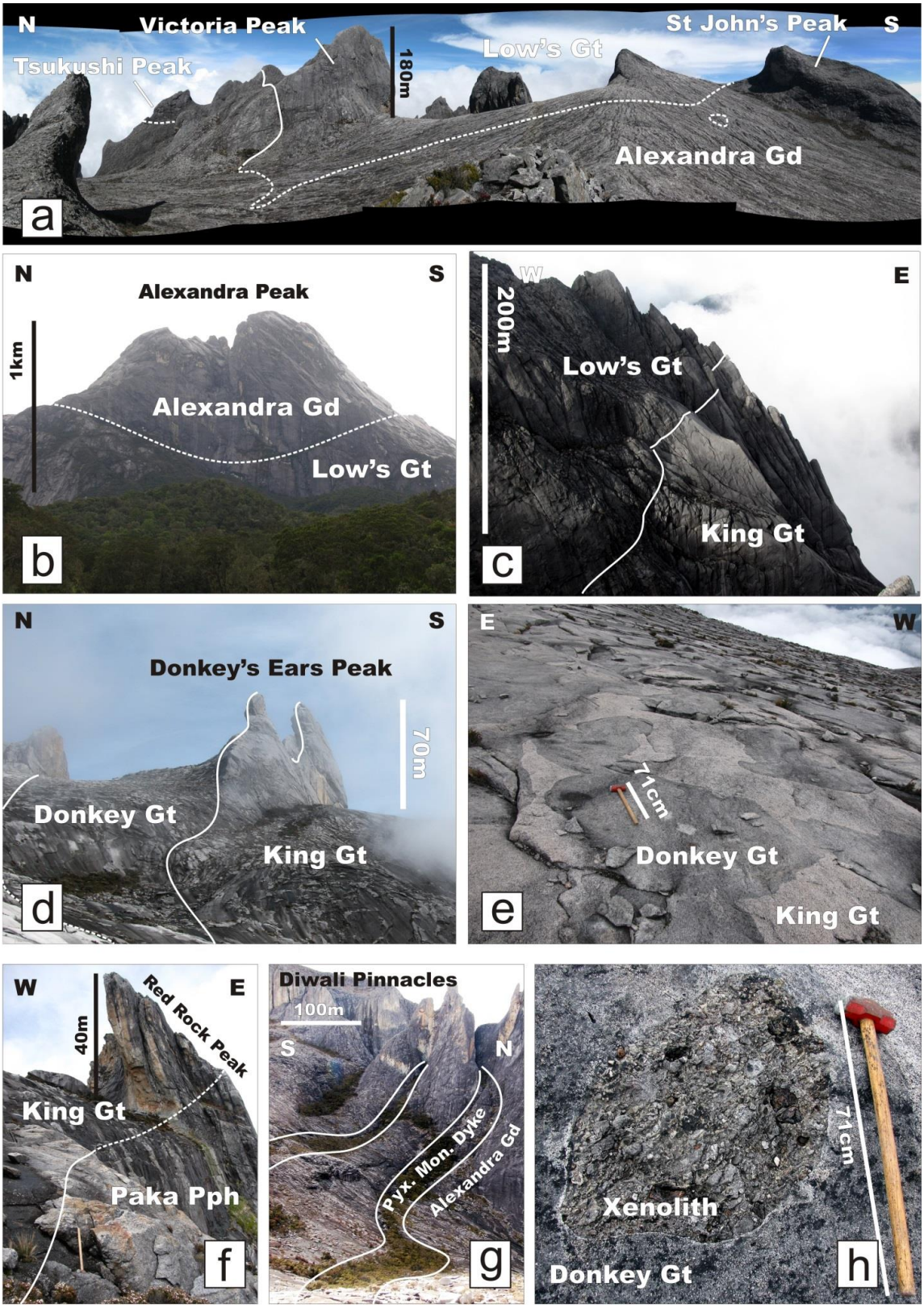
N
Victoria Peak
Tsukushi Peak
180m
Low's Gt
St John's Peak
S
Alexandra Gd
a
N
S
Alexandra Peak
1km
Alexandra Gd
Low's Gt
b
W
E
200m
Low's Gt
King Gt
c
N
S
Donkey's Ears Peak
70m
Donkey Gt
King Gt
d
E
W
71cm
Donkey Gt
King Gt
e
W
E
40m
Red Rock Peak
King Gt
Paka Pph
f
Diwali Pinnacles
100m
S
N
Pyx. Mon. Dyke
Alexandra Gd
g
71cm
Xenolith
Donkey Gt
h

Fig. 3.9. Selected field photos from Mt Kinabalu. Solid white lines indicate sharp contacts and dashed lines indicate inferred contacts.

(a) View of the Western Plateau looking east, showing the contact between the Alexandra Gd (foreground) and the Low's Gt. Field of view ~1.3km
(b) Inferred contact between the Alexandra Gd and Low's Gt on the west face of the Western Plateau. Photo looking East from Marai Parai. Field of view ~2.5km
(c) Contact of the Low's Gt and King Gt units on the eastern face of St Andrew's Peak, above Low's Gully. Photo looking N from Low's Peak. Field of view ~300m along cliff face.
(d) Contact of the Donkey Gt within the King Gt showing the resulting topographic feature of the Donkey's Ears Peak. Photo looking NE from the summit trail.
(e) Magma mingling between The Donkey Gt (dark grey unit) and the King Gt (light grey unit) on NW contact. Photo looking S. Sledgehammer (71cm long) for scale.
(f) Contact between the King Gt and Paka Pph on the E of the Eastern Plateau, showing the Paka Pph dipping beneath the King Gt. Photo looking N.
(g) Pyx. Mon. dykes intruding the Alexandra Gd on the N end of the Western Plateau, showing their effect on the topography. Photo looking W.
(h) Conglomerate xenolith within the Donkey Gt on the Western Plateau. Sledgehammer for scale.

Dykes

As well as the larger intrusions, numerous dykes of pyroxene monzonite, aplite, pegmatite, lamprophyre and diorite intrude the mountain.

Pyroxene Monzonite dykes (Pyx Mon dykes) form large, parallel ENE to WSW trending intrusions up to 20m wide crossing each summit plateau and are exposed for >1km vertically on the west face. Their preferential erosion compared to the other granitic units produces a number of the large linear depressions across the plateau and many of the gaps between the Diwali Pinnacles (Fig. 3.9g). These dykes contain porphyritic clinopyroxene and K-feldspar in a groundmass of quartz and feldspar and are composed of 2% quartz, 33% plagioclase, 40% K-feldspar and 10% clinopyroxene, plus 13% secondary chlorite with residual biotite and 2% magnetite. Some dykes were found with K-feldspar phenocrysts up to 15mm long preferentially orientated parallel to the walls of the dyke.

Aplite dykes are very common on the summit area, especially on the Western Plateau, ranging in width from 1cm veins to 20m dykes. These K-feldspar and quartz rich features represent late stage crystallisation of highly fractionated interstitial melt within faults and fractures.

Pegmatite also represents the emplacement of residual melt, but was only found in one piece of float on the Western Plateau and not observed *in situ*. The observed sample was composed of plagioclase and hornblende, with hornblende phenocrysts up to 15mm in length.

A **lamprophyre** dyke was observed on the Western Plateau and classified as a minette (Mitchell, 1994). This dark grey, 5 to 20cm wide dyke is composed of 4mm hornblende and 2mm plagioclase phenocrysts in a fine grained groundmass of plagioclase, K-feldspar, quartz, biotite and hornblende. Flow banding and King Gt xenoliths were observed in the dyke, as well as evidence of deformation indicating the dyke to be intruded along a shearing fault. We interpret this dyke to represent the late stage intrusion of volatile-rich residual melt produced through fractionation of its King Gt host (Mitchell, 1994).

Numerous **diorite** dykes, up to 10m wide, cut the summit trail in the 500m before the contact of the sedimentary unit with the ultramafics. Another intrudes the lower summit trail contact of the Paka Pph and the ultramafics and a number of small diorite dykes are found on the summit. These are fine grained, dark grey and composed of 0.5 to 2mm wide crystals with mineral proportions of approximately 10% quartz, 60% feldspar, 20% hornblende and 10% biotite. It is unclear whether these represent the same melt as any of the other units or satellite intrusions, although it clearly post-dates the Paka Pph.

Satellite Intrusions

Based on the map of the Bambangan Valley by Wong (1967), Jacobson (1970) mapped a small linear body of porphyritic granite 3km long by 0.5km wide, 5km south of the main pluton along the S. Bambangan river (Fig. 3.4). On investigation this was found to be a dark grey, fine grained granodiorite (the Bambangan Granodiorite) forming a small north-south trending ridge along the river valley at 1150m elevation. The unit is composed of 1 to 2mm long crystals with mineral proportions of approximately 10% quartz, 10% biotite, 50% feldspar and 30% hornblende. Imai (2000) describes a similar unit intruding the mineralised Mesilau Pph stock of the Mamut mine porphyry copper deposit.

Other satellite intrusions are summarised in Kirk (1968), including the mineralised biotite granite at Mt Nungkok 4.5 km to the west, as well as a highly chloritised satellite body of highly chloritised hornblende granite near the Poring Hot Springs (the Poring Hornblende Granite), 8km east (Fig. 3.4).

Enclaves and xenoliths

Mafic, fine grained sub-rounded enclaves are found in all of the major granitic units, usually only up to 5cm in length but occasionally up to 2m across. They have a similar mineralogy to the host granite but with a higher proportion of mafic minerals, being

composed of 50-55% amphibole, 10-30% plagioclase and 5-10% K-feldspar (Vogt and Flower, 1989). Meta-sedimentary xenoliths are described by Jacobson (1970). The only example seen during this work was a sub-rounded conglomerate xenolith (Fig. 3.9h), measuring 40cm by 60cm, composed of a poorly sorted, sub-angular quartz and fine grained quartzite clasts (3-70mm diameter) in a medium to coarse sand matrix. The origin of this conglomerate xenolith is unclear as similar lithologies are not observed in outcrop around Mt Kinabalu.

Contacts

External Contacts

Due to vegetation and weathering, few contacts of the granite units with the country rock are exposed and so were largely determined from topography and float. The contact of the sediments with the Paka Pph was observed in S. Tahobang on the south-west of the mountain (06^{o}03'54"N 116^{o}31'17"E, Fig. 3.5). Here they have been metamorphosed to a light grey, quartz-rich hornfels of vary fine sutured quartz grains and minor biotite with evidence for relict sedimentary beds. Chlorite forms 10-20% of the rock as interstitial material and veins, and muscovite appears as an interstitial secondary phase.

Ultramafic hornfels is found downstream of the contact of the ophiolite with the granite in the S. Bamabangan river on the south of the mountain (Fig. 3.2). The hornfels contains 60% relict olivine and orthopyroxene with secondary chlorite, serpentinite and talc.

A chilled margin was observed in the granite on the summit trail (06^{o}03'08"N 116^{o}33'51"E) where the Paka Pph is found on the southern contact of a large xenolith of ultramafic country rock interpreted to be approximately 500m long by 200m wide. The ultramafics near the contact have been preferentially weathered to regolith. The southernmost contact on the summit trail of the Paka Pph with the ultramafics has been intruded by a granodiorite dyke, and the ultramafics here are altered largely to talc.

North of the mountain the contact of the sedimentary formation and the pluton was determined from float and scattered outcrops. Sandstone within 2km of the contact has altered to quartzite. Microgranite float on the east side of the mountain indicates a chilled margin with the sedimentary country rock. Jacobson (1970) maps a continuation of this contact to the SW, and also maps observed contacts in S. Kilambuan and S. Penataran on the NW of the mountain. In S. Kilambuan he describes the occurrence of a mica-cordierite hornfels near the contact with cordierite porphyroblasts in a quartz and muscovite groundmass. Although the contact itself is not described by Jacobson (1970) in S. Penataran, he does describe boulders of plagioclase-hornblende gneiss, biotite-hornblende schist and actinolite schist downstream of the contact, representing metamorphic rocks of the ophiolite sequence similar to those observed in S. Mansahaban (Chapter 2).

Internal Contacts

Examples of internal contacts between all of the major granitic units were observed in the field with the exception of those between the Mesilau Pph and the King Gt or the Paka Pph. These contacts were obscured by vegetation but could be determined from topography and float. Most of the contacts are sharp and are indicated by clear changes in topography.

- **Alexandra Gd – Low's Gt contact**

  The eastern contact of the Alexandra Gd with the Low's Gt was observed at a number of locations on the Western Plateau, with the Alexandra Gd overlying the Low's Gt. Along its eastern edge the contact steepens to vertical and in some places, such as on Tsukushi Peak, the Low's Gt is found above the Alexandra Gd, enveloping the older unit (Fig. 3.9a).

  Jacobson (1970) describes the contact of the Alexandra Gd and Low's Gt as "gradational over a distance of 4 feet". The new observations show that the contact is quite variable and there appears to be a relationship between the dip

of the contact and its sharpness. Where the contact is steeply dipping it is sharp, such as across the summit and southern face of Victoria Peak in the northeast of the Western Plateau (Fig. 3.9a). Up to 40cm from the contact here the Low's Gt is highly fractured with numerous aplite dykes and veins cross cutting and running parallel to its surface. Channelling fluids along the contact has precipitated chlorite, epidote and haematite within the Low's Gt. In contrast, to the north and south of Victoria Peak where the dip shallows, the contact becomes gradational over 1 to 3m. Topography on much of the mountain is linked to the internal granitic contacts and on the Western Plateau the dip of the glaciated summit towards the west is sub-parallel to the Alexandra Gd – Low's Gt contact, revealing an irregular contact surface and windows of the upper surface of the Low's Gt exposed within the Alexandra Gd (Fig. 3.9a). From these windows of the later unit within the Alexandra Gd it can be determined that the contact surface beneath the two units dips at approximately 20^{o} to the WSW.

The location of the contact on the West Face is unclear due to the inaccessible 1.5km cliff, but when viewed from the west a noticeable protuberance above the large mass of the Low's Gt and a large band of fracturing crossing the face below this lump is conjectured to be fracturing along or parallel to the contact surface (Fig. 3.9b).

- **Low's Gt - King Gt contact**

  In the field these two units appear identical and so the location of the contact has been largely inferred from laboratory data rather than field observations. The geochemical and Anisotripic Magnetic Susceptibility (AMS) data from the Western Plateau (Chapters 4 and 5) show a clear discrepancy on the south eastern extent of the Western Plateau, constraining the location of this contact to within 200m. The only location on the summit where a likely contact is observed is the outcrop mapped as a leucocratic granite intrusion by Jacobson (1970) on the eastern cliff face of St Andrews Peak on the eastern side of the Western Plateau (Fig. 3.7 and 3.9c), although its location above Low's Gully

renders it inaccessible. The outcrop is observed from the SW as a lighter body of granite (the King Gt) in sharp contact with an overlying darker body (the Low's Gt). The light body darkens gradationally with distance from the contact, and the apparent dip of the contact is approximately 50^{o} to the NW. Dykes of the lighter body intrude the overlying unit, implying that the Low's Gt had solidified in the 0.2My (Cottam *et al.*, 2010) before the King Gt intruded.

- **Donkey Gt – King Gt contact**

  On the Western Plateau the unit Donkey Gt curves towards the NE, with a sharp western contact and a variable eastern contact. The eastern contact is largely gradational although it is observed to be sharp and sub-vertical where it forms the distinctive Donkeys Ears peak (Fig. 3.9d). The contact made the granite here more resistant to glacial erosion than the material around it resulting in the two distinctive planar peaks at the edge of the plateau.

  The western contact is sharp along its length with sub-vertical, contact-parallel flow banding within the Donkey Gt and magma mingling in places (Fig. 3.9e), forming a 10m wide band of rounded bodies of Donkey Gt up to 2m in diameter within the King Gt. This implies that neither body was solid at the time of the Donkey Gt intrusion. Intrusive bodies commonly exploit contacts as planes of weakness. Here the Donkey Gt is close to (~50m separation), but not along the contact between the two Low's Gt and King Gt, implying that the margin of the King Gt had crystallised further than its still liquid core at the time of the Donkey Gt intrusion, which also explains why its eastern contact is more gradational than its western contact.

  The contact was not well constrained in Easy Valley due to the steep topography, but was observed again within the King Gt on the Eastern Plateau where it is sharp and steeply dipping (66-80^{o} to the SE, Fig. 3.5).

- **King Gt – Paka Pph contact**

  The contact of the King Gt with the later Paka Pph was observed in multiple outcrops on the south and eastern flanks of the mountain (between 06°03'50"N 116°34'21"E and 06°04'27"N 116°34'57"E). At all locations it was found to be very sharp, often reflected in the topography due its preferential erosion which created many of the steep cliffs around the Eastern Plateau. Flow banding running sub-parallel to the contact is often present within the Paka Pph for the 50cm nearest the King Gt, and K-feldspar megacrysts in the Paka Pph are also commonly aligned parallel to the contact. On the southern flank where the contact was found below the Laban Rata accommodation, the Paka Pph was notably megacryst-rich close to the contact. Along the southern flanks of the mountain the King Gt – Paka Pph contact is steeply dipping (67-82° S) with the Paka Pph overlying the older unit. The steep cliffs on southern face of Mt Kinabalu mark this contact in the topography. The dip becomes more moderate on the Eastern Plateau (38-44° W) near the Red Rock Peak (Fig. 3.7 and 3.9f) where the Paka Pph underlies the King Gt. Hydrothermal fluids have been channelled along the contact resulting in strong haematite alteration and an orange appearance of the overlying unit, be it the Paka Pph near Laban Rata or the King Gt at the aptly named Red Rock Peak.

- **Mesilau Pph – Paka Pph contact**

  The contact between the Mesilau Pph and the Paka Pph was not observed due to dense vegetation although it may be found with further investigation within the Mesilau Pinnacles (Fig. 3.7) on the eastern edge of the Eastern Plateau. Large gaps within the pinnacles and a notable valley running north from them seem likely evidence of the location of the contact. A sharp change in float on the south of the mountain marks the contact between the two porphyritic units. The units are separated by a north-south trending stream, interpreted as marking the contact.

- **Mesilau Pph – King Gt contact**

  On its eastern extent the Mesilau Pph is in contact with the King Gt. The contact was traversed along the Eastern Ridge (Fig. 3.5). Vegetation and soil obscure the its exact location but float and scattered outcrops change on either side of a small north-south trending stream gully on the ridge indicating the contact's location through preferential erosion. The float and outcrops show no evidence of mineralogical or textural change on either side of the gully so the contact is probably sharp.

Structures

Country rocks

Bedding orientations were observed in the sandstone units (Fig. 3.5). Distal to the pluton the sedimentary beds dip at 42^{o} to 90^{o} to the SW. Near the pluton, these strike sub-parallel to the contact and dip at 42^{o} to 78^{o} away from the pluton, implying a degree of lateral compression to realign the beds. Foliation in the ultramafics, where developed, also strikes sub-parallel to the contact, dipping at 40^{o} to 85^{o} away from the pluton.

Faults are poorly preserved in the country rocks due to the high rates of weathering and dense vegetation in the rainforest. Jacobson (1970) recorded fault orientations from within the Cenozoic sediments (Fig. 3.10). This showed two dominant populations of faulting in the E-W (80^{o}-115^{o}) and NNW-SSE (180^{o}-155^{o}) directions, and a smaller NE-SW population (45^{o}-60^{o}). It is interesting to note that the NNW-SSE orientation is sub-parallel to the elongation direction of Mt Tambuyukon, which may have formed during the deformation that created this fault set.

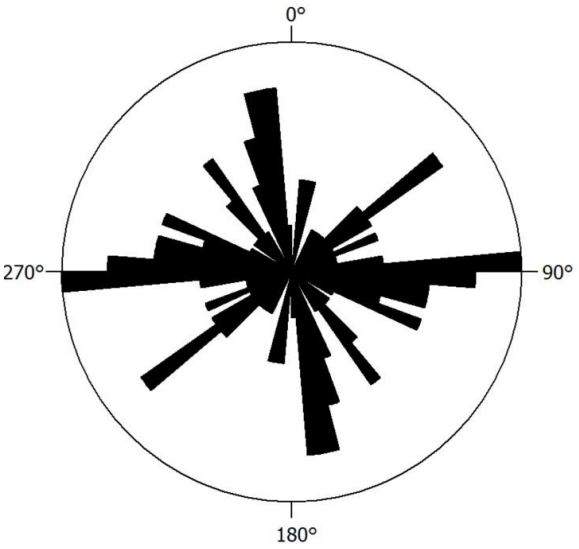

Fig. 3.10. Rose diagrams of strike measurements for faults (n=66) from the sedimentary country rocks around Mt Kinabalu from Jacobson (1970).

Granite

96 dyke and 49 fault orientations were recorded in the field. However, due to the mountain's limited exposure and accessibility most of the readings are limited to the Western Plateau area. Both planar data sets show a strong dominant sub-vertical dip with a strike orientation trending ENE – WSW, with a dominant strike of 050^{o} to 080^{o} for the faults, 040^{o} to 080^{o} for the aplite dykes and 040^{o} to 090^{o} for the intrusive (diorite and Pyx Mon) dykes (Fig. 3.11). A limited number of shear sense indicators from tension gashes on faults and displaced dykes and veins were observed. Six examples of sinistral displacement were found, all in the ENE-WSW direction, whilst twelve examples of dextral fault movement were observed. However, the orientation of dextral movement was more inconsistent with four examples of displacement to the ENE-WSW, three to the NNW-SSE, three to the E-W and one to the N-S. Although this is a limited data set, it does show that the strike-slip component of faulting within the intrusion was not in a dominant direction.

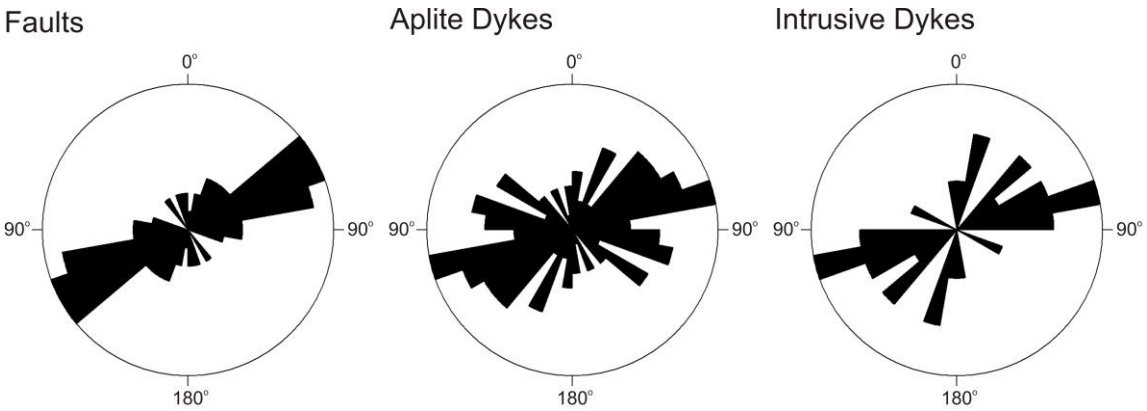

Fig. 3.11. Rose diagrams of strike measurements for faults (n=49), aplite dykes (n=81) and intrusive dykes (n=15) on Mt Kinabalu using 10^{o} bins.

The secondary fault and dyke direction to the NNW-SSE is similar to one of the two dominant fault directions by Jacobson (1970) from the sedimentary units (Fig. 3.10), and the observation of some dextral faults displaced in this direction implies there may still have been some movement along them at the time of intrusion. This orientation is also parallel to the steep cliff of the West Face and the linear valley of Low's Gully. Jacobson (1970) interpreted this 1800m deep canyon as preferential erosion of a "major north-south shear zone which possibly extends to the West Mesilau gorge" based on the close jointing visible in the King Gt forming its cliffs. However, no evidence of intensive deformation was found within Easy Valley (the south eastern upper branch of the gully) or the summit region on the southernmost tip of this gully to where the shear zone should project so it is unclear if this is the cause of this linear erosional feature.

Other large faults do exist in the region, including the N-S line of the Bambangan River (Fig. 3.2), which exploits a large fault in the ultramafic country rocks. Cottam et al. (2010) interpret the presence of large extensional faults on the south side of the mountain in their cross-section and Jacobson (1970) also makes this interpretation due to the mountain's steep southern face. However, evidence for such faults was not found in the field. Instead, we interpret these steep cliffs as preferential erosion of the steep King Gt – Paka Pph contact.

As most of the faulting described here from within the pluton strikes ENE-WSW, but the dominant fault sets within the sediments (Jacobson, 1970) strike N-S or E-W, most of the deformation recorded in the sediments occurred prior to the emplacement of Mt Kinabalu, as it would be expected for both the pluton and its country rocks to show the same fault orientations if they underwent the same periods of deformation.

Discussion

Emplacement depth

Vogt and Flower (1989) applied the hornblende alumina barometer of Hammarstrom and Zen (1986) and Hollister, Grissom et al. (1987) to hornblende compositions from Mt Kinabalu, and gave emplacement pressure estimates of 1-3kbar, equivalent to an emplacement depth of 3 to 10km. However, Hollister, Grissom et al. (1987) cautioned that only the rim composition should be used in these estimates so as to calculate the final crystallisation pressure, and so the same technique was applied to the published data of Imai (2000) on rim and core compositions of amphiboles from boulders of the main body and samples of the Mamut and Poring satellite stocks. Excluding negative values, this calculation gave estimates of 4.2-4.7kbar with a mean of 4.4kbar for the cores, and 0.1-2.6kbar with a mean of 1kbar for the rims. Hollister, Grissom et al. (1987) state that this technique can only be used for pressures of more than 2kbar, and so all that can be determined from this calculation is that the likely emplacement pressure was 2kbar or less. Assuming an intermediate value of crustal density of 2.8gcm^{-3} between dense ophiolite and less dense attenuated continental crust this is equivalent to a shallow emplacement depth of <7km, although it is at the shallow end of the 7-12km range of emplacement depths calculated by thermochronometric based estimates of uplift (Cottam *et al.*, 2013). As the intrusion is found in contact with the ophiolite and the overlying sediments this depth may represent the thickness of the sediments at the time of intrusion.

Contact metamorphic conditions

Maximum metamorphic temperatures of the country rocks, and thus minimum emplacement temperatures of the intrusion, can be estimated from the petrology of the rocks in contact with the pluton. Talc and anthophyllite in metamorphosed ultramafic bodies 2m from the Paka Pph contact represent the highest temperature metamorphic assemblage observed during this study and that of Jacobson (1970), implying a temperature of 630 - 700^{o}C at the calculated 2kbar emplacement pressure (Bucher and Grapes, 2011). 700^{o}C is only just above the expected ~675^{o}C whole rock solidus of the granite at the calculated pressure (Naney, 1983), and so the intruding magma was probably significantly hotter than the metamorphic temperature reached by the country rocks. Ultramafic and serpentinised ultramafic samples taken further from the contact do not contain talc, supporting the interpretation that this mineral is present as a result of contact metamorphism rather than previous alteration of the unit. In the quartzite on the northern contact of the pluton, authigenic biotite and chlorite have grown around the quartz. This assemblage is stable at temperatures of <510^{o}C at this pressure (Bucher and Grapes, 2011), and so probably formed during cooling of the pluton.

Jacobson (1970) notes different metamorphic mineral assemblages near the contacts in the West Mesilau Gorge. Here he describes a series of metamorphic lithologies including spotted cordierite biotite schists derived from sedimentary protoliths, and tremolite-talc, tremolite and anthophyllite schists from ultramafic protoliths. Elsewhere on the mountain mica-cordierite and corundum-cordierite schists are also described. The presence of cordierite, which is stable to temperatures of 900^{o}C at 2kbar, can only constrain the metamorphic temperature to between 900 and 550^{o}C (Bucher and Grapes, 2011).

Internal structure of the pluton and Emplacement Mechanism

The source and evolution of the melt will be the focus of the next chapter. However, based on the field relations the melt generated ascended through the ophiolite sequence until reaching its emplacement level at the contact of the ophiolite with the overlying Cenozoic sediments. Using the locations of the contacts between the internal units of the pluton and their orientations, interpretations of the pluton's internal structure can be derived (Fig. 3.12 and 3.13) and approximate volumes for each unit estimated (Table 3.1). All contact orientations shown, except for those with the Mesilau Pph are orientated from observed contact geometries.

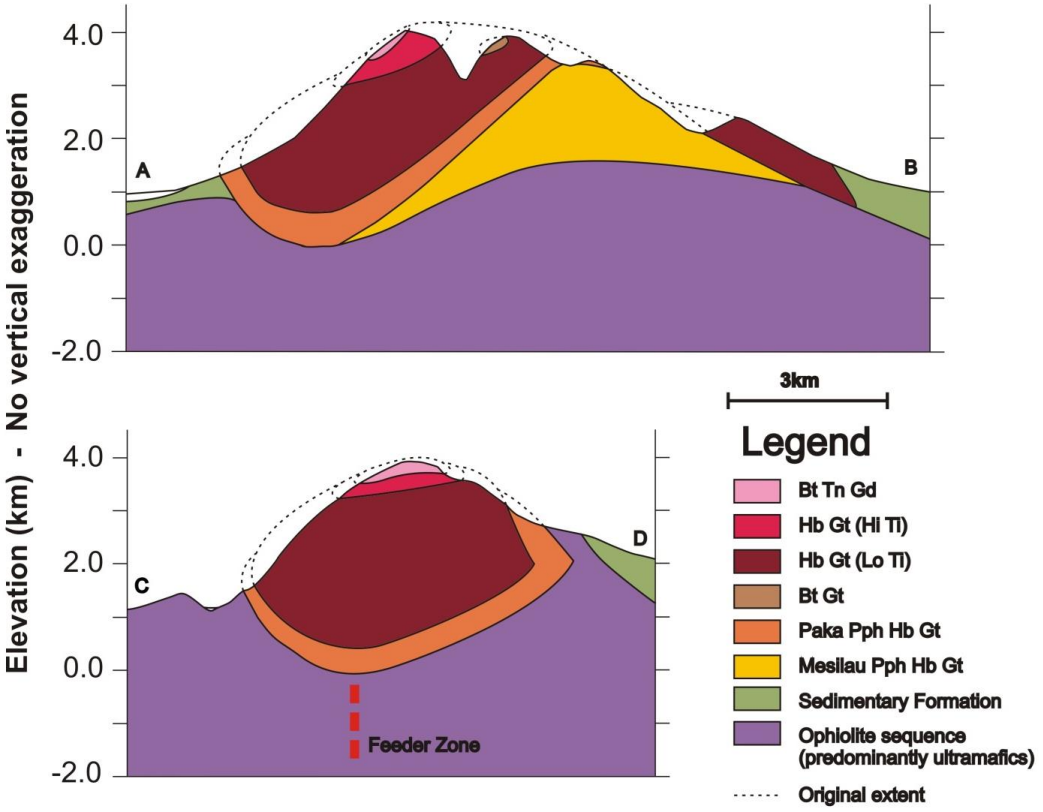

Fig. 3.12. Interpreted geological cross-sections of the mountain showing the internal structure of the pluton and extrapolated original extent. Lines of section as shown in Fig. 3.5. No vertical exaggeration.

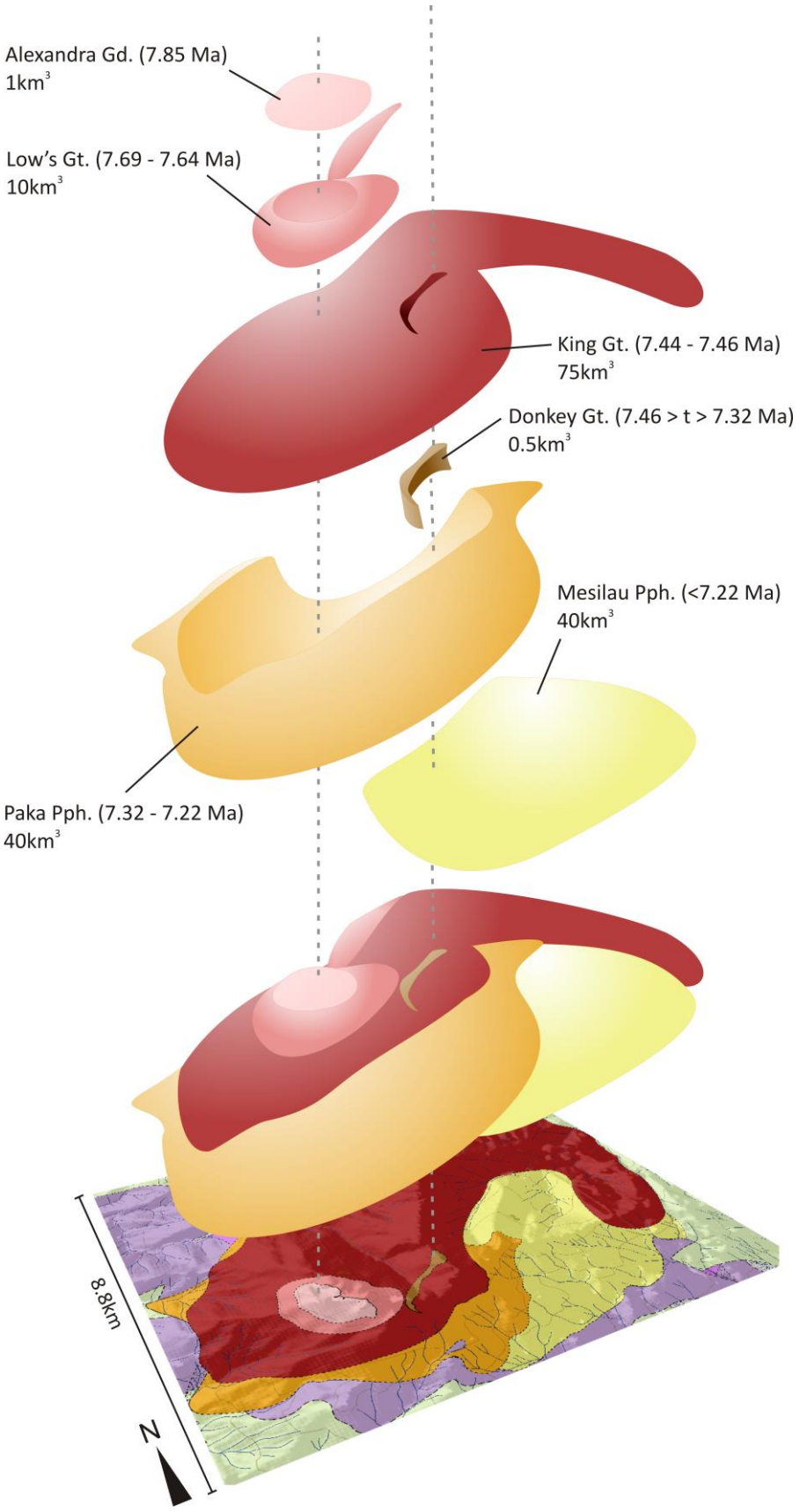

Fig. 3.13. Exploded view illustration of the pre-erosional structure of the Mt Kinabalu pluton and its composite units. Emplacement ages from Cottam *et al.* (2010).

It has been shown (McCaffrey and Petford, 1997, Cruden and McCaffrey, 2001) that a power law exists between the thickness of a pluton and its length, which can be estimated by the following equation from Cruden and McCaffrey (2001):

$$T = 0.6(\pm 0.15)L^{0.6(\pm 0.1)}$$

[Eq. 1]

Applying this equation to the long axis of Mt Kinabalu gives an estimated thickness of the pluton of 3km. The maximum vertical range of granite outcrops on the main body is 2.9km, and so this would imply that the pluton does not continue far beneath its lowest outcrops. This is supported by the orientation of the contact between the Paka Pph and the sedimentary hornfels in S. Bambangan on the west of the mountain where the contact dips towards the pluton (Fig. 3.5). Additionally Sperber (2009) estimated the amount of granitic material removed by glaciation and calculated that the original uppermost surface of the pluton was unlikely much higher than the present summit pinnacles. Both of these interpretations have been used in determining the cross section and pre-erosional structure of the pluton, and imply that most of the vertical extent of the intrusion is both exposed and preserved.

The bedding planes of the sediments around Mt Kinabalu have been re-aligned to be sub-parallel to their contact with the pluton, and the dip of these beds steepen towards the contact surface. This implies a degree of lateral compression was imposed by the pluton during emplacement but only for <3km from the contacts. As most of the vertical extent of the pluton is exposed the sedimentary structures we see are located laterally from the lower levels of the intrusion. As their beds dip away from the body, and because at this relatively shallow emplacement depth the ultramafic sequence would have been unlikely to deform in a ductile manner, accommodation space for emplacement was created through roof lifting of the overlying sediments in a laccolith style similar to Corry (1988) and Cruden (1998), as illustrated in Fig. 3.14.

The steep sides on the S, W and NW faces are in agreement with the description of punched emplacement laccoliths of Corry (1988), although as there isn't evidence that

the uplifting overburden was bounded by vertical faults on all sides, deformation was probably through flexure rather than faulting. This roof lifting process also affected earlier units as each subsequent pulse intruded resulting in the westward dip of the underlying contact surface of the Alexandra Gd and Low's Gt.

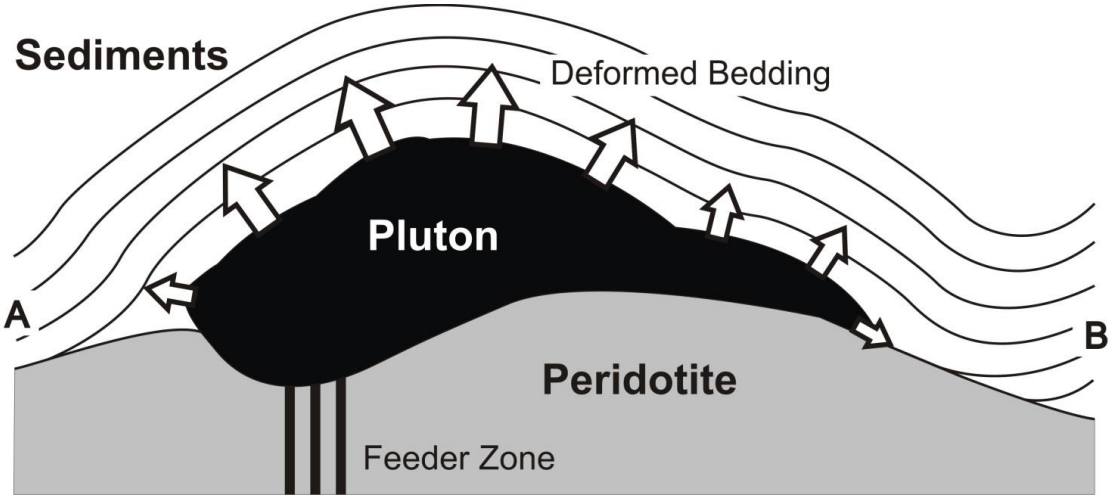

Fig. 3.14. Simplified illustration of emplacement mechanism, along section A–B. Arrow size illustrates the scale of stress.

The field evidence for the emplacement of Mt Kinabalu largely supports the top-down, laccolith-type layered emplacement model for composite plutons of Cruden (1998). However, it also highlights some of the complexities of this process. Although most of the units broadly agree with the model, and the uppermost two units are particularly tabular in shape, at Mt Kinabalu each subsequent unit often ascends around the sides of pre-existing units and even above them, producing irregular three-dimensional structures (Fig. 3.13). This is shown most clearly by the Low's Gt which rises on top of the eastern edge Alexandra Gd, and by the Paka Pph, which rises around the NW, S and E sides of the King Gt. This indicates that these later units were still under pressure from the magma column below when they intruded beneath the earlier units, and so were still trying to ascend. The solid earlier units would have restricted the ascent of

arriving magma which consequently exploited the contact of these earlier units as a plane of weakness and intruded along them.

Stress field during emplacement

From the structural data collected (Fig. 3.11) it is possible to interpret the tectonic setting during emplacement. In a compressive regime dykes propagate parallel to the σ1 direction and faults propagate at an angle oblique to it (Blès and Fuega, 1986, Park, 2001). In an extensional regime both will propagate perpendicular to the σ3 direction. As both faults and dykes share the same dominant orientation with steep dips and striking ENE-WSW it appears most likely that Kinabalu was emplaced in an extensional regime with a dominantly NNW-SSE direction for σ3. The ambiguous deformation direction of the shear sense indicators also supports this, as any obliquity in the extensional direction would result in apparent shearing in the plane of extension without a dominant shearing direction.

The dominant ENE-WSW dyke direction is parallel to the long axis of the pluton as a whole. If magma reached the pluton from below via a network of feeder dykes (Clemens and Mawer, 1992) this may imply that these feeder dykes shared both the orientation of the later dykes and the pluton's elongation direction, in support of the observations of Vigneresse (1995) that granitic feeder zones orient themselves parallel to the direction of maximum compression (σ1). This feeder orientation for Mt Kinabalu is supported by the relative orientation of the Donkey Gt outcrops (Fig. 3.7). These share the same elongation direction, and (assuming no structural control was imparted as the Donkey Gt rose though the King Gt) may mean this sub-vertical planar unit preserves the overall form of its underlying feeder system as the King Gt was only partially solid when the Donkey Gt intruded through it.

As the underlying feeder dykes represent the stress field pre- and syn-emplacement, the dykes represent syn-emplacement and faults represent post-emplacement the

common dominant ENE-WSW orientation for all three indicates that σ3 was predominantly orientated NNW-SSE throughout the whole period of intrusion and crystallisation of Mt Kinabalu's composite units and after emplacement.

This period of extension may result from multiple causes, including: (1) a local event related to post-orogenic extension of Sabah following the Sabah Orogeny; (2) isostatic uplift of NW Borneo in response to the earlier subduction of the attenuated continental crust of the Dangerous Grounds or (3) in response to the high erosion rates in the region; (4) delamination of a lithospheric root (Hall and Morley, 2004) or slab break-off following subduction of a proto-South China Sea (Morley and Back, 2008); or (5): response to a more regional period of extension in SE Asia, as suggested by Hall (2013) and Cottam *et al.* (2013). Hall and Morley (2004) noted the warm, weak lithosphere of SE Asia during the Cenozoic, which makes it particularly responsive to far-field stresses from its surrounding subduction zones. Extension was occurring between 12.5 Ma and 7 Ma in Sulawesi and the North Banda Sea, (Hinschberger *et al.*, 2000, Leeuwen *et al.*, 2007) related to rollback of the Banda slab (Hall, 2011), and the Bornean extension may relate to transfer of these subduction derived stresses. The NNW-SSE extension direction observed at Mt Kinabalu is similar to the NW-SE extension direction of many of the basins in SE Asia, including the Crocker Basin and Central Sabah Basin of onshore Borneo (Fig. 3.2), the NW Borneo Trough, the Sulu Sea (Fig 3.1) and the South China Sea (Balaguru, 2001, Hall and Morley, 2004), supporting the interpretation that the extension recorded here is in response to regional stresses.

Conclusions

This study presents new field observations and a new map of the Mt Kinabalu granitic intrusion of Sabah, N Borneo. The melt was emplaced in the shallow upper crust near the contact of the ultramafic Mesozoic ophiolite basement and overlying Cenozoic turbidite sediments at <12km depth as six main pulses of magma between 7.85 and 7.22 Ma, plus smaller dyke intrusions. Field observations and contact relations have corroborated the order of emplacement determined by zircon dating (Cottam *et al.*, 2010). The sharp nature of these contacts shows that the individual pulses were able to crystallise, at least on their margins, in the <0.2 My between pulses. Their orientations and geometry of the units and country rocks has shown the pulses were emplaced largely from the top down with accommodation space being created from lateral and upwards deformation of the overlying sediments in agreement with current models of laccolith emplacement. However, they also show that a simple layered model is an oversimplification as many of the units ascend around the sides and even on top of earlier units due to continuing pressure from the magma column. The pluton was emplaced during NNW-SSE directed extension which most likely primarily resulted from far-field extensional stresses affecting much of SE Asia in the Neogene.

Baillie, I., Evangelista, P. and Inciong, N. (2000). Differentiation of upland soils on the Palawan ophiolitic complex, Philippines. *Catena*. **39**, 4, 283-299.

Balaguru, A. (2001). Tectonic Evolution and Sedimentation of the Southern Sabah Basin, Malaysia. *Department of Geology, Royal Holloway, University of London.* PhD.

Balaguru, A. and Nichols, G. (2004). Tertiary stratigraphy and basin evolution, southern Sabah (Malaysian Borneo). *Journal of Asian Earth Sciences*. **23**, 4, 537-554.

Barckhausen, U. and Roeser, H.A. (2004). Seafloor spreading anomalies in the South China Sea revisited. *Geophysical Monograph Series*. **149**, 121-125.

Bergman, S.C., Dunn, D.P. and Krol, L.G. (1988). Rock and mineral chemistry of the Linhaisai Minette, Central Kalimantan, Indonesia, and the origin of Borneo diamonds. *The Canadian Mineralogist*. **26**, 1, 23-43.

Blès, J.-L. and Fuega, B. (1986). The fracture of rocks.

Briais, A., Patriat, P. and Tapponnier, P. (1993). Updated Interpretation of Magnetic Anomalies and Seafloor Spreading Stages in the South China Sea : Implications for the Tertiary Tectonics of Southeast Asia. *Journal of Geophysical Research*. **98B**, 6299-6328.

Bucher, K. and Grapes, R. (2011). Petrogenesis of Metamorphic Rocks. *Petrogenesis of Metamorphic Rocks*. 21-56.

Chiang, K.K. (2002). Geochemistry of the Cenozoic igneous rocks of Borneo and tectonic implications. *Department of Geology, Royal Holloway, University of London.* PhD.

Chung, S.-L., Cheng, H., Jahn, B.-m., O'Reilly, S.Y. and Zhu, B. (1997). Major and trace element, and Sr-Nd isotope constraints on the origin of Paleogene volcanism in South China prior to the South China Sea opening. *Lithos*. **40**, 2-4, 203-220.

Clemens, J. and Mawer, C. (1992). Granitic magma transport by fracture propagation. *Tectonophysics*. **204**, 3, 339-360.

Coggon, J., Nowell, G., Pearson, D. and Parman, S. (2011). Application of the 190Pt-186Os isotope system to dating platinum mineralization and ophiolite formation: an example from the Meratus Mountains, Borneo. *Economic Geology*. **106**, 1, 93-117.

Collenette, P. (1958). *The geology and mineral resources of the Jesselton-Kinabalu area, North Borneo*. Geological Survey Department, British Territories in Borneo.

Corry, C.E. (1988). *Laccoliths: Mechanics of Emplacement and Growth*. Geological Society of America.

Cottam, M., Hall, R., Sperber, C. and Armstrong, R. (2010). Pulsed emplacement of the Mount Kinabalu granite, northern Borneo. *Journal of the Geological Society*. **167**, 1, 49-60.

Cottam, M., Hall, R., Sperber, C., Kohn, B., Forster, M. and Batt, G. (2013). Neogene rock uplift and erosion in northern Borneo: evidence from the Kinabalu granite, Mount Kinabalu. *Journal of the Geological Society*.

Cruden, A. and McCaffrey, K. (2001). Growth of plutons by floor subsidence: implications for rates of emplacement, intrusion spacing and melt-extraction mechanisms. *Physics and Chemistry of the Earth, Part A: Solid Earth and Geodesy*. **26**, 4, 303-315.

Cruden, A.R. (1998). On the emplacement of tabular granites. *Journal of the Geological Society*. **155**, 5, 853-862.

Cullen, A., Macpherson, C., Taib, N.I., Burton-Johnson, A., Geist, D., Spell, T. and Banda, R.M. (2013). Age and Petrology of the Usun Apau and Linau Balui Volcanics: Windows to Central Borneo's Interior. *Journal of Asian Earth Sciences*.

Cullen, A.B. (2010). Transverse segmentation of the Baram-Balabac Basin, NW Borneo: refining the model of Borneo's tectonic evolution. *Petroleum Geoscience*. **16**, 1, 3-29.

Cullen, A.B., Reemst, P., Henstra, G., Gozzard, S. and Ray, A. (2010). Rifting of the South China Sea: new perspectives. *Petroleum Geoscience*. **16**, 3, 273-282.

Davis, D.W., Sewell, R.J. and Campbell, S.D.G. (1997). U-Pb dating of Mesozoic igneous rocks from Hong Kong. *Journal of the Geological Society*. **154**, 6, 1067-1076.

Hall, R. (2002). Cenozoic geological and plate tectonic evolution of SE Asia and the SW Pacific: computer-based reconstructions, model and animations. *Journal of Asian Earth Sciences*. **20**, 4, 353-431.

Hall, R. and Morley, C.K. (2004). Sundaland basins. *Continent-Ocean Interactions Within East Asian Marginal Seas*. **149**, 55-85.

Hall, R. (2009). Hydrocarbon basins in SE Asia: understanding why they are there. *Petroleum Geoscience*. **15**, 2, 131-146.

Hall, R. (2011). Australia–SE Asia collision: plate tectonics and crustal flow. *Geological Society, London, Special Publications*. **355**, 1, 75-109.

Hall, R. (2013). Contraction and extension in northern Borneo driven by subduction rollback. *Journal of Asian Earth Sciences*.

Hammarstrom, J.M. and Zen, E.-a. (1986). Aluminum in hornblende; an empirical igneous geobarometer. *American Mineralogist*. **71**, 11-12, 1297-1313.

Hinschberger, F., Malod, J.A., Réhault, J.P., Dyment, J., Honthaas, C., Villeneuve, M. and Burhanuddin, S. (2000). Origine et évolution du bassin Nord-Banda (Indonésie): apport des données magnétiques. *Comptes Rendus de l'Académie des Sciences-Series IIA-Earth and Planetary Science*. **331**, 7, 507-514.

Hollister, L.S., Grissom, G.C., Peters, E.K., Stowell, H.H. and Sisson, V.B. (1987). Confirmation of the empirical correlation of Al in hornblende with pressure of solidification of calc-alkaline plutons. *American Mineralogist*. **72**, 3-4, 231-239.

Hutchison, C. (1988). Stratigraphic-tectonic model for eastern Borneo. *Geological Society of Malaysia Bulletin*. **22**, 135-151.

Hutchison, C.S. (1974). Laboratory handbook of petrographic techniques.

Hutchison, C.S. (1978). Ophiolite metamorphism in northeast Borneo. *Lithos*. **11**, 3, 195-208.

Hutchison, C.S. (1989). *Geological evolution of South-east Asia*. Clarendon Press Oxford.

Hutchison, C.S. (1996). The 'Rajang accretionary prism'and 'Lupar Line'problem of Borneo. *Geological Society, London, Special Publications*. **106**, 1, 247-261.

Hutchison, C.S. (2005). *Geology of North-West Borneo: Sarawak, Brunei and Sabah*. Elsevier Science.

Imai, A. and Ozawa, K. (1991). Tectonic implications of the hydrated garnet peridotites near Mt Kinabalu, Sabah, East Malaysia. *Journal of Southeast Asian Earth Sciences*. **6**, 3, 431-445.

Imai, A. (2000). Genesis of the Mamut Porphyry Copper Deposit, Sabah, East Malaysia. *Resource Geology*. **50**, 1, 1-23.

Jacobson, G. (1970). *Gunung Kinabalu area, Sabah, Malaysia*. Sabah, Geological Survey of Malaysia.

Kasama, T., Akimoto, H., Hada, S. and Jacobson, G. (1970). Geology of the Mt. Kinabalu area, Sabah, Malaysia. *Journal of Geosciences, Osaka City University*. **13**, 113–148.

Kirk, H.J.C. (1968). The igneous rocks of Sarawak and Sabah. *Geological Survey Malaysia Bulletin*. **Memoir 14**,

Leeuwen, T., Allen, C.M., Kadarusman, A., Elburg, M. and Michael Palin, J. (2007). Petrologic, isotopic, and radiometric age constraints on the origin and tectonic history of the Malino Metamorphic Complex, NW Sulawesi, Indonesia. *Journal of Asian Earth Sciences*. **29**, 5, 751-777.

Leong, K. (1974). *The geology and mineral resources of the Upper Segama Valley and Darvel Bay area, Sabah, Malaysia*. US Government Printing Office.

Leong, K. (1998). Sabah crystalline basement: "Spurious" radiometric ages? Continental? *Warta Geologi (Geological Society of Malaysia Newsletter)*. **24**, 5-8.

Leuthold, J., Müntener, O., Baumgartner, L.P., Putlitz, B., Ovtcharova, M. and Schaltegger, U. (2012). Time resolved construction of a bimodal laccolith (Torres del Paine, Patagonia). *Earth and Planetary Science Letters*. **325**, 85-92.

Macpherson, C.G., Chiang, K.K., Hall, R., Nowell, G.M., Castillo, P.R. and Thirlwall, M.F. (2010). Plio-Pleistocene intra-plate magmatism from the southern Sulu Arc, Semporna peninsula, Sabah, Borneo: Implications for high-Nb basalt in subduction zones. *Journal of Volcanology and Geothermal Research*. **190**, 1-2, 25-38.

McCaffrey, K.J.W. and Petford, N. (1997). Are granitic intrusions scale invariant? *Journal of the Geological Society*. **154**, 1, 1-4.

Mitchell, R.H. (1994). The lamprophyre facies. *Mineralogy and Petrology*. **51**, 2, 137-146.

Morley, C.K. and Back, S. (2008). Estimating hinterland exhumation from late orogenic basin volume, NW Borneo. *Journal of the Geological Society*. **165**, 1, 353-366.

Moss, S.J., Chambers, J., Cloke, I., Satria, D., Ali, J.R., Baker, S., Milsom, J. and Carter, A. (1997). New observations on the sedimentary and tectonic evolution of the Tertiary Kutai Basin, East Kalimantan. *Geological Society, London, Special Publications*. **126**, 1, 395-416.

Moss, S.J. (1998). Embaluh group turbidites in Kalimantan: evolution of a remnant oceanic basin in Borneo during the Late Cretaceous to Palaeogene. *Journal of the Geological Society*. **155**, 509-524.

Naney, M. (1983). Phase equilibria of rock-forming ferromagnesian silicates in granitic systems. *American journal of science*. **283**, 10, 993-1033.

Nguyen, T.T.B., Satir, M., Siebel, W. and Chen, F. (2004). Granitoids in the Dalat zone, southern Vietnam: age constraints on magmatism and regional geological implications. *International Journal of Earth Sciences*. **93**, 3, 329-340.

Omang, S.A.K. and Barber, A. (1996). Origin and tectonic significance of the metamorphic rocks associated with the Darvel Bay Ophiolite, Sabah, Malaysia. *Geological Society, London, Special Publications*. **106**, 1, 263-279.

Park, R.G. (2001). *Foundations of Structural Geology*. Routledge.

Petford, N. and Clemens, J.D. (2000). Granites are not diapiric! *Geology Today*. **16**, 5, 180-184.

Petford, N., Cruden, A.R., McCaffrey, K.J.W. and Vigneresse, J.L. (2000). Granite magma formation, transport and emplacement in the Earth's crust. *Nature*. **408**, 6813, 669-673.

Reinhard, M. and Wenk, E. (1951). The geology of the Colony of North Borneo: Brit. Borneo Geol. *Survey Bull*. **1**,

Sperber, C.M. (2009). The thermotectonic development of Mount Kinabalu, Sabah, Malaysia: Constraints from low-temperature thermochronology. *Department of Earth Science, Royal Holloway, University of London.* PhD.

Streckeisen, A. (1976). To each plutonic rock its proper name. *Earth-Science Reviews*. **12**, 1, 1-33.

Suggate, S., Cottam, M., Hall, R., Sevastjanova, I., Forster, M., White, L., Armstrong, R., Carter, A. and Mojares, E. (2013). South China continental margin signature for sandstones and granites from Palawan, Philippines. *Gondwana Research*.

Tapponnier, P., Peltzer, G. and Armijo, R. (1986). On the mechanics of the collision between India and Asia. *Geological Society, London, Special Publications*. **19**, 1, 113-157.

Taylor, B. and Hayes, D.E. (1983). Origin and history of the South China Sea basin. *Geophysical Monograph Series*. **27**, 23-56.

Tu, K., Flower, M.F.J., Carlson, R.W., Xie, G., Chen, C.-Y. and Zhang, M. (1992). Magmatism in the South China Basin: 1. Isotopic and trace-element evidence for an endogenous Dupal mantle component. *Chemical Geology*. **97**, 1–2, 47-63.

van Hattum, M., Hall, R., Pickard, A. and Nichols, G. (2013). Provenance and geochronology of Cenozoic sandstones of northern Borneo. *Journal of Asian Earth Sciences*.

Vigneresse, J.L. (1995). Control of granite emplacement by regional deformation. *Tectonophysics*. **249**, 3, 173-186.

Vogt, E. and Flower, M.J. (1989). Genesis of the Kinabalu (Sabah) granitoid at a subduction-collision junction. *Contributions to Mineralogy and Petrology*. **103**, 4, 493-509.

Wong, N.P.Y. (1967). Geology and copper mineralisation of the Bambangan Valley, Kinabalu. *Borneo Regional Malaysia Geological Survey Bulletin*. **9**, 32-33.

Yan, Q., Shi, X., Wang, K., Bu, W. and Xiao, L. (2008). Major element, trace element, and Sr, Nd and Pb isotope studies of Cenozoic basalts from the South China Sea. *Science in China Series D: Earth Sciences*. **51**, 4, 550-566.

Yan, Q.S., Shi, X.F., Liu, J.H., Wang, K.S. and Bu, W.R. (2010). Petrology and geochemistry of Mesozoic granitic rocks from the Nansha micro-block, the South China Sea: Constraints on the basement nature. *Journal of Asian Earth Sciences*. **37**, 2, 130-139.

Zhou, X.M. and Li, W.X. (2000). Origin of Late Mesozoic igneous rocks in Southeastern China: implications for lithosphere subduction and underplating of mafic magmas. *Tectonophysics*. **326**, 3-4, 269-287.

Chapter 4:

Anisotropy of Magnetic Susceptibility of the Mt Kinabalu Pluton, Borneo: Constraining the stress field during granitic emplacement

South Peak viewed from the Donkey's Ears

Chapter 4: Anisotropy of Magnetic Susceptibility of the Mt Kinabalu Pluton, Borneo: Constraining the stress field during granitic emplacement

Abstract

The record of magmatic flow and tectonic stresses preserved in the mineral fabrics of the Mt Kinabalu pluton, Borneo, has been investigated using anisotropy of magnetic susceptibility (AMS) analyses on 94 samples from across the mountain and over its 2900m vertical range. This magnetic fabric, hosted variably by biotite and magnetite, shows a similar foliation to that observed in outcrops of the pluton's earliest unit and reveals clear mineral fabrics in other units where a mineral fabric cannot be determined visually. A dominant AMS fabric exists across most units of the pluton with shallow NW plunging lineations and shallowly dipping foliations. This indicates a fabric resulting from tectonic stresses and indicates emplacement of the pluton during NW-SE extension. Other evidence also exists in the AMS fabrics for magmatic orientation of minerals sub-parallel to the contact surfaces of each unit during emplacement, as well as tilting of the less voluminous early units during emplacement of the larger units below them.

This application of AMS analysis shows that tectonic mineral fabrics can be consistent and pervasive through large vertical ranges within a pluton. It has also shown the potential for combining AMS data with accurate emplacement ages for granitic plutons as a tool for determining paleo-stress fields at specific periods in a region's tectonic history.

Introduction

A new map and field observations from Mt Kinabalu (Chapter 3) reveal the complex internal structure of this pluton, the relative orientations and emplacement processes of the mountain's composite units and structural evidence for an extensional stress field during emplacement. This data provides fresh insight into its three dimensional emplacement structure and mechanisms for the emplacement of granitic plutons as well as details regarding the tectonic evolution of SE Asia during the Neogene.

Mineral fabrics in granitic plutons have long been mapped and studied to provide evidence of magma flow and deformation during their emplacement and crystallisation. However, these fabrics are often difficult to determine accurately and are biased by the two dimensional nature of an outcrop. Over the past decades the analysis of the Anisotropic Magnetic Susceptibility (AMS) has been applied to granitic intrusions. This method measures the variation of magnetic susceptibility of a core of sample in each of its three principal axes and from this the three dimensional magnetic fabric of a granitic outcrop can be determined. This magnetic fabric relates to the magnetic mineral fabric in the sample and so accurate three dimensional mineral fabrics can be determined, even when such fabric cannot be observed in outcrop.

Magmatic mineral fabrics form during crystallisation in response to the strain experienced by molten magma until it cools to its solidus. This strain can be a result of: (1) the primary magma flow into the pluton and the resultant pressure applied by the ascending magma column on the melt (e.g. Horsman *et al.*, 2005, Stevenson *et al.*, 2006, Stevenson *et al.*, 2007a, Clemens and Benn, 2010); (2) regional tectonic stress during emplacement and crystallisation (e.g. Vigneresse, 1995, Benn *et al.*, 1997, Benn, 2009); or (3) a combination of both (e.g. Wennerström and Airo, 1998, Petronis *et al.*, 2012). Stress-derived mineral orientations occur because crystals tend to align their longest principal axis with the long axis of the strain ellipse (*X*), itself oriented parallel to the axis of minimal stress, σ_3 (as illustrated in Fig. 4.1). The crystals will also tend to align their largest crystal face with the *X* and *Y* plane of the

strain ellipsoid, perpendicular to the direction of maximum stress, σ_1 (Paterson *et al.*, 1998). Whether a pluton's mineral fabric records magmatic or tectonic stresses will be determined by which force dominates the stress field during crystallisation.

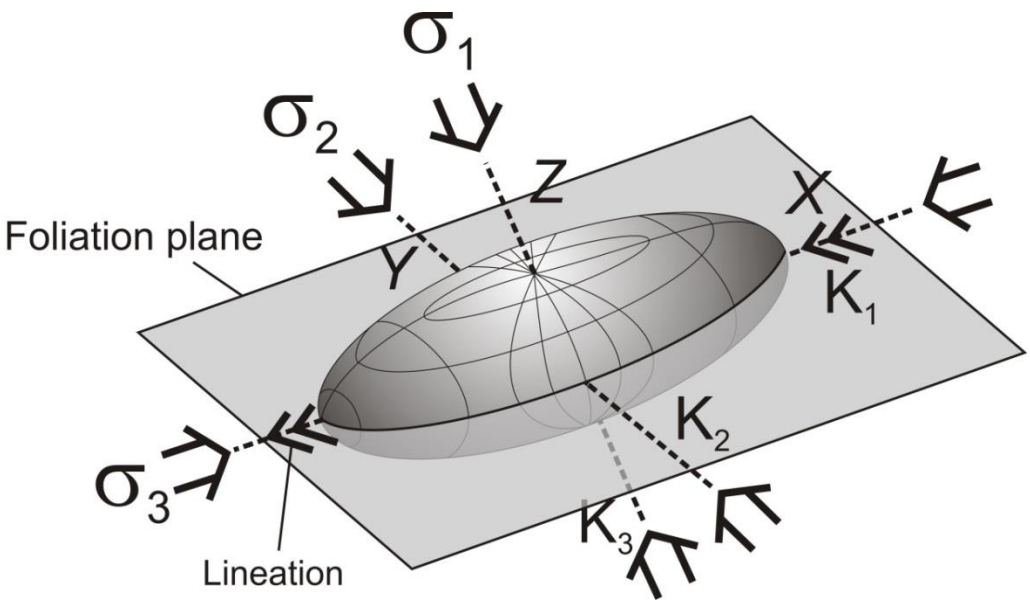

Fig. 4.1. Illustration of the relationship between the stress field (σ values) present during crystallisation (through either magmatic or tectonic stresses), the resultant strain ellipse (*X* > *Y* > *Z*) and magnetic mineral fabric (K values). Prolate fabric shown, where $K_1 > K_2 > K_3$.

Structure of the Mt Kinabalu pluton

As detailed in Chapter 3, the Mt Kinabalu pluton is composed of six major units and minor dyke intrusions (Fig. 4.2). U-Pb zircon ages (Cottam *et al.*, 2010) show that the pluton crystallised between 7.85 Ma and 7.22 Ma. Both the field evidence and zircon ages show that the pluton was constructed largely from the top-down with accommodation space being formed through uplift of the sedimentary overburden in a manner similar to models of laccolith emplacement (Cruden, 1998). The first unit emplaced was a relatively small planar unit, the biotite-rich "Alexandra Peak" Biotite Tonalitic Granodiorite (Alexandra Gd). This was followed by emplacement of the tabular "Low's Peak" High Ti Hornblende Granite (Low's Gt) beneath it and as a separate body in the North of the pluton. The largest unit, the "King George Peak" Low Ti Hornblende Granite (King Gt), was emplaced beneath the Low's Gt. It is

almost identical in hand specimen to the Low's Gt and forms the majority of granitic exposure on the mountain. A much smaller unit, the "Donkey's Ears Peak" Biotite Granite (Donkey Gt) intruded within the King Gt as a sub-vertical planar unit while the King Gt was still partially liquid. The first of two porphyritic units, the "Paka" Porphyritic Hornblende Granite (Paka Pph) was intruded beneath the King Gt, but rose around the sides of the earlier unit through persisting pressure from the magma column during emplacement resulting in an irregularly shaped body around the South and West of the pluton. Finally, the "Mesilau" Porphyritic Hornblende Granite (Mesilau Pph), notable for its 3cm long K-feldspar megacrysts, was intruded in the South-East of the pluton beneath the earlier units.

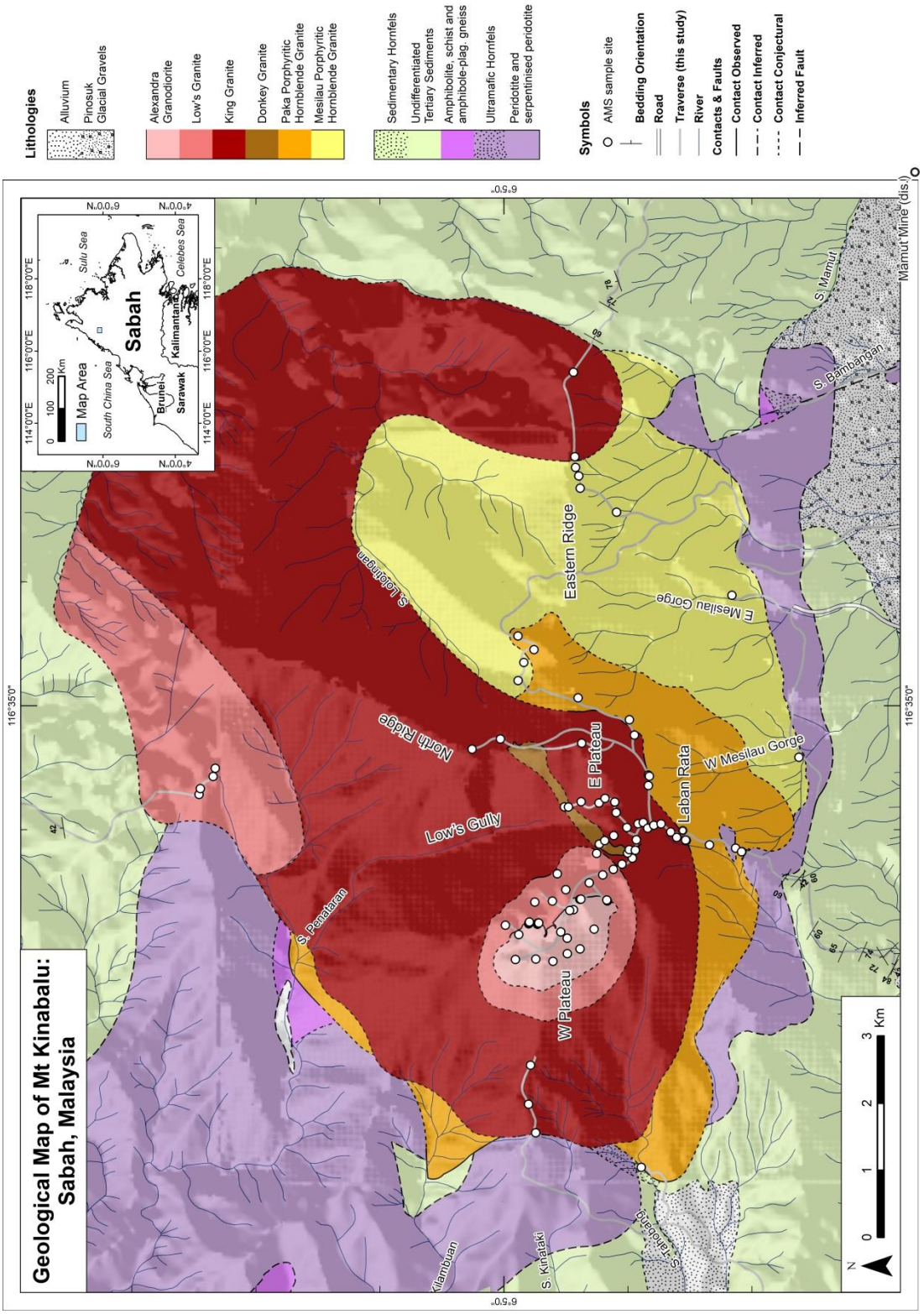

Fig. 4.2. Geological map of Mt Kinabalu showing transects taken during mapping and sample sites for AMS analyses.

Like Jacobson (1970), this study noted a planar fabric formed by biotite crystals in the Alexandra Gd dipping at 40 to 65^{o} to the SW. Sub horizontal orientations (<20^{o}) of feldspar megacrysts were also noted in the porphyritic units of the pluton, which re-orientate parallel to contact surfaces proximal to these. However, these fabrics are not visible in all outcrops of the porphyritic units and fabrics were not observed within most other units of the pluton either in hand specimen or petrographically. By applying an AMS study to the pluton the persistence of the observed fabrics, the presence of cryptic fabrics in other units and the structure of mineral fabrics in three dimensions can be determined to investigate evidence for magmatic flow and the stress regime during emplacement.

This application of mineral fabric analysis to Mt Kinabalu is of particular interest due to the vertical range of granitic outcrop displayed by Mt Kinabalu. Most studies on granitic emplacement are limited by the three dimensional relationships of the outcrops being sampled. Most previous studies were of highly eroded granites with limited vertical relief such that resultant datasets only reveal the mineral fabrics of a sub-horizontal planar section through the pluton. In contrast, Mt Kinabalu displays a 2900m vertical range of outcrop. Based on field evidence, thickness estimates (Cruden and McCaffrey, 2001) and estimates of eroded material (Sperber, 2009) this represents most of the total original extent of the emplaced pluton. Consequently, the Mt Kinabalu pluton provides a unique opportunity to investigate mineral fabrics in three dimensions throughout a whole pluton.

Methodology

Although the topography of the pluton provides a unique opportunity for a unique study, its steep cliffs and rainforest-covered flanks do limit the area which can be sampled. As such, the sampling strategy focussed on collecting transects on the North, South, East and West of the pluton (Fig. 4.2), sampling at 100m vertical intervals across the vertical range of outcrop as far as this was possible. Although the western, northern and eastern flanks of the mountain required trips of up to a week to complete, a popular trail exists on the southern side up to the summit. The

complete exposure on the previously glaciated summit and the presence of this trail allowed detailed sampling over much of the Western Plateau and sampling at 50m vertical intervals from the highest peak on the summit to the lowest exposure on the trail.

94 oriented block samples were collected (Fig. 4.2). From each block 10 to 24 cylindrical cores of approximately 11cm^3 were drilled (Owens, 1994), the number of sub-samples depending on the degree of surface weathering and alteration (normally 12 to 15). The oriented cores were analysed on an AGICO KLY-3s Kappabridge at the University of Birmingham, UK, to measure the magnetic susceptibility (*K*) along three principal axes (Fig. 4.1). Each sub-specimen's results were then normalised by the specimen's mean susceptibility (K_{mean}) and averaged for each block sample to determine mean values of the AMS ellipsoid (Jelínek, 1978, Owens, 2000) and 95% confidence ellipses calculated.

Results

AMS ellipsoid

Analysed results for all 94 samples are given in Appendix A3 along with their calculated parameters. The shape of the AMS fabric is described according to the relative dimensions of the three principal axes of the AMS ellipsoid (Fig. 4.3): K_1, the axis of maximum magnetic susceptibility; K_3 the axis of minimum susceptibility; and K_2, the intermediate axis. These axes represent the principal orientation of the iron-rich magnetically susceptible phases of the sample. All analysed fabrics lie along a spectrum from purely oblate ($K_1 = K_2 > K_3$) to purely prolate ($K_1 > K_2 > K_3$) and are described by the shape parameter, *T* (Jelinek, 1981):

$$T = (2\eta_2 - \eta_1 - \eta_3)/(\eta_1 - \eta_3)$$

[Eq. 1]

where $\eta_i = \ln(K_i)$ (i = 1 to 3). This calculation gives a range of potential values from 1 to -1, where positive values represent oblate fabrics and negative values represent prolate fabrics.

The degree of the measured anisotropy (P') is calculated from (Jelinek, 1981):

$$P' = exp\sqrt{2[(2\eta 1 - \eta_m)^2 + (\eta_2 - \eta_m)^2 + (\eta_3 - \eta_m)^2]}$$

[Eq. 2]

where $\eta_m = \sqrt[3]{(\eta_1\ \eta_2\ \eta_3)}$. This method for describing the degree of anisotropy is preferred to simply using K_1/K_3 as it makes reference to deviation of all axes from the mean susceptibilty, including the intermediate axis, K_2.

P' for the Mt Kinabalu is plotted against T and K_{mean} in Fig. 4.4. Plotting P' against K_{mean} shows that bulk magnetic susceptibility changes by two orders of magnitude within the sample set, from a minimum of 186 x 10^{-6} (in the dimensionless SI units of magnetic susceptibility) for the Alexandra Gd to a maximum of 41,250 x 10^{-6} for one of the Mesilau Pph samples. The largest change in susceptibility is between the low susceptibility values of the biotite-rich Alexandra Gd and Donkey Gt units with the much higher values of the other units and probably represents a change in the magnetic phases present.

Plotting P' against T (Fig. 4.4) shows that the mineral fabric is dominantly oblate. However, the 95% confidence data for the K_1 and K_2 values indicate that for almost all samples these axes are still statistically distinct enough to describe a lineation.

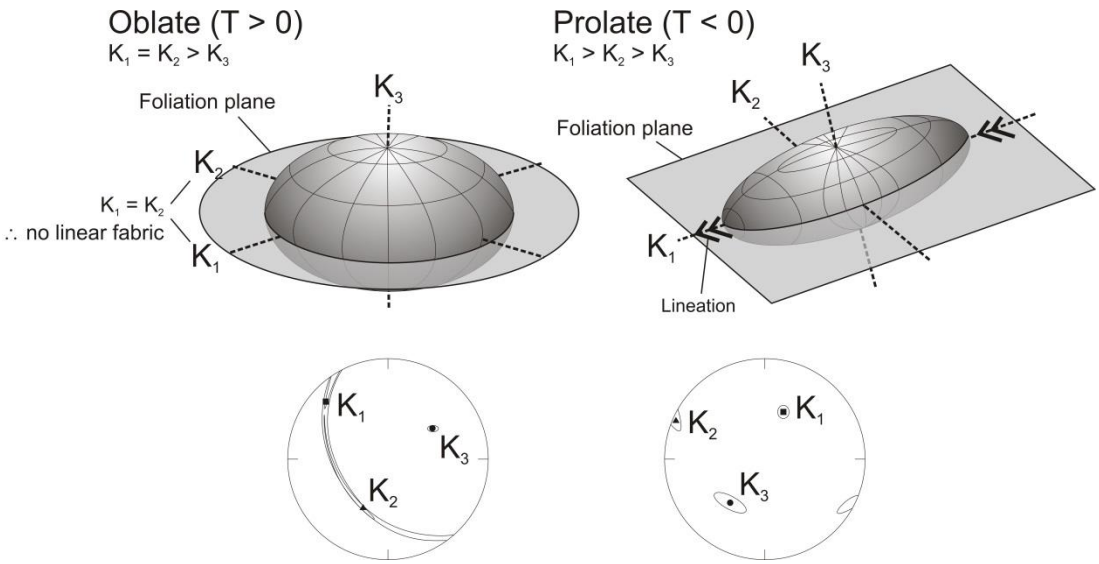

Fig. 4.3. Illustrations of the shape ellipsoids used to describe the magnetic fabrics (*T*) with examples of samples from this study displaying extreme examples of these fabrics (Samples A056b for oblate fabric and A244 for the prolate fabric). Stereographic projections of the sample fabrics show mean values for K_1, K_2 and K_3 and 95% confidence ellipsoids. Although most samples are classed as oblate (Fig. 4.4), most samples do not display overlap in their K_2 and K_3 95% confidence ellipsoids so all three poles can still be described with statistical significance.

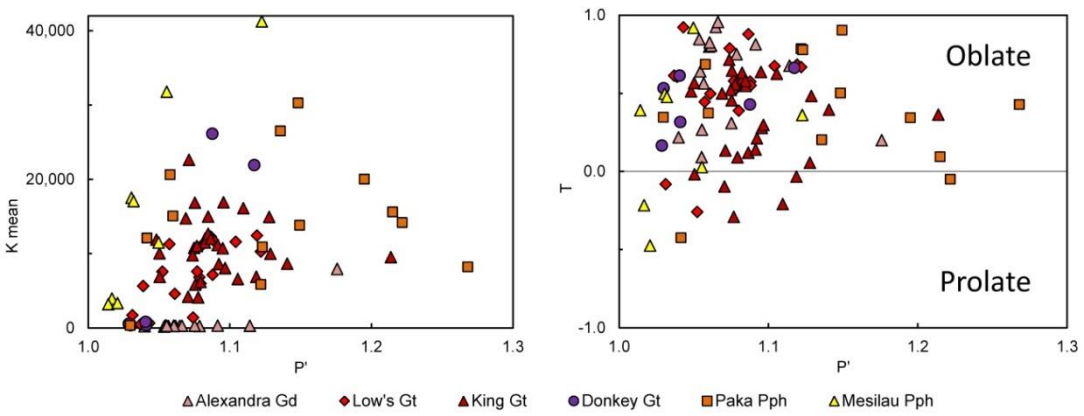

Fig. 4.4. Plots of the degree of magnetic anisotropy (*P'*) against K_{mean} (the mean magnetic susceptibility of K_1, K_2 and K_3) and *T*, the shape parameter for all samples.

Mineralogical source of the AMS fabric

An effective method for determining which phases host the magnetic susceptibility of a bulk rock sample is to analyse the magnetic susceptibility of a powdered sample during heating and cooling whilst observing the temperature at which there is a sharp decrease in susceptibility (the Curie Point). This remains an outstanding objective for this research that will be executed in the near future, but presently we must look for other evidence.

As noted, the biotite-rich Alexandra Gd and most of the Donkey Gt samples display much lower magnetic susceptibility than the other units. The low *K* values (<350 x 10^6 SI) indicate a paramagnetic phase, of which biotite is the most plausible (Rochette, 1987) given its prevalence in these units. Petrographic analysis of the different units shows that magnetite is notably absent in the Alexandra Gd and Donkey Gt samples but is prevalent in the other units as (1) inclusions with ferromagnesian phases (biotite and hornblende), (2) along their boundaries, and (3) as secondary precipitation within fractures. Despite their low modal abundance, the high magnetic susceptibility of ferromagnetic oxides means that they can dominate the AMS fabric (Stevenson *et al.*, 2007b, Petronis *et al.*, 2012). This would explain the much higher susceptibilities of these biotite-poor units and indicates that magnetite is likely to be the primary host of the magnetic fabric.

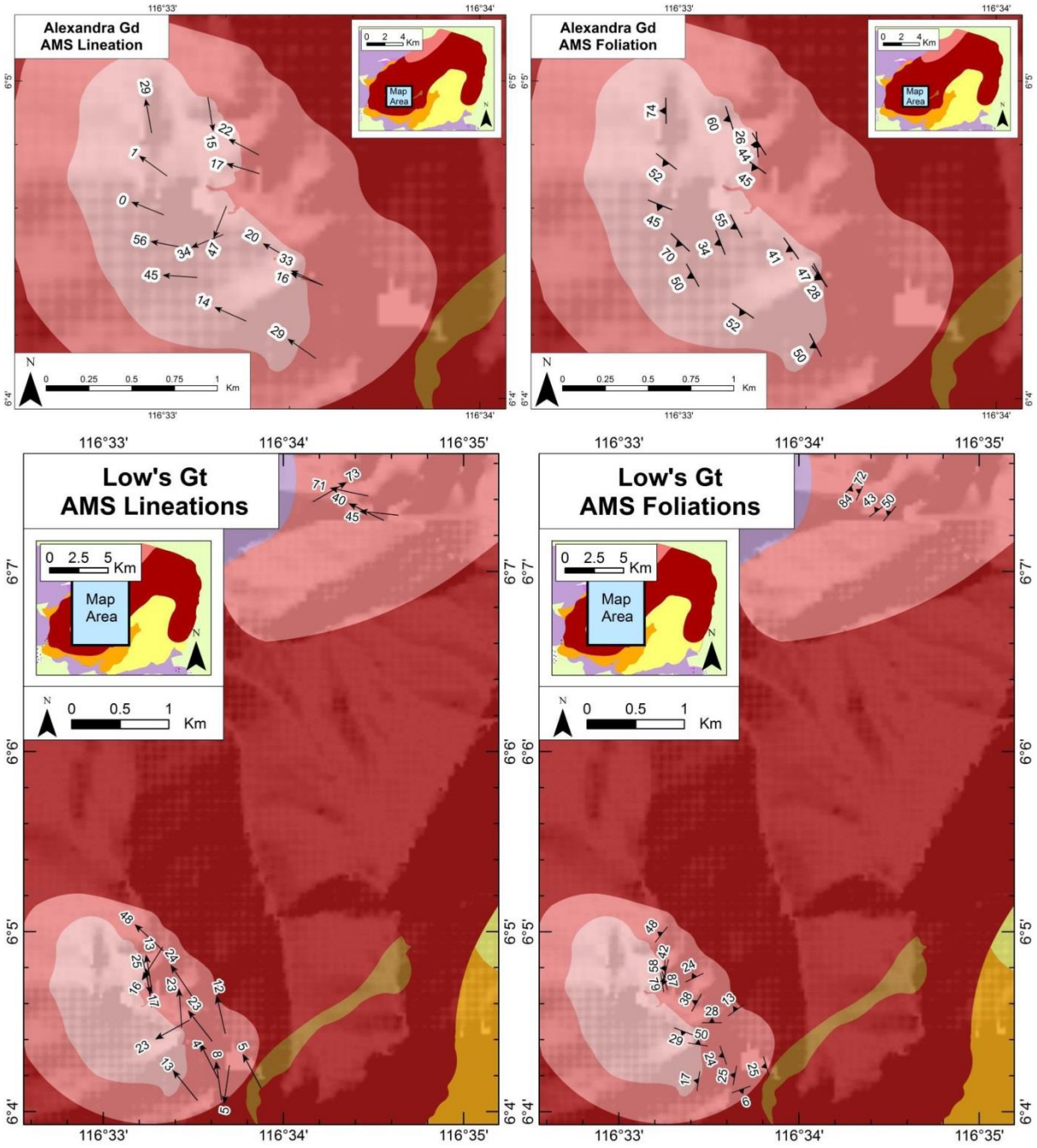

Fig. 4.5. Anisotropy of Magnetic Susceptibility (AMS) fabrics of the composite units forming the Mt Kinabalu pluton. Magnetic lineations and foliations shown for each unit separately. Samples where K_1 and K_2 values are not statistically significantly distinct at the 95% confidence level are excluded from the lineation data and samples where K_2 and K_3 values are not significantly distinct at the 95% confidence level are excluded from the foliation data.

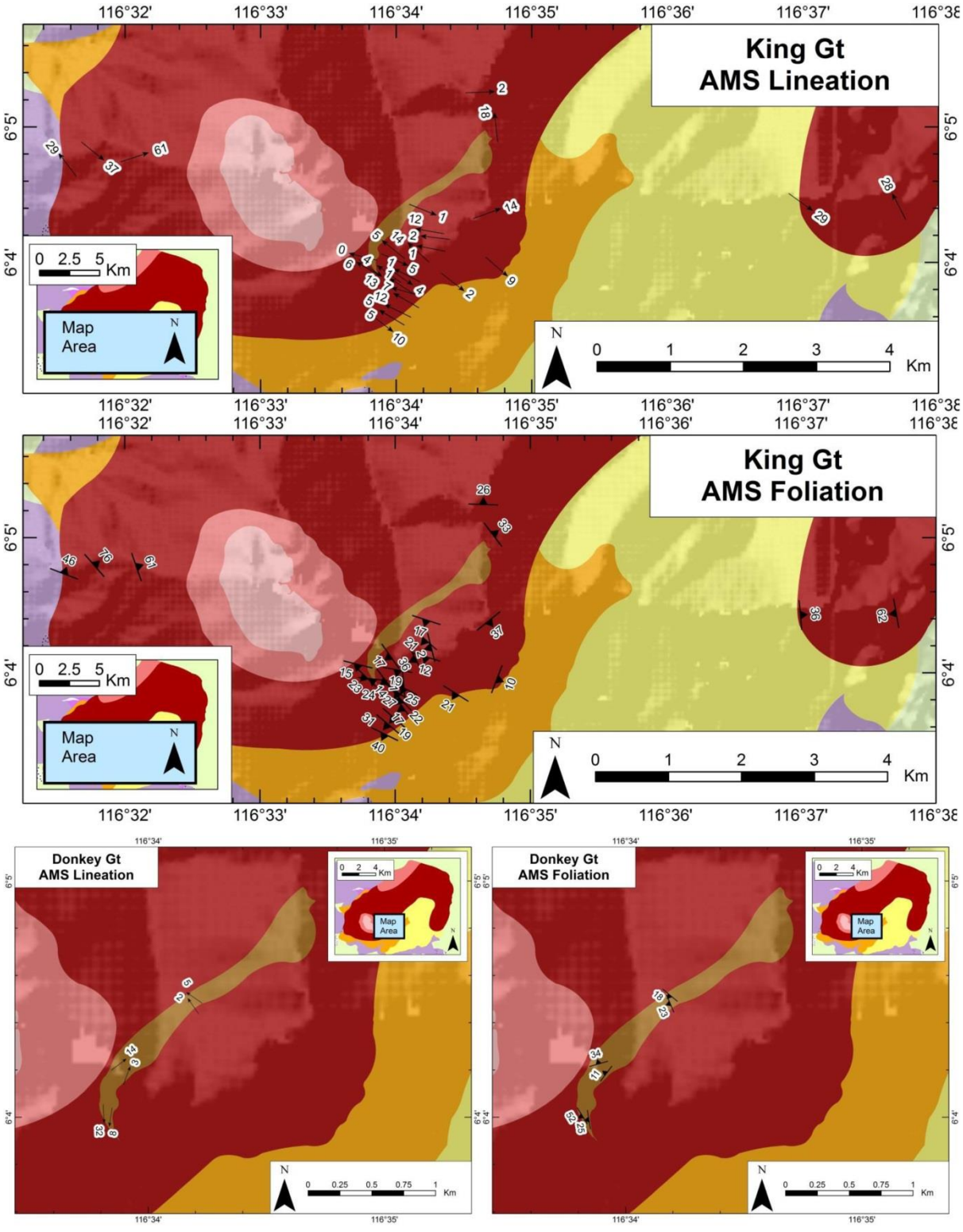

Fig. 4.5. (*continued*)

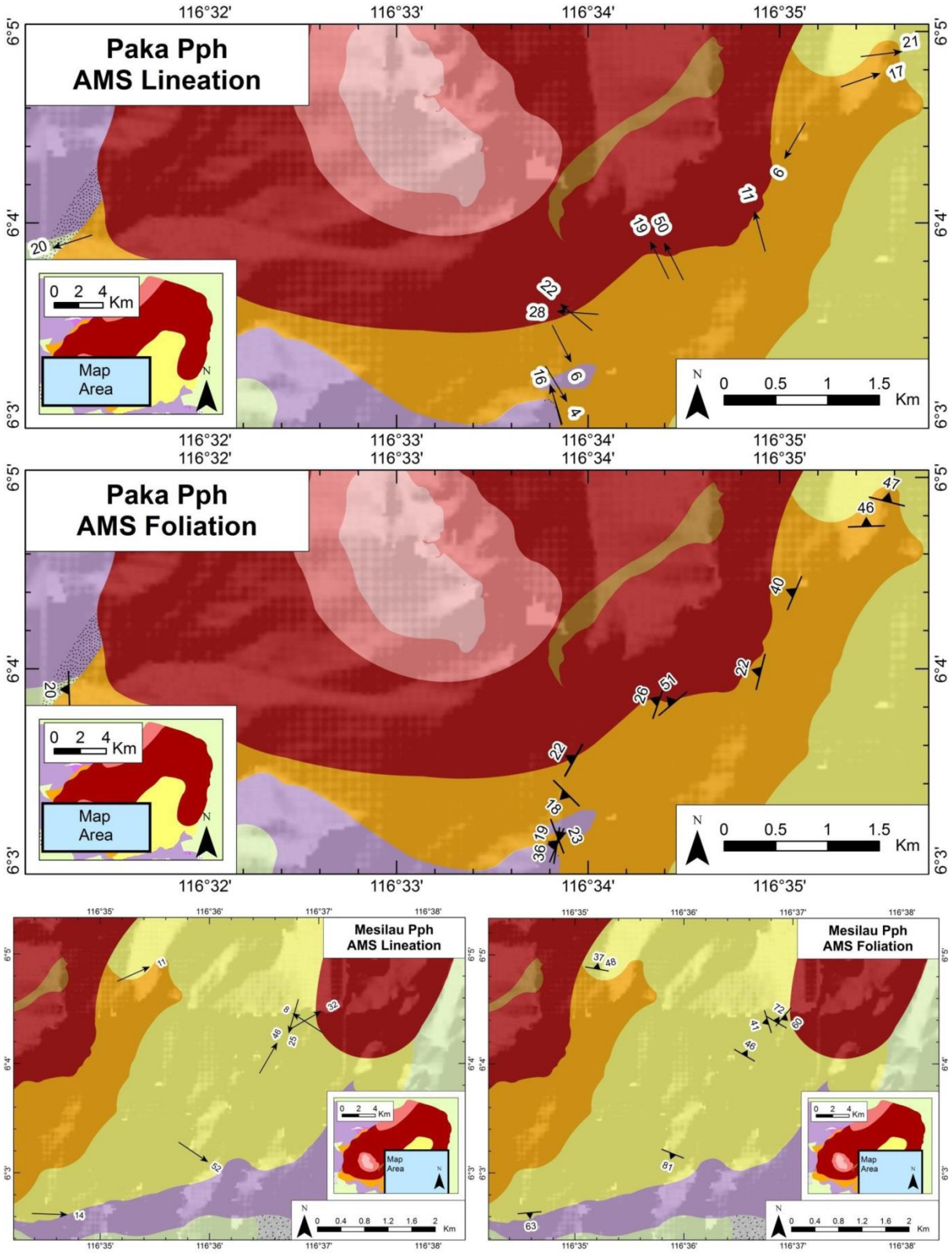

Fig. 4.5. (*continued*)

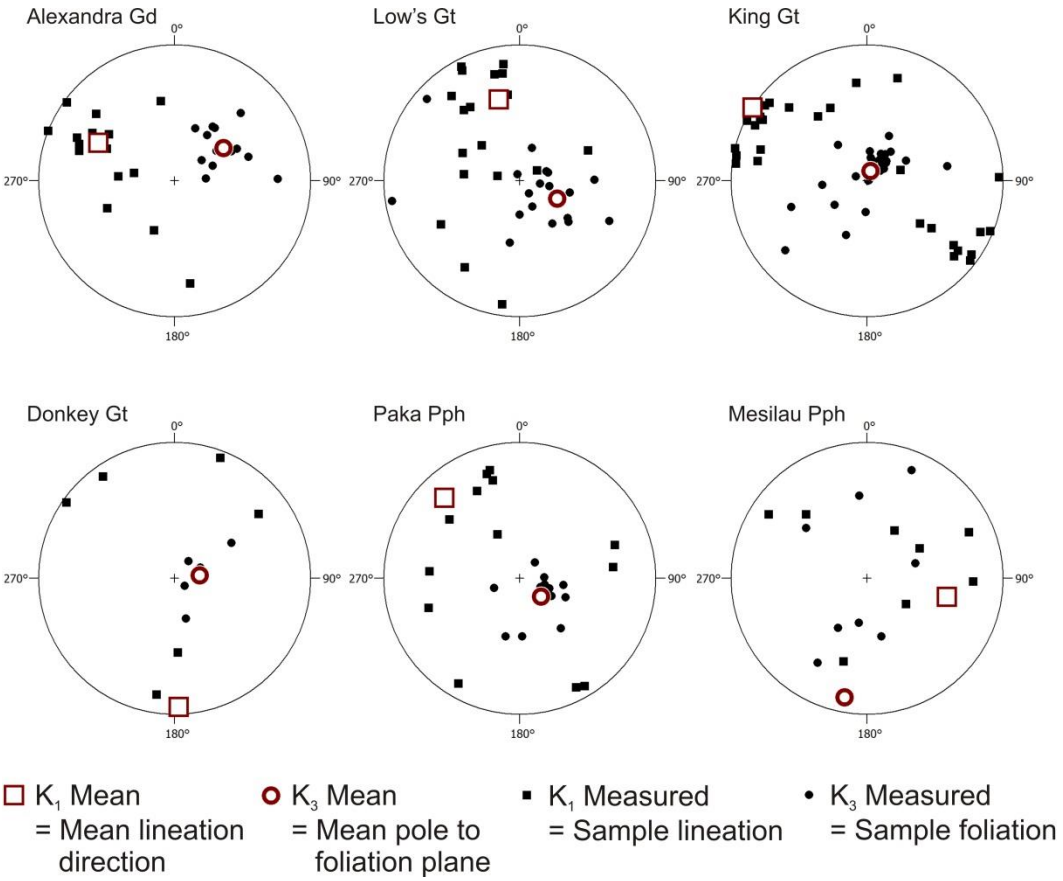

Fig. 4.6. Stereographic projections of the mean K_1 and K_3 values measured for each sample from Mt Kinabalu and the mean values for all samples of each unit. Samples where K_1 and K_2 values are not statistically significantly distinct at the 95% confidence level are excluded from the lineation data and samples where K_2 and K_3 values are not significantly distinct at the 95% confidence level are excluded from the foliation data.

AMS fabrics of the composite units

Fig. 4.5 shows the calculated lineation and foliation data for each major unit of Mt Kinabalu plotted on the geological map. The mean K_1 and K_3 data for each sample along with the mean values for each unit are plotted in Fig. 4.6. Lineation data is only plotted on the maps and stereographic projections where K_1 and K_2 are statistically significantly distinct at the 95% confidence level and foliation data is only plotted when K_2 and K_3 are significantly distinct at the same level.

The Alexandra Gd shows a very consistent foliation dipping 26 to 74^{o} towards the W and SW. Biotite appears to be the host of the magnetic fabric in this unit and this measured foliation is in agreement with biotite foliation observed in the field. This dip is towards a similar direction as the unit's underlying contact with the Low's Gt but at a steeper angle. The lineation data shows a dominant trend plunging at 0 to 56^{o} towards the NW across the extent of the unit.

The Low's Gt shows a dominant foliation dipping at moderate angles (13 to 48^{o}) toward the NW, and steepening in dip near the contacts with the Alexandra Gd (58 to 87^{o}) where the strike of the foliation orientates sub-parallel to the contact surface. The lineation data is largely consistent across the unit, plunging at shallow to moderate angles (4 to 48^{o}) towards the NNW.

The magnetic fabric of the King Gt shows four clear domains. On the western flanks of the mountain the foliations dip steeply towards the NE (46 to 61^{o}). Lineations here are inconsistent but two of the three samples trend in a NW-SE direction. The dense cluster of data in the southern King Gt indicates the location of the summit trail and Western Plateau. The data here represent a vertical range of 590m with a very consistent magnetic fabric of shallow (-14 to 14^{o}), dominantly NW plunging lineations and shallow to moderately SW dipping foliations (2 to 40^{o}). Data is sparse on the Eastern Plateau and the lobe of King Gt in the east. On the Eastern Plateau the foliation dips towards the E and NE and on the eastern lobe the foliation strikes N-S and the lineation data trends NW-SE.

The Donkey Gt shows lineations and strike of foliation oriented parallel to the contacts with the King Gt on the Western Plateau and perpendicular to this contact in Low's Gully, the deep valley between the two plateaux (Fig. 4.2). The lineations have a shallow plunge (3 to 32^{o}) and the foliation dips are shallow to moderate towards the W to NNW (18 to 52^{o}).

Most of the Paka Pph data shows a NW dipping foliation (19 to 51^{o}) and a NW plunging lineation (-4 to 50^{o}). However, the two samples in the NE show lineations plunging towards the ENE and foliations dipping towards the N.

The Mesilau Pph data is much more inconsistent. The location of this unit on the forested eastern flanks and Eastern Ridge (Fig. 4.2) means that the sample set is much sparser than the other units. There does however appear to be a dominant lineation orientation plunging towards the E and the foliation and lineation data for the two samples in the NW of the unit are similar to those measured for the Paka Pph in this region. However, neither of these two north-western samples displays both a significantly distinct foliation and lineation.

Discussion

The AMS data reveals some clear magnetic fabrics within the Mt Kinabalu pluton, some of which are consistent through large ranges of vertical extent, but are these fabrics of magmatic or tectonic origin? The key to making this distinction is determining how consistent the fabrics are with the regional tectonic strain during emplacement. The nature of this strain in the Miocene has been discussed numerous times and contrasting interpretations of compression (Tongkul, 1997, King *et al.*, 2010), transpression (Sperber, 2009) and extension (Cottam *et al.*, 2013, Hall, 2013) tectonics have been proposed. Although convincing fault lineations were lacking from within the pluton the common planar orientations of the dykes and faults measured from the intrusion indicate that the pluton was intruded into an extensional regime. This interpretation is based on the argument that in a compressive regime dykes propagate parallel to the σ_1 direction and faults propagate at an angle oblique to it (Blès and Fuega, 1986, Park, 2001). However, in an extensional regime both will propagate perpendicular to the σ_3 direction. As both faults and dykes display steep dips and share the same dominant orientation striking ENE-WSW, it appears most likely that Kinabalu was emplaced in an extensional regime with a dominantly NNW-SSE direction for σ_3, as illustrated in Fig. 4.7.

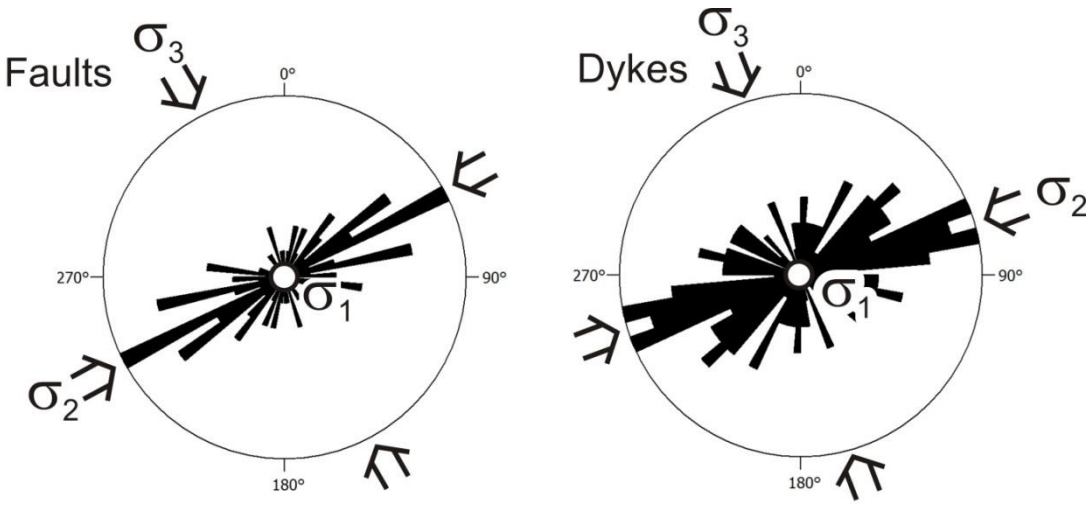

Fig. 4.7. Rose diagrams of strikes to the measured planes of faults and dykes from Mt Kinabalu with interpreted principal stress directions.

In an extensional regime the principal stress direction, σ_1 is sub-vertical. As noted earlier (Fig. 4.1) the shortest axis of the strain ellipsoid, and consequently the short axis of the crystallising mineral fabric will orientate parallel to this principal stress direction and so the mineral fabric in an extensional regime should show a sub-horizontal foliation. The data for Mt Kinabalu shows the AMS foliation across most of the pluton to be generally shallowly dipping with steep plunge angles of K_3 for most units (Fig. 4.6) indicating a dominant tectonically (not magmatically) oriented mineral fabric. However, the SW and NW dips of the foliation in the Alexandra Gd and Low's Gt respectively indicate that their original sub-horizontal fabric may have been tilted as the much more voluminous later units intruded beneath these relatively small tabular bodies.

This interpretation of a dominantly tectonic fabric is further supported by the dominant NW-SE azimuth of the lineation data. This orientation is parallel to the extension direction (and hence minimum stress direction, σ_3) interpreted from the structural data. As crystals tend to align their long axis parallel to the long axis of the strain ellipsoid (itself parallel to σ_3) this lineation direction supports the interpretation that the dominant AMS fabric preserved at Mt Kinabalu results from crystallisation during NW-SE extension at the time of emplacement. These fabrics

are very similar to those determined for extensional plutons elsewhere (e.g. Bouillin *et al.*, 1993).

However, although the dominant fabric appears to result from tectonic strain some of the variance in the data within individual units indicates that there may be subtle evidence of magma flow during emplacement. Paterson *et al.* (1998) showed that during magma flow along contact surfaces the wall of the contact results in a compressional force exerted on the magma perpendicular to the contact surface. As magma near a contact cools faster than in the central regions of a pluton these fabrics are less susceptible to realignment post-emplacement and so contact-parallel mineral fabrics can be preserved even when magmatic fabrics away from contacts are overprinted by tectonic fabrics. This is apparent within the Low's Gt where it contacts the Alexandra Gd (Fig. 4.5), within the Donkey Gt on the Western Plateau and along the SE contact between the King Gt and the Paka Pph, both in the King Gt where it aligned to the (now eroded) country rock and within the Paka Pph where the fabric aligned parallel to the surface of the King Gt.

Magnetic fabric variations elsewhere in the pluton may preserve similar mineral alignment now apparently distal to contacts. For instance, on the western flanks of the mountain the King Gt shows a moderate to steep foliation dip to the E. This may result from strain within the King Gt as the inflowing magma ascended around earlier (now indiscernible) composite magma pulses of this unit. Likewise, the similar foliation and lineation orientations of the NE Paka Pph and the Mesilau Pph samples nearby in the NW of their unit may represent orientation relative to the sub-horizontal contact that was present between them. This resulted in sub-parallel orientation of the Paka Pph foliation to the underlying contact and orientation of the Mesilau Pph foliation sub-parallel to the overlying contact surface with the Paka Pph, although the contact has since been eroded in this region.

Implications

Interpreting the dominant magnetic fabric in Mt Kinabalu as a result of regional tectonic NW-SE extension during emplacement supports the interpretation of Hall (2013) that SE Asia was undergoing extensional tectonics during the Neogene, specifically between 7.85 and 7.22 Ma (Cottam *et al.*, 2010). By combining the U-Pb zircon ages with the tectonically oriented AMS data (excluding the samples discussed to have oriented towards contact surfaces) we can propose the dominant extensional direction present during the emplacement of each unit (Fig. 4.8). As only two of the six Donkey Gt samples appear not to have preferentially aligned parallel to the contacts between the Donkey Gt and the King Gt this unit is excluded from this interpretation. The Mesilau Pph is also excluded due to its much more inconsistent orientations which may indicate that the fabric of the unit is dominated by secondary post-crystallisation precipitation of magnetite. However, if the fabric is primary then the dominant E-W lineations indicate a very different stress regime. The highly variable K_1 direction with a sub-horizontal mean orientation may then indicate compressional forces in a N-S direction during the latter stages of Mt Kinabalu's emplacement, although interpretation remains ambiguous without further sampling.

The predicted extension directions shown in Fig. 4.8 do not take into account tectonic rotation of the pluton post emplacement or rotation of each unit by upward deformation from the emplacement of later units. However, if AMS data and accurate ages of intrusion for granitic plutons could be combined with paleomagnetic data on the same samples (provided that the paleomagnetic orientation of the rock analysed was not reset through heating by the later intrusions) these factors could be corrected for. This application may have the potential to become a potent tool for determining stress regimes at specific points in time in regions of complex or ambiguous tectonic histories such as SE Asia.

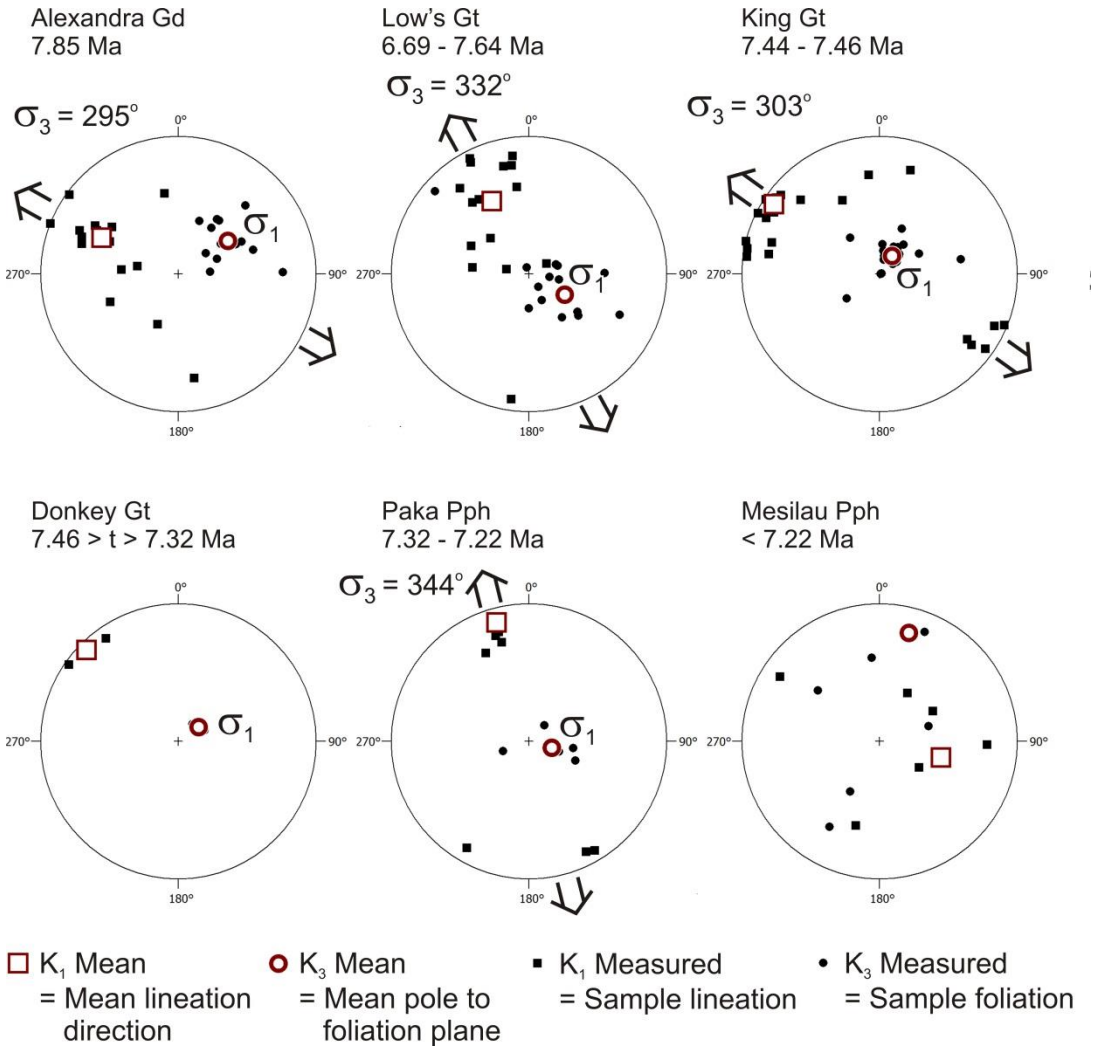

Fig. 4.8. *K_1* and *K_3* values for all units excluding contact oriented samples and interpreted principal stress directions (σ_1 and σ_3). Stress directions absent when data is deemed too ambiguous (see text). Age of emplacement from U-Pb zircon dates of Cottam *et al.* (2010). Samples where *K_1* and *K_2* values are not statistically significantly distinct at the 95% confidence level are excluded from the lineation data and samples where *K_2* and *K_3* values are not significantly distinct at the 95% confidence level are excluded from the foliation data.

Conclusions

1. The magnetic fabric at Mt Kinabalu is dominantly hosted by biotite in the Alexandra Granodiorite and the Donkey Granite and by magnetite in the later units, demonstrated by a much stronger magnetic susceptibility in the latter.
2. The AMS fabric of the Alexandra Granodiorite is in agreement with the orientation of the biotite foliation observed in outcrop.
3. The AMS data indicate that Mt Kinabalu was emplaced during NW-SE directed extension, shown by the prevalence of shallow NW plunging lineations and shallow dipping foliations in the AMS fabric of most units.
4. Tectonic magnetic fabrics in plutons are pervasive, as shown by the consistent AMS fabrics at Mt Kinabalu present over kilometres of vertical range and horizontal extent.
5. In addition to this tectonic fabric there is evidence for the orientation of the mineral fabric sub-parallel to contact surfaces from magma flow during emplacement.
6. The combination of AMS with U-Pb zircon dates allows temporal constraint of the paleo-stress field in the region. This technique may have application in tectonically ambiguous regions elsewhere.

Benn, K., Horne, R.J., Kontak, D.J., Pignotta, G.S. and Evans, N.G. (1997). Syn-Acadian emplacement model for the South Mountain batholith, Meguma Terrane, Nova Scotia: magnetic fabric and structural analyses. *Geological Society of America Bulletin*. **109**, 10, 1279-1293.

Benn, K. (2009). Anisotropy of magnetic susceptibility fabrics in syntectonic plutons as tectonic strain markers: the example of the Canso pluton, Meguma Terrane, Nova Scotia. *Earth and Environmental Science Transactions of the Royal Society of Edinburgh*. **100**, 1-2, 147-158.

Blès, J.-L. and Fuega, B. (1986). The fracture of rocks.

Bouillin, J.-P., Bouchez, J.-L., Lespinasse, P. and Pecher, A. (1993). Granite emplacement in an extensional setting: an AMS study of the magmatic structures of Monte Capanne (Elba, Italy). *Earth and Planetary Science Letters*. **118**, 1, 263-279.

Clemens, J.D. and Benn, K. (2010). Anatomy, emplacement and evolution of a shallow-level, post-tectonic laccolith: the Mt Disappointment pluton, SE Australia. *Journal of the Geological Society*. **167**, 5, 915-941.

Cottam, M., Hall, R., Sperber, C. and Armstrong, R. (2010). Pulsed emplacement of the Mount Kinabalu granite, northern Borneo. *Journal of the Geological Society*. **167**, 1, 49-60.

Cottam, M., Hall, R., Sperber, C., Kohn, B., Forster, M. and Batt, G. (2013). Neogene rock uplift and erosion in northern Borneo: evidence from the Kinabalu granite, Mount Kinabalu. *Journal of the Geological Society*.

Cruden, A. and McCaffrey, K. (2001). Growth of plutons by floor subsidence: implications for rates of emplacement, intrusion spacing and melt-extraction mechanisms. *Physics and Chemistry of the Earth, Part A: Solid Earth and Geodesy*. **26**, 4, 303-315.

Cruden, A.R. (1998). On the emplacement of tabular granites. *Journal of the Geological Society*. **155**, 5, 853-862.

Hall, R. (2013). Contraction and extension in northern Borneo driven by subduction rollback. *Journal of Asian Earth Sciences*.

Horsman, E., Tikoff, B. and Morgan, S. (2005). Emplacement-related fabric and multiple sheets in the Maiden Creek sill, Henry Mountains, Utah, USA. *Journal of structural geology*. **27**, 8, 1426-1444.

Jacobson, G. (1970). *Gunung Kinabalu area, Sabah, Malaysia*. Sabah, Geological Survey of Malaysia.

Jelinek, V. (1981). Characterization of the magnetic fabric of rocks. *Tectonophysics*. **79**, 3, T63-T67.

Jelínek, V. (1978). Statistical processing of anisotropy of magnetic susceptibility measured on groups of specimens. *Studia geophysica et geodaetica*. **22**, 1, 50-62.

King, R.C., Backé, G., Morley, C.K., Hillis, R.R. and Tingay, M.R. (2010). Balancing deformation in NW Borneo: Quantifying plate-scale vs. gravitational tectonics in a Delta and Deepwater Fold-Thrust Belt System. *Marine and Petroleum Geology*. **27**, 1, 238-246.

Owens, W. (2000). Statistical applications to second-rank tensors in magnetic fabric analysis. *Geophysical Journal International*. **142**, 2, 527-538.

Owens, W.H. (1994). Laboratory drilling of field-orientated block samples. *Journal of Structural Geology*. **16**, 12, 1719-1721.

Park, R.G. (2001). *Foundations of Structural Geology*. Routledge.

Paterson, S.R., Fowler Jr, T.K., Schmidt, K.L., Yoshinobu, A.S., Yuan, E. and Miller, R.B. (1998). Interpreting magmatic fabric patterns in plutons. *Lithos*. **44**, 1, 53-82.

Petronis, M., O'Driscoll, B., Stevenson, C. and Reavy, R. (2012). Controls on emplacement of the Caledonian Ross of Mull Granite, NW Scotland: Anisotropy of magnetic

susceptibility and magmatic and regional structures. *Geological Society of America Bulletin*. **124**, 5-6, 906-927.

Rochette, P. (1987). Magnetic susceptibility of the rock matrix related to magnetic fabric studies. *Journal of Structural Geology*. **9**, 8, 1015-1020.

Sperber, C.M. (2009). The thermotectonic development of Mount Kinabalu, Sabah, Malaysia: Constraints from low-temperature thermochronology. *Department of Earth Science, Royal Holloway, University of London.* PhD.

Stevenson, C.T., Hutton, D.H. and Price, A.R. (2006). The Trawenagh Bay Granite and a new model for the emplacement of the Donegal Batholith. *Transactions of the Royal Society of Edinburgh: Earth Sciences*. **97**, 04, 455-477.

Stevenson, C.T., Owens, W.H. and Hutton, D.H. (2007a). Flow lobes in granite: The determination of magma flow direction in the Trawenagh Bay Granite, northwestern Ireland, using anisotropy of magnetic susceptibility. *Geological Society of America Bulletin*. **119**, 11-12, 1368-1386.

Stevenson, C.T., Owens, W.H., Hutton, D.H., Hood, D.N. and Meighan, I.G. (2007b). Laccolithic, as opposed to cauldron subsidence, emplacement of the Eastern Mourne pluton, N. Ireland: evidence from anisotropy of magnetic susceptibility. *Journal of the Geological Society*. **164**, 1, 99-110.

Tongkul, F. (1997). Polyphase deformation in the Telupid area, Sabah,Malaysia. *Journal of Asian Earth Sciences*. **15**, 2-3, 175-183.

Vigneresse, J.L. (1995). Control of granite emplacement by regional deformation. *Tectonophysics*. **249**, 3, 173-186.

Wennerström, M. and Airo, M.-L. (1998). Magnetic fabric and emplacement of the post-collisional Pomovaara Granite Complex in northern Fennoscandia. *Lithos*. **45**, 1, 131-145.

Chapter 5:

Sourcing granitic melts from basalt fractionation, development of isotopic disequilibrium and the problems with crustal anatexis: Evidence from Mt Kinabalu, Borneo

Looking west along the Eastern Ridge towards the Eastern Plateau

Chapter 5: Sourcing granitic melts from basalt fractionation, development of isotopic disequilibrium and the problems with crustal anatexis: Evidence from Mt Kinabalu, Borneo

Abstract

The Mt Kinabalu granitic intrusion of Sabah, Malaysian Borneo, provides an opportunity to study the generation and evolution of felsic plutonic melts and the development of continental crust.

Six distinct major units and associated dykes compose the pluton. The trace and major element chemistry of the initial two units are distinctly more mafic than the later, more voluminous units, and the earliest unit has radiogenic isotope signatures more similar to continental crust than the later units. All show the relative trace element enrichments and depletions associated with arc magmatism and continental crust, despite this intrusion post-dating any subduction in the region by many millions of years.

The Mt Kinabalu intrusion is used to test the alternative theories for the generation of felsic plutonic melts. Tonalites of the offshore Dangerous Grounds attenuated continental crust share a similar isotopic signature to Mt Kinabalu and may have been subducted beneath NW Borneo, providing a suitable source through incongruent dehydration melting. A model is presented to test whether incongruent melting of tonalites whose mineral phases have developed isotopic disequilibrium would produce the observed signatures, and shows it to be an unsuitable source. Anatexis of other crustal sources is also disregarded based on experimental evidence, as melts generated from felsic crust, mafic crust and sediments are unable to generate metalluminous melts with the intermediate Cao/Na_2O and K_2O/Na_2O compositions of Mt Kinabalu.

Fractionation of a basaltic mantle melt generated by regional Neogene extension, similar to basalts from elsewhere in Borneo, is proposed as the process by which

the magma of Mt Kinabalu was generated. Felsic melts were produced through the crystallisation of plagioclase and hornblende-rich cumulates with simultaneous incongruent assimilation of immature, biotite-rich metasediments. A new method for modelling major element fractionation is presented and compared with published experimental data, revealing that the chemical variations between the units of Mt Kinabalu are determined by the degree of fractionation and assimilation. More voluminous and evolved melts are generated following recharge of the initial fractionated system of the earliest unit. These factors increase the initial K content and decrease the rate of assimilation, and so the water content of the melt. This enhances plagioclase stability and produces a more metalluminous melt for later units.

It is noted that the composition of continental crust shares similarities to the composition of Mt Kinabalu, meaning that it also cannot be produced through partial melting of crustal lithologies. Thus, the implications of the processes advocated for the generation of Mt Kinabalu are also explored for the generation of continental crust, and we propose that both the felsic and mafic units of the continental crust are generated from basaltic mantle melts.

Introduction

Granitic intrusions form the majority of the Earth's upper continental crust and provide many of our precious metals. In recent years their emplacement mechanisms and structure in the crust have become much better understood (Clemens and Mawer, 1992, McCaffrey and Petford, 1997, Petford and Clemens, 2000, Petford *et al.*, 2000), moving from models of slow moving diapirs to rapid dyke emplacement of laterally extensive laccoliths. However, the processes involved in producing these melts and the origin of the commonly observed geochemical signatures and heterogeneities are still disputed. This is not through a lack of potential processes but the opposite, with multiple potential means for deriving evolved melts of suitable compositions.

These can be divided into three major processes: (1) Fractionation of mafic mantle derived melts, (2) crustal anatexis and (3) mixing of mantle and anatectic melts. All three have been proposed for many different plutons worldwide (e.g. Chappell and White, 1992, Bogaerts *et al.*, 2006, Jagoutz *et al.*, 2009, Clemens and Benn, 2010, Leuthold *et al.*, 2013), with varying popularity. This study presents an investigation into the plausibility of each process in the formation of the Mt Kinabalu pluton in Sabah, Malaysia. A range of geochemical techniques are applied to determine its origin so that the global implications of these processes can be discussed.

The Mt Kinabalu pluton provides an ideal target for this study as it is composed of composite units with field evidence and U-Pb zircon dates (Cottam *et al.*, 2010) providing relative and absolute ages and timescales for intrusion. Complete exposure on its glaciated summit and spectacular exhumation with limited loss of high level material (Sperber, 2009) provides outcrops through much of its vertical extent.

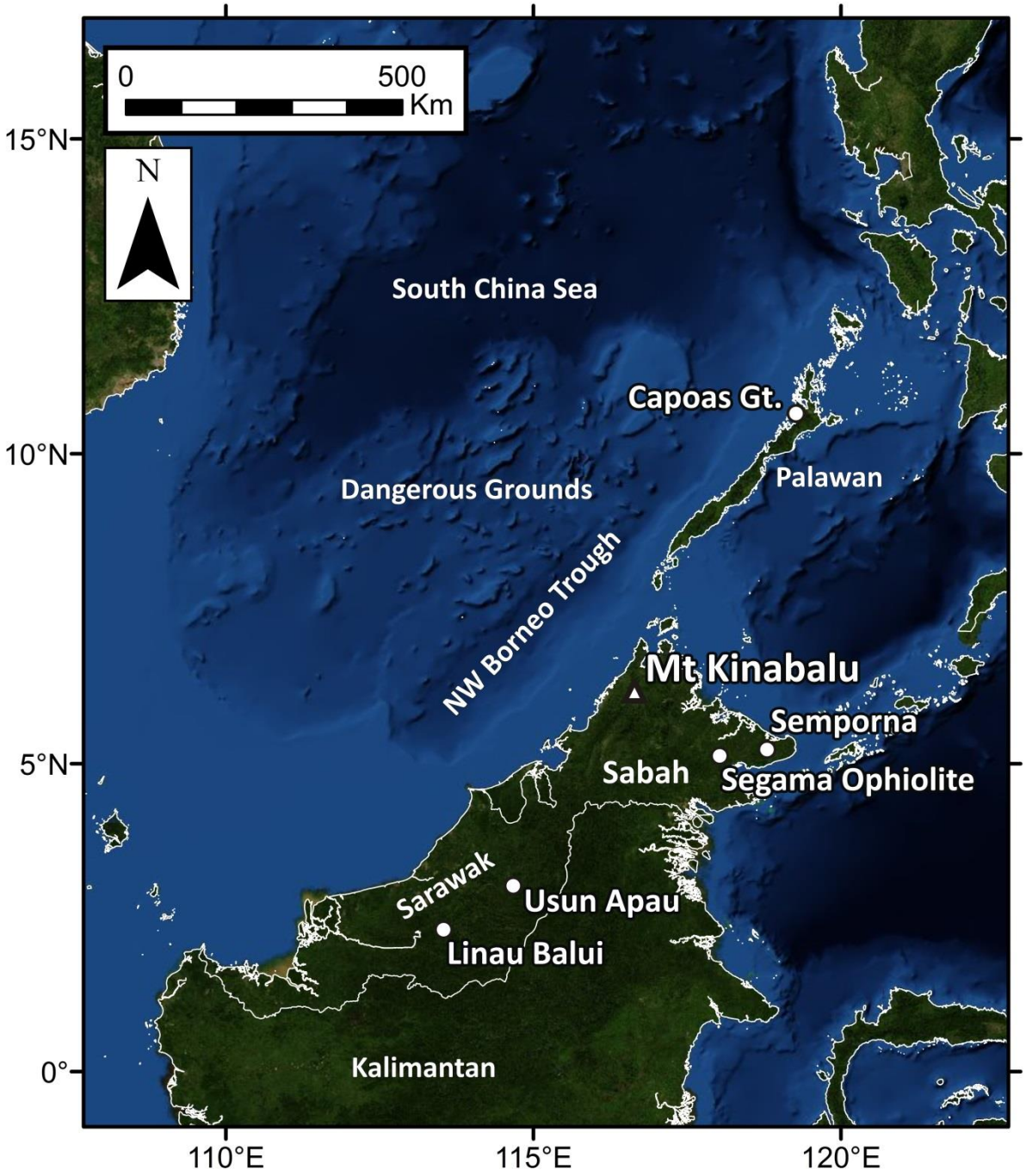

Fig. 5.1. Regional map of Borneo, Palawan and the South China Sea, with localities referred to in the text.

Regional Geological History and Tectonic Setting

The formation of Mt Kinabalu is intrinsically related to the geological and tectonic history of Sabah, NW Borneo and the South China Sea region (Fig. 5.1). Most of Sabah is underlain by an ophiolitic basement (Fig.5.2) dominantly composed of peridotites with associated amphibolitised gabbroic and basaltic units and overlying submarine volcanic rocks and cherts. This supra-subduction zone ophiolite was emplaced at approximately 200 Ma (Leong, 1974, Leong, 1998, Coggon *et al.*, 2011, see Chapter 2) during the initiation and early period of subduction of the western Pacific Plate beneath South China and SE Asia. The development of the early Pacific arc in this region resulted in later intrusive and extrusive magmatism in the ophiolite and the development of prolonged and extensive magmatism in East Asia, stretching from the Schwaner granite mountains of Kalimantan in SW Borneo (Moss, 1998), the Dalat granites of Vietnam (Nguyen *et al.*, 2004), the granitic crust of the South China Sea (Yan *et al.*, 2010), the volcanic and intrusive magmatism of Hong Kong (Davis *et al.*, 1997) and the widespread, largely granitic Yanshanian belt in S. China (Zhou and Li, 2000). This magmatic belt persisted across S. China and SE Asia until 79Ma (Zhou and Li, 2000) when the arc migrated eastwards.

Following this period the region underwent extension, resulting in deposition of the Late Cretaceous to Late Eocene Rajang group (Balaguru, 2001). This is a sequence of deep marine turbidite sedimentation into the large SW-NE trending Crocker Basin of NW Borneo. The Late Eocene unconformity marking its uppermost stratigraphic limit resulted from the Sarawak orogeny (Hutchison, 1996). This regional extension also resulted in the Paleogene volcanism of South China between 64 and 43 Ma (Chung *et al.*, 1997) followed by spreading of the South China Sea (SCS), dated using marine magnetic anomalies to between 31 and 20.5 Ma (Taylor and Hayes, 1983, Briais *et al.*, 1993, Barckhausen and Roeser, 2004). Three models are proposed for this extension (Fig. 5.3): 1. The extrusion model (Tapponnier *et al.*, 1986) in which the India-Asia collision resulted in the South China Sea being pulled open by displacement along laterally extensive strike slip faults; 2. The subduction model (Hall, 2009), in which southward directed subduction of the Proto-SCS along NW Borneo resulted in rifting through slab pull; 3. The continental rift basin model

(Cullen *et al.*, 2010) in which a combination of far-field stresses from slab roll back along Java and Sumatra and extrusion in SE Asia resulted in southward crustal extension. Whichever model is true, extension of the SCS thinned and rifted continental crust that had originally formed along the Mesozoic arc of S. China, ultimately forming the SCS oceanic basin along the SW-propagating spreading centre and causing NW-SE extension.

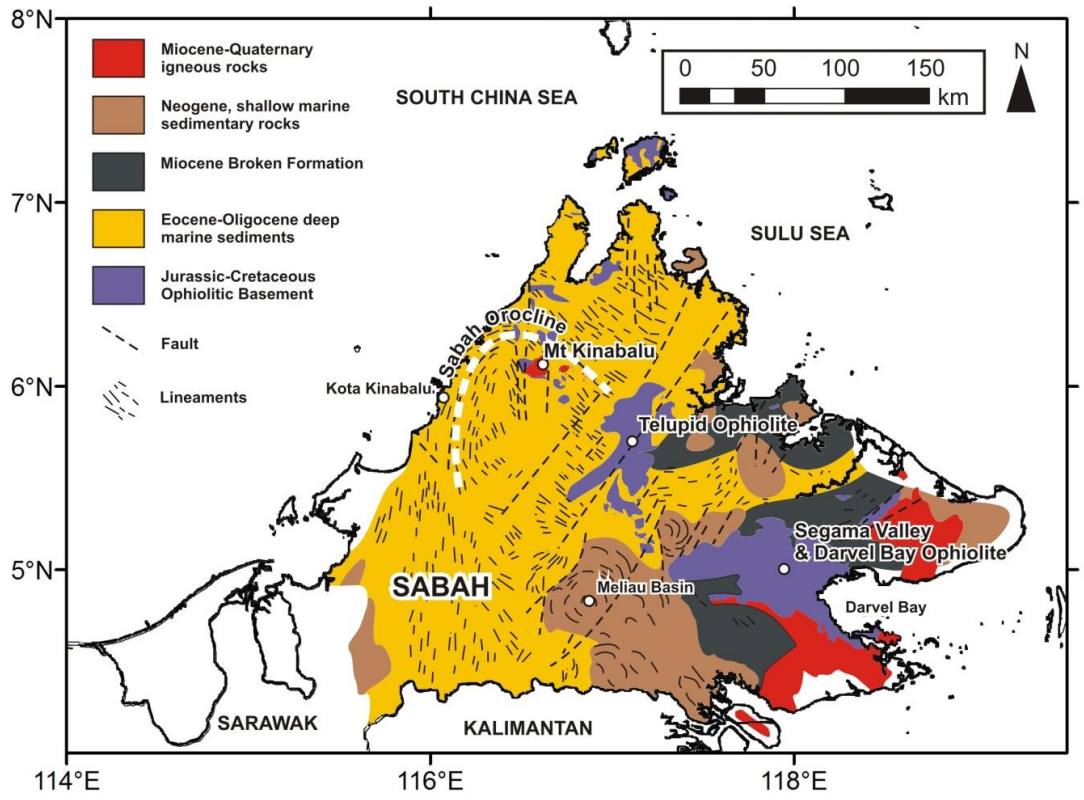

Fig. 5.2 Simplified geological map of Sabah, adapted from Kirk (1968) and Balaguru and Nichols (2004).

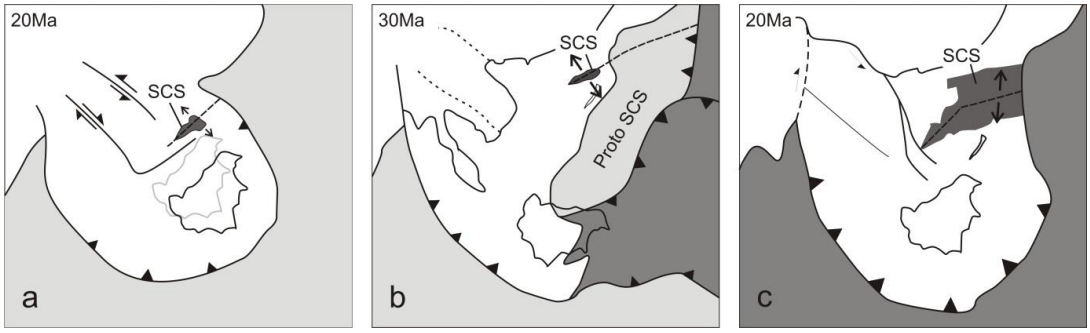

Fig. 5.3. Miocene tectonic illustrations of the proposed models for the opening of the South China Sea: (a) The extrusion model (Tapponnier *et al.*, 1986), (b) The subduction model (Hall, 2002), and (c) the continental rift model (Cullen, 2010). Adapted from Cullen (2010).

During this period of SCS extension, turbidite deposition of the Crocker Formation continued in Sabah (van Hattum *et al.*, 2013). The cessation of extension and SCS spreading is recorded in the sediments of onshore and offshore Sabah by the multiple unconformities of the protracted inversion event of the Sabah Orogeny between ~20 and 9 Ma (Hutchison, 1996, van Hattum *et al.*, 2013). In the subduction model this is attributed to the collision of the Dangerous Grounds attenuated continental crust from S. China, forming the continental shelf of the southern South China Sea (Fig. 5.1) with NW Borneo. Alternatively the unconformities may represent far-field compression associated with the NW-directed subduction of the Celebes Sea beneath SE Sabah (Cullen, 2010).

Renewed extension following the Sabah Orogeny in the Late Miocene (Hall, 2013) resulted in regional uplift in Sabah and progradation through the Miocene into the Pliocene and led to increasingly shallower deposition of carbonates and shallow marine to fluvial deltaic deposits of the Serudong Group (Balaguru, 2001). This renewed extension also coincided with the production of scattered Late Cenozoic magmatism in the South China Sea region, including the Mt Kinabalu intrusion (7.85 - 7.22 Ma, Cottam *et al.*, 2010), the Capoas intrusion of Palawan (13.5 Ma, Suggate *et al.*, 2013), the Scarborough Sea Mounts (13.9 - 1.6 Ma, Tu *et al.*, 1992, Yan *et al.*, 2008), extrusive and intrusive magmatism in Sarawak (Kirk, 1968) including the Usun Apau volcanics of Sarawak (4 Ma, Cullen *et al.*, 2013), the Semporna volcanics

of Eastern Sabah (3 Ma, Chiang, 2002, Macpherson *et al.*, 2010) and magmatism in Kalimantan, including the Metulang Plateau and Nuit volcanics (4.9 Ma, Moss *et al.*, 1997) and the Keramu river minette dykes (8 Ma, Bergman *et al.*, 1988).

Field relations, emplacement and previous work

The emplacement of the Mt Kinabalu pluton and the composition and field relations of its units are discussed in Chapter 3. The pluton intruded through an ophiolitic basement composed dominantly of peridotite and was emplaced at the contact between the basement and the overlying turbidite sandstones. These sediments were more able to deform through flexure than the peridotites and so provided accommodation space for the pluton. The pluton was constructed as a laccolith, similar to the models of Corry (1988) and Cruden (1998), through the emplacement of five major units plus minor units and dykes over a period of approximately 0.8 My (Cottam *et al.*, 2010).

The earliest unit, the 0.5km^3 "Alexandra Peak" Biotite Tonalitic Granodiorite (Alexandra Gd), was emplaced at 7.85 Ma and now forms the western summit plateau (Fig. 5.4). The second unit, the 9.5km^3 "Low's Peak" High Ti Hornblende Granite (Low's Gt), was emplaced between 7.69 and 7.64 Ma beneath the Alexandra Gd and at higher levels around its contacts. The much larger third unit, the 75km^3 "King George Peak" Low Ti Hornblende Granite (King Gt), was emplaced beneath the earlier units and forms the majority of the pluton's outcrops. Before full solidification of the King Gt the vertical sheet-like body of the "Donkey's Ears Peak" Biotite Granite (Donkey Gt) intruded within it. The first of two porphyritic units, the 40km^3 "Paka" Porphyritic Hornblende Granite (Paka Pph), was emplaced at 7.32 – 7.22 Ma beneath the pre-existing bodies and rose around their base and sides. Finally, the 40km^3 "Mesilau" Porphyritic Hornblende Granite (Mesilau Pph) was emplaced again, beneath and to the SE of the other units. Pyroxene Monzonite (Pyx Mon) dykes also intruded through the Alexandra Gd, Low's Gt and King Gt.

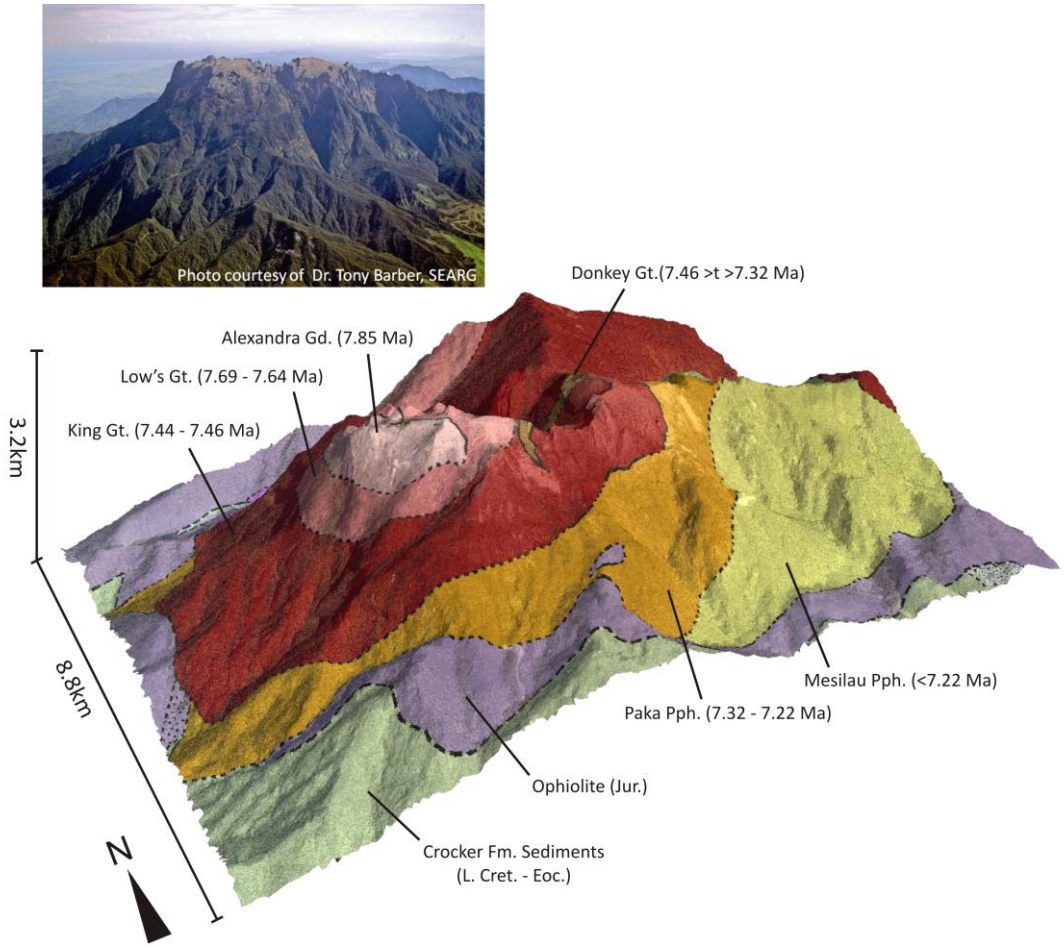

Fig. 5.4. Aerial photograph of Mt Kinabalu looking NE (courtesy of Dr Tony Barber, SEARG) and 3D geological map of the same view showing units and emplacement ages. U-Pb zircon ages from Cottam *et al.* (2010). Geological map from Burton-Johnson *et al.* (in prep.). DEM courtesy of SEARG (the South East Asia Research Group, Royal Holloway University, London).

Previous geochemical studies (Vogt and Flower, 1989, Chiang, 2002, Sperber, 2009, Cottam *et al.*, 2010, Cottam *et al.*, 2013) have analysed major and trace elements and strontium isotopes and obtained ages by apatite and zircon fission track and U-Pb zircon dating. Based on their evolved isotope signature, inherited zircon ages and arc-like trace element pattern the Mt Kinabalu pluton was interpreted as being derived from partial melts of unexposed crust, either old continental or andesitic crust underlying the ophiolite or subducted beneath it.

Methodology

To investigate the formation and evolution of Mt Kinabalu's magma we have collected and analysed a range of geochemical data including major and trace element concentrations, Sr, Nd and Pb radiogenic isotopes and oxygen isotope ratios.

Samples were crushed and milled to a fine powder using a fly press and agate ball mills. The powders were analysed for major element composition by XRF at Edinburgh University, and by ICP-MS and PIMMS *(*Plasma Ionisation Multi-collector Mass Spectrometry) at Durham University to obtain trace element and radiogenic isotope data respectively. For XRF analysis the samples were dried at 1100^{o}C to calculate Loss On Ignition (LOI) before being mixed with $LiBO_2$ flux and fused into glass discs for analysis (Gill, 1997). Trace element analysis followed the procedure presented in Ottley *et al.* (2003). Samples were dissolved using HF and HNO_3, and analysed on a ThermoScientific X-Series 2 ICP-MS using blanks, repeated samples and the standards BHVO-1, W2 and AGV-1 for calibration and quality control. For felsic samples where significant and observable depletions in Zr and Hf were the result of incomplete dissolution of zircon crystals, trace elements were determined by standard HF dissolution for all elements except those highly compatible in zircon (Ta, Cs, Zr, Hf, Th, U, Nb, Y and the REE except La, for which the $LiBO_2$ flux during flux fusion affects analytical accuracy). To analyse these elements the samples were prepared again but fused in the same way as for XRF to break down zircon and resistant accessory phases prior to dissolution. To determine accuracy and reproducibility the standards AGV-1, BHVO-1 and W2 as well as two samples from Mt Kinabalu were analysed multiple times in each analytical batch of samples as well as acid blanks and the flux material used for flux fusion prior to dissolution. This QC data is presented in Appendix A1.2.

Sample preparation for analysis of Sr and Nd radiogenic isotopes followed the column chemistry procedures detailed in Charlier *et al.* (2006). Whole rock powders were dissolved in HF and HNO_3 SpA acid and separated by column chemistry using Sr-spec resin and Hf-Nd cation resin (AG50 X-8). The lead fraction was collected in

100µl 8N HCl from the Sr columns following collection of the Nd and Sr fractions and waste elution using 200µl 2.5N HCl. The Pb fraction was then dried down, dissolved in 500µl 3% HNO_3, and spiked with ^{206}Tl to correct for mass bias (Hirata, 1996). PIMMS analytical procedures are as detailed in Nowell *et al.* (2003). For Nd and Sr, measured values for the NBS987 and J&M standards (±2SD error) during the same run as the samples were 0.710269 ±23 (n=35) and 0.511110 ±11 (n=44) respectively. Data are corrected to the respective NBS987 and J&M standard values of 0.71024 (Thirlwall, 1991) and 0.511110 (Royse *et al.*, 1998). For Pb, measured values for the NBS981 standards ±2SD for $^{206}Pb/^{204}Pb$, $^{207}Pb/^{204}Pb$, $^{208}Pb/^{204}Pb$, $^{207}Pb/^{206}Pb$ and $^{208}Pb/^{206}Pb$ (n=20) are 16.94049 ±88, 15.49813 ±87, 36.7177 ±23, 0.91486 ±3 and 2.16744 ±9 respectively. Data are corrected to the respective values of NBS981 of 16.94051, 15.49800, 36.71744, 0.91485 and 2.16743 (Galer, 1997).

Oxygen isotopes were analysed on picked mineral separates using laser fluorination at the SUERC laboratories in East Kilbride. Whole rock samples were crushed and minerals were picked by hand and cleaned in an ultrasonic bath, being careful to select only crystals without visible alteration. Oxygen was extracted using the laser-fluorination technique of Mattey and Macpherson (1993), heating ~1mg of sample with a laser in the presence of the fluorinating agent, ClF_3. Oxygen was converted to CO_2 by reaction on a hot graphite rod and the isotopic composition of the collected sample analysed on a VG PRISM 3 dual inlet isotope-ratio mass spectrometer. Results are reported relative to Vienna Standard Mean Ocean Water (V-SMOW) in the delta notation ($\delta^{18}O$, expressed in per mil, ‰). All samples were analysed at least twice to determine precision and four analyses of the reference standards SES, GP147 and UWG2 were made each day to allow daily calibration. The mean daily standard error is 0.15‰ and the maximum standard error for one day's analyses was 0.26%.

Results

Data for all whole rock major and trace element geochemical analyses are presented in Appendix A4.1 and mineral separate concentrations are presented in Appendix A4.2. Whole rock isotope data is recorded in Appendix A4.3 and mineral separate oxygen isotope data is recorded in Appendix A4.4. Major element mineral separate data acquired from ion microprobe analysis was provided by Prof. Robert Hall of the South Asia Research Group. Data from selected phases is presented in Appendix A4.5.

Major and trace elements

The samples show a wide range of major element compositions through all the units with the Alexandra Gd and Low's Gt generally plotting as high-K calc-alkaline diorites according to major element classifications and the later units plotting as shoshonitic granodiorites and syeno-diorites (Fig. 5.5). Harker plots (Fig. 5.6 & 5.7) also show a clear distinction between the Alexandra Gd and Low's Gt and the more homogenous later units, with the earliest two units possessing higher Fe, Mn, Ti, Mg, Ca and lower K content, plus a higher Al and lower P content for the Alexandra Gd.

PM normalised multi-element plots (Fig. 5.8) show the distinct enrichment in Cs, Rb, Th, U, K and Pb compared to relative depletion in Nb, Ta, La, Ce and Ti typical of the continental crust and arc magmatism. However, as discussed there was no active subduction zone present locally at the time of emplacement. The plots of all units are very similar, the only major distinction being the marked decrease of $(Ba/Th)_{PM}$ and $(Ba/Rb)_{PM}$, and an increase in the U and Th concentration between the Alexandra Gd and Low's Gt with the later units (Fig 5.8a to c).

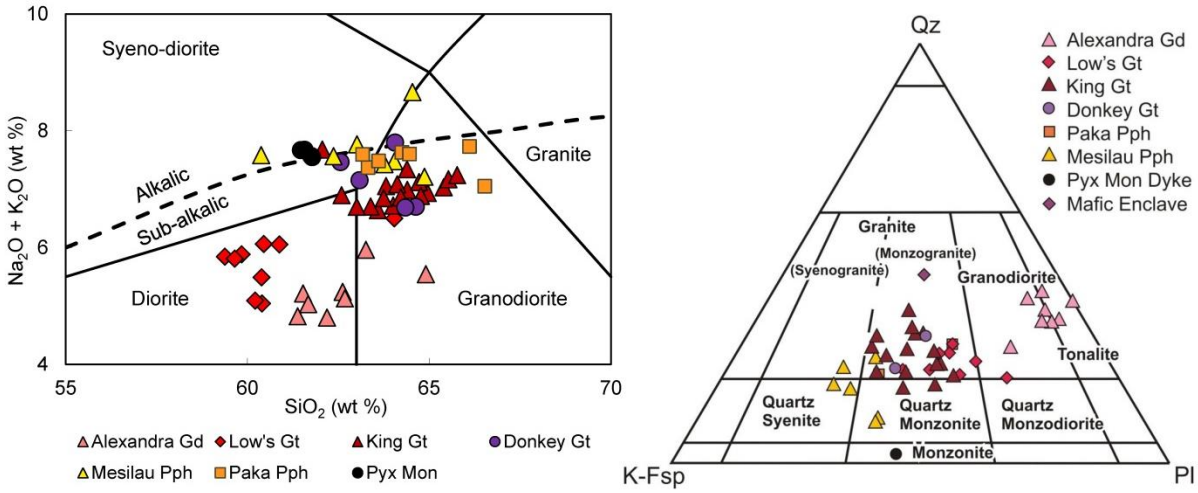

Fig. 5.5. (a) TAS (Miyashiro, 1974, Cox *et al.*, 1979) and (b) IUGS (Streckeisen, 1976) classifications of the Mt Kinabalu granitic units, based on major element and mineral modal abundances respectively. Point counted data for the QAP diagram from this study and Sperber (2009).

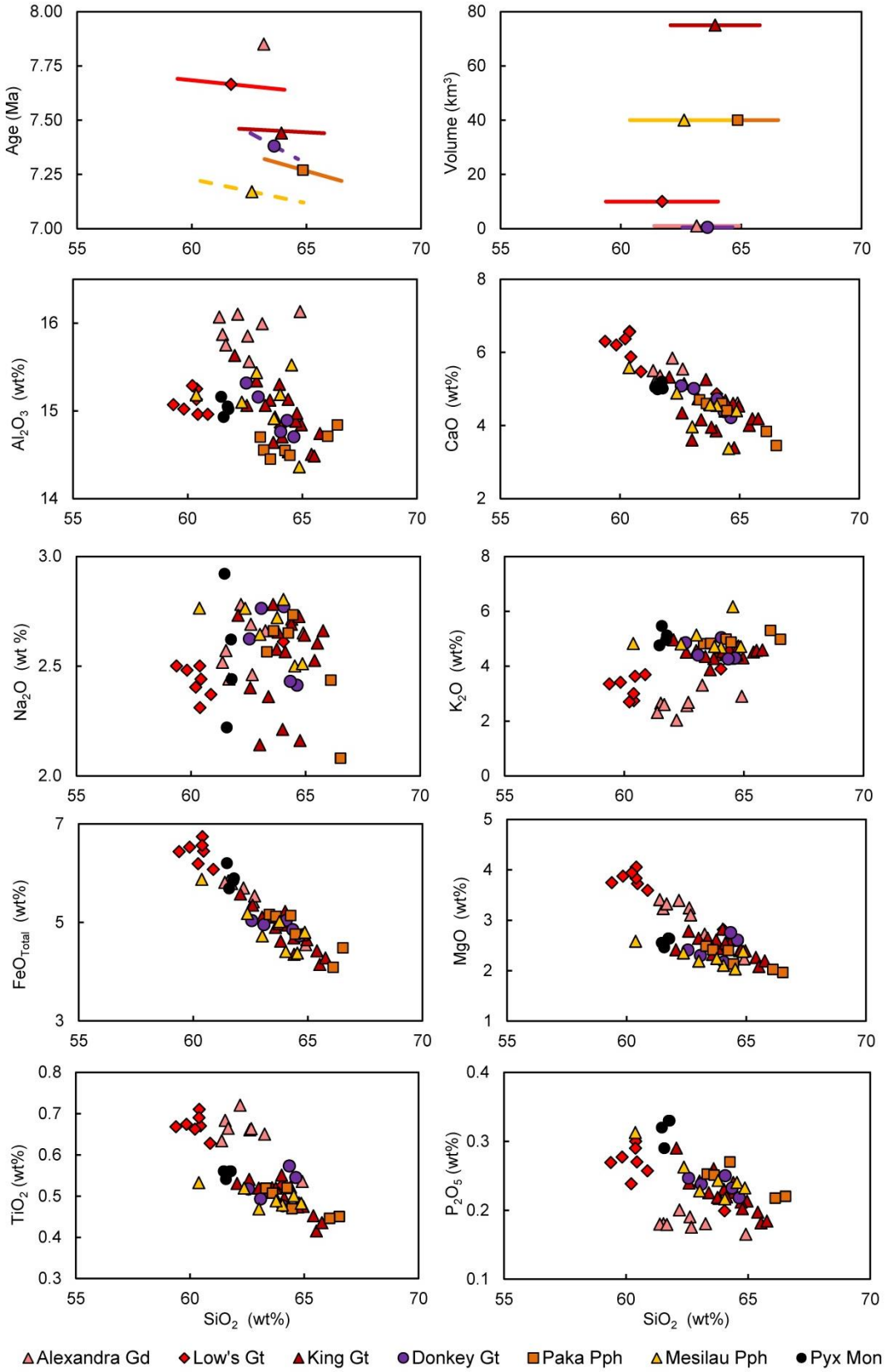

Fig. 5.6. Selected major element vs SiO_2 for the Mt Kinabalu granitic units, excluding samples determined to be cumulative for particular phases (discussed in results). Lines on age and volume plots show the range of values. Dotted lines show estimated age ranges.

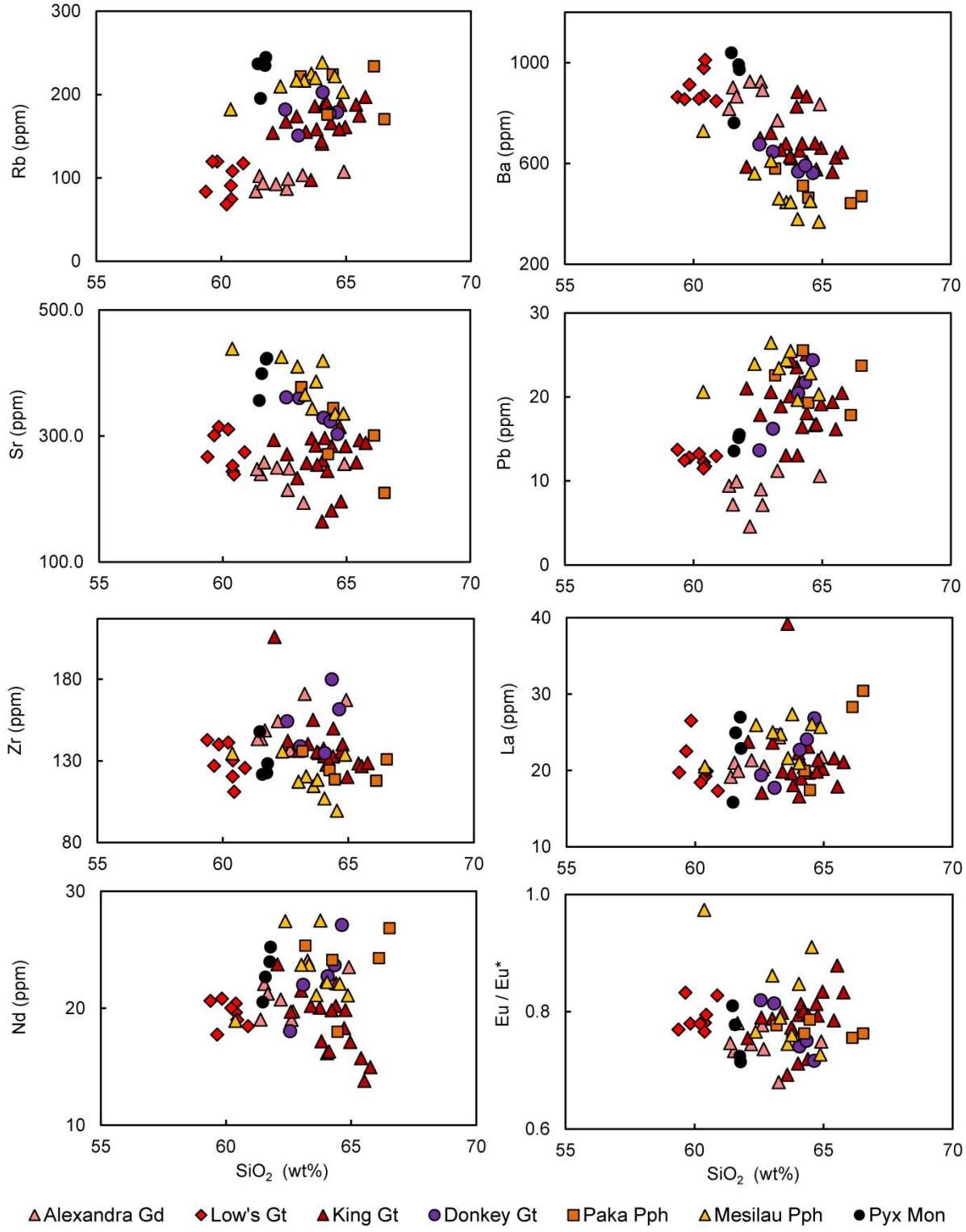

Fig. 5.7. Selected trace elements element vs SiO_2 for the Mt Kinabalu granitic units, excluding samples determined to be cumulative for particular phases (discussed in results). Eu* is defined as $\sqrt{((Sm_{sample}/Sm_{PM})*(Gd_{sample}/Gd_{PM}))}$.

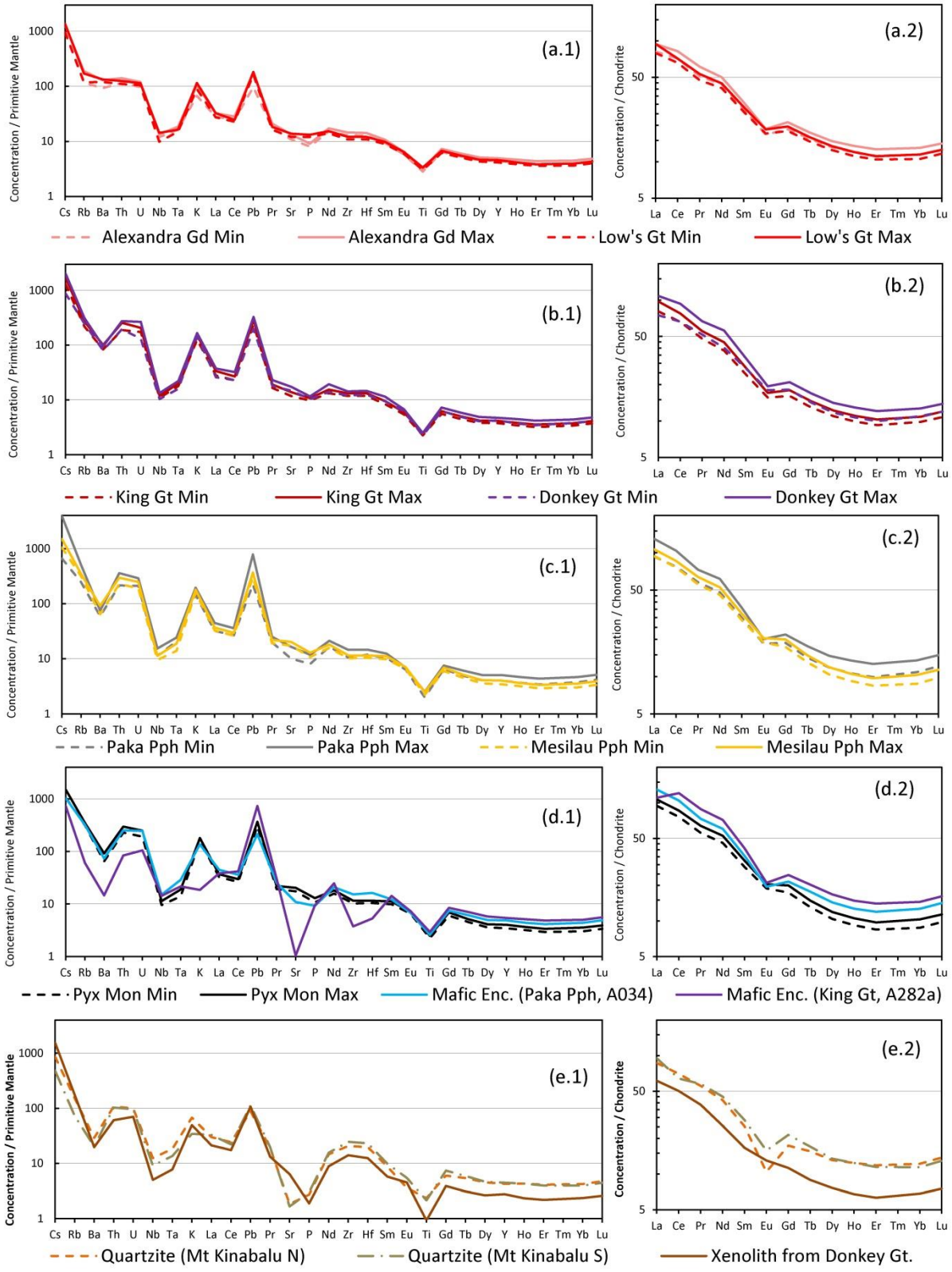

Fig. 5.8. Multi-element, primitive mantle normalised trace element plots and chondrite normalised REE plots for the Mt Kinabalu granitic units. Plots show the upper and lower 95% confidence limits for each unit. Normalising values from Sun and McDonough (1989).

All units have very similar chondrite normalised REE plots with a relative enrichment in the LREE compared to the HREE and a flat to slightly downward concave shape around the middle to heavy REE, also characteristic features of the upper continental crust and arc-type magmatism (Rudnick and Gao, 2003). There is a small Eu anomaly for all units, although this is markedly less for the Mesilau Pph (Eu/Eu* 95% confidence limits are 0.81 – 0.84 for the Mesilau Pph, compared to 0.72 – 0.79 for all other units), in which Sr also displays more elevated elemental concentrations.

Although during sample preparation of coarse grained lithologies larger volumes of material are processed than would be required for finer crystalline lithologies and milling to fine powder should homogenise a sample, there is still a greater risk for chemical analyses of coarse grained rocks to be overly enriched or deficient in a particular mineral phase compared to the original sample. Thus, it is particularly important when interpreting data from coarse intrusive samples to identify whether individual samples are representative of the chemistry of a unit. SBK122 (Low's Gt), CS080 (Pyx Mon) and A290b (Paka Pph) were identified as cumulative for hornblende based on their low K and high Ti and Dy contents; the Alexandra Gd sample, A049, and the King Gt samples CS070 and A085 are cumulative for plagioclase and deficient in alkali feldspar as indicated by their high Ca, Na and Sr and low K and Ba concentrations; the high K and Ba sample A198 (Mesilau Pph) is cumulative for alkali feldspar, and alteration has enriched the mineralised Mesilau Pph sample, A209 in fluid mobile elements including K and Pb. These cumulative samples are excluded from all figures but are included in Appendix A4.1.

Radiogenic Isotopes

The radiogenic isotopes of Sr, Nd and Pb plot in two clusters (Fig. 5.9 & 5.10), both with values expected for a continental crustal origin, with higher Sr and Pb and lower Nd isotope ratios than mantle or Bulk Silicate Earth values. The Alexandra Gd plots consistently in the cluster more similar to old continental crust (~0.7078 for $^{87}Sr/^{86}Sri$; ~0.51245 for $^{143}Nd/^{144}Nd$; ~18.756 $^{206}Pb/^{204}Pb$), while the later major

units, the mafic enclave from the King Gt, and the Pyx Mon dykes plot in the less continental cluster (~0.7065 for $^{87}Sr/^{86}Sr_i$; ~0.51250 for $^{143}Nd/^{144}Nd_i$; ~18.721 $^{206}Pb/^{204}Pb_i$). One Donkey Gt sample and the mafic enclave from the Paka Pph plot in the more continental cluster for Sr and Nd and between the two clusters for Pb (Fig.5.9).

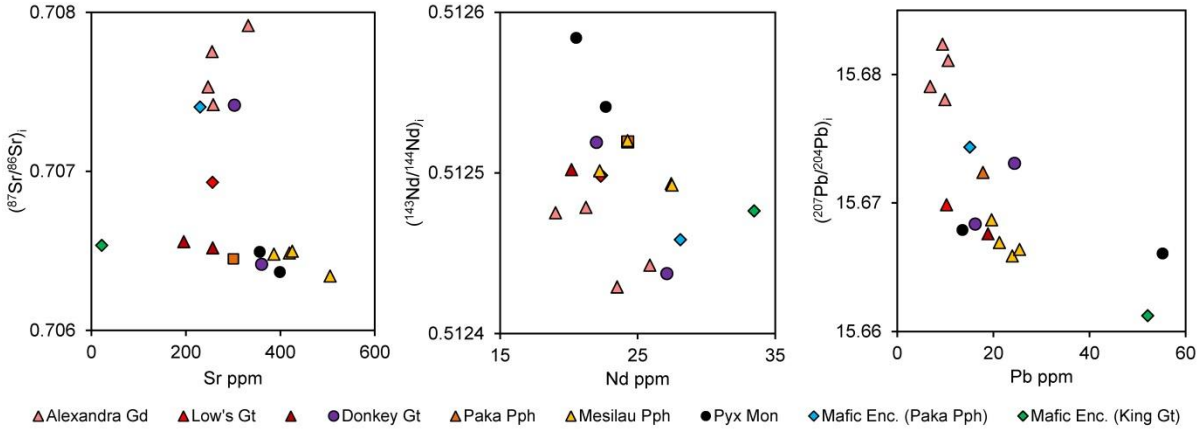

Fig. 5.9. Initial isotope values and respective trace element concentrations for the Mt Kinabalu units.

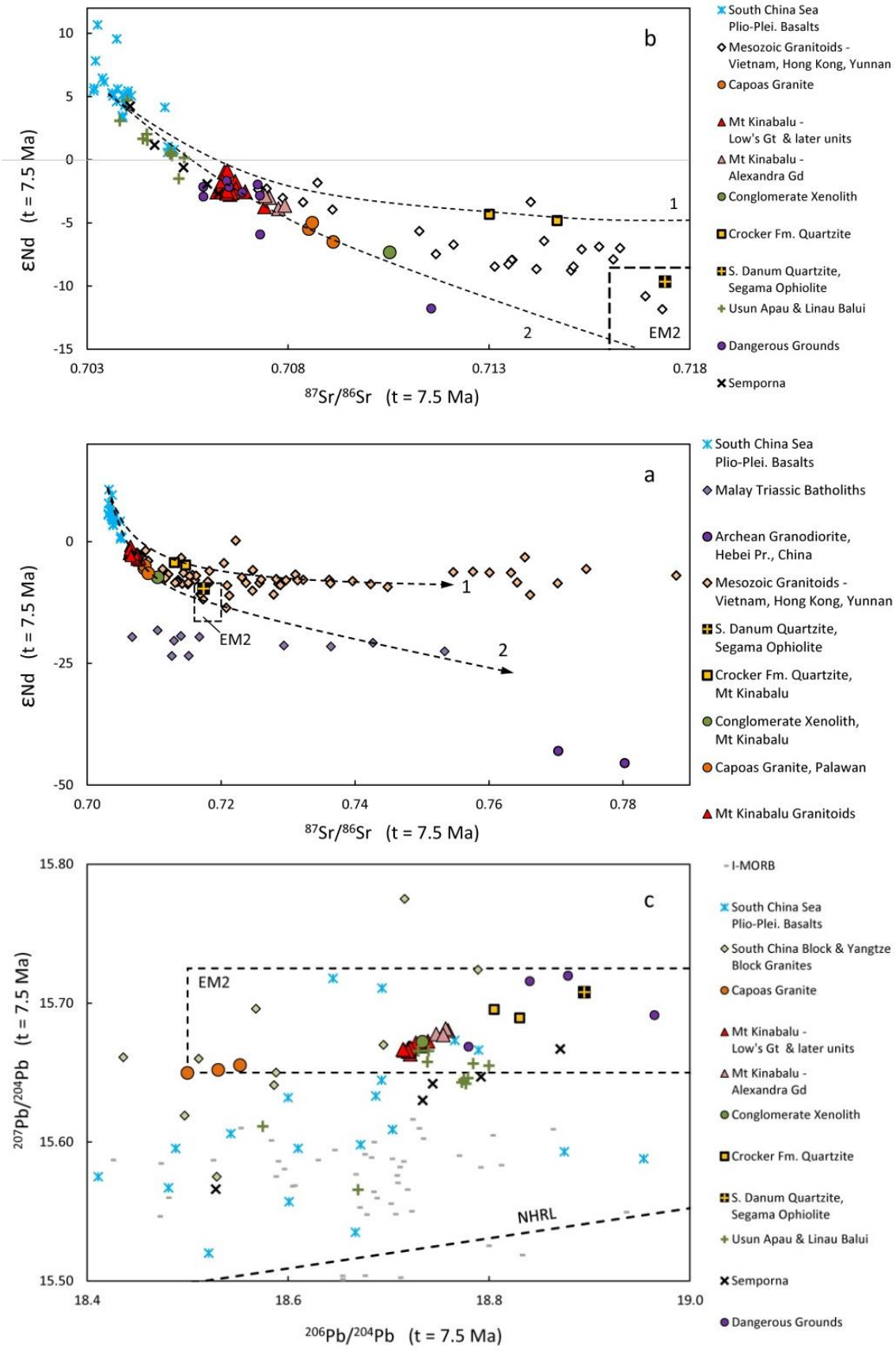

Fig. 5.10. Isotopic values at t = 7.5Ma for Mt Kinabalu, and regional lithologies for comparison. The two lines in (a) and (b) illustrate the two broad regional trends for samples

involving a larger component of Archean or Proterozoic crust, (2), and those with a lower contribution of older material based on their radiogenic isotope signature, (1). Data for comparison: South China Sea seamount basalts (Tu *et al.*, 1992, Yan *et al.*, 2008); Mesozoic granites of the South China Block and Yangtze Block (Zhu, 1995); Mesozoic Granitoids of Vietnam (Thuy *et al.*, 2004), Hong Kong (Darbyshire and Sewell, 1997) and Yunnan Province (Yanbo and Jingwen, 2010); Usun Apau and Linau Balui volcanics (Cullen *et al.*, 2013); granitic rocks of the Dangerous Grounds attenuated continental crust (Yan *et al.*, 2010, Yan *et al.*, 2011); Triassic Batholiths of the Malay Peninsula (Liew and McCulloch, 1985); Archean Granodiorite from Hebei Province, China (Jahn *et al.*, 1987); Spreading centre basalts of the Indian Ocean from the PetDB database (http://www.earthchem.org/petdb); Northern Hemisphere Reference line (NHRL) backdated to 7.5 Ma using the mean U & Pb concentrations of the I-MORB data (Hart, 1984). EM2 fields from Zindler and Hart (1986).

Comparison with regional data (Fig. 5.10) shows the Mt Kinabalu data to be within the range of Sr and Nd isotope data for the granitic rocks dredged from the South China Sea (Yan and Shi, 2009, Yan *et al.*, 2010) and similar to their Pb values, as well as some samples from the Mesozoic granitoids (Thuy *et al.*, 2004) and Cenozoic basalts (Nguyen *et al.*, 2004) of Vietnam and Mesozoic mafic samples from S China (Chen *et al.*, 2008, Wang *et al.*, 2008). Pb data for the region's magmatism, including Mt Kinabalu, diverges from the NHRL towards an EMII signature (Zindler and Hart, 1986) as also noted by previous authors (Hoang *et al.*, 1996, Yan *et al.*, 2008).

Oxygen Isotopes

15 hornblende, 12 quartz, 4 biotite and 1 pyroxene mineral separates were analysed for oxygen isotope ratios. By analysing different minerals the conditions of crystallisation and later alteration could be better constrained. Most of the samples form a cluster of $\delta^{18}O$ values around 9.1 to 10.3‰ for quartz and 6.6 to 8.2‰ for hornblende (Fig. 5.11), although one of the Alexandra Gd samples gave a lower value for hornblende and the Pyx Mon sample gave a lower quartz value. The pyroxene analysed from the Pyx Mon gave a much lower value of -1‰, and the biotite samples of the Alexandra Gd and Hb Gt gave a range of values from -1.3 – 5.9‰.

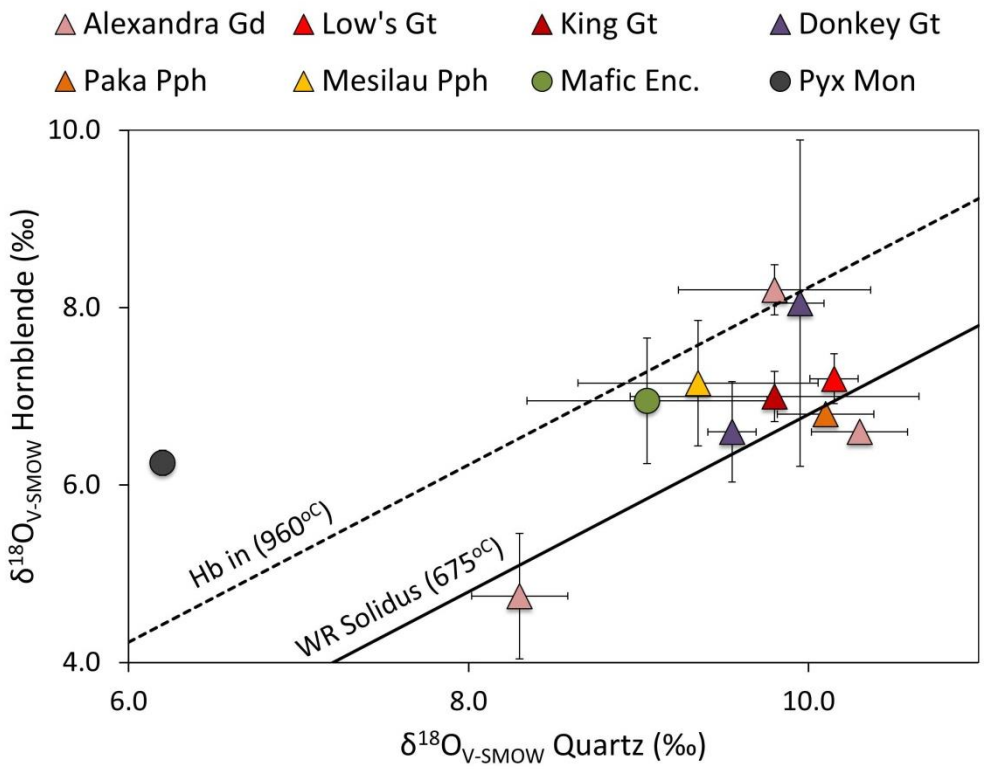

Fig. 5.11. δ-δ plot for quartz and hornblende. 2SD error bars based on two analyses of crystals from the same sample, indicating the combined analytical and natural variation. Isotherms calculated from Bottinga and Javoy (1975). Most data falls within the magmatic temperature range except two of the Alexandra Gd samples and the Pyx Mon dyke.

Country rocks

Samples of the ophiolite and turbidite sediments were also analysed for their major and trace element chemistry and their radiogenic isotope ratios. The ophiolite samples are discussed independently in Chapter 2. The turbidite sediments show arc-type trace element enrichments and depletions (Fig. 5.8e) inherited from their source, plus a positive Zr-Hf anomaly reflecting the concentration of zircon crystals in sediments as major mineral phases break down through weathering processes. Their Sr and Pb isotope ratios are more elevated than for Kinabalu but their Nd signature is very similar. The Pb isotopes of the conglomerate xenolith are within the range of the granitic samples but the Sr and Nd signatures are higher and lower respectively (Fig. 5.8).

Alteration

Prior to interpreting the data it is important to determine any alteration of the samples. For this, oxygen isotopes prove an invaluable tool as equilibration at magmatic temperatures will produce a distinctly higher and more restricted $\delta^{18}O$ isotope values than lower temperature equilibration with meteoric water.

Most of the samples fall within the $\delta^{18}O$ range of around 9.1 – 10.3‰ for quartz and 6.6 – 8.2‰ for hornblende. Thus, their $\Delta_{quartz\text{-}hornblende}$ values are equivalent to equilibrium temperatures of 610 - 1010^{o}C (Fig. 5.11) according to the hornblende-quartz equilibrium calculations of Bottinga and Javoy (1975). As the maximum thermal stability of hornblende is 960^{o}C (Naney, 1983) and the whole rock solidus is ~675^{o}C (Naney, 1983), this range represents magmatic temperatures. However, as can be seen in Fig. 5.11, some of the calculated quartz-hornblende equilibrium temperatures fall outside this expected range of magmatic temperatures.

The calculated temperatures for two of the two Alexandra Gd samples fall below the 675^{o}C whole rock solidus temperature. Oxygen diffusion in hornblende is much slower than the other major mineral phases with a much higher closure temperature (Farver and Giletti, 1985) and so is less affected by alteration by meteoric water. However, the higher diffusion rate of oxygen in quartz makes it more susceptible to resetting below the solidus. Zheng (1993a) and Zheng (1993b) published equations for determining mineral-water equilibrium temperatures and $\delta^{18}O_{water}$ values from measured $\Delta_{mineral\text{-}mineral}$ values of hydrous and anhydrous phases including quartz and hornblende. These calculations show that both Alexandra Gd samples equilibrated with water with a $\delta^{18}O$ composition of 7.0 – 8.9‰, equivalent to magmatic water, at temperatures of 720 – 760^{o}C, likely sourced from the later intrusive units below. This is supported by the alteration of much of the hornblende in this unit to biotite which has been shown experimentally (Brimhall *et al.*, 1985) to be the result of high temperature reactions in the periphery of a granitic intrusion between hornblende and magmatic fluid according to the equation:

$$NaCa_2Mg_5(AlSi_7O_{22})(OH)_2 + \tfrac{1}{2}K_2SO_4 + 4H_2SO_4 =$$
$$\text{edenite} \qquad (aq) \qquad (aq)$$

$$KMg_3(AlSi_3O_{10})(OH)_2 + 4SiO_2 + 2CaSO_4 + \tfrac{1}{2}Na_2SO_4 + 2MgSO_4 + 4H_2O$$
$$\text{phlogopite} \qquad \text{quartz} \quad \text{anhydrite} \quad (aq) \qquad (aq)$$

[Eq. 1]

The low $\delta^{18}O$ values for the quartz and pyroxene of the Pyx Mon sample and the biotite of the Alexandra Gd and King Gt, A047 and A282, cannot result from magmatic water, as the calculated $\delta^{18}O$ of the water they would be in equilibrium with remains below +5.5‰, the lower bound of magmatic water (Sheppard, 1986), even at temperatures up to 1000°C. If the quartz and pyroxene of the Pyx Mon sample are in equilibrium, then it is with water of a $\delta^{18}O$ composition of -0.5‰ at a temperature of 310°C. There is a strong link between the $\delta^{18}O$ of regional precipitation with latitude and altitude, and for this region the expected values would be approximately -5 to -10‰ (Bowen and Wilkinson, 2002). Equilibration with water at this composition would occur between 60 and 150°C for the biotite and pyroxene samples, and 135 and 200°C for the quartz sample, implying the presence of hot, hydrothermal meteoric water during cooling.

Excluding the values affected by post crystallisation equilibration, the $\delta^{18}O$ quartz values plot in one cluster of 9.1 – 10.2‰. However, having excluded the other two samples, the $\delta^{18}O$ of hornblende for the remaining Alexandra Gd sample, A049, plots 1‰ higher than the main cluster, as does the Donkey Gt, A093, although this sample is within 1σ error of the other data points. The Alexandra Gd value cannot be explained by alteration by sub-solidus alteration by water and so represents a magmatic value. However, it is unclear whether the other hornblende samples of the unit would have shared this value prior to alteration or whether an original discrepancy in the $\delta^{18}O$ quartz data has been masked by lower temperature diffusion.

Discussion

Crustal anatexis

As stated earlier, granitic melts can either be derived through fractionation of mantle derived melts, with or without crustal assimilation, or through partial melting of the crustal lithologies. Although a mantle derived origin for most volcanic magmatism is undisputed, melting of the overlying crustal material, with or without involvement of mantle derived melts, remains the dominant explanation for felsic plutons.

Based on the similarity between the radiogenic isotope signatures of the Mt Kinabalu samples and continental crust the ophiolitic country rocks are deemed an unsuitable source as they display a mantle affinity in their isotopic signatures (see Chapter 2). Chiang (2002) and Cottam *et al.* (2010) attributed the magmatism to melting of unexposed continental or andesitic crust of the Sabah lithosphere or subducted beneath it. An old felsic continental crust underlying the ophiolite of Sabah has been postulated based on geochemical (Macpherson *et al.*, 2010) and gravity data (Milsom *et al.*, 2001), and calc-alkaline intrusions within ophiolite outcrops of the Segama highlands have been attributed to exposures of or partial melts from this underlying crust. However, Chapter 2 showed that: (1) these small intrusions are calc-alkaline tonalites, representing supra-subduction zone arc magmatism associated with the Mesozoic subduction of the Pacific beneath SE Asia without evidence of contamination by felsic crust and, (2) the low gravity anomalies in the region can be explained by the overlying sedimentary basins and extension related asthenospheric upwelling (Macpherson *et al.*, 2010) without invoking an unexposed underlying crust. Therefore, if Mt Kinabalu is derived through melting of continental crust, this cannot be autochthonous material beneath the ophiolite. However, subduction of the Proto South China Sea beneath Borneo may also have subducted attenuated continental crust, providing a potential continental source.

Modelling anatexis of felsic crust and isotopic disequilibrium

Samples dredged from attenuated crust of the Dangerous Grounds in the South China Sea (Fig. 5.1) are monzogranites and tonalites (Yan and Shi, 2009, Yan *et al.*, 2010) that share similar radiogenic isotope signatures to Mt Kinabalu. Partial melting of tonalites has been advocated as a suitable source for granitic and granodioritic melts (Rutter and Wyllie, 1988, Roberts and Clemens, 1993, Singh and Johannes, 1996b), therefore subduction of this crust beneath NW Borneo could provide a suitable source for the Mt Kinabalu melts.

If the melts of Mt Kinabalu were derived from partial melting of a single tonalitic source, the question remains as to what caused the heterogeneity in the radiogenic isotopes of Mt Kinabalu as it should record the bulk isotopic signature of its source region. Hammouda *et al.* (1996), Knesel and Davidson (1996) and McLeod *et al.* (2012) showed that glasses produced by crustal melting can develop isotopic disequilibrium relative to their protolith though the incongruent melting of different constituent phases, providing that it occurs over shorter timescales than are required for equilibration through elemental diffusion. Isotopic disequilibrium of the anatectic glasses reflected isotopic disequilibrium between the source rock's constituent phases. This occurs because the parent and daughter elements of each isotopic system have different relative compatibilities for each phase and so are present in each phase in different relative proportions. For instance, Rb is much more compatible than Sr in biotite compared to hornblende. Consequently, the isotopic ratio for minerals with a higher parent/daughter ratio for that isotopic system will evolve to more radiogenic values in a given time than for minerals with a lower ratio. Thus, the higher Rb/Sr ratio of biotite than hornblende will result in higher $^{87}Sr/^{86}Sr$ values even though the rate of decay for ^{87}Rb is constant for all phases. Likewise, the higher Sm/Nd ratio of hornblende than biotite results in a higher $^{143}Nd/^{144}Nd$ value after a given time. The inheritance of Sr isotopic heterogeneity by granitic magmas by this process has previously been proposed by Farina and Stevens (2011) for hypothetical metasediment derived granitic melts.

It is also important to take account of the absolute concentration of the daughter element in each mineral phase when considering the isotopic composition derived from multiple mineral phases in isotopic disequilibrium. For instance, even if the $^{143}Nd/^{144}Nd$ isotopes of biotite and hornblende are very distinct the much higher concentration of Nd in hornblende than biotite means that the breakdown of hornblende will likely obscure any signature of biotite melting.

The evolution of isotopic disequilibrium in the South China Sea tonalites and the isotopic signature of melts derived by incongruent melting of different mineral proportions were modelled using the approach outlined in Supplementary A at the end of this chapter. As the composition of minerals in the South China Sea tonalites are unknown the most reasonable compositions to use are the mineral compositions of the Mt Kinabalu intrusion (Appendix A4.2) assuming that they share a similar composition to the minerals in their source. The similar appearance of the plagioclase and alkali feldspar separates means that they could not be differentiated and subsequently are modelled together as 'Undifferentiated Feldspar'.

The age of the source (t) has been taken as the mean age of the dredged South China Sea samples (Yan *et al.*, 2010) minus the age of the Alexandra Gd, 7.85Ma (Cottam *et al.*, 2010), and the initial isotopic compositions have been taken from within the range of values of the dredged samples. The variable for each model presented is the fraction of the melt derived from each mineral phase. For the Mt Kinabalu system we have modelled different mineral assemblages to represent the progressive dehydration melting of different mineral phases in a tonalite at 10kbar under increasing temperatures observed by Rutter and Wyllie (1988), resembling deep melting of the continental crust (Fig. 5.12). However, quantitative proportions of the minerals melting were not recorded. Instead we have chosen mineral assemblages to represent the melt progression qualitatively. Rutter and Wyllie (1988) carried out a series of melting experiments, observing after different temperatures the mineralogy present and the percentage of melt produced. They observed initial melting to result from biotite breakdown at 825^{o}C releasing water for melting, with step-like increase in the degree of melting above 925^{o}C when

hornblende breaks down. Of the original anhydrous mineral phases, K-feldspar was the first to be consumed followed by quartz while plagioclase remained present throughout. To simulate this order of events, we have modelled melts derived from four different mineral assemblages, summarised in the table of Fig. 5.13. We start with a melt derived from 25% biotite, decreasing to 5%, whilst the hornblende content synchronously changes from 0 to 15%. Along with biotite, the quartz content also decreases from 40 to 20% whilst the feldspar content increases from 35 to 60% to simulate the increasing degree of melting.

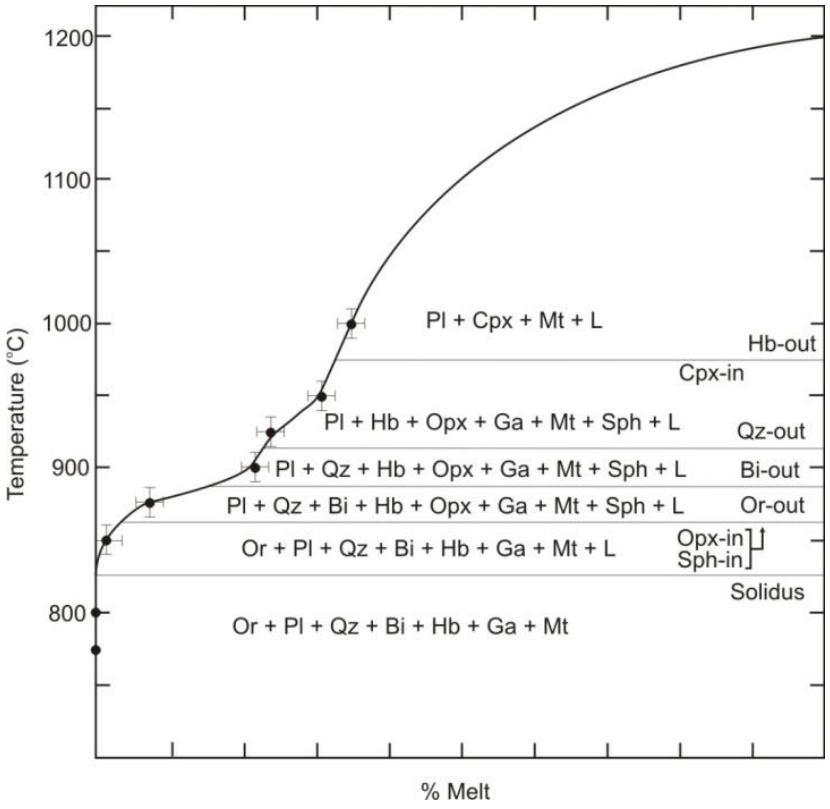

Fig. 5.12. Experimentally determined phase disappearance and appearance during dehydration partial melting of a tonalite at 10kbar. Adapted from Rutter and Wyllie (1988).

Watt and Harley (1993) and Bea (1996) have shown that the accessory phases of a granitic rock contain a significant proportion of its trace element budget. To quantify their proportions in the source, we have assumed a maximum possible apatite content, whereby all of the P_2O_5 in the Kinabalu samples is derived from

apatite breakdown. We have also assumed that all of the Zr and Hf in the samples is derived from zircon breakdown, and so have calculated the modal percentages of zircon required to meet this. The REE composition of a melt composed of this phase assemblage (calculated using the mineral separate data) would be deficient in the LREE compared to the observed compositions, so allanite has been included in the proportions required to meet the deficit.

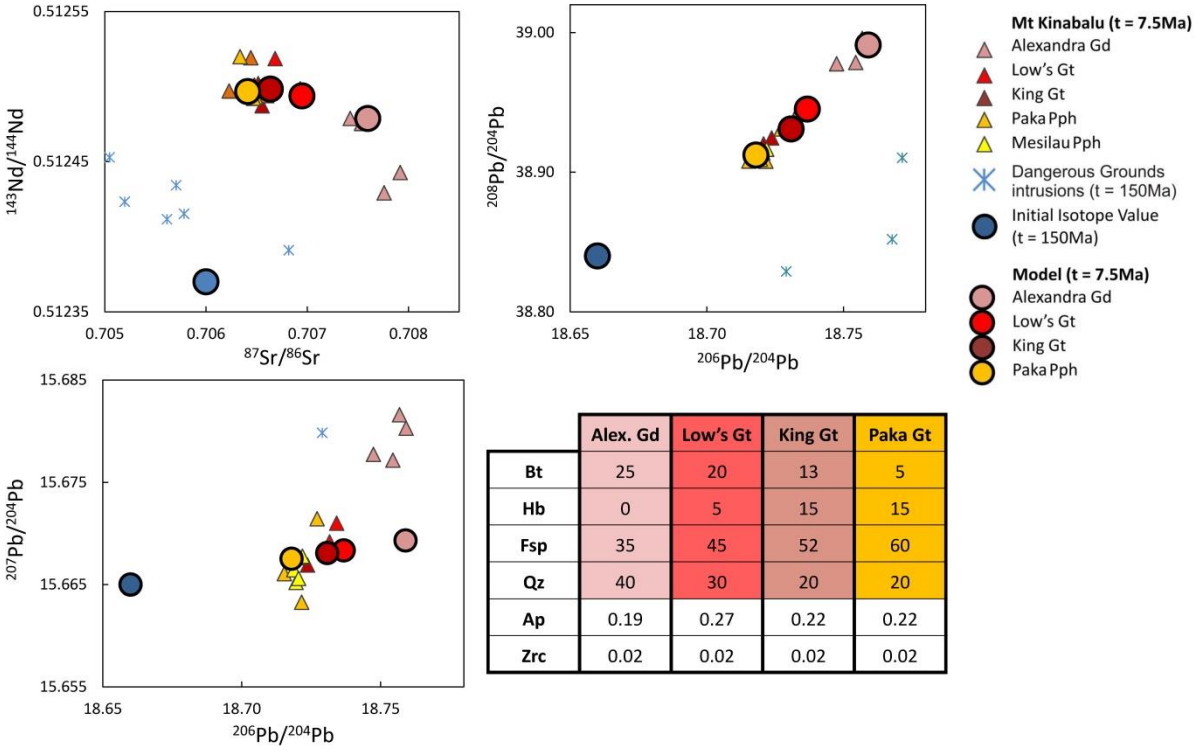

	Alex. Gd	Low's Gt	King Gt	Paka Gt
Bt	25	20	13	5
Hb	0	5	15	15
Fsp	35	45	52	60
Qz	40	30	20	20
Ap	0.19	0.27	0.22	0.22
Zrc	0.02	0.02	0.02	0.02

Fig. 5.13. Isotopic disequilibrium models, calculated according to Supplementary A. Circles indicate the resultant isotopic signature of melts derived from assemblages of mineral phases in the proportions given in the table. Isotopic signatures of the individual minerals all started at the "Initial Isotope Value" at t = 150Ma, and evolved on different vectors according to the relevant abundances of the parent and daughter elements of each isotopic system. The model value calculated incorporates their resultant signature at t = 7.5Ma, the mineral proportions and the absolute concentration of the daughter element in each mineral phase.

Modelling of the Sr, Nd and Pb isotope systems are shown in Fig. 5.13. along with the isotopic data from the Mt Kinabalu granitoids, the Dangerous Grounds samples and the initial isotopic composition of the models at t_0 (150Ma). As can be seen, this progression of mineral assemblages contributing to the melt may result in very similar patterns for $^{87}Sr/^{86}Sr$, $^{143}Nd/^{144}Nd$, $^{206}Pb/^{204}Pb$ and $^{208}Pb/^{204}Pb$ to those of the Mt Kinabalu samples (Fig. 5.13 a & b). This shows that since the emplacement of this tonalitic crust enough isotopic disequilibrium could have developed to create the isotopic heterogeneities observed, provided the melts extracted were sourced through progressive breakdown of the modelled mineral proportions.

The model illustrates how particular mineral phases would control each isotopic system. In the Sr system, high values of $^{87}Sr/^{86}Sr$ can only be achieved by biotite breakdown. However, the much higher Sr concentration and lower Rb/Sr ratio in the feldspars means that their increased contribution to the melt progressively dilutes the diminishing biotite signature and results in decreasing Sr isotope ratios. Similarly, the Sm/Nd ratio of hornblende is much higher than for the other major phases, as is its Nd concentration, and so even small degrees of hornblende breakdown will mask the lower Nd isotope ratios of feldspar and biotite and result in higher $^{143}Nd/^{144}Nd$ values. Finally, although the U/Pb and Th/Pb ratios are higher in hornblende than the other major phases that might be expected to produce an increase in the Pb ratios with progressive melting (e.g. the feldspars), the much higher concentration of Pb in the feldspars dominates the system so the increase in their contribution acts as a buffer and results in lower $^{206}Pb/^{204}Pb$ and $^{208}Pb/^{204}Pb$ ratios as the degree of melting increases.

As the whole rock chemistry of the Mt Kinabalu samples shows little variation in P, Zr and LREE between units, the percentage of the melt derived the accessory phases does not change much between each stage. As such their inclusion in the model has little effect on the relative concentrations of its results, although their absolute values, especially for the Pb system, are notably affected. However, we have assumed here all of the P and Zr are derived from apatite and zircon respectively, and so the abundance of these minerals entering the melt, and

subsequently their effect on the model, would be less if the concentration of these elements in the major mineral phases were included.

However, disequilibrium melting ceases to be a suitable cause of the isotopic heterogeneity of Mt Kinabalu when we consider the $^{207}Pb/^{204}Pb$ system (Fig. 5.13c). The $^{207}Pb/^{204}Pb$ ratio evolves slower than $^{206}Pb/^{204}Pb$ and $^{208}Pb/^{204}Pb$ in the model than for the Kinabalu samples, shown by the shallower gradient of the model in Fig. 5.13c. This is because ^{235}U has a much shorter half-life than the parent isotopes of ^{207}Pb and ^{208}Pb, and so its natural abundance has changed at a much faster rate over time. This results in a relatively low $^{235}U/^{207}Pb$ ratio at the time of the Dangerous Grounds tonalites' emplacement, and produces the shallow model gradient for $^{207}Pb/^{204}Pb$ against $^{206}Pb/^{204}Pb$. This feature makes the $^{207}Pb/^{204}Pb$ ratio much more sensitive than the other Pb isotope ratios to involvement of older material. U and Pb are fluid mobile, but processes resulting in their loss or gain would be unable to steepen the gradient. Loss of U would decrease the amount of ^{207}Pb produced, and as the abundance of ^{235}U is globally constant at any given time a gain of U would only result in faster evolution of both systems and not a steeper gradient. Loss of Pb would reduce the gradient by reducing the earlier signature, and gain of lead would reduce the rate of evolution in both systems and reduce the range of values. Consequently, there is no process by which the observed steep gradient and data range between $^{207}Pb/^{204}Pb$ and $^{206}Pb/^{204}Pb$ can be produced solely by disequilibrium melting.

Other sources of anatectic melting

The model has shown that partial melting of a single source region of crust similar to the dangerous Grounds would be an unsuitable source for the Mt Kinabalu magma. Alternative anatectic sources could either be melting of an unexposed lithology present in the subducted crust or melting of a heterogeneous crust, mixing melts from different lithologies.

^{235}U was much more abundant in the Archean and Proterozoic, and an isochron fitted to the $^{207}Pb/^{204}Pb$ and $^{206}Pb/^{204}Pb$ data produces an age of 3.6Ga. There are no known Archean outcrops in the South China Sea region, and so this age could reflect partial melting of an unexposed Archean lithology, a later igneous source that had itself been derived from Archean crust, or mixing of two sources that fall along this line.

Little Pb isotope data exists on the Dangerous Grounds crust (Yan *et al.*, 2011), but if an isochron is fitted through the data of its onshore equivalent in South China (Zhu, 1995) it also gives an Archean isochron of 3.7Ga, and so the Kinabalu melts could have inherited a similar signature if they melted the same source as these Mesozoic plutons. Alternatively, as the source region for a granitic partial melt would be significantly larger than the volume of the pluton produced, the melts would be derived from multiple plutons of a composite crust. Thus, melting of this composite but still lithologically homogenous crust such as the granitic crust of the Dangerous Grounds may allow the melts to inherit the overall isotopic trend of the source region rather than that of an individual pluton and so produce the observed Mt Kinabalu isochron. This means subducted continental crust may remain a potential source.

To test the plausibility of these alternative anatectic processes, and the ability for anatexis of felsic crust to produce suitable melt compositions, experimental data for partial melting of tonalites and felsic crustal sources was compiled, along with the available data for melting experiments of basalts, amphibolites and sediments as alternative sources (Vielzeuf and Holloway, 1988, Beard and Lofgren, 1991, Douce and Johnston, 1991, Rapp *et al.*, 1991, Rushmer, 1991, Skjerlie and Johnston, 1992, Rushmer, 1993, Sen and Dunn, 1994, Wolf and Wyllie, 1994, Douce and Beard, 1995, Gardien *et al.*, 1995, Rapp and Watson, 1995, Singh and Johannes, 1996a, Singh and Johannes, 1996b, Winther, 1996, Montel and Vielzeuf, 1997, Gardien *et al.*, 2000, Douce, 2005, Sisson *et al.*, 2005, Xiong *et al.*, 2005, Xiao and Clemens, 2007). All of the compiled data for all degrees of melting is plotted in Fig 5.14 classified as three broad source types: (1) felsic crust, (2) sediments and (3) mafic basaltic or amphibolitic crust.

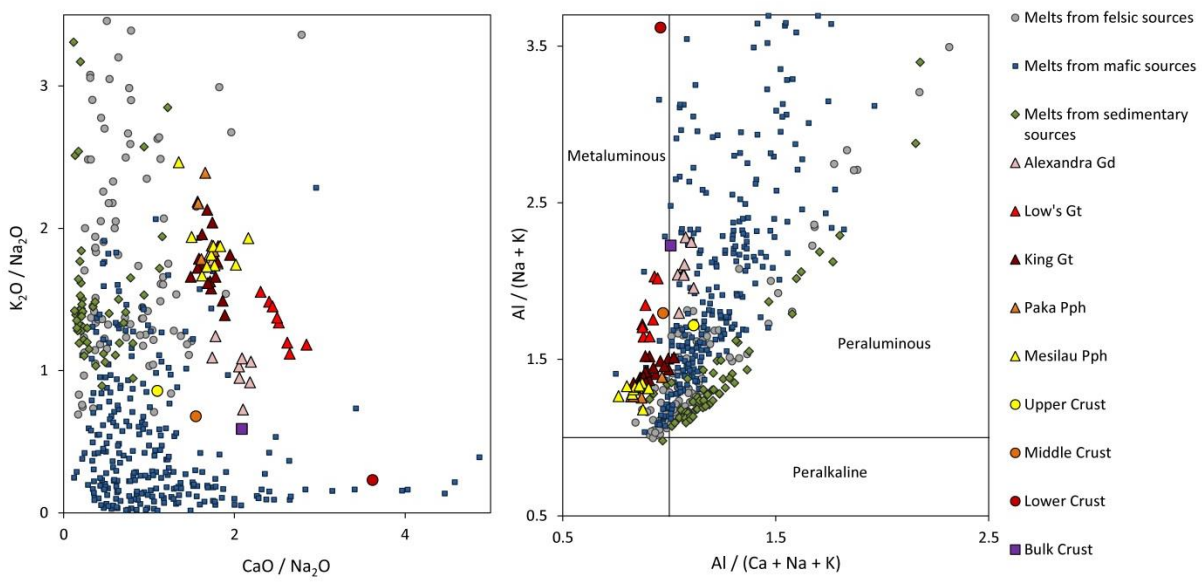

Fig. 5.14. Comparison of the Mt Kinabalu data with collated melting experiment data for melting experiments on potential felsic sources (tonalites and felsic gneisses), mafic sources (basalts and basaltic amphibolites), and sedimentary sources (sediments and metasediments) (Vielzeuf and Holloway, 1988, Beard and Lofgren, 1991, Douce and Johnston, 1991, Rapp *et al.*, 1991, Rushmer, 1991, Skjerlie and Johnston, 1992, Rushmer, 1993, Sen and Dunn, 1994, Wolf and Wyllie, 1994, Douce and Beard, 1995, Gardien *et al.*, 1995, Rapp and Watson, 1995, Singh and Johannes, 1996a, Singh and Johannes, 1996b, Winther, 1996, Montel and Vielzeuf, 1997, Gardien *et al.*, 2000, Douce, 2005, Sisson *et al.*, 2005, Xiong *et al.*, 2005, Xiao and Clemens, 2007). Note that the samples showing CaO/Na_2O values >2.4 are peraluminous and have molar Al/(Na+K) values >3.4 (Rushmer, 1991, Rushmer, 1993, Wolf and Wyllie, 1994). Crustal values from Rudnick and Gao (2003).

Plotting the ratios of the alkali metals, SiO_2 and the aluminium indices (molar Al/(Na + Ca + K)) and Al/(Na + K) shows that each source produces melts of particular compositions, regardless of their degree of melting. Sedimentary sourced melts are strongly peraluminous and produce high K_2O/Na_2O and very low CaO/Na_2O ratios. Melts derived from felsic crust also have high K_2O/Na_2O and low CaO/Na_2O ratios unless K_2O/Na_2O is >2, and are also strongly peraluminous. Consequently neither would be suitable sources for Mt Kinabalu. Melts derived from basalts or basaltic amphibolites are more weakly peraluminous and have a low K_2O/Na_2O ratio, but almost always have CaO/Na_2O ratios that are too low to be suitable primary melts for Mt Kinabalu. Only melts derived from exceptionally Ca rich and Na and K deficient basaltic amphibolites (Rushmer, 1991, Wolf and Wyllie, 1994) have

suitably high CaO/Na_2O ratios, but are strongly peraluminous with exceptionally high ratios of Al/(Na + K). Importantly, mixtures of these high CaO/Na_2O with high K_2O/Na_2O sources would remain peraluminous and so melts derived solely from crustal anatexis, be they from a single source or a mixture of sources (including the commonly invoked mafic lower crust), would be unable to create the major element composition of Mt Kinabalu and other metalluminous or intermediate to high CaO/Na_2O and K_2O/Na_2O magmatism.

Basaltic fractionation

If crustal anatexis is an unsuitable process to produce melt chemistry required for Mt Kinabalu, perhaps fractionation of a mantle derived melt would be a more plausible mechanism. The potential for fractional crystallisation of mafic magmas to produce evolved calc-alkaline magmas has been shown experimentally, and is determined by the relative proportions and compositions of the crystallising phases (especially pyroxene, amphibole, plagioclase and garnet). This is, in turn, determined by the pressure, temperature, H_2O activity and fO_2 of the system (Grove *et al.*, 2003, Müntener and Ulmer, 2006, Alonso-Perez *et al.*, 2009, Ulmer and Muntener, 2011, Krawczynski *et al.*, 2012).

As there is no evidence for contemporaneous mafic magmatism in the region of Mt Kinabalu, the nature and chemistry of a basaltic precursor is unclear. Instead we can look only slightly further afield to the Plio-Pleistocene basalts and basaltic andesites of Linau Balui and the Semporna Peninsula (Macpherson *et al.*, 2010, Cullen *et al.*, 2013). Basalts from both magmatic centres share similar chemical compositions, but the larger dataset for the Linau Balui basalts makes them preferable for chemical modelling. The most mafic sample from Linau Balui (LB64) is thus used as the initial major, trace and isotopic composition for the following models.

As the radiogenic and oxygen isotopes of Mt Kinabalu do not reflect a purely mantle source, petrogenesis through basaltic fractionation must also incorporate crustal

assimilation (AFC). The pluton's radiogenic isotope ratios plot at the end of the range of radiogenic isotope values of the basalts and dacites of Semporna and Usun Apau. This range of isotopic data displayed by the volcanic samples has been explained using AFC models of basaltic mantle derived melts assimilating felsic crust. The assimilant in these models has been proposed as either Archean felsic crust or Mesozoic granitic crust that has itself incorporated Archean or Proterozoic material, as evidenced by the high Sr and low Nd isotopic ratios of the South China and Malay granitoids (Liew and McCulloch, 1985, Zhu, 1995, Macpherson *et al.*, 2010, Cullen *et al.*, 2013). Accordingly, different potential assimilants from the region were tested in the modelling for Mt Kinabalu.

Modelling basalt fractionation and assimilation

Major element modelling

Due to their stoichiometric constraints, major elements cannot be modelled using partition coefficients in the same way as trace elements. For mafic systems the modelling program MELTS (Ghiorso and Sack, 1995) is commonly used but, unfortunately, this is not recommended for modelling of systems dominated by hornblende fractionation. Mass balance equations are commonly used instead, but do not reflect the changing compositions of mineral phases in response to the evolution of their parent liquid. Instead, we have developed an iterative major element AFC model that incorporates simultaneous trace element and isotopic modelling and incongruent, non-modal batch melting of the assimilant, as well as calculating the cumulate composition. The major element model is based on that of Grove and Donnelly-Nolan (1986). They presented an iterative fractionation model where the ratio of one major element pair in each fractionating phase (Fe-Mg or Ca-Na) was calculated to be in equilibrium with the melt at each increment of fractionation. This equilibrium composition was determined from experimentally determined paired-element partition coefficients between the mineral phase and the melt, and at each step an assimilant of fixed composition was added by mass balance. Their approach is developed here to (1) include a larger number of phases,

and (2) modify the concentration of all major and minor elements in each phase to be in equilibrium with the melt within stoichiometric constraints based on their changing major element compositions in the Mt Kinabalu mineral separates and experimental data. In addition at each step the trace element and isotopic composition is simultaneously calculated using the AFC equations of DePaolo (1981). Partition coefficients for the trace elements (Appendix A4.6) were collated for basalts and basaltic andesites and for dacites and rhyolites from the GERM database (http://eartref.org/GERM/). This combined modelling approach greatly limits the range of suitable solutions for the production of a target composition. The composition of the assimilated melt is calculated through non-modal batch melting for the trace elements and mass balance for the majors, with variable compositions of constituent phases entering the melt. The model is also divided into two stages, the first up to 63% SiO_2 representing fractionation of magma of basalt and andesite composition, and above 63% representing a dacitic or rhyolitic fractionating system, with appropriate trace element partition coefficients for each section (Appendix A4.6). At each increment the composition of the bulk cumulate assemblage is calculated for the major and trace elements, as well as the total fraction of melt remaining in the system and the total ratio of the mass of assimilated material to the initial magma mass (ρ).

The calculations are detailed in Supplementary B and produce an incremental mass balance equation that at each 1% reduction of F (fraction of melt remaining) simultaneously (1) removes small fractions of phases calculated to be in equilibrium with the melt, and (2) adds an assimilant in the fixed proportion *r* (ratio of the mass assimilated to the mass crystallised). The range for Fe-Mg, Al-Si and K-Na distribution coefficients was determined using the data of Grove *et al.* (2003) and Alonso-Perez *et al.* (2009) with values chosen to best reflect the mineral compositions of our samples. The Al-Si distribution coefficient was used for plagioclase equilibration in preference to Ca-Na, as the experimental data shows it to be far less variable. The relationship of the minor elements to the major element composition and the proportion of the major sites for which they substitute at

different compositions were determined from the experimental data and the mineral data for Mt Kinabalu.

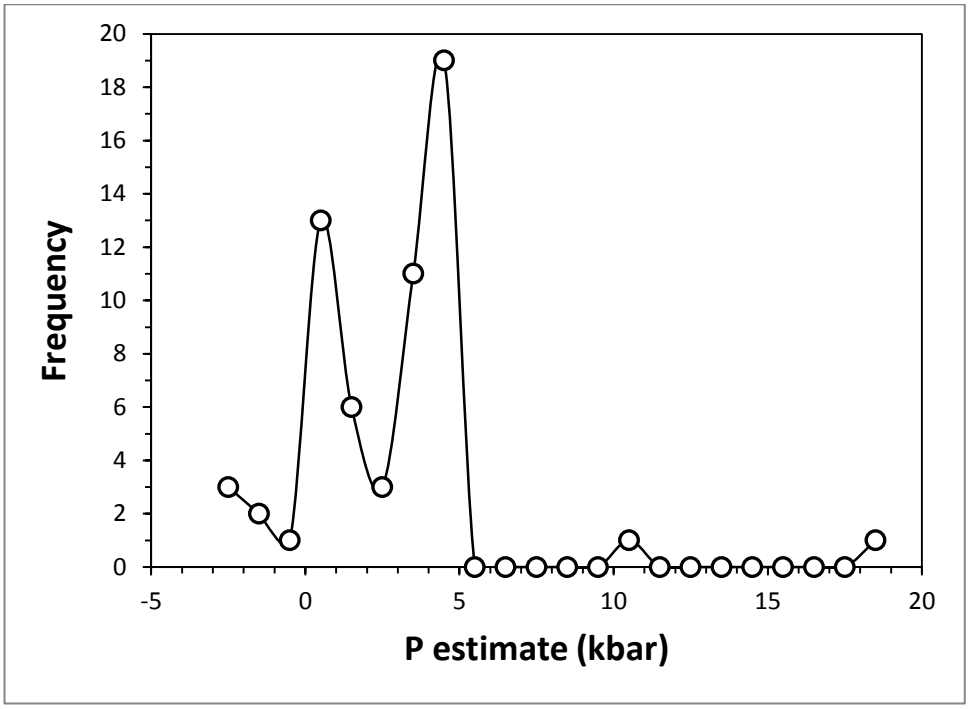

Fig. 5.15. Frequency chart of Al in hornblende pressure estimates (kbar), including data from whole crystals, rims and cores for hornblende samples from microprobe analysis of this study and Imai (2000). Data is calculated using the equation of Hollister *et al.* (1987). Values < 2kbar are below the specification of the technique, hence the presence of negative values.

It is very important when calculating an AFC model to determine a suitable value for *r*. This is determined by thermodynamic constraints and can be calculated using the EC-AFC model of Spera and Bohrson (2001), with specific heat capacities and fusion enthalpies calculated using the chemistry of potential assimilants and the published Linau Balui basalt data. The Al in hornblende barometer of Hollister *et al.* (1987) gives bimodal values for the Mt Kinabalu mineral data (Fig. 5.15) of <200Pa, representing hornblende fractionation at the emplacement depth, and 450Pa, interpreted to represent fractionation at depth prior to ascent and emplacement. This is equivalent to ~16km for a crustal density of 2.8gcm^{-3} and assuming a geothermal gradient of 25^{o}Ckm^{-1}, equates to an initial crustal temperature of

400^{o}C. This initial temperature was input into the model along with an assumed initial magma temperature of 1300^{o}C, crustal solidus of 700^{o}C and liquidus of 1000^{o}C and an equilibrium temperature of 800^{o}C. The equilibrium temperature (T_{eq}) determines the end point of the model and the volume of wall rock being modelled. These inputs result in a calculated *r* value of 0.65, which would become 0.4 and 0.8 for T_{eq} values of 750^{o}C or 850^{o}C respectively. Of course, these represent maximum values and require all of the heat to be lost to the same region of country rock. If heat is lost to multiple volumes of crust during ascent then the *r* value will be lower as the wall rock at all levels will need to be heated above its solidus prior to the onset of assimilation. Consequently, as assimilation has specific effects on the chemistry of the melt produced the value of *r* can be modified up to these maximum values when reproducing the observed chemistry of the data.

Although this method of chemical modelling lacks the thermodynamic constraints and complexity of the MELTs software, it does have advantages. In particular, it has the ability to model systems dominated by the fraction of hydrous mineral phases, inputs can be easily modified to achieve a target composition, and most importantly by allowing complete control of the fractionating system and its parameters it is easy to explore the particular effects each parameter or input has on the liquid line of descent (LLD) and the melt produced, subtleties which are much harder to grasp when using modelling software. Additionally, other than for determining a maximum *r* value, assumptions do not need to be made of the temperature, pressure, water content and oxidation state of the system, parameters which can be investigated based on the fractionating mineral assemblage used in a particular model.

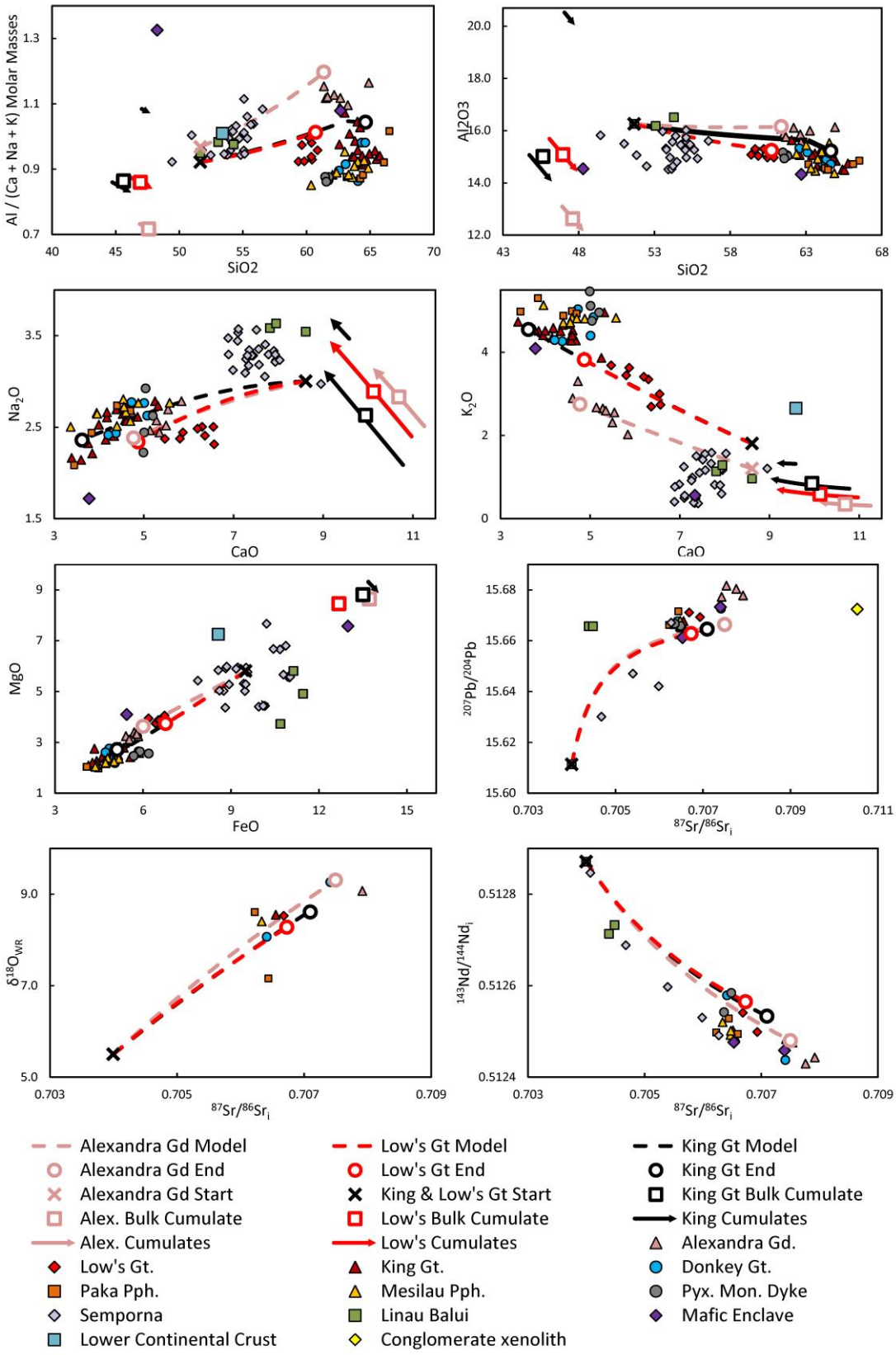

Fig. 5.16. Selected variation diagrams comparing the Mt Kinabalu data with the combined major, trace and isotope AFC models for the Alexandra Gd, Low's Gt and King Gt calculated according to Supplementary B. For each model all plots are calculated from the same F value, R (M_a/M_c) value and fractionating assemblage. The "End" circles indicate the same

point step in the model for all graphs and the trace and REE plots of Fig. 5.15. These points represent the best reproductions of the lowest Si composition of the Alexandra Gd (the most primitive composition for the major units) and the highest Si samples of the Low's Gt and King Gt. The composition of the Linau Balui basalt, LB64, is used as the starting composition for all models, with minor modifications discussed in the text. The conglomerate xenolith from the Donkey Gt, A098, is the assimilant for major and trace element modelling. The $\delta^{18}O_{V\text{-}SMOW}$ value used for the assimilant is 12‰. Lower continental crust included for reference (Rudnick and Gao, 2003).

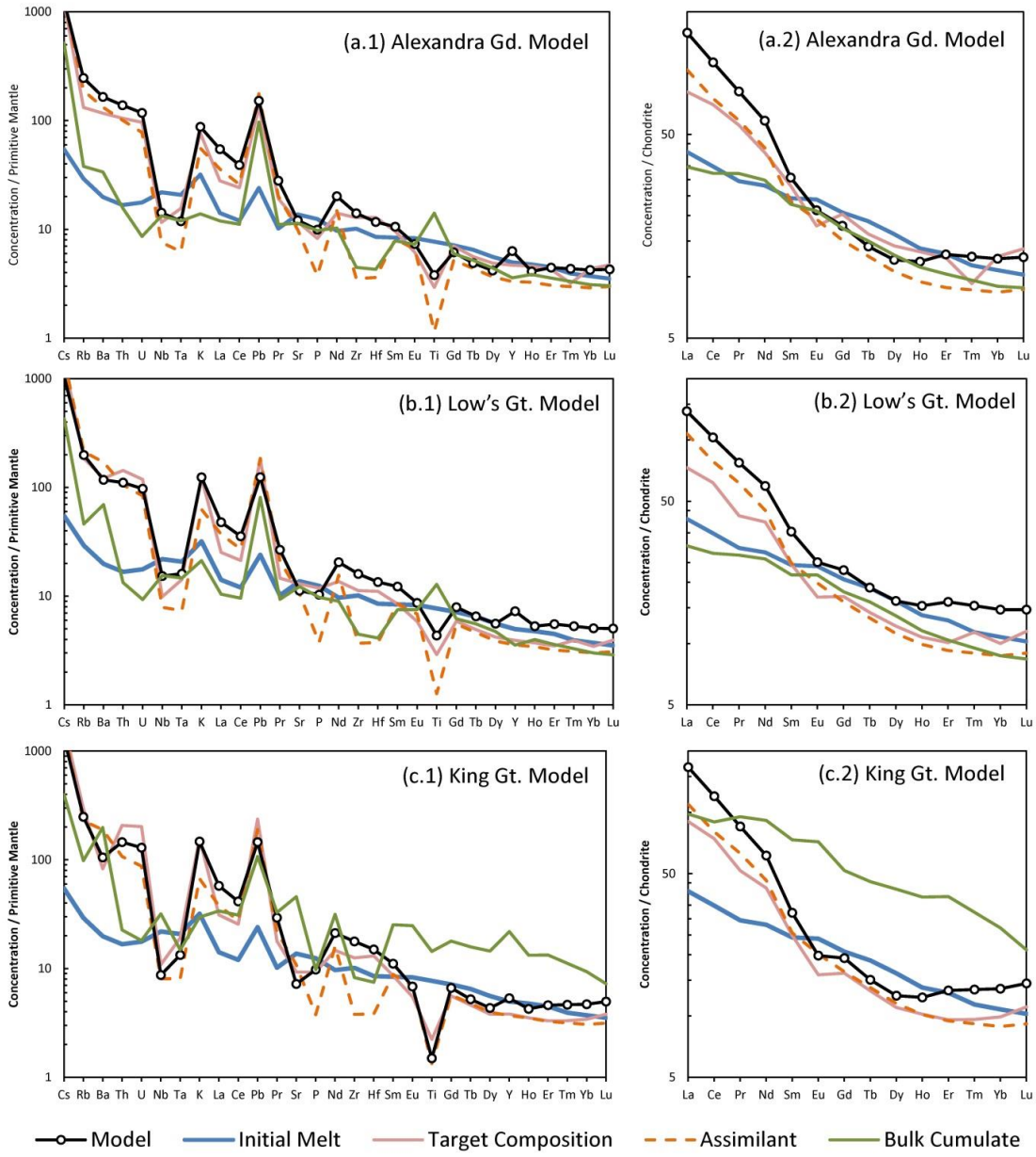

Fig. 5.17. Multi-element trace and REE plots, comparing the Mt Kinabalu fractionation models at the same points indicated in Fig. 5.16 with the Linau Balui basalt starting composition, conglomerate assimilant, target composition of the analysed samples and calculated bulk cumulate composition. Trace and REE plots normalised to primitive mantle and chondrite respectively according to the values of Sun and McDonough (1989).

Mineral %	Model					
	Alexa-ndra Gd	Low's Gt	King Gt.		LCC → UCC	
			SiO2 <63wt.%	SiO2 >63wt.%	SiO2 <63wt.%	SiO2 >63wt.%
Olivine	6	9	10	-	10	-
Clinopyroxene	11	9	10	-	16	-
Plagioclase	35	43	39	56	52	61
Orthopyroxene	-	-	-	-	6	19
Hornblende	40	30	29	28	12	14
Biotite	-	3	5	8	-	-
Apatite	0.004	0.004	0.005	0.004	0.003	0.003
Magnetite	6.2	6.0	6.7	5.6	4.3	5.43
Rutile	1.8	1.5	1.7	1.7	0.2	0.2
Parameters						
r (M_a / M_c)	0.65	0.5	0.5	0.00	0.00	0.00
Additional Assimilant Biotite	0.3	0.4	0.45	0.1	-	-
Assimilant F	0.5	0.5	0.5	0.5	-	-
F	0.60	0.54		0.43		0.27
$(Al^{Plag} \times Si^{Liq}) / (Si^{Plag} \times Al^{Liq})$	1.70	1.85	1.90	2.2	2.10	2.30
$(K^{Plag} \times Na^{Liq}) / (Na^{Plag} \times K^{Liq})$	0.02	0.02	0.02	0.02	0.02	0.02
$(Fe^{Hb} \times Mg^{Liq}) / (Mg^{Hb} \times Fe^{Liq})$	0.36	0.36	0.36	0.36	0.36	0.36
$(Fe^{Bt} \times Mg^{Liq}) / (Mg^{Bt} \times Fe^{Liq})$	2.30	2.30	2.30	2.30	2.30	2.30
$(Fe^{Cpx} \times Mg^{Liq}) / (Mg^{Cpx} \times Fe^{Liq})$	0.25	0.25	0.25	0.25	0.25	0.25
$(Al^{Cpx} \times Si^{Liq}) / (Si^{Cpx} \times Al^{Liq})$	0.10	0.10	0.10	0.10	0.10	0.10
$(Fe^{Opx} \times Mg^{Liq}) / (Mg^{Opx} \times Fe^{Liq})$	0.20	0.20	0.20	0.20	0.20	0.20
$(Al^{Opx} \times Si^{Liq}) / (Si^{Opx} \times Al^{Liq})$	0.13	0.13	0.13	0.13	0.13	0.13
$(F^{Bt} \times Mg^{Liq}) / (Mg^{Bt} \times Fe^{Liq})$	0.30	0.30	0.30	0.30	0.30	0.30
$(Fe^{Ol} \times Mg^{Liq}) / (Mg^{Ol} \times Fe^{Liq})$	0.30	0.30	0.30	0.30	0.30	0.30

Table 5.1. Summary of fractionating assemblages and parameters used in the fractionation models.

wt.%	Alex. Gd. A047	Model	Low's. Gt. CS077	Model	King Gt.	Model	LCC → UCC	Model
SiO_2	62.70	62.45	62.11	61.60	66.12	65.53	66.55	66.44
TiO_2	0.65	0.84	0.64	0.96	0.49	0.33	0.64	0.62
Al_2O_3	16.41	16.18	15.26	15.22	15.28	15.18	15.39	15.46
FeO	5.93	6.34	6.20	6.99	4.85	5.35	5.04	5.37
MnO	0.11	-0.02	0.12	-0.01	0.10	-0.08	0.10	-0.26
MgO	3.48	3.84	3.66	3.87	2.46	2.84	2.48	2.55
CaO	5.61	5.07	5.58	5.06	3.46	3.84	3.59	3.70
Na_2O	2.57	2.39	2.42	2.32	2.21	2.32	3.27	3.40
K_2O	2.36	2.69	3.76	3.78	4.82	4.49	2.80	2.59
P_2O_5	0.18	0.22	0.26	0.23	0.21	0.22	0.15	0.14
Total	100.0	100.0	100.0	100.0	100.0	100.0	100.0	100.0
$\sum D^2$		0.90		1.33		1.08		0.34
Total F		0.60		0.54		0.43		0.27
ρ		0.33		0.31		0.37		-

Table 5.2. Results of the models discussed with target compositions, both normalised to 100%, and sum of the differences squared for each major element oxide for comparison.

Results

The least evolved Alexandra Gd sample (A047), representing the earliest emplaced sample from the pluton, and the most evolved samples of the Low's Gt (CS077) and King Gt (A282) were successfully reproduced by the model (Fig. 5.16 and 5.17). Results and parameters used for all models discussed below are presented in Table 5.1 and 5.2, along with values for the sums of the differences squared ($\sum D^2$) of the major data normalised to 100%, which was used in determining the best fit of the models, and the an absolute *F* value and the ratio of the total mass assimilated to the mass of the original magma, ρ.

Primary magma

The basalt LB64 was used as the starting material for all the Mt Kinabalu models. However, it is apparent that it does not precisely represent a suitable primary melt for Mt Kinabalu, as the Na content is too high, requiring exceptionally sodic plagioclase fractionation to produce the observed compositions of Mt Kinabalu without overly decreasing the Ca concentration, and the Fe concentration is also

too high as approximately 15% magnetite fractionation would be required to achieve the observed composition of the granitoids without also overly decreasing the Mg concentration. Thus Na and Fe are decreased from 3.54 and 11.13 wt.% to 3 and 9.5 respectively, values still within the range of basaltic samples from Linau Balui and Semporna. It is also apparent by extrapolating the trend of the Alexandra Gd data on a plot of K_2O against CaO that the K_2O composition is too low, and so is increased from 0.96 to 1.2 wt.%. The $\delta^{18}O$ isotope value of LB64 is unknown, but due to the very limited variation in the oxygen isotope signature of the mantle the primary melts can be assumed to have a value of +5.5‰ (Mattey *et al.*, 1994, Macpherson and Mattey, 1998).

Assimilant

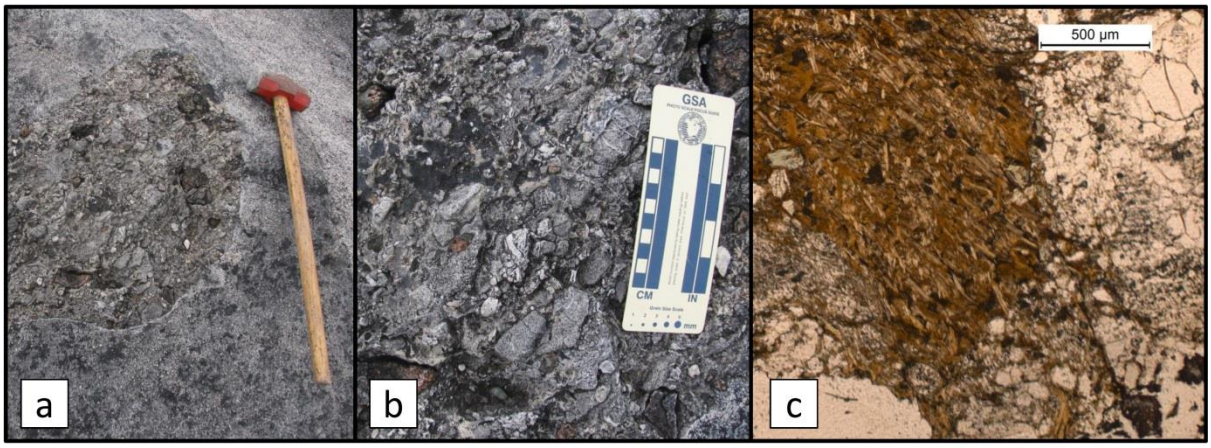

Fig. 5.18. Images of the conglomerate xenolith, A098, from Mt Kinabalu used in the AFC models. (a) Field photo of the xenolith within the Donkey Gt. Hammer for scale, 71cm long. (2) Clasts and and matrix of the conglomeritic xenolith. (c) Xenolith under 5x magnification under PPL, showing the abundant secondary biotite.

Although different possible assimilants from the region were modelled to determine the most suitable assimilant, the metamorphosed conglomerate xenolith found within the Donkey Gt (Fig. 5.18) is the only field evidence for crustal assimilation and was used successfully in all the following models presented for Mt Kinabalu. However, when modelled using the bulk composition of the sample the K

content of the model remains too low, and produces gradients shallower than the data on the plot of K_2O against CaO. Due to the decreasing water content at depth in the crust, melting of deep sedimentary material occurs through dehydration melting reactions driven by the breakdown of hydrous mineral phases, particularly biotite (Vielzeuf and Holloway, 1988, Douce and Johnston, 1991). Inspection of the xenolith in thin section reveals it to be composed of 60% quartz and 30 to 40% secondary biotite and <5% chlorite (Fig. 5.18c). The biotite and chlorite were likely derived through the reaction of ferromagnesian minerals and feldspars in the original sediment during prograde metamorphism (Deer *et al.*, 1966), and as the hydrous phases in the rock they would be the first to melt during assimilation. The high K content of biotite means that the melts produced through incongruent dehydration melting of this xenolith would be more K-enriched than its bulk composition, thus increasing the rate of K-enrichment in the fractionating magma of Kinabalu.

To model this incongruent melting, the fraction of the assimilant in the model composed of biotite was increased by mass balance. Without mineral data for the xenolith, major and trace data were taken as the mean analysed for the Mt Kinabalu mineral separate data. As variations between the biotite compositions of different lithologies will be less than between entirely different mineral phases this is a reasonable approximation, however as these secondary phases are produced through metamorphic reactions of other minerals they are undoubtedly distinct from the primary magmatic biotite of Mt Kinabalu. As noted earlier from the modelling of isotopic disequilibrium development, the high Rb/Sr ratio of biotite results in the development of very high $^{87}Sr/^{86}Sr$ value compared to other mineral phases in the same sample. As the AFC modelling of the Sr and Nd isotopes is successful using the bulk isotopic signature of the xenolith despite the biotite-rich derivation of the melt, this supports the interpretation of the melt being derived from late secondary, metamorphic biotite as this will have inherited the lower isotopic signature of the primary mineral assemblage This also supports the interpretation that the assimilant is not felsic crust where the biotite would be dominantly of primary, igneous origin.

Fractionating assemblages

Some constraints can be placed on the potential fractionating assemblages prior to modelling using the geochemical and petrographic data. The presence of weak negative Eu anomalies and depletions in the MREE implies the fractionation of plagioclase and amphibole respectively. This is notably supported by the Pyx Mon dykes, as they are rich in plagioclase phenocrysts and show the same MREE depletion as the other units (Fig. 5.8d.2) despite only the scarce skeletal remains of amphibole phenocrysts being present. These phenocrysts have altered to an assemblage of chlorite, biotite, clinopyroxene, plagioclase and magnetite, and likely began to react and resorb during ascent from depth as they left the amphibole stability field (Garcia and Jacobson, 1979). Mt Kinabalu is notably lacking in mafic enclaves compared to most granitic intrusions, however those that are present contain variable fine-grained phaneritic assemblages of plagioclase, hornblende, magnetite, biotite and clinopyroxene. This gives some indication of the likely fractionating phases if these represent higher temperature assemblages crystallised from the host melt earlier in its fractionation process. Additionally the presence of clinopyroxene in both the enclaves and Pyx Mon dykes but absence of orthopyroxene means it is unlikely that orthopyroxene crystallised, unless it has reacted preferentially over clinopyroxene to form hornblende at lower temperatures.

Within these constraints and input compositions the model was most successful in reflecting Alexandra Gd through fractionation of 6% olivine, 11% clinopyroxene, 35% plagioclase, 40% amphibole, 0.004% apatite, 6% magnetite and 1.8% rutile, with an *r* value of 0.65, an absolute *F* value of 0.60 and a ratio of the total mass assimilated to the mass of the original magma (ρ) of 0.33. The plagioclase composition varies from An_{64}-An_{47}, compared to An_{75}-An_{32} for the analysed data (excluding outliers).

The Alexandra Gd forms a separate but parallel LLD on the plot of K_2O against CaO compared to the later units. As they are parallel and not diverging the chemical disparity relates to a change in the source prior to the onset of the Low's Gt

fractionation rather than a change in the fractionating or assimilating assemblages and requires either an increase in Ca or K. It is not possible to produce the observed signature whilst maintaining the relatively low Si content of the Low's Gt if Ca is increased, and so this change reflects an increase in K_2O from 1.2 to 1.8 wt.%, potentially through recharge of an already fractionated system enriched in this incompatible element.

With this modification to the starting composition both the Low's Gt and the King Gt can be reproduced. Modelling of the Low's Gt is most successful with a fractionating assemblage of 2% clinopyroxene, 9% olivine, 9% clinopyroxene, 43% plagioclase, 30% amphibole, 3% biotite, 0.004% apatite, 6% magnetite and 1.5% rutile, with an *r* value of 0.5, an absolute *F* value of 0.54 and a ρ value of 0.31. The Al-Si plagioclase-melt distribution coefficient is increased from 1.8 to 1.9 and fractionates plagioclase compositions of An_{71}-An_{50}.

The evolved King Gt model starts with the same composition as that for the Low's Gt, but the higher Si of the sample to be reproduced requires two stage modelling. It is most successfully reproduced with an *r* value of 0.5 for the first stage and a fractionating assemblage of 10% olivine, 10% clinopyroxene, 39% plagioclase, 29% amphibole, 5% biotite, 0.005% apatite, 7% magnetite and 1.8% rutile, and for increments above 63% SiO_2 no assimilation (r = 0) and fractionation of an assemblage consisting of 56% plagioclase, 28% amphibole, 8% biotite, 0.004% apatite, 6% magnetite and 1.6% rutile. The absolute *F* value for this model is 0.43 and ρ is 0.37. The Al-Si plagioclase-melt distribution coefficient is increased to 1.9 for the lower Si stage (<63 wt.% SiO_2) and 2.2 for the more evolved system, and fractionates plagioclase compositions of An_{73}-An_{61}. The fractionating amphibole composition is hornblende for all three models. The observed Ba anomaly cannot be produced using reasonable Kd values (<30) if biotite appears in the assemblage only above 63% SiO_2, and it so must become a fractionating phase below this Si content.

Further constraints on the assimilant

As discussed previously, suitable alkali metal compositions for the Mt Kinabalu melts were only produced through an incongruent melting process, whereby an increased component of the melt was derived through biotite breakdown than is present in the modal mineralogy of the assimilant. Using this non-modal approach, with 30% of additional biotite being added to the assimilant in the Alexandra Gd model, 40% in the Low's Gt model and 45% in the King Gt model, the alkali metal data were successfully reproduced. Incongruent melting is modelled for the trace elements using the non-modal batch melting model and the same biotite addition as the major elements, using an *F* value (the fraction of melt remaining) of 0.5 for all three models. One notable effect on the trace elements of this process is the low PM normalised Rb/Ba ratio in the Alexandra Gd and Low's Gt model, as the high Ba content of the biotite-enriched assimilant compensates for its relative depletion compared to the more incompatible element Rb through fractionation.

Weathering processes increase the proportion of zircon crystals in a siliciclastic sedimentary rock compared to its igneous protolith, resulting in a positive Zr and Hf anomaly on multi-element, mantle normalised plots. As the Mt Kinabalu granitoids do not have such an anomaly (Fig. 5.6) but do contain inherited zircons (Cottam *et al.*, 2010) it can be assumed that many of the zircon crystals of its sedimentary assimilant did not breaking down and enter the melt. Assuming that all the Zr measured in the assimilant is derived from zircon, the model allows us to determine that only 20% of the crystals are breaking down, and thus the model could be adjusted to reflect this. However, as we do not know what proportion of the assimilant's other trace elements reside in zircon, we have instead used the trace element data collected using the standard dissolution procedure in preference to that collected using flux fusion as the negative Zr and Hf anomaly in the standard dissolution data indicates that this sample preparation process is unable to dissolve much of the zircon present in the sample.

For the values of *F* and *r* used in the models, the required $\delta^{18}O$ for the assimilant is 12‰. At the initial $^{87}Sr/^{86}Sr$ values of the Mt Kinabalu granitoids (0.706 to 0.708)

this would be a high value for igneous crust and a low value for deep ocean sediments, but would be reasonable for greywackes and immature terrestrial sediments (Magaritz *et al.*, 1978, Rollinson, 1993). The $\delta^{18}O$ and original mineralogy of the xenolith are unknown, but based on its texture and the high biotite and chlorite content it would fit this description and so remains a suitable assimilant. Additionally, although the xenolith provides a suitable assimilant in the Sr and Nd isotope models, the similarity of the Pb isotopes of the xenolith to those of the granitoids (Fig. 5.10c and Fig. 5.16) results in a small but important disparity in this system. This requires therefore that Pb isotopes be heterogeneous in the assimilant, which is reasonable given the immature and poorly mixed nature of the conglomerate.

An alternative continental derived sedimentary contaminant could be the Crocker turbidite sediments into which Mt Kinabalu intruded. However, the igneous rocks in SE Asia and South China shown in Fig. 5.10a fall on one of two Sr and Nd isotope trends: Trend 1, the standard Mesozoic trend shared by most of the Mesozoic continental crust of South China and SE Asia, or Trend 2, of samples that have incorporated older Proterozoic or Archean material. Mt Kinabalu, the Semporna basalts, the Usun Apau volcanics and the conglomerate xenolith all show involvement of the older isotope signatures of Trend 2, an observation further supported by the presence of both Mesozoic and Proterozoic inherited zircons in the Mt Kinabalu granitoids (Cottam *et al.*, 2010), whilst the two samples of the Crocker Formation turbidite sandstones into which the pluton has intruded fall on Trend 1. They are also much more mature sediments than the conglomerate xenolith, and lack the high biotite content required by the models. This implies that the inherited isotopic signature of Mt Kinabalu was not acquired by assimilation at emplacement level, and supports previous studies concluding that the high magma viscosities and slow diffusion rates of felsic melts at their level of emplacement are unable to assimilate and efficiently mix large volumes of crust, and that chemical evidence of crustal melting is thus inherited from deeper in the system (Clemens *et al.*, 2009).

Discussion and Implications of the Model

The formation of Mt Kinabalu

Using the model presented we have shown that mantle fractionation and assimilation of immature metamorphosed sediments can produce the composition of the Mt Kinabalu pluton with reasonable degrees of fractionation and assimilation. The fractionating assemblage, dominantly of plagioclase and hornblende with lesser amounts of olivine, clinopyroxene and magnetite is similar to that observed in fractionation experiments from basalt, via andesite to felsic compositions at 0.8 to 1.0 GPa and 3 to 4 initial wt% H_2O (Kägi, 2000, Alonso-Perez *et al.*, 2009). These experiments showed that at higher pressures or water contents garnet becomes stable and the lack of a strong and progressive HREE depletion for the Mt Kinabalu samples indicates that it is not a fractionating phase. The preference for rutile and magnetite fractionation over ilmenite and the dominance of amphibole in the fractionating assemblage implies a high fO_2 system (Toplis and Carroll, 1995, Krawczynski *et al.*, 2012).

It is interesting to note that although the Low's Gt has a lower Si content than the Alexandra Gd it has actually undergone a higher degree of fractionation. This is because it has fractionated a higher degree of the Si-rich phase, plagioclase, than the earlier unit. Higher degrees of fractionation imply that the melt reached cooler temperatures prior to extraction and emplacement, and hence biotite was able to crystallise and fractionate. The King Gt is much more evolved and so biotite is a more dominant fractionating phase, especially above 63 wt% SiO_2.

A distinct reduction in the Al content and aluminium index (molar Al/(Na+Ca+K)) occurs between the Alexandra Gd and all the subsequent units, switching from weakly peraluminous to weakly metalluminous. This is a result of the increased K content in the primary melt and an increase of plagioclase and decrease of amphibole in the fractionating assemblage both at high and low degrees of fractionation. Experiments have shown that the maximum temperature at which plagioclase becomes stable is reduced by increasing pressure or water contents in the melt whilst that of amphibole is increased (Grove *et al.*, 2003, Bogaerts *et al.*,

2006, Alonso-Perez *et al.*, 2009, Parman *et al.*, 2011, Krawczynski *et al.*, 2012), and so this change in the fractionating assemblage may result from either a decrease in the pressure or water content of the system. As stated earlier, the increased K required in the starting composition for the Low's Gt and subsequent units implies recharge of an already fractionated system, and so indicates that each subsequent melt batch continued to fractionate in the same region. Consequently, the pressure of the fractionating system is unlikely to change and the variation in the fractionating assemblage is more likely to have been caused by a decrease in the water content of the magma. This also agrees with the increasing biotite component of the fractionating assemblage, the stability of which increases with decreasing water content in granodiorite melts (Bogaerts *et al.*, 2006). As the *r* value also decreases between the Alexandra Gd and the later units the obvious source of this decrease in available water is a reduced amount being acquired from dehydration melting of the assimilant and so, in addition to controlling the distinct alkali metal trends of Mt Kinabalu and its continental isotopic signature, crustal assimilation also controlled its fractionating assemblages. This decrease in the degree of assimilation is likely to result from the reduced fertility of the assimilant, as the Alexandra Gd was the first unit and so the fertility of the wall rock will be depleted by each subsequent unit.

As discussed earlier, examination of the mafic enclaves of Mt Kinabalu provides some insight into the phases fractionating. However, by comparing the chemical data of two analysed enclaves to the LLD and chemistry of the cumulate assemblages revealed by the model it is clear that different populations of enclave exist in the pluton. One large fine grained enclave (A034), a 2m wide irregularly shaped body within the Paka Pph, is clearly a xenolith of an earlier unit that cooled quickly at depth and was entrained by the Paka Pph. Its trace element signature is similar to the King Gt and later units and its isotope ratios are similar to the Alexandra Gd and Donkey Gt. The enclave's major elements are similar to those of the King Gt so despite its dark appearance the enclave is equally evolved. The enclave is more enriched in Mg and K and contains less Na and Ca, reflecting a high abundance of biotite. Thus, it most probably represents crystallisation of the melt

of the previous unit to the Paka Pph, the Donkey Gt, against the conduit walls beneath the pluton, which was entrained by this subsequent unit during ascent, implying that each subsequent granitic unit exploited the same feeder system.

Smaller enclaves are more common but notably less abundant than expected in granitic plutons and contain particularly high amounts of hornblende, clinopyroxene and magnetite (approximately 50%) in addition to plagioclase. One of the enclaves (A282a) was analysed, a small 3cm wide dark rounded body within the King Gt. It has the same isotopic ratios as its host rock and so at the time it crystallised from the melt most of the crustal assimilation had already occurred. Comparing this smaller enclave to the LLD and predicted cumulates of the model shows it to have a similar major element composition to the fractionating assemblage. However, it's lower than predicted Ca, Na content and high Al index (Fig. 5.16) reflect its relatively low plagioclase composition, implying it crystallised early in the fractionation history at temperatures just below the stability field of plagioclase. As the final isotopic signature had already been achieved this supports the hypothesis that most assimilation occurs early in a melt's fractionation history (Reiners *et al.*, 1995). By collecting more data on these enclaves and comparing them with the model the fractionation and assimilation history of the melts could be further constrained.

One final point of discussion on the formation of Mt Kinabalu is the origin of the basaltic magmatism from which it is derived. As shown, the elemental and isotopic composition of all the Mt Kinabalu units modelled can be successfully reproduced using the composition of the Linau Balui basalt (Cullen *et al.*, 2013) possessing the most mantle-like isotopic signature (LB64), with only minor changes to its Fe, K and Na contents. Mt Kinabalu, the Linau Balui basalts, dacites and andesites of Usun Apau, basalts of the Semporna peninsula (Macpherson *et al.*, 2010) and basaltic seamounts of the South China Sea (Tu *et al.*, 1992, Yan *et al.*, 2008), the Capoas granite of Palawan (Encarnacion *et al.*, 1995) and basaltic volcanism in Vietnam (Hoang *et al.*, 1996) all represent Neogene magmatism post-dating the Sabah Orogeny and the cessation of spreading in the South China Sea. Furthermore, compared to primitive mantle (PM) they all possess progressive enrichment of

elements that are more incompatible in the mantle. This has been attributed to low degree melting of upwelling, fertile, OIB-like mantle beneath Borneo and the South China Sea region (Macpherson *et al.*, 2010).

Enrichment of a mantle melt in incompatible elements may either represent low degrees of melting, a fertile source not depleted by previous melting events or a combination of both. We compared the data for the basalts of Linau Balui and other regional, post-SCS spreading Cenozoic basalts with the models for FMM (Fertile MORB Mantle) melting by Pearce and Parkinson (1993) This model normalises the relative proportions of progressively more incompatible elements in a melt to FMM, classifying the elements as VHI (Very Highly Incompatible – Nb & Zr), HI (Highly Incompatible – Ti, Y and Yb) and MI (Moderately Incompatible – Ca, Al, Ga, V and Sc). Neogene basaltic volcanism from the region become progressively more enriched relative to FMM as the elements become more incompatible (Fig. 5.19), with VHI ≫ HI > MI. This corresponds to low to moderate degree melting of a FMM source that had not previously had melt extracted, and implies the upwelling of fresh, fertile mantle beneath the entire region following cessation of the South China Sea spreading.

Structural and AMS (Anisotropic Magnetic Susceptibility) data from Mt Kinabalu (Chapters 3 and 4) indicate that at its time of emplacement the stress field of the region was in extension NNW-SSE. Although this may partly result from post orogenic collapse following crustal thickening during the Sabah Orogeny there is evidence that this was a regional event including NW-SE spreading of the Sulu Sea NE of Borneo, crustal thinning beneath the sediment wedge offshore of NW Borneo and the rapid uplift of Mt Kinabalu and its surrounding area (Cottam *et al.*, 2013, Hall, 2013). This regional extension would have been accommodated by crustal thinning with subsequent upwelling of fresh, fertile mantle. Upwelling would induce low degree melting and produce the scattered OIB-like magmatism in the region, including the basaltic precursor to Mt Kinabalu.

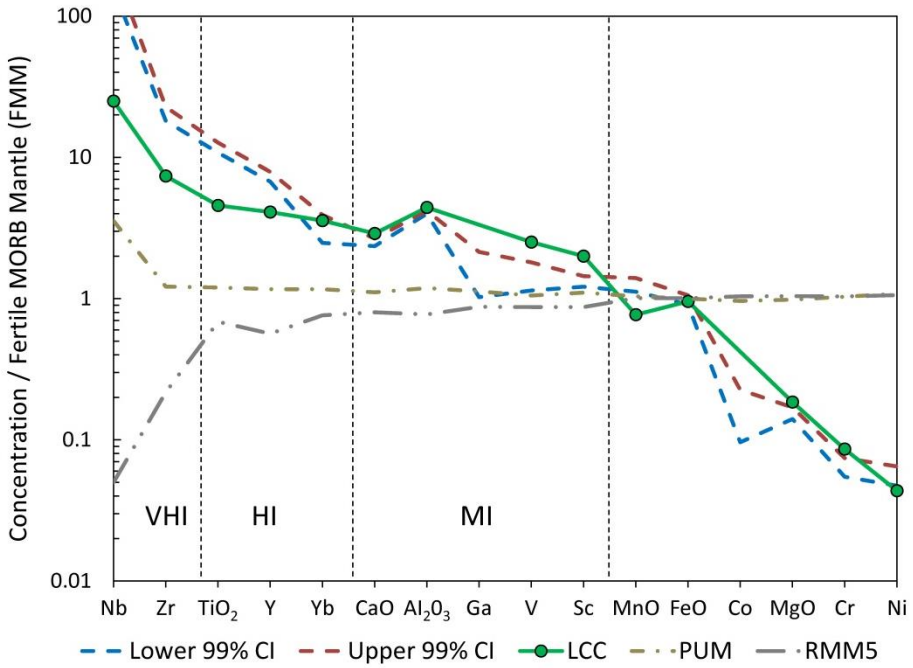

Fig. 5.19. Fertile MORB mantle (FMM) normalised plot based on Pearce and Parkinson (1993), showing the composition of the average lower continental crust (LCC) (Rudnick and Gao, 2003) and the upper and lower 99% confidence intervals (CI) of Neogene volcanics from the South China Sea region (n = 115). Data included from Semporna (Macpherson *et al.*, 2010), Usun Apau and Linau Balui (Cullen *et al.*, 2013), South China Sea basaltic seamounts (Tu *et al.*, 1992, Yan *et al.*, 2008) and Vietnamese basalts (Hoang *et al.*, 1996). Elemental incompatibility with FMM increases towards the left, and is categorised as very highly incompatible (VHI), highly incompatible (HI) and moderately incompatible (MI). Primitive upper mantle (PUM) and residual MORB mantle after 5% melt depletion (RMM5) included for reference (Pearce and Parkinson, 1993).

Mt Kinabalu is located at the core of an oroclinal bend where the trend of the fold and thrust belt rotates abruptly about 90^{o} from a SSW trend to an ESE trend (marked by the lineaments in Fig. 5.2). The core of an orocline will be its thickest point, as well as a site of high deformation (Gutiérrez-Alonso *et al.*, 2004). This will have resulted in a thicker crustal root than the surrounding regions, making further out of isostatic equilibrium than regions away from the bend. To compensate for this disequilibrium, the immediate Mt Kinabalu region would have to ascend at a faster rate than its environs during the regional extension, focussing upwelling of fertile magma, and resulting in the location of the Mt Kinabalu magmatism. The combination of focussed deformation in the oroclinal core, and extensional

deformation during uplift would also have produced a more deformed crustal structure, conducive for magma ascent.

Global implications for granitic magmatism and formation of the continental crust

The experimental petrology presented in Fig. 5.14 demonstrates that it is not feasible for purely anatectic derived melts to generate the Mt Kinabalu magmas. By plotting the upper, middle, lower and bulk crustal values (Rudnick and Gao, 2003) on the same plots the plausibility for crustal melting to produce bulk crustal signatures can also be investigated and compared with Mt Kinabalu. From this we can see that although the low CaO / Na_2O and peraluminous composition of the upper crust (UCC) may be produced by crustal melting, the weakly metalluminous and intermediate to high CaO / Na_2O values for middle (MCC), lower (LCC) and bulk (BCC) crust are more similar to Mt Kinabalu and do not plot within the range of the experimental data. Thus, they also cannot be produced purely from partial melts of crustal sources without mantle involvement and so, like Mt Kinabalu, could also be formed through differentiation of mantle derived basaltic melts. As the UCC value plots along the same trend as the MCC, LCC and BCC on the alkali metal plot, the UCC appears to represent the most evolved end-member of a suite of crustal values rather than being derived through an entirely different process and so is likely to share the same origin as the other crustal units.

The Mt Kinabalu samples show a much steeper gradient than the crustal values on the plot of alkali metal ratios (Fig 5.14). As discussed, this a combined result of the high plagioclase content, high rate of assimilation and the enriched biotite component in the assimilating melt, caused by the incongruent melting of immature biotite-rich metasediments. The shallower gradient of the crustal trend can be reproduced by both reducing the biotite proportion of the assimilated melt and the rate of assimilation, by fractionating less plagioclase and making the plagioclase concentration more Ca and Al rich, or through combinations of these processes. Reducing the proportion of plagioclase in the fractionating assemblage also results in more peraluminous melts. Thus, although the combination of the

fractionating assemblage involved in the evolution of the Mt Kinabalu magma, and the origin and process of crustal assimilation result in a disparity between this pluton and the average values of UCC and MCC, simple changes to the system would be able to produce the same chemistry as these dominantly granitic crustal units.

If the same process of basalt fractionation advocated for the formation of Mt Kinabalu also formed the middle and upper crust, this would provide a means of developing felsic continental crust directly from the mantle without invoking large scale intra-crustal recycling. In addition to the felsic fractionated melts, a mafic cumulate assemblage would be produced. Potential evidence of this cumulate material is the LCC as this has been shown from xenoliths and seismic studies to be mafic and to possess positive Sr and Eu anomalies, evidence for plagioclase-bearing cumulates and counterparts to the negative anomalies of the UCC (Rudnick and Fountain, 1995, Rudnick and Gao, 2003). However, comparing the estimated major and trace element composition of the LCC with the calculated bulk cumulate assemblages of the Mt Kinabalu models (Fig. 5.16 & 5.20) indicates that the LCC is of unsuitable composition to be dominantly composed of cumulate material. Most notably, the LCC is too felsic, especially in its Si, Fe and Mg contents compared to the restricted mafic compositions of the calculated Mt Kinabalu cumulates. In addition, unlike the calculated cumulates the LCC shows negative anomalies for Nb, La, Ce and Ti on PM normalised plots.

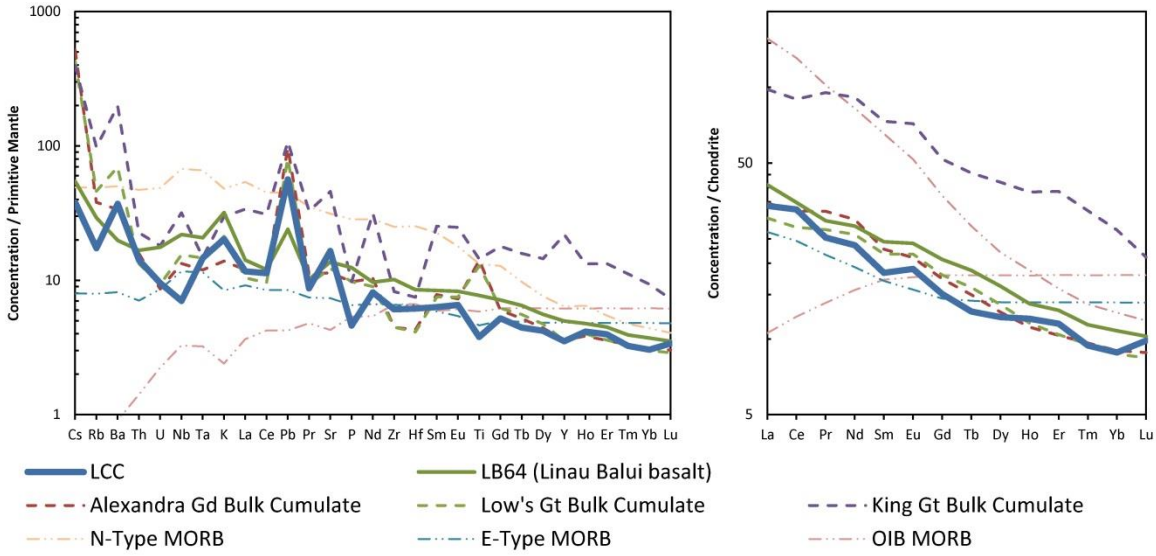

Fig. 5.20. Multi-element trace and REE plots, comparing the estimated average composition of the lower continental crust (Rudnick and Gao, 2003) with compositions of the bulk cumulate assemblages and the Linau Balui basalt starting composition (LB64) of the Mt Kinabalu models from Fig. 5.16. Normal, depleted MORB (N-Type), enriched MORB (E-Type) and N-type NORB. Plots normalised to primitive mantle and chondrite respectively. N-MORB and normalising values from Sun and McDonough (1989).

An alternative interpretation of the lower crust and its clear chemical relationship to the UCC and MCC is that instead of being the cumulate formed by their fractionation it represents their source. As discussed, partial melts of mafic sources (as would form through melting of the LCC) would be peraluminous and possess low CaO/Na_2O ratios. Thus, the LCC would have to undergo almost 100% partial melting before the resultant magma resembled the original composition and plotted along the same trend relative to the other crustal values. This is a requirement if these melts are to have the composition of the more felsic crustal units or represent the primary melt from which they formed through fractionation. Alternatively, we propose that most of its constituent material represents the composition of the primary melts from which the UCC and MCC fractionated and that the resultant cumulate material is a more minor component of the bulk LCC (as illustrated in Fig. 5.21).

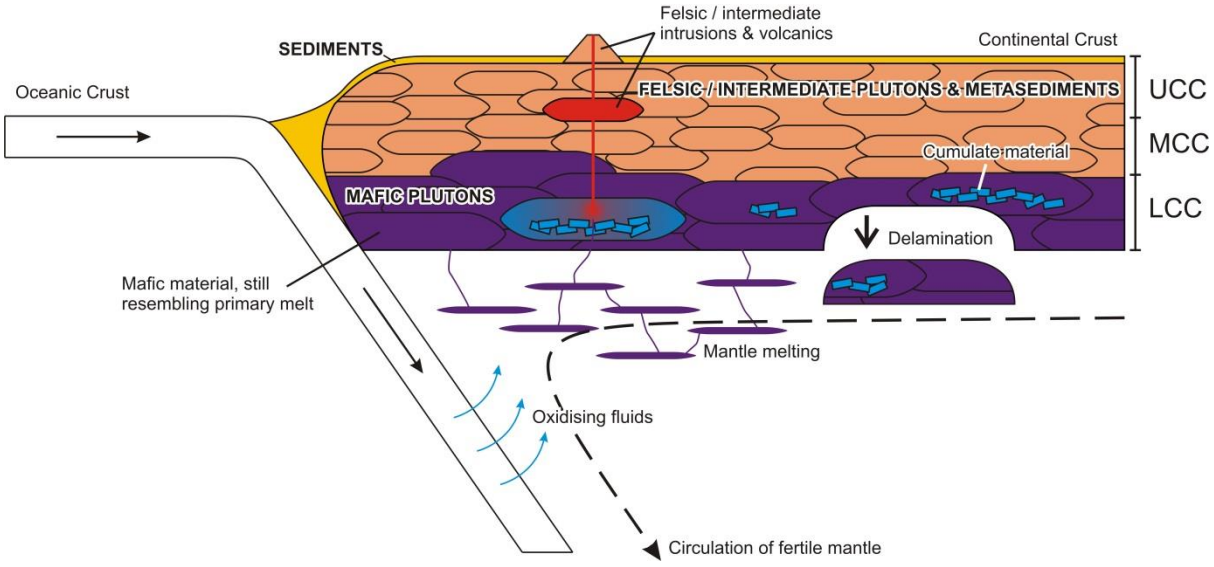

Fig. 5.21. Schematic diagram illustrating our proposed model for continental arc magmatism and generation of the continental crust. Active subduction circulates and hydrates fresh, fertile mantle in the mantle wedge. This produces basaltic mantle melts, most of which remain in the lower crust (LCC) but some fractionate, producing felsic and intermediate magmas that ascend in to the middle and upper crust (MCC and UCC) and leave a cumulate component in the LCC. Continued melting thickens the LCC, which eventually delaminates back in to the mantle. Relative thicknesses of the UCC, MCC and LCC from Rudnick and Gao (2003).

To test this hypothesis we have attempted to model the formation of the UCC with the LCC as the starting composition. The assimilant of a magmatic system is dependent on the specific crust hosting it, and invoking a degree of recycling in the system only passes the formation of the continental crust back a stage as it fails to explain the process from which the assimilant was derived. Instead we have attempted to produce the UCC without assimilation (i.e. r = 0), which means the model is also applicable to the formation of early crust, when there is no available crustal assimilant from which to inherit a chemical signature.

With the recommended average LCC composition of Rudnick and Gao (2003) as the starting composition and an r value of 0, the major and trace element composition of the UCC can be successfully reproduced (Fig. 5.22 & 5.23) through a two-stage model with the following mineral assemblages: Stage 1 (SiO_2 <63 wt.%): 10% olivine, 16% clinopyroxene, 5% orthopyroxene; 52% plagioclase, 12% amphibole, , 0.003% apatite, 4.3% magnetite, 0.22% rutile and 0.7% garnet; and Stage 2 (SiO_2

>63 wt.%): 19% orthopyroxene; 61% plagioclase, 14% amphibole, , 0.003% apatite, 5.4% magnetite, 0.2% rutile and 0.7% garnet. The absolute *F* value for this model is 0.28. The Al-Si plagioclase-melt distribution coefficient is 2.1 for the lower Si stage and 2.3 for the more evolved system, and fractionates plagioclase compositions of An_{81}-An_{65}. An alternative model without amphibole as a fractionating phase was also attempted and successfully reproduced the major element signature, but resulted in overly enriched REE concentrations. The high plagioclase content of the gabbroic cumulate produced in this amphibole-bearing model reflects the decreasing Al content between the LCC to the MCC and UCC and increasingly peraluminous compositions. If this Al decrease is instead achieved through fractionation of a garnet rich assemblage an unsuitably strong depletion in the HREE is produced. To successfully reproduce the UCC, the K_2O content of the LCC was increased from 0.61 to 0.8 wt.%. The K content of the LCC is the least well constrained of the major elements, and the values proposed by different studies vary by an order of magnitude (Rudnick and Gao, 2003), and so this relatively small change is reasonable.

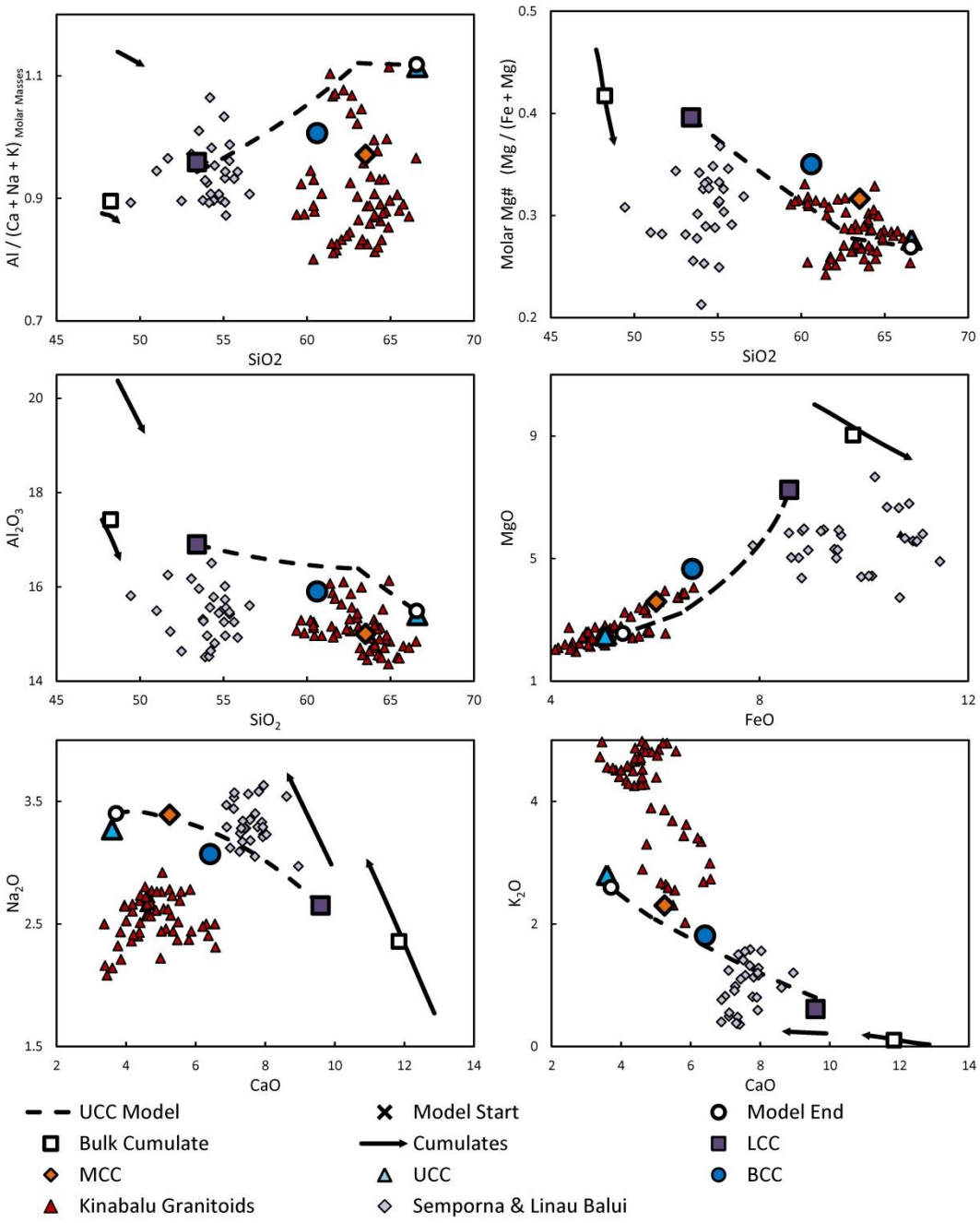

Fig. 5.22. Selected variation diagrams showing modelling of the generation of the average upper continental crust (UCC) through fractional crystallisation of the average lower continental crust (LCC) without assimilation, showing the evolution of the fractionating assemblage and the bulk cumulate composition. Compositions of the Mt Kinabalu granitoids and the basalts of Linau Balui and Semporna are shown for reference. "Model End" marks the same point in the model on all plots, where F= 0.28.

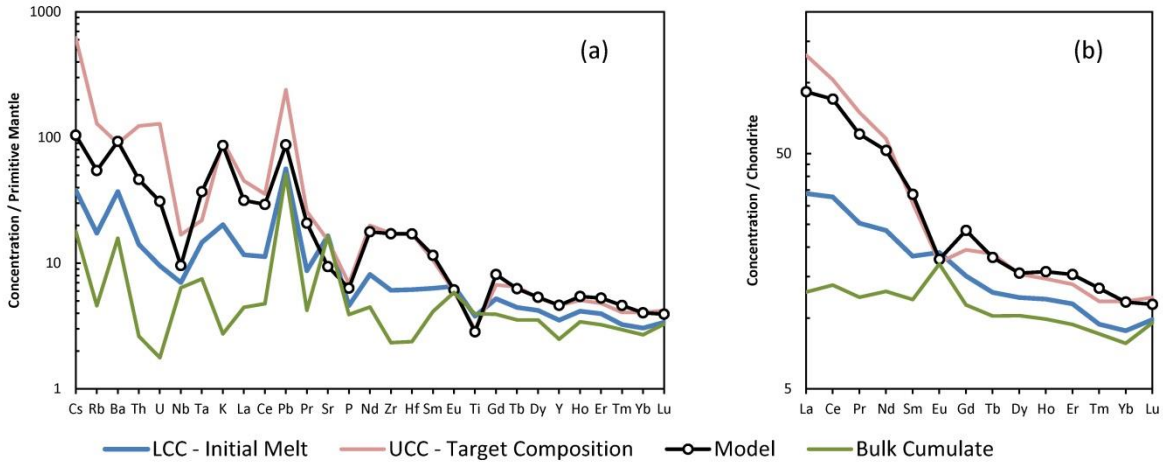

Fig. 5.23. Multi-element trace and REE plots, comparing the LCC to UCC fractionation models at the same increment indicated by the "Model End" point in Fig. 5.21, along with the average LCC starting composition, average UCC target composition and calculated bulk cumulate composition. Trace and REE plots normalised according to the values of Sun and McDonough (1989).

Although the major element composition and most of the trace element concentrations of the UCC can be successfully reproduced through fractionation of a reasonable mineral assemblage, there are some important discrepancies between the UCC composition and the model as the PM normalised concentrations of the model show a comparative deficit in Cs, Rb, U and Th, and an overly high Ta/Nb ratio. These can be explained by comparing this model with the King Gt model, UCC, LCC and predicted cumulate assemblage. The high Cs and Rb concentrations of the King Gt model were a result of assimilation, as these elements are much more enriched in the crust than the mantle, indicating a degree of assimilation of pre-existing crust in creating the modern UCC signature. The same is also true of U and Th, although the LCC starting composition and the cumulate material of the UCC model are more depleted in these elements than in the King Gt model, which may be the result of dilution of these elements by a cumulate component in the LCC. The Nb-Ta discrepancy is a result of the negative Nb and Ti anomalies of the LCC (i.e. PM normalised La/Nb and Eu/Ti ratios >1), features absent from the Linau Balui basalt used in the Mt Kinabalu models (Fig. 5.20), and its contemporaneous magmatism in Semporna (Macpherson *et al.*, 2010). This indicates the presence of

residual Ti and Nb-rich rutile in the source of the LCC, but not in the mantle source for the Neogene SE Asian magmatism, a result of the more oxidising conditions above subduction zones produced by the metasomatic fluids released from the subducting slab compared to the more reduced conditions of the deeper asthenosphere (Frost and McCammon, 2008).

From this modelling it can be seen that both the UCC and MCC may be derived through different degrees of fractional crystallisation of a mantle melt very similar to the LCC However, it also indicates a discrepancy between the compositions of the LCC and this primary magma, resulting from a component of cumulate material also hosted in the LCC.

A similar model for the generation of the felsic continental crust has previously been proposed by Lee *et al.* (2007) using the example of continental growth in the North American Cordillera. They proposed that continental growth in the Phanerozoic develops through multiple stages. Firstly, subduction initiation produces an island arc. This initial period of subduction is extensional, due to slab rollback driven by old subducting oceanic crust, but as the subducting material becomes younger the slab angle decreases and subduction becomes compressional, accreting the island arc to the continent and producing a continental arc setting. Subsequent arc magmas assimilate this accreted mafic crust. As the crust thickens and the differentiation column and pressure at the level of fractionation increase more felsic melts are produced through fractionation of garnet-bearing mafic cumulates in the lower crust, which eventually delaminate and leave a more felsic bulk crustal composition.

We broadly agree with this proposed order of events, but despite the similarities there are some important differences between the two models. Firstly, their model is based largely on the presence of garnet pyroxenite cumulates in the Sierra Nevada batholith, which have been shown to be early cumulates formed during fractionation of this large granitic massif (Lee *et al.*, 2006). Although these are undoubtedly important in the generation of this batholith and a small degree of garnet fractionation is predicted by our model, the average UCC composition lacks

the strong HREE depletion in that would be required if garnet is a major phase in its fractionating assemblage.

However, the most important difference is in their implications of the LCC composition. Their model predicts that following development of the continental arc the LCC will become dominantly composed of cumulate material. As discussed previously, although the LCC undoubtedly contains a cumulate component its composition is unsuitable to be dominantly composed of cumulate material, and is very dissimilar to the composition of the low Si, HREE enriched garnet pyroxenite cumulates of their model.

One additional point of discussion is the process by which the composite granitic plutons are generated in their study. Lee *et al.* (2006) were able to model the major element evolution of the Sierra Nevada batholith from an assumed primitive mantle-derived basalt primary melt through fractionation of the garnet pyroxenite cumulates. However, the high Mg content of these cumulates required an important recharge component to maintain the constant Mg# observed in their data for the pluton. An interesting application of the major element fractionation model presented here would be to test whether the amount of recharge necessary would be reduced if the Mg/Fe ratio of each fractionating phase is calculated to equilibrate with the melt.

Clemens *et al.* (2011) and Chappell *et al.* (2012) noted that most granitic magmas, both S-type and I-type, are peraluminous, and become increasingly so as they become more evolved. This is illustrated by the aluminium index and silica content of the global diorite, tonalite, granodiorite and granite dataset of GEOROC (http://georoc.mpch-mainz.gwdg.de) plotted in Fig. 5.24. The average crustal values and the LLD of the UCC model are also plotted, and show that the same model also closely reproduces the average trend for global felsic and intermediate plutonic magmatism.

Interestingly, both the LCC composition used to generate the UCC and the Linau Balai basalt used to model generation of the Mt Kinabalu granitoids show progressive enrichment in their more incompatible elements, unlike depleted N-

MORB values and more similar to enriched E-MORB or OIB magmatism (Fig. 5.20), although applying the model presented here to both N-MORB and E-MORB starting compositions (Hofmann, 1988, Sun and McDonough, 1989, Niu *et al.*, 1999) failed to produce the UCC especially for elements highly incompatible in the mantle (e.g. Cs, Rb, Ba, Th, U, K and Pb). Like the Linau Balui basalts, if the LCC is compared with modelled melting of Fertile MORB Mantle (Pearce and Parkinson, 1993) it also indicates low to moderate degree melting of fertile mantle that has not been depleted by previous melting events (Fig. 5.19). This implies a constant influx of fresh, fertile mantle during the continental magmatism that generated the LCC, and consequently the MCC and UCC. As most continental magmatism occurs along continental arcs, this is likely the result of mantle circulation in the mantle wedge, driven by the pull of the subducting slab (Fig. 5.21).

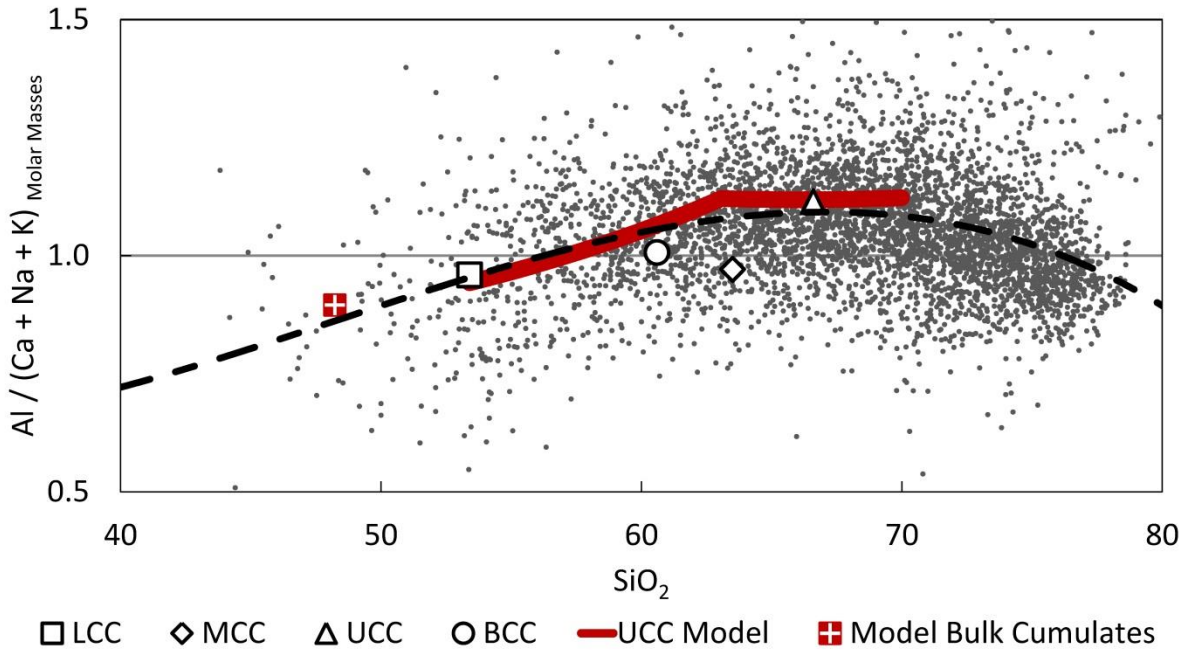

Fig. 5.24. Global dataset for granites, granodiorites, diorites and tonalites from the GEOROC database (http://georoc.mpch-mainz.gwdg.de; 6656 whole rock samples; Data accessed on 05/08/2013) for molar aluminium index, Al/(Ca+Na+K), vs SiO_2, fitted with a third order polynomial trendline to highlight the overall pattern. The same model shown in Fig. 5.21 for generating the UCC from the LCC is shown, along with the calculated bulk cumulate assemblage of the model.

An additional implication of these models is the scale of continental magmatic activity. It can be assumed based on the UCC composition that most continental magmatism is felsic plutonism, not mafic or intermediate volcanism. The models presented here have shown the volume of cumulate material produced during evolution of felsic plutons will be approximately 40 to 70% of the extracted melts. Thus, if the LCC still more closely resembles the primary melt from which both itself and the UCC and MCC were derived than the cumulates produced generating the felsic crust, most mantle melts generated during continental magmatism must remain in the LCC so as to dilute the cumulate component. Therefore, any estimate of the total continental magmatic activity based on the volumes of plutonic and volcanic activity will grossly underestimate the true volume of mantle melting occurring unless we can determine what proportion of the LCC is composed of cumulate material. Also, if most mantle derived magma is unable to rise above the LCC strong structural controls must exist in the crust to determine magma ascent.

Conclusions

1. Magma forming the composite units of the Miocene Mt Kinabalu granitic pluton was derived through fractional crystallisation of plagioclase and amphibole rich cumulates from basaltic melts. The primary melts were similar to the Plio-Pleistocene basalts of Linau Balui and the Semporna peninsula, and were generated by low degree melting of fertile mantle, upwelling beneath SE Asia during regional Neogene extension.
2. High degrees of assimilation of immature Mesozoic conglomeritic meta-sediments occurred during the early, high-temperature period of melt fractionation and were efficiently mixed with the melt. The alkali metal content of Mt Kinabalu indicates that assimilation was an incongruent process, with a higher component of metamorphic biotite than present in the assimilant's bulk assemblage contributing to the melt through dehydration breakdown reactions.

3. After the first unit the fertility of the assimilant was reduced. This reduced the rate of assimilation and consequently the amount of water entering the melt for subsequent units, allowing enhanced plagioclase fractionation and producing more metalluminous melts. Magma recharge into an already fractionated system increased the initial K content of these later units. The combination of these two processes and the higher degrees of fractionation for the later units has resulted in the observed chemical heterogeneities within the pluton.
4. It may be possible for isotopic disequilibrium and geochemical heterogeneities between melt batches to be generated by incongruent melting of a single crustal source, but this would require extended periods of time and anatectic breakdown of a changing mineral assemblage to produce a discernible contrast in their chemical signatures. The relatively short half-life of ^{235}U renders the $^{207}Pb/^{206}Pb$ system most sensitive to determining the effect of this process and shows it to be an unsuitable solution in developing the Mt Kinabalu magmas. However, this process may have important implications for crustal assimilation.
5. Experimental data shows that metalluminous melts with both CaO/Na_2O > 1.5 and K2O/Na2O > 0.5 cannot be produced through crustal anatexis, including from mixed sources. Therefore, Mt Kinabalu cannot be produced through crustal anatexis alone.
6. Like Mt Kinabalu, bulk (BCC), middle (MCC) and lower (LCC) continental crust also possess CaO/Na_2O > 1.5 and K2O/Na2O > 0.5 and are too metalluminous to be produced solely though crustal anatexis. Their major element compositions, as well the upper crust (UCC), fall along one trend, indicating a cogenetic relationship. However, this conclusion from the experimental data indicates that the middle crust, and consequently its more fractionated upper crustal counterpart, cannot be generated by partial melting of the basaltic lower crust. Consequently, as for Mt Kinabalu, fractionation of a basaltic melt would be a more suitable process to invoke to generate the felsic crust.

7. The major and trace element composition of the LCC renders it of unsuitable composition to be mainly composed of cumulate material fractionated during generation of the felsic crust. Instead, we propose that it more closely represents the composition of the primary melts from which both it and the felsic crust were derived. With the exception of some trace elements the composition of the UCC can be derived through fractionation of the LCC without crustal assimilation. The modelled LLD also reproduces the global trend of felsic and intermediate plutons.
8. If the LCC closely represents the composition of the primary magma from which the UCC differentiated, then most mantle melts produced beneath the continents remain trapped in the LCC and are not expressed as fractionated volcanic or plutonic magmatism. If this is true, then the volume of mantle melting beneath continental arcs is much greater than would be believed based on observed magmatic activity, although this cannot be quantified without constraints on how much of the LCC is composed of cumulate material.

9.

Alonso-Perez, R., Müntener, O. and Ulmer, P. (2009). Igneous garnet and amphibole fractionation in the roots of island arcs: experimental constraints on andesitic liquids. *Contributions to Mineralogy and Petrology*. **157**, 4, 541-558.

Balaguru, A. (2001). Tectonic Evolution and Sedimentation of the Southern Sabah Basin, Malaysia. *Department of Geology, Royal Holloway, University of London.* PhD.

Balaguru, A. and Nichols, G. (2004). Tertiary stratigraphy and basin evolution, southern Sabah (Malaysian Borneo). *Journal of Asian Earth Sciences*. **23**, 4, 537-554.

Barckhausen, U. and Roeser, H.A. (2004). Seafloor spreading anomalies in the South China Sea revisited. *Geophysical Monograph Series*. **149**, 121-125.

Bea, F. (1996). Residence of REE, Y, Th and U in granites and crustal protoliths; implications for the chemistry of crustal melts. *Journal of Petrology*. **37**, 3, 521-552.

Beard, J.S. and Lofgren, G.E. (1991). Dehydration Melting and Water-Saturated Melting of Basaltic and Andesitic Greenstones and Amphibolites at 1, 3, and 6. 9 kb. *Journal of Petrology*. **32**, 2, 365-401.

Bergman, S.C., Dunn, D.P. and Krol, L.G. (1988). Rock and mineral chemistry of the Linhaisai Minette, Central Kalimantan, Indonesia, and the origin of Borneo diamonds. *The Canadian Mineralogist*. **26**, 1, 23-43.

Bogaerts, M., Scaillet, B. and Vander Auwera, J. (2006). Phase equilibria of the Lyngdal granodiorite (Norway): implications for the origin of metaluminous ferroan granitoids. *Journal of Petrology*. **47**, 12, 2405-2431.

Bottinga, Y. and Javoy, M. (1975). Oxygen isotope partitioning among the minerals in igneous and metamorphic rocks. *Reviews of Geophysics*. **13**, 2, 401-418.

Bowen, G.J. and Wilkinson, B. (2002). Spatial distribution of δ18O in meteoric precipitation. *Geology*. **30**, 4, 315-318.

Briais, A., Patriat, P. and Tapponnier, P. (1993). Updated Interpretation of Magnetic Anomalies and Seafloor Spreading Stages in the South China Sea : Implications for the Tertiary Tectonics of Southeast Asia. *Journal of Geophysical Research*. **98B**, 6299-6328.

Brimhall, G.H., Agee, C. and Stoffregen, R. (1985). The hydrothermal conversion of hornblende to biotite. *The Canadian Mineralogist*. **23**, 3, 369-379.

Chappell, B. and White, A. (1992). I-and S-type granites in the Lachlan Fold Belt. *Transactions of the Royal Society of Edinburgh: Earth Sciences*. **83**, 1-2, 1-26.

Chappell, B.W., Bryant, C.J. and Wyborn, D. (2012). Peraluminous I-type granites. *Lithos*.

Charlier, B., Ginibre, C., Morgan, D., Nowell, G., Pearson, D., Davidson, J. and Ottley, C. (2006). Methods for the microsampling and high-precision analysis of strontium and rubidium isotopes at single crystal scale for petrological and geochronological applications. *Chemical Geology*. **232**, 3, 114-133.

Chen, C.-H., Lee, C.-Y. and Shinjo, R. (2008). Was there Jurassic paleo-Pacific subduction in South China?: Constraints from 40Ar/39Ar dating, elemental and Sr–Nd–Pb isotopic geochemistry of the Mesozoic basalts. *Lithos*. **106**, 1, 83-92.

Chiang, K.K. (2002). Geochemistry of the Cenozoic igneous rocks of Borneo and tectonic implications. *Department of Geology, Royal Holloway, University of London.* PhD.

Chung, S.-L., Cheng, H., Jahn, B.-m., O'Reilly, S.Y. and Zhu, B. (1997). Major and trace element, and Sr-Nd isotope constraints on the origin of Paleogene volcanism in South China prior to the South China Sea opening. *Lithos*. **40**, 2-4, 203-220.

Clemens, J. and Mawer, C. (1992). Granitic magma transport by fracture propagation. *Tectonophysics*. **204**, 3, 339-360.

Clemens, J., Stevens, G. and Farina, F. (2011). The enigmatic sources of I-type granites: the peritectic connexion. *Lithos*. **126**, 3, 174-181.

Clemens, J.D., Helps, P.A. and Stevens, G. (2009). Chemical structure in granitic magmas - a signal from the source? *Earth and Environmental Science Transactions of the Royal Society of Edinburgh*. **100**, Special Issue 1-2, 159-172.

Clemens, J.D. and Benn, K. (2010). Anatomy, emplacement and evolution of a shallow-level, post-tectonic laccolith: the Mt Disappointment pluton, SE Australia. *Journal of the Geological Society*. **167**, 5, 915-941.

Coggon, J., Nowell, G., Pearson, D. and Parman, S. (2011). Application of the 190Pt-186Os isotope system to dating platinum mineralization and ophiolite formation: an example from the Meratus Mountains, Borneo. *Economic Geology*. **106**, 1, 93-117.

Corry, C.E. (1988). *Laccoliths: Mechanics of Emplacement and Growth*. Geological Society of America.

Cottam, M., Hall, R., Sperber, C. and Armstrong, R. (2010). Pulsed emplacement of the Mount Kinabalu granite, northern Borneo. *Journal of the Geological Society*. **167**, 1, 49-60.

Cottam, M., Hall, R., Sperber, C., Kohn, B., Forster, M. and Batt, G. (2013). Neogene rock uplift and erosion in northern Borneo: evidence from the Kinabalu granite, Mount Kinabalu. *Journal of the Geological Society*.

Cox, K.G., Bell, J.D. and Pankhurst, R.J. (1979). *The interpretation of igneous rocks*. G. Allen & Unwin.

Cruden, A.R. (1998). On the emplacement of tabular granites. *Journal of the Geological Society*. **155**, 5, 853-862.

Cullen, A., Macpherson, C., Taib, N.I., Burton-Johnson, A., Geist, D., Spell, T. and Banda, R.M. (2013). Age and Petrology of the Usun Apau and Linau Balui Volcanics: Windows to Central Borneo's Interior. *Journal of Asian Earth Sciences*.

Cullen, A.B. (2010). Transverse segmentation of the Baram-Balabac Basin, NW Borneo: refining the model of Borneo's tectonic evolution. *Petroleum Geoscience*. **16**, 1, 3-29.

Cullen, A.B., Reemst, P., Henstra, G., Gozzard, S. and Ray, A. (2010). Rifting of the South China Sea: new perspectives. *Petroleum Geoscience*. **16**, 3, 273-282.

Darbyshire, D.P.F. and Sewell, R.J. (1997). Nd and Sr isotope geochemistry of plutonic rocks from Hong Kong: implications for granite petrogenesis, regional structure and crustal evolution. *Chemical Geology*. **143**, 1-2, 81-93.

Davis, D.W., Sewell, R.J. and Campbell, S.D.G. (1997). U-Pb dating of Mesozoic igneous rocks from Hong Kong. *Journal of the Geological Society*. **154**, 6, 1067-1076.

Deer, W.A., Howie, R.A. and Zussman, J. (1966). An introduction to the rock-forming minerals.

DePaolo, D.J. (1981). Trace element and isotopic effects of combined wallrock assimilation and fractional crystallization. *Earth and planetary science letters*. **53**, 2, 189-202.

Douce, A.E.P. and Johnston, A.D. (1991). Phase equilibria and melt productivity in the pelitic system: implications for the origin of peraluminous granitoids and aluminous granulites. *Contributions to Mineralogy and Petrology*. **107**, 2, 202-218.

Douce, A.E.P. and Beard, J.S. (1995). Dehydration-melting of biotite gneiss and quartz amphibolite from 3 to 15 kbar. *Journal of Petrology*. **36**, 3, 707-738.

Douce, A.E.P. (2005). Vapor-absent melting of tonalite at 15–32 kbar. *Journal of Petrology*. **46**, 2, 275-290.

Encarnacion, J.P., Essene, E.J., Mukasa, S.B. and Hall, C.H. (1995). High-Pressure and -Temperature Subophiolitic Kyanite--Garnet Amphibolites Generated during Initiation of Mid-Tertiary Subduction, Palawan, Philippines. *J. Petrology*. **36**, 6, 1481-1503.

Farina, F. and Stevens, G. (2011). Source controlled 87Sr/86Sr isotope variability in granitic magmas: The inevitable consequence of mineral-scale isotopic disequilibrium in the protolith. *Lithos*. **122**, 3, 189-200.

Farver, J.R. and Giletti, B.J. (1985). Oxygen diffusion in amphiboles. *Geochimica et Cosmochimica Acta*. **49**, 6, 1403-1411.

Faure, G. and Mensing, T.M. (2005). Isotopes: principles and applications.

Frost, D.J. and McCammon, C.A. (2008). The redox state of Earth's mantle. *Annu. Rev. Earth Planet. Sci.* **36**, 389-420.

Galer, S. (1997). Optimal triple spiking for high precision lead isotope ratio determination. *Terra Nova*. **9**, 441.

Garcia, M.O. and Jacobson, S.S. (1979). Crystal clots, amphibole fractionation and the evolution of calc-alkaline magmas. *Contributions to Mineralogy and Petrology*. **69**, 4, 319-327.

Gardien, V., Thompson, A.B., Grujic, D. and Ulmer, P. (1995). Experimental melting of biotite+ plagioclase+ quartz±muscovite assemblages and implications for crustal melting. *Journal of Geophysical Research: Solid Earth (1978–2012)*. **100**, B8, 15581-15591.

Gardien, V., Thompson, A. and Ulmer, P. (2000). Melting of biotite+ plagioclase+ quartz gneisses: the role of H2O in the stability of amphibole. *Journal of Petrology*. **41**, 5, 651-666.

Ghiorso, M.S. and Sack, R.O. (1995). Chemical mass transfer in magmatic processes IV. A revised and internally consistent thermodynamic model for the interpolation and extrapolation of liquid-solid equilibria in magmatic systems at elevated temperatures and pressures. *Contributions to Mineralogy and Petrology*. **119**, 2-3, 197-212.

Gill, R. (1997). *Modern Analytical Geochemistry: an introduction to quantitative chemical analysis techniques for Earth, environmental and materials scientists*. Addison Wesley Longman.

Govindaraju, K. (1994). 1994 compilation of working values and sample description for 383 geostandards. *Geostandards newsletter*. **18**, S1, 1-158.

Grove, T. and Donnelly-Nolan, J. (1986). The evolution of young silicic lavas at Medicine Lake Volcano, California: Implications for the origin of compositional gaps in calc-alkaline series lavas. *Contributions to Mineralogy and Petrology*. **92**, 3, 281-302.

Grove, T.L., Elkins-Tanton, L.T., Parman, S.W., Chatterjee, N., Müntener, O. and Gaetani, G.A. (2003). Fractional crystallization and mantle-melting controls on calc-alkaline differentiation trends. *Contributions to Mineralogy and Petrology*. **145**, 5, 515-533.

Gutiérrez-Alonso, G., Fernández-Suárez, J. and Weil, A.B. (2004). Orocline triggered lithospheric delamination. *Orogenic curvature: Integrating paleomagnetic and structural analyses. Geol. Soc. Am. Spec. Pap, Boulder, Colorado*. **383**, 121-130.

Hall, R. (2002). Cenozoic geological and plate tectonic evolution of SE Asia and the SW Pacific: computer-based reconstructions, model and animations. *Journal of Asian Earth Sciences*. **20**, 4, 353-431.

Hall, R. (2009). Hydrocarbon basins in SE Asia: understanding why they are there. *Petroleum Geoscience*. **15**, 2, 131-146.

Hall, R. (2013). Contraction and extension in northern Borneo driven by subduction rollback. *Journal of Asian Earth Sciences*.

Hammouda, T., Pichavant, M. and Chaussidon, M. (1996). Isotopic equilibration during partial melting: an experimental test of the behaviour of Sr. *Earth and Planetary Science Letters*. **144**, 1, 109-121.

Hart, S.R. (1984). A large-scale isotope anomaly in the Southern Hemisphere mantle. *Nature*. **309**, 753-757.

Hirata, T. (1996). Lead isotopic analyses of NIST standard reference materials using multiple collector inductively coupled plasma mass spectrometry coupled with a modified external correction method for mass discrimination effect. *Analyst*. **121**, 10, 1407-1411.

Hoang, N., Flower, M.F. and Carlson, R.W. (1996). Major, trace element, and isotopic compositions of Vietnamese basalts: Interaction of hydrous EM1-rich asthenosphere with thinned Eurasian lithosphere. *Geochimica et Cosmochimica Acta*. **60**, 22, 4329-4351.

Hofmann, A.W. (1988). Chemical differentiation of the Earth: the relationship between mantle, continental crust, and oceanic crust. *Earth and Planetary Science Letters*. **90**, 3, 297-314.

Hollister, L.S., Grissom, G.C., Peters, E.K., Stowell, H.H. and Sisson, V.B. (1987). Confirmation of the empirical correlation of Al in hornblende with pressure of solidification of calc-alkaline plutons. *American Mineralogist*. **72**, 3-4, 231-239.

Hutchison, C.S. (1996). The 'Rajang accretionary prism'and 'Lupar Line'problem of Borneo. *Geological Society, London, Special Publications*. **106**, 1, 247-261.

Imai, A. (2000). Genesis of the Mamut Porphyry Copper Deposit, Sabah, East Malaysia. *Resource Geology*. **50**, 1, 1-23.

Jagoutz, O.E., Burg, J.-P., Hussain, S., Dawood, H., Pettke, T., Iizuka, T. and Maruyama, S. (2009). Construction of the granitoid crust of an island arc part I: geochronological and geochemical constraints from the plutonic Kohistan (NW Pakistan). *Contributions to Mineralogy and Petrology*. **158**, 6, 739-755.

Jahn, B., Auvray, B., Cornichet, J., Bai, Y., Shen, Q. and Liu, D. (1987). 3.5 Ga old amphibolites from eastern Hebei Province, China: field occurrence, petrography, Sm-Nd isochron age and REE geochemistry. *Precambrian Research*. **34**, 3, 311-346.

Kägi, R. (2000). The Liquid Line of Descent of Hydrous, Primary, Calc-alkaline Magmas Under Elevated Pressure: An Experimental Approach. *University of Basel.*

Kirk, H.J.C. (1968). The igneous rocks of Sarawak and Sabah. *Geological Survey Malaysia Bulletin*. **Memoir 14**,

Knesel, K.M. and Davidson, J.P. (1996). Isotopic disequilibrium during melting of granite and implications for crustal contamination of magmas. *Geology*. **24**, 3, 243-246.

Krawczynski, M.J., Grove, T.L. and Behrens, H. (2012). Amphibole stability in primitive arc magmas: effects of temperature, H2O content, and oxygen fugacity. *Contributions to Mineralogy and Petrology*. **164**, 2, 317-339.

Lee, C.-T.A., Cheng, X. and Horodyskyj, U. (2006). The development and refinement of continental arcs by primary basaltic magmatism, garnet pyroxenite accumulation, basaltic recharge and delamination: insights from the Sierra Nevada, California. *Contributions to Mineralogy and Petrology*. **151**, 2, 222-242.

Lee, C.-T.A., Morton, D.M., Kistler, R.W. and Baird, A.K. (2007). Petrology and tectonics of Phanerozoic continent formation: from island arcs to accretion and continental arc magmatism. *Earth and Planetary Science Letters*. **263**, 3, 370-387.

Leong, K. (1974). *The geology and mineral resources of the Upper Segama Valley and Darvel Bay area, Sabah, Malaysia*. US Government Printing Office.

Leong, K. (1998). Sabah crystalline basement: "Spurious" radiometric ages? Continental? *Warta Geologi (Geological Society of Malaysia Newsletter)*. **24**, 5-8.

Leuthold, J., Müntener, O., Baumgartner, L., Putlitz, B. and Chiaradia, M. (2013). A Detailed Geochemical Study of a Shallow Arc-related Laccolith; the Torres del Paine Mafic Complex (Patagonia). *Journal of Petrology*. **54**, 2, 273-303.

Liew, T.C. and McCulloch, M.T. (1985). Genesis of granitoid batholiths of Peninsular Malaysia and implications for models of crustal evolution: Evidence from a Nd---Sr isotopic and U---Pb zircon study. *Geochimica et Cosmochimica Acta*. **49**, 2, 587-600.

Macpherson, C.G. and Mattey, D.P. (1998). Oxygen isotope variations in Lau Basin lavas. *Chemical Geology*. **144**, 3, 177-194.

Macpherson, C.G., Chiang, K.K., Hall, R., Nowell, G.M., Castillo, P.R. and Thirlwall, M.F. (2010). Plio-Pleistocene intra-plate magmatism from the southern Sulu Arc, Semporna peninsula, Sabah, Borneo: Implications for high-Nb basalt in subduction zones. *Journal of Volcanology and Geothermal Research*. **190**, 1-2, 25-38.

Magaritz, M., Whitford, D. and James, D. (1978). Oxygen isotopes and the origin of high 87Sr/86Sr andesites. *Earth and Planetary Science Letters*. **40**, 2, 220-230.

Mattey, D. and Macpherson, C. (1993). High-precision oxygen isotope microanalysis of ferromagnesian minerals by laser-fluorination. *Chemical Geology*. **105**, 4, 305-318.

Mattey, D., Lowry, D. and Macpherson, C. (1994). Oxygen isotope composition of mantle peridotite. *Earth and Planetary Science Letters*. **128**, 3, 231-241.

McCaffrey, K.J.W. and Petford, N. (1997). Are granitic intrusions scale invariant? *Journal of the Geological Society*. **154**, 1, 1-4.

McLeod, C.L., Davidson, J.P., Nowell, G.M. and de Silva, S.L. (2012). Disequilibrium melting during crustal anatexis and implications for modeling open magmatic systems. *Geology*. **40**, 5, 435-438.

Milsom, J., Holt, R., Hutchison, C.S., Bergman, S.C., Swauger, D.A. and Graves, J.E. (2001). Discussion of a Miocene collisional belt in north Borneo: uplift mechanism and isostatic adjustment quantified by thermochronology: Journal, Vol. 157, 2000, 783-793. *Journal of the Geological Society*. **158**, 2, 396-400.

Miyashiro, A. (1974). Volcanic rock series in island arcs and active continental margins. *American Journal of Science*. **274**, 4, 321-355.

Montel, J.-M. and Vielzeuf, D. (1997). Partial melting of metagreywackes, Part II. Compositions of minerals and melts. *Contributions to Mineralogy and Petrology*. **128**, 2-3, 176-196.

Moss, S.J., Chambers, J., Cloke, I., Satria, D., Ali, J.R., Baker, S., Milsom, J. and Carter, A. (1997). New observations on the sedimentary and tectonic evolution of the Tertiary Kutai Basin, East Kalimantan. *Geological Society, London, Special Publications*. **126**, 1, 395-416.

Moss, S.J. (1998). Embaluh group turbidites in Kalimantan: evolution of a remnant oceanic basin in Borneo during the Late Cretaceous to Palaeogene. *Journal of the Geological Society*. **155**, 509-524.

Müntener, O. and Ulmer, P. (2006). Experimentally derived high-pressure cumulates from hydrous arc magmas and consequences for the seismic velocity structure of lower arc crust. *Geophysical Research Letters*. **33**, 21, L21308.

Naney, M. (1983). Phase equilibria of rock-forming ferromagnesian silicates in granitic systems. *American journal of science*. **283**, 10, 993-1033.

Nguyen, T.T.B., Satir, M., Siebel, W. and Chen, F. (2004). Granitoids in the Dalat zone, southern Vietnam: age constraints on magmatism and regional geological implications. *International Journal of Earth Sciences*. **93**, 3, 329-340.

Niu, Y., Collerson, K.D., Batiza, R., Wendt, J.I. and Regelous, M. (1999). Origin of enriched-type mid-ocean ridge basalt at ridges far from mantle plumes: The East Pacific Rise at 11 20' N. *Journal of Geophysical Research: Solid Earth (1978–2012)*. **104**, B4, 7067-7087.

Nowell, G., Pearson, D., Ottley, C., Schweiters, J. and Dowall, D. (2003). Long-term performance characteristics of a plasma ionisation multi-collector mass spectrometer (PIMMS): the ThermoFinnigan Neptune. *Plasma Source Mass Spectrometry: Applications and Emerging Technologies. Cambridge: Royal Society of Chemistry*. 307-320.

Ottley, C., Pearson, D. and Irvine, G. (2003). A routine method for the dissolution of geological samples for the analysis of REE and trace elements via ICP-MS. *Plasma source mass spectrometry: Applications and emerging technologies*. 221-230.

Parman, S., Grove, T., Kelley, K. and Plank, T. (2011). Along-arc variations in the pre-eruptive H2O contents of Mariana arc magmas inferred from fractionation paths. *Journal of Petrology*. **52**, 2, 257-278.

Pearce, J.A. and Parkinson, I.J. (1993). Trace element models for mantle melting: application to volcanic arc petrogenesis. *Geological Society, London, Special Publications*. **76**, 1, 373-403.

Petford, N. and Clemens, J.D. (2000). Granites are not diapiric! *Geology Today*. **16**, 5, 180-184.

Petford, N., Cruden, A.R., McCaffrey, K.J.W. and Vigneresse, J.L. (2000). Granite magma formation, transport and emplacement in the Earth's crust. *Nature*. **408**, 6813, 669-673.

Potts, P.J., Tindle, A.G. and Webb, P. (1992). *Geochemical Reference Material Compositions: Rocks, minerals, sediments, soils, carbonates, refractories, and ores used in research and industry*. Taylor & Francis US.

Rapp, R.P., Watson, E.B. and Miller, C.F. (1991). Partial melting of amphibolite/eclogite and the origin of Archean trondhjemites and tonalites. *Precambrian Research*. **51**, 1, 1-25.

Rapp, R.P. and Watson, E.B. (1995). Dehydration melting of metabasalt at 8–32 kbar: implications for continental growth and crust-mantle recycling. *Journal of Petrology*. **36**, 4, 891-931.

Reiners, P.W., Nelson, B.K. and Ghiorso, M.S. (1995). Assimilation of felsic crust by basaltic magma: thermal limits and extents of crustal contamination of mantle-derived magmas. *Geology*. **23**, 6, 563-566.

Roberts, M.P. and Clemens, J.D. (1993). Origin of high-potassium, calc-alkaline, I-type granitoids. *Geology*. **21**, 9, 825-828.

Rollinson, H.R. (1993). *Using geochemical data: evaluation, presentation, interpretation*. Longman Scientific & Technical Essex.

Royse, K., Kempton, P. and Darbyshire, D. (1998). Procedure for the analysis of rubidium–strontium and samarium–neodymium isotopes at the NERC Isotope Geosciences Laboratory. *NIGL Report Series*. **121**, 28.

Rudnick, R. and Gao, S. (2003). Composition of the continental crust. *Treatise on geochemistry*. **3**, 1-64.

Rudnick, R.L. and Fountain, D.M. (1995). Nature and composition of the continental crust: a lower crustal perspective. *Reviews of Geophysics*. **33**, 3, 267-309.

Rushmer, T. (1991). Partial melting of two amphibolites: contrasting experimental results under fluid-absent conditions. *Contributions to Mineralogy and Petrology*. **107**, 1, 41-59.

Rushmer, T. (1993). Experimental high-pressure granulites: some applications to natural mafic xenolith suites and Archean granulite terranes. *Geology*. **21**, 5, 411-414.

Rutter, M.J. and Wyllie, P.J. (1988). Melting of vapour-absent tonalite at 10 kbar to simulate dehydration–melting in the deep crust. *Nature*. **331**, 6152, 159-160.

Sen, C. and Dunn, T. (1994). Dehydration melting of a basaltic composition amphibolite at 1.5 and 2.0 GPa: implications for the origin of adakites. *Contributions to Mineralogy and Petrology*. **117**, 4, 394-409.

Sheppard, S.M. (1986). Characterization and isotopic variations in natural waters. *Reviews in Mineralogy and Geochemistry*. **16**, 1, 165-183.

Singh, J. and Johannes, W. (1996a). Dehydration melting of tonalites. Part I. Beginning of melting. *Contributions to Mineralogy and Petrology*. **125**, 1, 16-25.

Singh, J. and Johannes, W. (1996b). Dehydration melting of tonalites. Part II. Composition of melts and solids. *Contributions to Mineralogy and Petrology*. **125**, 1, 26-44.

Sisson, T., Ratajeski, K., Hankins, W. and Glazner, A. (2005). Voluminous granitic magmas from common basaltic sources. *Contributions to Mineralogy and Petrology*. **148**, 6, 635-661.

Skjerlie, K.P. and Johnston, A.D. (1992). Vapor-absent melting at 10 kbar of a biotite-and amphibole-bearing tonalitic gneiss: implications for the generation of A-type granites. *Geology*. **20**, 3, 263-266.

Spera, F.J. and Bohrson, W.A. (2001). Energy-constrained open-system magmatic processes I: General model and energy-constrained assimilation and fractional crystallization (EC-AFC) formulation. *Journal of Petrology*. **42**, 5, 999-1018.

Sperber, C.M. (2009). The thermotectonic development of Mount Kinabalu, Sabah, Malaysia: Constraints from low-temperature thermochronology. *Department of Earth Science, Royal Holloway, University of London.* PhD.

Streckeisen, A. (1976). To each plutonic rock its proper name. *Earth-Science Reviews*. **12**, 1, 1-33.

Suggate, S., Cottam, M., Hall, R., Sevastjanova, I., Forster, M., White, L., Armstrong, R., Carter, A. and Mojares, E. (2013). South China continental margin signature for sandstones and granites from Palawan, Philippines. *Gondwana Research*.

Sun, S.-S. and McDonough, W. (1989). Chemical and isotopic systematics of oceanic basalts: implications for mantle composition and processes. *Geological Society, London, Special Publications*. **42**, 1, 313-345.

Tapponnier, P., Peltzer, G. and Armijo, R. (1986). On the mechanics of the collision between India and Asia. *Geological Society, London, Special Publications*. **19**, 1, 113-157.

Taylor, B. and Hayes, D.E. (1983). Origin and history of the South China Sea basin. *Geophysical Monograph Series*. **27**, 23-56.

Thirlwall, M. (1991). Long-term reproducibility of multicollector Sr and Nd isotope ratio analysis. *Chemical Geology: Isotope Geoscience section*. **94**, 2, 85-104.

Thuy, N.T.B., Satir, M., Siebel, W., Vennemann, T. and Long, T.V. (2004). Geochemical and isotopic constraints on the petrogenesis of granitoids from the Dalat zone, southern Vietnam. *Journal of Asian Earth Sciences*. **23**, 4, 467-482.

Toplis, M. and Carroll, M. (1995). An experimental study of the influence of oxygen fugacity on Fe-Ti oxide stability, phase relations, and mineral—Melt equilibria in ferro-basaltic systems. *Journal of Petrology*. **36**, 5, 1137-1170.

Tu, K., Flower, M.F.J., Carlson, R.W., Xie, G., Chen, C.-Y. and Zhang, M. (1992). Magmatism in the South China Basin: 1. Isotopic and trace-element evidence for an endogenous Dupal mantle component. *Chemical Geology*. **97**, 1–2, 47-63.

Ulmer, P. and Muntener, O. (2011). Derivation of granitoid magmas by deep crustal crystallization-differentiation of basaltic parental magmas: an experimental perspective. *Seventh Hutton Symposium on Granites and related rocks*.

van Hattum, M., Hall, R., Pickard, A. and Nichols, G. (2013). Provenance and geochronology of Cenozoic sandstones of northern Borneo. *Journal of Asian Earth Sciences*.

Vielzeuf, D. and Holloway, J.R. (1988). Experimental determination of the fluid-absent melting relations in the pelitic system. *Contributions to Mineralogy and Petrology*. **98**, 3, 257-276.

Vogt, E. and Flower, M.J. (1989). Genesis of the Kinabalu (Sabah) granitoid at a subduction-collision junction. *Contributions to Mineralogy and Petrology*. **103**, 4, 493-509.

Wang, Y., Fan, W., Cawood, P.A. and Li, S. (2008). Sr–Nd–Pb isotopic constraints on multiple mantle domains for Mesozoic mafic rocks beneath the South China Block hinterland. *Lithos*. **106**, 3, 297-308.

Watt, G. and Harley, S. (1993). Accessory phase controls on the geochemistry of crustal melts and restites produced during water-undersaturated partial melting. *Contributions to Mineralogy and Petrology*. **114**, 4, 550-566.

Winther, K.T. (1996). An experimentally based model for the origin of tonalitic and trondhjemitic melts. *Chemical Geology*. **127**, 1, 43-59.

Wolf, M.B. and Wyllie, P.J. (1994). Dehydration-melting of amphibolite at 10 kbar: the effects of temperature and time. *Contributions to Mineralogy and Petrology*. **115**, 4, 369-383.

Xiao, L. and Clemens, J. (2007). Origin of potassic (C-type) adakite magmas: experimental and field constraints. *Lithos*. **95**, 3, 399-414.

Xiong, X., Adam, J. and Green, T. (2005). Rutile stability and rutile/melt HFSE partitioning during partial melting of hydrous basalt: implications for TTG genesis. *Chemical Geology*. **218**, 3, 339-359.

Yan, Q., Shi, X., Wang, K., Bu, W. and Xiao, L. (2008). Major element, trace element, and Sr, Nd and Pb isotope studies of Cenozoic basalts from the South China Sea. *Science in China Series D: Earth Sciences*. **51**, 4, 550-566.

Yan, Q. and Shi, X. (2009). Mineralogy, Pb and O isotopic characteristics of granitic rocks from the Nansha block (South China Sea): magmatic process and tectonic affiliation. *AGU Fall Meeting Abstracts*. **1**, 2133.

Yan, Q., Shi, X. and Li, N. (2011). Oxygen and lead isotope characteristics of granitic rocks from the Nansha block (South China Sea): Implications for their petrogenesis and tectonic affinity. *Island Arc*. **20**, 2, 150-159.

Yan, Q.S., Shi, X.F., Liu, J.H., Wang, K.S. and Bu, W.R. (2010). Petrology and geochemistry of Mesozoic granitic rocks from the Nansha micro-block, the South China Sea: Constraints on the basement nature. *Journal of Asian Earth Sciences*. **37**, 2, 130-139.

Yanbo, C. and Jingwen, M. (2010). Age and geochemistry of granites in Gejiu area, Yunnan province, SW China: Constraints on their petrogenesis and tectonic setting. *Lithos*. **120**, 3, 258-276.

Zheng, Y.-F. (1993a). Calculation of oxygen isotope fractionation in anhydrous silicate minerals. *Geochimica et Cosmochimica Acta*. **57**, 1079-1091.

Zheng, Y.-F. (1993b). Calculation of oxygen isotope fractionation in hydroxyl-bearing silicates. *Earth and Planetary Science Letters*. **120**, 3, 247-263.

Zhou, X.M. and Li, W.X. (2000). Origin of Late Mesozoic igneous rocks in Southeastern China: implications for lithosphere subduction and underplating of mafic magmas. *Tectonophysics*. **326**, 3-4, 269-287.

Zhu, B. (1995). The mapping of geochemical provinces in China based on Pb isotopes. *Journal of Geochemical Exploration*. **55**, 1, 171-181.

Zindler, A. and Hart, S. (1986). Chemical geodynamics. *Annual review of earth and planetary sciences*. **14**, 493-571.

Supplementary A – Modelling the evolution of isotopic heterogeneities and disequilibrium partial melting

Presented here is the process by which the development of isotopic disequilibrium in an igneous rock, and the signature that would be imparted on partial melts through the breakdown of different phases can be modelled.

Assuming that all minerals in an igneous rock will be in isotopic equilibrium at its time of formation then isotopic disequilibrium will only develop given enough time. By knowing the age of a rock (t), its initial isotopic ratio, its modal mineral composition, the elemental composition of its constituent minerals and the decay constant of the isotopic system (λ) then the isotopic ratio of each phase can be calculated. Using the calculated ratios and the concentration of the daughter element in each phase it is then possible to calculate the isotopic ratio of a melt produced from a combination of these phases, similar to the modelling of the $^{87}Sr/^{86}Sr$ system for the partial melting of a metagreywacke by Farina and Stevens (2011).

The isotopic ratio developed in each phase since crystallisation, t, is calculated through the following steps. It is here illustrated for the $^{87}Sr/^{86}Sr$ system, but can also be applied to other radiogenic isotope systems.

The ratio of the parent and daughter elemental isotopes for each phase is calculated using equation 5.8 of Faure and Mensing (2005):

$$\left(\frac{^{87}\mathrm{Rb}}{^{86}\mathrm{Sr}}\right)_{\mathrm{i}} = \left(\frac{\mathrm{Rb}}{\mathrm{Sr}}\right)_{\mathrm{Min.conc.}} \times \frac{\mathrm{Ab}\ ^{87}\mathrm{Rb} \times \mathrm{WSr}}{\mathrm{Ab}\ ^{86}\mathrm{Sr} \times \mathrm{WRb}}$$

[Eq. 2]

where $^{87}Rb/^{86}Sr$ is the isotopic ratio of the parent and daughter isotopes, Ab ^{87}Rb and Ab ^{86}Sr are the isotopic abundances of ^{87}Rb and ^{86}Sr, and WRb and WSr are their respective atomic weights. $(Rb/Sr)_{Min.Conc.}$ is the measured ratio of the elemental concentrations in each mineral phase. Ab ^{86}Sr is calculated from:

$$\mathrm{Ab}\ ^{\mathrm{x}}\mathrm{Sr} = \left(\frac{^{\mathrm{x}}\mathrm{Sr}}{^{88}\mathrm{Sr}}\right) / \left(\frac{^{84}\mathrm{Sr}}{^{88}\mathrm{Sr}} + \frac{^{86}\mathrm{Sr}}{^{88}\mathrm{Sr}} + \frac{^{87}\mathrm{Sr}}{^{88}\mathrm{Sr}} + \frac{^{88}\mathrm{Sr}}{^{88}\mathrm{Sr}}\right)$$

[Eq. 3]

where ^{x}Sr substitutes for each Sr isotope, and:

$$\left(\frac{^{87}\mathrm{Sr}}{^{88}\mathrm{Sr}}\right) = \left(\frac{^{87}\mathrm{Sr}}{^{86}\mathrm{Sr}}\right)_{i} \left(\frac{^{86}\mathrm{Sr}}{^{88}\mathrm{Sr}}\right)$$

[Eq. 4]

where $(^{87}Sr/^{86}Sr)_i$ is the calculated initial whole rock isotope ratio of the source.

Finally, WSr for Eq. 2 is calculated from:

$$\mathrm{WSr} = \sum(\mathrm{M}\ ^{\mathrm{x}}\mathrm{Sr}\mathrm{Ab}\ ^{\mathrm{x}}\mathrm{Sr})$$

[Eq. 5]

where $M\ ^{x}Sr$ is the weight of each Sr isotope in atomic mass units (amu).

Once the initial $^{87}Rb/^{86}Sr$ isotope ratio for each mineral phase has been calculated, the $^{87}Sr/^{86}Sr$ after t My, $(^{87}Sr/^{86}Sr)_{tmin}$, can be calculated from:

$$\left(\frac{^{87}\mathrm{Sr}}{^{86}\mathrm{Sr}}\right)_{tmin.} = \left(\frac{^{87}\mathrm{Sr}}{^{86}\mathrm{Sr}}\right)_{i} + \left(\left(\frac{^{87}\mathrm{Rb}}{^{86}\mathrm{Sr}}\right)_{\mathrm{i}} (1 - e^{-\lambda t \times 10^{6}}\right)$$

[Eq. 6]

where λ is the decay constant of ^{87}Rb.

Once the isotopic composition of each mineral phase has been calculated it is possible to calculate the isotopic composition of a melt derived from a chosen assemblage of different phases, using the concentration of the daughter element in each constituent mineral and the fraction of the melt derived from each phase, F. The sum of the F values for all the phases contributing to the melt should equal one.

The concentration of the daughter element in each phase determines the proportion that it contributes to the total budget of that element in a melt derived from an assemblage of phases. This proportion, P, as a fraction of the total budget, is calculated from:

$$P_{min.x} = \frac{F_{min.x} Sr_{min.x}}{\sum F_{min.} Sr_{min.}}$$

[Eq. 7]

where x denotes each individual mineral phase and $\sum F_{min.} Sr_{min.}$ is the sum of the fraction of the total melt for each phase multiplied by its daughter element concentration, in this case Sr. The sum of the P values for all the phases contributing to the melt should also equal one.

The resultant isotopic signature of the melt derived from an assemblage of phases can then be calculated from:

$$\left(\frac{^{87}\mathrm{Sr}}{^{86}\mathrm{Sr}}\right)_{melt} = \sum \left(\left(\frac{^{87}\mathrm{Sr}}{^{86}\mathrm{Sr}}\right)_{tmin.} \mathrm{P}_{min} \right)$$

[Eq. 8]

where the calculated isotopic ratio for each phase is multiplied by the contribution that each phase makes to the total budget of the daughter isotope in the melt, and the sum of these values for all phases contributing to the melt is its resultant isotopic signature.

Supplementary B – Modelling major element fractionation

The major element fractional crystallisation and assimilation model discussed in this paper is based on the model of Grove and Donnelly-Nolan (1986), modified for the Mt Kinabalu system. It differs from their model in that it attempts to model expected variation of elements in all sites of each phase, including minor elements.

The model is calculated using the molar masses of the major elements, calculated from a starting basaltic composition, and only converted back to oxides at the end of modelling. It is calculated iteratively at 1% changes of F (the remaining melt fraction) and at each stage the composition of the potential fractionating phases is calculated to be in equilibrium with the melt based on paired element distribution coefficients. The weakness of the model is that the specific values of these coefficients in this system are unknown and will vary according to temperature, pressure, composition, water content and fO_2. For this model the values are adjusted to best represent the data whilst remaining similar to experimental values and producing mineral compositions similar to the mineral separate data of this study. The relative abundances for the major elements not determined directly from this distribution and mineral formula are calculated based on their distributions in the mineral data with respect to these ratios or by constants values. The formulae for each phase and the sites in to which elements can substitute are determined from Deer *et al.* (1966) and the ionic charge of each element. The calculations used to equilibrate the major and minor elements are summarised in Table 5.3.

The liquid composition is converted from molar masses to atomic abundances prior to the equilibration calculations, and the mineral composition is calculated in this manner to conform to the stoichiometric constraints of each mineral's known possible compositions. Calculated values are converted back to 100% normalised molar masses of the mineral composition prior to fractionation.

Plagioclase is removed as $((K,Na)_{1-(x-1)},(Mg+Mn+Ca)_{x-1})_1((Fe+Al)_x,Si_{4-x})_4O_8$. It is equilibrated with the liquid using the paired distribution coefficient $K_D = Al^{Plag}Si^{Liq}/Si^{Plag}Al^{Liq}$. The Al-Si distribution was used in preference to the Ca-Na

distribution as the experiments of Grove *et al.* (2003) and Alonso-Perez *et al.* (2009) show it to be far less variable (1.9-4.5, compared to 0.6-10.2). The Na-K distribution is calculated from $K_D = K^{Plag}Na^{Liq}/Na^{Plag}K^{Liq}$. Fe substitutes for Al, and Mg and Mn substitute for Ca in proportions determined from the Mt Kinabalu mineral data.

Hornblende is removed as $(Na,K)_{0\text{-}1}Ca_2((Mn,(Mg,Fe)),(Ti(Al,Si)))_{13}O_{22}(OH)$. It is equilibrated with the liquid using the equation $K_D = Fe^{Hb}Mg^{Liq}/Mg^{Hb}Fe^{Liq}$. Orthopyroxene and clinopyroxene are calculated as $((Ca,Na),(Mn,(Mg,Fe)))_2(Si,(Ti,Al))_2O_6$ and use the Fe-Mg mineral-melt distribution coefficients $K_D = Fe^{Opx}Mg^{Liq}/Mg^{Opx}Fe^{Liq}$, and the Al-Si $K_D = Al^{Cpx}Si^{Liq}/Si^{Cpx}Al^{Liq}$. Biotite is defined as $(K,Na)_2((((Mg,Fe)Ti)Mn)_{4\text{-}6},(Al,Si)_{8\text{-}10})_{14}O_{20}(OH)_4$, and equilibrated with the liquid using $K_D = Al^{Plag}Si^{Liq}/Si^{Plag}Al^{Liq}$. Olivine is calculated as $((Mg,Fe),Ca,Mn)_2(Si,Al,Ti)O_4$, and garnet as $(Mg,Fe)_3Al_2\ Si_3O_{12}$. They are both equilibrated using the Fe-Mg distributions $K_D = Fe^{Min}Mg^{Liq}/Mg^{Min}Fe^{Liq}$.

We shall use the example of plagioclase to illustrate how these equilibrium compositions are calculated:

As stated, plagioclase is described in these models by the formula:

$$((K,Na)_{1\text{-}(x\text{-}1)},(Mg,Mn,Ca)_{x\text{-}1})_1((Fe,Al)_x,Si_{4\text{-}x})_4O_8$$

[Eq. 9]

Its equilibrium composition is calculated from its Al-$Si_{mineral\text{-}melt}$ paired element partition coefficient ($kd^{Plag}_{min-melt}$), so the Al/Si ratio of the mineral is calculated first from:

$$Al^{Plag}/Si^{Plag} = kd^{Plag}_{min-melt}(Si^{Melt}/Al^{Melt})$$

[Eq. 10]

According to the mineral formula, Al and Si have a constant abundance in plagioclase of 4 formula units, so the Si component can be calculated from:

$$Si_{(formula\ units)} = 4/(Al^{Plag}/Si^{Plag} + 1)$$

[Eq. 11]

Iron is a very minor constituent of plagioclase. This model treats all the iron in plagioclase as Fe^{3+}, which substitutes for Al in the Mt Kinabalu data in a fixed proportion of the Al and Si site according to:

$$Fe_{(Formula\ units)} = 0.005(4 - Si_{(Formula\ units)})$$

[Eq. 12]

Al can then be calculated from:

$$Al_{(Formula\ units)} = (4 - Si_{(Formula\ units)}) - Fe_{(Formula\ units)}$$

[Eq. 13]

The Ca and Na site makes up one formula unit of plagioclase. As can be seen in the mineral formula, the Ca/Na ratio of plagioclase is directly linked to its Al/Si content. However, Mg and Mn are able to substitute for Ca in very small proportions, and K is able to substitute for Na.

The total Ca, Mg and Mn content is calculated from:

$$(Ca + Mg + Mn)_{(Formula\ units)} = Si_{(Formula\ units)} - 1$$

[Eq. 14]

Mn and Mg substitute in fixed proportions for Ca, and so the proportions of each element can be calculated based on their proportions in the Mt Kinabalu mineral data according to:

$$Mg_{(Formula\ units)} = 0.014(Ca + Mg + Mn)_{(Formula\ units)}$$

$$Mn_{(Formula\ units)} = 0.003(Ca + Mg + Mn)_{(Formula\ units)}$$

$$Ca_{(Formula\ units)} = (Ca + Mg + Mn)_{(Formula\ units)} - Mg_{(Formula\ units)} - Mn_{(Formula\ units)}$$

[Eq. 15, a, b and c respectively]

Finally, in addition to Al and SI, the K/Na ratio of plagioclase is also determined by the melt composition, and so is calculated from its Na-$K_{mineral\text{-}melt}$ paired element partition coefficient ($kd^{Plag}_{min-melt}$):

$$K^{Plag}/Na^{Plag} = kd^{Plag}_{min-melt}(Na^{Melt}/K^{Melt})$$

[Eq. 16]

The formula units of K and Na are then calculated from:

$$(Na+K)_{(Formula\ units)} = 1 - (Ca + Mg + Mn)_{(Formula\ units)}$$

$$Na_{(Formula\ units)} = ((1/(K^{Plag}/Na^{Plag} + 1)\ (Ca + Mg + Mn)_{(Formula\ units)})$$
$$(Na+K)_{(Formula\ units)}$$

$$K_{(Formula\ units)} = (Na+K)_{(Formula\ units)} - Na_{(Formula\ units)}$$

[Eq. 17, a and b respectively]

Each element is then multiplied by its molar mass and a total is calculated for all elements. A 100% normalised predicted total is then calculated ($Predicted \sum Major\ and\ minor\ elements_{(Molar\ mass)}$) by dividing this total by the predicted total (sum of the calculated elements in molar mass units plus the required oxygen content – i.e. 8 formula units for plagioclase) and multiplying by 100.

$$Predicted \sum Major\ and\ minor\ elements_{(Molar\ mass)} = \frac{100 \times \sum Major\ and\ minor\ elements_{(Molar\ mass)}}{\sum Major\ \&\ minor\ elements_{(Molar\ mass)} + (O_{(Formula\ units)} \times (O_{(Molar\ mass)})}$$

[Eq. 18]

Finally, the 100% normalised molar mass of each element is calculated by multiplying its calculated molar mass by the predicted normalised total divided by the calculated total.

i.e.

$$Element^{Plag}_{Molar\ mass,100\%\ normalised} = \frac{Element^{Plag}_{Molar\ mass,not\ normalised} \times Predicted \sum Major\ and\ minor\ elements_{(Molar\ mass)}}{\sum Major\ \&\ minor\ elements_{(Molar\ mass)}}$$

[Eq. 19]

These steps change for each mineral according to their formula and the calculations in Table 5.3, but follow broadly the same technique in their calculation.

The molar mass of each major element in the melt following fractional crystallisation ($C_{m(FC)}$) is calculated for each iteration by subtracting the sum of the major element concentrations of the fractionating minerals in their relative proportions in the cumulate assemblage ($\sum C_a$) using the mass balance equation:

$$C_{m(FC)} = (C^0 - (1 - F)\sum C_c)/F$$

[Eq. 20]

At each iteration, following fractional crystallisation an assimilant is added to the melt based on the proportion r, the ratio of the mass assimilated to the mass crystallised ($(M_a/\ M_c)$. The major element concentration of the melt following assimilation is calculated by mass balance, whilst the trace element and isotopic composition is calculated using equations (6a), (15a) and (20) of DePaolo (1981).

The mass balance equation used for assimilation of major elements is:

$$C_{m(AFC)} = C_{m(FC)}(1 - (1 - F)r) + ((1 - F)r)\sum C_a$$

[Eq. 21]

Additionally, at each iteration the molar mass of the major elements ($\sum M_c$) in the bulk cumulate assemblage is calculated using the mass balance equation:

$$\sum M_c = M_c^0 \left(1 - \frac{dF_T}{1 - F_T}\right) + C_c \left(\frac{dF_T}{1 - F_T}\right)$$

[Eq. 22]

where M_c^0 is the concentration at the previous iteration, C_c is the elemental molar mass in the fractionating assemblage and F_T is the total fraction of melt remaining in the system, including previous iterations. The cumulate composition is then calculated to oxides and normalised to 100%

The trace element concentration of the fractionating assemblage (C_c) is calculated by rearranging equation (4) of DePaolo (1981), which gives:

$$C_c = DC_m = (\left(\frac{r}{r-1}\right) C_a - \left(\frac{dC_m}{d\ln F}\right)(r-1) + C_m - rC_m$$

[Eq. 23]

where C_m is the concentration of the element in the melt and C_a is its concentration in the assimilant. The composition of the bulk cumulate assemblage is the calculated in the same way as for the major elements (Eq. 22).

Mineral	Table 5.3. - Calculations used for major element modelling (in formula units)	
Plagioclase	**Composition**	$((K,Na)_{1-(x-1)},(Mg,Mn,Ca)_{x-1})_1((Fe,Al)_x,Si_{4-x})_4O_8$
	Al-Si Kd	$K_D = (Al^{Plag} \times Si^{Liq}) / (Si^{Plag} \times Al^{Liq})$
	K-Na Kd	$K_D = (K^{Plag} \times Na^{Liq}) / (Na^{Plag} \times K^{Liq})$
	Fe	= 0.005 x (Fe + Al)
	Mg	= 0.014 x (Mg + Mn + Ca)
	Mn	= 0.003 x (Mg + Mn + Ca)
Hornblende	**Composition**	$(Na,K)_{0-?}Ca_2((Mn,(Mg,Fe)),(Ti(Al,Si)))_{13}O_{22}(OH)$
	Fe-Mg Kd	$K_D = (Fe^{Hb} \times Mg^{Liq}) / (Mg^{Hb} \times Fe^{Liq})$
	Si/Al	$= 0.0861 \times (Fe/Mg)^{-9.021} + 4$
	(Fe + Mg + Mn) / (Al +Si +Ti)	= -0.3386 x (Al/Si) + 0.6139
	Mn	= 0.014 x (Fe + Mg + Mn)
	Ti / (Al + Si + Ti)	= 0.0923 x (Al/Si) – 0.0018
	(Na + K) / Total major elements exc. O &	= 0.1569 x (Al/Si) + 0.005
	H	$= 0.8153 \times (Al/Si)^{-0.6259}$
	Na/K	
Clinopyroxene	**Composition**	$((Ca,Na),(Mn,(Mg,Fe)))_2(Si,(Ti,Al))_2O_6$
	Fe-Mg Kd	$K_D = (Fe^{Cpx} \times Mg^{Liq}) / (Mg^{Cpx} \times Fe^{Liq})$
	Al-Si Kd	$K_D = (Al^{Cpx} \times Si^{Liq}) / (Si^{Cpx} \times Al^{Liq})$
	Mn/(Fe+Mg+Mn)	= 0.0619 x (Fe/Mg) – 0.0063
	Ti/(Ti+Al)	= 0.21707 x ((Ti+Al)/Si) – 0.00341
	Na/(Na+Ca)	= 0.0515 x (Fe/Mg) + 0.0044
	(Ca+Na)/(Fe+Mg+Mn+Ca+Na)	= 0.0423 x (Fe/Mg) + 0.4623
Orthopyroxene	**Composition**	$((Ca,Na),(Mn,(Mg,Fe)))_2(Si,(Ti,Al))_2O_6$
	Fe-Mg Kd	$K_D = (Fe^{Opx} \times Mg^{Liq}) / (Mg^{Opx} \times Fe^{Liq})$
	Mn/(Fe+Mg+Mn)	= 0.01371 x (Fe/Mg) – 0.00053
	Ti/(Ti+Al)	= 0.08
	Na/(Na+Ca)	= 8405 x (Fe/Mg) – 0.1718
	(Ca+Na)/(Fe+Mg+Mn+Ca+Na)	= 0.1072 x (Fe/Mg) + 0.0236
Olivine	**Composition**	$((Mg,Fe),Ca,Mn)_2(Si,Al,Ti)O_4$
	Fe-Mg Kd	$K_D = (Fe^{Cpx} \times Mg^{Liq}) / (Mg^{Cpx} \times Fe^{Liq})$
	Ca/(Fe+Mg+Mn+Ca)	= 0.006
	Mn/(Fe+Mg+Mn+Ca)	= 2 x (0.0099 x (Fe/Mg)+0.0004)
	Al/(Al+Ti+Si)	= 0.002
	Ti/(Al+Ti+Si)	= 0.001
Biotite	**Composition**	$(K,Na)_2((((Mg,Fe)Ti)Mn)_{4-6},(Al,Si)_{8-10})_{14}O_{20}(OH)_4$
	Al-Si Kd	$K_D = (Al^{Bt} \times Si^{Liq}) / (Si^{Bt} \times Al^{Liq})$
	Al + Si	= (1 + 5/7) x Al/Si + (7 + 3/7)
	Mg+Fe+Mn+Ti	= 14 – (Al + Si)
	Fe + Ti	= 4 – (2 x (Si – 4))
	Mn / (Mg+Fe+Mn+Ti)	= 0.0133
	Ti	= (0.178 x (Fe + Ti)) x (Mg+Fe+Ti)/(Mg+Fe+Ti+Mn)
	Na / (Na+K)	= 0.03
Garnet	**Composition**	$(Mg,Fe)_3Al_2\ Si_3O_{12}$
	Fe-Mg Kd	$K_D = (Fe^{Cpx} \times Mg^{Liq}) / (Mg^{Cpx} \times Fe^{Liq})$

Chapter 6 - Regional Synopsis:

Magmatism in SE Asia: An Extended History

Phallus Peak on the Eastern Plateau, looking SW

Chapter 6: Regional Synopsis:

Magmatism in SE Asia: An Extended History

This synopsis chapter explores findings from Mt Kinabalu in their regional context, comparing the pluton with other magmatism in SE Asia and South China and discussing the origins of this magmatism since the Mesozoic.

Abstract

The geochemistry of the Mesozoic Capoas Granite of Palawan was analysed and compared with the Miocene pluton of Mt Kinabalu and the Plio-Pleistocene dacites of Usun Apau to test the hypothesis that all were derived through fractional crystallisation of basaltic primary melts and simultaneous assimilation of crustal material, most likely sediments deposited on the South China margin prior to rifting of the South China Sea.

Modelling this AFC process for the Capoas Granite and Usun Apau has shown it to be plausible but has also highlighted differences in the magmatic systems of each location. These include assimilation of sediments of older provenance by the Capoas Granite magma and a higher clinopyroxene and lower hornblende content in the fractionating systems of Usun Apau and Capoas compared to Mt Kinabalu, probably implying higher water contents in the Mt Kinabalu system.

The incompatible element enriched basaltic primary melts for these systems and other basaltic magmatism in Borneo resulted from low degree melting of fertile mantle. This fertile mantle upwelled during regional extension and so, by looking for evidence of similar enriched basalts elsewhere in the region, the extent of this extensional magmatism can be investigated. Collating data from South China and around the South China Sea shows low degree extensional magmatism to have occurred across the entire region since at least the Jurassic until the present day.

With no proximal subduction zones associated with much of this magmatism a combination of backarc extension from the Pacific Plate and Indian Ocean subduction zones and extrusion tectonics from the India-Asia collision may provide a source for these extensional stresses. This implies that crustal stress can be transferred over vast distances, with global implications for tectonics and intraplate magmatism.

From this we can see that Mt Kinabalu is just one expression of a more extensive and prolonged history of extensional magmatism in the region.

Introduction

The previous chapters of this thesis have investigated the formation of the Mt Kinabalu pluton in northern Borneo and have shown it to be the product of fractional crystallisation of a basaltic melt generated during a period of regional extension. Evidence highlighted in previous chapters for extension in Borneo in the Cenozoic and during the emplacement of the Mt Kinabalu pluton has included:

- Dyke and fault orientations from the mountain (Chapter 3).
- The orientation of the AMS fabric in most units (Chapter 4).
- The OIB-like incompatible element enrichment of the basalts of Linau Balui and Semporna Peninsula indicating low degree melting of a fertile source of upwelling asthenosphere. A basaltic melt similar in composition to these regional basalts has also been shown to be the primary melt from which the Mt Kinabalu magma evolved (Chapter 5).
- Widespread low gravity anomalies despite the dense ophiolitic basement of Sabah resulting from thick overlying sedimentary basins and asthenospheric upwelling beneath extended lithosphere (Chapter 2).

But how widespread was this extensional period and what other magmatism was produced? Is the Mt Kinabalu pluton an anomaly or part of a larger magmatic event? This will be discussed here. First we will compare the geochemical data of Mt Kinabalu with two other Neogene magmatic centres with intermediate to felsic melts to investigate whether they share a common derivation: (1) the Capoas granitic intrusion of Palawan and (2) the Usun Apau dacites of Sarawak. We will then compare the results of this study to the regional magmatism and tectonics of the South China Sea region since the onset of Pacific subduction in the Early Jurassic to investigate how prevalent the magmatic signatures recorded in Borneo are regionally.

The Capoas Granite of Palawan

The Capoas Granite (Capoas Gt) of northern Palawan is comprised of three small bodies along the western coast in the North of the island (Fig. 6.1). These are the approximately 49km^2 Mount Capoas Granite, the 28km^2 Bay Peak Granite and the 9km^2 Binga Point Granite. These bodies intruded a sequence of Permian to Jurassic cherts and shales deposited on the South China margin prior to extension of the South China Sea (Isozaki *et al.*, 1988, Encarnación and Mukasa, 1997, Suggate *et al.*, 2013). The field relations and petrography are discussed in detail in Encarnación and Mukasa (1997) as well as previous geochemical data and zircon and monazite ages. Published concordant monazite ages of 13.4 (±0.4) Ma are older than the 7.85 (±0.08) to 7.22 (±0.07) Ma U-Pb zircon ages of Mt Kinabalu analysed by sensitive high-resolution ion microprobe (SHRIMP, Cottam *et al.*, 2010). Consequently Suggate *et al.* (2013) analysed new samples of the Capoas Gt for U-Pb zircon ages by the same technique to investigate whether this more accurate methodology would also yield younger ages for the Capoas Gt. The results supported the previous study, yielding ages of 13.5 (±0.25) Ma for the Mt Capoas Granite and 13.8 (±0.25) Ma for the Bay Peak Granite. Although the Capoas Gt is older than Mt Kinabalu both intrusions indicate Miocene magmatism postdating extension of the South China Sea (SCS). We have analysed samples from the Suggate *et al.* (2013) study for major and trace chemistry and radiogenic isotopes to determine their petrogenesis.

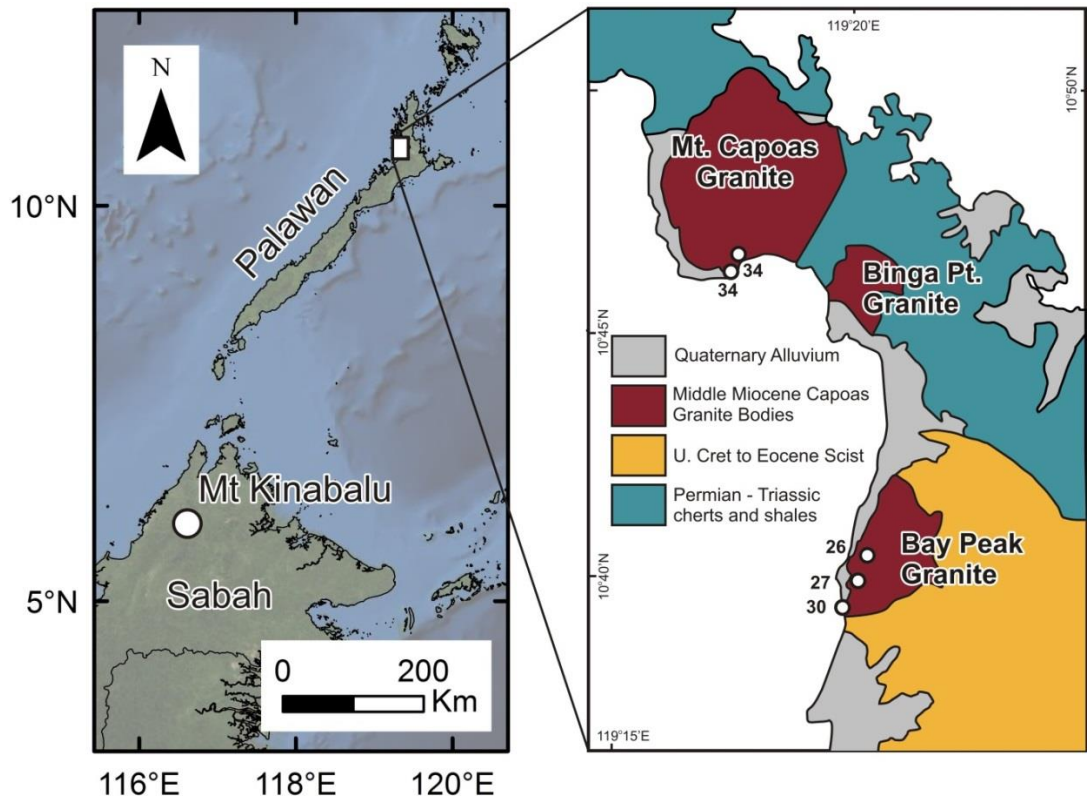

Fig. 6.1 Location and geological maps of the granitic bodies of the Capoas intrusion, Palawan. Sample locations marked by hollow circles. Geological map adapted from Encarnación and Mukasa (1997) and Suggate *et al.* (2013).

Methodology

Samples were crushed and milled to a fine powder using a fly press and agate ball mills. The powders were analysed for major element composition by XRF at Edinburgh University and by ICP-MS and PIMMS *(*Plasma Ionisation Multi-collector Mass Spectrometry) at Durham University to obtain trace element and radiogenic isotope data respectively. Methodology and QC data for these techniques is described in Chapter 5. Errors for isotopic analysis are as in Chapter 5.

Three thin sections were stained with sodium cobaltnitrate and potassium rhodizonate solutions to differentiate their plagioclase and K-feldspar minerals according to the procedure in Hutchison (1974).

Results

Results of thin section point counting are presented in Table 6.1 and geochemical results are presented in Appendix A5.1 and A5.2. The samples are classified as granitic composition (Fig. 6.2) according to the TAS system (Cox *et al.*, 1979) or granite to granodiorite according to their modes (Streckeisen, 1976). See Fig 6.1 for sample locations.

Multi-element plots of the trace elements are plotted in Fig. 6.3 with the composition of the Alexandra Gd of Mt Kinabalu for comparison. Both the Alexandra Gd and the Capoas Gt show similar relative enrichments and depletions in their trace elements and similar patterns to those expected for Upper Continental Crust. However, the Capoas Gt samples show stronger enrichments in their most incompatible elements, steeper chondrite normalised La/Yb ratios and stronger depletions in their normalised concentrations of Ba relative to Rb and Th and in their MREE to HREE.

The Sr and Nd isotopes of the Capoas Gt plot along the same trend as other regional magmatism (Fig. 6.4a), including the Mt Kinabalu pluton, granitic rocks of the SCS (Yan *et al.*, 2010) and the basalts, andesites and dacites of the Semporna Peninsula (Macpherson *et al.*, 2010), Linau Balui and Usun Apau (Cullen *et al.*, 2013). Like these other examples of regional Neogene magmatism the Pb isotopes for the Capoas Gt plot within EM2 field, although with notably lower $^{206}Pb/^{204}Pb$.

	PAL26 Bay Peak Gt.	PAL34 Mt Capoas Gt.	PAL35 Mt. Capoas Gt.	Encarnación & Mukasa (1997)
Quartz	26	38	34	29
Plag.	47	24	23	33
K-Fsp.	14	23	36	23
Biotite	14	14	7	15
Magnetite	-	0.7	-	-
Chlorite	-	-	0.3	-
TOTAL	100	100	100	100

Table 6.1. Modal mineral proportions from point counting of thin sections stained for plagioclase and K-feldspar (based on 300 points per sample). Modal abundances for the Capoas Intrusion for Encarnación and Mukasa (1997) for comparison.

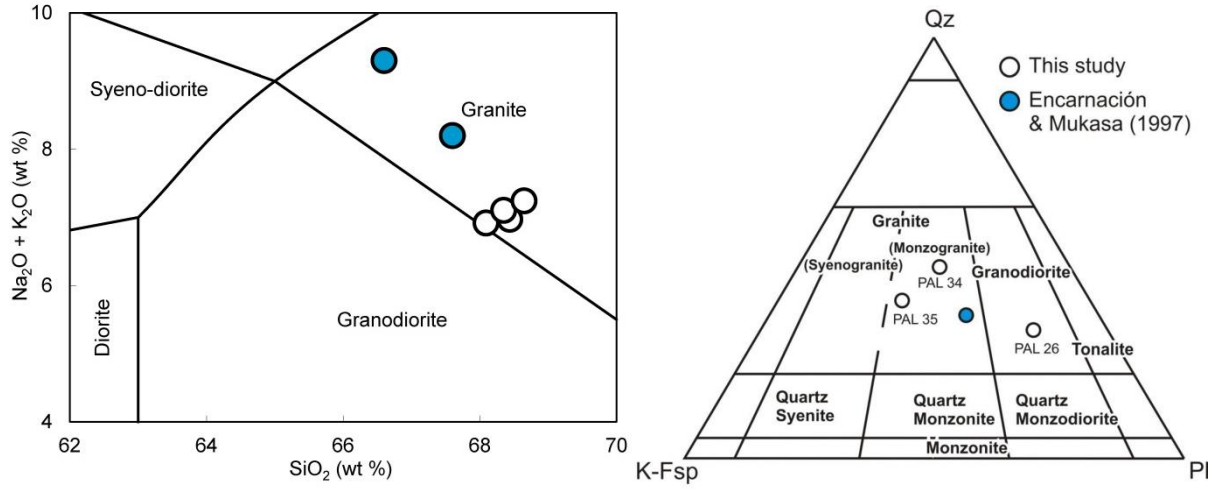

Fig. 6.2. TAS (Cox *et al.*, 1979) and IUGS QAP (Streckeisen, 1976) classifications of the Capoas Gt based on major element and mineral modal abundances respectively. Point counted data for the QAP diagram from this study and Sperber (2009).

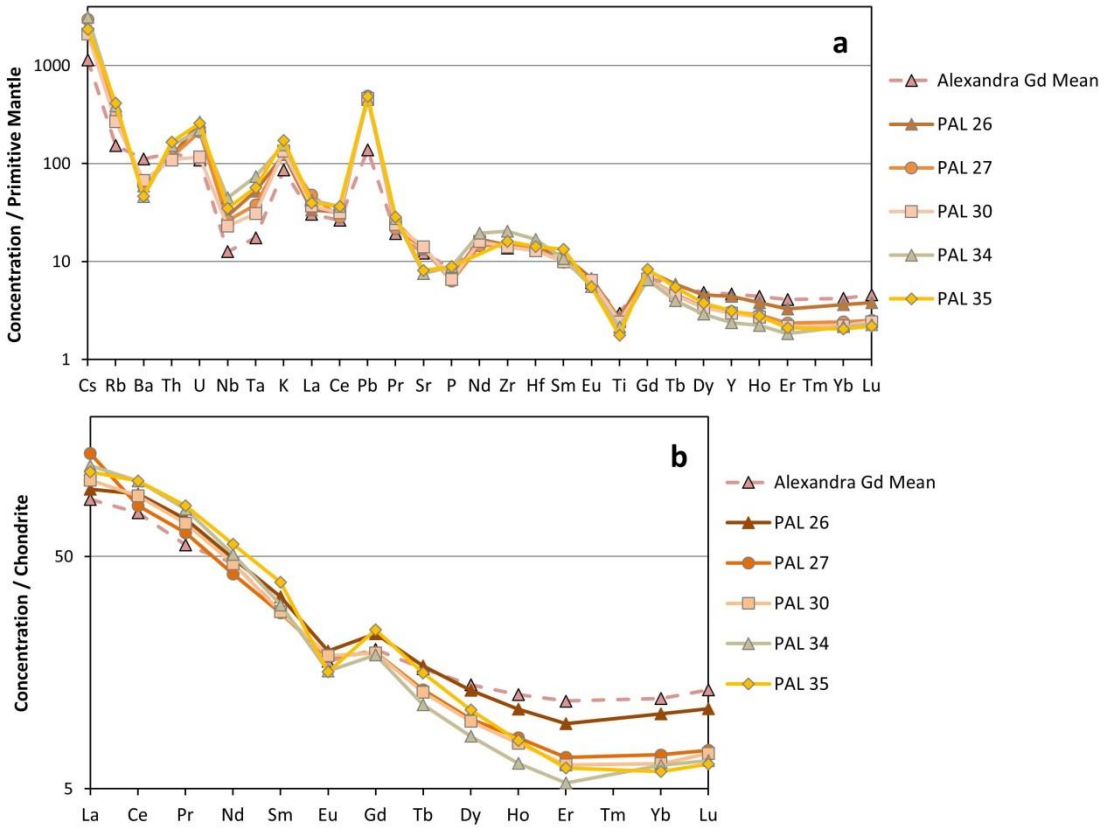

Fig. 6.3. Multi-element, primitive mantle normalised trace element plots and chondrite normalised REE plots for the Capoas Granite of Palawan, with the mean plot of the Alexandra Gd unit of Mt Kinabalu for comparison. Normalising values from Sun and McDonough (1989).

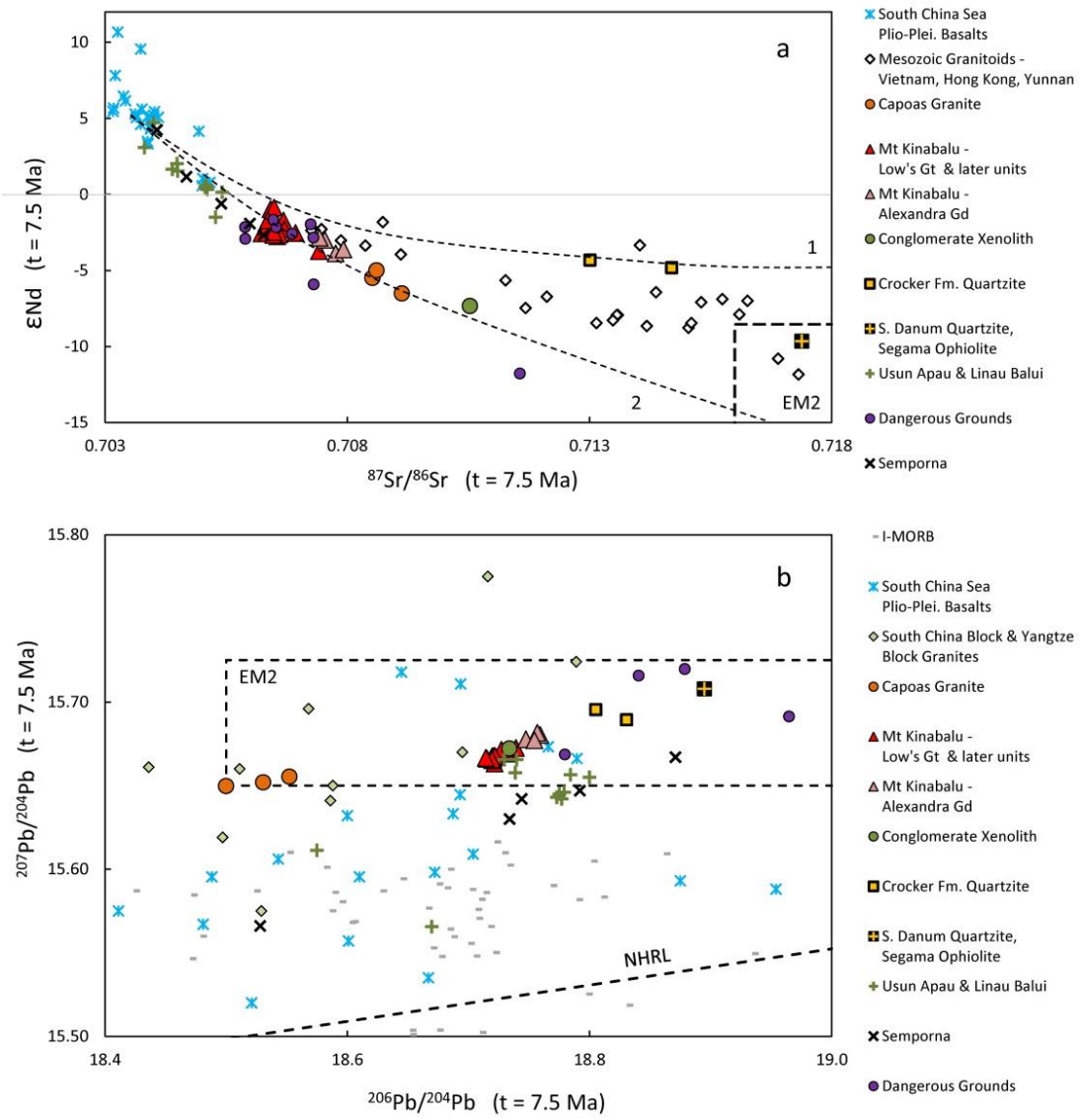

Fig. 6.4. Isotopic values (t = 7.5 Ma, the age of Mt Kinabalu's emplacement) for the Capoas Gt, Usun Apau, Mt Kinabalu and regional lithologies for comparison. The two lines in (a) illustrate the two broad regional trends for samples involving a larger component of Archean or Proterozoic crust, (2), and those with a lower contribution of older material based on their radiogenic isotope signature, (1). Data for comparison: South China Sea seamount basalts (Tu *et al.*, 1992, Yan *et al.*, 2008); Mesozoic granites of the South China Block and Yangtze Block (Zhu, 1995); Mesozoic Granitoids of Vietnam (Thuy *et al.*, 2004), Hong Kong (Darbyshire and Sewell, 1997) and Yunnan Province (Yanbo and Jingwen, 2010); Usun Apau and Linau Balui volcanics (Cullen *et al.*, 2013); granitic rocks of the Dangerous Grounds attenuated continental crust (Yan *et al.*, 2010, Yan *et al.*, 2011); Spreading centre basalts of the Indian Ocean from the PetDB database (http://www.earthchem.org/petdb); Northern Hemisphere Reference line (NHRL) backdated to 7.5 Ma using the mean U & Pb concentrations of the I-MORB data (Hart, 1984). EM2 fields from Zindler and Hart (1986).

Discussion

An anatectic source for the Mt Kinabalu pluton was shown to be unsuitable based on its major element chemistry compared with available experimental data from various sources (Chapter 5). However, the Capoas Gt plots within the experimental data for melts derived from felsic crust, or for a mixture of melts from basalts and basaltic amphibolites with melts from sedimentary sources (Fig. 6.5). This does not disprove derivation though fractional crystallisation of a mantle derived basaltic source and simultaneous assimilation of crustal material (AFC) as was determined for Mt Kinabalu, but mean that we cannot rule out an anatectic source.

To test the AFC process the same model applied to the evolution of the Mt Kinabalu magma (Chapter 5) has been applied to the Capoas Gt samples and the dacites of Usun Apau (Cullen *et al.*, 2013). Like the Linau Balui basalts, the Plio-Pleistocene Usun Apau dacites and associated andesites and basalts form a large plateau (770km^2) in Sarawak overlying steeply dipping sandstones and shales that were erupted between 4.1 and 2.1 Ma. These have previously been interpreted as evolving through AFC processes involving a mantle derived basalt and assimilation of felsic crust similar to the Triassic batholiths of Peninsular Malaysia (Liew and McCulloch, 1985, Cullen *et al.*, 2013). As for the Mt Kinabalu models, the Linau Balui basalt, LB64, was used as the initial melt in this model and the conglomerate xenolith (A098, see Chapter 5) was again used as the assimilant. As the same primary melt and assimilant are used, the maximum relative value of assimilation to crystallisation, *r*, (mass assimilated / mass crystallised) of 0.8 determined in Chapter 5 is still applicable.

Like Mt Kinabalu the magmatism of Usun Apau and the Capoas Gt can also be derived through AFC processes involving a mantle melt and a crustal assimilant. However, differences between these model parameters and those for Mt Kinabalu indicate differences in their magmatic systems. Discrepancies between the models and the analysed data highlight the less well constrained variables of each model and the ambiguities in the results.

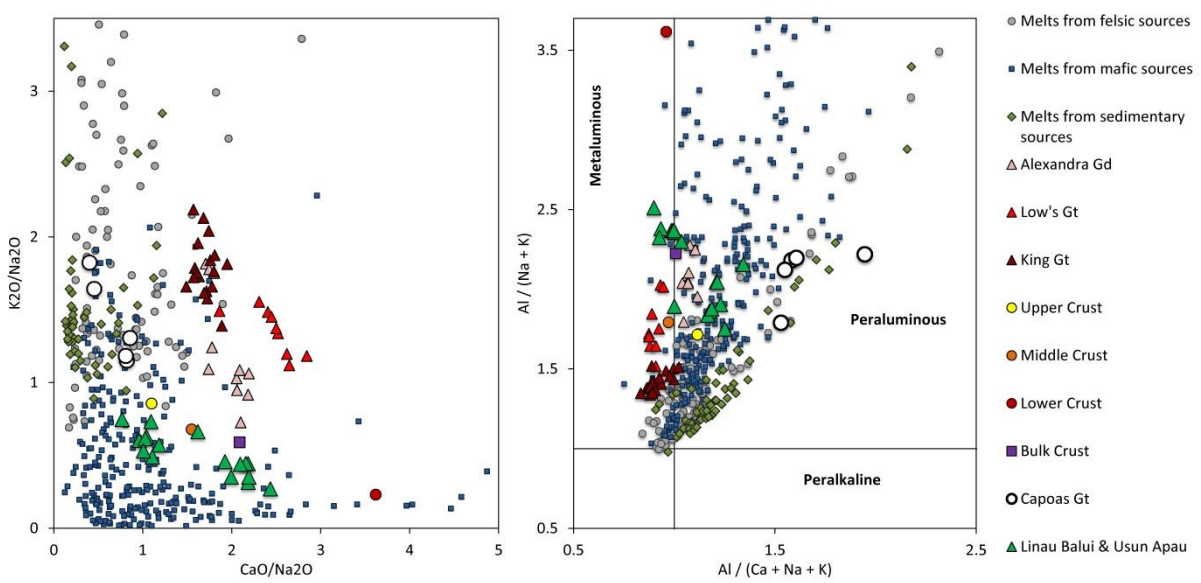

Fig. 6.5. Comparison of the Capoas Gt and Usun Apau data (Cullen *et al.*, 2013) with the Mt Kinabalu granitoids and collated melting experiment data for melting experiments on potential felsic sources (tonalites and felsic gneisses), mafic sources (basalts and basaltic amphibolites), and sedimentary sources (sediments and metasediments) (Vielzeuf and Holloway, 1988, Beard and Lofgren, 1991, Douce and Johnston, 1991, Rapp *et al.*, 1991, Rushmer, 1991, Skjerlie and Johnston, 1992, Rushmer, 1993, Sen and Dunn, 1994, Wolf and Wyllie, 1994, Douce and Beard, 1995, Gardien *et al.*, 1995, Rapp and Watson, 1995, Singh and Johannes, 1996a, Singh and Johannes, 1996b, Winther, 1996, Montel and Vielzeuf, 1997, Gardien *et al.*, 2000, Douce, 2005, Sisson *et al.*, 2005, Xiong *et al.*, 2005, Xiao and Clemens, 2007). Note that the samples showing CaO/Na_2O values >2.4 are peraluminous and have molar Al/(Na+K) values >3.4 (Rushmer, 1991, Rushmer, 1993, Wolf and Wyllie, 1994). Crustal values from Rudnick and Gao (2003).

The most significant differences between the fractionating assemblages are the decrease in hornblende (Hb) and increase in clinopyroxene (Cpx) fractionating in the Usun Apau and Capoas Granite models. This is required to produce the more peraluminous melts, a consequence of lower Ca, not higher Al as would be a consequence of decreased plagioclase fractionation. This increase in Cpx fractionation requires a decrease of Hb in the assemblage so as not to overly deplete Mg, Fe and other elements compatible in both phases (e.g. HREE). A simultaneous decrease in Hb and increase in Cpx may imply a lower water content of the fractionating system compared to that of Mt Kinabalu (Alonso-Perez *et al.*, 2009).

Although the same assimilant for the Mt Kinabalu model (a biotite-rich meta-conglomerate) was used to model Usun Apau and the Capoas Granite, the exact lithology probably differs in each location and may explain some of the discrepancies between the models and the observed data. Our previous AFC models of the radiogenic isotope data for the Usun Apau dacites (Cullen *et al.*, 2013, see Appendix A6) had shown a requirement for an older assimilant than that used here to explain the high Sr and low Nd isotopic ratios. However, use of the thermodynamic EC-AFC model (Spera and Bohrson, 2001) to constrain a maximum value of *r* has shown that it is reasonable to use a higher rate of assimilation. This shows the importance of constraining these thermodynamic parameters when modelling assimilation.

The *r* value used in the Capoas Gt model is the maximum deemed reasonable for the inputs used in the EC-AFC model (Chapter 5) but this value is much higher than for the other two magmatic centres. However, the presence of Archean inherited zircons in the Capoas Gt but not the Mt Kinabalu pluton (Cottam *et al.*, 2010, Suggate *et al.*, 2013) implies that the assimilant in Palawan may possess an older isotopic signature with higher Sr and Pb and lower Nd isotope ratios, and so a lower *r* value may be reasonable if the assimilant could be constrained.

Another notable discrepancy is in the REE of the Usun Apau model, as both the dacites of Usun Apau and the basalts of Linau Balui share very similar REE

concentrations. Modelling fractional crystallisation shows that the degree of fractionation required to reproduce the major element composition from the basaltic primary melt will inevitably increase the REE concentrations. This is shown by the much higher REE concentrations of the model compared to the data (Fig. 6.7) and indicates that the dacites did not evolve from a melt with exactly the same composition as the contemporaneous basalts. The notable negative Eu anomaly in the model but not in the data may also indicate this. However, as the characteristic negative Eu anomaly associated with plagioclase fractionation is a result of substitution of Eu^{2+} (not Eu^{3+}) for Ca this discrepancy between the model and the data may indicate relatively oxidising conditions and so a prevalence of Eu^{3+} over Eu^{2+} in the melt.

	Model						
	Capoas Gt.		Usun Apau		Alex. Gd	King Gt	
Mineral %	**SiO2 <63wt.%**	**SiO >63wt.%**	**SiO2 <63wt.%**	**SiO >63wt.%**	**SiO <63wt.%**	**SiO <63wt.%**	**SiO >63wt.%**
Olivine	17	-	12	-	6	10	-
Clinopyroxene	26	-	29	12	11	10	-
Plagioclase	26	55	37	54	35	39	56
Orthopyroxene	9	16	15	24	-	-	-
Hornblende	13	9	-	-	40	29	28
Biotite	-	11	-	2.4	-	5	8
Apatite	0.004	0.008	0.01	0.008	0.004	0.005	0.004
Magnetite	5.2	6.5	4.4	4.8	6.2	6.7	5.6
Rutile	-	-	-	-	1.8	1.7	1.7
Garnet	0.3	-	-	-	-	-	-
Ilmenite	3.2	3.0	3.0	2.4	-	-	-
Parameters							
r (M_a / M_c)	0.8	0.4	0.55	0.0	0.65	0.65	0.65
Additional Assimilant Biotite	0.33	0.33	0.1	N/a	0.3	0.3	0.3
Assimilant F	0.9	0.9	1.0	N/a	0.5	0.5	0.5
$(Al^{Plag} \times Si^{Liq}) / (Si^{Plag} \times Al^{Liq})$	1.80	2.40	1.70	2.40	1.70	1.70	1.70
$(K^{Plag} \times Na^{Liq}) / (Na^{Plag} \times K^{Liq})$	0.02	0.02	0.02	0.02	0.02	0.02	0.02
$(Fe^{Hb} \times Mg^{Liq}) / (Mg^{Hb} \times Fe^{Liq})$	0.36	0.36	0.36	0.36	0.36	0.36	0.36
$(Fe^{Bt} \times Mg^{Liq}) / (Mg^{Bt} \times Fe^{Liq})$	2.30	2.30	2.30	2.30	2.30	2.30	2.30
$(Fe^{Cpx} \times Mg^{Liq}) / (Mg^{Cpx} \times Fe^{Liq})$	0.25	0.25	0.25	0.25	0.25	0.25	0.25
$(Al^{Cpx} \times Si^{Liq}) / (Si^{Cpx} \times Al^{Liq})$	0.10	0.10	0.10	0.10	0.10	0.10	0.10
$(Fe^{Opx} \times Mg^{Liq}) / (Mg^{Opx} \times Fe^{Liq})$	0.20	0.20	0.20	0.20	0.20	0.20	0.20
$(Al^{Opx} \times Si^{Liq}) / (Si^{Opx} \times Al^{Liq})$	0.13	0.13	0.13	0.13	0.13	0.13	0.13
$(F^{Bt} \times Mg^{Liq}) / (Mg^{Bt} \times Fe^{Liq})$	0.30	0.30	0.30	0.30	0.30	0.30	0.30
$(Fe^{Ol} \times Mg^{Liq}) / (Mg^{Ol} \times Fe^{Liq})$	0.30	0.30	0.30	0.30	0.30	0.30	0.30

Table 6.1. Summary of fractionating assemblages and parameters used in the fractionation models for the Capoas Gt and Usun Apau dacites with the model parameters used for the Alexandra Gd and King Gt in Chapter 5 for comparison.

wt.%	Capoas Gt. PAL 26	Model	Usun Apau UA81	Model	Alex. Gd. A047	Model	King Gt.	Model
SiO_2	69.34	68.80	70.44	70.40	62.70	62.45	66.12	65.53
TiO_2	0.57	0.73	0.50	0.60	0.65	0.84	0.49	0.33
Al_2O_3	15.42	16.00	16.10	16.83	16.41	16.18	15.28	15.18
FeO_{Tot}	2.65	3.76	2.87	2.86	5.93	6.34	4.85	5.35
MnO	0.05	-0.19	0.03	-0.45	0.11	-0.02	0.10	-0.08
MgO	2.07	1.18	0.99	0.53	3.48	3.84	2.46	2.84
CaO	2.68	2.92	2.73	2.83	5.61	5.07	3.46	3.84
Na_2O	3.28	3.29	3.57	3.55	2.57	2.39	2.21	2.32
K_2O	3.78	3.37	2.67	2.74	2.36	2.69	4.82	4.49
P_2O_5	0.15	0.15	0.11	0.12	0.18	0.22	0.21	0.22
Total	100.00	100.00	100.00	100.00	100.0	100.0	100.0	100.0
$\sum D^2$		2.94		1.00		0.90		1.08
Total F		0.46		0.40		0.60		0.43
ρ		0.51		0.29		0.33		0.37

Table 6.2. Results of the major element models discussed with target compositions (both normalised to 100%) and sum of the differences squared for each major element oxide for comparison. Alexandra Gd and King Gt models from Chapter 5 for comparison.

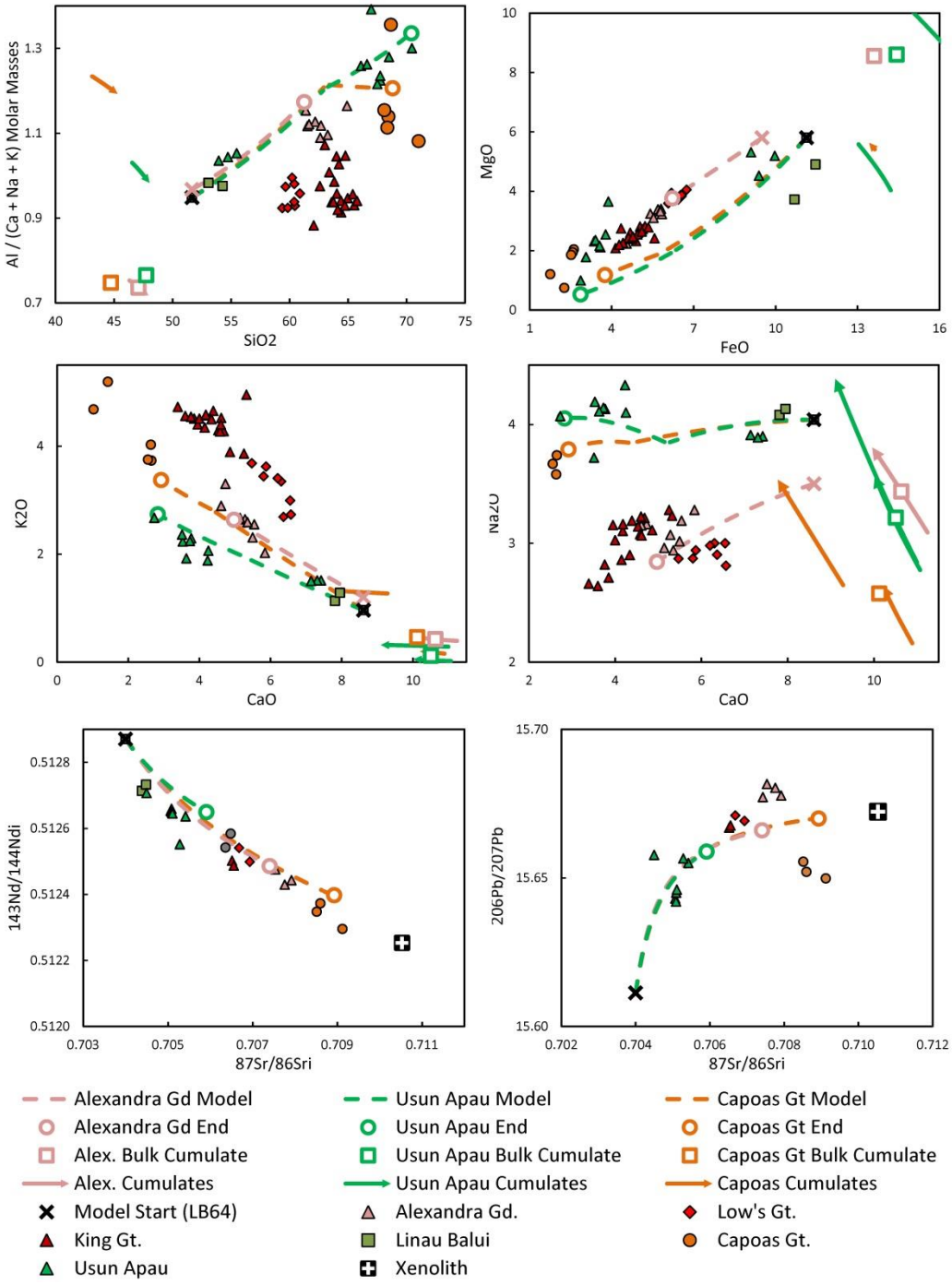

Fig. 6.6. Selected variation diagrams comparing the measured major element data with the combined major, trace and isotope AFC models for the Capoas Gt and Usun Apau dacites calculated according to Supplementary B of Chapter 5. For each model all plots are calculated from the same F value, R (M_a/M_c) value and fractionating assemblage. The "End" circles indicate the same point step in the models for all graphs and the trace and REE plots of Fig. 6.7. These points represent the best reproductions of the highest Si samples from each suite. The composition of the Linau Balui basalt, LB64, is used as the starting composition for all models. The conglomerate xenolith from the Donkey Gt of Mt Kinabalu, A098, is the assimilant for major and trace element modelling. Units from the Kinabalu pluton and the Alexandra Gd model from Chapter 5 for comparison.

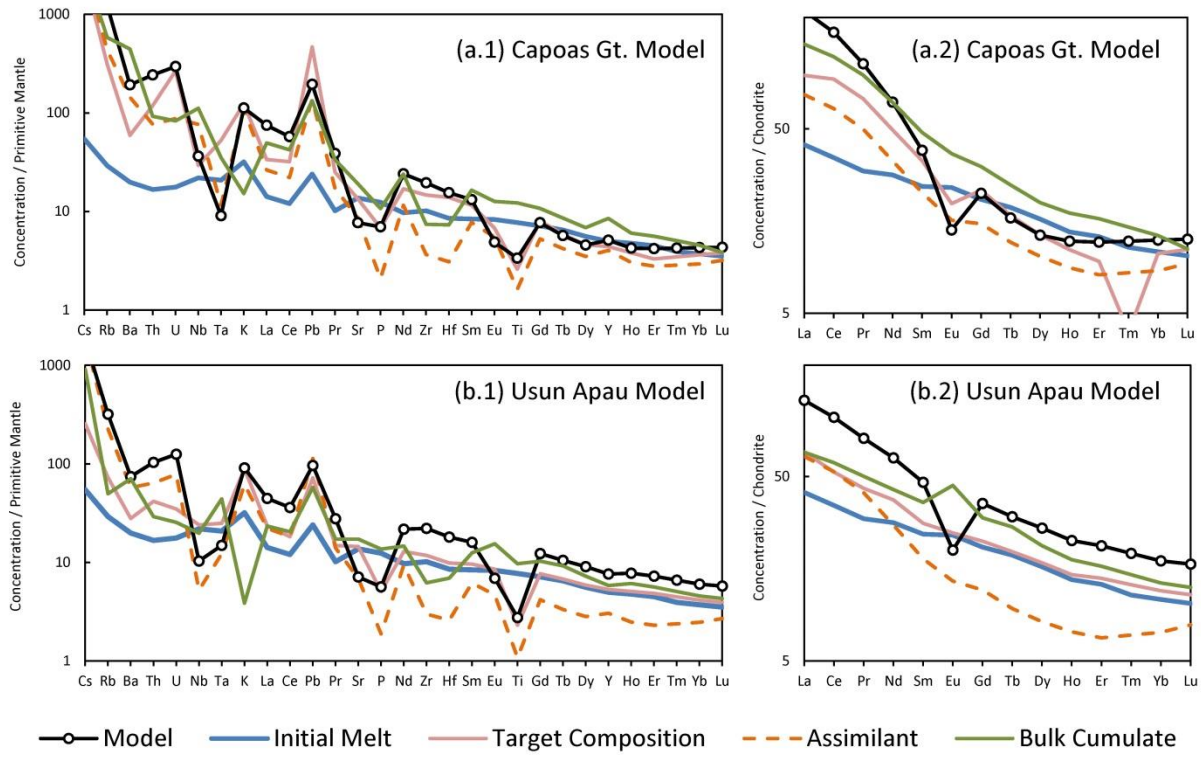

Fig. 6.7. Multi-element trace and REE plots comparing the Capoas Gt and Usun Apau dacite fractionation models at the same points indicated in Fig. 6.6 with the Linau Balui basalt starting composition, conglomerate assimilant, target composition of the analysed samples and calculated bulk cumulate composition. Trace and REE plots normalised to primitive mantle and chondrite respectively according to the values of Sun and McDonough (1989).

Regional signature

The model has shown that with modifications to the fractionating assemblage, assimilant and rate of assimilation the Plio-Pleistocene felsic magmatism of Usun Apau and the Miocene plutons of Palawan can be produced in a similar manner to the Mt Kinabalu pluton. This involves an AFC process affecting mantle derived melts similar to the incompatible element enriched Linau Balui basalts and assimilation of meta-sediments.

The assimilant is shown in Mt Kinabalu to probably be a meta-conglomerate similar to a xenolith exposed on the mountain's summit plateau and enriched in metamorphic biotite. Although similar lithologies are not exposed in the mountain's immediate area similar rocks are described in Central Palawan (Suzuki *et al.*, 2000) and interpreted to have originally been deposited during the Upper Cretaceous to Eocene along the South China continental margin prior to extension of the SCS.

As noted in Chapter 5 for the Mt Kinabalu models, the enriched incompatible element composition of the Linau Balui volcanics is a requirement to successfully reproduce the compositions of the felsic magmatism. Thus if the felsic magmatism of Mt Kinabalu, the Usun Apau dacites and the Capoas Gt were all produced by AFC processes involving a mantle derived basaltic parental melt, as advocated here, this parental melt cannot be from a depleted source. In Chapter 5 we proposed, in agreement with Macpherson *et al.* (2010), that this requires low degree melting of a fertile source and that this was a result of asthenospheric upwelling during regional extension. But how widespread is this extensional magmatism, and for how long has it persisted?

To test this we have compiled data for basaltic magmatism in South China and the South China Sea region since the Jurassic. Fig. 6.8 shows that although there are variable enrichments in the highly fluid mobile elements and depletions in Nb and Ta, indicating variable involvement of subduction derived fluids, the whole region has been characterised by incompatible element enriched mafic magmatism from the Mesozoic until the present day. This OIB-like signature has resulted in some authors proposing mantle plume involvement, especially for the magmatism of

Hainan (e.g. Zou and Fan, 2010). However, we agree with previous authors' (Chung *et al.*, 1997, Zhou *et al.*, 2006, Chen *et al.*, 2008) that these fertile melts are the products of extensional magmatism. The enriched mantle affinity shared by the Bornean magmatism and widespread magmatism in SE Asia and South China indicates that the Neogene magmatism recorded in Borneo, including that of Mt Kinabalu, is just a small part of a much more protracted and widespread history of magmatic activity in the region.

An alternative explanation to lithospheric extension driving intraplate magmatism and mantle upwelling may be shear driven upwelling of the asthenosphere, whereby mantle convection or plate motion can create shearing forces within the asthenosphere that result in the upwelling of deep fertile mantle (Conrad *et al.*, 2011). This may aided by existing low viscosity pockets in the asthenosphere producing mantle circulation or upwelling in to existing lithospheric thin spots (Conrad *et al.*, 2010, Bianco *et al.*, 2011, King, 2011, Ekici *et al.*, 2012). Along with extensional magmatism this process should be investigated further with relation to SE Asia to determine the viability of each process or a combination of both in controlling the region's intra-plate magmatism.

It should be noted from Fig. 6.8 how persistent the enriched signatures of the regions magmatism are in both time and space. If the enriched basalt signatures do indicate continued extensional magmatism since the Jurassic initiation of western Pacific subduction then this has important implications for determining the region's tectonic evolution. Given the lack of subduction zones proximal to much of this magmatism during their eruption or emplacement (such as that in the last 5 Ma in Vietnam, Hainan, Semporna, Sarawak, the SCS and the Sulu Arc) these extensional forces cannot simply be from spreading immediately behind an arc. Instead this indicates stress is able to be transferred through the crust over very large distances as the most likely sources of extension are from backarc spreading associated with the Indian Ocean and Pacific subduction zones encircling the region and extrusion tectonics associated with the India-Asia collision.

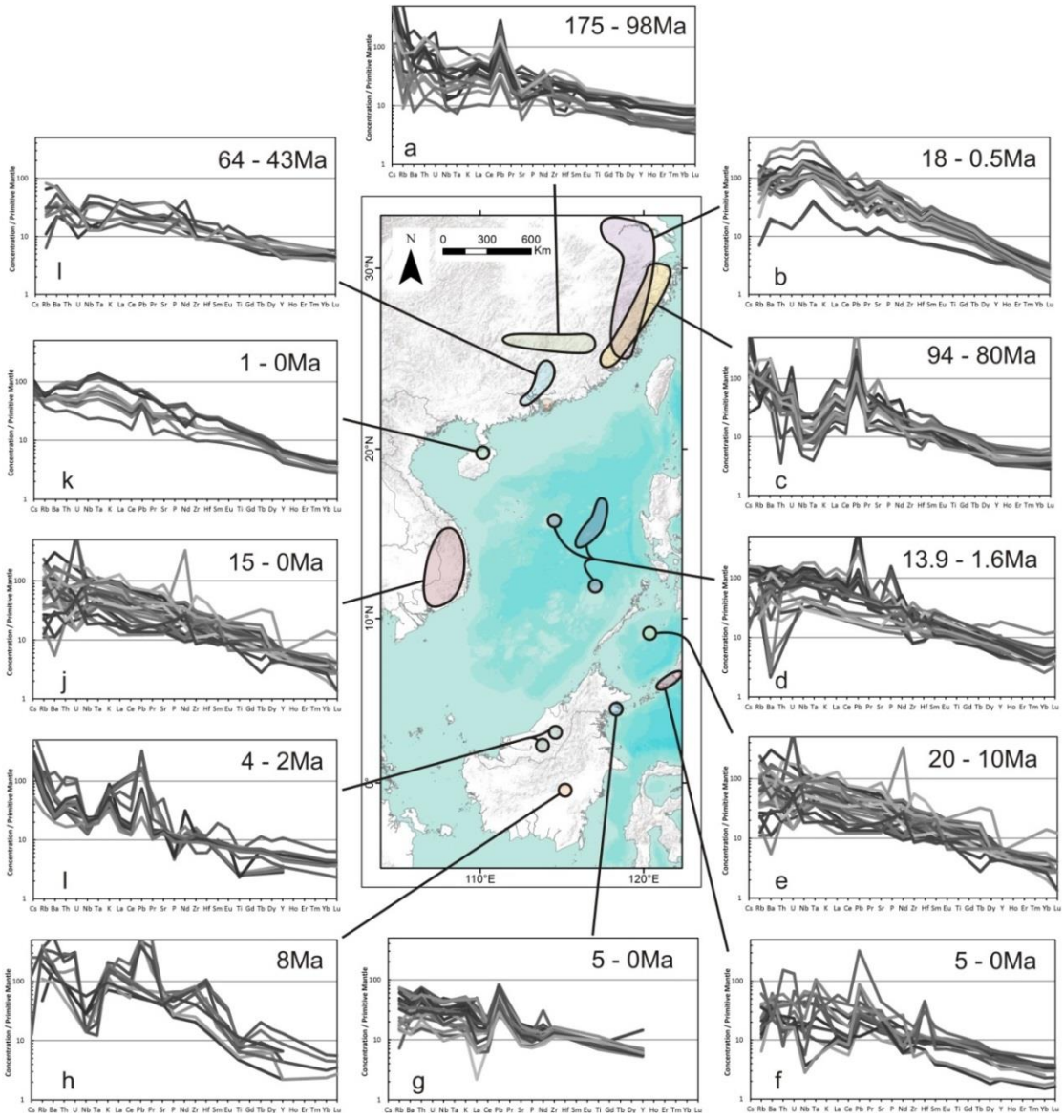

Fig. 6.8. Distribution, magmatic ages and trace element chemistry of mafic magmatism in the South China Sea region since the Jurassic. Localities shown are:

(a) Cathaysia Folded Belt basalts (Chen *et al.*, 2008, and sources therein)
(b) Cenozoic SE China basalts (Zou *et al.*, 2000)
(c) Southeast Coast Magmatic Belt basalts of S. China (Chen *et al.*, 2008, and sources therein)
(d) SCS post-spreading basaltic seamounts (Tu *et al.*, 1992, Yan *et al.*, 2008)
(e) Cagayan ridge basalts (Smith *et al.*, 1988, Kudrass *et al.*, 1990, Spadea *et al.*, 1991)
(f) Plio-Pleistocene basalts of the Sulu Arc (Castillo *et al.*, 2007)
(g) Semporna Plio-Pleistocene basalts (Macpherson *et al.*, 2010)
(h) Linhaisai minettes, Kalimantan (Bergman *et al.*, 1988)
(i) Usun Apau and Linau Balui basalts, andesites and dacites (Cullen *et al.*, 2013)
(j) Vietnamese basalts (Hoang *et al.*, 1996)
(k) Hainan basalts (Zou and Fan, 2010)
(l) Paleogene basalts from South China (Chung *et al.*, 1997)

Conclusions

- The Capoas Granite of Palawan shares similar trace element and radiogenic isotope to Mt Kinabalu.
- The chemical compositions of Mt Kinabalu the Capoas Granite, and the dacites of Usun Apau, can be reproduced by AFC modelling involving an incompatible element enriched basaltic primary melt and a sedimentary assimilant.
- This assimilant was probably deposited on the South China continental margin prior to extension of the South China Sea (SCS), similar to Upper-Cretaceous to Eocene sediments of Palawan.
- Although both Mt Kinabalu and the Capoas Granite probably derived from similar processes, the higher Sr and Pb and lower Nd isotope ratios indicate involvement of an older assimilant at Capoas, which is supported by its Archean inherited zircons.
- The basaltic primary melt for the Neogene magmatic centres along the southern SCS was an incompatible element enriched basaltic melt, similar to those of Linau Balui. This was produced by low degree melting of fertile upwelling asthenosphere during regional extension, although shear driven mantle upwelling may provide an alternative process.
- Similarly enriched incompatible element signatures of an OIB-like affinity are found in basaltic magmatism across the whole region of South China and the South China Sea since the Jurassic.
- This common signature indicates that most of the magmatic activity in the region (including Mt Kinabalu) has resulted from continuing widespread and protracted crustal extension in SE Asia and South China since the Mesozoic.
- The occurrence of magmatism far from active subduction indicates the extension driving the magmatism is able to be transferred through the lithosphere over very large distances. The most obvious sources for this extension are backarc extension associated with subduction of the Indian Ocean and Pacific Plate or extrusion tectonics associated with the India-Asia

collision. This evidence for distal stress transfer has global implications for tectonics and intraplate magmatism.

Alonso-Perez, R., Müntener, O. and Ulmer, P. (2009). Igneous garnet and amphibole fractionation in the roots of island arcs: experimental constraints on andesitic liquids. *Contributions to Mineralogy and Petrology*. **157**, 4, 541-558.

Beard, J.S. and Lofgren, G.E. (1991). Dehydration Melting and Water-Saturated Melting of Basaltic and Andesitic Greenstones and Amphibolites at 1, 3, and 6. 9 kb. *Journal of Petrology*. **32**, 2, 365-401.

Bergman, S., Dunn, D. and Krol, L. (1988). Rock and mineral chemistry of the Linhaisai minette and the origin of Borneo diamonds, Central Kalimantan, Indonesia. *Can Mineral*. **26**, 23-44.

Bianco, T.A., Conrad, C.P. and Smith, E.I. (2011). Time dependence of intraplate volcanism caused by shear-driven upwelling of low-viscosity regions within the asthenosphere. *Journal of Geophysical Research: Solid Earth (1978–2012)*. **116**, B11,

Castillo, P., Rigby, S. and Solidum, R. (2007). Origin of high field strength element enrichment in volcanic arcs: Geochemical evidence from the Sulu Arc, southern Philippines. *Lithos*. **97**, 3, 271-288.

Chen, C.-H., Lee, C.-Y. and Shinjo, R. (2008). Was there Jurassic paleo-Pacific subduction in South China?: Constraints from 40Ar/39Ar dating, elemental and Sr–Nd–Pb isotopic geochemistry of the Mesozoic basalts. *Lithos*. **106**, 1, 83-92.

Chung, S.-L., Cheng, H., Jahn, B.-m., O'Reilly, S.Y. and Zhu, B. (1997). Major and trace element, and Sr-Nd isotope constraints on the origin of Paleogene volcanism in South China prior to the South China Sea opening. *Lithos*. **40**, 2-4, 203-220.

Conrad, C.P., Wu, B., Smith, E.I., Bianco, T.A. and Tibbetts, A. (2010). Shear-driven upwelling induced by lateral viscosity variations and asthenospheric shear: A mechanism for intraplate volcanism. *Physics of the Earth and Planetary Interiors*. **178**, 3, 162-175.

Conrad, C.P., Bianco, T.A., Smith, E.I. and Wessel, P. (2011). Patterns of intraplate volcanism controlled by asthenospheric shear. *Nature Geoscience*. **4**, 5, 317-321.

Cottam, M., Hall, R., Sperber, C. and Armstrong, R. (2010). Pulsed emplacement of the Mount Kinabalu granite, northern Borneo. *Journal of the Geological Society*. **167**, 1, 49-60.

Cox, K.G., Bell, J.D. and Pankhurst, R.J. (1979). *The interpretation of igneous rocks*. G. Allen & Unwin.

Cullen, A., Macpherson, C., Taib, N.I., Burton-Johnson, A., Geist, D., Spell, T. and Banda, R.M. (2013). Age and Petrology of the Usun Apau and Linau Balui Volcanics: Windows to Central Borneo's Interior. *Journal of Asian Earth Sciences*.

Darbyshire, D.P.F. and Sewell, R.J. (1997). Nd and Sr isotope geochemistry of plutonic rocks from Hong Kong: implications for granite petrogenesis, regional structure and crustal evolution. *Chemical Geology*. **143**, 1-2, 81-93.

Douce, A.E.P. and Johnston, A.D. (1991). Phase equilibria and melt productivity in the pelitic system: implications for the origin of peraluminous granitoids and aluminous granulites. *Contributions to Mineralogy and Petrology*. **107**, 2, 202-218.

Douce, A.E.P. and Beard, J.S. (1995). Dehydration-melting of biotite gneiss and quartz amphibolite from 3 to 15 kbar. *Journal of Petrology*. **36**, 3, 707-738.

Douce, A.E.P. (2005). Vapor-absent melting of tonalite at 15–32 kbar. *Journal of Petrology*. **46**, 2, 275-290.

Ekici, T., Macpherson, C.G. and Otlu, N. (2012). Polybaric melting of a single mantle source during the Neogene Siverek phase of the Karacadağ Volcanic Complex, SE Turkey. *Lithos*. **146**, 152-163.

Encarnación, J. and Mukasa, S.B. (1997). Age and geochemistry of an 'anorogenic'crustal melt and implications for I-type granite petrogenesis. *Lithos*. **42**, 1, 1-13.

Gardien, V., Thompson, A.B., Grujic, D. and Ulmer, P. (1995). Experimental melting of biotite+ plagioclase+ quartz±muscovite assemblages and implications for crustal melting. *Journal of Geophysical Research: Solid Earth (1978–2012)*. **100**, B8, 15581-15591.

Gardien, V., Thompson, A. and Ulmer, P. (2000). Melting of biotite+ plagioclase+ quartz gneisses: the role of H2O in the stability of amphibole. *Journal of Petrology*. **41**, 5, 651-666.

Hart, S.R. (1984). A large-scale isotope anomaly in the Southern Hemisphere mantle. *Nature*. **309**, 753-757.

Hoang, N., Flower, M.F. and Carlson, R.W. (1996). Major, trace element, and isotopic compositions of Vietnamese basalts: Interaction of hydrous EM1-rich asthenosphere with thinned Eurasian lithosphere. *Geochimica et Cosmochimica Acta*. **60**, 22, 4329-4351.

Hutchison, C.S. (1974). Laboratory handbook of petrographic techniques.

Isozaki, Y., Amiscaray, E. and Rillon, A. (1988). Permian, Triassic and Jurassic bedded radiolarian cherts in North Palawan Block, Philippines: evidence of Late Mesozoic subduction-accretion. *IGCP Project*. **224**, 3, 99-115.

King, S.D. (2011). Volcanism: Eruptions above mantle shear. *Nature Geoscience*. **4**, 5, 279-280.

Kudrass, H., Muller, P., Kreuzer, H. and Weiss, W. (1990). Volcanic rocks and tertiary carbonates dredged from the Cagayan Ridge and the Southwest Sulu Sea, Philippines. *Rangin, C, Silver, EA, von Breymann, MT, et al., Proc. ODP, Init. Repts*. **124**, 93-100.

Liew, T.C. and McCulloch, M.T. (1985). Genesis of granitoid batholiths of Peninsular Malaysia and implications for models of crustal evolution: Evidence from a Nd---Sr isotopic and U---Pb zircon study. *Geochimica et Cosmochimica Acta*. **49**, 2, 587-600.

Macpherson, C.G., Chiang, K.K., Hall, R., Nowell, G.M., Castillo, P.R. and Thirlwall, M.F. (2010). Plio-Pleistocene intra-plate magmatism from the southern Sulu Arc, Semporna peninsula, Sabah, Borneo: Implications for high-Nb basalt in subduction zones. *Journal of Volcanology and Geothermal Research*. **190**, 1-2, 25-38.

Montel, J.-M. and Vielzeuf, D. (1997). Partial melting of metagreywackes, Part II. Compositions of minerals and melts. *Contributions to Mineralogy and Petrology*. **128**, 2-3, 176-196.

Rapp, R.P., Watson, E.B. and Miller, C.F. (1991). Partial melting of amphibolite/eclogite and the origin of Archean trondhjemites and tonalites. *Precambrian Research*. **51**, 1, 1-25.

Rapp, R.P. and Watson, E.B. (1995). Dehydration melting of metabasalt at 8–32 kbar: implications for continental growth and crust-mantle recycling. *Journal of Petrology*. **36**, 4, 891-931.

Rudnick, R. and Gao, S. (2003). Composition of the continental crust. *Treatise on geochemistry*. **3**, 1-64.

Rushmer, T. (1991). Partial melting of two amphibolites: contrasting experimental results under fluid-absent conditions. *Contributions to Mineralogy and Petrology*. **107**, 1, 41-59.

Rushmer, T. (1993). Experimental high-pressure granulites: some applications to natural mafic xenolith suites and Archean granulite terranes. *Geology*. **21**, 5, 411-414.

Sen, C. and Dunn, T. (1994). Dehydration melting of a basaltic composition amphibolite at 1.5 and 2.0 GPa: implications for the origin of adakites. *Contributions to Mineralogy and Petrology*. **117**, 4, 394-409.

Singh, J. and Johannes, W. (1996a). Dehydration melting of tonalites. Part I. Beginning of melting. *Contributions to Mineralogy and Petrology*. **125**, 1, 16-25.

Singh, J. and Johannes, W. (1996b). Dehydration melting of tonalites. Part II. Composition of melts and solids. *Contributions to Mineralogy and Petrology*. **125**, 1, 26-44.

Sisson, T., Ratajeski, K., Hankins, W. and Glazner, A. (2005). Voluminous granitic magmas from common basaltic sources. *Contributions to Mineralogy and Petrology*. **148**, 6, 635-661.

Skjerlie, K.P. and Johnston, A.D. (1992). Vapor-absent melting at 10 kbar of a biotite-and amphibole-bearing tonalitic gneiss: implications for the generation of A-type granites. *Geology*. **20**, 3, 263-266.

Smith, T., Huang, C. and Sajona, F. (1988). Geochemistry and petrogenesis of the volcanic rocks from holes 768 and 769, Sulu Sea. *Proceedings of the Ocean Drilling Program: Scientific results*. **124**, 297.

Spadea, P., Beccaluva, L., Civetta, L., Coltorti, M., Dostal, J., Sajona, F., Serri, G., Vaccaro, C. and Zeda, O. (1991). Petrology of basic igneous rocks from the floor of the Sulu Sea. *Proceedings of Ocean Drilling Program Science Results*. **124**, 251-65.

Spera, F.J. and Bohrson, W.A. (2001). Energy-constrained open-system magmatic processes I: General model and energy-constrained assimilation and fractional crystallization (EC-AFC) formulation. *Journal of Petrology*. **42**, 5, 999-1018.

Sperber, C.M. (2009). The thermotectonic development of Mount Kinabalu, Sabah, Malaysia: Constraints from low-temperature thermochronology. *Department of Earth Science*. **PhD**,

Streckeisen, A. (1976). To each plutonic rock its proper name. *Earth-Science Reviews*. **12**, 1, 1-33.

Suggate, S., Cottam, M., Hall, R., Sevastjanova, I., Forster, M., White, L., Armstrong, R., Carter, A. and Mojares, E. (2013). South China continental margin signature for sandstones and granites from Palawan, Philippines. *Gondwana Research*.

Sun, S.-S. and McDonough, W. (1989). Chemical and isotopic systematics of oceanic basalts: implications for mantle composition and processes. *Geological Society, London, Special Publications*. **42**, 1, 313-345.

Suzuki, S., Takemura, S., Yumul, G.P., David, S.D. and Asiedu, D.K. (2000). Composition and provenance of the Upper Cretaceous to Eocene sandstones in Central Palawan, Philippines: Constraints on the tectonic development of Palawan. *Island Arc*. **9**, 4, 611-626.

Thuy, N.T.B., Satir, M., Siebel, W., Vennemann, T. and Long, T.V. (2004). Geochemical and isotopic constraints on the petrogenesis of granitoids from the Dalat zone, southern Vietnam. *Journal of Asian Earth Sciences*. **23**, 4, 467-482.

Tu, K., Flower, M.F.J., Carlson, R.W., Xie, G., Chen, C.-Y. and Zhang, M. (1992). Magmatism in the South China Basin: 1. Isotopic and trace-element evidence for an endogenous Dupal mantle component. *Chemical Geology*. **97**, 1–2, 47-63.

Vielzeuf, D. and Holloway, J.R. (1988). Experimental determination of the fluid-absent melting relations in the pelitic system. *Contributions to Mineralogy and Petrology*. **98**, 3, 257-276.

Winther, K.T. (1996). An experimentally based model for the origin of tonalitic and trondhjemitic melts. *Chemical Geology*. **127**, 1, 43-59.

Wolf, M.B. and Wyllie, P.J. (1994). Dehydration-melting of amphibolite at 10 kbar: the effects of temperature and time. *Contributions to Mineralogy and Petrology*. **115**, 4, 369-383.

Xiao, L. and Clemens, J. (2007). Origin of potassic (C-type) adakite magmas: experimental and field constraints. *Lithos*. **95**, 3, 399-414.

Xiong, X., Adam, J. and Green, T. (2005). Rutile stability and rutile/melt HFSE partitioning during partial melting of hydrous basalt: implications for TTG genesis. *Chemical Geology*. **218**, 3, 339-359.

Yan, Q., Shi, X., Wang, K., Bu, W. and Xiao, L. (2008). Major element, trace element, and Sr, Nd and Pb isotope studies of Cenozoic basalts from the South China Sea. *Science in China Series D: Earth Sciences*. **51**, 4, 550-566.

Yan, Q., Shi, X. and Li, N. (2011). Oxygen and lead isotope characteristics of granitic rocks from the Nansha block (South China Sea): Implications for their petrogenesis and tectonic affinity. *Island Arc*. **20**, 2, 150-159.

Yan, Q.S., Shi, X.F., Liu, J.H., Wang, K.S. and Bu, W.R. (2010). Petrology and geochemistry of Mesozoic granitic rocks from the Nansha micro-block, the South China Sea: Constraints on the basement nature. *Journal of Asian Earth Sciences*. **37**, 2, 130-139.

Yanbo, C. and Jingwen, M. (2010). Age and geochemistry of granites in Gejiu area, Yunnan province, SW China: Constraints on their petrogenesis and tectonic setting. *Lithos*. **120**, 3, 258-276.

Zhou, b.X., Sun, T., Shen, W., Shu, L. and Niu, Y. (2006). Petrogenesis of Mesozoic granitoids and volcanic rocks in South China: a response to tectonic evolution. *Episodes*. **29**, 1, 26.

Zhu, B. (1995). The mapping of geochemical provinces in China based on Pb isotopes. *Journal of Geochemical Exploration*. **55**, 1, 171-181.

Zindler, A. and Hart, S. (1986). Chemical geodynamics. *Annual review of earth and planetary sciences*. **14**, 493-571.

Zou, H., Zindler, A., Xu, X. and Qi, Q. (2000). Major, trace element, and Nd, Sr and Pb isotope studies of Cenozoic basalts in SE China: mantle sources, regional variations, and tectonic significance. *Chemical Geology*. **171**, 1, 33-47.

Zou, H. and Fan, Q. (2010). U–Th isotopes in Hainan basalts: Implications for sub-asthenospheric origin of EM2 mantle endmember and the dynamics of melting beneath Hainan Island. *Lithos*. **116**, 1, 145-152.

Chapter 7:

Conclusions

Alexandra Peak and the Western Plateau, looking E from Marai Parai

Chapter 7: Conclusions

During the preceding chapters the original questions laid out in the introduction have been investigated. The principal conclusions can be summarised as follows:

1. **What processes produced the felsic magma of Mt Kinabalu?**

- The felsic magma of the Mt Kinabalu pluton was derived through fractional crystallisation of incompatible element enriched basaltic melts, similar to Plio-Pleistocene basalts from elsewhere in Borneo.
- These primary basaltic melts were formed through low degree melting of a fertile mantle source.
- Structural and AMS (Anisotropy of Magnetic Susceptibility) evidence shows that Mt Kinabalu was emplaced during a period of crustal extension in a NW-SE direction, and so this fertile mantle melt probably upwelled due to lithospheric extension and subsequent thinning.
- The evolved, felsic melts were derived through fractional crystallisation of plagioclase and amphibole rich cumulates.
- The magma assimilated high degrees of Mesozoic, conglomeritic metasediments during its early, high temperature period of fractionation. Assimilation occurred incongruently with metamorphic biotite contributing to the melt in a greater percentage than its modal proportion in the bulk assimilant through dehydration breakdown reactions.
- The composite units of the Mt Kinabalu show distinct geochemical signatures. The most pronounced difference is for the first unit to be emplaced, the Alexandra Peak Granodiorite of the Western Plateau, which exhibits both distinct elemental abundances and isotopic signatures. The later units show very similar isotopic signatures although the second unit of the pluton, the Low's Peak Granite, is notably more mafic in its major element composition.
- Magma recharge in to an already fractionated system resulted in a higher initial K content for the Low's Peak Granite and the later units to be emplaced compared with the Alexandra Peak Granodiorite
- Reduced fertility of the assimilant following emplacement of the first unit resulted in a lower rate of assimilation for subsequent units and less water entering the melt. This resulted in a higher degree of plagioclase fractionation and, combined with the higher initial K content, produced more metalluminous melts.

2. How was this magma emplaced in the crust?

- The pluton was emplaced at the contact of the ophiolitic basement with overlying turbidite sediments. This level in the stratigraphy resulted in the weaker rheology of the sediments than the largely peridotite composed ophiolite.
- Upwards deformation of the sediments provided the accommodation space for the pluton.
- The pluton is composed of six major units plus minor dykes and satellite bodies.
- Field relations of the internal contacts of the pluton support previous U-Pb zircon ages.
- Internal contacts are mostly sharp, with only narrow gradational contacts (<4m) observed and rare occurrences of magma mingling. This indicates that at least the margins of each unit had crystallised in the 0.2 My between each unit's emplacement.
- The only exception is the Donkey Peak Gt (Donkey Gt). This forms a relatively small, sub-vertical planar body within the King George Peak Granite (King Gt), the largest unit of the pluton. The magma mingling texture of the contact between these units implies the Donkey Gt intruded when the King Gt was only partially solid, allowing the later unit to ascend through it.
- The pluton was constructed in a broadly top-down, laccolith style. However, pressure from the upwelling magma column resulted in each unit ascending around the external contacts of earlier units creating irregular three-dimensional bodies.
- Evidence for magma flow is preserved by deflection of the AMS fabric sub-parallel to the contact surfaces for outcrops in their proximity.

3. What implications do these findings have for the generation and emplacement of granitic melts globally?

- These findings show further geochemical evidence for the derivation of granitic melts through extensive fractional crystallisation of basaltic primary melts.
- A new method for calculating the simultaneous evolution of major elements, trace elements, isotopes and bulk cumulates produced by a basaltic melt undergoing fractional crystallisation and non-modal assimilation is presented.

- The trace element data could only be successfully reproduced using enriched basaltic compositions.
- The derivation of isotopic heterogeneities from anatexis of a single source with inter-mineral isotopic disequilibrium is discussed and a new model for its calculation presented. However, the relatively short half-life of ^{235}U renders the $^{207}Pb/^{206}Pb$ system particularly sensitive to determining the effect of this process and proved it to be unsuitable for the derivation of Mt Kinabalu. However, this process may have important implications for assimilation processes.
- Experimental data shows that metalluminous melts with both $CaO/Na_2O > 1.5$ and K2O/Na2O > 0.5, such as those of Mt Kinabalu, cannot be produced through crustal anatexis alone. Any other plutons of this composition proposed to result partial melts of the crust, including the mafic lower crust or underplated basalts, must also involve a component of primary mantle melts.
- Although the structure of Mt Kinabalu broadly agrees with models of laccolith style emplacement for granitic plutons, the irregular three dimensional forms of its composite bodies and the processes by which they ascend around the external contacts of earlier units highlight the greater complexity of the natural system.

4. What implications do they have for the generation of continental crust?

- Like Mt Kinabalu, bulk (BCC), middle (MCC) and lower (LCC) continental crust also possess $CaO/Na_2O > 1.5$ and K2O/Na2O > 0.5 and are too metalluminous to be produced solely though crustal anatexis. The upper crust (UCC) falls along the same major element trend as the other crustal units, indicating a cogenetic relationship. Consequently, as for Mt Kinabalu, fractionation of a basaltic melt would be a more plausible process to generate the felsic UCC and MCC than melting and differentiation from the mafic LCC.
- The major and trace element composition of the LCC renders it of unsuitable composition to be mainly composed of cumulate material fractionated during generation of the felsic crust. Instead, we propose that although the LCC contains a cumulate component, as evidenced by enrichment in Eu and Sr, it more closely represents the composition of the primary melts from which both it and the felsic crust were derived.

- Derivation of the chemical composition of the UCC through fractionation of gabbroic cumulates the LCC composition has been successfully modelled. Although this was broadly successful without an assimilating component, crustal assimilation would explain the trace element discrepancies between the modelled results and the estimated average LCC composition.
- The liquid line of descent predicted by the model deriving the UCC from the LCC also closely matches the trend of the global dataset of felsic and intermediate plutons.

5. What can we learn from this study about the regional geology and tectonic history of Borneo and SE Asia?

- Felsic plutons within the ophiolite of the Segama Valley in East Sabah have been shown to be arc tonalites of mantle origin, not partial melts or windows of an underlying granitic continental crust.
- The low gravity anomalies in Sabah can be explained as a combination of deep sedimentary basins and upwelling asthenosphere beneath extended and thinned lithosphere without advocating a felsic underlying basement.
- Our data on Mt Kinabalu has shown that the crustal assimilant shown by the region's magmatism is probably sediments overlying the ophiolite or incorporated in to it.
- Mafic units from the Sabah ophiolite show a range of chemical compositions from MORB affinity to arc affinity in their trace element signatures. This indicates initial emplacement during the early stages of subduction zone development followed by continuing magmatic activity in a supra-subduction zone magmatic arc.
- The age of emplacement of the Sabah ophiolite is reviewed in light of the new data and compared with ophiolites and magmatism in Kalimantan. From this it is proposed that the ophiolite was initially emplaced at approximately 200 Ma during the initiation of western Pacific subduction, but that magmatism persisted until the subduction zone migrated east in the Late Cretaceous.
- It is proposed that this Paleo-Pacific subduction zone is marked by ophiolite outcrops in Sabah and the Meratus ophiolite of Kalimantan, and probably also the ophiolite of South Palawan and West Java.
- Combining the AMS data of the pluton with U-Pb zircon ages for each unit allows the orientation of the regional stress field at specific points in time to be accurately

determined. This application has the potential to be a powerful tool for determining paleo-stress fields in regions of complex or ambiguous tectonic regimes.

- The AMS and structural data support interpretations that Borneo has been undergoing regional NW-SE directed extension since the Late Miocene.
- The upwelling asthenosphere beneath Borneo is indicated geochemically by the OIB-like affinity of the incompatible element enriched Plio-Pleistocene basalts of Sabah and Sarawak produced by low degree melting of a fertile mantle source. By mapping similar basalts in the region of South China and the South China Sea it can be seen that similar magmatism has been continuing across the whole region since the Jurassic at the youngest. As these OIB-like basalts have probably been produced by crustal extension this implies widespread extensional magmatism in SE Asia since the Mesozoic, of which Mt Kinabalu is just a part.

Future Work

Although the conclusions presented by this thesis provide answers to the initial questions of the study, it does present the potential for future work on the region and in the fields of granite generation and crustal growth. Potential areas of study include:

- Collection of paleomagnetic data on the pluton's composite units which may be able to provide evidence for the roof-lifting model of emplacement as each unit tilted those above it. By combing this data with the AMS data and U-Pb zircon ages the orientation of the regional stress field relative to north can be determined.
- A more detailed study on the pluton's mafic enclaves. Geochemical and petrographic analysis of these bodies may provide more information on the assimilation and fractional crystallisation processes that occurred during the evolution of the magma.
- Investigation regionally for more evidence of the extensional tectonics of SE Asia since the Jurassic and whether it can be traced further back in history.
- New geochronological analysis of the Sabah ophiolite, particularly using the Pt-Os technique employed to date the Meratus ophiolite, to better constrain the initiation of its emplacement.
- Reinvestigation of granitic magmatism globally to determine the extent of mantle derived magmatism compared to anatectic melting, and hence the origin of the felsic continental crust.

Appendices

Appendix A1: Major and trace element QC data

	SiO_2	Al_2O_3	Fe_2O_3	MgO	CaO	Na_2O	K_2O	TiO_2	MnO	P_2O_5
BHVO-1										
n	3	3	3	3	3	3	3	3	3	3
Mean	49.86	13.76	12.23	7.28	11.27	2.31	0.53	2.69	0.17	0.26
1SD	0.10	0.06	0.01	0.01	0.02	0.02	0.00	0.00	0.00	0.00
Accepted Value*	49.94	13.80	12.23	7.23	11.40	2.26	0.52	2.71	0.17	0.27
SD Acc-An	0.05	0.03	0.00	0.04	0.09	0.04	0.00	0.02	0.00	0.01
SG										
n	3	3	3	3	3	3	3	3	3	3
Mean	69.53	14.17	2.33	1.13	1.69	3.28	5.34	0.51	0.05	0.22
1SD	0.04	0.01	0.00	0.01	0.01	0.02	0.00	0.00	0.00	0.00
Accepted Value*	69.27	14.16	2.37	1.19	1.73	3.43	5.33	0.52	0.05	0.22
SD Acc-An	0.19	0.00	0.03	0.04	0.03	0.11	0.01	0.01	0.00	0.00

* Govindaraju (1994)

A1.1. Major element standards for QC.

Data analysed by XRF at Edinburgh University, as detailed in Chapters 2 and 5. “SD Acc-An” is the standard deviation between the mean measured value and the accepted value.

Appendix A1.2. QC data for trace element analysis, including standards, blanks and repeated samples for both standard dissolution sample preparation and by flux fusion prior to acid dissolution. Accepted satandard values from Potts (1992).

	AGV-1				BHVO-1				W2			
n	8				8				12			
	Mean	1SD	Accepted value	1SD Acc-An	Mean	1SD	Accepted value	1SD Acc-An	Mean	1SD	Accepted value	1SD Acc-An
Cs	1.21	0.02	1.26	0.04	0.07	0.04	0.13	0.04	0.94	0.03	0.99	0.03
Rb	65.67	2.35	67	0.94	9.33	0.64	11	1.18	20.93	0.94	20	0.66
Ba	1198.85	40.44	1221	15.66	146.09	6.26	139	5.01	184.26	8.35	182	1.60
Th	6.21	0.40	6.5	0.20	1.34	0.11	1.08	0.19	2.35	0.21	2.2	0.10
U	1.86	0.08	1.89	0.02	0.46	0.03	0.42	0.03	0.54	0.03	0.53	0.01
Nb	13.65	0.15	15	0.95	19.86	0.23	19	0.61	7.94	0.13	7.9	0.03
Ta	0.85	0.02	0.92	0.05	1.27	0.03	1.23	0.03	0.52	0.02	0.5	0.02
La	26.22	8.59	38	8.33	22.98	6.99	15.8	5.08	12.96	3.91	11.4	1.10
Ce	63.86	1.39	66	1.51	39.64	1.39	39	0.45	23.92	0.84	24	0.06
Pb	36.55	1.07	36	0.39	14622	22652	2.6	10337	8.24	0.25	9.3	0.75
Pr	7.78	0.17	6.5	0.90	5.60	0.09	5.7	0.07	3.10	0.05	5.9	1.98
Sr	640.80	15.97	662	14.99	424.04	13.51	403	14.88	210.40	5.66	194	11.60
Nd	31.18	1.12	34	1.99	26.66	1.53	25.2	1.03	13.81	1.09	14	0.13
Zr	219.59	4.45	225	3.82	180.50	2.57	179	1.06	99.92	1.78	94	4.18
Hf	4.80	0.09	5.1	0.21	4.51	0.13	4.38	0.09	2.62	0.13	2.56	0.04
Sm	5.48	0.09	5.9	0.30	6.45	0.17	6.2	0.18	3.47	0.08	3.25	0.16
Eu	1.50	0.02	1.66	0.11	2.14	0.06	2.06	0.06	1.15	0.02	1.1	0.03
Gd	4.46	0.13	5.2	0.53	6.61	0.17	6.4	0.15	3.95	0.11	3.6	0.25
Tb	0.62	0.01	0.71	0.07	0.99	0.02	0.96	0.02	0.65	0.02	0.63	0.02
Dy	3.28	0.07	3.8	0.37	5.38	0.09	5.2	0.13	3.93	0.09	3.8	0.09
Y	18.36	0.61	21	1.87	28.51	0.72	27.6	0.64	23.17	0.70	24	0.59
Ho	0.63	0.01	0.73	0.07	1.00	0.02	0.99	0.01	0.81	0.02	0.76	0.04
Er	1.60	0.05	1.61	0.01	2.44	0.05	2.4	0.03	2.16	0.05	2.5	0.24
Tm	0.23	0.01	0.32	0.06	0.31	0.06	0.33	0.02	0.30	0.06	0.38	0.06
Yb	1.53	0.02	1.67	0.10	2.04	0.03	2.02	0.02	2.14	0.04	2.05	0.06
Lu	0.25	0.01	0.28	0.02	0.31	0.01	0.291	0.01	0.34	0.01	0.33	0.01

A1.2.1. Comparison of standard data compiled from each trace element analysis with accepted standard values (Potts, 1992).

A1.2.1a. QC data from standards prepared for ICP-MS analysis by flux fusion prior to HF and HNO_3 acid dissolution.

	Blanks				Fused Flux		CS011		SBK127	
n	19				28		7		6	
	Mean	1SD	Accepted value	1SD Acc-An	Mean	1SD	Mean	1SD	Mean	1SD
Cs	-0.06	0.09	0.00	0.04	-0.03	0.11	12.76	0.45	13.87	0.42
Rb	-0.82	0.73	0.00	0.58	-0.75	0.84	185.12	6.78	271.49	10.36
Ba	0.26	2.16	0.00	0.19	-0.19	0.90	690.43	56.55	1121.32	48.84
Th	-0.01	0.00	0.00	0.01	0.00	0.01	24.53	7.39	18.69	2.54
U	0.00	0.01	0.00	0.00	0.00	0.01	4.89	0.45	54.40	121.84
Nb	-0.07	0.14	0.00	0.05	2.06	4.00	8.53	0.12	7.67	0.33
Ta	-0.01	0.03	0.00	0.01	0.00	0.01	0.90	0.05	0.79	0.16
La	-4.95	11.25	0.00	3.50	0.02	0.19	23.84	2.07	31.14	7.91
Ce	0.00	0.07	0.00	0.00	0.01	0.08	45.70	3.43	49.30	1.47
Pb	21461	25431	0.00		7009	16136	24.38	7.72	17.72	0.76
Pr	-0.01	0.01	0.00	0.00	0.00	0.01	5.12	0.31	5.84	0.14
Sr	-0.32	0.60	0.00	0.23	-0.24	0.72	297.89	6.72	461.90	14.31
Nd	-0.13	0.48	0.00	0.09	-0.42	0.66	20.08	1.33	23.94	0.75
Zr	-0.50	0.21	0.00	0.36	-0.03	0.36	135.78	13.39	121.25	4.20
Hf	-0.07	0.05	0.00	0.05	0.00	0.03	3.94	0.35	3.55	0.17
Sm	-0.01	0.05	0.00	0.01	-0.01	0.05	4.02	0.26	4.90	0.18
Eu	0.00	0.00	0.00	0.00	0.00	0.00	1.00	0.05	1.04	0.04
Gd	-0.03	0.06	0.00	0.02	-0.02	0.07	3.75	0.21	4.25	0.09
Tb	-0.02	0.02	0.00	0.01	-0.01	0.03	0.55	0.03	0.57	0.03
Dy	0.00	0.00	0.00	0.00	0.00	0.00	3.17	0.11	3.17	0.09
Y	-0.18	0.29	0.00	0.13	-0.07	0.53	19.09	0.52	18.89	0.70
Ho	0.00	0.00	0.00	0.00	0.00	0.00	0.64	0.03	0.64	0.02
Er	-0.02	0.03	0.00	0.01	-0.04	0.04	1.74	0.06	1.74	0.05
Tm	-0.01	0.04	0.00	0.01	-0.02	0.08	0.28	0.02	0.27	0.02
Yb	-0.01	0.01	0.00	0.00	0.00	0.01	1.89	0.06	1.84	0.05
Lu	0.00	0.00	0.00	0.00	0.00	0.00	0.32	0.01	0.31	0.01

A1.2.1b. QC data on blanks, fusion blanks and fused repeat samples from the flux fusion procedure of sample preparation. “Fused flux” data represents analysis of flux powder processed alongside mixtures of sample and flux through the fusion and standard dissolution process and analysed as a procedural blank.

	AGV-1				BHVO-1				W2			
n	11				11				20			
	Mean	1SD	Accepted value	1SD Acc-An	Mean	1SD	Accepted value	1SD Acc-An	Mean	1SD	Accepted value	1SD Acc-An
Cs	1.25	0.03	1.26	0.01	0.10	0.00	0.13	0.02	0.89	0.03	0.99	0.07
Rb	67.99	1.11	67.00	0.70	9.46	0.37	11.00	1.09	20.21	0.74	20.00	0.15
Ba	1217.35	19.93	1221.00	2.58	130.00	5.65	139.00	6.36	171.63	9.03	182.00	7.33
Th	6.45	0.12	6.50	0.04	1.25	0.04	1.08	0.12	2.19	0.07	2.20	0.01
U	1.91	0.04	1.89	0.01	0.42	0.01	0.42	0.00	0.49	0.02	0.53	0.03
Nb	14.84	0.47	15.00	0.12	19.52	0.12	19.00	0.36	7.70	0.11	7.90	0.14
Ta	0.91	0.02	0.92	0.00	1.25	0.02	1.23	0.02	0.50	0.01	0.50	0.00
La	37.88	0.48	38.00	0.08	15.31	0.53	15.80	0.35	10.54	0.45	11.40	0.61
Ce	66.75	0.92	66.00	0.53	36.84	1.24	39.00	1.53	22.54	0.90	24.00	1.03
Pb	36.11	0.42	36.00	0.07	2.19	0.13	2.60	0.29	7.57	0.24	9.30	1.22
Pr	8.78	0.34	6.50	1.61	5.60	0.04	5.70	0.07	3.13	0.07	5.90	1.96
Sr	672.09	17.92	662.00	7.13	405.09	12.94	403.00	1.47	203.54	5.28	194.00	6.74
Nd	33.38	0.69	34.00	0.44	25.99	0.53	25.20	0.56	13.73	0.42	14.00	0.19
Zr	233.56	5.61	225.00	6.05	173.37	4.19	179.00	3.98	89.57	2.62	94.00	3.13
Hf	5.11	0.14	5.10	0.01	4.43	0.06	4.38	0.03	2.48	0.21	2.56	0.06
Sm	5.90	0.15	5.90	0.00	6.23	0.11	6.20	0.02	3.36	0.09	3.25	0.08
Eu	1.62	0.05	1.66	0.03	2.10	0.04	2.06	0.03	1.13	0.04	1.10	0.02
Gd	4.94	0.22	5.20	0.19	6.49	0.22	6.40	0.07	3.88	0.14	3.60	0.20
Tb	0.68	0.02	0.71	0.02	0.97	0.02	0.96	0.01	0.64	0.02	0.63	0.01
Dy	3.57	0.11	3.80	0.17	5.31	0.06	5.20	0.08	3.85	0.06	3.80	0.03
Y	20.32	0.75	21.00	0.48	27.57	0.37	27.60	0.02	22.74	0.36	24.00	0.89
Ho	0.68	0.02	0.73	0.04	0.99	0.01	0.99	0.00	0.79	0.01	0.76	0.02
Er	1.77	0.06	1.61	0.12	2.44	0.03	2.40	0.03	2.15	0.03	2.50	0.25
Tm	0.26	0.01	0.32	0.04	0.34	0.01	0.33	0.01	0.33	0.00	0.38	0.04
Yb	1.66	0.05	1.67	0.01	2.01	0.03	2.02	0.01	2.07	0.03	2.05	0.02
Lu	0.27	0.01	0.28	0.01	0.31	0.00	0.29	0.01	0.33	0.00	0.33	0.00

A1.2.1c. QC data from standards prepared for ICP-MS analysis by the standard HF and HNO_3 acid dissolution procedure without prior flux fusion.

	Blanks				CS011		SBK127	
n	61				7		4	
	Mean	1SD	Accepted value	1SD Acc-An	Mean	1SD	Mean	1SD
Cs	0.00	0.00	0.00	0.00	10.28	0.18	11.75	0.12
Rb	0.01	0.04	0.00	0.01	160.88	4.92	245.03	0.72
Ba	0.07	0.11	0.00	0.05	642.69	30.35	969.93	20.57
Th	0.00	0.01	0.00	0.00	17.38	3.73	19.32	0.17
U	0.00	0.00	0.00	0.00	3.95	0.28	4.09	0.02
Nb	0.00	0.02	0.00	0.00	7.64	0.18	7.19	0.06
Ta	0.00	0.00	0.00	0.00	0.78	0.02	0.67	0.01
K			0.00					
La	0.00	0.00	0.00	0.00	20.94	1.12	23.00	0.55
Ce	0.00	0.01	0.00	0.00	41.26	2.32	44.26	0.36
Pb	0.01	0.05	0.00	0.01	18.31	0.27	15.61	0.16
Pr	0.00	0.00	0.00	0.00	5.13	0.20	5.72	0.10
Sr	0.04	0.07	0.00	0.03	268.46	11.11	427.15	6.71
P			0.00					
Nd	0.00	0.03	0.00	0.00	19.52	0.92	22.32	0.27
Zr	0.01	0.03	0.00	0.00	10.32	0.45	78.09	0.79
Hf	-0.02	0.05	0.00	0.01	0.64	0.08	2.59	0.03
Sm	0.00	0.00	0.00	0.00	3.92	0.15	4.61	0.04
Eu	0.00	0.00	0.00	0.00	0.95	0.02	1.01	0.02
Ti			0.00					
Gd	0.00	0.00	0.00	0.00	3.39	0.12	4.04	0.06
Tb	0.00	0.00	0.00	0.00	0.51	0.01	0.56	0.02
Dy	0.00	0.00	0.00	0.00	2.91	0.03	3.03	0.03
Y	-0.01	0.02	0.00	0.01	17.56	0.55	17.88	0.11
Ho	0.00	0.00	0.00	0.00	0.59	0.01	0.60	0.01
Er	0.00	0.00	0.00	0.00	1.63	0.05	1.64	0.03
Tm	0.00	0.00	0.00	0.00	0.26	0.01	0.26	0.00
Yb	0.00	0.00	0.00	0.00	1.65	0.04	1.71	0.01
Lu	0.00	0.00	0.00	0.00	0.26	0.00	0.28	0.01
			0.00					
La	0.00	0.00	0.00	0.00	20.94	1.12	23.00	0.55
Ce	0.00	0.01	0.00	0.00	41.26	2.32	44.26	0.36
Pr	0.00	0.00	0.00	0.00	5.13	0.20	5.72	0.10
Nd	0.00	0.03	0.00	0.00	19.52	0.92	22.32	0.27
Sm	0.00	0.00	0.00	0.00	3.92	0.15	4.61	0.04
Eu	0.00	0.00	0.00	0.00	0.95	0.02	1.01	0.02
Gd	0.00	0.00	0.00	0.00	3.39	0.12	4.04	0.06
Tb	0.00	0.00	0.00	0.00	0.51	0.01	0.56	0.02
Dy	0.00	0.00	0.00	0.00	2.91	0.03	3.03	0.03
Ho	0.00	0.00	0.00	0.00	0.59	0.01	0.60	0.01
Er	0.00	0.00	0.00	0.00	1.63	0.05	1.64	0.03
Tm	0.00	0.00	0.00	0.00	0.26	0.01	0.26	0.00
Yb	0.00	0.00	0.00	0.00	1.65	0.04	1.71	0.01
Lu	0.00	0.00	0.00	0.00	0.26	0.00	0.28	0.01

A1.2.1d. QC data on blanks and repeat samples from the acid dissolution procedure without prior flux fusion of the samples.

Appendix A2: Whole rock elemental and isotopic data for the Sabah ophiolite samples from the Segama Valley and Mt Kinabalu area

Lat.			4.947333	4.948492	5.014017	5.094228	5.084223	5.094897
Long.			117.74274	117.75042	117.725785	118.013355	118.019607	118.03004
Height (AMSL), m			1183	1570	737	291	178	282
			Gd	Dyke	Gd	Gd	Bt Gd	Gt Dyke
			S. Purut	S. Danum	S. Danum	S. LKK.	S. LKK.	S. Babayas
Element	Prep.	Analysis	A245	A248b	A249	A261	A265	A275
(wt%)								
SiO_2	F	XRF	56.20	63.79	61.57	67.95	55.59	71.39
TiO_2	F	XRF	0.83	0.50	0.51	0.18	0.63	0.16
Al_2O_3	F	XRF	16.95	17.54	15.21	15.86	17.55	15.53
FeO_{TOT}	F	XRF	7.03	4.10	4.32	1.50	6.40	1.51
MnO	F	XRF	0.15	0.07	0.08	0.05	0.14	0.03
MgO	F	XRF	3.95	1.89	1.86	0.53	3.35	0.58
CaO	F	XRF	6.66	2.82	4.13	3.15	6.96	2.60
Na_2O	F	XRF	3.50	5.26	4.91	6.28	3.41	5.06
K_2O	F	XRF	1.49	1.37	1.96	1.96	2.11	1.30
P_2O_5	F	XRF	0.17	0.16	0.12	0.06	0.17	0.03
Total			99.84	99.95	99.47	99.80	99.25	99.55
LOI			2.13	1.99	4.33	2.12	2.22	1.17
ppm								
Ta	F	ICP-MS	0.22	0.07	0.27	0.08	0.24	0.08
Sc	HF	ICP-MS	22.59	5.66	10.99	1.47	18.54	1.49
V	HF	ICP-MS	180.80	88.93	87.87	26.95	241.50	13.21
Cr	HF	ICP-MS	89.33	0.06	26.75	0.68	8.09	0.57
Ga	HF	ICP-MS	15.56	18.46	14.06	14.53	18.61	14.22
Co	HF	ICP-MS	22.46	11.57	11.81	2.34	20.39	1.74
Ni	HF	ICP-MS	36.98	5.94	13.28	1.03	9.09	0.91
Cu	HF	ICP-MS	35.57	49.51	10.63	20.49	84.94	31.52
Zn	HF	ICP-MS	54.62	59.66	43.77	35.45	61.22	24.33
Cs	F	ICP-MS	0.28	0.32	2.08	-0.05	1.86	0.43
Rb	HF	ICP-MS	33.04	29.84	55.68	13.16	31.66	17.16
Ba	HF	ICP-MS	181.10	151.70	204.40	363.50	416.40	330.20
Sr	HF	ICP-MS	345.40	516.90	220.90	673.30	567.30	542.80
Zr	F	ICP-MS	159.90	95.49	223.20	112.50	75.65	115.80
Hf	F	ICP-MS	4.03	2.37	5.53	2.72	2.11	2.76
Th	F	ICP-MS	3.40	1.77	4.19	0.73	3.88	0.92
U	F	ICP-MS	1.22	0.54	1.19	0.28	0.95	0.37
Pb	HF	ICP-MS	2.75	3.88	3.32	5.41	6.86	6.69
Nb	F	ICP-MS	3.21	1.39	3.48	1.57	4.11	1.97
Y	F	ICP-MS	30.13	11.09	28.67	4.72	19.31	4.64
La	HF	ICP-MS	9.48	9.58	13.41	5.36	11.90	7.97
Ce	F	ICP-MS	25.04	22.77	32.16	11.89	28.24	16.73
Pr	F	ICP-MS	3.82	3.23	4.45	1.56	3.98	2.23
Nd	F	ICP-MS	15.79	11.64	16.83	4.68	14.68	6.99
Sm	F	ICP-MS	4.66	2.73	4.39	1.23	3.77	1.50
Eu	F	ICP-MS	1.30	0.94	1.06	0.50	1.11	0.55
Gd	F	ICP-MS	5.03	2.41	4.37	1.03	3.58	1.25
Tb	F	ICP-MS	0.80	0.32	0.71	0.13	0.51	0.13
Dy	F	ICP-MS	4.77	1.91	4.31	0.81	2.99	0.82
Ho	F	ICP-MS	0.99	0.36	0.91	0.17	0.63	0.17
Er	F	ICP-MS	2.72	0.94	2.58	0.37	1.67	0.37
Tm	F	ICP-MS	0.26	0.01	0.25	-0.07	0.11	-0.07
Yb	F	ICP-MS	2.88	1.01	2.88	0.56	1.84	0.54
Lu	F	ICP-MS	0.46	0.17	0.47	0.11	0.29	0.10

F = Fused
HF = Standard HF dissolution

A2.1.a. Major and trace elements for the Segama Valley felsic intrusions

Lat.			5.013		4.948201	4.948658	5.092971	5.094332	5.094155
Long.			117.7		117.744875	117.746	118.0133	118.029994	118.030048
Height (AMSL), m			725		1182	1328	202	186	246
			Quartzite		Hnfs	Volc	Hnfs	Calc-sil	Hnfs
			S. Danum		S. Purut	S. Purut	S. LKK.	S. Babayas	S. Babayas
Element	Prep.	Analysis	A251	Prep.	A246	A247	A264	A271	A272
(wt%)									
SiO_2	F	XRF	87.49	F	53.65	46.28	59.97	22.77	49.57
TiO_2	F	XRF	0.33	F	1.22	0.73	0.84	0.22	0.78
Al_2O_3	F	XRF	5.96	F	13.86	16.39	16.09	4.43	19.76
FeO_{TOT}	F	XRF	1.56	F	9.55	7.11	7.10	1.79	7.14
MnO	F	XRF	0.02	F	0.18	0.21	0.16	0.05	0.15
MgO	F	XRF	0.77	F	6.60	2.07	3.69	1.16	3.18
CaO	F	XRF	0.08	F	7.55	12.82	4.09	46.50	9.94
Na_2O	F	XRF	0.92	F	2.35	2.72	3.62	0.03	3.67
K_2O	F	XRF	1.31	F	1.75	0.59	0.88	0.01	0.46
P_2O_5	F	XRF	0.04	F	0.20	0.14	0.15	0.47	0.17
Total			99.91		99.66	99.63	99.49	99.56	99.75
LOI			1.26		1.69	9.76	2.11	21.93	4.13
ppm									
Ta	F	ICP-MS	0.48	HF	0.18	0.09	0.37	0.05	0.34
Sc	HF	ICP-MS	4.48	HF	26.63	24.53	19.62	4.91	20.57
V	HF	ICP-MS	31.36	HF	296.60	225.60	231.80	56.65	232.60
Cr	HF	ICP-MS	26.63	HF	19.17	35.02	51.53	6.47	19.45
Ga	HF	ICP-MS	6.48	HF	13.81	14.98	21.48	4.90	18.35
Co	HF	ICP-MS	4.78	HF	28.55	18.56	20.16	4.90	22.14
Ni	HF	ICP-MS	11.47	HF	16.21	17.07	37.65	7.60	15.80
Cu	HF	ICP-MS	7.00	HF	55.50	18.44	3.52	22.35	45.25
Zn	HF	ICP-MS	32.88	HF	131.60	97.94	130.00	42.61	84.11
Cs	F	ICP-MS	2.46	HF	0.94	0.23	0.38	0.00	0.18
Rb	HF	ICP-MS	53.41	HF	22.15	12.23	14.57	0.10	10.76
Ba	HF	ICP-MS	59.62	HF	256.20	56.24	121.70	27.77	44.36
Sr	HF	ICP-MS	27.31	HF	231.70	320.80	468.90	1017.00	453.50
Zr	F	ICP-MS	307.70	HF	10.64	43.59	100.30	26.25	24.96
Hf	F	ICP-MS	7.91	HF	0.50	1.17	2.75	0.71	0.87
Th	F	ICP-MS	6.52	HF	0.45	0.34	5.20	0.37	1.04
U	F	ICP-MS	1.57	HF	0.17	0.14	1.41	0.37	0.36
Pb	HF	ICP-MS	10.97	HF	1.78	1.13	3.52	1.08	2.13
Nb	F	ICP-MS	5.46	HF	2.72	1.45	5.25	0.68	5.57
Y	F	ICP-MS	14.24	HF	25.81	16.27	30.39	14.67	18.88
La	HF	ICP-MS	16.86	HF	6.05	3.41	17.32	6.97	8.17
Ce	F	ICP-MS	34.36	HF	14.53	8.12	37.13	8.81	17.82
Pr	F	ICP-MS	4.25	HF	2.45	1.34	4.89	1.75	2.61
Nd	F	ICP-MS	15.59	HF	12.10	6.84	20.42	7.76	11.87
Sm	F	ICP-MS	2.86	HF	3.32	1.92	4.74	1.72	2.89
Eu	F	ICP-MS	0.56	HF	1.16	0.65	1.38	0.44	1.02
Gd	F	ICP-MS	2.65	HF	3.99	2.36	4.86	1.95	3.09
Tb	F	ICP-MS	0.41	HF	0.67	0.40	0.81	0.31	0.50
Dy	F	ICP-MS	2.34	HF	4.07	2.50	4.87	1.89	3.05
Ho	F	ICP-MS	0.49	HF	0.87	0.53	1.03	0.42	0.64
Er	F	ICP-MS	1.36	HF	2.43	1.49	2.89	1.19	1.76
Tm	F	ICP-MS	0.22	HF	0.36	0.22	0.43	0.17	0.26
Yb	F	ICP-MS	1.51	HF	2.36	1.46	2.78	1.14	1.71
Lu	F	ICP-MS	0.26	HF	0.38	0.24	0.43	0.19	0.28

F = Fused
HF = Standard HF dissolution

A2.1.b. Major and trace elements for the Segama Valley ophiolite.

Lat.			5.978759		6.055028	5.978759	5.978759	5.997251	5.980212	6.081992
			116.681		116.564	116.681	116.681	116.696	116.678	116.52
Long.			65		58	65	65	14	74	06
Height (AMSL), m			552.39		0	552.39	552.39	568.74	567.05	1667.51
			Am-Pl-Gneiss		Peridotite	Chert	Eclogite	Peridotite	Volc	Umf
Element	Prep.	Analysis	A203c	Prep.	SBK129	A203a	A203e	A204b	A207	A287
(wt%)										
SiO2	F	XRF	49.35	F	43.86	87.40	41.71	40.33	49.98	42.35
TiO2	F	XRF	1.37	F	0.16	0.24	0.04	0.16	2.04	0.13
Al2O3	F	XRF	16.30	F	4.17	4.89	21.39	3.80	15.70	3.17
FeOTOT	F	XRF	0.04	F	0.04	0.01	0.02	0.04	0.05	0.04
MnO	F	XRF	0.16	F	0.12	0.23	0.07	0.15	0.16	0.16
MgO	F	XRF	8.18	F	37.33	1.22	13.70	35.24	7.66	36.59
CaO	F	XRF	10.32	F	4.11	0.68	14.69	3.65	1.86	2.55
Na2O	F	XRF	3.45	F	0.07	0.39	0.81	-0.11	5.70	-0.16
K2O	F	XRF	0.10	F	0.10	0.92	0.00	0.01	0.37	0.00
P2O5	F	XRF	0.15	F	0.02	0.19	0.00	0.00	0.32	0.00
Total			100.06		98.99	99.92	100.15	99.97	99.95	99.92
LOI			1.34		1.58	1.15	3.29	8.29	4.79	6.35
ppm										
Ta	F	ICP-MS	0.05	HF	0.01	0.24	0.00	0.01	1.74	0.00
Sc	HF	ICP-MS	30.06	HF	12.01	6.95	3.72	13.28	31.74	11.98
V	HF	ICP-MS	216.60	HF	68.12	26.63	12.09	74.45	193.50	68.82
Cr	HF	ICP-MS	295.85	HF	2049.88	28.03	704.30	2521.00	317.45	2436.00
Ga	HF	ICP-MS	14.86	HF	2.58	7.12	8.07	3.25	17.42	2.83
Co	HF	ICP-MS	38.56	HF	84.34	15.22	46.66	104.60	42.84	106.70
Ni	HF	ICP-MS	123.20	HF	1837.10	60.31	689.60	1886.00	247.80	2005.00
Cu	HF	ICP-MS	51.22	HF	205.12	717.15	60.48	12.80	19.48	31.09
Zn	HF	ICP-MS	113.50	HF	66.94	92.09	15.46	68.53	123.70	67.73
Cs	F	ICP-MS	0.04	HF	5.30	1.18	0.05	0.11	0.61	0.34
Rb	HF	ICP-MS	0.70	HF	8.66	35.09	0.13	0.32	8.34	0.16
Ba	HF	ICP-MS	3.83	HF	4.21	120.40	1.71	2.12	90.73	0.51
Sr	HF	ICP-MS	170.50	HF	6.72	47.80	165.40	4.54	202.00	4.53
Zr	F	ICP-MS	116.60	HF	5.73	41.66	1.20	6.24	161.10	3.62
Hf	F	ICP-MS	2.86	HF	0.22	1.06	0.03	0.20	3.72	0.14
Th	F	ICP-MS	0.07	HF	0.02	3.26	0.00	0.00	2.89	0.00
U	F	ICP-MS	0.02	HF	0.04	1.40	0.00	0.00	0.98	0.00
Pb	HF	ICP-MS	0.29	HF	0.99	5.93	0.00	0.17	1.70	0.07
Nb	F	ICP-MS	0.27	HF	0.15	3.35	0.03	0.02	27.50	0.01
Y	F	ICP-MS	29.92	HF	3.75	25.32	0.68	4.12	29.22	3.11
La	HF	ICP-MS	3.20	HF	0.50	15.75	0.14	0.09	19.69	0.07
Ce	F	ICP-MS	12.04	HF	1.58	26.91	0.34	0.46	40.11	0.30
Pr	F	ICP-MS	2.29	HF	0.30	4.11	0.06	0.11	5.52	0.07
Nd	F	ICP-MS	11.85	HF	1.69	17.13	0.33	0.73	23.47	0.54
Sm	F	ICP-MS	3.83	HF	0.54	3.62	0.08	0.31	5.31	0.23
Eu	F	ICP-MS	1.32	HF	0.15	0.84	0.16	0.14	1.77	0.10
Gd	F	ICP-MS	4.88	HF	0.70	3.69	0.10	0.48	5.63	0.35
Tb	F	ICP-MS	0.85	HF	0.12	0.56	0.02	0.09	0.87	0.07
Dy	F	ICP-MS	5.20	HF	0.75	3.31	0.11	0.61	5.05	0.46
Ho	F	ICP-MS	1.11	HF	0.16	0.70	0.02	0.14	1.01	0.10
Er	F	ICP-MS	3.01	HF	0.46	1.95	0.06	0.40	2.63	0.31
Tm	F	ICP-MS	0.47	HF	0.07	0.29	0.01	0.06	0.36	0.05
Yb	F	ICP-MS	2.92	HF	0.48	1.91	0.06	0.41	2.34	0.33
Lu	F	ICP-MS	0.47	HF	0.08	0.31	0.01	0.07	0.36	0.05

F =
Fused
HF = Standard HF dissolution

A2.1.c. Major and trace elements for ophiolite samples from S. Mansahaban and Mt Kinabalu.

	Lithology	Sample	$^{87}Sr/^{86}Sr_m$	2SE	$^{143}ND/^{144}Nd_m$	2SE	$^{206}Pb/^{204}Pb_m$	2SE	$^{207}Pb/^{204}Pb_m$	2SE	$^{208}Pb/^{204}Pb_m$	2SE
S. Mansahaban	Basalt	A207	0.708149	0.000012	0.512702	0.000008	19.5181	0.0055	15.6936	0.0046	39.7395	0.0150
	Eclogite	A203e	0.702576	0.000014	0.513167	0.000017						
	Peridotite	A204b	0.704287	0.000027	0.513394	0.000029						
Mt Kinabalu	Peridotite	SBK129	0.704105	0.000021	0.513063	0.000023						
Segama Ophiolite	Gd (S. Purut)	A245	0.703845	0.000009	0.512990	0.000007	19.3276	0.0023	15.5857	0.0024	38.9625	0.0075
	Gd (S. Danum)	A249	0.705354	0.000010	0.512960	0.000013	18.9355	0.0026	15.5659	0.0024	38.7117	0.0069
	Gd (S. LKK)	A261	0.703227	0.000011	0.513097	0.000013	18.6973	0.0012	15.5621	0.0011	38.3783	0.0041
	Bt Gd (S. LKK)	A265	0.703486	0.000012	0.512920	0.000008	18.7302	0.0014	15.5837	0.0012	38.6578	0.0045
	Volc Spilite (S. Purut)	A247	0.703768	0.000013	0.513036	0.000015	19.0022	0.0025	15.5537	0.0020	38.4495	0.0054
	Quartzite (S. Danum)	A251	0.717985	0.000230	0.512139	0.000003	18.9056	0.0007	15.7084	0.0008	39.2130	0.0030
	Hornfels (S.LKK)	A264	0.703698	0.000017	0.512710	0.000009	19.4363	0.0025	15.6275	0.0024	39.2771	0.0066

A2.2. Isotopic data from the ophiolite samples of the Segama Valley, Mt Kinabalu and S. Mansahaban.

Appendix A3: AMS results and calculated parameters

Lat.	Long.	Height (AMSL) m	Sample	Magnetic Susceptibility, x 10^6 SI (K)				K_1		95% angles in plane	K_2		K_3	95% angles in plane		K_3		95% angles in plane		Jelenick parameters	
				K_{mean}	K_1	K_2	K_3	Dec.	Dip	K_1-K_2	Dec.	Dip	Dec.	K_1-K_2	K_2-K_3	Dec.	Dip	K_1-K_3	K_2-K_3	P'	T
6.0557	116.5646	3115	A026a	20018	21570	20369	18115	152.7	5.8	3.6	244.5	17.3	44.7	3.5	1.6	44.7	71.7	1.9	0.8	1.19	0.35
6.0522	116.5642	2997	A031	8205	9015	8440	7161	149.0	4.3	4.3	57.2	22.2	249.2	4.0	1.7	249.2	67.3	2.1	1.5	1.27	0.43
6.0513	116.5637	2966	A035	14171	15635	14076	12801	344.7	16.5	5.1	244.5	30.9	98.8	8.8	2.1	98.8	54.0	9.2	1.2	1.22	-0.05
6.0790	116.5493	3850	A040	305	314	312	290	306.4	1.4	19.4	214.7	51.9	37.5	19.7	2.5	37.5	38.1	5.0	1.6	1.09	0.80
6.0818	116.5492	3684	A042	259	266	264	248	350.3	28.8	8.8	204.0	56.6	89.1	9.4	2.5	89.1	15.5	4.4	2.7	1.08	0.75
6.0813	116.5526	3819	A044	323	329	327	312	171.3	15.1	19.1	284.2	55.2	72.1	19.1	5.6	72.1	30.5	5.7	3.2	1.06	0.81
6.0831	116.5538	3945	A046	4601	4710	4643	4449	312.9	48.3	10.2	220.1	2.5	127.9	9.9	2.5	127.9	41.6	4.3	1.9	1.06	0.50
6.0767	116.5490	3991	A047	298	306	298	290	291.5	0.1	3.1	201.4	45.0	21.7	3.8	2.8	21.7	45.0	3.9	2.5	1.06	0.07
6.0748	116.5500	3835	A049	186	189	188	180	280.6	56.3	29.9	144.7	25.6	44.4	30.1	6.1	44.4	20.4	8.5	6.2	1.05	0.87
6.0748	116.5521	3964	A051	260	266	263	252	247.7	33.7	9.8	338.0	0.4	68.6	11.7	8.2	68.6	56.3	10.8	4.4	1.06	0.54
6.0757	116.5529	3978	A052	295	300	300	284	202.4	46.9	43.7	317.0	21.3	63.1	43.7	3.3	63.1	35.4	4.2	1.4	1.06	0.93
6.0731	116.5506	3767	A053	7930	8530	7997	7262	274.5	45.1	11.5	165.9	17.6	60.6	9.9	9.2	60.6	39.6	10.0	7.9	1.18	0.24
6.0712	116.5533	3892	A054	340	346	343	330	293.9	14.0	28.5	187.5	48.5	35.1	28.6	6.9	35.1	38.1	10.6	3.3	1.05	0.64
6.0731	116.5573	4019	A055	305	314	307	293	295.2	32.6	4.8	183.5	30.0	61.3	4.5	1.9	61.3	42.6	4.0	1.8	1.08	0.31
6.0800	116.5540	3971	A056a	280	285	284	270	298.1	22.5	18.0	202.8	12.4	86.2	18.1	5.1	86.2	64.0	5.5	2.2	1.06	0.78
6.0800	116.5541	3964	A056b	303	308	308	292	310.5	15.9	91.8	206.8	39.8	57.6	91.8	2.6	57.6	45.9	3.9	2.8	1.07	0.97
6.0799	116.5541	3964	A056d	1398	1431	1421	1341	350.9	12.9	21.3	242.1	54.6	89.2	21.2	2.9	89.2	32.3	3.3	2.4	1.07	0.81
6.0799	116.5543	3978	A056e	5651	5732	5691	5529	212.2	15.9	20.5	314.6	37.2	103.5	20.4	5.1	103.5	48.4	5.2	2.8	1.04	0.61
6.0788	116.5540	3884	A057a	273	279	277	264	287.3	17.4	24.8	182.2	39.7	35.7	25.0	4.6	35.7	45.1	5.8	1.7	1.06	0.82
6.0788	116.5541	3906	A057b	2154	2195	2141	2126	167.1	17.1	19.5	312.5	69.5	44.6	9.5	4.0	260.9	10.9	44.0	9.8	1.03	-0.51
6.0787	116.5541	3911	A057c	7559	7768	7525	7386	352.2	25.1	5.7	164.7	64.7	9.5	5.7	1.3	153.8	2.9	8.7	2.8	1.05	-0.24
6.0792	116.5569	3872	A058	12419	12918	12705	11634	326.2	23.8	5.7	57.5	2.8	153.8	5.7	1.3	66.0	1.9	1.9	1.0	1.12	0.68
6.0768	116.5571	3947	A060	8586	8937	8633	8187	356.5	23.1	3.0	253.1	28.7	119.2	3.7	2.3	119.2	51.7	3.2	2.1	1.09	0.22
6.0762	116.5608	3867	A061	11268	11527	11356	10922	346.7	12.4	14.9	255.6	5.0	143.9	26.4	13.2	143.9	76.6	25.8	3.9	1.06	0.41
6.0750	116.5586	4102	A062	7151	7381	7257	6815	321.8	23.0	5.2	58.6	15.5	179.7	6.8	4.7	179.7	61.8	6.9	3.2	1.09	0.58
6.0730	116.5573	4026	A064a	235	240	236	231	290.9	16.2	20.2	194.0	22.4	53.6	20.5	5.6	53.6	61.9	7.3	5.4	1.04	0.24
6.0730	116.5573	4028	A064b	653	662	661	637	66.2	32.5	64.1	312.1	32.6	189.1	64.1	4.4	189.1	40.5	4.9	3.4	1.04	0.89
6.0740	116.5559	3972	A067	474	480	477	464	240.9	22.9	10.5	143.6	16.7	20.7	10.0	5.9	20.7	61.1	7.1	3.5	1.04	0.59
6.0745	116.5558	3979	A068	292	299	293	283	300.1	20.2	5.8	195.6	34.3	54.9	4.1	3.4	54.9	48.6	5.5	2.9	1.06	0.26
6.0694	116.5571	3811	A069	305	317	312	287	305.3	29.1	4.4	190.7	36.8	62.7	4.4	1.8	62.7	39.5	2.1	0.9	1.11	0.67
6.0695	116.5572	3859	A070	11073	11435	11175	10607	321.2	12.7	8.2	228.6	11.5	97.7	7.6	4.1	97.7	72.7	6.5	1.9	1.08	0.41

A3.1. AMS data, 95% confidence ranges and shape parameters (Jelineck, 1981).

A3.1. (*cont.*)

				Magnetic Susceptibility, x 10^6 SI (K)				K_1	K_1	95% angles in plane		K_2	K_2	95% angles in plane		K_3	K_3	95% angles in plane		Jelenick parameters	
Lat.	Long.	Height (AMSL) m	Sample	K_{mean}	K_1	K_2	K_3	Dec.	Dip	K_1-K_2	K_1-K_3	Dec.	Dip	K_1-K_2	K_2-K_3	Dec.	Dip	K_1-K_3	K_2-K_3	P'	T
6.0719	116.5595	3969	A071	10263	10689	10499	9601	333.0	3.5	6.2	1.1	241.4	23.4	6.3	2.0	71.0	66.3	2.1	1.2	1.12	0.66
6.0700	116.5606	3939	A072	11578	11990	11812	10934	352.1	8.3	30.9	3.1	258.4	23.4	31.5	5.9	100.4	65.0	9.9	3.3	1.10	0.67
6.0686	116.5614	3900	A073	12256	12574	12517	11676	188.0	4.9	30.5	4.2	97.7	2.6	30.5	2.4	340.3	84.4	4.6	1.2	1.09	0.87
6.0675	116.5621	3848	A074	12038	12399	12213	11503	283.7	0.1	8.5	4.0	193.7	15.4	8.5	2.5	14.2	74.6	4.6	3.1	1.08	0.61
6.0661	116.5628	3793	A075	11478	11814	11653	10968	300.0	6.1	14.0	1.9	207.5	22.1	14.0	3.5	44.5	67.0	3.8	1.8	1.08	0.61
6.0667	116.5635	3786	A077	376	383	378	368	177.4	32.5	10.8	7.4	294.6	35.7	9.3	7.6	58.1	37.5	9.3	7.7	1.04	0.31
6.0665	116.5640	3756	A079	376	381	378	370	188.7	8.1	19.6	6.4	282.3	23.9	19.4	9.2	81.2	64.6	9.2	7.0	1.03	0.56
6.0657	116.5639	3743	A080	12664	13064	12837	12090	126.7	13.1	7.3	3.5	221.7	20.3	7.3	2.4	6.0	65.5	4.0	1.5	1.08	0.55
6.0655	116.5653	3689	A081	6590	6835	6715	6219	306.5	4.0	21.1	4.4	215.6	13.1	21.1	2.9	53.3	76.3	4.5	2.7	1.11	0.63
6.0653	116.5675	3655	A082	11992	12471	12024	11480	296.6	0.9	6.7	2.9	206.6	0.6	6.7	4.3	85.4	88.9	4.3	2.9	1.09	0.13
6.0646	116.5677	3592	A083	4199	4348	4189	4062	125.2	3.5	6.2	3.2	216.8	24.9	7.4	5.8	27.6	64.8	7.7	3.3	1.07	-0.13
6.0640	116.5669	3556	A084	4112	4231	4164	3940	303.2	0.8	20.6	3.1	212.8	26.6	20.9	6.4	34.7	63.4	8.0	2.2	1.08	0.54
6.0632	116.5673	3512	A085	16850	17352	17022	16175	286.3	11.7	9.2	4.4	192.4	18.2	9.2	2.6	47.3	68.1	4.6	2.7	1.08	0.43
6.0622	116.5675	3454	A086	16889	17581	17018	16067	300.3	6.9	6.2	2.4	208.4	15.1	6.4	4.9	54.0	73.3	5.8	1.9	1.10	0.29
6.0609	116.5664	3357	A087	6880	7274	6864	6502	296.3	5.0	6.1	1.9	204.6	18.7	6.2	2.0	40.8	70.6	4.1	1.9	1.12	-0.01
6.0601	116.5656	3298	A088	8623	9103	8756	8008	300.8	5.2	4.2	1.0	207.8	30.3	4.4	1.6	39.5	59.1	2.1	1.0	1.14	0.38
6.0588	116.5652	3246	A089a	13813	14398	14313	12728	310.0	22.1	15.8	1.5	218.5	3.7	15.8	3.1	119.4	67.5	3.4	1.0	1.15	0.91
6.0589	116.5652	3256	A089b	5863	6087	6019	5482	274.2	27.7	7.1	1.8	10.0	10.8	7.1	1.1	119.2	59.9	2.1	1.1	1.12	0.75
6.0589	116.5653	3242	A089c	9513	10308	9704	8529	127.7	9.7	2.6	1.1	225.5	38.6	2.6	1.7	26.1	49.7	2.0	1.1	1.21	0.37
6.0705	116.5647	3946	A093	565	573	566	557	52.6	14.2	15.4	4.6	314.0	30.4	17.3	7.4	164.3	55.8	11.1	4.5	1.03	0.22
6.0698	116.5652	3976	A096	831	843	837	812	20.9	3.1	17.3	4.9	290.3	10.4	17.2	6.0	127.2	79.2	6.3	5.2	1.04	0.63
6.0709	116.5635	3979	A099	11805	12192	11973	11250	332.5	5.2	11.1	1.6	240.3	24.0	11.4	3.1	73.9	65.4	4.3	1.5	1.09	0.54
6.0686	116.5659	3889	A106	8046	8376	8113	7648	308.6	5.1	12.5	2.4	217.2	16.4	13.0	4.6	55.3	72.8	7.9	2.1	1.10	0.39
6.0668	116.5670	3741	A112	10756	11063	10881	10325	114.4	5.0	7.7	2.2	206.1	18.7	7.6	2.5	9.9	70.6	2.9	2.1	1.07	0.54
6.0514	116.5637	2964	A115	15610	17097	15656	14079	342.6	12.6	5.0	2.9	249.4	14.1	4.7	1.8	112.8	71.0	4.5	1.2	1.21	0.09
6.0752	116.5697	3369	A126	26139	27052	26429	24936	305.0	1.7	19.0	1.6	214.4	18.4	22.8	2.5	39.9	71.5	13.4	1.7	1.09	0.42
6.0747	116.5697	3389	A127	21919	22798	22403	20556	324.9	5.3	4.3	1.2	232.7	22.7	4.3	1.2	67.4	66.6	1.9	1.4	1.12	0.66
6.0729	116.5704	3489	A128	14960	15424	15176	14280	112.3	1.2	7.7	1.6	202.7	17.3	8.3	6.5	18.5	72.7	7.2	1.7	1.08	0.57
6.0705	116.5703	3611	A129	14927	15814	14942	14025	280.1	11.5	3.9	1.1	186.4	17.5	4.1	1.8	41.9	68.8	2.7	1.0	1.13	0.05
6.0697	116.5709	3677	A130	16096	16994	15966	15328	277.4	1.8	1.8	1.5	187.4	0.7	3.2	1.6	76.5	88.0	3.2	1.6	1.11	-0.21
6.0684	116.5704	3768	A131	11010	11454	10927	10649	280.9	1.3	3.7	1.5	190.6	12.3	3.6	3.1	16.8	77.6	3.1	1.8	1.08	-0.27

A3.1. (*cont.*)

				Magnetic Susceptibility, x 10^6 SI (K)				K_1		95% angles in plane		K_2		95% angles in plane		K_3		95% angles in plane		Jelenick parameters	
Lat.	Long.	Height (AMSL) m	Sample	K_{mean}	K_1	K_2	K_3	Dec.	Dip	K_1-K_2	K_1-K_3	Dec.	Dip	K_1-K_2	K_2-K_3	Dec.	Dip	K_1-K_3	K_2-K_3	P'	T
6.0682	116.5690	3862	A132	5844	6000	5928	5604	313.2	13.7	6.8	0.8	214.4	32.3	6.9	1.9	63.0	54.3	1.9	0.8	1.08	0.63
6.0639	116.5726	3482	A138	10890	11312	11180	10177	333.9	19.1	6.1	0.9	237.8	17.2	6.1	1.3	108.8	63.8	1.5	0.7	1.12	0.80
6.0639	116.5740	3531	A139	9955	10442	10131	9293	127.7	2.3	3.4	2.5	218.6	20.9	4.0	3.4	31.7	69.0	4.6	1.1	1.13	0.48
6.0876	116.5775	3779	A140	11864	12086	11954	11553	88.5	1.7	7.5	1.9	357.7	25.9	9.5	4.8	182.0	64.0	7.9	2.3	1.05	0.52
6.0838	116.5789	3697	A141	22616	23359	22676	21813	353.8	18.3	5.3	2.1	93.2	26.3	10.9	3.6	233.1	57.1	10.2	2.4	1.07	0.15
6.0729	116.5783	4061	A148	14737	15131	14889	14192	69.5	13.6	7.3	3.5	168.9	33.8	5.6	0.8	320.9	52.8	5.9	0.8	1.07	0.50
6.0665	116.5815	3769	A152	26515	28086	26706	24754	344.6	11.1	3.0	1.4	250.9	18.2	2.8	2.8	104.4	68.5	2.9	1.7	1.14	0.21
6.0658	116.5794	3779	A154	11144	11609	11182	10641	131.0	9.4	11.3	3.3	40.4	3.4	11.2	5.5	290.9	80.0	5.9	3.2	1.09	0.12
6.0638	116.5739	3508	A155	30282	31952	30912	27982	333.3	50.2	2.8	0.9	235.7	6.3	2.9	2.4	140.5	39.1	2.5	0.9	1.15	0.51
6.0734	116.5844	3888	A162	20620	21034	20862	19965	210.1	6.2	11.3	3.5	305.3	39.6	11.5	2.8	112.7	49.8	3.9	2.7	1.06	0.70
6.0814	116.5867	3332	A167	11470	11639	11619	11151	316.5	24.1	79.6	3.5	59.2	26.2	79.6	4.6	190.1	53.0	4.7	3.7	1.05	0.91
6.0807	116.5892	3278	A168	3961	3996	3956	3931	65.7	11.1	11.6	7.5	324.1	45.6	32.4	10.1	166.0	42.3	31.9	7.4	1.02	-0.17
6.0793	116.5909	3513	A170	15051	15426	15154	14575	70.8	17.0	3.0	1.7	325.1	41.5	3.6	2.8	177.7	43.6	3.4	1.8	1.06	0.38
6.0814	116.5927	3512	A171	12094	12368	12025	11890	83.2	20.7	4.1	1.6	334.6	40.2	8.8	3.8	193.5	42.6	8.7	2.0	1.04	-0.44
6.0494	116.5891	2716	A190	41251	43309	41769	38674	91.9	13.9	3.8	1.3	206.1	58.9	3.7	1.7	354.6	27.2	1.8	1.4	1.12	0.36
6.0527	116.5982	2047	A198	31777	32629	31784	30917	123.7	52.0	7.4	3.1	285.8	36.6	13.1	6.8	22.4	8.8	12.8	3.2	1.06	0.03
6.0024	116.6361	1160	A210	1007	1020	1015	987	249.5	4.8	12.1	2.0	339.7	2.5	12.7	4.4	97.3	84.6	6.1	1.6	1.04	0.69
6.0022	116.6361	1147	A211	3280	3370	3305	3164	285.8	30.3	4.9	4.0	27.6	19.3	4.9	2.7	145.1	52.9	4.3	2.5	1.07	0.38
6.1243	116.5714	2536	A216	1727	1755	1726	1702	60.0	73.0	6.5	3.8	219.8	16.0	11.3	5.2	311.4	5.6	11.0	4.4	1.03	-0.09
6.1221	116.5750	2767	A217	6835	7037	6919	6547	276.4	45.1	9.9	1.9	25.0	17.6	9.8	3.4	130.3	39.6	3.9	2.0	1.08	0.51
6.1224	116.5738	2724	A218	6000	6178	6077	5745	295.7	40.1	8.6	2.9	37.5	13.7	8.5	4.2	142.6	46.6	5.5	1.7	1.08	0.54
6.1241	116.5722	2605	A219	7589	7804	7689	7274	281.9	71.3	11.7	4.0	23.0	3.7	12.1	3.6	114.2	18.3	5.2	3.5	1.08	0.58
6.0740	116.6282	3008	A236	6185	6415	6196	5945	333.2	28.2	4.7	2.3	206.5	48.1	4.8	3.8	79.9	28.2	3.9	2.3	1.08	0.10
6.0738	116.6168	3126	A237	6885	7056	6881	6717	126.3	29.0	14.8	3.0	24.6	20.2	17.2	4.5	264.8	53.5	10.1	2.5	1.05	0.01
6.0737	116.6154	3109	A240	17521	17732	17603	17227	60.4	32.1	7.5	2.1	186.8	43.4	7.5	3.2	309.5	29.7	3.3	2.2	1.03	0.52
6.0733	116.6143	3134	A241	17060	17278	17141	16761	303.0	8.5	24.9	3.3	56.5	69.6	24.9	4.6	210.1	18.5	4.8	3.3	1.03	0.52
6.0731	116.6126	3132	A242	3202	3221	3208	3178	195.6	25.1	29.3	11.3	301.2	29.9	37.8	19.6	72.8	49.1	32.0	9.9	1.01	0.43
6.0682	116.6094	2855	A244	3356	3395	3346	3328	30.2	45.8	5.6	4.2	300.2	0.1	14.5	4.4	210.1	44.2	14.5	5.4	1.02	-0.50
6.0791	116.5259	1886	A282	10022	10212	10109	9746	322.6	28.7	10.7	5.3	73.1	32.6	11.0	3.4	200.9	43.8	5.5	3.9	1.05	0.57
6.0800	116.5298	2150	A285	9756	10000	9906	9363	129.1	36.7	9.5	2.1	336.1	50.1	9.6	2.2	229.4	13.5	2.8	1.7	1.07	0.70
6.0798	116.5350	2444	A286	10710	11068	10898	10164	72.3	61.1	4.8	1.6	341.1	0.7	5.0	1.5	250.7	28.9	2.2	1.6	1.09	0.66
6.0649	116.5213	1152	A290b	353	357	354	347	252.0	19.7	6.4	2.0	343.9	5.2	6.4	3.7	88.1	69.6	3.9	2.0	1.03	0.32

Appendix A4: Geochemical data from Mt Kinabalu

A4.1. Whole rock Major and trace element data from Mt Kinabalu.

* Majors from Sperber (2009)			*		*	*					
Lat.			6.0728	6.0784	6.0763	6.0756	6.0790	6.0818	6.0767	6.0748	6.0712
			116.55	116.55	116.55	116.55	116.55	116.54	116.54	116.55	116.55
Long.			70	13	02	37	00	92	90	00	33
Height (AMSL), m			4030	3827	3929	3959	3803	3684.11	3991.24	3835.27	3891.51
			Alex. Gd	Alex. Gd	Alex. Gd	Alex. Gd	Alex. Gd	Alex. Gd	Alex. Gd	Alex. Gd	Alex. Gd
Element	Prep.	Analysis	CS016	CS021	CS022	CS023	CS036	A042	A047	A049	A054
(wt%)											
SiO_2	F	XRF	63.26	61.53	62.62	62.19	62.68	64.91	61.38	63.11	61.67
TiO_2	F	XRF	0.65	0.68	0.66	0.72	0.66	0.54	0.63	0.68	0.66
Al_2O_3	F	XRF	15.99	15.87	15.85	16.10	15.56	16.13	16.07	16.15	15.75
FeO_{TOT}	F	XRF	5.14	5.84	5.42	5.70	5.53	4.54	5.81	3.37	5.79
MnO	F	XRF	0.10	0.10	0.10	0.10	0.10	0.06	0.11	0.06	0.11
MgO	F	XRF	2.72	3.23	3.24	3.39	3.10	2.23	3.40	3.19	3.32
CaO	F	XRF	4.73	5.28	5.54	5.84	5.14	4.61	5.49	7.27	5.35
Na_2O	F	XRF	2.66	2.57	2.69	2.78	2.46	2.65	2.52	3.86	2.44
K_2O	F	XRF	3.30	2.64	2.55	2.02	2.67	2.89	2.31	0.65	2.59
P_2O_5	F	XRF	0.18	0.18	0.19	0.20	0.18	0.17	0.18	0.19	0.18
Total			99.30	99.44	99.46	99.67	99.53	99.90	107.60	99.50	99.42
LOI			0.73	0.87	0.57	1.00	0.84	0.66	1.06	0.60	0.92
ppm											
Ta	F	ICP-MS	0.78	0.71	0.66	0.68	0.66	0.82	0.64	0.70	0.67
Sc	HF	ICP-MS	14.20	22.04	17.91	21.34	21.54	12.94	20.47	21.04	20.45
V	HF	ICP-MS	100.34	187.45	142.53	166.38	167.06	101.80	176.00	185.70	173.00
Cr	HF	ICP-MS	42.20	58.87	50.84	56.45	57.66	35.12	62.96	68.52	65.45
Ga	HF	ICP-MS	13.97	17.75	14.50	17.62	17.67	17.68	17.94	19.26	17.71
Co	HF	ICP-MS	10.89	15.47	13.14	15.11	15.29	10.71	16.32	10.03	16.01
Ni	HF	ICP-MS	24.91	16.65	18.99	15.39	14.60	11.44	17.18	33.45	16.82
Cu	HF	ICP-MS	3.73	35.34	12.23	5.12	23.57	7.39	22.66	4.21	17.64
Zn	HF	ICP-MS	40.50	48.60	44.49	34.90	50.79	38.10	54.04	26.07	59.54
Cs	F	ICP-MS	9.17	9.45	9.41	7.71	8.25	9.57	9.71	4.10	9.00
Rb	HF	ICP-MS	103.26	102.26	86.82	92.40	98.63	107.30	83.80	22.90	93.55
Ba	HF	ICP-MS	770.96	901.42	924.83	925.12	890.96	834.60	816.00	257.10	865.50
Sr	HF	ICP-MS	193.66	239.28	214.07	249.52	248.24	255.50	247.10	332.00	257.90
Zr	F	ICP-MS	171.00	143.40	136.20	154.30	136.60	167.20	143.30	154.90	148.60
Hf	F	ICP-MS	4.51	4.14	3.68	4.23	3.64	4.50	3.97	4.18	4.05
Th	F	ICP-MS	11.58	10.09	8.86	9.87	10.22	11.53	8.92	10.45	12.42
U	F	ICP-MS	2.12	2.20	1.87	2.10	1.86	2.39	2.02	2.64	2.49
Pb	HF	ICP-MS	11.20	7.18	8.98	4.58	7.14	10.59	9.42	6.87	9.94
Nb	F	ICP-MS	10.13	8.80	8.07	8.56	8.40	10.10	8.24	9.03	8.65
Y	F	ICP-MS	22.52	20.87	19.88	20.27	20.08	18.52	21.26	25.60	21.19
La	HF	ICP-MS	24.34	21.00	20.17	21.33	20.53	21.73	19.17	15.94	19.94
Ce	F	ICP-MS	53.38	49.06	40.01	44.14	42.32	53.30	42.83	45.58	45.92
Pr	F	ICP-MS	5.97	5.52	4.16	4.60	4.39	5.82	5.27	5.81	5.10
Nd	F	ICP-MS	24.07	22.08	19.01	20.75	19.73	23.51	19.03	25.89	21.24
Sm	F	ICP-MS	4.59	4.36	3.91	4.14	4.01	4.44	4.28	5.36	4.20
Eu	F	ICP-MS	0.98	1.01	0.96	0.97	0.93	0.99	1.03	1.16	1.03
Gd	F	ICP-MS	4.20	4.11	3.63	3.86	3.74	3.67	4.17	5.00	3.88
Tb	F	ICP-MS	0.60	0.62	0.56	0.60	0.59	0.55	0.61	0.76	0.60
Dy	F	ICP-MS	3.55	3.60	3.29	3.47	3.35	3.09	3.60	4.35	3.52
Ho	F	ICP-MS	0.73	0.74	0.67	0.71	0.67	0.62	0.75	0.88	0.71
Er	F	ICP-MS	1.96	1.94	1.85	1.94	1.83	1.67	2.05	2.41	1.95
Tm	F	ICP-MS	0.28	0.28	0.31	0.34	0.31	0.26	0.24	0.38	0.31
Yb	F	ICP-MS	2.12	2.09	1.92	2.00	1.91	1.75	2.14	2.54	2.05
Lu	F	ICP-MS	0.34	0.36	0.31	0.32	0.32	0.28	0.35	0.40	0.34

F = Flux fusion + acid dissolution
HF = Standard HF dissolution

A4.1.a. Whole rock Alexandra Gd data.

* Majors from Sperber (2009)

Lat.			6.1235	6.0831	6.1224	6.0310	6.0741	6.0750	6.0768	6.0788	6.1214
			116.572	116.553	116.573	116.725	116.558	116.558	116.557	116.557	116.577
Long.			0	8	8	1	4	7	1	0	6
Height (AMSL), m			2586	3945	0	0	0	4096	3947	3847	3025
			Low's Gt	Low's Gt	Low's Gt	Low's Gt	Low's Gt	Low's Gt	Low's Gt	Low's Gt	Low's Gt
Element	Prep	Analysis	CS077	A046	A218	SBK121	SBK122	CS018	CS019	CS020	CS081
(wt%)											
SiO_2	F	XRF	60.88	60.21	59.65	60.40	57.48	60.45	60.39	59.38	59.84
TiO_2	F	XRF	0.63	0.66	0.68	0.71	0.83	0.67	0.69	0.67	0.67
Al_2O_3	F	XRF	14.96	15.29	15.29	15.25	15.48	14.96	15.13	15.07	15.02
FeO_{TOT}	F	XRF	6.07	6.19	6.56	6.74	7.59	6.44	6.56	6.43	6.52
MnO	F	XRF	0.11	0.13	0.12	0.13	0.16	0.12	0.13	0.12	0.12
MgO	F	XRF	3.59	3.94	3.87	4.05	5.16	3.72	3.83	3.74	3.87
CaO	F	XRF	5.47	6.36	5.80	6.57	7.74	5.87	6.55	6.30	6.20
Na_2O	F	XRF	2.37	2.40	2.37	2.31	2.52	2.44	2.50	2.50	2.48
K_2O	F	XRF	3.68	2.69	3.44	2.73	1.79	3.62	2.99	3.34	3.40
P_2O_5	F	XRF	0.26	0.24	0.28	0.30	0.29	0.27	0.29	0.27	0.28
Total			99.75	99.84	100.02	99.94	99.89	99.28	99.79	99.12	99.75
LOI			1.05	1.05	1.23	1.24	0.98	0.50	0.93	0.58	0.61
ppm											
Ta	F	ICP-MS	0.58	0.62	0.63	0.66	0.67	0.62	0.60	0.70	0.70
Sc	HF	ICP-MS	21.35	21.79	22.11	17.88	22.24	17.97	18.30	17.12	25.38
V	HF	ICP-MS	184.49	188.30	201.10	151.50	177.51	151.41	155.76	151.54	211.19
Cr	HF	ICP-MS	75.68	92.40	82.55	62.35	99.86	61.20	63.80	60.12	86.95
Ga	HF	ICP-MS	16.65	16.93	17.67	13.74	14.70	13.81	14.17	14.05	17.65
Co	HF	ICP-MS	20.25	20.39	20.47	16.33	19.04	16.95	17.04	16.47	23.59
Ni	HF	ICP-MS	18.23	22.27	20.15	13.11	20.77	14.60	13.89	13.14	21.19
Cu	HF	ICP-MS	43.11	28.37	52.02	1052.8	9.31	29.28	62.40	38.56	59.84
Zn	HF	ICP-MS	50.76	59.52	54.50	71.75	57.12	45.11	45.67	48.48	58.31
Cs	F	ICP-MS	11.32	5.46	11.75	9.12	5.27	11.57	8.93	9.73	10.08
Rb	HF	ICP-MS	117.35	68.08	119.50	74.43	48.31	107.97	90.63	83.41	119.46
Ba	HF	ICP-MS	847.28	856.00	854.30	977.93	773.49	1010.8	867.50	863.25	912.61
Sr	HF	ICP-MS	273.97	310.30	300.70	243.30	256.47	238.73	252.41	266.49	314.28
Zr	F	ICP-MS	125.60	141.20	126.90	130.20	122.20	111.00	120.40	142.70	140.00
Hf	F	ICP-MS	3.42	3.78	3.44	3.53	3.45	3.16	3.34	3.93	3.92
Th	F	ICP-MS	12.17	10.20	8.98	9.58	8.72	10.01	10.14	10.00	10.14
U	F	ICP-MS	2.48	2.30	2.24	2.44	2.01	2.24	2.26	2.27	2.44
Pb	HF	ICP-MS	12.95	13.22	12.43	12.22	10.27	11.73	11.47	13.71	12.79
Nb	F	ICP-MS	7.03	7.81	14.89	7.99	8.83	7.09	7.81	8.04	8.01
Y	F	ICP-MS	17.84	19.71	20.40	20.37	22.93	17.88	19.79	19.44	19.82
La	HF	ICP-MS	17.32	18.41	22.52	19.26	21.52	19.90	20.12	19.73	26.52
Ce	F	ICP-MS	37.70	43.87	40.88	40.60	45.65	39.31	41.47	44.03	44.20
Pr	F	ICP-MS	4.03	4.82	5.12	4.67	5.36	4.19	4.80	4.87	5.11
Nd	F	ICP-MS	18.46	20.01	17.74	19.63	22.32	19.01	20.40	20.63	20.81
Sm	F	ICP-MS	3.76	4.07	4.23	4.09	4.77	3.87	4.18	4.22	4.22
Eu	F	ICP-MS	0.98	0.99	1.13	1.01	1.15	0.97	1.00	1.03	1.03
Gd	F	ICP-MS	3.50	3.73	4.04	3.84	4.36	3.62	3.82	3.93	3.88
Tb	F	ICP-MS	0.53	0.56	0.60	0.55	0.65	0.54	0.58	0.57	0.57
Dy	F	ICP-MS	3.10	3.24	3.31	3.23	3.75	3.15	3.28	3.28	3.34
Ho	F	ICP-MS	0.61	0.64	0.65	0.66	0.75	0.62	0.66	0.66	0.67
Er	F	ICP-MS	1.67	1.78	1.76	1.78	1.97	1.70	1.80	1.79	1.78
Tm	F	ICP-MS	0.29	0.27	0.13	0.25	0.27	0.29	0.27	0.27	0.24
Yb	F	ICP-MS	1.70	1.83	1.91	1.93	2.11	1.74	1.84	1.82	1.94
Lu	F	ICP-MS	0.29	0.30	0.31	0.33	0.34	0.29	0.30	0.31	0.32

F = Flux fusion + acid dissolution
HF = Standard HF dissolution

A4.1.b. Whole rock Low's Gt data

* Majors from Sperber (2009)					*	*	*	*			
Lat.			6.0733	6.0640	6.0640	6.0766	6.0788	6.0943	6.0970	6.0741	6.0632
			116.557	116.567	116.570	116.575	116.581	116.580	116.583	116.579	116.567
Long.			5	0	4	8	0	7	3	0	3
Height (AMSL), m			0	3577	3460	3918	3769	3657	3527	4007	3511.5
			King Gt	King Gt	King Gt	King Gt	King Gt	King Gt	King Gt	King Gt	King Gt
Element	Prep	Analysis	SBK123	CS011 c	CS028	CS031	CS066	CS069	CS070	CS072	A085
(wt%)											
SiO_2	F	XRF	64.04	64.40	64.39	63.59	62.06	64.01	65.56	64.96	64.92
TiO_2	F	XRF	0.53	0.52	0.52	0.52	0.53	0.55	0.55	0.47	0.52
Al_2O_3	F	XRF	14.81	14.53	15.13	15.12	15.63	15.30	15.22	14.84	15.12
FeO_{TOT}	F	XRF	5.04	4.35	4.68	4.89	5.57	5.22	3.90	4.64	3.55
MnO	F	XRF	0.09	0.07	0.09	0.10	0.12	0.11	0.08	0.10	0.05
MgO	F	XRF	2.81	2.74	2.60	2.32	2.41	2.82	2.83	2.39	2.68
CaO	F	XRF	4.86	4.68	4.39	5.25	5.32	3.85	4.91	4.53	5.15
Na_2O	F	XRF	2.61	2.71	2.69	2.78	2.73	2.21	3.58	2.64	4.09
K_2O	F	XRF	3.89	4.28	4.65	3.86	4.95	4.51	0.95	4.29	2.49
P_2O_5	F	XRF	0.20	0.23	0.24	0.26	0.29	0.23	0.24	0.21	0.22
Total			99.96	99.64	99.90	99.24	100.23	99.39	99.87	100.09	99.95
LOI			0.52	0.64	1.11	0.77	0.36	1.87	1.62	0.49	0.76
ppm											
Ta	F	ICP-MS	0.78	0.96	0.82	0.96	0.75	0.81	0.83	0.81	0.72
Sc	HF	ICP-MS	16.83	17.04	13.84	14.24	14.64	15.98	17.87	15.56	17.04
V	HF	ICP-MS	141.75	145.30	115.51	128.08	132.57	112.15	121.07	128.95	131.80
Cr	HF	ICP-MS	58.35	53.81	39.79	31.06	26.75	81.18	57.41	46.97	49.34
Ga	HF	ICP-MS	15.71	16.45	12.25	13.66	13.95	11.85	14.41	15.66	16.24
Co	HF	ICP-MS	15.37	12.67	12.58	10.94	12.59	13.63	13.73	14.30	10.39
Ni	HF	ICP-MS	14.41	12.77	8.78	5.70	4.66	42.73	17.58	12.31	14.64
Cu	HF	ICP-MS	41.01	30.50	21.90	5.70	40.82	8.18	3.68	33.83	8.18
Zn	HF	ICP-MS	41.66	43.02	44.54	30.50	34.30	80.77	32.93	44.58	32.12
Cs	F	ICP-MS	17.65	12.97	15.04	5.56	9.66	10.34	5.49	13.63	6.42
Rb	HF	ICP-MS	140.99	165.50	166.03	97.37	153.96	144.18	36.68	160.97	82.79
Ba	HF	ICP-MS	883.93	605.60	865.41	677.98	586.81	825.67	216.26	661.57	407.80
Sr	HF	ICP-MS	261.09	283.90	181.39	295.92	293.62	164.05	412.67	283.56	292.90
Zr	F	ICP-MS	132.80	149.80	132.70	155.10	205.90	137.50	149.00	120.10	136.80
Hf	F	ICP-MS	3.65	4.28	3.77	4.38	5.63	3.84	4.06	3.33	3.73
Th	F	ICP-MS	17.71	23.69	13.14	26.48	19.45	14.86	19.68	15.58	14.43
U	F	ICP-MS	3.83	5.20	3.17	5.18	4.99	3.30	2.78	3.57	3.36
Pb	HF	ICP-MS	13.04	18.06	25.07	13.03	21.02	23.53	9.10	19.13	20.50
Nb	F	ICP-MS	7.64	8.71	8.76	9.99	8.31	8.79	8.58	7.89	8.13
Y	F	ICP-MS	15.39	19.69	18.72	23.68	19.73	20.74	16.85	15.90	19.79
La	HF	ICP-MS	16.58	19.70	23.10	39.21	23.75	22.24	20.04	20.21	17.66
Ce	F	ICP-MS	37.63	50.81	42.66	73.18	51.13	47.99	39.64	37.50	41.98
Pr	F	ICP-MS	4.07	5.51	4.41	7.69	5.91	5.54	4.07	3.88	5.25
Nd	F	ICP-MS	16.15	22.13	20.19	30.22	23.75	22.37	18.02	17.11	19.19
Sm	F	ICP-MS	3.15	4.38	4.11	5.63	4.90	4.49	3.59	3.39	4.31
Eu	F	ICP-MS	0.78	1.07	0.90	1.16	1.13	0.98	0.78	0.87	1.06
Gd	F	ICP-MS	2.84	3.88	3.58	4.66	4.25	3.97	3.17	2.98	3.84
Tb	F	ICP-MS	0.40	0.60	0.55	0.71	0.60	0.57	0.48	0.45	0.55
Dy	F	ICP-MS	2.45	3.28	3.15	3.90	3.44	3.34	2.72	2.57	3.13
Ho	F	ICP-MS	0.48	0.67	0.61	0.78	0.68	0.68	0.56	0.52	0.65
Er	F	ICP-MS	1.29	1.84	1.73	2.13	1.85	1.80	1.53	1.43	1.75
Tm	F	ICP-MS	0.19	0.29	0.29	0.34	0.27	0.25	0.26	0.24	0.20
Yb	F	ICP-MS	1.47	1.95	1.85	2.26	2.11	1.96	1.68	1.54	1.89
Lu	F	ICP-MS	0.25	0.33	0.30	0.36	0.37	0.33	0.28	0.26	0.30

F = Flux fusion + acid dissolution
HF = Standard HF dissolution

A4.1.c. Whole rock King Gt data

* Majors from Sperber (2009)										
Lat.			6.0589	6.0729	6.0705	6.0684	6.0740	6.0738	6.0791	6.0800	6.0798
			116.56	116.57	116.57	116.57	116.62	116.61	116.52	116.52	116.53
Long.			53	04	03	04	82	68	59	98	50
Height (AMSL), m			3241.9	3488.96	3611.29	3767.98	3007.82	3126.3	1886.21	2150.33	2443.77
			King Gt	King Gt	King Gt	King Gt	King Gt	King Gt	King Gt	King Gt	King Gt
Element	Prep.	Analysis	A089c	A128	A129	A131	A236	A237	A282	A285	A286
(wt%)											
SiO_2	F	XRF	64.12	64.72	65.53	65.77	63.39	63.01	64.77	62.59	64.22
TiO_2	F	XRF	0.50	0.47	0.41	0.44	0.51	0.52	0.48	0.54	0.49
Al_2O_3	F	XRF	14.70	14.88	14.48	14.74	15.06	15.34	14.97	15.06	15.10
FeO_{TOT}	F	XRF	4.94	4.74	4.14	4.27	5.10	5.10	4.75	5.34	4.78
MnO	F	XRF	0.09	0.09	0.08	0.09	0.10	0.10	0.10	0.10	0.10
MgO	F	XRF	2.54	2.40	2.08	2.19	2.64	2.64	2.41	2.78	2.47
CaO	F	XRF	4.61	4.60	4.18	4.18	4.15	3.60	3.39	4.34	3.76
Na_2O	F	XRF	2.56	2.72	2.60	2.66	2.36	2.14	2.16	2.40	2.32
K_2O	F	XRF	4.52	4.40	4.57	4.58	4.34	4.56	4.73	4.50	4.54
P_2O_5	F	XRF	0.22	0.21	0.18	0.18	0.23	0.24	0.20	0.24	0.21
Total			99.90	100.32	99.32	100.05	100.02	100.15	100.30	100.03	100.10
LOI			0.54	0.56	0.60	0.47	1.57	2.33	1.81	1.55	1.59
ppm											
Ta	F	ICP-MS	0.75	0.64	0.69	0.82	0.73	0.75	0.78	0.68	0.68
Sc	HF	ICP-MS	15.81	14.28	12.29	12.75	15.73	16.03	14.67	17.29	15.47
V	HF	ICP-MS	134.80	123.80	110.70	111.30	134.50	132.90	125.40	147.00	125.80
Cr	HF	ICP-MS	45.75	41.78	37.58	38.94	47.08	47.23	43.60	51.33	44.68
Ga	HF	ICP-MS	16.09	15.76	15.33	15.49	16.10	15.91	16.15	16.56	15.92
Co	HF	ICP-MS	13.29	14.05	12.07	12.74	14.72	15.20	13.62	15.01	14.33
Ni	HF	ICP-MS	12.27	11.72	10.25	11.86	12.83	12.77	11.87	13.62	11.87
Cu	HF	ICP-MS	56.78	26.90	22.19	9.50	18.93	14.43	11.64	16.00	14.52
Zn	HF	ICP-MS	43.56	39.86	32.78	40.89	48.25	49.98	44.44	43.56	42.65
Cs	F	ICP-MS	18.75	8.65	9.55	17.32	8.88	10.45	13.48	9.93	12.66
Rb	HF	ICP-MS	188.70	158.30	174.60	197.10	155.20	173.70	187.40	167.30	189.50
Ba	HF	ICP-MS	650.50	680.00	623.10	644.00	653.50	720.80	576.50	700.20	679.00
Sr	HF	ICP-MS	296.70	314.10	293.20	288.70	256.80	232.80	195.70	271.00	244.30
Zr	F	ICP-MS	127.60	135.70	126.70	128.60	140.30	136.10	140.10	142.20	130.40
Hf	F	ICP-MS	3.45	3.63	3.42	3.68	3.81	3.83	4.03	3.91	3.67
Th	F	ICP-MS	42.61	21.66	15.98	18.84	18.69	17.14	17.57	9.04	16.97
U	F	ICP-MS	5.14	4.47	3.87	5.19	3.78	3.50	4.23	2.74	4.00
Pb	HF	ICP-MS	21.76	16.64	16.14	20.48	18.89	20.58	16.74	17.85	16.41
Nb	F	ICP-MS	8.01	7.17	6.77	7.54	7.86	8.06	7.73	7.57	7.57
Y	F	ICP-MS	17.37	16.30	15.03	14.99	18.18	18.35	17.36	18.14	16.82
La	HF	ICP-MS	18.95	19.85	17.88	21.09	19.84	23.63	21.35	17.06	20.48
Ce	F	ICP-MS	37.62	38.99	34.07	38.23	43.21	49.15	45.40	40.82	46.25
Pr	F	ICP-MS	4.67	4.42	4.05	4.51	4.85	5.21	4.91	4.72	4.87
Nd	F	ICP-MS	16.30	18.30	13.79	14.96	20.19	21.50	19.84	19.69	19.83
Sm	F	ICP-MS	3.79	3.66	3.22	3.38	4.03	4.13	3.80	3.98	3.82
Eu	F	ICP-MS	0.96	0.91	0.87	0.88	0.97	1.00	0.92	0.97	0.93
Gd	F	ICP-MS	3.42	3.18	2.83	3.10	3.40	3.62	3.33	3.56	3.30
Tb	F	ICP-MS	0.49	0.48	0.41	0.44	0.51	0.54	0.50	0.52	0.49
Dy	F	ICP-MS	2.87	2.70	2.37	2.58	2.97	3.08	2.79	3.01	2.77
Ho	F	ICP-MS	0.56	0.54	0.48	0.51	0.60	0.62	0.58	0.61	0.56
Er	F	ICP-MS	1.56	1.49	1.30	1.36	1.65	1.73	1.58	1.61	1.54
Tm	F	ICP-MS	0.16	0.24	0.11	0.12	0.26	0.27	0.25	0.26	0.25
Yb	F	ICP-MS	1.67	1.63	1.48	1.55	1.74	1.83	1.68	1.76	1.65
Lu	F	ICP-MS	0.27	0.26	0.24	0.25	0.28	0.30	0.28	0.29	0.27

F = Flux fusion + acid dissolution
HF = Standard HF dissolution

A4.1.c. (*cont.*)

* Majors from Sperber (2009)							
Lat.			6.0880	6.0705	6.0747	6.0819	6.0665
Long.			116.5780	116.5647	116.5697	116.5780	116.5640
Height (AMSL), m			3767	3946.06	3389.22	3805.71	3755.96
			Donkey Gt	Donkey Gt	Donkey Gt	Donkey Gt	Donkey Gt
Element	Prep.	Analysis	CS033	A093	A127	A145	A079
(wt%)							
SiO_2	F	XRF	64.06	64.63	63.08	62.56	64.34
TiO_2	F	XRF	0.48	0.54	0.49	0.52	0.57
Al_2O_3	F	XRF	14.76	14.70	15.16	15.32	14.89
FeO_{TOT}	F	XRF	5.04	4.72	4.95	5.03	4.85
MnO	F	XRF	0.11	0.09	0.10	0.10	0.09
MgO	F	XRF	2.17	2.60	2.30	2.41	2.75
CaO	F	XRF	4.73	4.21	5.01	5.08	4.38
Na_2O	F	XRF	2.77	2.41	2.76	2.62	2.43
K_2O	F	XRF	5.03	4.29	4.39	4.84	4.26
P_2O_5	F	XRF	0.25	0.22	0.24	0.25	0.23
Total			100.25	99.71	99.36	99.80	99.93
LOI			0.29	0.76	0.33	0.51	0.59
ppm							
Ta	F	ICP-MS	0.92	0.83	0.62	0.75	0.83
Sc	HF	ICP-MS	15.30	16.01	14.74	15.22	16.11
V	HF	ICP-MS	139.25	117.00	139.30	144.40	119.10
Cr	HF	ICP-MS	27.98	47.09	35.63	35.96	50.97
Ga	HF	ICP-MS	15.96	16.57	16.61	17.40	16.77
Co	HF	ICP-MS	14.41	12.50	14.04	14.02	12.68
Ni	HF	ICP-MS	7.88	11.29	10.00	10.09	12.36
Cu	HF	ICP-MS	23.21	16.69	26.39	31.78	26.31
Zn	HF	ICP-MS	44.63	59.55	40.96	32.48	58.49
Cs	F	ICP-MS	12.25	17.95	8.15	7.87	13.81
Rb	HF	ICP-MS	202.78	178.60	150.80	182.00	177.10
Ba	HF	ICP-MS	567.97	561.90	646.80	675.60	591.90
Sr	HF	ICP-MS	328.89	302.80	360.20	361.20	322.80
Zr	F	ICP-MS	134.70	161.60	138.90	154.30	179.90
Hf	F	ICP-MS	4.07	4.62	3.80	4.19	4.77
Th	F	ICP-MS	24.40	20.90	17.42	17.01	14.69
U	F	ICP-MS	6.14	4.10	3.66	2.73	3.14
Pb	HF	ICP-MS	20.45	24.38	16.22	13.65	21.75
Nb	F	ICP-MS	8.80	9.76	7.49	7.59	10.29
Y	F	ICP-MS	20.18	21.73	20.01	19.24	22.27
La	HF	ICP-MS	22.70	26.84	17.73	19.40	24.07
Ce	F	ICP-MS	47.97	60.79	44.21	41.95	54.53
Pr	F	ICP-MS	5.62	6.67	5.08	5.17	6.63
Nd	F	ICP-MS	22.74	27.12	22.00	18.05	23.68
Sm	F	ICP-MS	4.60	5.24	4.38	4.21	5.22
Eu	F	ICP-MS	1.03	1.13	1.09	1.08	1.21
Gd	F	ICP-MS	3.94	4.45	3.84	3.83	4.63
Tb	F	ICP-MS	0.55	0.66	0.57	0.55	0.66
Dy	F	ICP-MS	3.04	3.73	3.23	3.12	3.77
Ho	F	ICP-MS	0.62	0.76	0.67	0.62	0.75
Er	F	ICP-MS	1.74	2.08	1.80	1.67	2.14
Tm	F	ICP-MS	0.25	0.32	0.29	0.16	0.24
Yb	F	ICP-MS	2.05	2.20	1.88	1.90	2.26
Lu	F	ICP-MS	0.34	0.36	0.31	0.30	0.36

F = Flux fusion + acid dissolution
HF = Standard HF dissolution

A4.1.d. Whole rock Donkey Gt data.

* Majors from Sperber (2009)			*	*				
Lat.			6.0565	6.0514	6.0555	6.0638	6.0734	6.0649
Long.			116.5646	116.5639	116.5647	116.5739	116.5844	116.5213
Height (AMSL), m			0	0	3096	3508.18	3888.38	1152.49
			Paka Pph	Paka Pph	Paka Pph	Paka Pph	Paka Pph	Paka Pph
Element	Prep.	Analysis	SBK128	SBK130	CS027	A155	A162	A290b
(wt%)								
SiO_2	F	XRF	64.25	66.53	66.11	64.46	63.17	67.10
TiO_2	F	XRF	0.52	0.45	0.45	0.47	0.50	0.39
Al_2O_3	F	XRF	14.55	14.84	14.71	14.49	14.70	14.69
FeO_{TOT}	F	XRF	5.14	4.48	4.08	4.76	5.09	4.58
MnO	F	XRF	0.10	0.09	0.07	0.10	0.10	0.16
MgO	F	XRF	2.40	1.96	2.02	2.13	2.44	1.82
CaO	F	XRF	4.60	3.45	3.84	4.41	4.70	3.19
Na_2O	F	XRF	2.65	2.08	2.43	2.73	2.67	2.46
K_2O	F	XRF	4.98	4.97	5.30	4.87	4.92	3.65
P_2O_5	F	XRF	0.27	0.22	0.22	0.24	0.25	0.22
Total			100.03	99.57	100.07	99.56	99.59	100.04
LOI			0.20	1.38	0.38	0.38	0.47	1.26
ppm								
Ta	F	ICP-MS	1.01	1.11	0.90	0.82	0.88	0.89
Sc	HF	ICP-MS	11.49	9.98	12.89	13.89	15.35	13.08
V	HF	ICP-MS	109.92	95.34	122.22	138.00	152.50	117.70
Cr	HF	ICP-MS	24.65	22.29	31.93	32.81	43.18	29.30
Ga	HF	ICP-MS	13.15	13.15	14.79	15.77	16.46	15.66
Co	HF	ICP-MS	9.20	9.55	14.23	13.87	15.40	11.24
Ni	HF	ICP-MS	6.99	5.18	9.78	9.73	12.53	8.57
Cu	HF	ICP-MS	105.34	47.95	143.70	35.64	44.41	6.03
Zn	HF	ICP-MS	26.23	30.63	31.11	39.30	36.46	77.49
Cs	F	ICP-MS	7.90	11.14	10.74	16.77	12.16	10.66
Rb	HF	ICP-MS	175.83	170.41	233.82	224.00	221.80	164.20
Ba	HF	ICP-MS	511.13	469.77	441.85	463.70	579.50	484.40
Sr	HF	ICP-MS	270.88	209.50	300.51	344.00	377.30	343.40
Zr	F	ICP-MS	124.30	130.90	117.80	118.60	135.90	151.40
Hf	F	ICP-MS	3.89	4.09	3.52	3.43	4.05	4.59
Th	F	ICP-MS	27.64	30.93	28.21	10.54	26.72	31.73
U	F	ICP-MS	6.46	5.80	4.82	3.94	6.30	5.83
Pb	HF	ICP-MS	25.55	23.71	17.83	19.31	22.55	91.73
Nb	F	ICP-MS	9.00	9.74	8.19	8.33	8.85	8.86
Y	F	ICP-MS	18.11	22.11	18.19	18.70	18.91	26.69
La	HF	ICP-MS	19.98	30.43	28.31	17.42	24.71	32.08
Ce	F	ICP-MS	48.93	57.24	54.11	36.46	55.81	71.19
Pr	F	ICP-MS	5.85	6.70	5.55	4.81	6.23	7.87
Nd	F	ICP-MS	24.13	26.84	24.28	17.98	25.34	31.88
Sm	F	ICP-MS	4.97	5.14	4.45	4.37	4.97	6.30
Eu	F	ICP-MS	1.13	1.16	1.00	1.07	1.13	1.19
Gd	F	ICP-MS	4.16	4.21	3.67	3.94	4.00	5.06
Tb	F	ICP-MS	0.56	0.60	0.52	0.51	0.56	0.76
Dy	F	ICP-MS	3.13	3.37	2.90	3.00	3.14	4.26
Ho	F	ICP-MS	0.63	0.68	0.59	0.59	0.63	0.89
Er	F	ICP-MS	1.69	1.87	1.66	1.62	1.71	2.47
Tm	F	ICP-MS	0.25	0.27	0.29	0.14	0.28	0.41
Yb	F	ICP-MS	1.93	2.19	1.83	1.82	1.90	2.68
Lu	F	ICP-MS	0.33	0.37	0.31	0.29	0.30	0.43

F = Flux fusion + acid dissolution
HF = Standard HF dissolution

A4.1.e. Whole rock Paka Pph data

* Majors from Sperber (2009)						*					
Lat.			6.0665	6.0793	6.0595	6.0595	6.0814	6.0800	6.0723	6.0494	6.0527	6.0733
			116.58	116.59	116.59	116.59	116.58	116.59	116.60	116.58	116.59	116.61
Long.			15	09	36	40	67	99	12	91	82	43
Height (AMSL), m			3769	3513	2393	2393	3332	3133	3413	2715	2046	3134
			Mes Pph	Mes Pph	Mes Pph	Mes Pph	Mes Pph	Mes Pph	Mes Pph	Mes Pph	Mes Pph	Mes Pph
Element	Prep.	Analysis	A152	A170	CS055	CS056	A167	A172	A173	A190	A198	A241
(wt%)												
SiO_2	F	XRF	63.61	63.32	64.04	64.54	64.87	62.37	63.01	60.38	57.72	63.77
TiO_2	F	XRF	0.51	0.52	0.48	0.50	0.48	0.52	0.47	0.53	0.63	0.49
Al_2O_3	F	XRF	14.45	14.55	15.19	15.52	14.36	15.10	15.43	15.18	15.58	14.91
FeO_{TOT}	F	XRF	5.12	5.16	4.40	4.37	4.80	5.18	4.72	5.87	6.57	5.01
MnO	F	XRF	0.11	0.11	0.08	0.07	0.11	0.11	0.10	0.12	0.13	0.11
MgO	F	XRF	2.41	2.48	2.10	2.03	2.38	2.35	2.19	2.58	3.09	2.24
CaO	F	XRF	4.60	4.70	4.54	3.37	4.40	4.88	3.96	5.58	6.02	4.56
Na_2O	F	XRF	2.66	2.56	2.80	2.50	2.51	2.76	2.64	2.76	2.78	2.72
K_2O	F	XRF	4.82	4.81	4.67	6.16	4.70	4.80	5.13	4.82	5.37	4.71
P_2O_5	F	XRF	0.25	0.25	0.22	0.24	0.23	0.26	0.23	0.31	0.35	0.24
Total			99.49	99.55	100.08	99.79	100.06	99.41	99.43	99.21	99.47	99.96
LOI			0.38	0.50	1.06	1.68	0.69	0.50	1.02	0.43	0.50	0.64
ppm												
Ta	F	ICP-MS	1.00	0.76	0.59	0.61	0.81	0.77	0.59	0.45	0.46	0.80
Sc	HF	ICP-MS	15.17	15.93	14.02	10.44	14.47	14.90	14.12	16.24	19.88	14.88
V	HF	ICP-MS	146.10	153.50	135.70	92.37	139.40	151.30	134.20	177.70	204.20	145.70
Cr	HF	ICP-MS	41.46	49.28	36.54	20.51	44.92	37.89	39.13	28.72	47.90	35.15
Ga	HF	ICP-MS	16.72	16.07	16.62	13.17	15.97	17.40	16.70	17.01	16.82	16.87
Co	HF	ICP-MS	15.38	15.63	14.21	8.93	14.46	15.27	13.94	17.80	20.19	14.80
Ni	HF	ICP-MS	12.38	13.34	10.00	2.43	11.87	11.06	11.20	9.39	13.76	10.52
Cu	HF	ICP-MS	51.80	1.96	262.78	347.06	206.10	57.62	81.57	54.91	79.49	53.99
Zn	HF	ICP-MS	46.21	44.33	35.21	19.91	42.32	49.67	50.75	49.10	54.69	52.40
Cs	F	ICP-MS	12.99	9.55	7.34	8.36	12.39	12.42	10.94	8.89	10.93	13.41
Rb	HF	ICP-MS	225.00	216.60	238.44	221.90	203.00	209.60	216.90	182.20	206.80	219.70
Ba	HF	ICP-MS	446.30	460.90	379.01	450.60	368.30	560.10	610.70	729.00	853.70	446.10
Sr	HF	ICP-MS	343.20	365.50	419.03	334.79	335.40	425.20	410.10	438.30	505.40	386.30
Zr	F	ICP-MS	114.60	120.50	107.00	99.45	133.70	135.70	117.20	134.50	138.40	118.40
Hf	F	ICP-MS	3.34	3.42	3.03	2.83	3.76	3.86	3.28	3.48	3.49	3.50
Th	F	ICP-MS	19.12	28.49	26.15	26.17	15.11	25.16	21.88	22.20	15.67	28.05
U	F	ICP-MS	6.48	5.01	5.20	4.95	3.92	4.53	4.41	3.61	2.84	5.72
Pb	HF	ICP-MS	24.41	23.42	19.64	22.82	20.32	23.94	26.45	20.60	21.26	25.46
Nb	F	ICP-MS	9.32	7.94	6.75	6.69	8.02	8.65	7.04	5.82	6.36	8.38
Y	F	ICP-MS	20.02	16.92	14.53	13.87	17.93	19.62	16.67	13.81	17.35	19.24
La	HF	ICP-MS	21.62	24.77	20.97	26.07	25.69	25.95	25.01	20.53	20.57	27.37
Ce	F	ICP-MS	46.64	51.36	47.20	46.94	49.55	57.97	51.57	40.90	45.95	58.16
Pr	F	ICP-MS	5.92	5.69	5.04	4.96	5.99	6.54	5.76	4.48	5.45	6.59
Nd	F	ICP-MS	21.11	23.72	22.24	22.09	21.10	27.44	23.72	18.91	24.27	27.50
Sm	F	ICP-MS	4.83	4.66	4.38	4.07	4.75	5.35	4.65	3.72	4.92	5.30
Eu	F	ICP-MS	1.11	1.08	1.08	1.07	1.08	1.19	1.17	1.08	1.32	1.17
Gd	F	ICP-MS	4.31	3.74	3.44	3.15	4.31	4.19	3.69	3.07	4.12	4.14
Tb	F	ICP-MS	0.57	0.52	0.46	0.44	0.56	0.59	0.52	0.43	0.56	0.57
Dy	F	ICP-MS	3.12	2.86	2.53	2.36	3.06	3.18	2.81	2.31	3.02	3.20
Ho	F	ICP-MS	0.62	0.57	0.51	0.46	0.59	0.62	0.57	0.45	0.59	0.64
Er	F	ICP-MS	1.69	1.53	1.33	1.27	1.59	1.71	1.53	1.21	1.54	1.71
Tm	F	ICP-MS	0.15	0.24	0.23	0.22	0.14	0.28	0.24	0.19	0.24	0.27
Yb	F	ICP-MS	1.91	1.60	1.44	1.33	1.81	1.88	1.63	1.26	1.52	1.84
Lu	F	ICP-MS	0.31	0.27	0.24	0.23	0.30	0.31	0.28	0.22	0.25	0.30

F = Flux fusion + acid dissolution
HF = Standard HF dissolution

A4.1.f. Whole rock Mesilau Pph data

* Majors from Sperber (2009)					*	*		*		*	
Lat.			5.9769	6.0684	6.0682	6.0681	6.0838	6.0667	6.0478	6.0719	6.0684
			116.68	116.56	116.56	116.56	116.57	116.56	116.56	116.56	116.56
Long.			27	15	17	16	83	17	30	03	15
Height (AMSL), m			543.02	0	3823.5	3873	3728	0	2888	3980	0
			Mineralised Mes. Pph	Pyx Mon	Pyx Mon	Pyx Mon	Pyx Mon	Aplite	Aplite	Aplite	Lamp-rophyre
Element	Prep.	Analysis	A209	SBK126	SBK127c	CS014	CS071	SBK124	CS007	CS059	SBK125
(wt%)											
SiO_2	F	XRF	62.04	61.75	61.78	61.47	61.57	76.78	74.80	73.18	60.30
TiO_2	F	XRF	0.49	0.56	0.56	0.56	0.54	0.10	0.17	0.17	0.59
Al_2O_3	F	XRF	14.80	15.05	15.02	15.16	14.93	12.51	13.07	13.88	13.81
FeO_{TOT}	F	XRF	5.05	5.85	5.89	6.20	5.69	0.72	1.40	1.28	5.77
MnO	F	XRF	0.10	0.12	0.12	0.11	0.08	0.01	0.04	0.02	0.12
MgO	F	XRF	2.27	2.64	2.63	2.55	2.46	0.15	0.40	0.35	5.08
CaO	F	XRF	3.91	5.20	5.01	5.04	4.99	0.83	0.77	2.07	5.59
Na_2O	F	XRF	2.26	2.62	2.44	2.92	2.22	2.68	2.31	2.70	2.26
K_2O	F	XRF	6.11	4.95	5.11	4.75	5.46	5.58	4.78	5.39	3.89
P_2O_5	F	XRF	0.24	0.33	0.33	0.32	0.29	0.02	0.03	0.07	0.26
Total			99.40	99.72	99.55	99.77	99.98	99.46	99.14	99.25	99.25
LOI			1.57	0.37	0.50	0.74	1.12	0.11	1.21	0.30	0.93
ppm											
Ta	F	ICP-MS	0.56	0.73	0.74	0.93	0.72	2.42	1.32	1.01	0.84
Sc	HF	ICP-MS	13.93	17.42	17.63	13.43	16.78	0.10	1.04	0.88	16.73
V	HF	ICP-MS	139.60	166.85	174.70	131.44	162.61	3.09	17.59	21.22	114.80
Cr	HF	ICP-MS	29.86	25.23	26.24	16.68	31.73	-0.92	0.98	4.70	155.82
Ga	HF	ICP-MS	16.23	16.26	16.28	12.99	15.59	11.17	11.53	10.50	12.99
Co	HF	ICP-MS	11.78	15.45	15.14	11.87	14.95	0.87	2.19	2.76	15.15
Ni	HF	ICP-MS	8.96	8.76	9.25	2.03	10.37	-4.22	8.05	-2.71	10.02
Cu	HF	ICP-MS	804.50	5.53	6.98	4.82	28.34	37.76	2.53	4.82	16.04
Zn	HF	ICP-MS	57.29	66.19	74.77	55.26	29.56	3.21	11.49	6.57	45.84
Cs	F	ICP-MS	3.35	13.13	14.67	12.34	9.75	37.78	32.36	18.18	28.31
Rb	HF	ICP-MS	181.00	234.83	244.60	236.81	195.29	264.78	221.15	197.10	155.42
Ba	HF	ICP-MS	685.40	992.04	972.40	1039.16	761.28	122.92	51.54	675.84	547.03
Sr	HF	ICP-MS	396.90	421.87	423.40	356.17	398.83	32.75	39.73	191.62	225.42
Zr	F	ICP-MS	117.50	122.60	128.30	147.90	121.70	78.28	105.10	76.80	160.60
Hf	F	ICP-MS	3.20	3.59	3.72	4.19	3.56	3.88	4.06	2.45	4.33
Th	F	ICP-MS	17.29	23.08	23.07	24.25	22.59	36.12	48.54	25.17	17.51
U	F	ICP-MS	4.10	5.20	4.88	5.31	4.90	7.33	10.95	5.70	3.58
Pb	HF	ICP-MS	33.31	15.16	15.52	55.20	13.56	23.48	31.42	19.70	12.18
Nb	F	ICP-MS	6.63	7.85	7.78	8.62	7.84	9.62	11.11	6.33	10.58
Y	F	ICP-MS	16.49	19.90	19.79	19.45	18.39	2.62	9.81	3.71	23.90
La	HF	ICP-MS	22.89	26.98	22.88	15.84	24.94	28.83	23.32	18.28	26.20
Ce	F	ICP-MS	48.52	50.07	51.29	47.77	48.89	35.16	36.91	27.12	57.27
Pr	F	ICP-MS	5.99	5.93	5.93	5.30	5.62	2.55	3.45	2.22	6.62
Nd	F	ICP-MS	20.49	23.98	25.23	20.53	22.68	6.26	11.30	6.40	26.78
Sm	F	ICP-MS	4.64	4.94	5.15	4.24	4.75	0.66	1.81	0.85	5.39
Eu	F	ICP-MS	1.21	1.07	1.09	1.05	1.11	0.10	0.27	0.38	1.10
Gd	F	ICP-MS	4.00	4.16	4.25	3.71	3.99	0.39	1.40	0.66	4.80
Tb	F	ICP-MS	0.52	0.59	0.60	0.55	0.55	0.00	0.17	0.03	0.71
Dy	F	ICP-MS	2.67	3.21	3.31	3.18	3.10	0.33	1.34	0.55	4.02
Ho	F	ICP-MS	0.53	0.64	0.65	0.66	0.61	0.07	0.28	0.12	0.80
Er	F	ICP-MS	1.41	1.68	1.79	1.72	1.62	0.19	0.86	0.27	2.10
Tm	F	ICP-MS	0.08	0.24	0.28	0.24	0.24	0.05	0.15	0.06	0.30
Yb	F	ICP-MS	1.57	1.93	1.88	1.92	1.81	0.51	1.38	0.46	2.31
Lu	F	ICP-MS	0.25	0.32	0.31	0.33	0.30	0.11	0.25	0.09	0.38

F = Flux fusion + acid dissolution
HF = Standard HF dissolution

A4.1.g. Whole rock data from dykes and sulphide mineralised Mesilau Pph float.

* Majors from Sperber (2009)			*	*	*				
Lat.			6.0507	6.0507	6.0310	6.0626	6.0022	6.0514	6.0791
			116.70	116.70	116.72	116.69	116.63	116.56	116.52
Long.			26	26	51	17	61	40	59
Height (AMSL), m			0	0	0	945	1146.72	2970.57	1886.21
			Sat Gdt	Sat Gdt	Sat Gdt	Poring Hb Gt	Bt Di, S. Bambangan	Mafic enc	Mafic enc
Element	Prep.	Analysis	SBK118	SBK119	SBK120	CS042	A211	A034	A282a
(wt%)									
SiO_2	F	XRF	61.65	65.40	63.40	63.78	62.75	62.69	48.28
TiO_2	F	XRF	0.70	0.54	0.53	0.56	0.61	0.56	0.63
Al_2O_3	F	XRF	14.94	13.74	14.83	13.94	15.69	14.31	14.53
FeO_{TOT}	F	XRF	6.01	5.07	5.44	5.05	5.07	5.44	12.99
MnO	F	XRF	0.12	0.11	0.13	0.10	0.09	0.11	0.32
MgO	F	XRF	3.70	3.27	2.39	3.13	2.78	4.09	7.56
CaO	F	XRF	4.56	3.58	4.98	3.34	4.47	3.78	7.34
Na_2O	F	XRF	2.01	2.81	2.71	3.15	2.66	1.72	0.45
K_2O	F	XRF	5.09	4.37	4.68	5.01	2.97	4.09	0.56
P_2O_5	F	XRF	0.30	0.25	0.28	0.24	0.18	0.20	0.20
Total			99.75	99.70	99.98	99.92	100.07	99.92	99.34
LOI			1.54	1.47	0.34	1.07	2.22	2.32	5.03
ppm									
Ta	F	ICP-MS	1.04	0.80	0.78	0.94	0.70	1.18	0.89
Sc	HF	ICP-MS	18.00	14.12	11.88	17.21	17.57	20.46	45.85
V	HF	ICP-MS	134.04	106.41	116.90	131.70	150.50	156.00	213.40
Cr	HF	ICP-MS	57.12	47.49	29.76	61.19	45.05	166.00	214.00
Ga	HF	ICP-MS	14.14	12.10	13.58	15.64	17.64	16.79	21.40
Co	HF	ICP-MS	15.16	12.35	13.14	14.78	14.12	19.86	38.11
Ni	HF	ICP-MS	16.05	61.97	15.49	33.71	13.43	33.15	32.35
Cu	HF	ICP-MS	3.79	3.45	43.10	22.14	29.28	78.22	278.20
Zn	HF	ICP-MS	55.52	37.64	43.73	54.15	56.93	53.89	126.00
Cs	F	ICP-MS	6.18	2.96	26.24	4.96	10.82	8.13	5.72
Rb	HF	ICP-MS	226.09	121.57	180.99	238.20	109.40	203.30	38.42
Ba	HF	ICP-MS	727.31	457.06	497.58	547.90	931.70	515.60	101.60
Sr	HF	ICP-MS	292.45	242.79	304.44	231.80	291.70	230.00	21.86
Zr	F	ICP-MS	167.50	158.30	132.20	141.00	153.80	170.00	41.76
Hf	F	ICP-MS	4.62	4.26	3.81	4.19	4.04	5.01	1.63
Th	F	ICP-MS	19.92	16.85	29.73	17.08	8.60	21.38	7.09
U	F	ICP-MS	3.77	2.62	6.67	3.85	2.26	5.14	2.20
Pb	HF	ICP-MS	21.54	22.41	26.12	28.23	16.26	15.11	52.09
Nb	F	ICP-MS	11.36	9.57	8.55	9.34	8.81	10.66	10.17
Y	F	ICP-MS	26.34	22.56	21.98	21.36	22.19	22.11	24.55
La	HF	ICP-MS	32.31	25.02	28.20	25.16	19.82	30.67	26.18
Ce	F	ICP-MS	66.98	53.74	57.13	55.36	42.38	63.88	73.84
Pr	F	ICP-MS	7.18	6.40	6.38	6.77	5.22	6.95	8.39
Nd	F	ICP-MS	32.29	26.66	25.83	24.55	18.20	28.11	33.47
Sm	F	ICP-MS	6.43	5.39	5.20	5.39	4.25	5.43	6.30
Eu	F	ICP-MS	1.44	1.12	1.14	1.17	1.07	1.13	1.22
Gd	F	ICP-MS	5.49	4.68	4.36	4.92	4.24	4.42	5.03
Tb	F	ICP-MS	0.82	0.67	0.58	0.69	0.60	0.66	0.76
Dy	F	ICP-MS	4.58	3.69	3.30	3.72	3.44	3.64	4.25
Ho	F	ICP-MS	0.91	0.74	0.66	0.74	0.69	0.72	0.84
Er	F	ICP-MS	2.50	1.95	1.77	2.07	1.88	1.98	2.32
Tm	F	ICP-MS	0.43	0.28	0.24	0.27	0.14	0.32	0.37
Yb	F	ICP-MS	2.69	2.15	1.84	2.24	2.00	2.15	2.46
Lu	F	ICP-MS	0.45	0.36	0.31	0.36	0.33	0.36	0.41

F = Flux fusion + acid dissolution
HF = Standard HF dissolution

A4.1.h. Whole rock data from satellite bodies and mafic enclaves.

* Majors from Sperber (2009)									
Lat.			6.132023	6.03124	6.070546		6.132023	6.03124	6.070546
Long.			116.5698	116.5483	116.5642		116.5698	116.5483	116.5642
Height (AMSL), m			2239	1874	3968		2239	1874	3968
			Quartzite	Sst	Xenolith		Quartzite	Sst	Xenolith
Element	Prep.	Analysis	A221	A291	A098	Prep.	A221	A291	A098
(wt%)									
SiO_2	F	XRF	77.95	83.81	83.42	F	77.95	83.81	83.42
TiO_2	F	XRF	0.51	0.46	0.20	F	0.51	0.46	0.20
Al_2O_3	F	XRF	10.62	8.40	8.08	F	10.62	8.40	8.08
FeO_{TOT}	F	XRF	4.15	1.75	1.26	F	4.15	1.75	1.26
MnO	F	XRF	0.05	0.01	0.01	F	0.05	0.01	0.01
MgO	F	XRF	1.59	0.64	0.99	F	1.59	0.64	0.99
CaO	F	XRF	0.03	-0.05	1.90	F	0.03	-0.05	1.90
Na_2O	F	XRF	0.21	1.79	1.37	F	0.21	1.79	1.37
K_2O	F	XRF	2.03	1.03	1.49	F	2.03	1.03	1.49
P_2O_5	F	XRF	0.06	0.07	0.04	F	0.06	0.07	0.04
Total			99.87	99.70	99.88		99.87	99.70	99.88
LOI			2.21	1.60	0.98		2.21	1.60	
ppm									
Ta	HF	ICP-MS	0.72	0.59	0.32	F	0.75	0.56	0.31
Sc	HF	ICP-MS	8.39	4.94	3.77	HF	8.39	4.94	3.77
V	HF	ICP-MS	67.99	49.69	29.08	HF	67.99	49.69	29.08
Cr	HF	ICP-MS	51.51	29.31	25.95	HF	51.51	29.31	25.95
Ga	HF	ICP-MS	11.48	8.32	8.00	HF	11.48	8.32	8.00
Co	HF	ICP-MS	7.79	2.04	4.82	HF	7.79	2.04	4.82
Ni	HF	ICP-MS	21.91	7.25	34.96	HF	21.91	7.25	34.96
Cu	HF	ICP-MS	19.44	7.20	6.37	HF	19.44	7.20	6.37
Zn	HF	ICP-MS	44.64	32.70	10.61	HF	44.64	32.70	10.61
Cs	HF	ICP-MS	5.68	3.29	12.21	F	6.79	3.77	9.03
Rb	HF	ICP-MS	96.26	46.23	111.50	HF	96.26	46.23	111.50
Ba	HF	ICP-MS	201.90	141.20	137.40	HF	201.90	141.20	137.40
Sr	HF	ICP-MS	38.71	35.01	133.90	HF	38.71	35.01	133.90
Zr	HF	ICP-MS	5.30	42.17	157.00	F	230.80	274.80	24.11
Hf	HF	ICP-MS	0.16	1.26	3.83	F	6.08	7.13	0.67
Th	HF	ICP-MS	8.58	8.42	5.15	F	9.16	8.74	5.12
U	HF	ICP-MS	1.44	1.48	1.47	F	2.08	2.01	1.15
Pb	HF	ICP-MS	6.23	7.96	7.59	HF	6.23	7.96	7.59
Nb	HF	ICP-MS	9.21	7.13	3.56	F	8.85	6.47	3.25
Y	HF	ICP-MS	12.24	16.46	12.58	F	19.29	20.23	10.26
La	HF	ICP-MS	20.54	22.52	14.53	HF	20.54	22.52	14.53
Ce	HF	ICP-MS	41.18	41.33	30.75	F	42.96	39.21	27.94
Pr	HF	ICP-MS	5.12	5.68	3.65	F	5.27	5.48	3.43
Nd	HF	ICP-MS	19.16	21.82	11.95	F	19.69	21.09	12.53
Sm	HF	ICP-MS	3.63	4.30	2.54	F	3.87	4.37	2.31
Eu	HF	ICP-MS	0.57	0.89	0.75	F	0.60	0.92	0.67
Gd	HF	ICP-MS	3.00	3.88	2.31	F	3.57	4.39	2.02
Tb	HF	ICP-MS	0.44	0.53	0.33	F	0.58	0.64	0.31
Dy	HF	ICP-MS	2.32	2.86	1.94	F	3.32	3.42	1.71
Ho	HF	ICP-MS	0.44	0.55	0.38	F	0.70	0.70	0.33
Er	HF	ICP-MS	1.13	1.45	1.05	F	1.96	1.90	0.89
Tm	HF	ICP-MS	0.16	0.20	0.07	F	0.32	0.30	0.14
Yb	HF	ICP-MS	0.97	1.34	1.16	F	2.07	1.94	0.84
Lu	HF	ICP-MS	0.15	0.22	0.19	F	0.35	0.33	0.13

F = Flux fusion + acid dissolution
HF = Standard HF dissolution

A4.1.i. Whole rock data from sediments on the mountain's flanks and the conglomerate xenolith from within the Donkey Gt. Data from samples prepared by just the standard acid dissolution and by a combination of standard dissolution and flux fusion are shown.

Element (ppm)	Bt. A053 B Alex. Gd	Bt. A054 B Alex. Gd	Bt. A047 B Alex. Gd	Bt. A218 B Low's Gt	Bt. A282 b King Gt	Bt. A046 B Low's Gt	Hb. A053 H Alex. Gd	Hb. A054 H Alex. Gd	Hb. A047 H Alex. Gd	Hb. A218 H Low's Gt	Hb. A282 H King Gt	Hb. A046 H Low's Gt	Qtz A053 Q Alex. Gd
Ta	1.49	1.69	1.73	1.70	1.72	1.74	1.02	1.39	1.34	1.19	0.97	0.95	0.03
Sc	16.05	20.22	25.75	7.18	6.25	8.86	109.40	109.60	104.70	71.37	93.45	70.01	0.15
V	517	532	517	456	430	412	529	450	500	447	443	435	2.86
Cr	195	225	198	225	175	242	192	176	189	190	125	239	2.96
Ga	25.89	27.91	29.24	31.06	36.19	27.31	17.37	15.51	18.29	18.29	20.45	16.47	3.11
Mn	1402	1928	1797	1502	2153	1549	2896	3237	3299	2625	3113	2316	85.2
Co	57.38	59.06	57.90	74.56	78.16	70.84	39.07	36.35	38.14	49.22	52.35	46.16	0.37
Ni	56.91	67.19	58.25	73.37	51.53	55.55	39.85	31.75	47.89	37.82	35.37	37.30	8.66
Ti	21285	21765	18941	23119	23832	20338	5754	4963	7151	8973	7672	9261	246
Cu	366.6	40.49	71.73	135.5	40.82	89.20	246.4	23.36	12.06	84.74	27.68	35.27	23.55
Zn	103.8	124.7	115.8	111.4	128.2	108.1	96.47	101.0	95.39	98.14	107.4	92.64	52.23
Cs	17.73	23.00	18.56	46.11	84.52	22.31	11.21	13.31	1.70	5.07	11.09	2.86	2.69
Rb	145.60	163.40	115.00	189.90	227.80	149.20	91.90	81.05	9.29	23.73	26.13	20.69	6.71
Ba	2863	2654	1863	3196	1750	4279	306	214	192	149	87	181	96.0
Sr	31	42	125	67	70	43	106	61	188	164	152	154	202
Zr	3.06	2.70	6.98	6.21	3.72	5.76	27.03	23.16	27.32	56.26	51.17	50.76	1.37
Hf	0.21	0.23	0.42	0.36	0.23	0.28	1.96	1.97	2.05	3.02	3.04	2.64	0.06
Th	0.43	1.69	1.83	1.03	2.16	7.20	1.50	2.62	4.08	2.40	1.39	1.79	0.62
U	0.18	0.44	0.64	0.54	0.99	1.52	0.53	0.95	1.29	1.47	0.47	0.88	0.16
Pb	3.59	4.06	8.17	8.17	16.74	13.41	5.29	3.45	7.10	5.29	7.40	6.19	4.17
Nb	29.37	32.93	29.85	27.72	33.00	23.67	12.24	12.25	14.80	16.83	17.38	14.30	0.15
Y	2.71	5.48	9.06	4.16	7.22	2.08	97.48	102.2	100.1	59.81	86.57	51.51	0.51
La	3.83	5.58	8.84	9.77	17.40	12.90	27.66	27.60	30.96	27.59	34.02	22.39	2.12
Ce	8.87	13.13	19.11	17.22	30.47	20.31	89.16	88.94	96.88	76.89	98.72	62.32	3.18
Pr	1.19	1.84	2.57	2.15	3.67	2.06	15.06	15.02	15.98	12.16	16.04	9.98	0.34
Nd	4.49	7.16	9.70	7.43	12.58	6.18	66.62	67.30	71.27	52.00	69.75	43.35	1.08
Sm	0.77	1.34	1.84	1.18	1.89	0.81	16.48	16.49	17.05	11.98	16.96	10.12	0.16
Eu	0.35	0.38	0.44	0.54	0.60	0.47	1.42	1.17	1.24	2.46	2.68	1.99	0.22
Gd	1.01	1.53	2.07	1.45	2.01	1.18	17.12	17.31	17.24	12.08	16.84	10.32	0.17
Tb	0.09	0.17	0.26	0.14	0.21	0.08	2.67	2.74	2.75	1.82	2.55	1.57	0.02
Dy	0.45	0.91	1.45	0.70	1.05	0.38	15.64	16.23	16.50	10.26	14.63	8.93	0.09
Ho	0.09	0.18	0.29	0.14	0.21	0.07	3.16	3.27	3.37	2.05	2.90	1.78	0.02
Er	0.24	0.48	0.81	0.37	0.55	0.18	8.53	8.98	9.29	5.49	7.82	4.81	0.05
Tm	0.04	0.07	0.13	0.06	0.08	0.03	1.34	1.43	1.47	0.85	1.22	0.75	0.01
Yb	0.22	0.46	0.83	0.35	0.46	0.16	8.43	9.09	9.56	5.42	7.49	4.74	0.05
Lu	0.04	0.08	0.13	0.06	0.08	0.03	1.28	1.41	1.50	0.85	1.14	0.74	0.01

A4.2. Mineral separate trace element data collected from crushed and handpicked minerals prepared by the standard acid dissolution procedure prior to ICP-MS analysis.

Element (ppm)	Qtz A054 Q Alex. Gd	Qtz A047 Q Alex. Gd	Qtz A218 Q Low's Gt	Qtz A282 Q King Gt	Qtz A046 Q Low's Gt	Fsp. A053 F Alex. Gd	Fsp. A054 F Alex. Gd	Fsp. A047 F Alex. Gd	Fsp. A218 P Low's Gt	Fsp. A282 F King Gt	Fsp. A046 P Low's Gt	Fsp. A218 K Low's Gt	Fsp. A046 K Low's Gt
Ta	0.03	0.06	0.04	0.06	0.03	0.06	0.04	0.04	0.10	0.04	0.05	0.01	0.01
Sc	0.24	0.32	0.01	0.02	0.01	0.09	0.09	0.31	0.09	0.01	0.11	0.02	0.08
V	3.56	9.32	2.49	2.13	1.49	2.62	2.34	4.82	5.71	1.78	5.19	1.95	2.52
Cr	3.85	5.57	2.94	2.50	2.64	6.02	2.18	2.48	2.13	2.29	1.71	2.11	1.57
Ga	4.86	8.06	0.60	0.73	0.84	19.69	21.68	19.10	18.72	12.48	20.14	10.79	9.94
Mn	54.2	62.0	15.5	7.7	23.2	185.9	69.7	100.7	69.7	15.5	108.4	46.5	85.2
Co	0.26	0.39	0.13	0.05	0.07	2.61	0.76	0.65	0.46	0.09	0.59	0.20	0.17
Ni	10.90	13.22	8.40	7.77	8.45	9.96	7.39	7.77	6.66	7.39	6.11	6.01	4.88
Ti	228	701	138	144	90	126	120	168	545	108	174	108	96
Cu	3.95	1.89	3.13	1.31	2.00	147.4	5.02	2.14	82.35	2.69	46.05	11.13	7.43
Zn	52.46	51.72	50.19	49.86	51.26	53.95	51.07	51.37	51.37	51.02	51.54	51.00	51.91
Cs	0.52	4.36	0.69	1.21	1.11	4.82	0.73	7.25	5.52	6.76	3.74	5.48	4.79
Rb	10.16	5.32	7.61	12.10	4.69	12.37	11.57	13.50	101.5	129.4	21.68	108.9	99.43
Ba	307.4	103.4	70.2	24.9	24.4	336.0	300.2	293.8	998.2	2190.	337.2	2035.	896.2
Sr	262	209	48	18	55	561	604	539	632	412	721	406	273
Zr	4.93	0.96	0.20	0.70	0.82	1.76	1.55	1.79	2.72	0.57	2.63	0.26	0.58
Hf	0.28	0.05	0.02	0.05	0.05	0.08	0.07	0.09	0.14	0.03	0.10	0.01	0.03
Th	0.60	1.20	0.19	0.71	11.89	1.17	1.06	2.70	1.44	0.42	7.39	0.13	1.33
U	0.59	0.25	0.05	0.17	1.79	0.26	0.28	0.42	0.57	0.17	1.56	0.07	0.22
Pb	5.18	6.30	1.21	1.17	1.74	13.05	14.74	13.15	19.14	37.36	13.43	34.49	35.47
Nb	0.16	0.56	0.07	0.17	0.07	0.31	0.80	0.23	0.70	0.08	0.28	0.04	0.07
Y	0.81	1.01	0.07	0.13	0.19	0.96	0.77	1.06	2.24	0.67	0.55	0.34	0.15
La	2.67	4.54	0.66	0.74	1.57	8.41	9.74	10.09	6.90	3.59	7.08	2.16	2.56
Ce	3.95	6.91	0.66	0.99	2.00	11.35	13.15	14.17	8.28	3.76	8.56	2.22	2.80
Pr	0.42	0.74	0.08	0.10	0.17	1.10	1.26	1.36	1.00	0.36	0.77	0.24	0.25
Nd	1.35	2.37	0.24	0.27	0.45	3.12	3.59	3.82	3.27	1.04	2.08	0.71	0.68
Sm	0.19	0.33	0.03	0.04	0.06	0.36	0.38	0.44	0.54	0.16	0.23	0.11	0.08
Eu	0.36	0.54	0.03	0.02	0.03	1.22	1.40	1.26	0.62	0.83	0.65	0.62	0.51
Gd	0.22	0.32	0.03	0.04	0.06	0.39	0.41	0.46	0.61	0.23	0.26	0.18	0.10
Tb	0.02	0.04	0.00	0.00	0.01	0.04	0.03	0.04	0.07	0.02	0.02	0.01	0.01
Dy	0.13	0.18	0.01	0.02	0.03	0.17	0.14	0.19	0.38	0.10	0.10	0.05	0.03
Ho	0.03	0.04	0.00	0.00	0.01	0.03	0.03	0.04	0.07	0.02	0.02	0.01	0.01
Er	0.08	0.09	0.01	0.01	0.02	0.09	0.07	0.09	0.21	0.06	0.05	0.03	0.01
Tm	0.02	0.02	0.00	0.00	0.00	0.01	0.01	0.02	0.03	0.01	0.01	0.01	0.00
Yb	0.11	0.09	0.01	0.02	0.02	0.09	0.06	0.09	0.20	0.05	0.05	0.03	0.01
Lu	0.02	0.02	0.00	0.00	0.00	0.01	0.01	0.02	0.03	0.01	0.01	0.00	0.00

A4.2. (*cont.*)

A4.3. Radiogenic isotope data from Mt Kinabalu.

Lithology	Sample	$^{87}Sr/^{86}Sr_m$	2SE	$^{143}ND/^{144}Nd_m$	2SE	$^{206}Pb/^{204}Pb_m$	2SE	$^{207}Pb/^{204}Pb_m$	2SE	$^{208}Pb/^{204}Pb_m$	2SE
Alexandra Gd	A042	0.707888	0.000011	0.512435	0.000008	18.7761	0.0006	15.6811	0.0007	39.0200	0.0034
Alexandra Gd	A047	0.707640	0.000010	0.512482	0.000007	18.7729	0.0011	15.6823	0.0010	39.0192	0.0043
Alexandra Gd	A049	0.707939	0.000007	0.512449	0.000011	18.7763	0.0006	15.6791	0.0007	39.0151	0.0031
Alexandra Gd	A054	0.707536	0.000018	0.512488	0.000004	18.7732	0.0012	15.6780	0.0012	39.0094	0.0031
Alexandra Gd	A054 (Fused)	0.707555	0.000016	0.512500	0.000017						
Low's Gt	A218	0.706805	0.000018	0.512548	0.000006	18.7477	0.0009	15.6716	0.0009	38.9647	0.0030
Low's Gt	SBK122	0.706989	0.000009	0.512505	0.000008	18.7463	0.0006	15.6698	0.0008	38.9574	0.0034
Low's Gt	A218 (Fused)	0.706824	0.000016	0.512518	0.000013						
King Gt	A236	0.706702	0.000012	0.512508	0.000008	18.7387	0.0008	15.6676	0.0008	38.9488	0.0047
King Gt	A282	0.706849	0.000008	0.512493	0.000010	18.7397	0.0008	15.6685	0.0007	38.9460	0.0027
Donkey Gt	A093	0.707595	0.000016	0.512443	0.000009	18.7518	0.0012	15.6731	0.0012	38.9766	0.0041
Donkey Gt	A127	0.706542	0.000017	0.512584	0.000004	18.7366	0.0010	15.6683	0.0009	38.9451	0.0032
Paka Pph	A162	0.706644	0.000009	0.512503	0.000010	18.7363	0.0006	15.6670	0.0008	38.9371	0.0035
Paka Pph	A290b	0.706938	0.000011	0.512500	0.000008	18.7264	0.0006	15.6635	0.0007	38.9163	0.0027
Paka Pph	CS027	0.706682	0.000016	0.512533	0.000005	18.7474	0.0008	15.6724	0.0007	38.9699	0.0027
Mesilau Pph	A172	0.706642	0.000010	0.512499	0.000010	18.7337	0.0007	15.6659	0.0008	38.9351	0.0032
Mesilau Pph	A198	0.706462	0.000008	0.512526	0.000008	18.7288	0.0010	15.6669	0.0010	38.9306	0.0033
Mesilau Pph	A241	0.706646	0.000009	0.512498	0.000007	18.7373	0.0008	15.6664	0.0007	38.9409	0.0029
Mesilau Pph	CS055	0.706653	0.000009	0.512507	0.000007	18.7417	0.0008	15.6687	0.0008	38.9491	0.0032
Pyx Mon Dyke	CS014	0.706690	0.000009	0.512590	0.000010	18.7266	0.0006	15.6661	0.0007	38.9215	0.0027
Pyx Mon Dyke	CS071	0.706511	0.000019	0.512548	0.000003	18.7413	0.0008	15.6679	0.0008	38.9505	0.0036
Mafic enc	A034	0.707669	0.000010	0.512464	0.000008	18.7525	0.0010	15.6743	0.0010	38.9718	0.0038
Mafic enc	A282a	0.707072	0.000011	0.512482	0.000008	18.7247	0.0006	15.6612	0.0008	38.9066	0.0032
Xenolith	A098	0.710785	0.000017	0.512259	0.000009	18.7482	0.0015	15.6729	0.0014	38.9582	0.0045
Quartzite	A221	0.715460	0.000072	0.512387	0.000027	18.8302	0.0011	15.6966	0.0011	39.1173	0.0034
Quartzite	A291	0.713415	0.000075	0.512413	0.000006	18.8495	0.0010	15.6903	0.0009	39.1089	0.0026
Quartzite	A291 (Fused)	0.713093	0.000017	0.512424	0.000008						

		Hornblende		Quartz		Biotite		Clinopyroxene	
Sample	Lithology	$\delta^{18}O_{V\text{-}SMOW}$	SD	$\delta^{18}O_{V\text{-}SMOW}$	SD	$\delta^{18}O_{V\text{-}SMOW}$	SD	$\delta^{18}O_{V\text{-}SMOW}$	SD
A042	Alex. Gd			11.35	0.07				
A047	Alex. Gd	4.45	0.35	9.20	0.81	-2.05	0.35		
A049	Alex. Gd	7.93	0.64	10.20	0.28				
A054	Alex. Gd	7.00	0.00	10.40	0.14	4.35	0.35		
A046	Low's Gt	6.85	0.49						
A218	Low's Gt	7.10	0.14	10.20	0.00	5.45	0.35		
A282	King Gt	7.05	0.07	9.90	0.14	-0.35	0.21		
A093	Donkey Gt	7.90	0.99		0.00				
A096	Donkey Gt	7.30	0.14						
A127	Donkey Gt	6.70	0.28	9.80	0.14				
A162	Paka Pph	7.10	0.00	10.50	0.14				
CS027	Paka Pph	5.35	0.21						
A198	Mesilau Pph	7.20	0.28	9.55	0.35				
A239	Mesilau Pph	6.75	0.21						
A034	Mafic Enc	7.25	0.35	8.95	0.35				
A039	Pyx Gt Dyke	6.05	0.07	6.10	0.00			-0.30	0.00

A4.4. Oxygen isotope values for different phases from of Mt Kinabalu ($\delta^{18}O_{V\text{-}SMOW}$, expressed in per mil, ‰). SD based on two analyses from each sample.

A4.5. Mineral separate ion microprobe data on selected phases of the Mt Kinabalu granite.

Data courtesy of Prof. Robert Hall, South East Asia Research Group.

Rock	Sample	SiO_2	Na_2O	MgO	Al_2O_3	FeO_{TOT}	MnO	K_2O	CaO	Total
CS19	19-2.8	65.06	1.33	0.00	19.29	0.14	0.00	14.46	0.99	101.42
CS19	19-3.9	64.80	1.79	0.16	18.36	0.04	0.05	14.31	0.25	99.80
CS19	19-5.4	65.39	1.48	0.13	18.61	0.34	0.06	15.13	0.00	101.54
CS31	31-1.5	63.59	1.08	0.00	17.89	0.00	0.09	15.73	2.06	100.44
CS31	31-2.2	64.28	0.84	0.10	18.07	0.11	0.00	16.42	0.00	99.96
CS31	31-3.4	63.94	1.20	0.03	17.77	0.11	0.00	15.45	0.00	98.61
CS31	31-3.5	64.14	1.23	0.00	17.86	0.15	0.06	16.02	0.13	99.76
CS31	31-3.7	64.07	0.86	0.05	18.15	0.32	0.00	15.55	0.00	99.36
CS31	31-10.6	65.41	0.71	0.08	18.16	0.24	0.08	16.23	0.00	101.16
CS31	31-11.4	64.71	0.86	0.00	18.39	0.04	0.00	16.13	0.00	100.18
CS31	31-11.5	58.61	0.82	0.17	17.09	0.00	0.48	14.87	0.00	92.05
CS67	67-36	70.54	1.16	0.00	20.07	0.11	0.01	10.43	0.13	102.56
CS67	67-37	66.77	2.18	0.00	19.36	0.08	0.02	12.94	0.11	101.55
KK127	127-91	69.43	0.98	0.00	20.33	0.16	0.01	11.56	0.40	103.03

a. K-feldspar

Rock	Sample	SiO_2	Na_2O	MgO	Al_2O_3	FeO_{TOT}	MnO	K_2O	TiO_2	Total
CS19	19-1.4	38.12	0.12	11.23	14.75	21.06	0.18	10.13	4.52	100.11
CS19	19-1.9	36.94	0.31	11.30	13.96	19.87	0.38	10.05	4.32	97.14
CS19	19-2.2	37.24	0.20	10.91	13.61	19.57	0.10	10.22	5.06	96.91
CS19	19-3.6	37.93	0.28	11.50	14.00	19.70	0.32	9.98	4.52	98.24
CS19	19-3.10	36.72	0.16	10.71	13.83	21.08	0.42	10.08	4.56	97.55
CS19	19-3.11	37.93	0.21	11.31	14.22	20.27	0.32	9.93	4.49	98.68
CS19	19-5.3	36.71	0.47	11.21	14.22	19.65	0.17	9.91	5.27	97.60
CS22	22-04	36.34	0.11	10.12	14.71	19.36	0.24	9.10	3.47	93.46
CS22	22-28	37.12	0.12	11.31	14.53	18.18	0.22	9.03	3.59	94.10
CS22	22-29	35.27	0.12	9.96	14.29	19.27	0.21	9.33	4.02	92.46
CS56	56-5.1	37.80	0.18	12.62	14.18	17.57	0.34	10.35	5.10	98.14
CS56	56-5.3	38.29	0.47	13.52	14.17	17.54	0.25	10.23	4.43	98.89
CS67	67-40	36.61	0.20	12.65	14.50	15.96	0.23	9.26	4.61	94.03
CS67	67-41	36.55	0.25	12.25	14.15	15.69	0.23	9.23	4.62	92.97
CS67	67-45	36.30	0.18	12.21	14.19	16.71	0.24	9.43	4.55	93.80
KK127	127-62	36.73	0.19	12.37	13.82	16.69	0.22	9.18	4.19	93.37
KK127	127-63	36.75	0.10	11.53	13.93	17.25	0.38	9.17	4.28	93.39
KK127	127-65	36.09	0.21	11.96	14.54	16.67	0.21	9.31	4.29	93.29
KK127	127-66	36.41	0.21	12.33	14.30	16.59	0.22	9.38	4.38	93.82
KK128	128-58	37.63	0.08	11.83	13.16	18.25	0.21	9.77	3.75	94.67

b. Biotite

Rock	Sample	SiO_2	Na_2O	MgO	Al_2O_3	FeO_{TOT}	MnO	K_2O	CaO	TiO_2	CrO_2	Total	Notes
CS19	19-1.1	45.01	1.44	10.62	9.66	16.92	0.23	1.17	11.80	1.55	0.12	72.31	
CS19	19-1.2	47.16	1.19	11.43	8.07	15.53	0.64	0.87	11.39	0.78	0.03	67.19	
CS19	19-1.3	48.90	0.82	12.39	6.78	15.25	0.32	0.62	11.55	0.38	0.13	65.19	
CS19	19-1.7	50.30	0.92	13.13	5.54	14.97	0.64	0.42	11.84	1.08	0.00	65.17	
CS19	19-2.3	45.48	1.62	11.87	8.98	15.63	0.36	1.14	11.36	1.75	0.15	70.23	CORE
CS19	19-2.4	44.99	1.71	10.86	9.63	16.10	0.26	1.08	11.62	1.34	0.28	70.78	RIM
CS19	19-2.5	44.69	1.65	11.22	9.75	15.91	0.37	1.28	11.64	2.02	0.04	71.55	CORE
CS19	19-2.7	44.98	1.29	10.87	8.86	17.11	0.50	1.23	11.68	1.56	0.00	72.12	RIM
CS19	19-3.1	45.31	1.64	11.40	9.21	15.52	0.44	1.26	11.44	1.60	0.15	69.91	RIM
CS19	19-3.2	44.74	1.66	11.10	9.50	16.38	0.46	1.07	11.54	1.44	0.04	71.39	CORE
CS19	19-3.3	44.86	1.49	10.94	8.73	16.42	0.43	1.12	11.46	1.73	0.10	70.67	RIM
CS19	19-3.4	46.22	1.49	11.92	8.87	15.48	0.40	1.06	11.53	1.49	0.00	69.45	CORE
CS19	19-3.7	46.01	1.49	11.51	8.15	15.77	0.39	1.13	11.46	1.02	0.13	68.58	RIM
CS19	19-3.8	44.08	1.45	11.08	9.26	16.10	0.47	1.19	11.64	1.70	0.11	70.91	CORE
CS19	19-4.4	46.33	1.41	11.83	8.19	15.31	0.58	0.83	11.52	1.54	0.19	68.40	
CS22	22-03	51.31	0.36	13.17	3.46	14.22	0.47	0.21	11.84	0.25	0.02	59.80	
CS22	22-21	52.19	0.31	13.76	2.50	13.99	0.47	0.14	11.78	0.19	0.03	58.72	
CS22	22-30	50.51	0.66	12.63	5.09	15.32	0.59	0.29	10.84	0.28	0.03	62.77	
CS22	22-31	51.37	0.28	13.91	2.70	14.08	0.48	0.15	11.95	0.18	0.04	59.42	
CS31	31-2.3	52.70	0.92	13.49	3.71	15.33	0.54	0.20	12.25	0.34	0.00	63.83	
CS31	31-2.4	51.63	0.79	13.19	3.05	14.99	0.77	0.38	12.29	0.45	0.02	62.59	
CS31	31-3.3	50.10	1.40	12.75	5.08	16.12	0.86	0.41	11.44	1.02	0.00	66.99	
CS31	31-4.2	48.89	1.26	10.88	5.99	16.95	0.49	0.64	12.10	0.82	0.04	68.01	
CS31	31-5.1	46.74	1.24	11.43	6.66	16.97	0.66	0.96	11.51	1.22	0.17	69.68	RIM
CS31	31-5.2	49.08	1.21	12.42	5.73	15.88	0.66	0.58	11.79	0.86	0.01	66.80	CORE
CS31	31-6.1	52.04	0.81	13.76	3.54	14.43	0.92	0.33	12.18	0.28	0.16	62.46	
CS31	31-6.2	51.59	0.79	13.66	3.82	15.33	0.64	0.21	12.02	0.38	0.03	63.90	
CS31	31-7.1	48.25	1.01	11.72	5.94	16.78	0.53	0.72	12.15	0.61	0.00	68.09	
CS31	31-7.2	48.94	1.24	12.27	5.37	15.69	0.60	0.76	11.93	0.57	0.21	66.07	
CS31	31-8.1	50.99	0.95	12.60	3.46	15.78	0.48	0.33	11.83	0.50	0.12	63.61	RIM
CS31	31-8.2	53.15	0.62	13.56	2.85	14.69	0.39	0.19	12.20	0.43	0.13	61.39	CORE
CS31	31-9.2	52.27	0.76	13.67	3.01	14.95	0.55	0.26	11.95	0.70	0.00	62.48	
CS31	31-9.4	57.06	6.21	0.14	27.30	0.18	0.00	0.61	9.32	0.05	0.00	44.02	
CS31	31-10.5	52.11	0.79	12.71	3.09	15.89	0.55	0.22	11.63	0.36	0.11	63.00	
CS56	56-2.3	44.54	1.59	9.52	9.40	18.06	0.35	1.11	12.17	1.73	0.00	74.00	CORE
CS56	56-2.4	44.17	1.73	9.44	9.32	17.87	0.40	1.20	11.65	1.90	0.00	73.37	CORE
CS56	56-2.8	56.17	0.58	19.49	3.05	5.09	1.09	0.27	12.90	0.24	0.12	48.49	
CS56	56-2.9	43.48	1.48	9.58	9.02	18.21	0.27	1.39	11.53	1.53	0.09	73.34	
CS56	56-2.12	42.15	0.00	11.43	16.06	13.75	0.00	5.13	5.55	0.01	0.27	67.48	
CS56	56-3.7	49.13	1.20	12.81	5.83	15.42	0.47	0.59	12.37	0.79	0.04	66.65	
CS56	56-3.8	43.81	1.48	9.55	9.50	18.12	0.66	1.38	11.79	1.80	0.00	74.43	
CS56	56-4.2	44.92	1.36	10.20	8.68	17.06	0.53	1.45	11.96	1.85	0.12	72.17	
CS56	56-4.4	44.73	1.51	10.39	9.18	17.47	0.62	1.41	11.93	1.43	0.00	73.35	
CS67	67-33	43.84	1.57	10.61	9.38	15.78	0.42	1.17	11.60	1.57	0.03	69.67	
CS67	67-34	45.03	1.10	10.56	8.85	15.62	0.37	0.83	10.76	1.07	0.00	66.53	
CS67	67-42	48.63	1.11	12.82	5.11	14.08	0.56	0.44	11.41	0.91	0.02	62.10	
CS67	67-43	45.49	1.27	11.84	7.88	14.74	0.44	0.93	11.79	1.12	0.01	66.42	
CS67	67-44	44.37	1.39	10.59	9.28	16.18	0.41	1.11	11.36	1.36	0.02	69.68	
KK128	128-53	44.68	1.33	11.21	8.55	15.68	0.40	1.00	11.43	1.14	0.00	68.17	
KK128	128-54	47.31	1.16	13.33	6.35	13.27	0.41	0.66	11.93	1.12	0.00	62.98	
KK128	128-55	46.64	1.37	11.56	6.75	15.83	0.56	0.73	11.46	1.04	0.00	66.89	
KK128	128-56	47.49	1.14	12.50	5.66	15.40	0.62	0.58	11.33	0.96	0.00	65.31	
KK128	128-57	46.67	1.30	11.79	6.20	15.73	0.52	0.72	11.51	1.12	0.00	66.37	

c. Hornblende

Rock	Sample	SiO_2	Na_2O	MgO	Al_2O_3	FeO_{TOT}	MnO	K_2O	CaO	Total	Notes
CS19	19-3.13	54.23	4.96	0.05	28.94	0.15	0.07	0.25	11.71	100.53	
CS19	19-4.1	57.69	6.06	0.11	26.71	0.25	0.00	0.40	9.64	101.15	CORE
CS19	19-4.2	59.22	7.01	0.02	25.59	0.34	0.14	0.36	7.65	100.70	RIM
CS19	19-4.3	59.62	7.02	0.15	26.53	0.16	0.07	0.34	8.29	102.37	RIM
CS19	19-5.1	55.14	5.20	0.11	28.50	0.15	0.00	0.22	11.40	100.87	RIM
CS19	19-5.2	55.08	5.05	0.00	28.13	0.35	0.00	0.35	10.75	100.10	CORE
CS22	22-06	45.41	1.63	0.00	34.54	0.12	0.00	0.03	17.26	99.13	
CS22	22-07	55.70	5.62	0.00	29.27	0.05	0.02	0.16	10.37	101.24	
CS22	22-08	63.02	7.29	0.00	25.92	0.02	0.01	0.30	5.86	102.42	
CS22	22-13	48.51	2.89	0.00	30.71	0.06	0.00	0.06	14.97	97.27	
CS22	22-14	52.73	4.55	0.00	28.67	0.11	0.00	0.12	11.95	98.26	
CS22	22-15	59.55	6.82	0.00	26.01	0.07	0.00	0.27	7.58	100.39	
CS31	31-1.6	67.15	9.65	0.07	19.99	0.00	0.00	0.33	2.35	99.54	
CS31	31-2.1	57.26	6.09	0.16	27.39	0.17	0.29	0.16	9.38	101.09	
CS31	31-3.2	55.82	5.59	0.12	28.08	0.16	0.14	0.17	10.84	101.10	
CS31	31-3.6	55.99	5.81	0.12	26.55	0.51	0.00	0.43	9.51	99.48	
CS31	31-4.3	57.02	5.91	0.23	27.16	0.11	0.04	0.42	9.47	100.48	
CS31	31-8.3	58.81	7.03	0.10	25.66	0.12	0.00	0.53	7.84	100.24	RIM
CS31	31-8.4	56.29	5.74	0.05	27.71	0.16	0.00	0.45	10.15	100.71	CORE
CS31	31-8.5	56.63	6.37	0.13	26.13	0.19	0.00	0.50	8.98	99.15	
CS31	31-8.6	52.63	4.08	0.07	30.18	0.24	0.15	0.29	12.98	100.89	
CS31	31-8.7	61.13	7.92	0.15	24.52	0.21	0.00	0.51	6.21	100.88	
CS31	31-8.8	0.06	0.13	0.18	0.19	87.68	0.00	0.00	0.00	185.68	
CS31	31-10.1	57.28	6.17	0.11	26.75	0.15	0.00	0.53	9.03	100.19	
CS31	31-10.3	60.45	7.17	0.21	24.80	0.34	0.00	0.34	7.18	100.86	
CS56	56-2.1	60.13	7.61	0.00	24.68	0.19	0.02	0.34	6.76	99.95	RIM
CS56	56-2.2	59.32	6.97	0.06	25.39	0.19	0.00	0.64	7.75	100.54	CORE
CS56	56-2.14	59.55	6.79	0.09	25.61	0.27	0.14	0.26	7.99	101.00	
CS56	56-6.1	63.27	8.85	0.18	22.46	0.24	0.13	0.66	4.33	100.39	
CS56	56-6.2	62.45	8.56	0.18	23.41	0.15	0.00	0.37	4.73	100.01	
CS56	56-6.3	59.11	7.20	0.18	26.01	0.31	0.06	0.27	7.84	101.34	
CS56	56-6.4	62.72	8.67	0.19	23.19	0.34	0.00	0.42	5.09	100.99	
CS67	67-38	59.12	4.46	0.00	25.72	0.18	0.01	0.30	8.17	98.15	
CS67	67-39	56.08	5.38	0.00	27.01	0.19	0.01	0.32	9.48	98.66	
CS67	67-49	54.14	5.84	0.02	27.13	0.19	0.00	0.33	9.76	97.61	
CS67	67-50	54.95	5.51	0.03	27.48	0.23	0.00	0.30	10.27	99.01	
KK127	127-76	57.73	5.91	0.01	26.13	0.24	0.02	0.78	8.85	99.92	
KK127	127-77	55.85	5.45	0.02	26.88	0.22	0.00	0.58	9.99	99.24	
KK127	127-78	54.97	5.39	0.01	26.47	0.24	0.00	0.62	10.03	97.98	
KK127	127-80	56.28	5.51	0.01	27.31	0.25	0.01	0.60	9.87	100.11	

d. Plagioclase

	Ol	Cpx	Plg	Opx	Hb	Ap	Mag	Rut	Ilm	Grt	Bio	KFsp
Cs	0.097	0.273	0.094	0.257	0.792		0.510				3.000	0.195
Rb	0.020	0.052	0.117	0.026	0.243		0.150			0.900	3.707	0.448
Ba	0.014	0.045	0.307	0.067	0.204	0.300	0.155				15.28	9.744
Th	0.022	0.083	0.051	0.074	0.185	17.10	0.177				0.828	0.023
U	0.061	0.040	0.098	0.017	0.053	1.820	0.120				0.788	0.048
Nb	0.039	2.100	0.451	0.268	0.145		0.310	26.50	3.450		6.186	0.062
Ta	0.082	0.430	0.049	0.080	0.314	142.0	0.343	44.00	4.650		1.750	0.010
K		0.011	0.110	0.025	0.469		0.045		0.022		3.320	
La	0.013	0.166	0.182	0.144	0.312	8.817	0.205		0.007	0.053	0.748	0.080
Ce	0.009	0.246	0.166	0.143	0.469	23.45	0.229		0.008	0.083	0.894	0.039
Pb	0.151	0.870	0.620	0.405	0.360		2.900				0.917	1.245
Pr	0.006	0.360	0.138	0.177	0.735	27.17	0.290		0.008	0.128	0.960	0.036
Sr		0.125	2.143	0.055	0.400	1.350	0.110			0.027	1.237	5.931
P	0.055		0.045	0.009		100.0			0.050			
Nd	0.013	0.474	0.118	0.212	1.001	30.90	0.350		0.009	0.200	1.026	0.033
Zr	0.045	0.355	0.056	0.069	0.626	0.636	0.157			0.600	0.977	0.046
Hf	0.017	0.297	0.023	0.185	0.772	0.565	0.322			0.570	0.765	0.033
Sm	0.015	0.571	0.098	0.226	1.554	26.58	0.423		0.009	1.206	1.210	0.024
Eu	0.018	0.626	0.572	0.280	1.748	25.35	0.390		0.008	1.520	0.724	3.786
Ti		0.477	0.062	0.347	2.227		16.50		108.0	0.500	2.500	
Gd	0.019	0.641	0.064	0.257	2.132	25.92	0.468		0.008	5.200	1.238	0.022
Tb	0.022	0.625	0.071	0.352	2.343	25.29	0.513		0.009	7.100	1.254	0.022
Dy	0.019	0.704	0.089	0.334	2.300	24.67	0.440		0.010	13.17	1.125	0.045
Y	0.032	1.138	0.056	0.397	1.018	24.17	0.322		0.005	5.867	1.571	0.037
Ho	0.028	0.702	0.086	0.410	2.023	23.68	0.388		0.012	14.65	1.000	0.040
Er	0.036	0.736	0.084	0.409	1.681	22.70	0.342		0.015	18.69	0.896	0.035
Tm	0.041	0.819	0.085	0.509	1.577	18.28	0.302		0.019	23.83	0.808	0.031
Yb	0.046	0.903	0.086	0.608	1.474	13.85	0.266		0.023	30.40	0.734	0.028
Lu	0.095	0.925	0.063	0.847	1.416	7.050	0.305		0.029	57.00	0.698	0.033
La	0.013	0.166	0.182	0.144	0.312	8.817	0.205		0.007	0.053	0.748	0.080
Ce	0.009	0.246	0.166	0.143	0.469	23.45	0.229		0.008	0.083	0.894	0.039
Pr	0.006	0.360	0.138	0.177	0.735	27.18	0.290		0.008	0.128	0.960	0.036
Nd	0.013	0.474	0.118	0.212	1.001	30.90	0.350		0.009	0.200	1.026	0.033
Sm	0.015	0.571	0.098	0.226	1.554	26.58	0.423		0.009	1.206	1.210	0.024
Eu	0.018	0.626	0.572	0.280	1.748	25.35	0.390		0.008	1.520	0.724	3.786
Gd	0.019	0.641	0.064	0.257	2.132	25.92	0.468		0.008	5.200	1.238	0.022
Tb	0.022	0.625	0.071	0.352	2.343	25.29	0.513		0.009	7.100	1.254	0.022
Dy	0.019	0.704	0.089	0.334	2.300	24.67	0.440		0.010	13.17	1.125	0.045
Ho	0.028	0.702	0.086	0.410	2.023	23.68	0.388		0.012	14.65	1.000	0.040
Er	0.036	0.736	0.084	0.409	1.681	22.70	0.342		0.015	18.69	0.896	0.035
Tm	0.041	0.819	0.085	0.509	1.577	18.28	0.302		0.019	23.83	0.808	0.031
Yb	0.046	0.903	0.086	0.608	1.474	13.85	0.266		0.023	30.40	0.734	0.028
Lu	0.095	0.925	0.063	0.847	1.416	7.050	0.305		0.029	57.00	0.698	0.033

A4.6.a Kd values used to model melt at <63wt% SiO_2 (i.e. basalt and andesite). Compiled from the GERM database (http://eartref.org/GERM/).

	Cpx	Plg	Opx	Hb	Ap	Mag	Rut	Ilm	Grt	Bio	KFsp
Cs	2.387	0.094	0.407	0.010			0.008		0.670	3.000	0.195
Rb	0.037	0.092	0.035	0.154		0.050	0.004		0.034	3.707	0.448
Ba	0.347	0.944	0.130	0.356					0.014	15.28	9.744
Th	0.138	0.043	0.133	0.160	41.00	0.130	0.540	7.500	0.100	0.828	0.023
U		0.093	0.145		43.70	0.360		3.200	0.610	0.788	0.048
Nb	0.605	0.338	0.489	3.700	0.100	2.383	102.0	51.81	0.070	6.186	0.062
Ta	0.323	0.034	0.147	0.430		3.600	39.00	106.0	0.090	1.750	0.010
K	0.037	0.263		0.081					0.020	3.320	1.490
La	0.430	0.326	0.263	1.047	22.90	0.885	0.006	7.100	0.260	0.748	0.080
Ce	0.762	0.251	0.318	1.671	30.79	1.110	0.087	7.800	0.348	0.894	0.039
Pb	0.498	0.709	0.307	0.760	0.030	0.937	0.015	0.719	0.010	0.917	1.245
Pr	1.105	0.226	0.376	2.939	38.70	1.380	0.182	7.700	0.437	0.960	0.036
Sr	0.985	4.000	0.118	0.604		0.165	0.036	0.449	0.013	1.237	5.931
P											
Nd	1.456	0.194	0.434	4.207	46.65	1.650	0.277	7.600	0.525	1.026	0.033
Zr	0.460	0.177	0.094	0.642	0.547	0.681	4.240	2.106	1.200	0.977	0.046
Hf	0.548	0.131	0.170	0.520	0.804	2.350	5.320	3.100		0.765	0.033
Sm	2.329	0.135	0.547	6.924	50.65	2.000	0.016	6.900	2.660	1.210	0.024
Eu	2.100	3.248	0.327	5.541	28.90	0.470	0.000	2.500	1.500	0.724	3.786
Ti	0.700	0.050	0.400	15.80	0.100	12.50			1.200	2.500	
Gd	2.570	0.143	0.616	8.231	45.63	2.225	0.004	6.700	10.50	1.238	0.022
Tb	2.834	0.125	0.682	9.326	43.72	2.450	0.007	6.500	19.55	1.254	0.022
Dy	2.792	0.115	0.717	10.51	41.80	1.750	0.010	4.900	28.60	1.125	0.045
Y	2.743	0.150	1.000	12.90	40.00	0.955	0.007	1.034	52.10	1.571	0.037
Ho	2.679	0.107	0.804	9.866	36.56	1.558	0.011	4.686	35.70	1.000	0.040
Er	2.575	0.097	0.891	9.226	31.33	1.387	0.012	4.482	42.80	0.896	0.035
Tm	2.449	0.092	0.993	7.792	26.68	1.235	0.011	4.287	41.35	0.808	0.031
Yb	2.328	0.085	1.095	6.358	22.03	1.100	0.009	4.100	39.90	0.734	0.028
Lu	2.253	0.084	1.153	4.564	17.75	1.055	0.012	3.600	29.60	0.698	0.033
La	0.430	0.326	0.263	1.047	22.90	0.885	0.006	7.100	0.260	0.748	0.080
Ce	0.762	0.251	0.318	1.671	30.79	1.110	0.087	7.800	0.348	0.894	0.039
Pr	1.105	0.226	0.376	2.939	38.70	1.380	0.182	7.700	0.437	0.960	0.036
Nd	1.456	0.194	0.434	4.207	46.65	1.650	0.277	7.600	0.525	1.026	0.033
Sm	2.329	0.135	0.547	6.924	50.65	2.000	0.016	6.900	2.660	1.210	0.024
Eu	2.100	3.248	0.327	5.541	28.90	0.470	0.000	2.500	1.500	0.724	3.786
Gd	2.570	0.143	0.616	8.231	45.63	2.225	0.004	6.700	10.50	1.238	0.022
Tb	2.834	0.125	0.682	9.326	43.72	2.450	0.007	6.500	19.55	1.254	0.022
Dy	2.792	0.115	0.717	10.51	41.80	1.750	0.010	4.900	28.60	1.125	0.045
Ho	2.679	0.107	0.804	9.866	36.56	1.558	0.011	4.686	35.70	1.000	0.040
Er	2.575	0.097	0.891	9.226	31.33	1.387	0.012	4.482	42.80	0.896	0.035
Tm	2.449	0.092	0.993	7.792	26.68	1.235	0.011	4.287	41.35	0.808	0.031
Yb	2.328	0.085	1.095	6.358	22.03	1.100	0.009	4.100	39.90	0.734	0.028
Lu	2.253	0.084	1.153	4.564	17.75	1.055	0.012	3.600	29.60	0.698	0.033

A4.6.b. Kd values used to model melt at >63wt% SiO_2 (i.e. dacite and rhyolite). Compiled from the GERM database (http://eartref.org/GERM/).

Appendix A5: Whole rock geochemical data from The Capoas Granite

Element	Prep.	Analysis	Capoas Gt PAL 26	Capoas Gt PAL 27	Capoas Gt PAL 30	Capoas Gt PAL 34	Capoas Gt PAL 35
(wt%)							
SiO2	F	XRF	68.44	68.0922	68.3496	68.64885	71.0226
TiO2	F	XRF	0.563	0.5544	0.52767	0.467365	0.38313
Al2O3	F	XRF	15.22	15.2064	15.0777	16.0782	14.949
FeOTOT	F	XRF	2.61845	2.574449	2.521001	2.268828	1.754901
MnO	F	XRF	0.051	0.05049	0.04851	0.04009	0.02871
MgO	F	XRF	2.04	1.9404	1.8513	1.2027	0.7425
CaO	F	XRF	2.65	2.5542	2.6334	1.02335	1.4256
Na2O	F	XRF	3.24	3.168	3.0789	2.56365	3.1581
K2O	F	XRF	3.731	3.74913	4.02336	4.67787	5.19057
P2O5	F	XRF	0.148	0.13761	0.14256	0.19412	0.19305
Total			99.613	99.10393	99.3147	99.52765	99.51356
LOI			0.62	0.79	0.78	2.11	0.47
ppm							
Ta	F	ICP-MS	2.155	1.555	1.265	3.032	2.328
Sc	HF	ICP-MS	7.288	6.579	6.639	2.223	0.424
V	HF	ICP-MS	47.56	45.1	41.98	26.82	18.95
Cr	HF	ICP-MS	56.15	53.405	39.035	22.355	8.79
Ga	HF	ICP-MS	19.49	19.65	18.5	20.64	20.51
Co	HF	ICP-MS	9.685	9.312	8.105	5.725	3.618
Ni	HF	ICP-MS	42.24	39.21	25.64	15.72	3.928
Cu	HF	ICP-MS	3.1875	3.617	6.5215	0.511	0.19
Zn	HF	ICP-MS	45.35	42.62	41.77	39.03	34.68
Cs	F	ICP-MS	20.09	23.26	16.53	24.66	18.45
Rb	HF	ICP-MS	197.8	193.1	170.2	246	261.5
Ba	HF	ICP-MS	413.1	416.6	471.2	321.5	325.5
Sr	HF	ICP-MS	283.6	289.5	298.3	159.4	171.9
Zr	F	ICP-MS	164.5	167.1	158.3	228.9	179.1
Hf	F	ICP-MS	4.2825	4.187	3.969	5.2035	4.402
Th	F	ICP-MS	10.06	9.953	9.265	12.92	14.11
U	F	ICP-MS	5.585	4.442	2.462	4.64	5.432
Pb	HF	ICP-MS	33.12333	34.61333	32.93667	31.79333	34.25333
Nb	F	ICP-MS	20.91	18.68	16.37	31.86	24.79
Y	F	ICP-MS	20.02	14.05	13.5	10.81	14.29
La	HF	ICP-MS	23.05	32.86	25.22	29.11	27.38
Ce	F	ICP-MS	56.79	50.59	55.73	64.72	64.68
Pr	F	ICP-MS	6.895	6.012	6.583	7.596	7.859
Nd	F	ICP-MS	22.95	19.65	21.75	23.81	26.36
Sm	F	ICP-MS	5.125	4.369	4.43	4.7355	5.9275
Eu	F	ICP-MS	1.138	1.075	1.086	0.932	0.924
Gd	F	ICP-MS	4.77	3.968	3.943	3.873	4.962
Tb	F	ICP-MS	0.633	0.498	0.487	0.43	0.589
Dy	F	ICP-MS	3.3745	2.5405	2.4825	2.142	2.7735
Ho	F	ICP-MS	0.624	0.47	0.445	0.364	0.456
Er	F	ICP-MS	1.5795	1.1275	1.0495	0.8775	1.0155
Tm	F	ICP-MS	0.101	0.023	0.013	-0.004	-0.004
Yb	F	ICP-MS	1.7895	1.19	1.0905	1.073	1.009
Lu	F	ICP-MS	0.281	0.186	0.18	0.168	0.162

F = Fused
HF = Standard HF dissolution

A5.1. Whole rock major and trace element compositions of the Capoas Granite, Palawan

	Sample	$^{87}Sr/^{86}Sr_m$	2SE	$^{143}ND/^{144}Nd_m$	2SE	$^{206}Pb/^{204}Pb_m$	2SE	$^{207}Pb/^{204}Pb_m$	2SE	$^{208}Pb/^{204}Pb_m$	2SE
Capoas Gt	PAL26	0.708731	0.000011	0.512354	0.000008	18.5647	0.0015	15.6560	0.0014	38.9138	0.0038
Capoas Gt	PAL 34	0.709075	0.000010	0.512378	0.000008	18.5413	0.0017	15.6525	0.0015	38.9269	0.0049
Capoas Gt	PAL 35	0.709591	0.000011	0.512302	0.000007	18.5116	0.0007	15.6503	0.0008	38.9161	0.0031

A5.2. Whole rock radiogenic isotope data from the Capoas Granite of Palawan.

Appendix A6:

Cullen, A., Macpherson, C., Taib, N.I., Burton-Johnson, A., Geist, D., Spell, T. and Banda, R.M. (2013). Age and Petrology of the Usun Apau and Linau Balui Volcanics: Windows to Central Borneo's Interior. *Journal of Asian Earth Sciences*.

This publication includes samples analysed by the author of this thesis and isotopic modelling and interpretations made by the author on the Usun Apau and Linau Balui magmatism as part of a collaborative study. Reinterpretation of this data is discussed in Chapter 6.

Journal of Asian Earth Sciences 76 (2013) 372–388

Contents lists available at SciVerse ScienceDirect

Journal of Asian Earth Sciences

journal homepage: www.elsevier.com/locate/jseaes

Age and petrology of the Usun Apau and Linau Balui volcanics: Windows to central Borneo's interior

Andrew Cullen [a,*], Colin Macpherson [b], Nur Iskandar Taib [c], Alex Burton-Johnson [b], Dennis Geist [d], Terry Spell [e], Richard Mani Banda [f]

[a] Chesapeake Energy, Oklahoma City, OK, USA
[b] University of Durham, Durham, UK
[c] University of Malaya, Kuala Lumpur, Malaysia
[d] Idaho State University, Moscow, ID, USA
[e] University Las Vegas, Las Vegas, NV, USA
[f] Department of Minerals & Geoscience Malaysia, Kuching, Sarawak, Malaysia

ARTICLE INFO

Article history:
Available online 16 May 2013

Keywords:
Borneo
Usun Apau
Linau Balui
Volcanism
Sr
Nd
Pb isotope geochemistry
Luconia

ABSTRACT

The Usun Apau plateau lies in a remote area of Sarawak along the Tinjar Line, which defines the onshore part of a suture between the Luconia and Dangerous Grounds blocks. Reconnaissance studies in late 1950s established that the plateau is composed of a bimodal suite of young volcanic rocks, but no further work exists to constrain the age and petrogenesis of the Usun Apau volcanics. We present and discuss new data from a suite of volcanic rocks recently collected from the Usun Apau region. These data include ^{40}Ar–^{39}Ar age dates of mineral separates, major and trace element geochemistry, and Sr, Nd, Pb isotope geochemistry. The Usun Apau plateau is constructed largely of dacite and andesite erupted between 3.9 and 4.1 Ma. Minor basaltic dikes and flows (*ca.* 2.1 Ma) represent a distinctly younger episode of volcanism that is similar in age and character to the Linau Balui basalts about 100 km SE of the plateau. Although the trace element and isotopic suites from both areas indicate the parental melts were generated from a garnet-bearing, LILE-enriched, non-HIMU OIB-like mantle source, depletion in the HREEs and a negative Nb anomaly impart some characteristics of an island arc-type source contribution. The Usun Apau and Linau Balui volcanics are too young to be directly linked to subduction beneath Borneo; indicating a source region possibly modified by an older episode of subduction. Sr, Nd, Pb inter-isotope correlations plot within the same arrays as Pliocene basalts from the Southern Sulu Arc (500 km NE) which suggests much of northern and central Borneo is underlain by similar lithosphere. Assimilation–fractional crystallization modeling indicates that differentiation of the Usun Apau dacite magmas included assimilation of continental crust with very low $^{143}Nd/^{144}Nd$. Modeling different basement compositions as contaminants yielded non-unique results. Triassic Malay granite and different Archean granites represent plausible types of assimilants; whereas crust of Dangerous Grounds and Kontum Plateau do not.

1. Introduction

The Usun Apau plateau, one of several volcanic edifices of the interior of Sarawak, separates the headwaters of the Baram and the Pelagus-Rajang rivers (Figs. 1 and 2). The plateau is renowned for spectacular waterfalls that spill over its rim; the Julan Falls have a sheer plunge of more than 200 m (Hazenbroek and Morshidi, 2001). The plateau averages about 1000 m elevation and is constructed of flat-lying volcanic rocks that nonconformably overlie strongly deformed Paleogene flysch of the Rajang-Crocker Group. With annual rainfall on the plateau exceeding 2 m (Camerlengo et al., 2000), a youthful age for the plateau is inferred by the preservation of small calderas, which form the Dupoi valley, and constructional cones, such as Bukit Selidang, on the eastern side of the plateau (Fig. 2). Campbell (1956) and Kirk (1968) reported the Usun Apau volcanics include hypersthene-bearing dacites cut by subordinate late-stage basaltic dikes. Subsequent studies establishing the age and petrogenetic lineage of the Usun Apau volcanics are lacking, however. Hutchison (2005) noted the need for a modern petrologic and radiometric-dating program targeting the Usun Apau, but expressed doubt that such a program would be undertaken owing to the plateau's remote setting in Borneo's rugged interior highlands. In 2007 a small expedition attempting to climb Bukit Selidang (1373 m) collected a suite of samples suitable for the program envisioned by Charles Hutchison. This study reports

* Corresponding author.
E-mail address: abcullen@hotmail.com (A. Cullen).

1367-9120/$ - see front matter © 2013 Elsevier Ltd. All rights reserved.
http://dx.doi.org/10.1016/j.jseaes.2013.05.003

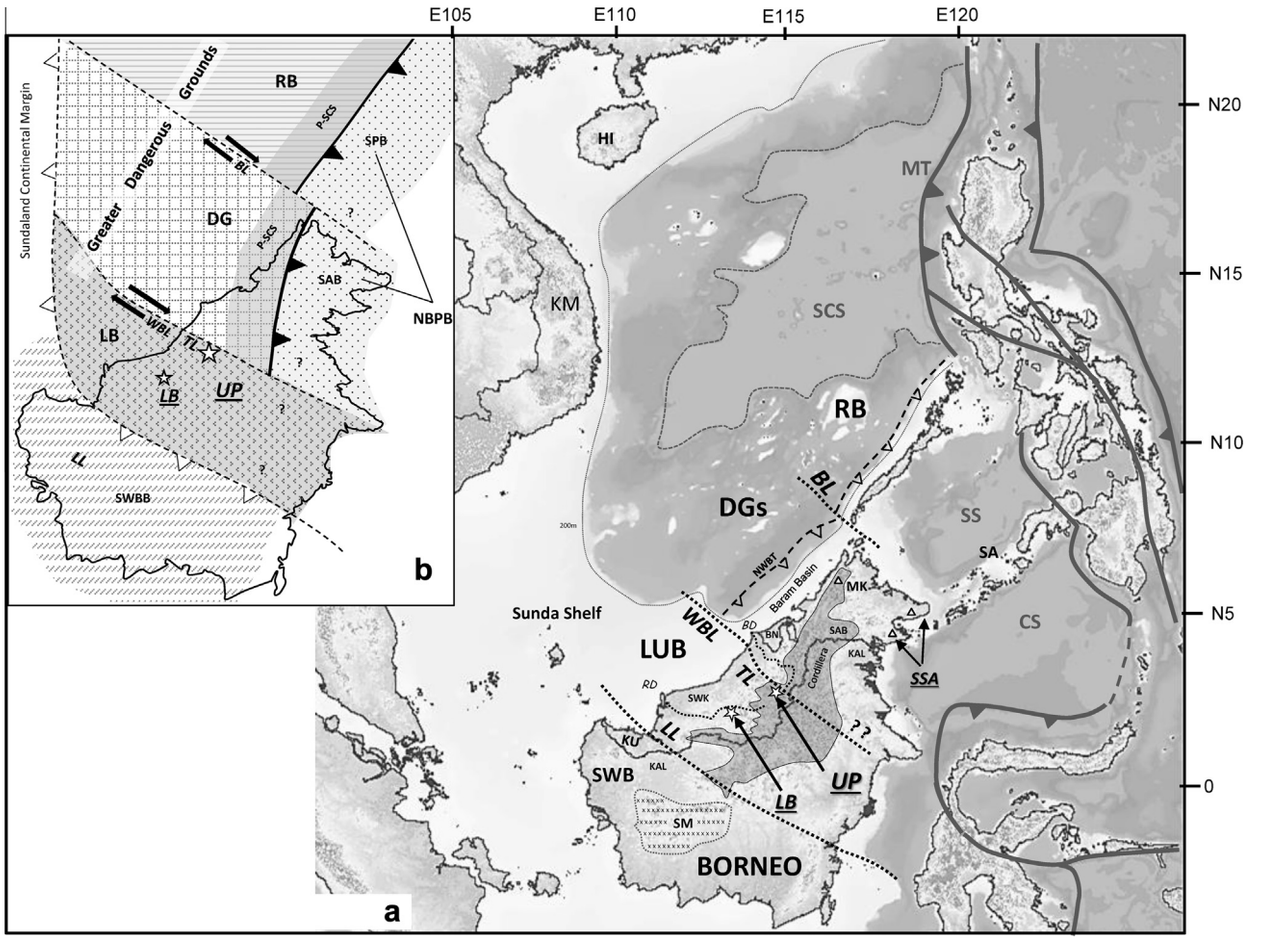

Fig. 1. (a) Maps showing location of study area in relation principal tectonic component of the Borneo region. *Abbreviation*: BD – Baram Delta, BL – Balabac Line, CS – Celebes Sea, DGs – Dangerous Grounds, HI – Hainan Island, KAL – Kalimantan, KM – Kontum Massif, KU – Kuching, LB – Linau – Balui plateau, LUB – Luconica Block, LL – Lupar Line, MK – Mount Kinabalu, MT – Manila trench, NWBT – Northwest Borneo Trough with limit of deepwater fold-thrust belt in dashed line with open triangles, RB – Reed Bank, RJD – Rajang Delta, SCS – South China Sea with oceanic crust outline in gray dashed line and 200 m isobaths in dotted line, SA – Sulu Arc, SAB – Sabah, SM – Schwaner Mountains, SS – Sulu Sea, SSA – Southern Sulu Arc SWB – Southwest Borneo Block, SWK – Sarawak, UP – Usun Apau, WBL – West Baram Line; strongly deformed Paleogene flysch of Borneo highlands shown as gray shaded areas. Question marks (?) highlight areas of uncertain relationships. (b) Schematic illustration of NW Borneo region's crustal blocks and tectonic setting *ca.* 35 Ma: abbreviations as before; NBPB – North Borneo Palawan Blocks, SPB – South Palawan Block. Lines with solid triangles denote upper plate of suture zones (Longley, 1997; Hall, 1997; Morley, 2002; Hall et al., 2009).

the analytical results from those samples within the framework of recent studies of Pliocene basalts from the Linau-Balui plateau (Taib, 2012) and the Southern Sulu Arc (Macpherson et al., 2010).

2. Regional setting

The lithosphere of the Borneo region comprises several blocks accreted to SE Asia prior to the Cenozoic (Fig. 1b; Metcalfe, 2010; Hall et al., 2009). The SW Borneo Block is a Paleozoic-cored fragment of Australian Gondwanaland sutured to Sundaland during the Middle Cretaceous (Metcalfe, 2010). The greater Dangerous Grounds, which comprises the Luconia, the Dangerous Grounds, and Reed Banks (Fig. 1b), collided with the SW Borneo Block along the Lupar Line in the Late Cretaceous (Metcalfe, 2010; Hall et al., 2009) ending an episode of subduction beneath SW Kalimantan that produced the Schwaner Mountain granites (Hutchison, 1996). An interval of relative tectonic quiescence that followed collision of the greater Dangerous Grounds ended with the initiation of SE-directed subduction of the oceanic crust of the proto-South China Sea (*ca.* 45 Ma; Hall et al., 2009) and ultimately to the progressive collision of the Dangerous Grounds and Reed Banks continental blocks with NW Borneo and Palawan, respectively. The history of subduction of the proto-South China Sea (SCS) beneath NW Borneo is poorly understood. Some workers envision an extensive proto-SCS (Taylor and Hayes, 1983; Hall, 2002; Clift et al., 2008) with protracted subduction that extended into the Early Miocene, whereas Rangin et al. (1999) and Cullen (2010) envision a narrower proto-SCS with less subduction prior to collision of the Dangerous Grounds and Reed Bank with the upper plate of the North Borneo Palawan Block.

Hutchison et al. (2000) interpreted the suture between the Dangerous Grounds and North Borneo Palawan Block as passing through the central part of Sabah (Fig. 1b). Mesozoic granitic rocks have been dredged from fault scarps on the Dangerous Grounds (Kudrass et al., 1986; Yan et al., 2010). Zircons from the Late Miocene Mt. Kinabalu pluton with inherited Late Cretaceous and older cores (Cottam et al., 2010) are strong evidence that Dangerous Grounds basement extends to the suture proposed by Hutchison et al. (2000). Although the North Borneo Palawan Block has an oceanic character marked by exposures of Lower Cretaceous ophiolites, the nature of the basement supporting the Sabah and South Palawan ophiolites is unclear. Several lines of evidence suggest this

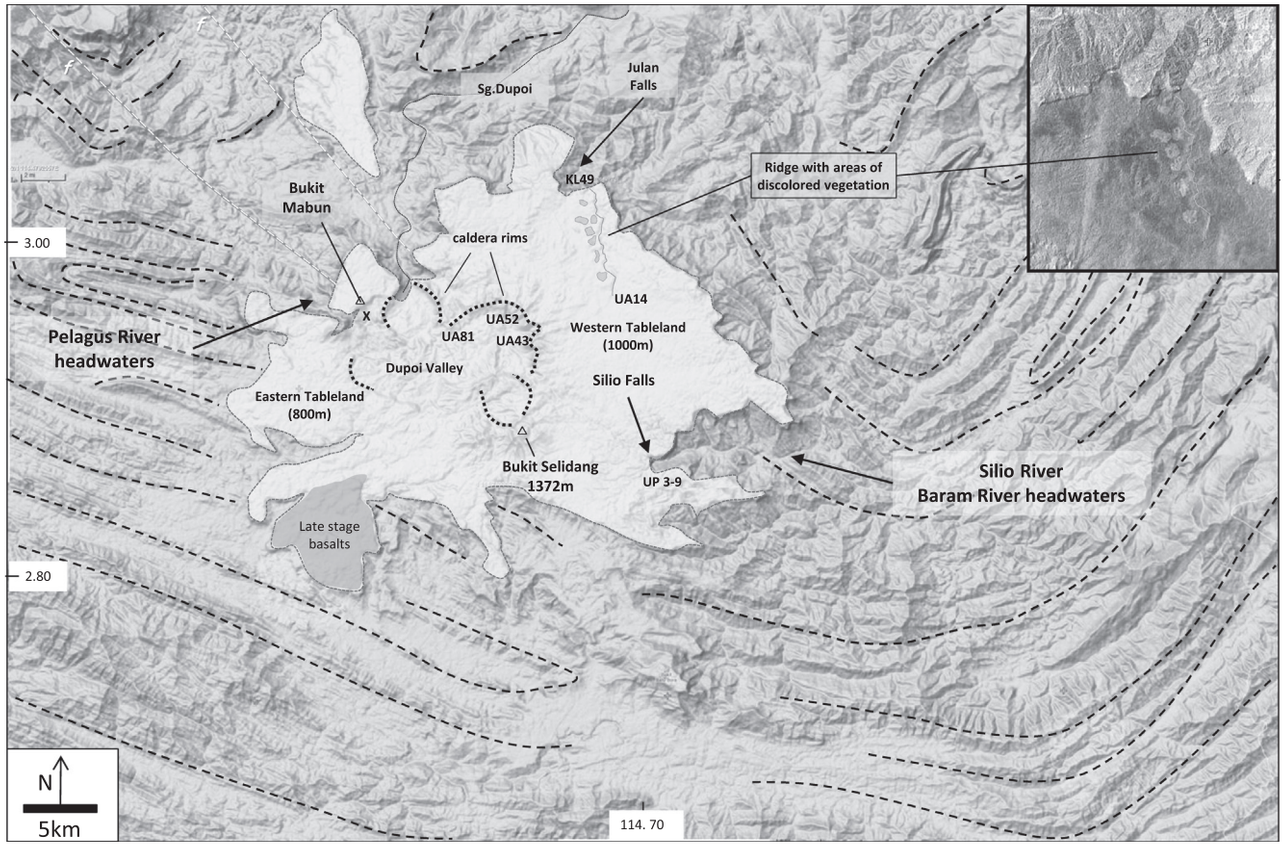

Fig. 2. Geological features of the Usun Apau area: Topographic relief map as background, volcanic plateau in light gray with sample locations posted, fold axes of strongly deformed Paleogene deepwater clastic rocks in dashed black lines. Dashed gray lines and (*f*) mark faults that bound the NE edge of the Dulit plateau approximately 20 km northwest of the Usun Apau plateau. Inset is a Google Earth image of eastern side of plateau.

basement is of a continental affinity; Jurassic to Triassic age granitoids crop out in small windows beneath the ophiolites (Hutchison, 2005), Pliocene basalts from the Southern Sulu Arc have isotopic signatures indicating assimilation of Archean continental crust (Macpherson et al., 2010), Bouguer gravity data indicate that most of Sabah is underlain by low density crust (Milsom and Holt, 2001), and to the NE the Sulu Sea and Palawan have been interpreted as part of micro-continental plate (Bird et al., 1993; Yumul et al., 2009).

The Usun Apau plateau lies along the Tinjar Line where a deflection in the structural grain of the underlying Rajang-Crocker Group defines a large oroclinal bend (Fig. 1a; Hutchison, 2010). The Tinjar Line is often shown extending offshore extension to link with the West Baram Line (Figs. 1 and 3). These "lines" are poorly understood features that have never been rigorously defined. In early tectonic models (Hamilton, 1979; Holloway, 1982; Daly et al., 1991) the lines are not featured; whereas some subsequent models interpret these lines as lying along a transform boundary that accommodated differential motion between the Luconia Block and the Dangerous Grounds during subduction of the proto-SCS (Fig. 1b; Morley, 2002; Clift et al., 2008; Hall et al., 2009). With respect to current plate boundaries, however, the Usun Apau plateau represents an intra-plate tectonic setting that is ideally located to study the nature of the Luconia Block in relation Borneo's other possible basement fragments.To the extent that volcanic rocks represent direct, albeit modified, samples of the lower crust and upper mantle, the distribution, age, and composition of Borneo's igneous rocks provide information with which to constrain models for the region's tectonic evolution. Borneo's Cenozoic igneous record is intriguing and somewhat problematic. Igneous rocks of various ages, although widespread, are limited and not a volumetrically significant portion of the rock record. Episodes of bimodal volcanism that occurred in the Late Eocene and Late Miocene to Pleistocene are separated by Oligocene–Miocene calc-alkaline igneous activity. For the purposes of this paper we group Borneo's Cenozoic igneous rocks into 5 informal units (Fig. 3).

1. The Usun Apau and Linau Balui plateaus belong to a group of dissected Plio-Pleistocene volcanic tablelands that cap parts of Borneo's interior highlands. These tablelands include the Nieuwenhuis Mountains, and the Nankan plateau, and thus mostly lie SW of the Tinjar line (Fig. 3). Owing to their remote location, the volcanic rocks of tablelands remain relatively under-studied. Basalts, dacites, and andesites have been reported (reviewed by Tate, 2001; Hutchison, 2005) and a limited number of age determinations indicate Pliocene to Pleistocene magmatic activity (Weerd and Armin, 1992).
2. The Southern Sulu Arc (SSA) comprises Early to Middle Miocene andesites, which record short-lived subduction of part of the Celebes Sea beneath SE Sabah, as well as Plio-Pleistocene basaltic rocks that post-date subduction (Chiang, 2002; Hutchison, 2005). Those basalts have been interpreted as being derived by partial melting of from an OIB-like mantle, and some of the more evolved basaltic andesites have radiogenic isotopic ratios indicative of assimilation of ancient continental crust basement (Macpherson et al., 2010).

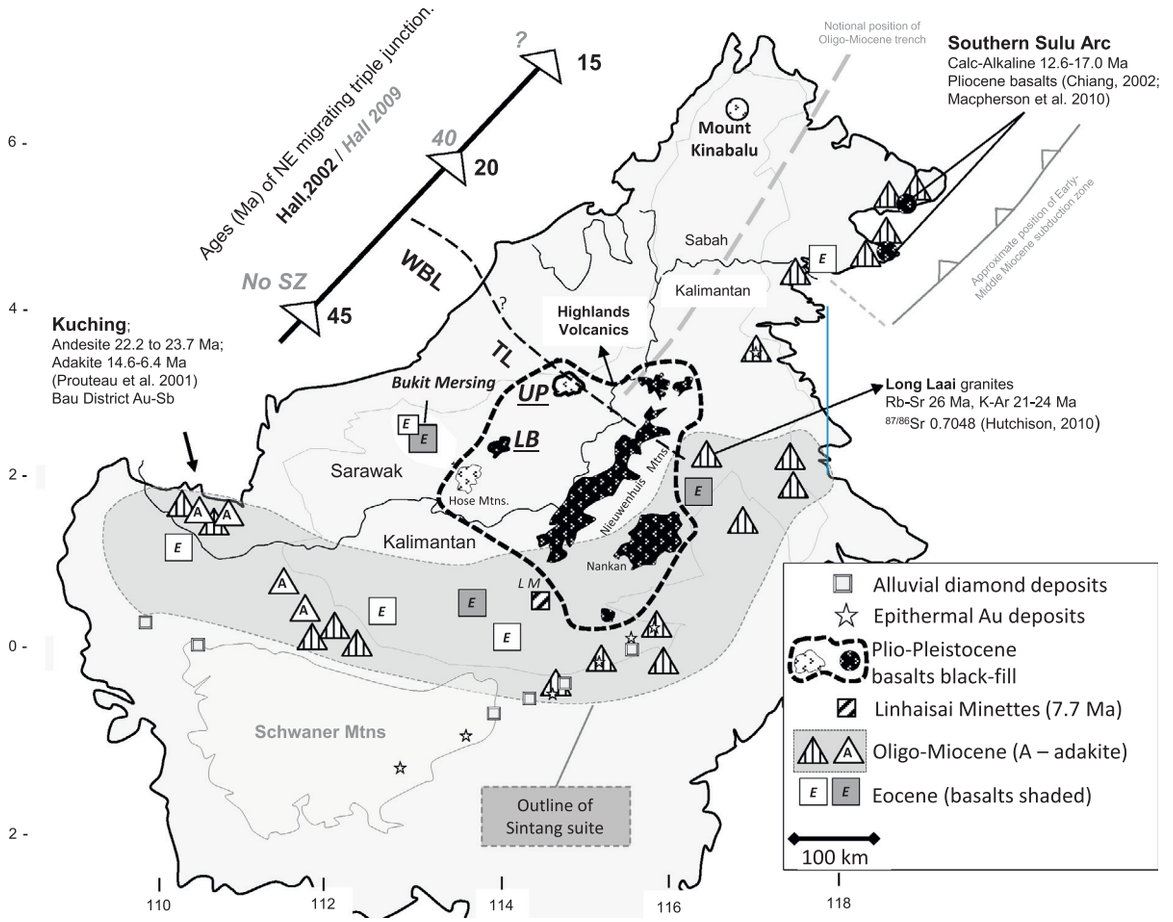

Fig. 3. Map showing distribution and age of Cenozoic igneous rocks in relation to tectonic elements discussed in text. Abbreviations as before and those shown in legend. Open triangles show the different ages of position of subduction tip line in the different tectonic reconstructions of Hall (2002, 2009).

3. The Sintang suite is represented primarily by Oligocene to Miocene calc-alkaline stocks, plugs, and dikes (Van Bemmelen, 1949; Soeria-Atmadja et al., 1999) that are associated with epithermal gold mineralization (van Leeuwen et al., 1990). The Sintang suite occurs mostly in Kalimantan, but extends into Sarawak, Malaysia, near the city of Kuching where two distinct phases of igneous activity are recorded; Early Miocene (23.7–23.3 Ma) calc-alkaline diorites and Middle to Late Miocene (14.6–6.4 Ma) microtonalites and dacites, which have an adakite signature (Prouteau et al., 2001). The Kuching adakites are associated with gold-antimony mineralization and have been interpreted as re-melting of oceanic lithosphere modified during an earlier episode of subduction (Prouteau et al., 2001). Alternatively, the Linhaisai minettes (*ca.* 8 Ma, ultra-potassic philogopite-bearing mafic dikes) in the Central Kalimantan (Fig. 3) suggests the region is underlain by enriched subcontinental mantle lithosphere (Bergman et al., 1988).
4. Mt. Kinabalu is an isolated, sheeted, granitic pluton in northern Sabah, Malaysia, that was emplaced in several short pulses between 7 and 8 Ma (Cottam et al., 2010); it can regarded as post-dating subduction and collision of Dangerous Grounds continental crust. Isotopic data show that older pulses have more radiogenic Sr and Pb and less radiogenic Nd and Hf than the younger pulses, which may reflect either differences in crustal assimilation or incongruent dehydration melting of a sole source (Burton-Johnson and Macpherson, 2012). Inherited zircon ages from the Mt. Kinabalu pluton indicate it is underlain by subducted Mesozoic Dangerous Grounds continental crust (Cottam et al., 2010).
5. Bi-modal Eocene volcanic rocks crop out at several widely separated locations (Pieters and Supriatna, 1990) and have been penetrated by exploration wells in nearly all of Kalimantan's onshore basins (Satyana et al., 1999). This episode of volcanism is likely related to the early rift phase of basinal extension (Hutchison, 1996). The Bukit Mersing basalts, approximately 100 km east of the Linau Balui plateau (Fig. 3), have trace element characteristic of ocean island basalts (Taib, 2010). These basalts are important because their geochemical signature predates any modification of the lithosphere during Oligocene–Early Miocene tectonism.

3. Field program & sampling

The Usun Apau plateau covers an area of about 770 km^2. Its original extent, although undoubtedly larger, is not known. The plateau's margins are steep; sheer drops up to 300 m reflect the thickness of the lavas and welded tuffs that make up the plateau and cap steeply dipping sandstones and shales of the Belaga Formation. Fresh outcrops are limited to stream cuts in deep ravines. Access is limited and dangerous. Because high runoff and strong currents quickly round material transported from the plateau and remove weathering rinds, river cobbles collected near the base

Fig. 4. Outcrop photo at Silio Falls (*ca.* 200 m) shows contact between crudely jointed lava flows (UP-D) and overlying welded tuffs (UP-WT).

of the plateau provide fresh, albeit out of place, samples. Owing to the relatively small size of the plateau and numerous drainages the river cobbles represent samples transported only short distances. On the south side of the plateau, 8 km from Bukit Selideng, the seven UP samples were collected from the Silio River near the base of the Silio Falls (Fig. 2) where crudely bedded welded tuffs overlie weakly jointed lava flows (Fig. 4). In hand sample the welded tuffs have well developed flow banding defined by black fiamme; UP4 had visible quartz and was classified as dacite. The lavas, 15% plagioclase phenocrysts set in an aphanitic groundmass, were classified in the field as andesite owing to their light gray color. Additional samples from Usun Apau caldera walls and from Linau-Balui plateau were collected during field work between 1982 and 1987 (Banda and Aji, 2012) and analyzed by Taib (2012).

4. Analytical methods

Appendix A summarizes our analytical techniques and results are given in Tables 1–3. Age determinations used performed using the Ar–Ar method (University of Nevada Las Vegas), major and trace elements were measured by X-ray Fluorescence Spectroscopy (Washington State University and University of Malaya); and trace elements and radiogenic isotopes were measured by Inductively Coupled Plasma Mass Spectrometry (Washington State University, Vrij University Amsterdam, and Durham University).

5. Results

5.1. Petrography

Examination of standard, but unstained, thin sections confirmed the field classifications of andesite and welded tuff (Fig. 5). The welded tuffs have a glassy groundmass with numerous small opaque crystals presumed to be Fe–Ti oxides. Euhedral to subhedral hypersthene phenocrysts set in the groundmass suggest pyroxene was an equilibrium phase at the time of eruption. Plagioclase phenocrysts (*ca.* An_{40} from extinction angles) are also present; some show strong oscillatory zoning indicative of minor fluctuations in the magma chamber prior to eruption (Fig. 5C). Groundmass plagioclase is slightly more sodic (*ca.* An_{30}). Although rare, small grains of biotite are present; these yielded reliable age dates. Several samples have large anhedral quartz grains with highly embayed rims around which the glassy groundmass shows viscous flow features (Fig. 5A). Abundant inclusions of rutile are present in some quartz grains indicating a plutonic source (Fig. 5B). The Usun Apau plateau is constructed upon a thick section of the Belaga Formation which has sandstones derived largely from a granitic provenance such as the Schwaner Mountains (van Hattum et al., 2006). We interpret the quartz grains as xenocrysts from the Belaga Formation, rather than an equilibrium phase at the time of eruption. The lava flows have a pilotaxitic texture owing to alignment of plagioclase laths (*ca.* An_{40}) and subhedral hypersthene (Fig. 5D). The phenocrysts in the lavas are smaller than those in the welded tuffs. Rounded quartz grains are present, but rare, whereas biotite was not seen in thin section.

5.2. ^{39}Ar–^{40}Ar age determinations

Three samples were analyzed using conventional furnace stepwise heating analyses on bulk mineral separates (Table 1). Although the samples had U-shaped age spectra commonly associated with excess argon (Fig. 6), stable plateau ages could be determined for each sample; UP 7 yielded a 3 point isochron age. An isochron age is the best estimate of the age of a sample, even if a plateau age is obtained.

The age spectrum for the UP-4 biotite is characterized by high initial ages (step 2 ~6.2 Ma) that decrease progressively to ages of ~4 Ma by ~10% gas released. This decline is followed by a flat, concordant age spectrum for the remainder of the gas released. The total gas age, which is equivalent to a conventional K/Ar age, is 3.96 ± 0.03 Ma. Steps 8–13 (77% of the ^{39}Ar released) define a slightly younger, but statistically indistinguishable, plateau age of 3.90 ± 0.04 Ma. There is no isochron defined by these data. Ca/K ratios are slightly high in the first few steps, but otherwise generally consistent with outgassing of a homogeneous biotite mineral separate. Radiogenic yields ($\%^{40}Ar^{*}$) are somewhat low for a high-K phase of this age, which may indicate some alteration is present. The high initial ages are likely caused by recoil of reactor-generated ^{39}Ar out of the biotite crystals, which based on $\%^{40}Ar^{*}$ could contain chlorite intergrowths that would result in a depleted layer near the surface of the crystals, the first material to outgas on step heating. Thus, initial ages from recoil affected samples are anomalously high. The possibility that the shape of this age spectrum is a result of excess argon in the sample cannot be confirmed, as no isochron is defined by these data. The overall concordant nature of the age spectrum and the observation that recoil artifacts are common in biotites, the plateau age (3.90 ± 0.04 Ma) is considered the most reliable for this sample.

The UP-8 biotite sample produced an age spectrum similar to the UP-4 biotite and is interpreted similarly. The total gas age for this sample is 3.94 ± 0.04 Ma. Steps 6–10 (69% of the ^{39}Ar released) define a slightly younger (statistically indistinguishable) plateau age of 3.86 ± 0.05 Ma. Steps 6–8 (57% of the ^{39}Ar released) define a statistically valid isochron, which yields an age of 3.84 ± 0.06 Ma and an initial $^{40}Ar/^{36}Ar$ ratio of 301.0 ± 4.5, indistinguishable from atmospheric argon at the 2σ uncertainty level. Although the isochron is defined by only 3 points, it is important that the isochron does not suggest excess argon is present. Ca/K

Table 1
Results of ^{39}Ar–^{40}Ar age determinations.

Step	T (C)	t (min.)	^{36}Ar	^{37}Ar	^{38}Ar	^{39}Ar	^{40}Ar	$\%^{40}Ar^{*}$	% ^{39}Ar rlsd	Ca/K	$^{40}Ar^{*}/^{39}ArK$	Age (Ma)	1s.d.
UP4: Andesite–Biotite, 11.80 mg, J = 0.001580 ± 0.59%													
1	650	12	4.846	3.448	1.185	12.075	1381.58	0.6	1.0	0.943909	0.666563	1.90	1.27
2	725	12	1.297	4.154	0.422	8.255	384.301	4.9	0.7	1.663759	2.163354	6.16	0.31
3	790	12	1.093	5.607	0.788	28.377	358.384	14.7	2.3	0.653096	1.759361	5.01	0.09
4	850	12	0.437	4.995	1.124	50.301	197.358	42.0	4.1	0.328194	1.483612	4.22	0.05
5	900	12	0.331	3.665	0.886	40.390	151.006	44.5	3.3	0.299895	1.439306	4.10	0.05
6	950	12	0.388	2.588	1.047	47.544	178.074	43.7	3.9	0.179896	1.438603	4.10	0.05
7	1000	12	0.556	1.781	1.657	75.984	264.970	44.1	6.2	0.077461	1.416099	4.03	0.05
8	1040	12	0.979	1.204	3.976	187.271	537.285	50.1	15.2	0.021247	1.387971	3.95	0.05
9	1070	12	0.839	0.874	5.187	247.004	575.287	60.5	20.0	0.011693	1.366173	3.89	0.04
10	1090	12	0.391	0.668	2.739	130.556	292.479	66.8	10.6	0.016909	1.391487	3.96	0.05
11	1120	12	0.304	0.872	2.570	121.423	251.759	72.0	9.9	0.023733	1.363360	3.88	0.04
12	1160	12	0.269	1.905	3.487	165.381	302.453	80.5	13.4	0.038067	1.367931	3.90	0.04
13	1215	12	0.180	2.124	2.130	100.804	186.929	82.7	8.2	0.069633	1.348946	3.84	0.04
14	1400	12	0.155	1.767	0.390	17.054	67.650	74.0	1.4	0.342440	1.447393	4.12	0.07
											Total gas age =	3.96	0.03
									Steps 8–13		Plateau age =	3.90	0.04
UP7: Dacite–Plagioclase, 24.68 mg, J = 0.001635 ± 0.69%													
1	600	12	9.122	51.242	4.027	141.252	2853.28	9.6	14.9	1.174744	1.948062	5.74	0.14
2	640	12	1.011	29.476	1.568	101.188	446.574	37.7	10.7	0.943240	1.615873	4.76	0.06
3	680	12	0.743	35.317	1.728	120.701	397.662	49.8	12.7	0.947450	1.583581	4.67	0.05
4	720	12	0.578	36.476	1.723	120.984	340.901	56.3	12.7	0.976261	1.501671	4.42	0.05
5	770	12	0.493	34.620	1.526	106.960	291.288	57.2	11.3	1.048097	1.457492	4.29	0.05
6	830	12	0.466	31.984	1.073	69.876	227.971	47.9	7.4	1.482366	1.430986	4.22	0.05
7	900	12	0.378	23.637	0.723	43.449	164.627	41.9	4.6	1.761971	1.394287	4.11	0.07
8	990	12	0.429	16.084	0.504	28.684	160.479	29.3	3.0	1.816132	1.417053	4.18	0.07
9	1090	12	1.039	16.534	0.723	32.136	342.947	15.6	3.4	1.666327	1.568286	4.62	0.09
10	1180	12	3.196	20.858	1.400	49.885	1012.63	11.0	5.3	1.354058	2.199788	6.48	0.15
11	1260	12	5.845	31.728	2.389	80.686	1840.74	10.3	8.5	1.273412	2.341004	6.89	0.15
12	1400	12	3.736	28.766	1.557	53.240	1182.22	11.0	5.6	1.749952	2.408051	7.09	0.16
											Total gas age=	5.11	0.05
											No plateau		
											No isochron		
UP8: Dacite–Biotite, 8.90 mg, J = 0.00152 ± 0.93%													
1	730	12	1.885	16.062	0.671	14.138	553.797	4.1	2.1	3.782874	1.559721	4.27	0.23
2	800	12	0.353	12.167	0.306	11.736	119.372	21.5	1.7	3.451690	1.811623	4.96	0.11
3	860	12	0.276	9.402	0.503	22.300	112.978	39.4	3.3	1.402894	1.631004	4.47	0.06
4	920	12	0.318	7.185	0.656	29.125	113.242	39.5	4.3	0.820723	1.508548	4.13	0.07
5	970	12	0.356	4.081	0.981	46.958	170.899	47.3	6.9	0.289085	1.501238	4.11	0.06
6	1010	12	0.395	2.053	1.490	72.577	215.676	53.5	10.7	0.094088	1.432161	3.92	0.05
7	1040	12	0.682	1.464	3.186	154.238	411.703	55.7	22.7	0.031571	1.417177	3.88	0.05
8	1070	12	0.540	1.219	3.131	156.065	374.564	62.5	23.0	0.025980	1.416446	3.88	0.05
9	1100	12	0.253	0.957	1.204	60.404	155.342	62.8	8.9	0.052697	1.387210	3.80	0.05
10	1130	12	0.155	0.743	0.557	26.473	80.626	64.3	3.9	0.093353	1.385749	3.80	0.05
11	1170	12	0.199	1.153	1.087	52.899	127.995	68.3	7.8	0.072497	1.353591	3.71	0.05
12	1220	12	0.119	1.530	0.532	25.747	69.315	78.2	3.8	0.197661	1.385018	3.79	0.07
13	1400	12	0.128	1.712	0.131	5.531	45.640	43.7	0.8	1.029822	1.716188	4.70	0.19
											Total gas age=	3.94	0.04
									Steps 6–10		Plateau age=	3.86	0.05
									Steps 6–8		Isochron age=	3.84	0.06

$\%^{39}Ar$ rlsd (released).
4 amu discrimination = 1.0433 ± 0.20%, 40/39 K = 0.0148 ± 79.07%, 36/37Ca = 0.00026 ± 3.15%, 39/37Ca = 0.00067 ± 1.70%.
Note: isotope beams in mV, rlsd = released, error in age includes J error, all errors 1 sigma (^{36}Ar through ^{40}Ar are measured beam intensities, corrected for decay for the age calculations).
K concentration is not measured directly in the $^{40}Ar/^{39}Ar$ method.
Measurement of ^{39}Ar indirectly gives the ^{40}K via the irradiation and calibration with the fluence monitor standard.

ratios are initially high, and again with the final step, suggesting the presence of another mineral phase in this biotite separate. The affected steps account for ~12% of the total gas released. Radiogenic yields are somewhat low, suggesting some alteration may be present. Although all 3 ages are identical within 2σ uncertainties, the plateau age (3.86 ± 0.05 Ma) is considered the most reliable for this sample.

UP-7, a plagioclase separate, is characterized by a discordant age spectrum with high initial age of ~5.7 Ma, followed by steps of progressively decreasing age until step 7 (4.11 ± 0.07 Ma), and then progressively increasing ages to a final step at 7.1 Ma. The total gas age is 5.11 ± 0.05 Ma. There are no plateau or isochron ages defined by these data. Ca/K ratios are somewhat low and varied for a plagioclase, unless this is a very high-K plagioclase which is not consistent with petrographic observations. Radiogenic yields are as expected for a plagioclase of this age. However, the very low radiogenic yields in the final steps, which are generally of higher radiogenic yield, suggest some alteration of the mineral separate. The form of the age spectrum is distinctly U-shaped, suggesting excess argon is present, although this cannot be confirmed via an isochron. The most conservative interpretation in this case is to assume excess argon is present, and thus the youngest age on the age spectrum (step 7, 4.11 ± 0.07 Ma) is a maximum age for the sample. The age Ar–Ar age dates are consistent with outcrop

Table 2
Major and trace element analyses: major element oxides normalized to 100% on a volatile-free basis.

Location	UP3 2.85N 114.71E Andesite	UP4 2.85N 114.71E Andesite	UP5 2.85N 114.71E Dacite	UP6 2.85N 114.71E Dacite	UP7 2.85N 114.71E Dacite	UP8 2.85N 114.71E Dacite	UP9 2.85N 114.71E Andesite	UA81 2.931N 114.58 Dacite	UA43 2.94N 114.62E Basalt	UA52 2.95N 114.63E Basaltic Andesite	UA14 2.95N 114.67E Basaltic Andesite	TN96 3.24N 114.35E Basaltic Andesite	LB98 2.46N 114.10E Basalt	LB64 2.42N 114.07E Basalt	LB85 2.43N 114.08E Basaltic Andesite	KL49 3.04N 114.65E Basaltic Andesite	AN35 2.99N 114.86E Basaltic Andesite
wt%																	
SiO_2	66.10	66.62	68.49	67.75	67.50	67.74	66.97	70.45	53.94	54.73	55.48	59.63	53.07	51.66	54.28	56.08	54.93
TiO_2	0.54	0.55	0.53	0.53	0.59	0.53	0.57	0.50	1.44	1.41	1.37	1.04	1.51	1.67	1.53	1.37	1.37
Al_2O_3	16.94	17.01	16.52	16.17	15.10	16.18	17.41	16.10	16.90	16.88	16.82	16.10	16.17	16.25	16.50	16.93	16.81
FeO^*	3.78	3.59	3.06	3.36	3.88	3.41	3.56	2.87	9.97	9.10	9.39	7.67	11.46	11.13	10.69	9.19	9.75
MnO	0.07	0.06	0.05	0.07	0.07	0.07	0.06	0.03	0.00	0.13	0.14	0.09	0.13	0.11	0.16	0.13	0.14
MgO	2.54	2.11	1.78	2.31	3.65	2.35	2.16	0.99	5.19	5.31	4.52	3.83	4.90	5.80	3.72	4.37	4.66
CaO	4.25	4.23	3.53	3.77	3.51	3.73	3.63	2.73	7.42	7.31	7.14	5.63	7.81	8.61	7.95	6.67	7.23
Na_2O	3.60	3.83	3.69	3.63	3.22	3.64	3.61	3.57	3.40	3.39	3.41	3.48	3.58	3.54	3.63	3.47	3.63
K_2O	2.06	1.88	2.23	2.29	2.36	2.24	1.92	2.67	1.51	1.51	1.50	2.31	1.13	0.96	1.28	1.59	1.28
P_2O_5	0.12	0.12	0.11	0.12	0.12	0.12	0.10	0.11	0.24	0.23	0.24	0.24	0.24	0.27	0.26	0.22	0.20
LOI	1.51	3.09	2.56	1.78	1.95	2.51	2.53	2.97	0.66	0.57	1.84	3.37	0.98	1.55	1.83	1.74	2.05
ppm																	
Ni	42.9	39.0	22.9	33.4	45.0	28.6	33.7	*NA*	*NA*	78.4	77.8	*NA*	*NA*	*NA*	*NA*	55.9	54.6
Cr	60.0	57.1	53.9	54.2	130.3	55.9	56.7	*NA*	*NA*	140.9	131.0	*NA*	*NA*	*NA*	*NA*	92.4	114.7
Sc	9.2	9.3	8.2	9.1	10.3	8.7	9.3	19.0	19.0	18.7	18.3	7.7	21.0	20.6	22.5	17.6	18.8
V	64.1	55.0	55.1	56.5	70.2	56.9	56.3	*NA*	*NA*	122.4	115.2	*NA*	*NA*	*NA*	*NA*	115.2	122.5
Ba	337.5	321.4	362.7	379.8	365.6	361.3	365.8	194.7	989.5	184.1	191.6	427.4	157.6	138.3	167.7	215.1	178.3
Rb	85.6	72.4	88.7	92.6	92.6	90.4	69.7	46.1	73.8	41.9	44.1	133.2	28.5	18.5	31.5	48.8	36.9
Sr	456.0	451.5	395.7	406.5	300.3	400.0	405.8	304.8	1040.7	304.6	300.7	364.4	261.2	288.8	266.3	294.0	275.2
Zr	172.9	174.2	167.8	164.3	158.7	163.9	179.7	131.7	142.1	119.2	119.4	67.0	134.0	113.5	138.0	116.5	102.1
Y	12.9	14.5	16.2	14.4	16.5	14.6	14.0	24.1	49.0	22.6	19.8	15.8	25.1	22.6	28.8	20.4	20.0
Nb	9.0	8.9	9.3	9.5	10.8	9.5	9.7	17.1	12.7	14.7	14.4	10.5	15.8	15.6	16.5	14.4	12.1
Ga	17.0	15.7	16.2	17.2	16.1	17.0	16.7	*NA*	*NA*	18.1	19.5	*NA*	*NA*	*NA*	*NA*	19.7	19.6
Cu	17.7	22.6	15.3	18.2	14.5	17.3	33.1	*NA*	*NA*	49.1	49.3	*NA*	*NA*	*NA*	*NA*	47.4	50.8
Zn	60.4	60.3	48.2	60.4	52.5	58.3	62.4	*NA*	*NA*	94.2	93.6	*NA*	*NA*	*NA*	*NA*	90.3	98.1
Pb	9.3	10.4	12.0	11.2	9.4	11.4	12.0	5.1	23.2	4.1	4.6	23.0	4.5	1.7	4.7	5.3	4.1
La	*NA*	*NA*	*NA*	*NA*	*NA*	*NA*	*NA*	16.1	45.5	15.6	14.2	29.0	12.6	9.7	13.7	13.7	11.3
Ce	*NA*	*NA*	*NA*	*NA*	*NA*	*NA*	*NA*	32.3	89.1	30.2	27.6	56.7	26.3	21.3	27.7	26.1	21.9
Pr	*NA*	*NA*	*NA*	*NA*	*NA*	*NA*	*NA*	4.09	10.4	3.9	3.5	6.2	3.4	2.8	3.5	3.3	2.8
Nd	*NA*	*NA*	*NA*	*NA*	*NA*	*NA*	*NA*	17.4	42.6	16.3	14.5	22.8	14.8	13.1	15.5	13.7	12.0
Sm	*NA*	*NA*	*NA*	*NA*	*NA*	*NA*	*NA*	4.26	8.49	4.26	3.79	4.43	3.89	3.72	4.00	3.62	3.41
Eu	*NA*	*NA*	*NA*	*NA*	*NA*	*NA*	*NA*	1.43	2.55	1.43	1.28	1.17	1.33	1.39	1.37	1.23	1.20
Gd	*NA*	*NA*	*NA*	*NA*	*NA*	*NA*	*NA*	4.57	8.65	4.61	4.02	3.72	4.41	4.25	4.65	3.98	3.84
Tb	*NA*	*NA*	*NA*	*NA*	*NA*	*NA*	*NA*	0.73	1.23	0.75	0.67	0.55	0.72	0.70	0.76	0.67	0.65
Dy	*NA*	*NA*	*NA*	*NA*	*NA*	*NA*	*NA*	4.32	7.02	4.50	4.02	2.98	4.31	4.11	4.59	4.05	3.96
Ho	*NA*	*NA*	*NA*	*NA*	*NA*	*NA*	*NA*	0.83	1.37	0.89	0.79	0.54	0.85	0.78	0.92	0.80	0.79
Er	*NA*	*NA*	*NA*	*NA*	*NA*	*NA*	*NA*	2.32	3.85	2.30	2.07	1.46	2.38	2.15	2.58	2.14	2.11
Tm	*NA*	*NA*	*NA*	*NA*	*NA*	*NA*	*NA*	0.33	0.52	0.32	0.29	0.20	0.34	0.29	0.36	0.30	0.29
Yb	*NA*	*NA*	*NA*	*NA*	*NA*	*NA*	*NA*	2.04	3.15	1.93	1.75	1.24	2.15	1.83	2.23	1.83	1.79
Lu	*NA*	*NA*	*NA*	*NA*	*NA*	*NA*	*NA*	0.29	0.47	0.30	0.27	0.17	0.31	0.26	0.33	0.29	0.28
Th	*NA*	*NA*	*NA*	*NA*	*NA*	*NA*	*NA*	3.53	7.32	3.46	3.82	9.81	2.72	1.42	2.86	4.19	3.19
Hf	*NA*	*NA*	*NA*	*NA*	*NA*	*NA*	*NA*	3.04	3.65	3.02	3.11	1.87	3.09	2.63	3.16	3.05	2.72
Ta	*NA*	*NA*	*NA*	*NA*	*NA*	*NA*	*NA*	1.02	0.97	0.93	0.92	0.92	0.90	0.85	0.95	0.98	0.79
U	*NA*	*NA*	*NA*	*NA*	*NA*	*NA*	*NA*	0.73	1.96	0.85	0.95	2.25	0.55	0.37	0.60	1.16	0.84
Cs	*NA*	*NA*	*NA*	*NA*	*NA*	*NA*	*NA*	2.01	2.57	1.81	2.00	5.47	1.20	0.43	1.49	2.43	1.67

LOI – Loss on Ignition.
NA – No Analysis.

Table 3
Radiogenic isotope analyses.

Sample	Lithology	$^{87}Sr/86Sr$	$^{143}ND/^{144}Nd$	$^{206}Pb/^{204}Pb$	$^{207}Pb/^{204}Pb$	$^{208}Pb/^{204}Pb$
UP3	Andesite	0.705122	0.512653	18.773	15.643	38.929
UP4	Andesite	0.705135	0.512659	18.777	15.642	38.927
UP5	Dacite	0.705159	0.512649	18.775	15.645	38.936
UP7	Dacite	0.705511	0.512636	18.800	15.655	38.972
UP9	Andesite	0.705161	0.512645	18.779	15.646	38.937
UA43	Basalt	0.704555	0.512713	18.745	15.658	38.947
UA81	Dacite	0.705365	0.512559	18.795	15.657	38.977
TN96	Andesite	0.704204	0.512792	18.677	15.566	38.691
LBA64	Basalt	0.704100	0.512879	18.591	15.612	38.738
LBA85	Basalt	0.704521	0.512740	18.739	15.666	38.946
LBA98	Basalt	0.704533	0.512721	18.749	15.666	38.958

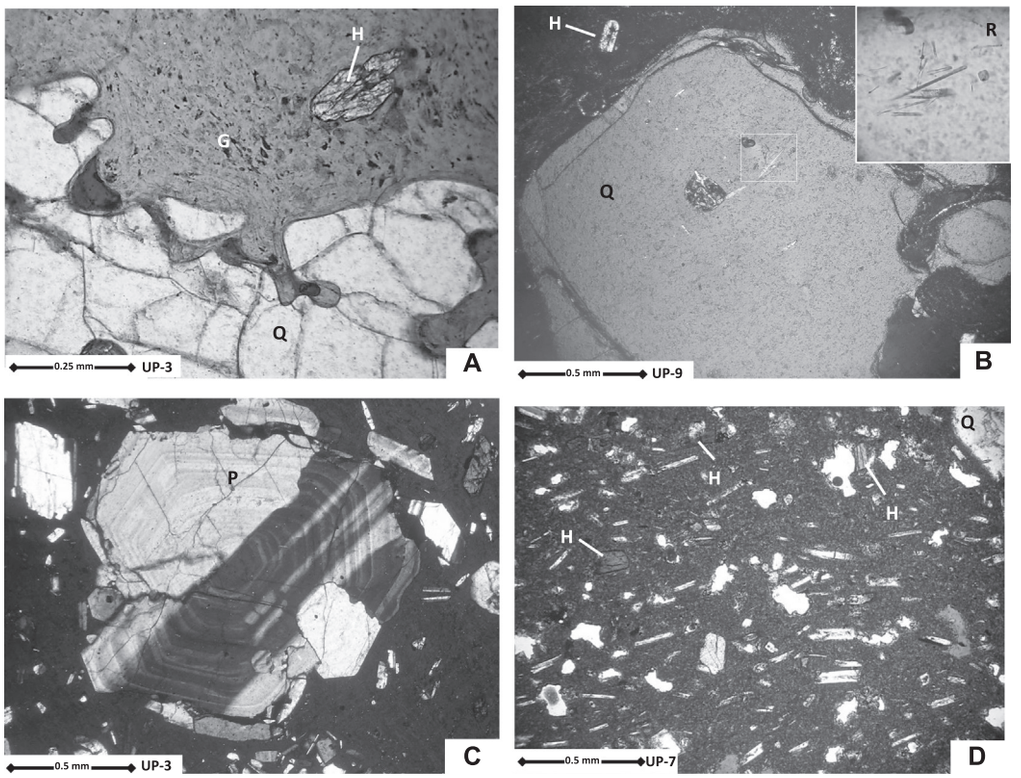

Fig. 5. Photomicrographs of Usun Apau volcanic rocks. (A) polarized light, welded tuff with embayed quartz xenocryst (Q) in glassy ground mass with exquisite flow patterns with euhedral hypersthene phenocryst (H); (B) cross-polarized light, welded tuff, quartz xenocryst with fine rutile inclusions (R); (C) polarized light, oscillatory-zoned Carlsbad twinned plagioclase phenocryst; (D) plain light, trachytic plagioclase laths in fine-grained groundmass.

observations at Silo Falls that welded tuffs (UP-4, 3.90 ± 0.04 Ma and UP-8, 3.84 ± 0.06 Ma) overlie lava flows (4.11 ± 0.07 Ma). Preliminary dating of a basalt from the Usun Apau plateau yields an Ar–Ar age of 2.0–2.5 Ma (Taib, 2012) similar to the age of the basalts from the Linau Balui plateau (Taib, 2012).

5.3. Major and trace element geochemistry

Table 2 summarizes the major and trace element analyses. Our sample set represents widespread coverage, albeit from a limited number of locations. Considering the difficult access to the interior highlands, this sample set must serve as a representative suite until future expeditions sample other areas. Samples from the Silio Falls on the southeastern side of the plateau present an excellent vertical succession. The Silio Falls samples straddle the dacite and andesite boundary on a plot of $Na_2O + K_2O$ vs. SiO_2 and are similar to the adakites of the Sintang suite near Kuching (Fig. 7). Two dacite samples from the northern area around Bukit Mabun (Fig. 2) analyzed by Kirk (1957) are relatively enriched in the alkalis and plot in the trachyte field (Fig. 7). The late-stage basalt to basaltic andesite dikes from the Usun Apau plot with the Linau Balui basalts (Fig. 7; Taib, 2012). The major and trace element abundances vs. SiO_2 show the distinct groupings for samples from the different areas of the Usun Apau plateau; however intra-area compositional differences are narrow (Fig. 8a and b). For example, UP81, higher in silica and presumably more evolved, is depleted in Zr relative to the Silo Falls dacites (Fig. 8b). Samples from Bukit Mabun on the northern side of the plateau are enriched in alkalis, but depleted in magnesium, relative to the Silio Falls dacites (Fig. 8a). An andesite (TN96) from the Tinjar area has elevated

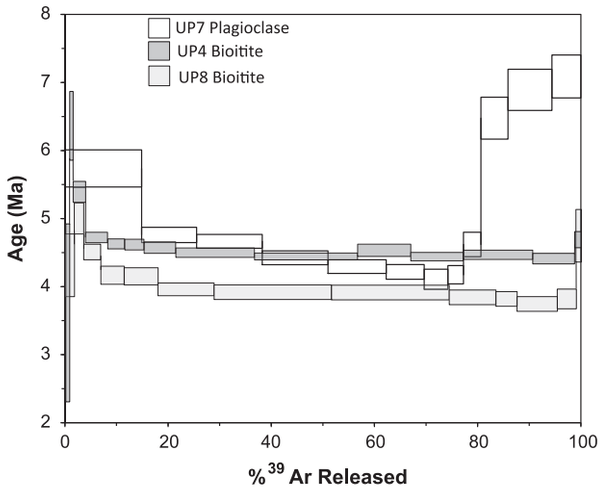

Fig. 6. Plot of Ar–Ar age as a function of % ^{39}Ar released during stepwise heating for 3 mineral separate samples.

Rb, but low Zr concentrations, which imparts a unique signature relative to other samples (Fig. 8b). All samples have relatively low Nb, Sc, and Y concentrations (Fig. 8b).

The N-MORB normalized multi-element plots for the Linau Balui and Usun Apau samples show enrichment in large-ion-lithophile elements (LILE) and depletion in the high-field strength elements (HFSE) and the heavy rare earth elements (HREE); UA43 shows very strong enrichment in LILE relative OIB (Fig. 9). The Usun Apau basalts are more enriched in LILE the Linau Balui basalts; both are enriched in LILE relative to OIB. The more evolved samples show much stronger LILE enrichment, but similar depletion in HFSE and HREE. All samples show strong relative depletion in Nb and a modest positive Zr anomaly relative to Ti; the Usun Apau dacites show very strong depletion in Ti. Although such negative anomalies are commonly associated with island arc tholeites, the steep LILE to Nb trend is largely a reflection of LILE enrichment. Only two samples (UA43 and TN96) have $(La/Nb)_n$ ratios >1, although generally an indicator of a subduction signal, crustal contamination cannot be excluded. Overall, the volcanic rocks from both plateaus appear to be derived from a similar LILE-enriched OIB-like mantle source.

5.4. Isotope geochemistry

The Usun Apau and Linau Balui samples display wide ranges in their radiogenic isotopic ratios, $^{87}Sr/^{86}Sr$, $^{143}Nd/^{144}Nd$, $^{206}Pb/^{204}Pb$, $^{207}Pb/^{204}Pb$, and $^{208}Pb/^{204}Pb$ (Figs. 10 and 11; Table 3). Both sample suites show trends towards higher $^{87}Sr/^{86}Sr$ and lower $^{143}Nd/^{144}Nd$ as a function of SiO_2 (Fig. 10). Because such isotopic variations should not occur during fractional crystallization of magmas derived from similar source regions, the observed trends strongly indicate assimilation played a role in their differentiation, particularly the Usun Apau dacites. Strong inter-isotope correlations for the Usun Apau and Linau Balui volcanics define arrays similar to those of the SSA basalts (Fig. 11), which have been interpreted as the result of fractional crystallization coupled with assimilation of continental crust (Macpherson et al., 2010).

6. Discussion

Our study of the volcanic rocks from the Usun Apau and Linau Balui areas reveals important information regarding a previously unknown part of central Borneo and fills an important data gap between the southern Sulu Arc and the Sintang Intrusives near Kuching. Specifically, we are able to address five important considerations: (1) age of magmatic activity, (2) nature of their source regions, (3) the nature of the subsurface crust via melt-crust interaction, (4) the relationship of Luconia to other crustal blocks, and (5) causes of volcanism.

6.1. Episodes of volcanic activity

The Usun Apau plateau records two short-lived episodes of volcanism. Eruption of andesitic to dacitic lavas and tuffs

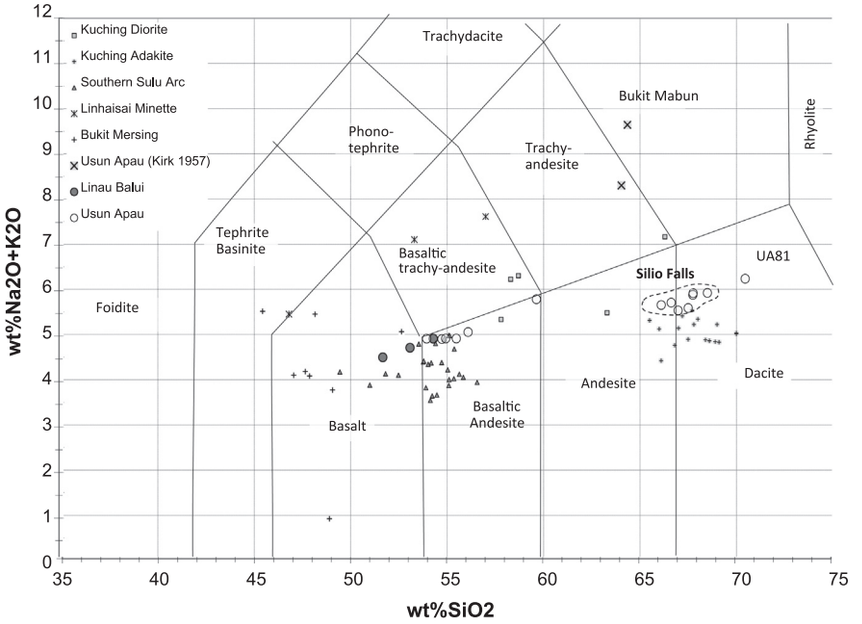

Fig. 7. Total alkali silica classification (Le Bas and Streckeisen, 1991) of samples from Linau Balui and Usun Apau plateaus plotted with data from the Sintang suite near Kuching (Prouteau et al., 2001), Linhaisai minettes (Bergman et al., 1988), Southern Sulu Arc (Macpherson et al., 2010), and Bukit Mersing (Taib, 2010).

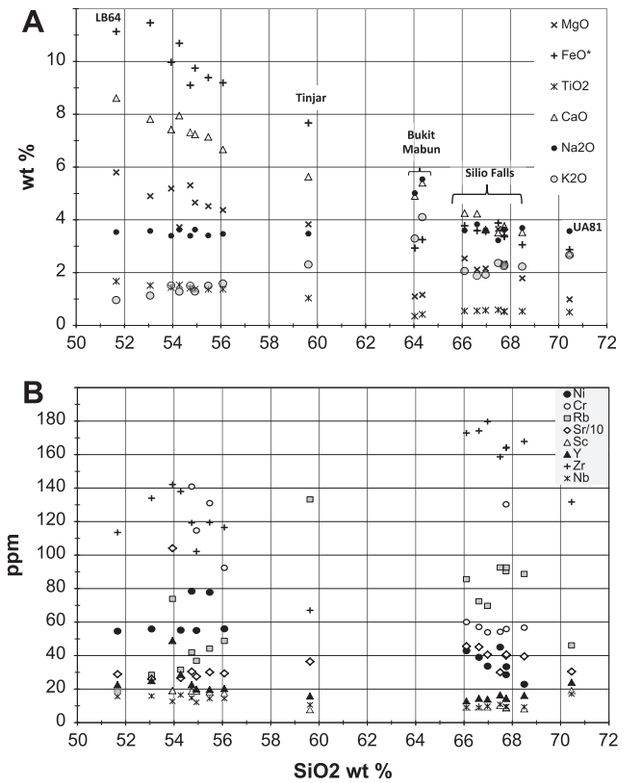

Fig. 8. Plot of major and trace element data for the Usun Apau and Linau-Balui volcanics; TN, Tinjar; BM Bukit Mabun. (a) Selected major elements vs. SiO_2. (b) Selected trace elements vs. wt% SiO_2.

(4.11 ± 0.07 Ma and 3.90 ± 0.04 Ma), which form most of the plateau, was followed by a period of quiescence that ended with a very small volume of basaltic volcanism (*ca.* 2.0 Ma). The N–S alignment of light-colored elliptical tonal anomalies on the NE edge of the plateau (Fig. 2, inset) may indicate recent geothermal activity. Although the basalts and more evolved rocks appear to form relatively coherent differentiation arrays (Figs. 7 and 8a), several lines of evidence lead us to interpret these as two distinct magmatic episodes rather than eruption from a single stratified magma chamber. First and foremost, the more evolved rocks are distinctly older than the basalts. The similar timing of basaltic volcanism at the Usun Apau, Linau Balui, and Nankan plateaus (Fig. 3) suggests that this activity is related to a younger more widespread episode. Moreover, several incompatible trace elements have trends opposite that predicted from fractional crystallization. For example, Nb decreases with decreasing MgO through the spectrum of basalt to dacite with different ages, but stays relatively constant within each suite (Fig. 12a). For the Linau Balui basalts K/Nb, which should be relatively invariant, decreases with MgO (Fig. 12a). We interpret Usun Apau volcanism as pulsed sampling of a single mantle source at *ca.* 4 and *ca.* 2 Ma. The earlier silicic phase of magmatism, more enriched in incompatible trace elements (Fig. 9), supplied a larger volume of melt to the surface producing an andesitic plateau capped by welded tuffs. The evolved character of this magmatism suggests that there was a period of prolonged differentiation at crustal levels. Basalts of the later phase did not experience a similar extent of differentiation, so may have ascended more rapidly to the surface.

6.2. Nature of source region

The basaltic rocks from Usun Apau and Linau Balui provide the best estimate of the nature of their mantle sources. The least evolved rocks show relatively smooth normalized trace element patterns that indicate an LILE-enriched OIB-like mantle region (Fig. 9). Depletion of the heavy rare earth elements in the Usun Apau and Linau Balui volcanics indicates the presence of garnet and/or amphibole in the source region. Relative to the amphibole-bearing Kuching adakites, the Usun Apau dacites are enriched in Rb (Fig. 12c), but have a lower K/Rb (Fig. 12d). The presence of pyroxene rather than amphibole as a phenocryst phase in the Usun Apau dacites coupled with their lower K/Rb ratios likely reflects the absence of buffering by amphibole, which preferentially retains Rb. The low concentrations of Ti and Nb (Figs. 8 and 9) point to

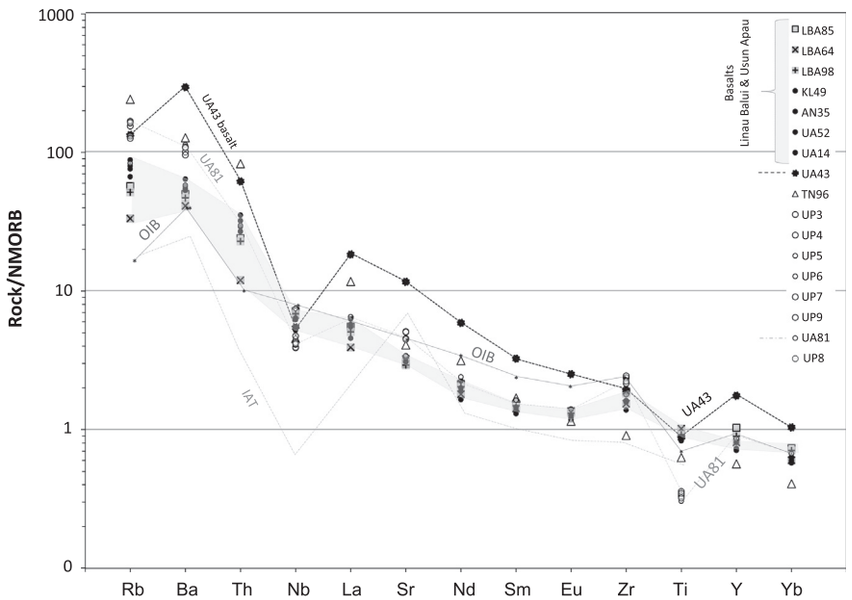

Fig. 9. Normalized Rock/N-MORB plot for selected trace elements comparing Usun Apau and Linau Balui; N-MORB and OIB from Sun and McDonough (1989); Island Arc Basalt-IAB (Elliott, 2003).

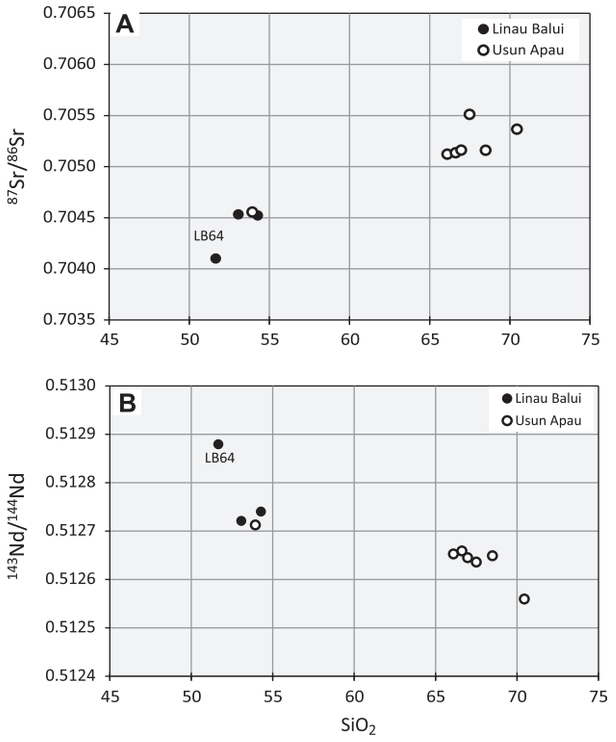

Fig. 10. Plots of (12a) $^{87}Sr/^{86}Sr$ vs. SiO_2 and (12b) $^{143}Nd/^{144}Nd$ vs. SiO_2 for the Usun Apau and Linau Balui volcanics.

either rutile and/or ilmenite in the source region, or enrichment by metasomatic fluids depleted in the relatively insoluble HSFEs. The absence of a negative Eu anomaly (Fig. 9) and mildly elevated Sr/Y in the dacites (Fig. 12b) are interpreted to reflect the lack of extensive plagioclase fractionation and/or its absence in the source region. Considering the stability fields for garnet, plagioclase, and amphibole (Green and Falloon, 2005; Stern, 2002), the trace element data suggest Usun Apau and Linau Balui parent magmas were derived from depths of at least 60 km to 80 km. The fact that the Usun Apau volcanics have an average Cr/Ni ratio (1.84) similar to that for primitive mantle, suggests equilibration of melt in the presence of mantle peridotite (Yogodzinski et al., 1995; Rapp et al., 1999).

With the exception of UA43, a basalt, which stands out as anomalous, the MORB-normalized trace element data for the Linau Balui basalts, the Usun Apau basalts, and the Usun Apau dacites plot in sufficiently tight groupings that we have plotted the average for these groups along with trace element data from other areas (Fig. 13). The Linau Balui and Usun Apau basalts resemble the Plio-Pleistocene basalts of the SSA, which suggests that the Usun Apau and Linau Balui basalts are derived from a mantle source similar to that invoked for Southern Sulu Arc by Macpherson et al. (2010). Higher LILE contents in Usun Apau volcanics indicate further enrichment of this source in highly incompatible elements. In the Usun Apau samples, increasing HFSE depletion with decreasing MgO (Fig. 12a) suggests that this signature may have been acquired in the crust owing to interaction with a HSFE depleted contaminant (see Section 6.3).

Macpherson et al. (2010) attributed the source of the SSA lavas to enrichment in the convecting mantle available over a wide region, from the Sulu Arc to Hainan Island (Fig. 1), and proposed that the same mantle exists under central Borneo. We confirm this prediction is true at least as far southwest as Linau Balui. The Usun Apau basalts are more enriched in the most incompatible elements than the SSA lavas, suggesting that there may be subtle variations in the composition of this source. Alternatively, the Usun Apau and Linau Balui basalts may have originated from the same source through slightly smaller degrees of partial melting than experienced at the SSA. This would be consistent with the greater lithospheric thickness expected in southern Sarawak, compared to SSA, where Miocene subduction would have thinned the overriding plate, onto which the latter were ultimately erupted.

6.3. Differentiation: Mixing and assimilation

As established in the previous section, the mafic lavas are probably related to a mantle component sampled by small degrees of partial melting. As isotopic fractionation should not occur during fractional crystallization, the range of the isotope ratios in the Usun Apau and Linau Balui volcanics provides unambiguous evidence that mixing of one or more components contributed to their evolution. Strong inter-isotope correlations indicate binary mixing. The fact that the Usun Apau and Linau Balui data plot in the same arrays as the SSA (Fig. 11) is strong evidence that the magmas from these regions experienced similar evolutionary pathways with respect to source region and crustal assimilation.

In an attempt to constrain the origin of contamination in the SSA, Macpherson et al. (2010) employed assimilation with fractional crystallization (AFC) modeling (DePaolo, 1981). The SSA lavas are all basaltic or basaltic andesites, which restricts the amount of differentiation that can be accommodated in such models. Hence, viable contaminants require large isotopic differences from the uncontaminated melt. In practice, this meant a contaminant with very low $^{143}Nd/^{144}Nd$ and, therefore, of great age, such as the Archean age granite Macpherson et al. (2010) used to match the trends observed in the SSA. The situation is different for Usun Apau. Because the volcanic rocks there also include more evolved dacites, a greater amount of differentiation can be accommodated in AFC models which, in turn, decreases the amount of isotopic leverage required of the contaminant. Therefore, it is more difficult to constrain the isotopic composition of the contaminant or other parameters for the model e.g. bulk distribution coefficients or the extent of assimilation.

We used Linau Balui basalt LB64 as a possible uncontaminated composition to test possible AFC Models (Fig. 14). LBA64 is considered suitable because, along with its lower silica and magnesium contents, it has the highest $^{143}Nd/^{144}Nd$ and lowest $^{87}Sr/^{86}Sr$ in the area, with values that lie within the field of South China Sea basalts (Fig. 11a). Because little is known about the composition of potential crustal contaminants in this part of Borneo, data were compiled from a number of regional granitic belts that might offer approximate bulk crust compositions. Since each of these display a spread in isotopic compositions, samples that produced AFC models with the lowest $^{143}Nd/^{144}Nd$ at low $^{87}Sr/^{86}Sr$ were used because these, like the Southern Sulu Arc (Macpherson et al., 2010), provide the best fit to the Linau Balui–Usun Apau array. The one exception to this was for Triassic batholiths from the Malayan peninsula, for which two compositions were used which span the range of Nd isotopic ratios. Ratios of assimilation to crystallization (r) were varied between 0.15 and 0.3 but this has a negligible impact upon the conclusions reached by this modeling (Fig. 14).

Proterozoic metamorphic rocks of the Kontum massif in Vietnam and Mesozoic crust similar to that of the South China margin, represented here by granitic rocks from Hong Kong and the Dangerous Grounds attenuated crust, would be unsuitable contaminants as even their lowest Nd isotopic values are too high for the required Sr signature (Fig. 14b). Archean rocks, which Macpherson et al. (2010) postulated to lie beneath the Southern Sulu Arc, can reproduce the Linau Balui–Usun Apau array well (Fig. 14a). An alternative contaminant, however, is provided by the Malay

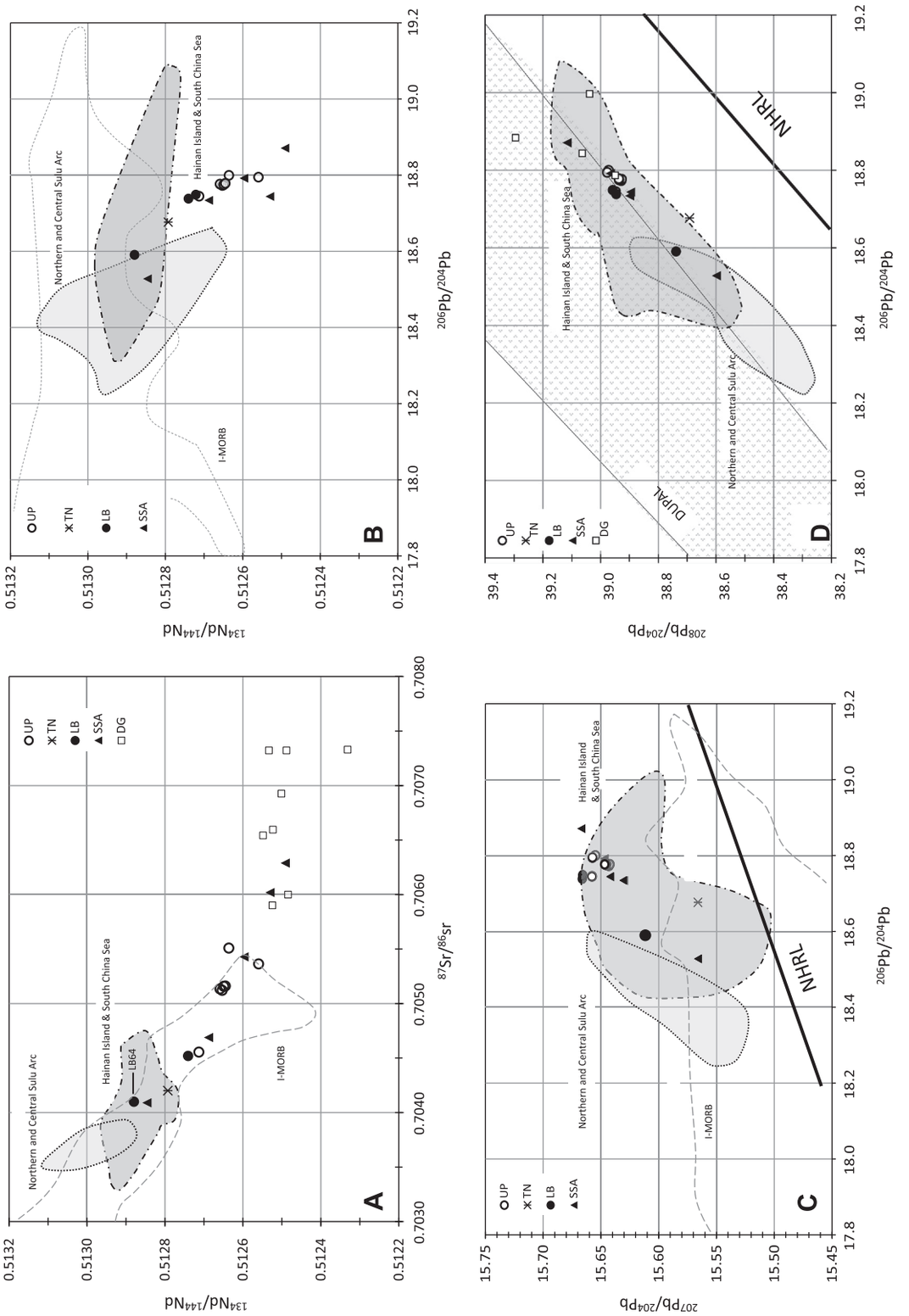

Fig. 11. $^{87}Sr/^{86}Sr$, $^{143}Nd/^{144}Nd$, $^{206}Pb/^{204}Pb$, $^{207}Pb/^{204}Pb$, and $^{208}Pb/^{204}Pb$ isotopic data from Usun Apau, Linau Balui, and Tinar Line plotted with data from other Cenozoic igneous rocks from the greater SCS region: DG – Dangerous Grounds (Yan et al., 2010, 2011), Bukit Mersing Taib (2012), shaded polygons for the Northern & Central Sulu Arc and Hainan Island & South China Sea (Macpherson et al., 2010 and references therein); NHRL – Northern Hemisphere Reference Line (Hart, 1984); I-MORB – Indian Ocean MORB (GERM: http://earthref.org/GERM).

Triassic batholiths. Less than 50% crystallization of the Linau Balui basalt composition is required to generate the range of isotopic compositions in Usun Apau dacites if melts resembling these granites were assimilated. The combination of a modest amount of differentiation with modest values for *r* but of a silicic component could elevate SiO_2 contents into the dacites range (Fig. 14a). The

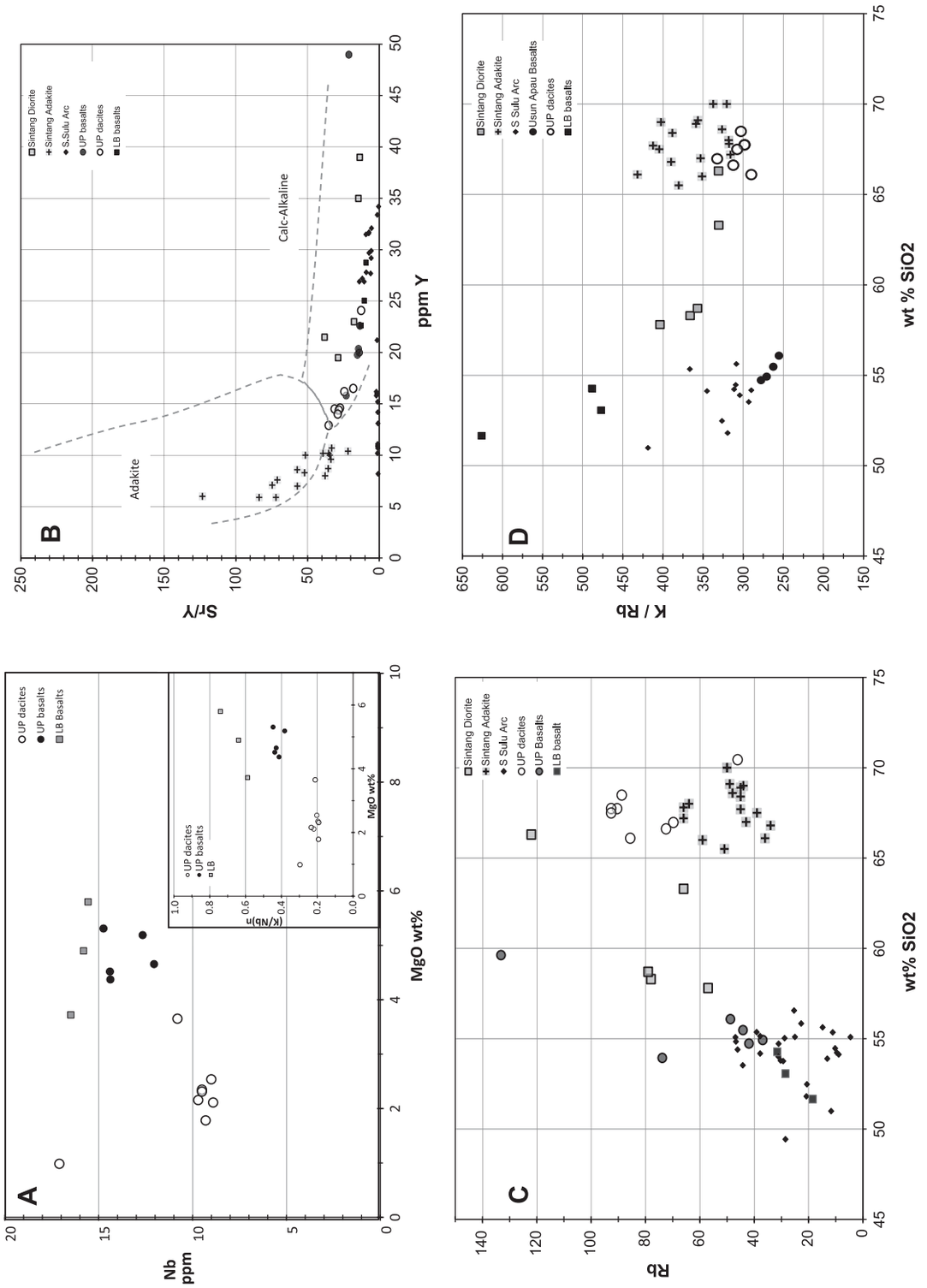

Fig. 12. Trace element plots comparing Usun Apau (UP) and Linau Balui (LB) samples with other igneous rocks from NW Borneo (Prouteau et al., 2001; Macpherson et al., 2010). (10a) Nb vs. wt% MgO, (10b) Sr/Y vs. Y discrimination diagram (Defant and Drummond, 1990), (10c) ppm Rb vs. wt% SiO_2, (11d) K/Rb vs. wt% SiO_2.

Malay Triassic batholiths, which had protoliths of mid-Proterozoic crust (Liew and McCulloch, 1985), are associated with a world-class belt of tin mineralization. We highlight the tin-bearing granites at Long Laai, 250 km east of Usun Apau (Bambang and Le Bel, 1987; see Fig. 3), as an intriguing occurrence indicating that similar crust may underlie parts of the Luconia block.

6.4. Luconia's relationship to other crustal blocks

Regardless of the choice of protolith, the isotopic data support the interpretation that differentiation of the Usun Apau, Linau Balui, and South Sulu Arc magmas included assimilation of relatively old continental crust. Macpherson et al. (2010) suggested that the

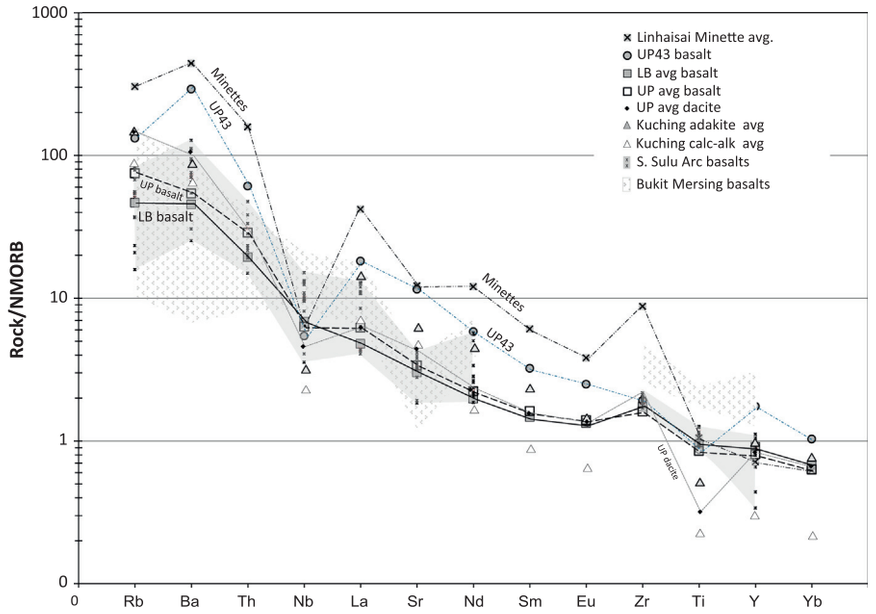

Fig. 13. Averaged normalized Rock/N-MORB plot for selected trace elements comparing the Usun Apau and Linau Balui plateaus with areas previously discussed and referenced in Figs. 11 and 12.

Sulu Arc, the South China Sea region and its extended margins are underlain by a common OIB-like mantle source with Dupal-like characteristics (Tu et al., 1992), and that in some cases, depending on the ease of ascent through the overlying crust, the isotopic signature of that source is significantly altered by interaction with Precambrian continental crust. The OIB-like character of the Usun Apau and Linau-Balui basalts (Fig. 9) coupled with the trace element and isotopic signatures of the regional data set (Figs. 11 and 13) strongly suggests that similar lithosphere extends beyond the Tinjar Line and underlies the Luconia block. The Linhaisai minettes in Kalimantan, interpreted as derived from subcontinental lithosphere (Bergman et al., 1988), and tin-bearing granites at Long Laai having a $^{87}Sr/^{86}Sr$ ratio of 0.7048 (Hutchison, 2010) further extends the potential geographic extent of this continental

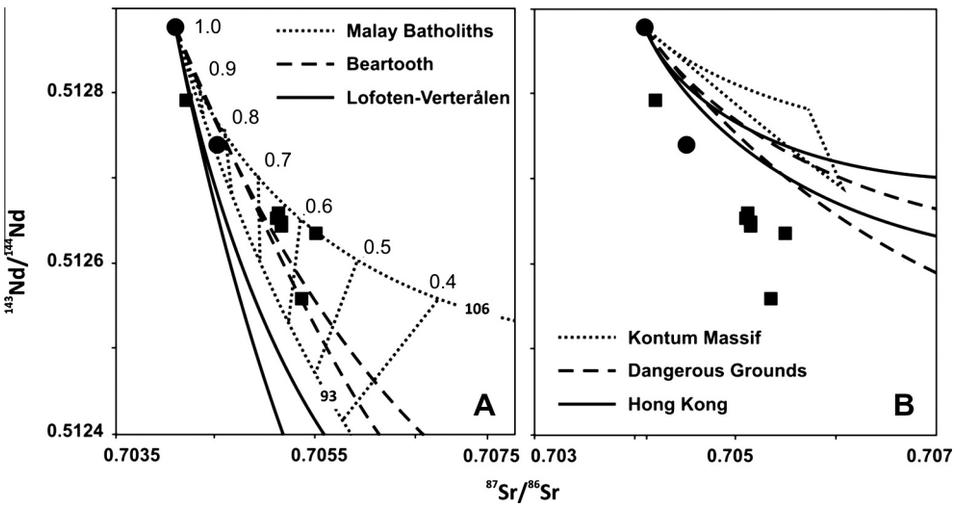

Fig. 14. Assimilation fractional crystallization models. $^{143}Nd/^{144}Nd$ vs. $^{87}Sr/^{86}Sr$ for volcanic rocks from Usun Apau (squares) and Linau Balui (circles). Lines represent assimilation and fractional crystallization models (DePaolo, 1981) of (a) suitable, and (b) unsuitable contaminants to generate the Usun Apau – Linau Balui array. Initial basalt is Linau Balui basalt (LBA64; this work) $^{87}Sr/^{86}Sr = 0.704100$, $^{143}Nd/^{144}Nd = 0.512879$, Sr = 289 ppm, Nd = 13 ppm. In all models, $D_{Sr} = 1.5$ and $D_{Nd} = 0.1$. Contaminant compositions are Triassic batholiths of the East Coast of Peninsular Malaysia, samples 93 and 106 (Liew and McCulloch, 1985); $^{87}Sr/^{86}Sr = 0.706760$ and 0.811870, $^{143}Nd/^{144}Nd = 0.5116300$ and 0.511490, Sr = 31 and 719 ppm, Nd = 28 and 35 ppm; Archean crust, Beartooth Mountains, USA (Wooden et al., 1988) $^{87}Sr/^{86}Sr = 0.724600$, $^{143}Nd/^{144}Nd = 0.510250$, Sr = 400 ppm, Nd = 43 ppm; Archean migmatite, Lofoten-Verterålen, Norway (Jacobsen and Wasserburg, 1978) $^{87}Sr/^{86}Sr = 0.708900$, $^{143}Nd/^{144}Nd = 0.510410$, Sr = 573 ppm, Nd = 29 ppm; Metamorphic rocks of the Kontum Massif, Vietnam (Lan et al., 2003) $^{87}Sr/^{86}Sr = 0.706210$, $^{143}Nd/^{144}Nd = 0.512323$, Sr = 848 ppm, Nd = 16 ppm; Dangerous Grounds attenuated crust (Yan et al., 2010) $^{87}Sr/^{86}Sr = 0.711624$, $^{143}Nd/^{144}Nd = 0.512030$, Sr = 470 ppm, Nd = 33 ppm. Granitic rocks from Hong Kong (Darbyshire and Sewell, 1997) $^{87}Sr/^{86}Sr = 0.711491$, $^{143}Nd/^{144}Nd = 0.512344$, Sr = 271 ppm, Nd = 41 ppm. Two curves are shown for each contaminant representing different values for r; the ratio of mass assimilated to mass crystallized. Except for the Malay Batholiths the end members are the same with $r = 0.15$ for the higher-$^{143}Nd/^{144}Nd$ model and $r = 0.3$ for the lower-$^{143}Nd/^{144}Nd$ model. The Malay Batholith models are for different contaminants ($r = 0.3$ and 0.15, respectively for the pairs of values listed above). Models run cover range of F; fraction of liquid remaining, from 1 to 0.1. F values are indicated on Malay Batholith models decreasing in 0.1 increments.

basement (Fig. 3). Thus, although the tectonic models generally treat the Borneo region as comprised of multiple lithospheric blocks, it appears likely that the Greater Dangerous Grounds, including the Luconia block and the Palawan micro-continent, represent lithospheric fragments that share a distant Southeast Asian ancestry.

6.5. Causes of volcanism

Intra-plate Plio-Pleistocene volcanic activity in the greater South China Sea region poses an interesting question. How can such regional activity be represented by widely scattered relatively small volumes of magma erupted in abrupt short-lived pulses that appear to ultimately share a similar mantle source? We do not have a clear answer to this question, but make some observations that point to several possibilities. Hainan Island is underlain by a deep mantle plume that may represent melting of an EM2 mantle source (Zou and Fan, 2010), whereas the Scarborough Seamounts appear to be related to paleo-transform faults of the South China Sea spreading system. Borneo's interior volcanic tablelands, including the Usun Apau and Linau Balui plateaus, are largely restricted to the region SW of the Tinjar Line (Fig. 3), which is consistent with tectonic model that treat Luconia as a discrete lithospheric block. With the exception of the Usun Apau calderas, which lie along the projection of faults that mark the edge of Dulit plateau (Fig. 2), the Tinjar Line does not appear to directly control the locus of the volcanic activity. The varied settings for Pliocene volcanism point towards a deep seated mechanism. Recent studies of shear wave velocity anisotropy in the region's upper mantle and lower crust show that there are distinct areas with strong lateral gradients that persist vertically for more than 200 km (Wu et al., 2005). Whilst these steep-sided lateral velocity gradients could reflect temperature differences, we consider differences in volatile content related to dehydration of an old deeply subducted slab to be a plausible complicating factor that is consistent with the trace element geochemistry of the Usun Apau and Linau Balui volcanics. Regardless of their ultimate origin, once primary melts are generated regional differences in lithospheric thickness, as well as deeply rooted faults, related the region's protracted and complex tectonic history influence further differentiation by controlling routes and rates of ascent.

7. Conclusions

- ^{39}Ar–^{40}Ar age determinations show that two distinct pulses of volcanism are represented. The Usun Apau dacites erupted at *ca*. 4.0 Ma; the Linau Balui and Usun Apau basalts erupted at *ca*. 2.0 Ma.
- The Usun Apau and Linau Balui volcanic suites are the product of small percentage melting of an LILE-enriched, OIB-like, garnet-bearing mantle possibly modified by fluids related to much older subduction.
- Volcanic rocks from the Usun Apau and Linau Balui plateaus have isotopic signatures indicating assimilation of relatively old continental crust.
- AFC modeling shows the Usun Apau dacites could be the product of fractional crystallization coupled with assimilation of continental crust similar to the tin-bearing Triassic Malay granites.
- The Tinjar Line does not appear to have played a direct role in magma genesis, but may have localized emplacement by providing a route of ascent for the dacites.
- The Linau Balui and Usun Apau volcanics share radiogenic isotopic similarities not only with the Southern Sulu Arc basalts, but also with other Pliocene basalts in the greater SCS region. Thus, Luconia, the Dangerous Grounds, and the Palawan microplate appear to represent crustal fragments that may ultimately share a Southeast Asian ancestry.

Acknowledgements

Morrison Ngau arranged most of the logistics and guided the expedition to Silio Falls of the Usun Apau plateau. Without his help, good cheer, and perseverance that expedition would not have achieved its objectives. We gratefully thank Morrison for all his hard work. Barry Weaver of the University of Oklahoma was kind enough to review an early version of this paper. His comments helped with improvements to several figures. Criticisms from an anonymous reviewer helped to sharpen our discussion. Steve Bergman is acknowledged for his constructive review that highlighted the importance of the Linhaisai minettes. Lastly, Robert Hall is thanked for his encouragement and comments which helped to disambiguate several passages in the final submission.

Appendix A. Analytical methods

A.1. Age determinations

Radiometric age determinations were analyzed by the $^{40}Ar/^{39}Ar$ method at the Nevada Isotope Geochronology Laboratory (University of Nevada Las Vegas). Samples were wrapped in Al foil and stacked in 6 mm inside diameter sealed fused silica tubes. Individual packets averaged 3 mm thick and neutron fluence monitors (FC-2, Fish Canyon Tuff sanidine) were placed every 5–10 mm along the tube. Synthetic K-glass and optical grade CaF_2 were included in the irradiation packages to monitor neutron induced argon interferences from K and Ca. Loaded tubes were packed in an Al container and irradiated at the U.S. Geological Survey TRIGA Reactor, Denver, CO in the In-Core Irradiation Tube (ICIT) of the 1 MW TRIGA type reactor. Correction factors for interfering neutron reactions on K and Ca were determined by repeated analysis of K-glass and CaF_2 fragments. Measured $(^{40}Ar/^{39}Ar)_K$ values were 1.48 (±79.07%) × 10^{-2}. Ca correction factors were $(^{36}Ar/^{37}Ar)_{Ca} = 2.60$ (±3.15%) × 10^{-4} and $(^{39}Ar/^{37}Ar)_{Ca} = 6.70$ (±1.70%) × 10^{-4}. J factors were determined by fusion of 4–8 individual crystals of neutron fluence monitors which gave reproducibility's of 0.25–0.48% at each standard position. Variation in neutron fluence along the 100 mm length of the irradiation tubes was <4%. Matlab curve fit was used to determine J and uncertainty in J at each standard position. No significant neutron fluence gradients were present within individual packets of crystals as indicated by the excellent reproducibility of the single crystal fluence monitor fusions.

Irradiated FC-2 sanidine standards together with CaF_2 and K-glass fragments were placed in a Cu sample tray in a high vacuum extraction line and were fused using a 20 W CO_2 laser. Sample viewing during laser fusion was by a video camera system and positioning was via a motorized sample stage. Samples analyzed by the furnace step heating method utilized a double vacuum resistance furnace similar to the (Staudacher et al., 1978) design. Reactive gases were removed by three GP-50 SAES getters prior to being admitted to a MAP 215-50 mass spectrometer by expansion. The relative volumes of the extraction line and mass spectrometer allow 80% of the gas to be admitted to the mass spectrometer for laser fusion analyses and 76% for furnace heating analyses. Peak intensities were measured using a Balzers electron multiplier by peak hopping through 7 cycles; initial peak heights were determined by linear regression to the time of gas admission. Mass spectrometer discrimination and sensitivity was monitored by repeated analysis of atmospheric argon aliquots from an on-line

pipette system. Measured $^{40}Ar/^{36}Ar$ ratios were 283.23 ± 0.20% during this work, thus a discrimination correction of 1.0433 (4 AMU) was applied to measured isotope ratios. The sensitivity of the mass spectrometer was $\sim 6 \times 10^{-17}$ mol mV^{-1} with the multiplier operated at a gain of 36 over the Faraday. Line blanks averaged 26.20 mV for mass 40 and 0.02 mV for mass 36 for laser fusion analyses and 24.32 mV for mass 40 and 0.08 mV for mass 36 for furnace heating analyses. Discrimination, sensitivity, and blanks were relatively constant over the period of data collection. Computer automated operation of the sample stage, laser, extraction line and mass spectrometer as well as final data reduction and age calculations were done using LabSPEC software written by B. Idleman (Lehigh University). An age of 28.02 Ma (Renne et al., 1998) was used for the Fish Canyon Tuff sanidine fluence monitor in calculating ages for samples.

For $^{40}Ar/^{39}Ar$ analyses a plateau segment consists of 3 or more contiguous gas fractions having analytically indistinguishable ages (i.e. all plateau steps overlap in age at $\pm 2\sigma$ analytical error) and comprising a significant portion of the total gas released (typically >50%). Total gas (integrated) ages are calculated by weighting by the amount of ^{39}Ar released, whereas plateau ages are weighted by the inverse of the variance. For each sample inverse isochron diagrams are examined to check for the effects of excess argon. Reliable isochrons are based on the MSWD criteria of (Wendt and Carl, 1991) and, as for plateaus, must comprise contiguous steps and a significant fraction of the total gas released. All analytical data are reported at the confidence level of 1σ (standard deviation). Furnace step heating analyses produce an apparent age spectrum. The "apparent" derives from the fact that ages on an age spectrum plot are calculated assuming that the non-radiogenic argon (trapped initial argon) is atmospheric in isotopic composition ($^{40}Ar/^{36}Ar = 295.5$). Isochrons can verify (or rule out) excess argon, and isochron ages are usually preferred if a statistically valid regression is obtained. If there is excess argon in the sample ($^{40}Ar/^{36}Ar > 295.5$) then these apparent ages will be older than the actual age of the sample. U-shaped age spectra are commonly associated with excess argon (the first few and final few steps often have lower radiogenic yields, thus apparent ages calculated for these steps are affected more by any excess argon present). When such a sample yields no reliable isochron, the youngest measured age provides a maximum estimate for the age of the sample. Plateau ages are simply a segment of the age spectrum which consists of 3 or more steps, comprising >50% of the total gas released. An isochron age is the best estimate of the age of a sample, even if a plateau age is obtained. $^{40}Ar/^{39}Ar$. Total gas ages are equivalent to K/Ar ages determined by older analytical methods.

A.2. Major and trace elements

KL49, UA14, AN35, UA52, UP3, UP4, UP5, UP6, UP7, UP8 and UP9 were analyzed for major elements by X-ray Fluorescence Spectroscopy (XRF) at the Geoanalytical Lab at Washington State University, United States, using the low-dilution fused bead method described in Johnson et al. (1999). UA81, UA43, Tn96 and LBA64, LBA84 and LBA98 were analyzed for major elements using a PanAnalytical Axios Max WD-RXF at University of Malaya, Malaysia, using 1:9 dilution fused beads with a lithium tetraborate flux (Fluxana FX-X100). Powdered samples were heated at 950 °C to determine Loss on Ignition values, after which they were mixed with flux in platinum crucibles and fused over a propane–oxygen flame in a HD Elektronik Vulcan automatic fusion machine. After an automated cycle of heating and agitation, the molten charge was poured onto heated platinum moulds to produce 32 mm buttons. Calibration used nine USGS rock standards prepared in the same way as the samples. These samples were also analyzed for trace elements using a Thermo Scientific – XSeries II ICP-MS at the *Vrije Universiteit*, Amsterdam.

The UP samples trace elements were also measured by XRF; precision was determined by triplicate analysis of separate glass beads prepared from sample of Galapagos basalt, run at the same time as the Usun Apau samples. The relative standard deviation on the triplicate analyses is <1% except for FeO_t (2.0%), K_2O (1.1%), and Na_2O (2.6%). Samples KL49, UA14, AN35, UA52 were analyzed for trace elements, including rare earth elements, by Inductively Coupled Plasma Mass Spectrometry (ICP-MS); methods and standards can be found at http://www.sees.wsu.edu/Geolab/note/icpms.html.

A.3. Radiogenic isotopes

UA81, UA43, Tn96, LBA64, LBA84, and LBA98 were analyzed for Pb, Nd and Sr isotopes at the *Vrije Universiteit*, Amsterdam, using ultra-clean dissolution in Teflon beakers and ion-exchange resin columns. Sr isotopes were measured using TIMS (Finnigan MAT 262) and Pb and Nd isotopes were measured using a Finnigan Neptune multi-collector ICP-MS. BHVO-2 and BCR-2 were used as internal check standards for trace and isotope analyses. The UP samples were analyzed for Sr, Nd and Pb isotopes at Northern Centre for Isotopic and Elemental Tracing, Durham University, United Kingdom. Isotope ratios in the fractions for Sr, Nd and Pb were measured using the ThermoElectron Neptune PIMMS (Plasma Ionisation Multi-collector Mass Spectrometer). Details of operating procedures and instrument configuration are given in McLeod (2012). Measured values for the NBS 987 Sr and J&M Nd standards ± 2SD error obtained during the same runs as the UP samples were 0.710269 ± 0.000028 ($n = 11$) and 0.511112 ± 0.000008 ($n = 15$), respectively. The NBS 981 Pb standard gave ratios averaging 16.94051 ± 0.000906 for $^{206}Pb/^{204}Pb$, 15.49800 ± 0.000754 for $^{207}Pb/^{204}Pb$ and 36.71744 ± 0.002327 for $^{208}Pb/^{204}Pb$.

References

Bambang, S., Le Bel, L.M., 1987. Discovery of a new tin province Long Laai area east, Kalimantan, Indonesia. In: Hutchison, C.S. (Ed.), Tin and Tungsten Granites Proceedings IGCP Project 220 Meeting, September, 1986. Technical Bulletin, 6. SEATRAD.

Banda, R.M., Aji, E., 2012. The geology and mineral resources of the Northern Usun Apau Area, Sarawak, Malaysia. Minerals and Geoscience, Department of Malaysia Map Report 21, 1–135.

Bergman, S.C., Dun, D.P., Krol, L.G., 1988. Rock and mineral of the Linhaisai Minette, Central Kalimantan, Indonesia, and the origin of Borneo Diamonds. Canadian Mineralogist 26, 23–43.

Bird, P.R., Quinton, M.N., Bee, M.N., Bristow, J., 1993. Mindoro: a rifted microcontinent in collision with the Philippines volcanic arc; basin evolution and hydrocarbon potential. Journal of Southeast Asian Earth Sciences 8, 449–468.

Burton-Johnson, A., Macpherson, C.J., 2012. Mt. Kinabalu Multi-phased Post-collisional I-Type Granite. Abstract American Geophysical Union Annual Meeting.

Camerlengo, A.L., Ambak, A.M., Saadon, M.N., 2000. Rainfall in Sarawak. Pertanika Journal of Science and Technology 8, 125–135.

Campbell, C.J., 1956. Geology of the Usun Apau Area. British Borneo Geological Survey, Annual Report. pp. 86–120.

Chiang, K.K., 2002. Geochemistry of the Cenozoic Igneous Rocks of Borneo and Tectonic Implications. Unpublished PhD Thesis. Royal Holloway University of London, pp. 364.

Clift, P., Lee, G.H., Nguyan, A.D., Barckhausen, U., Long, H., Zhen, S., 2008. Seismic reflection evidence for a dangerous grounds miniplate: no extrusion origin for the South China Sea. Tectonics 27, 1–16.

Cottam, M., Hall, R., Sperber, C., Armstrong, R., 2010. Pulsed emplacement of layered granite: new high-precision age data from Mount Kinabalu, North Borneo. Journal of the Geological Society of London 176, 49–60.

Cullen, A.B., 2010. Transverse segmentation of the Baram-Balabac Basin, Northwest Borneo: refining the model of Borneo's tectonic evolution. Petroleum Geoscience 16, 3–29.

Daly, M.C., Cooper, M.A., Wilson, I., Smith, D.G., Hooper, B.G., 1991. Cenozoic plate tectonics and basin evolution in Indonesia. Marine and Petroleum Geology 8, 2–21.

Darbyshire, D.P.F., Sewell, R.J., 1997. Nd and Sr isotope geochemistry of plutonic rocks from Hong Kong: implications for granite petrogenesis, regional structure and crustal evolution. Chemical Geology 143, 81–93.
Defant, M.J., Drummond, M.S., 1990. Derivation of some modern arc magmas by melting of young subducted lithosphere. Nature 347, 662–665.
DePaolo, D.J., 1981. Trace element and isotopic effects of combined wallrock assimilation and fractional crystallization. Earth and Planetary Science Letters 53, 189–202.
Elliott, T., 2003. Tracers of the slab. Geophysical Monograph 238, 23–45.
Green, D.H., Falloon, T.J., 2005. Primary magmas at mid-ocean ridges, ''hotspots'', and other intraplate settings: constraints on mantle potential temperature. Geological Society of America Special Paper 338, 32.
Hall, R., 1997. Cenozoic plate reconstructions of SE Asia. In: Hall, R., Blundell, D.J. (Eds.), Tectonic Evolution of Southeast Asia. Geological Society of London Special Publication 106, pp. 153–184.
Hall, R., 2002. Cenozoic geological and plate tectonic evolution of SE Asia and the SW Pacific: computer-based reconstructions, model and animations. Journal of Asian Earth Sciences 20, 353–431.
Hall, R., 2009. The Eurasian SE Asian margin as a modern example of an accretionary orogeny. In: Cawood, P.A., Kroner, A. (Eds.), Earth Accretionary Systems in Space and Time. Geological Society of London Special Publication 318, pp. 351–372.
Hall, R., Clements, B., Smyth, H.R., 2009. Sundaland basement character, structure and plate tectonic development. In: Proceedings Indonesian Petroleum Association, 33rd Annual Convention, IPA09-G-134, pp. 1–27.
Hamilton, W., 1979. Tectonics of the Indonesian region. United States Geological Survey Professional Paper 1078, 345.
Hart, S.R., 1984. A large-scale isotope anomaly in the Southern Hemisphere mantle. Nature 309, 753–757.
Hazenbroek, H.P., Morshidi, A.K., 2001. National Parks of Sarawak. Natural History Publications (Borneo), Kota Kinabalu, p. pp. 502.
Holloway, N.H., 1982. North Palawan Block, Philippines – its relation to Asian Mainland and role in the evolution of South China Sea. American Association of Petroleum Geologists Bulletin 66, 1355–1383.
Hutchison, C.S., 1996. The 'Rajang Accretionary Prism' and 'Lupar Line' problem of Borneo. In: Hall, R., Blundell, D.J. (Eds.), Tectonic Evolution of Southeast Asia. Geological Society of London Special Publication 106, pp. 247–261.
Hutchison, C.S., 2005. Geology of North-West Borneo. Elsevier, Amsterdam, Netherlands, pp. 421.
Hutchison, C.S., 2010. Oroclines and paleomagnetism in Borneo and South-East Asia. Tectonophysics 496, 53–67.
Hutchison, C.S., Bergman, S.C., Swauger, D., Graves, J.E., 2000. A Miocene collisional belt in north Borneo, uplift mechanism and isostatic adjustment quantified by thermochronology. Journal of the Geological Society of London 157, 783–793.
Jacobsen, S.B., Wasserburg, G., 1978. Interpretation of Nd, Sr and Pb isotope data from Archean migmatites in Lofoten-Vesterålen, Norway. Earth and Planetary Science Letters 41 (3), 245–253.
Johnson, D.M., Hooper, P.R., Conrey, R.M., 1999. XRF analysis of rocks and minerals for major and trace elements on a single low dilution Li-tetraborate fused bead. Advances in X-Ray Analysis 41, 843–867.
Kirk, H.J., 1957. The geology and mineral resources of the upper Rajang and adjacent areas. Geological Survey Department British Territories in Borneo, Memoir 8, 181.
Kirk, H.J., 1968. The igneous rocks of Sarawak and Sabah. Geological Survey of Borneo Region, Malaysia, Bulletin 5, 210.
Kudrass, H.R., Wiedicke, M., Cepek, P., Kreuzer, H., Muller, P., 1986. Mesozoic and Cainozoic rocks dredged from the South China Sea (Reed Bank area) and Sulu Sea and their significance for the plate-tectonic reconstructions. Marine and Petroleum Geology 3, 19–30.
Lan, C.Y., Chung, S.L., Long, T.C., Lo, C.H., Lee, T.Y., Mertzman, S.A., Shen, J.J., 2003. Geochemical Sr–Nd isotopic constraints from the Kontum Massif, central Vietnam, on the crustal evolution of the Indochina block. Precambrian Research 122, 7–27.
Le Bas, M.J., Streckeisen, A.L., 1991. The IUGS systematic of igneous rocks. Journal of the Geological Society London 148, 825–833.
Liew, T.C., McCulloch, M.T., 1985. Genesis of granitoid batholiths of Peninsular Malaysia and implications for models of crustal evolution: evidence from a Nd–Sr isotopic and U–Pb zircon study. Geochimica et Cosmochimica Acta 49, 587–600.
Longley, I.M., 1997. The tectonostratigraphic evolution of SE Asia. In: Murphy, R.W. (Ed.), Petroleum Geology of Southeast Asia. Geological Society of London Special Publication 126, pp. 311–339.
Macpherson, C.G., Chaing, K., Hall, R., Nowell, G.M., Castillo, P.R., Thirwall, M.F., 2010. Plio-Pleistocene intra-plate magmatism from the southern Sulu Arc, Semporna peninsula, Sabah, Borneo: implications for high-Nb basalt in subduction zones. Journal of Volcanology and Geothermal Research 190, 25–38.
McLeod, C.l., 2012. An investigation of Crustal Contamination through Petrology and Geochemistry. PhD Thesis, Durham University, UK.
Metcalfe, I., 2010. Tectonic framework and Phanerozoic evolution of Sundaland. Gondwana Research 19, 3–21.
Milsom, J., Holt, R., 2001. Discussion of a Miocene collisional belt in north Borneo, uplift mechanism and isostatic adjustment quantified by thermochronology. Journal of the Geological Society London 158, 396–400.
Morley, C.K., 2002. A tectonic model for the Tertiary evolution of strike-slip faults and rift basins in SE Asia. Tectonophysics 347, 189–215.
Pieters, P.E., Supriatna, S., 1990. Preliminary Geological Map of West, Central, and East Kalimantan Area. Indonesia Geological Development and Research Centre.
Prouteau, G., Maury, R.C., Sajona, F.G., Pubellier, M., Cotten, J., Bellon, H., 2001. Le magmatisme post-collisionnel du Nord-Ouest de Bornéo, produit de la fusion d'un fragment de croûte océanique ancré dans le manteau supérieur. Bulletin de la Société Géologique de France 172, 319–332.
Rangin, C., Spakman, W., Pubellier, M., Bijward, H., 1999. Tomographic and geologic constraints on subduction along the eastern Sundaland continental margin, South-East Asia. Bulletin de la Société Geologique de France 170, 755–788.
Rapp, R.P., Shimizu, N., Norman, M.D., Applegate, G.S., 1999. Reaction between slab-derived melts and peridotite in the mantle wedge: experimental constraints at 3.8 GPa. Chemical Geology 160, 335–356.
Renne, P.R., Swisher, C.C., Deino, A.L., Karner, D.B., Owens, T.L., DePaolo, D.J., 1998. Intercalibration of standards, absolute ages and uncertainties in $^{40}Ar/^{39}Ar$ dating. Chemical Geology 145, 117–152.
Satyana, A.H., Nugroho, D., Imanhardjo, S., 1999. Tectonic controls on the hydrocarbon habitats of the Barito, Kutei, and Tarakan Basins, Eastern Kalimantan, Indonesia: major dissimilarities in adjoining basins. Journal of Asian Earth Sciences 17, 99–122.
Soeria-Atmadja, R., Noeradi, D., Pridai, P., 1999. Cenozoic magmatism in Kalimantan and its related geodynamic evolution. Journal of Asian Earth Science 17, 25–45.
Staudacher, T.H., Jessberger, E.K., Dorflinger, D., Kiko, J., 1978. A refined ultrahigh-vacuum furnace for rare gas analysis. Journal Physics of Earth Science Instrumentation 11, 781–784.
Stern, R.J., 2002. Subduction zones. Reviews in Geophysics 40, 1–42.
Sun, S.S., McDonough, W.F., 1989. Chemical and isotopic systematics of oceanic basalts: implications for mantle composition and processes. In: Saunders, A.D., Norry, M.J. (Eds.), Magmatism in the Ocean Basins. Geological Society of London Special Publication 42, pp. 313–345.
Taib, N.I., 2010. K-rich basalt in the Bukit Mersing area, Third Division, Sarawak. Geological Society Malaysia Bulletin 52, 67–73.
Taib, N.I., 2012. Bimodal Cenozoic volcanism in Central Sarawak: hot spots or extension? Proceedings of GEOSEA 2012, 60.
Tate, R.B., 2001. Geological Map of Borneo Island. CD-ROM. Geological Society of Malaysia.
Taylor, B., Hayes, D.E., 1983. Origin and history of the South China Sea basin. In: Hayes, D.E. (Ed.),The Tectonic and Geologic Evolution of Southeast Asian Seas and Islands: Part 2, Geophysical. Monograph Series 27, AGU, Washington D. C, pp. 23– 56.
Tu, K., Flower, M.F.J., Carlson, R.W., Xie, G.H., Chen, C.Y., Zhang, M., 1992. Magmatism in the South China Basin, 1. Isotopic and trace element evidence for an endogenous Dupal mantle component. Chemical Geology 97, 47–63.
Van Bemmelen, R.W., 1949. The Geology of Indonesia, 1A, General Geology of Indonesia and Adjacent Archipelagoes. Government Printing Office, The Hague, 732 pp.
van Hattum, M., Hall, R., Pickard, A., Nichols, G., 2006. Southeast Asian sediments not from Asia: provenance and geochronology of north Borneo sandstones. Geology 34, 589–592.
van Leeuwen, T.M., Leach, T., Hawke, A.A., Hawke, M.M., 1990. The Kelian disseminated gold deposit, East Kalimantan, Indonesia: an example of a deeply eroded epithermal system. In: Hedenquist, J.W., White, N.C., Siddeley, G. (Eds.), Epithermal Gold Deposits of the Circum-Pacific: Geology, Geochemistry, Origin and Exploration, Journal Geochemical Exploration, vol. 35, pp. 1–61.
Weerd, A., Armim, R.A., 1992. Origin and Evolution of Tertiary Hydrocarbon-bearing Basins in Kalimantan (Borneo), Indonesia. American Association Petroleum Geologists Bulletin 77, 1778–1803.
Wendt, I., Carl, C., 1991. The statistical distribution of the mean squared weighted deviation. Chemical Geology 86, 275–285.
Wooden, J.P., Mueller, J.P., 1988. Pb, Sr, and Nd isotopic compositions of a suite of Late Archean, igneous rocks, eastern Beartooth Mountains: implications for crust-mantle evolution. Earth and Planetary Science Letters 87, 59–72.
Wu, H.H., Tsai, Y., Lee, T.Y., Lo, C.H., Hseih, C.H., Toan, D., 2005. 3-D shear wave velocity structure of the crust and upper mantle in South China Sea and its surrounding regions by surface wave dispersion analysis. Marine Geophysical Research 25, 5–27.
Yan, Q.S., Shi, X.F., Liu, J.H., Wang, K.S., Bu, W.R., 2010. Petrology and geochemistry of Mesozoic granitic rocks from the Nansha micro-block, the South China Sea: constraints on the basement nature. Journal of Asian Earth Sciences 37, 130–139.
Yan, Q., Shi, X., Li, N., 2011. Oxygen and lead isotope characteristics of granitic rocks from the Nansha block (South China Sea): implications for their petrogenesis and tectonic affinity. Island Arc 20, 150–159.
Yogodzinski, G.M., Kay, R.W., Volynets, O.N., Koloskov, A.V., Kay, S.M., 1995. Magnesian andesite in the western Aleutian Komandorsky region: implications for slab melting and processes in the mantle wedge. Geological Society of America Bulletin 107, 505–519.
Yumul, G.P., Dimalanta, C.B., Marquez, E.J., Queaño, K.L., 2009. Onland signatures of the Palawan microcontinental block and Philippine mobile belt collision and crustal growth process: a review. Journal of Asian Earth Sciences 34, 610–623.
Zou, H., Fan, Q., 2010. U–Th isotopes in Hainan basalts: implications for sub-asthenospheric origin of EM2 mantle end-member and the dynamics of melting beneath Hainan Island. Lithos 116, 145–152.